UCRL-50021-78

Laser Program
Annual Report-1978

Volume 3

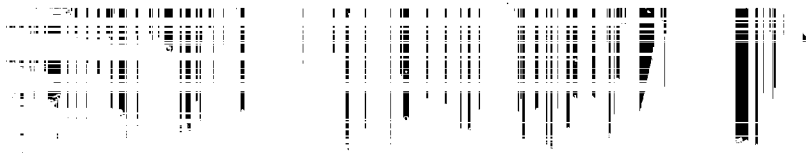

UCRL-50021-78
Distribution Category
UC-21,22

Laser Program
Annual Report – 1978
Volume 3

Scientific Editor: Michael J. Monsler
Publication Editor: Brian D. Jarman

MS date: March 1979

LAWRENCE LIVERMORE LABORATORY
University of California · Livermore, California · 94550

Available from : National Technical Information Serivce · U.S. Department of Commerce
5285 Port Royal Road · Springfield, VA 22161 · **$14.00** per copy · (Microfiche **$3.00**)

FOREWORD

This volume consists of Sections 8 through 10 of the 1978 Laser Program Annual Report. The remaining sections are published under separate cover in Volume 1 (Sections 1 through 4) and Volume 2 (Sections 5 through 7).

CONTENTS

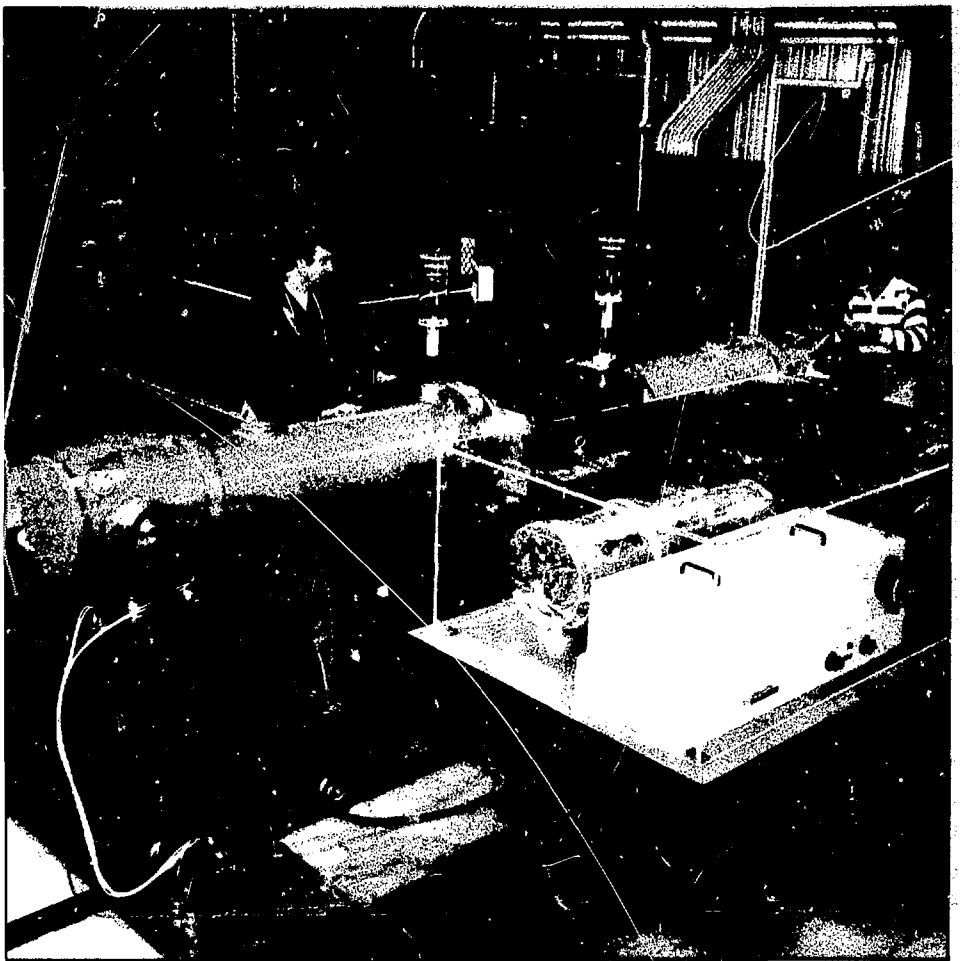

Section 8

Advanced Quantum Electronics

SECTION 8

CONTENTS

SECTION 8

ADVANCED QUANTUM ELECTRONICS

8.1 Introduction

The broad objectives of the LLL advanced-laser effort are to identify, demonstrate, and assess laser driver systems for use in laser-fusion power reactors. A further aspect of this effort is to participate, as required, in program activities directed toward demonstration of the effectiveness of selected advanced-laser systems for pellet implosions. To carry out assessments of candidate laser systems, we have assembled, over the past four years, an integrated capability to conduct experimental, theoretical, and computational studies spanning the relevant aspects of fusion laser systems, including atomic and molecular collision physics, quantum electronic processes, and device and systems technologies.

The technical performance requirements placed on candidate laser systems (energy, power, wavelength, etc.) were derived initially from computer simulations of pellet implosions. These requirements are continually being refined as we obtain additional experimental pellet-implosion data and improved computer simulations. On the basis of these sources of guidance, our advanced laser driver effort has focused throughout its history on laser systems operating at relatively short wavelengths (0.25 to 2 μm).

The programmatic and technical basis of our current effort stems from laser system studies conducted in 1977, in which we compared on a common basis the projected efficiencies and scalabilities of four short-wavelength laser systems: Group VI (Se), solid state hybrids (Tm), rare-earth molecular vapors (Tb), and pulse compressors (KrF/CH_4). On the basis of these studies we were able to conclude that:

- All four systems appear to be scalable to reactor size with efficiencies exceeding 1%.
- The technologies for scaling the four systems are moderately distinct. They are largely undeveloped at present, but they appear to be tractable.
- Of the candidate systems studied, driver laser systems based on the hybrid pulse compression concept (backward-wave Raman compression and angle-coded pulse stacking), using a KrF laser to pump a CH_4 Raman medium, offer the highest efficiency potential (4 to 6%), shortest operating wavelength (0.27 μm), and greatest richness in technological options for implementation.
- The other system candidates considered are inferior in efficiency because they use relatively inefficient optical pump sources. These, or similar candidate media, may be rendered more competitive if more efficient and scalable pump sources are found.

On the basis of this assessment, we directed our efforts in 1978 along two complementary paths: (1) the research, development, and further assessment of hybrid Raman pulse-compressor systems, and (2) a renewed search for new laser media and pumping techniques capable of yielding driver systems that operate with efficiencies in excess of 10%.

Our 1978 progress is reported as follows. In §8.2, we outline some results of laser theory and design analysis that help to provide technical perspective for our efforts. Subjects selected for review here include laser-beam propagation and focusing, an update on our computational capabilities for describing the kinetics of electrically excited laser media, models for Raman pulse compressors, and a treatment of injection locking and control of amplified spontaneous emission in high-gain media.

The central focus of our continuing assessment of pulse-compressor laser systems is the design, construction, and operation of an experimental laser-system test bed, RAPIER, phased over a four-year period. The experimental data, system model normalization, and operational systems experience gained in developing the RAPIER test bed are intended to provide a sound basis for design and construction of the larger, repetitively pulsed laser-system modules needed for reactor service.

Efforts associated with pulse compressor systems are described in §8.3. Topics selected for discussion include pulse-compressor system design, theoretical analysis of issues associated with the Raman scattering medium, analysis of the KrF-excimer pump medium and amplifier devices, and

progress in the design, construction, and testing of RAPIER hardware.

A major research activity conducted in the past few years has addressed the utility of Group VI atomic lasers for reactor driver applications. Significant experimental and analytical results on both sulfur and selenium storage lasers have been achieved in 1978. In §8.4, we describe the results of laser and kinetics experiments, the theoretical analysis of the important kinetic processes, and laser scaling analyses.

We recognize a continuing need to identify and investigate new advanced-laser concepts that might lead to fusion lasers higher in efficiency (>10%) and less complex and expensive than those projected for the baseline excimer pulse-compressor systems. The various candidate energy-storage systems studied to date at LLL (Tm^{3+} solid state, rare-earth vapors, Group VI) have been shown to be technically sound in terms of their microscopic properties; that is, they can store excitation energy for microsecond-long time scales at excited state densities in the range of 10^{16} to 10^{17} cm^{-3}. Their potential is limited rather by modest efficiencies of the excimer pumps that excite them and by the inefficiency of converting pump energy into short output pulses. In §8.5, we discuss progress made on new pump sources, the development of rare-gas-halogen discharge lasers, and the development of theoretical and computational models that will help us to better understand the important microscopic processes in electrically and optically excited active media.

Authors

W. F. Krupke
E. V. George
C. F. Bender

8.2 Laser Theory and Analysis

Our laser theory and analysis activity was formed to provide a capability to help identify new laser media, plan experiments, analyze experimental results quantitatively, assess the feasibility of laser driver systems for fusion reactors, and analyze and optimize laser systems. To provide a timely and in-depth quantitative evaluation of advanced laser concepts, several technical disciplines are brought together in this effort. laser theory, radiation propagation and transport, plasma physics of electrically excited media, chemical kinetics of excited media, gas dynamics and heat transfer, and laser-system analysis and optimization. As a consequence of this effort, we have developed and exercised several significant computational tools for analyzing advanced laser-driver concepts. The results of applying these tools are described throughout this section. In this subsection, the generic details of these analyses, as well as some representative sample calculations, are discussed. Several articles are included, dealing with laser beam propagation and focusing, laser media kinetics, Raman compressor analysis, and injection locking and gain control of large-aperture, high-gain laser media.

8.2.1 Propagation Issues for Solid Media

The laser performance requirements (pulse length, energy, and repetition rate) for inertial-confinement fusion reactor applications are well known.[1-3] Ideally, these performance characteristics should be easily variable, to accommodate changes in target design. In addition to these constraints, the fusion laser must also be relatively inexpensive. Experience to date indicates that such a laser requires a simple pump technology and must operate at a high energy density to minimize scale

Table 8-1. Characteristics of several potential storage lasers for laser fusion applications.

Laser medium	Wavelength, μm	Nominal lifetime (τ_L), μs	Saturation fluence (Γ_s), J/cm^2	Specific laser output ($\mathcal{E}_L$), J/liter	Excited-state density (n^*),[a] cm^{-3}
Iodine (gas)	1.3	10	0.5	10	6.8×10^{16}
Selenium (gas)	0.489	1	1	10	2.5×10^{16}
Nd^{3+}:glass (solid)	1.06	300	5	200	10^{18}
Tm^{3+}:YLF (solid)	0.451	67	3.6	240	5.4×10^{17}

[a]Upper laser level.

size. All of these additional features are most easily satisfied by a storage laser system.[2] The characteristics of several possible storage-laser systems are listed in Table 8-1. At present, all of these systems are relatively inefficient (<2%) because of inefficient pumping techniques. However, if efficient pumps could be found, these media would be ideal for fusion-laser applications.

From Table 8-1, it is interesting to note that solid state lasers have the highest energy density and longest energy-storage lifetimes. To date, these solid state lasers have operated at significantly higher energy densities (>10 times) and storage lifetimes (>10 times) than have corresponding gas lasers. Consequently, solid state amplifiers can be more compact; they can operate with a medium length typically more than an order of magnitude smaller than required by a gas laser of corresponding output. On the basis of considerations such as these and the analysis of media and conditioning for average-power lasers presented in last year's annual report, we have concluded that solid state laser systems should be considered as serious candidates for fusion applications in which repetition rates of 1 to 10 Hz are acceptable. In this subsection, we review some of the propagation issues for solid and gaseous laser media and compare them to establish their relative importance.

As noted in last year's annual report,[1] the Talanov moment theorems[4] can be employed to derive an approximate condition for laser beam focusability. Neglecting the usual small contribution from diffraction, this condition is given as

$$r_t > f_L \, \Delta\Theta_\perp \ , \tag{1}$$

where r_t is the target radius, f_L is the focal length of the final focusing optics, and $\Delta\Theta_\perp$ is the "averaged" angular divergence for the ray elements of the beam. The approximate constraint this condition imposes on refractive index fluctuations is

$$\frac{\Delta n}{n} < \left(\frac{r_t}{f_L}\right)\left(\frac{L_\perp}{L}\right) \tag{2}$$

for ordered disturbances and

$$\left[\left\langle\left(\frac{\Delta n}{n}\right)^2\right\rangle\right]^{1/2} < \left(\frac{r_t}{f_L}\right)\left(\frac{\ell}{L}\right)^{1/2} \tag{3}$$

for random disturbances. In Eqs. (2) and (3), the quantity L is the length of the laser medium traversed and Δn is the characteristic magnitude of the index fluctuation whose characteristic transverse-scale size is $L_\perp$. The random disturbances are assumed to have a Gaussian correlation function with scale size ℓ. Random fluctuations produce less distortion than do nonrandom, ordered refractive-index inhomogeneities of comparable scale size. In general, the density fluctuations generated in an average-power laser amplifier will not be fully ordered or random and will have properties specific to the scale size of the device. Therefore, conditions derived from Eqs. (1)-(3) are only useful in estimating the bounds that distortions can have and the approximate conditions that must be achieved to have adequate beam quality. For reactor-size targets, final focusing optical systems, and laser amplifier conditions, Eqs. (2) and (3) generally require[1,3] that refractive index fluctuations be less than 2×10^{-6} or at most 3×10^{-5}. As noted in Refs. 1 and 3, these focusability conditions are relatively insensitive to wavelength and depend only on the length of the laser medium and the transverse refractive index gradients.

In gaseous media, relative refractive index fluctuations $\Delta n/n$ are related to relative gas density fluctuations $\Delta\rho/\rho_0$ by the Gladstone–Dale constant β, namely,

$$\begin{aligned} \frac{\Delta n}{n} &\approx \beta\left(\frac{\rho_0}{\rho_s}\right)\left(\frac{\Delta\rho}{\rho_0}\right) \\ &\approx (4 \times 10^{-5} \text{ to } 4 \times 10^{-4})\,(1 \text{ to } 2)\,(10^{-4} \text{ to } 10^{-3}) \\ &\approx 4 \times 10^{-9} \text{ to } 8 \times 10^{-7} \ , \end{aligned} \tag{4}$$

where ρ_s is standard density and ρ_0 is the operating density of the laser. It is important to note that β is approximately an order of magnitude smaller in helium and neon compared to other gases and generally lies in the range 4×10^{-5} to 4×10^{-4}. In gaseous media, density disturbances are created by base flow turbulence and thermal inhomogeneities, thermal energy deposited in the laser medium during excitation, and shock waves from hot electrodes and e-beam foils. The technology for controlling these disturbances is well developed; for average-power gas lasers, values of $\Delta\rho/\rho_0$ in the 10^{-4} to 10^{-3} range have been achieved.[5,6] Thus for average-power gas lasers, index fluctuations will be in the

range 4×10^{-9} to 8×10^{-7}, which is acceptable for fusion reactor applications.[1-3]

In solid media, the index of refraction can be written as $n = n_0 + \gamma I$, where $n_0\gamma$ (cm^2/W) = $4.2 \times 10^{-3}\, n_2$ (esu) and I is the local laser light intensity. For typical, solid state optical materials, n_2 lies in the range of 3×10^{-14} to 10^{-13} esu. The nonlinear index variations will lie in the range

$$\frac{\Delta n}{n_0} \approx \frac{\gamma \Delta I}{n_0} \approx \frac{(8 \times 10^{-17} \text{ to } 3 \times 10^{-16}\ cm^2/W)}{1.5} \times (10^9 \text{ to } 10^{10}\ W/cm^2) \approx 5 \times 10^{-8} \text{ to } 2 \times 10^{-6} \quad . \tag{5}$$

These fluctuations are comparable to those in a gas amplifier. However, because nonlinear refractive index fluctuations depend on intensity, it has been found that they lead to a self-focusing instability[7] which develops from intensity modulations on the beam, created by noise sources (switches, dust, etc.). Experimental and theoretical studies associated with Nd:glass lasers show that beam degradation from self-focusing can be controlled by proper choice of host materials[8] and by using optical-relay spatial filtering techniques.[9]

Nonuniform temperature T and mechanical and thermally induced stress distributions σ_{ij} in a solid medium can produce variations in the medium's length L and linear refractive index n_0.[10] In addition, stress-induced birefringence[11] can occur if nonuniform stress distributions are created. If mechanical and thermally induced stresses are not important, then refractive index fluctuations are approximated by

$$\frac{\Delta n}{n_0} \approx \left[\frac{1}{n_0}\left(\frac{\partial n_0}{\partial T}\right)_{\sigma=0} + \frac{1}{L}\left(\frac{\partial L}{\partial T}\right)\right] \Delta T \quad . \tag{6}$$

For most solid media, $(\partial n_0/\partial T)/n_0$ and $(\partial L/\partial T)/L$ have values in the range 10^{-6} to 10^{-5}/°C. If solid temperature variations can be controlled to within 1°C, then these index fluctuations would be

$$\frac{\Delta n}{n_0} \approx (10^{-6} \text{ to } 10^{-5}\ °C^{-1})\,(1°C) \approx 10^{-6} \text{ to } 10^{-5} \quad . \tag{7}$$

These fluctuations are larger than those for gaseous media. However, because solid media may be 10 to 100 times shorter in length, the target focusability condition would be comparable. Usually, the physical properties of solid media are such that $\partial n_0/\partial T < 0$ and $\partial L/\partial T > 0$. Consequently, for average power applications, the possibility exists that solid media may be developed for which the thermal and strain contributions, Eq. (6), effectively cancel. The phosphate glass host LHG-7 is an example of this type of medium.

When mechanical and thermally induced stresses are present in solid state media, the media become birefringent.[11] The direction of polarization of the laser radiation may then rotate as the radiation propagates through each disk of a solid state amplifier. Because the disks are inclined at Brewster's angle, two disks in series act as a polarizer/analyzer combination. The second or analyzer disk in the series may then reject a significant fraction of the depolarized laser light. This relative intensity loss for an isotropic solid medium, which is caused by depolarization produced by stress-induced birefringence, is approximately[11]

$$\left(\frac{\delta I}{I}\right)_{\text{loss}} \approx \sin^2 2\theta \, \sin^2\left(\frac{\delta\phi}{2}\right) , \tag{8}$$

where θ is chosen as the angle between the initial laser beam polarization and the y stress axis. For a beam propagating along the z axis, the difference in phase shift for the laser beam's electric field components oriented along the x and y axes is

$$\delta\phi \approx \frac{\pi L}{\lambda}\,(q_{11} - q_{12})\, n_0^3\, (\sigma_{xx} - \sigma_{yy}) = kL\Delta B \Delta\sigma \quad . \tag{9}$$

The stress components along the x and y axes are σ_{xx} and σ_{yy}, respectively. The quantity $\Delta\sigma$ is simply the difference $\sigma_{xx} - \sigma_{yy}$. The quantities q_{11} and q_{12} are the stress optic coefficients of the solid medium. For ED-2 glass,[12] $\Delta B \approx 2$ nm·cm/kg, and then

$$\frac{\delta\phi}{\pi} \approx 3 \times 10^{-4}\ \frac{L(\text{cm})\ \Delta\sigma\ (\text{psi})}{\lambda(\mu\text{m})} \quad . \tag{10}$$

Because large-scale amplifier disks may have an L value of about 10 cm, induced stress fields with

$\Delta\sigma \approx$ 100-1000 psi will produce significant depolarization losses if the laser wavelength λ is in the visible or near-infrared regime. The control of stress-induced birefringence is an important problem for average-power solid state laser systems. It will require development of well-designed mounting and cooling systems for the amplifier disks. Materials may also be developed for which ΔB is minimized by minimizing the refractive index n_0, or the stress optic coefficient difference $q_{11} - q_{12}$, or both. For example, the fluorophosphate glass E-181 has a ΔB value of 0.7 nm·cm/kg.[12]

In summary, we note that solid state lasers can offer the possibility of high energy density and long storage lifetime. To date, solid state storage lasers have operated at higher energy densities (> 10 times) and storage lifetimes (> 10 times) than have corresponding gas storage lasers. When account is taken of the relative scale sizes of solid and gas amplifiers, linear phase distortions for average-power solid and gas amplifiers are comparable. The critical issue for solid state lasers is the simultaneous minimization of two propagation effects: (1) nonlinear self-focusing[7,8] and (2) birefringence[11] caused by thermally induced stress. At present, there does not appear to be a fundamental reason that forbids average-power solid state lasers from operating in the 1-to-10-Hz regime. Clearly, however, a significant amount of innovation will be required to make solid state systems a viable technological option.

References

1. *Laser Program Annual Report—1977*, Lawrence Livermore Laboratory, Livermore, Calif., UCRL-50021-77, §7 (1978).
2. W. F. Krupke and E. V. George, *Opt. Eng.* **17**, 238 (1978).
3. W. F. Krupke, E. V. George, and R. A. Haas, "Advanced Lasers for Fusion," in *Laser Handbook Vol. III* (to be published).
4. S. N. Vlasov, V. A. Petrishchev, and V. I. Talanov, *Izv. VUZ Radiofiz.* **14**, 1353 (1971).
5. R. M. Feinberg, R. S. Lowder, and O. L. Zappa, *Low Pressure Loss Cavity for Repetitively Pulsed Electric Discharge Lasers*, Air Force Weapons Laboratory, Kirtland AFB, N. Mex., AFWL-TR-75-99 (1975).
6. D. R. Aushermann, I. E. Alker, and E. Baum, "Acoustic Suppression in Pulsed Chemical Lasers," AIAA Paper No. 78-237, presented at the *AIAA 16th Aerospace Sciences Meeting, Huntsville, Ala., Jan. 1978.*
7. J. A. Fleck, J. R. Morris, and E. S. Bliss, *IEEE J. Quant. Electron.* **QE-14**, 353 (1978).
8. M. J. Weber, D. Milam, and W. L. Smith, *Opt. Eng.* 17, 463 (1978).
9. J. T. Hunt, P. A. Renard, and W. W. Simmons, *Appl. Opt.* **16**, 779 (1977).
10. F. W. Quelle, *Appl. Opt.* **5**, 633 (1966).
11. M. Born and E. Wolf, *Principles of Optics* (Pergamon Press, New York, 1970).
12. S. E. Stokowski, R. A. Saroyan, and M. J. Weber, *Nd-Doped Laser Glass Spectroscopic and Physical Properties*, Lawrence Livermore Laboratory, Livermore, Calif., M-095 (1978).

Author

R. A. Haas

8.2.2 Laser Media Kinetics

During our analysis of excimer and Group VI laser media, we have developed several kinetics codes applicable to electrical excitation of media and photon pumping of optically thick media, respectively. In this section, we describe these codes in more detail.

Boltzmann-Rate-Equation Analysis of Electrically Excited Media Kinetics. The computational model that we use to study electrically excited laser media was described briefly in the 1977 annual report. In this subsection, we update that discussion and present some illustrative results.

The computer code based on this computational model includes a Boltzmann analysis of the electron kinetics and a time-dependent rate equation solution for the heavy particle kinetics. The Boltzmann analysis calculation is coupled as a subroutine to a time-dependent chemical kinetics code, so that the electron-impact rate coefficients can be recomputed as time progresses, to reflect changes in excited-state densities and electron density. The transient kinetics code used in this study is based upon the stiff differential equation solver of Gear[13] and has input in the form of symbolic chemical reactions with rate coefficients in Arrhenius form. Using this code, we can treat time-varying beam current and discharge electric field even into the afterglow regime.

The Boltzmann equation is solved numerically for the electron energy distribution function, using the techniques described in Refs. 14 to 16. The electron impact processes included in this solution are momentum transfer, inelastic and superelastic collisions, ionization, attachment, recombination, electron–electron collisions, and the effects of an external e-beam source. The e-beam source function is computed by slowing down a high-energy electron from some energy $\mathcal{E}_p^{max}$ to a low energy $\mathcal{E}_p^{min}$, using the discrete slowing-down technique.[17–19] This calculation then gives a secondary electron spectrum $f_s(\mathcal{E})$ (electrons/eV) for low-energy electrons

in the energy range $(0, \mathcal{E}_p^{min})$. The distribution f_s is normalized to unity. For $Ar/Kr/F_2$ mixtures, $\mathcal{E}_p^{min}$ is chosen to be the ionization potential of argon. If the electron beam's volumetric power deposition is P_{eb} (kW/cm^3), then the source function $Q(\mathcal{E})$ (electrons/eV·cm^3·s) required in the Boltzmann equation is

$$Q(\mathcal{E}) = P_{eb}\, f_s(\mathcal{E})/U_i \ , \qquad (11)$$

where U_i is the energy loss per electron-ion pair created during the slowing down of each primary electron. The electron slowing-down calculation makes extensive use of the analytic formulas for differential ionization cross sections developed by Green and co-workers.[20,21]

A summary of the electron-impact cross-sectional data currently used to study KrF laser media is shown in Table 8-2. Detailed calculations of electron-beam-pumped KrF amplifier performance have been carried out using this kinetics code, and some results relevant to pulse compressor systems applications are presented in §8.2.3. We have also examined the effect that an applied auxiliary electric field has on KrF laser performance. Figures 8-1 and 8-2 show some typical results from this study. Figure 8-1 shows the difference in electron energy flow for pure e-beam (E/N = 0) and discharge-augmented e-beam excitation. The details of such a plot are model-dependent. The relative importances of ionization, attachment, dissociation, elastic loss, and electronic excitation processes are shown in this figure. As the electric field strength is increased, the fractional electron power transfer into the rare-gas metastable states increases. Because production of these states results in a smaller electron energy loss than does the production of ionic species, which dominates in pure e-beam excitation, the KrF production efficiency increases as illustrated in Fig. 8-2. The ratio of small-signal gain to loss, g_0/γ, also increases (Fig. 8-2) because of increased gain, primarily from enhanced power deposition. At high values of E/N, an instability is observed that has the characteristics of the multistep ionization instability first studied by Daugherty, Mangano, and Jacob.[38] Discharge instability is expected to limit scalability of these devices.[38,39]

Table 8-2. Electron kinetic processes included in model of electrically excited $Ar/Kr/F_2$ medium.

Electron impact process	References	Remarks
1. Momentum transfer—Ar	22	
2. $Ar \rightarrow Ar(^3P_0 + {}^3P_2)$	23, 24	Ar*
3. $Ar \rightarrow Ar(^3P_1)$		
4. $Ar \rightarrow Ar(^1P_1)$		
5. $Ar \rightarrow Ar(4p)$	23, 24	Ar**
6. $Ar \rightarrow Ar^+$	25	
7. $Ar^* \rightarrow Ar^{**}$	26	K(4s → 4p) cross section
8. $Ar^* \rightarrow Ar^+$	27	
9. $Ar^{**} \rightarrow Ar^+$		Scaling of cross section[27]
10. Momentum transfer—Kr	22	
11. $Kr \rightarrow Kr^*$	23	Total excitation cross section including Kr(5p)
12. $Kr \rightarrow Kr^+$	25	
13. $Kr^* \rightarrow Kr^{**}$	28	Rb(5s → 5p) cross section
14. $Kr^* \rightarrow Kr^+$	27	
15. $Kr^{**} \rightarrow Kr^+$		Scaling of cross section[35]
16. Momentum transfer—F_2	29	Resonance not included[30]
17. F_2 vibrational excitation	31	
18. $F_2 \rightarrow F + F^-$	32	
19. $F_2(x) \rightarrow F_2(^3\Pi_u) \rightarrow 2F$	34	
20. $F_2(x) \rightarrow F_2(^1\Pi_u) \rightarrow 2F$		
21. $F_2(x) \rightarrow F_2^{**} \rightarrow 2F$	33	

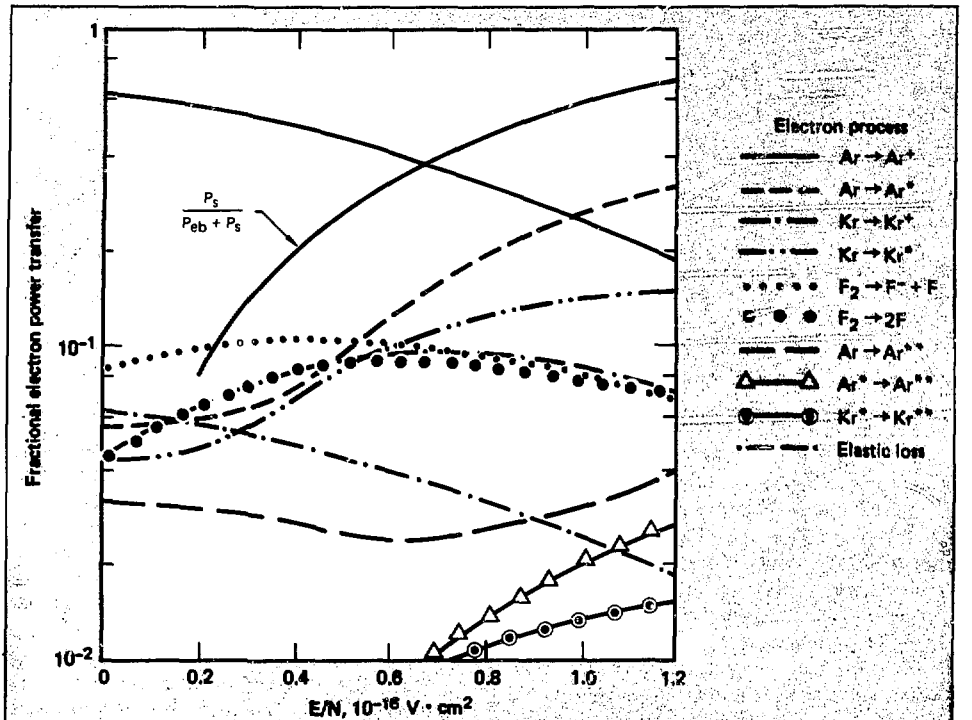

Fig. 8-1. The net self-consistent fractional electron power transfer in an electrically excited KrF laser mixture (Ar/Kr/F_2 = 0.945/0.05/0.005) at a pressure of 1 atm. The volumetric e-beam power deposition was held constant at P_{eb} = 30 kW/cm^3 as E/N was varied.

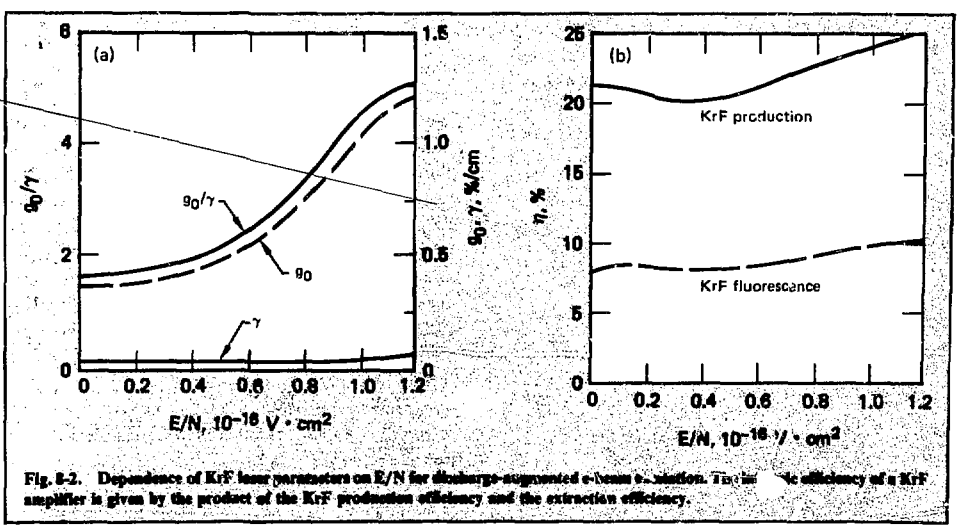

Fig. 8-2. Dependence of KrF laser parameters on E/N for discharge-augmented e-beam excitation. The [illegible] efficiency of a KrF amplifier is given by the product of the KrF production efficiency and the extraction efficiency.

Bleaching-Wave Kinetics Analysis of Photolytically Pumped Media. Photolytically pumped Group VI lasers[40] are excited by photodissociation of a parent molecule, thereby producing the ^1S state of the Group VI atom such as O, S, or Se. For large-scale amplifier systems, the parent medium is optically thick, initially, to the pump radiation. Generally, the pump absorption length is less than a centimeter. Under these circumstances, excitation proceeds by propagating a photodissociation or bleaching wave through the medium[41,42] (§8.3). For fluorescence pumping,[42] this bleaching wave typically propagates at a speed of approximately 1 $m/\mu s$; therefore, excitation of large volumes takes a significant fraction of a microsecond. Recent experiments (§8.3.1) indicate that, after passage of the bleaching or excitation wave front, photoionization of ^1S states by pump radiation produces free electrons. These electrons exercise several kinetic channels, which ultimately shorten ^1S lifetimes to values less than or comparable to a microsecond. Consequently, as discussed in detail in §8.3, the understanding and control of these processes are of fundamental importance for fusion applications of Group VI laser media.

To provide a computational means for studying kinetic processes in Group VI experiments and their impact on large-scale laser devices, a special kinetics code was developed. The code treats the spatial and temporal characteristics of bleaching or photodissociation wave excitation. In this computational model, the pump radiation transport and absorbing molecule continuity equations are solved analytically. Pump radiation photoionization losses are generally small and are neglected in this calculation. The resulting solutions for the pump intensity, absorber density, and production rate of ^1S states by photodissociation are

$$I_p(z, t) = I_{p0}(t - z/c) \times \frac{1}{A_1} \times \frac{1}{A_2} , \tag{12}$$

where

$$A_1 = 1 - \exp\left[\frac{\sigma_a}{h\nu_p} \int_0^{t-z/c} I_{p0}(t')\, dt'\right] ,$$

$$A_2 = 1 - \exp(-\sigma_a n_{a0} z) ,$$

$$n_a(z, t) = n_{a0} \times \frac{1}{A_3} \times \frac{1}{A_4} , \tag{13}$$

where

$$A_3 = 1 + \exp(-\sigma_a n_{a0} z) ,$$

$$A_4 = \exp\left[\frac{\sigma_a}{h\nu_p} \int_0^{t-z/c} I_{p0}(t')\, dt'\right] - 1 ,$$

$$S^*(z, t) = \frac{\sigma_a}{h\nu_p} I_p(z, t)\, n_a(z, t) , \tag{14}$$

respectively, where the initial absorber density n_{a0} is assumed to be uniform. The photodissociation cross section is σ_a and the pump photon energy is $h\nu_p$. These solutions are then used as source terms in the appropriate local continuity and energy equations for the medium during the bleaching-wave excitation process. These kinetic equations, which include all collisional processes of interest (e.g., see Table 8-2), are then integrated simultaneously in time from appropriate initial conditions that hold at the beginning of the excitation process for each spatial position along the path of the pump-driven bleaching wave. This computational procedure is very fast and, to a good approximation, models accurately the circumstances of interest in Group VI fusion-laser media and experiments. Typical bleaching-wave solutions, using a simplified kinetic model for the Se atom laser, are shown for illustration purposes in Fig. 8-3. The results show the spatial distribution of kinetic densities and electron temperature T_e at a time 200 ns after initiation of photolysis. In these examples, the initial OCSe density was 2×10^{15} cm^{-3} (0.6 Torr) and the Xe_2^* excimer pump's input intensity was held constant at 1.5 MW/cm^2. The kinetic model employed in these calculations is similar to that described in §8.3.3 but does not include gas heating and CO vibration kinetics processes. Figure 8-3(a) shows for this simple model that, without CO addition, electron superelastic heating and multiplication by ionization processes produce electron densities sufficient to rapidly quench the Se(^1S) state. As shown in this figure, the rapid temporal and spatial decay of the Se(^1S) population, following the passage of the bleaching wave, leads to a highly nonuniform

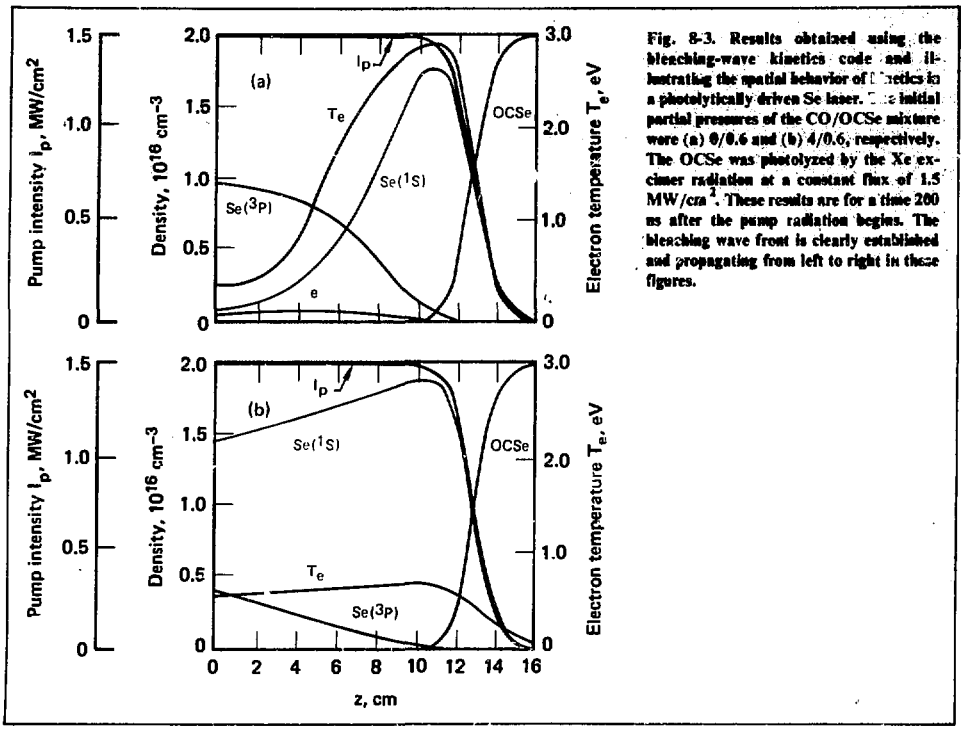

Fig. 8-3. Results obtained using the bleaching-wave kinetics code and illustrating the spatial behavior of kinetics in a photolytically driven Se laser. The initial partial pressures of the CO/OCSe mixture were (a) 0/0.6 and (b) 4/0.6, respectively. The OCSe was photolyzed by the Xe excimer radiation at a constant flux of 1.5 MW/cm^2. These results are for a time 200 ns after the pump radiation begins. The bleaching wave front is clearly established and propagating from left to right in these figures.

transverse gain profile, which reduces device efficiency as well as complicating the laser-beam extraction scenario. Figure 8-3(b) shows the effect of adding 4 Torr of CO to the 0.6-Torr of OCSe. The Se(^{1}S) lifetime is clearly increased, thereby increasing efficiency and reducing gain profile nonuniformity. The results presented in Fig. 8-3 are intended to illustrate the computational capabilities of the bleaching-wave kinetics code described in this section. For a more detailed, accurate, and complete treatment of the kinetics of these media, consult §8.3.3.

References

13. C. W. Gear, *Numerical Initial Value Problems in Ordinary Differential Equations* (Prentice-Hall, Englewood Cliffs, N.J., 1971).
14. W. L. Morgan, Joint Institute for Laboratory Astrophysics Information Center Report No. 18, in press.
15. S. D. Rockwood, *Phys. Rev. A* **8**, 2348 (1973).
16. C. J. Elliot and A. E. Greene, *J. Appl. Phys.* **47**, 2946 (1976).
17. L. R. Peterson, *Phys. Rev.* **187**, 105 (1969).
18. R. H. Garvey and A. E. S. Green, *Phys. Rev. A* **14**, 946 (1976).
19. W. L. Morgan, *A Study of the Plasma Chemistry of the Argon Oxide Laser*, Wayne State University, Detroit, Mich., RIES Report 75-109 (1975).
20. A. E. S. Green and T. Sawada, *J. Atmos. Terr. Phys.* **34**, 1719 (1972).
21. L. R. Peterson and J. E. Allen, *J. Chem. Phys.* **12**, 6068 (1972).
22. L. S. Frost and A. V. Phelps, *Phys. Rev.* **136**, A1538 (1964).
23. M. Schaper and H. Scheibner, *Beit. Plasma Phys.* **9**, 45 (1969).
24. E. Eggarter, *J. Chem. Phys.* **62**, 833 (1975).
25. D. Rapp and P. Englander-Golden, *J. Chem. Phys.* **43**, 1464 (1965).
26. I. P. Zapesochnyi, E. N. Postoi, and I. S. Aleksakhin, *Sov. Phys. JETP* **41**, 865 (1976).
27. D. Ton-That and M. R. Flannery, *Phys. Rev. A* **15**, 517 (1977).
28. J. H. Jacob and J. A. Mangano, *Appl. Phys. Lett.* **28**, 724 (1976).
29. T. N. Rescigno, C. F. Bender, C. W. McCurdy, and V. McKoy, *J. Phys. B* **9**, 2141 (1976).
30. T. N. Rescigno, Lawrence Livermore Laboratory, Livermore, Calif., private communication, 1978.
31. P. J. Chantry, *Attachment Measurements in Halogen Bearing Molecules*, Westinghouse R&D Center, final technical report 78-9C6-ATACH-R1 (1978).
32. R. J. Hall, *J. Chem. Phys.* **68**, 1803 (1978).
33. T. N. Rescigno, C. F. Bender, and V. McKoy, *Chem. Phys. Lett.* **45**, 307 (1977).

34. The $F_2(1\,^1\Sigma_g^+ \rightarrow {}^1\pi_u)$ and $F_2(1\,^1\Sigma_g^+ {}^3\pi_u)$ cross sections used in this study are based on the calculations of T. N. Rescigno and Fliflet (Lawrence Livermore Laboratory, Livermore, Calif., private communication). These computed cross sections, parameterized using the analytic expression of Green and Barth,[35] have been varied in Boltzmann and electron-stopping calculations to fit the F_2 dissociation data of Chen et al.[36] and Wilson et al.[37]
35. A. E. S. Green and C. A. Barth, *J. Geophys. Res.* **70**, 1083 (1965).
36. H. L. Chen, R. E. Center, D. W. Trainor, and W. I. Fyfe, *J. Appl. Phys.* **48**, 2297 (1977).
37. J. Wilson, H. L. Chen, W. Fyfe, and R. L. Taylor, *J. Appl. Phys.* **44**, 5447 (1973).
38. J. D. Daugherty, J. A. Mangano, and J. H. Jacob, *Appl. Phys. Lett.* **28**, 581 (1976).
39. R. T. Brown and W. L. Nighan, *Appl. Phys. Lett.* **32**, 730 (1978).
40. J. R. Murray and C. K. Rhodes, *J. Appl. Phys.* **47**, 5041 (1976).
41. V. E. Khartsiev, *Sov. Phys. JETP* **27**, 464 (1968).
42. *Laser Program Annual Report—1977*, Lawrence Livermore Laboratory, Livermore, Calif., UCRL-50021-77, §7.3.4 (1978).

Authors

R. A. Haas
W. L. Morgan
J. Harvey
R. D. Franklin

8.2.3 Raman Compressor Analysis

During our analysis of Raman-pulse-compressor laser systems, we have developed several computational models and computer codes that describe the dynamics of the Raman compression process and the performance characteristics of complete pulse-compressor systems. The results of our studies using these codes are described in Ref. 43 and §8.2.1 through 8.2.3 of this report. In this subsection (§8.2.3), we discuss the computational models and computer codes developed to treat Raman-compressor-cell dynamics and system performance. A brief discussion of the analysis of the effects of spatial and temporal inhomogeneities is also included.

Dynamics. Analytical studies[43,44] of Raman compressor dynamics, (§8.1 and 8.2) indicate that forward Stokes and backward second-Stokes parasitic waves (generated from spontaneous scattering of the pump and backward Stokes waves, respectively) can seriously limit the conversion efficiency and compression ratio of a Raman compressor. To model these processes in more detail, we have developed a one-dimensional, four-wave electromagnetics code that simulates the self-consistent dynamics of the electric field amplitudes of the pump (E_p), forward Stokes (E_S^f), backward Stokes (E_S^b), and backward second-Stokes (E_{2S}^b) waves. The corresponding molecular excitation waves Q_1, Q_2, Q_3, and Q_4 are also treated, including transient effects. If we define the differential operators

$$D_a^{f,b} = \partial/\partial z \pm \partial/\partial(ct) \tag{15}$$

and the Manley–Rowe factors or frequency ratios

$$M_{a,b} = (\nu_p/\nu_S, \nu_S/\nu_{2S}) , \tag{16}$$

then the field equations derived[44,45] from appropriate Maxwell equations are

$$D_p^f E_p = -\frac{1}{2}\gamma M_a \left(RQ_1 E_S^f + Q_3 E_S^b\right) , \tag{17}$$

$$D_S^f E_S^f = \frac{1}{2}\gamma \left(RQ_1^* E_p - M_b Q_4 E_{2S}^b\right) , \tag{18}$$

$$D_S^b E_S^b = -\frac{1}{2}\gamma \left(Q_3^* E_p - RM_b Q_2 E_{2S}^b\right) , \tag{19}$$

$$D_{2S}^b E_{2S}^b = -\frac{1}{2}\gamma \left(Q_4^* E_S^f + Q_2^* E_S^b\right) , \tag{20}$$

where γ is the backward gain coefficient and R is the ratio of the forward to backward gain coefficients. The molecular excitation is a set of four mutually incoherent quadrupole waves,

$$(Q_1, Q_2, Q_3, Q_4) = \Gamma \int_{-\infty}^{t} dt' e^{-\Gamma(t-t')} \times \left(E_p E_S^{f*}, E_S^b E_{2S}^{b*}, E_p E_S^{b*}, E_S^f E_{2S}^{b*}\right) , \tag{21}$$

where Γ is the transition line width. The electric field and molecular quantities contain both phase and amplitude information and are generally complex. The superscript * denotes a complex conjugate quantity. Equations (15) to (21) have been solved numerically.

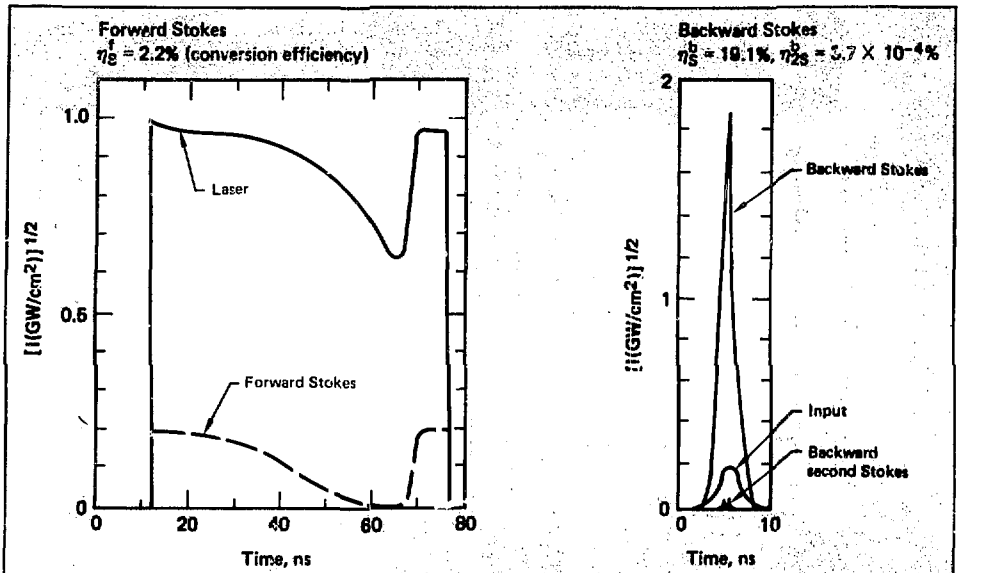

Fig. 8-4. Raman compressor simulation calculations made with four-wave electromagnetics code, showing that forward Stokes buildup depletes the pump laser pulse. Backward Stokes input pulse was Gaussian in shape; pump pulse was rectangular. The Raman cell parameters were: compression ratio K = 15, forward/backward gain ratio R = 4, and backward Stokes small-signal gain $\gamma^b I_1 L$ = 8.

The results of two calculations performed with this four-wave electromagnetics code are shown in Figs. 8-4 and 8-5. The conversion efficiencies into the various wave channels are shown in each figure. In Fig. 8-4, the intensity of the input backward Stokes pulse is such that very little second-Stokes radiation is generated as the backward Stokes pulse is amplified. The conversion efficiency into the backward Stokes pulse agrees very well with an estimate obtained using an extension of the Frantz–Nodvik theory.[44–46] In Fig. 8-5, the backward Stokes input intensity was increased from that in Fig. 8-4, and one can see that a significant amount of second-Stokes radiation was generated. According to the code, this process has a very rapid onset, and the threshold agrees quite well with predictions based on our Frantz–Nodvik analysis[44–46] when transient effects are not important. When transient effects become important (i.e., for $\gtrsim$1-ns pulse lengths for the KrF–CH_4 system), the Frantz–Nodvik theory becomes inaccurate.

Although the four-wave electromagnetics code is very useful in detailing the parasitics problem and validating simpler analytic treatments, it is quite slow. Therefore, we replaced it with a faster, two-wave code that is used to generate design analysis data for the Raman cell. This two-wave code has been used to study both standard and nonstandard geometries, such as the conical amplifier (§8.3.1) in which the field intensity is maintained at a nearly constant value to minimize second-Stokes generation. The results from the conical amplifier studies indicate that such a geometry offers only a slight improvement in performance when compared with conventional constant-area devices. Also, we have used the two-wave code to study several multipass configurations, to study pulse shape effects, and to model experiments. In addition to the two-wave code, another code has been developed to treat stochastic processes involving the pump and Stokes waves.

Systems Analysis. For systems analysis, several compressor–stacker design codes have been developed specifically for use in systems where the pump is a single pulse or a repetitively pulsed laser with nonsaturating loss.

The code for the single-pulse pump laser treats all sections of the system, except the oscillators, and ignores mirror losses. It computes Raman parasitic gains and the overall energy conversion efficiency

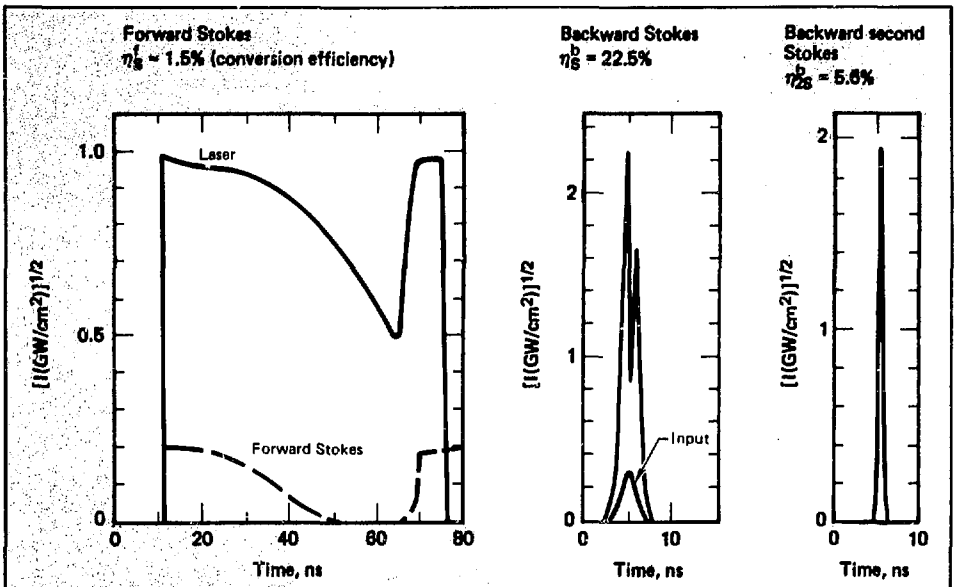

Fig. 8-5. Raman compressor simulation calculations made with four-wave electromagnetics code, showing that backward second-Stokes buildup depletes the backward Stokes pulse at high intensities. The pump pulse was rectangular; the backward Stokes input pulse was Gaussian. The Raman cell parameters were: compression ratio K = 15, forward/backward gain ratio R = 4, and backward Stokes small-signal gain $\gamma^b I_L L$ = 5.

from the pump laser pulse to the backward Stokes pulse. The Raman cell is treated with the Frantz–Nodvik theory, and the parasitics are evaluated perturbatively. The KrF laser is treated using the Schulz–Dubois[47] theory for homogeneously broadened cw lasers with distributed nonsaturable loss. The code is constructed in a modular fashion where mutually compatible macros or laser components may be arranged in various orders. Thus, the code is capable of simulating the flow of optical energy in widely differing system configurations.

The repetitively excited pump laser code treats system architectures in which the pump may be repetitively pulsed, and multipass extraction is employed in the Raman cell. Mirror losses and focusing of the pump radiation are included.

These codes have helped us realize that focusing of the KrF pump radiation is required if near-optimal system efficiency is to be attained. Another result pointed up by the codes is that the optical damage limits have a critical influence on the system efficiency. The pump fluence is equal to the product of the gain and the saturation fluence, so, for fixed gain, the required pump fluence must increase as the pressure decreases. Because the pump fluence must be less than the damage fluence, the pressure is required to exceed a certain value, calculated to be a few atmospheres. Figure 8-6 shows a typical output for a stacker-compressor-compressor configuration in which the pump is focused by a telescope whose two lenses sandwich the Raman cell window. Thus, the pump fluence experienced by the Stokes wave is three times as large as that seen by the cell windows. Each Raman cell is double-passed to avoid the use of preamplifiers, but the inputs (of the order of kW/cm^2 intensity) are assumed given. This system compresses a 400-ns KrF laser pulse to a 5-ns pulse at the second Stokes frequency, with a gain exponent of 13.3R at the second Stokes in the first compressor and 16.1R for the third Stokes in the second compressor, where R is the ratio of forward to backward gain. Over 25% of the energy available in the KrF preamplifier and amplifier is extracted as focusable energy.

In conclusion, we have developed a complete set of one-dimensional compressor system codes to

```
    KRF AMPLIFIER
ALPHA/GAMMA          5.0000
GAMMA*LENGTH         1.1000
PULSE LENGTH       400.       NSEC
AVAILABLE FLUENCE 1.408000J/CM**2
INPUT FLUENCE     0.003679J/CM**2
OUTPUT FLUENCE    0.143534J/CM**2
EFFICIENCY        0.0993
    KRF AMPLIFIER
ALPHA/GAMMA         20.0000
GAMMA*LENGTH         1.1000
PULSE LENGTH       400.       NSEC
AVAILABLE FLUENCE 5.632000J/CM**2
INPUT FLUENCE     0.143534J/CM**2
OUTPUT FLUENCE    2.934751J/CM**2
EFFICIENCY        0.4956

STACKING /FOCUSSING NUMBERS.... 5. / 3.00
```

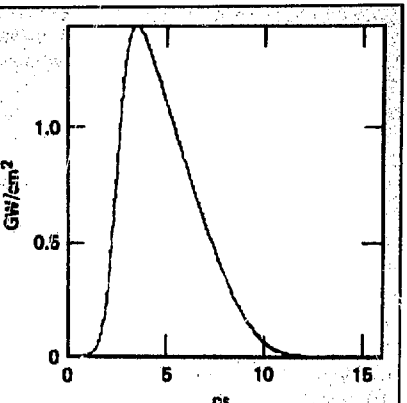


```
    RAMAN CELL                          RAMAN CELL
PUMP FLUENCE        8.804254J/CM**2   PUMP FLUENCE        7.124374J/CM**2
GAMMA*C (=2/SATFLUX) 2.2000  CM**2/JOULE GAMMA*C (=2/SATFLUX) 3.2000  CM**2/JOULE
GAIN EXPONENT       9.6847            GAIN EXPONENT      11.3990
PULSE COMPRESSION   5.0               PULSE COMPRESSION   5.0
INPUT FLUENCE       0.000017J/CM**2   INPUT FLUENCE       0.000003J/CM**2
OUTPUT FLUENCE      0.237903J/CM**2   OUTPUT FLUENCE      0.245881J/CM**2
EFFICIENCY          0.0270            EFFICIENCY          0.0345
SECOND STOKES GAIN  0.1393.(F-B RATIO) SECOND STOKES GAIN  *.     .(F-B RATIO)
    RAMAN CELL                          RAMAN CELL
PUMP FLUENCE        8.539012J/CM**2   PUMP FLUENCE        6.841892J/CM**2
GAMMA*C (=2/SATFLUX) 2.2000  CM**2/JOULE GAMMA*C (=2/SATFLUX) 3.2000  CM**2/JOULE
GAIN EXPONENT       9.3929            GAIN EXPONENT      10.9470
PULSE COMPRESSION   5.0               PULSE COMPRESSION   5.0
INPUT FLUENCE       0.237903J/CM**2   INPUT FLUENCE       0.245881J/CM**2
OUTPUT FLUENCE      7.124371J/CM**2   OUTPUT FLUENCE      6.095927J/CM**2
EFFICIENCY          0.0065            EFFICIENCY          0.0536
SECOND STOKES GAIN 13.2440.(F-B RATIO) SECOND STOKES GAIN 16.1293.(F-B RATIO)

                OVERALL SYSTEM EFFICIENCY 26.02%
```

Fig. 8-6. Output of Raman compressor system design code for a stacker-compressor-compressor system, double-passing the Raman cell at each compression.

assess the performance of Raman compressors as a component of a fusion driver laser. A discussion of the pertinent results of the analysis[44] is given in a following subsection (§8.3.1).

Spatial and Temporal Inhomogeneities. The theory of stimulated Raman scattering involving spatially and temporally inhomogeneous waves is comparatively undeveloped. Early work by Dyakov[48] derived an equation of the Fokker–Planck type for the Stokes intensity based on an analogy with turbulent-medium propagation. The stochastic theory was developed further by Pasmanik and Friedman,[49] using projection operator techniques to develop equations of the Feynman–Dyson type. In general, previous work has concentrated on stochasticity in the dynamical equation parameters rather than in the boundary conditions. For compressor analysis, the medium may be treated as a deterministic system, but the injected waves, which appear in the boundary values of the problem, must be taken as stochastic variables. Space does not permit a full discussion of these theories here; consequently, only a summary of the relevant work is presented.

An exact treatment of forward processes, where a monochromatic Stokes wave is pumped by a temporally stochastic pump, has been given using the well-known exact solution for this case.[50] This theory uses a novel technique for separating the effects of noise and those of the coherent term by rewriting the equations for the mean values in terms of functional derivatives. A second approach,

somewhat less rigorous but more generally applicable, develops a multimode parametric theory in which the gain experienced by a multimode or broadband Stokes wave is expressed in terms of parametrically coupled multiwave mixing.[51] In regions where these theories overlap, the agreement is good. Namely, both predict that the gain in the forward direction is independent of pump bandwidth, if the Stokes wave grows from noise.

A very important conclusion of the parametric theory is that the gain depends sensitively on the pump character. It is not possible a priori to predict the gain caused by a particular pump, or the outcome of an experiment, without a full knowledge of the autocorrelation functions of the pump. Thus, if these functions are not measured in a particular experiment, the experiment is, strictly speaking, not interpretable. The majority of experiments fall into this category. However, several experiments, at LLL and elsewhere, have demonstrated that under inhomogeneous pumping the gain may be either increased or reduced.[51] With reference to compressor design, in particular for the conditions in a KrF/CH_4 compressor, it appears that temporal pump stochasticity increases the forward gain but reduces the backward gain, whereas *spatial* inhomogeneity may reduce the forward gain but leaves the backward gain unaffected. The tentative nature of these conclusions is emphasized.

A discussion of the implications of inhomogeneities for RAPIER is also given in a following subsection (*§8.3.1*).

References

43. *Laser Program Annual Report—1977*, Lawrence Livermore Laboratory, Livermore, Calif., UCRL-50021-77, §7.6 (1978)
44. D. Eimerl, *Design Considerations for Raman Compressors in Inertial Confinement Fusion*, Lawrence Livermore Laboratory, Livermore, Calif., UCRL-81264 Preprint (1978).
45. W. Kaiser and M. Maier, "Stimulated Rayleigh, Brillouin, and Raman Spectroscopy," in *Laser Handbook*, F.T. Arecchi and E. O. Shulz-DuBois, Eds. (North-Holland, Amsterdam, 1972), pp. 1077-1150.
46. M. Maier, W. Kaiser, and J. A. Giordmaine, *Phys. Rev.* **117**, 580 (1969).
47. E. O. Schulz-Dubois, *Bell. Syst. Tech. J.* **43**, 625 (1964).
48. Yu. E. Dyakov, *Kratk. Soobshch. Fiz.* **7**, 49 (1971); **12**, 41 (1971); **4**, 23 (1973); **5**, 39 (1973).
49. G. A. Pasmanik and G. I. Friedman, *Sov. J. Quant. Electron.* **4**, 304 (1974).
50. D Eimerl, "Theory of Temporal Pump Stochasticity in Stimulated Raman Scattering in Dispersionless Media," *J. Math. Phys.* (to be published); also Lawrence Livermore Laboratory, Livermore, Calif., UCRL-80957 Preprint (1978).
51. D. Eimerl, *Inhomogeneously Pumped Stimulated Raman Scattering*, Lawrence Livermore Laboratory, Livermore, Calif., UCRL-81921 Preprint (1978).

Authors

D. Eimerl
R. A. Haas

8.2.4 Injection Locking and Amplified Spontaneous Emission (ASE)

The KrF^* laser medium gives high gain (10% cm^{-1}), broad bandwidth (~50 cm^{-1}), and short spontaneous-emission lifetime (~8 ns). Thus, the spontaneous emission is strong, has a large bandwidth, and is amplified to greater than a saturation intensity in just a few gain lengths. For extraction times greater than a few nanoseconds, the KrF laser saturates in a homogeneous manner. Consequently, the saturation of the gain is not strongly dependent on the bandwidth of the saturating field, and ASE may load the gain and reduce the extracted energy substantially

The combination of streng spontaneous emission and high (unloaded) gain has several implications for scaling the KrF laser. For large-solid-angle amplifiers (i.e., those having a large ratio of output aperture to length) with walls of low reflectivity, the ASE passing through the exit windows is strong, and the resulting gain loading is also large. Thus, ASE severely limits the extraction efficiency of unidirectional single-pass amplifiers. This limitation is considerably less stringent in bidirectional amplifiers. Also, depending on the wall reflectivity, parasitic oscillations or transverse modes may develop. Their suppression requires precise control of the optical signal field, to fill the gain region completely with high intensity radiation; it also requires baffles or other geometrical arrangements to increase the number of reflections experienced by the parasitic mode per gain length in the medium. If the KrF laser is used to drive a Raman compressor, then narrow line width is required (~0.3 cm^{-1}). This requirement is met most directly by injecting a signal with the desired spatial and temporal properties. The effects that the control mechanisms for ASE, parasitics, and line width have on the efficiency and size of large lasers are critical scaling

issues for fusion laser design. In 1978, we mounted a theoretical effort, coordinated with the experimental program, to analyze these and related issues.

Line width control in a large oscillator is achieved most directly by injecting a field of the desired line width and spatial quality before the medium is pumped. For a laser pulse of 50 ns, which is one or two meters in length, the number of round trips the field makes during operation is quite small. Also, for KrF, some species' kinetic response times are comparable to the round trip time. Thus, oscillators are operated in a transient regime, both optically and kinetically preventing good mode definition. The output contains not only the amplified injected signal but also the ASE, which has the generally undesirable properties of large bandwidth and large solid angle. Thus, control of the oscillator implies that the ASE component of the output is small. Also, efficient operation implies that the gain is sufficiently loaded by the optical field at all times during the transient operation of the oscillator, to prevent parasitic modes from growing and depleting the available optical energy, or damaging the laser components.

Successful control of the oscillator in this manner is termed injection locking. Previously, that term has been applied to frequency control of oscillators, in steady state operation, by driving the oscillators at a frequency other than their natural frequency.[52–54] It has also been applied to line width control of broadband oscillators (such as dye lasers) by injection of a short pulse of radiation, thereby indefinitely locking the oscillator to the injected pulse's characteristics.[55–57] Here, it is extended to include the transient phenomena just described, as well as ASE control. It is also extended to the control of amplifiers and other mirrorless devices, some of which are described below.

The analysis of gain control, ASE, and parasitic suppression in the general case involves transient, multidirectional wave propagation and spectral behavior. However, considerable insight into these problems may be obtained in a simple, quasi-one-dimensional model. In this model, a steady-state geometric optics approximation is made, treating nonparaxial rays as a bundle defined by a solid angle. Within this model, mirrorless amplifiers, plane oscillators, injection-locked plane oscillators, and bidirectional amplifiers have been analyzed and some general conclusions have been developed. The remainder of this subsection decribes the analysis of these devices and concludes with a discussion of comparative systems.

Mirrorless Amplifiers. Amplified spontaneous emission is very similar in character to oscillator noise. An elementary introduction to noise and spontaneous emission has been given by Yariv,[58,59] in terms of differential equations that contain a noise source and a gain term for each frequency interval $\delta\nu$. In the differential equation formulation, the noise source is the spontaneous emission power, within the relevant frequency interval, deposited into a volume element and into the solid angle subtended by the exit aperture at a point in that volume element.[60,61] However, the spontaneous emission that leaves the volume element and travels through the gain medium but not through the exit aperture is neglected. This neglected contribution to the ASE saturates the gain substantially and depletes the available energy. To include it, we abandoned the differential approach in favor of an integral formulation.[62]

Consider a thin uniform rod containing a medium that has homogeneously saturating gain and nonsaturating loss, operating on a bound-free molecular transition. Also, consider a thin cross-sectional element at the point z. The ASE through this element, originating in a similar element at z', is the relevant source multiplied by the gain experienced between z' and z. If $dI/d\nu$ is the noise intensity per unit frequency interval, then

$$\frac{dI^+}{d\nu} = \int_0^z dz'\, \rho(z')\, \delta\Omega(z - z') \exp\left[\int_{z'}^{z} g(\nu, z'')\, dz''\right] . \tag{22}$$

Here, ρ is the spontaneous source per unit frequency interval and solid angle, $\delta\Omega$ (z,z') is the solid angle subtended by the first element at z', and g is the net gain at the appropriate frequency. Thus,

$$\rho = \frac{n^* h\nu}{4\pi\tau_r}\, h(\nu) = \sigma n^* \left(\frac{\tau}{\tau_r}\right) I_S\, h(\nu) , \tag{23}$$

where τ_r is the upper level lifetime and h is the line shape function, normalized to unity:

$$\int h(\nu)\, d\nu = 1 . \tag{24}$$

The net gain, assumed to be transversely uniform in the chosen medium, is

$$g = \sigma n^* h(\nu) - \gamma(\nu) \ , \tag{25}$$

where γ is the nonsaturating loss coefficient. In the steady state case, the upper level population is given by

$$n_0^*/n_0 = 1 + \int d\nu \, h(\nu) \left[\frac{dI^+}{d\nu} + \frac{dI^-}{d\nu} + \frac{dI}{d\nu} \right] , \tag{26}$$

where n_0^*, the population in the absence of any optical fields, is determined by the kinetics and pumping of the laser.

Equation (26) includes the loading from the forward and backward noise $dI^{\pm}/d\nu$ and the signal $dI/d\nu$. When combined with the specified input intensity, these standard equations define the system.

An important assumption is that the walls of the amplifier are nonreflecting. To include reflecting walls, the solid angle may be increased to include the rays that do not proceed directly from plane z to z'. The effective solid angle $\delta\Omega_{eff}$ is determined by the nature of the walls (diffuse, specular) and the magnitude of the gain. In the simplest approximation, a simple geometrical argument leads to a sum over the number of reflections a wave may experience between z and z',

$$\delta\Omega_{eff}(z, z') = \sum_n R^n \delta\Omega(s/n)$$

$$\approx \delta\Omega(s) \, [1 + R(1 - R)^{-3}] \ , \tag{27}$$

where s is the separation (z – z') and R is the reflection coefficient. In units of the saturation intensity and the FWHM $\Delta\nu$ of the gain profile, these equations reduce to the following set:

$$i_{in} = \lambda G_0 \int_0^1 dx' \, \phi(x') \frac{\delta\Omega(x, x')}{4\pi}$$

$$X \exp[Y(x', y) - Y(x, y)] \, \epsilon(x' - x) \ , \tag{28}$$

$$i = i_{in}(y_{in}) \exp [Y(x, y_{in})] \ , \tag{29}$$

$$\phi^{-1} = 1 + \int dy \, h(y) \, [i_{in} + i] \ , \tag{30}$$

$$Y(x, y) = \int_0^x dx' \, [G_0 \phi(x') - \epsilon \, \ell(y)] \ , \tag{31}$$

where the dimensionless length is x = z/L and

$$\lambda = \frac{\tau}{\tau_r} \, [1 + R \, (1 - R)^{-3}] \ . \tag{32}$$

Here, G_0 is the small-signal gain $\sigma n_0^* L$ and Σ is the loss γL. The loss line shape is $\ell(y)$, where $\nu - \nu_p = y\Delta\nu$. Thus, the dimensionless parameters G_0, Σ, and λ characterize the amplifier and, with i_{in} and y_{in}, completely determine the system behavior.

These equations may be solved iteratively, alternately determining the loading $\phi = n^*/n_0^*$ and the intensities. The system is not convergent, unless the change in ϕ from one iteration to the next is restricted to a specified fraction of the difference between the present and the previous iteration. Otherwise, an oscillatory behavior develops. The calculations are quite rapid and can detail the extraction behavior of a particular amplifier in about one minute of CDC-7600 time.

This approximation to the thin rod (small aspect ratio) is expected to be good, as long as the transverse dimension is less than about half the length. The occurrence of parasitic oscillations in the transverse direction may be tested, after the solution for ϕ has been determined, by requiring that there be net loss for the transverse modes, namely,

$$G\phi(x)a/L - \epsilon + \ln R < 0 \ , \tag{33}$$

which must hold for all x. Within the thin-rod model, it is not realistic to treat oblique parasitics and whisper modes. Control of these modes depends critically on the reflectivity of the walls as a function of the angle of incidence, and on the details of the cavity geometry. Purely transverse parasitics give the stated condition on $\phi(x)$ and, within the model's limits, serve to define the maximum transverse dimension.

The model contains an expression for the broadband portion of the forward waves at the exit. Note that the ASE is spatially divergent, and that the ratio of the forward broadband noise to the signal therefore decreases as the point of observation recedes from the amplifier. By evaluating the integrals approximately, one can show that the forward noise is approximately equal to the backward noise,

$$i^+ \approx i^- \approx \lambda \frac{\delta\Omega}{4\pi} P \ , \tag{34}$$

where [illegible] power gain at line center. The output signal

$$i = \quad ^{\sigma} \ , \tag{35}$$

where $\sigma = h(y_{in})/h_p$, the ratio of the gain at the injected frequency to the peak gain. Thus, the forward noise ratio is

$$f_n^{(0)} = i^+/i^- = \lambda \frac{\delta\Omega_0}{4\pi} \frac{I_s}{I_{in}} P^{1-\sigma} \ , \tag{36}$$

where $\delta\Omega_0$ is the solid angle of the amplifier exit aperture at the entrance. Simple geometry gives f_n away from the exit aperture. The amplifier is injection-locked if the output is essentially narrowband. Quantitatively, this requires

$$f_n^{(0)} < f \ , \tag{37}$$

where f is the maximum tolerable forward noise at the exit aperture. The extraction efficiency for various input and solid angles is plotted in Fig. 8-7, which shows clearly the debilitating effect of ASE on unidirectional amplifier performance.

Plane Oscillators. If ASE is neglected in the plane mirror oscillator, the intensity is given by a generalization of the Rigrod analysis.[63,64] In units of the saturation intensity, the forward and backward waves satisfy

$$\frac{1}{i^+}\frac{di^+}{dx} = -\frac{1}{i^-}\frac{di^-}{dx} = g \equiv \frac{G}{1 + i^+ + i^-} - \epsilon \ , \tag{38}$$

where $0 < x < 1$. Thus, i^+i^- is a constant, and the coupled equations reduce to a single equation in one unknown, which is exactly solvable. The boundary conditions are

$$i^+(0) = R_1 \, i^-(0) \ , \tag{39}$$

$$i^-(1) = R_2 \, i^+(1) \ , \tag{40}$$

where R_1 and R_2 are the mirror reflectivities. These conditions are appropriate both for noisy signals spanning many vacuum modes and for well-defined single-mode behavior. The solution is as follows. If we define

$$x = G/\epsilon - 1 \ , \tag{41}$$

$$i^+i^- = a^2 \ , \tag{42}$$

and

$$F(x) = \ln\left[\frac{(K^2 - 4a^2)^{1/2} + 2x - K}{(K^2 - 4a^2)^{1/2} - 2x + K}\right] \ , \tag{43}$$

then

$$p\{F[i^+(1)] - F[i^+(0)]\} - \ln\left[\frac{i^+(1)}{i^+(0)}\right] - \epsilon = 0 \ , \tag{44}$$

where

$$p = (K + 1)(K^2 - 4a^2)^{-1/2} \ . \tag{45}$$

This equation gives the parameter a, thus completely specifying the Rigrod solutions for i^+ and i^-.

The solution obtained from the Rigrod analysis does not take account of the ASE. However, if we assume that the ASE is small (i.e., it does not change the degree of gain saturation), then it may be calculated directly from the Rigrod analysis. This approach is consistent only if the result is small. In the Rigrod analysis, the gain loading is

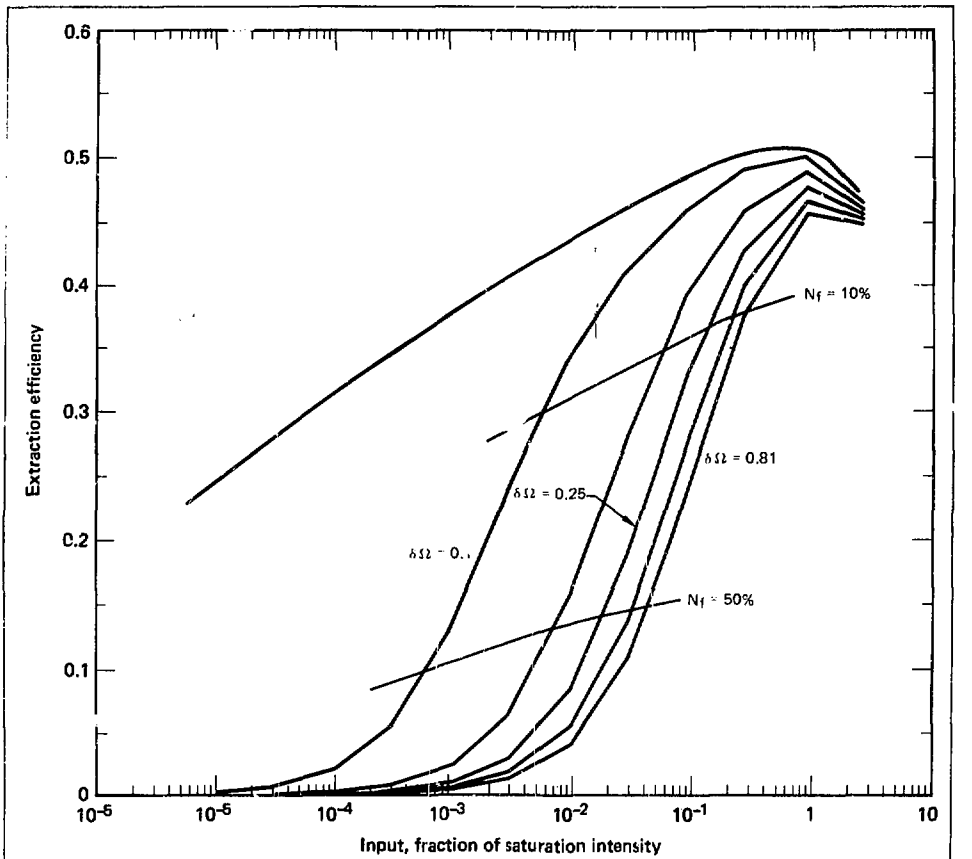

Fig. 8-7. Extraction efficiency of a mirrorless amplifier with parameters $G_0 = 20$, $\epsilon = 1$, $\lambda = 0.25$. The lines $N_f = 10\%$ and 50% show the efficiency below which the ASE at the exit aperture is 10% and 50% of the signal, respectively.

$$\phi^{-1} = 1 + i^+ + i^- \ , \tag{46}$$

and the saturated gain is $\frac{1}{2}|\ln(R_1R_2)|$. An approximate formula for the forward ASE at the exit aperture may be obtained:

$$i_n^+ \approx \lambda \frac{\delta\Omega_0}{4\pi} T_2 (R_1R_2)^{-\frac{1}{2}} \ , \tag{47}$$

where T_2 is the forward output coupling. Thus, the forward noise fraction is

$$f_n = \lambda \frac{\delta\Omega_0}{4\pi} T_2 (R_1R_2)^{-\frac{1}{2}} (1/\eta_f G) \ , \tag{48}$$

where η_f is the forward extraction efficiency and G is the unloaded gain exponent. Clearly f_n is small under conditions of interest, and ASE may indeed be calculated perturbatively.

The optical extraction efficiency is

$$\eta = \eta^- + \eta^+ = a\left[\frac{T_1}{R_1^{\frac{1}{2}}} + \frac{T_2}{R_2^{\frac{1}{2}}}\right] . \tag{49}$$

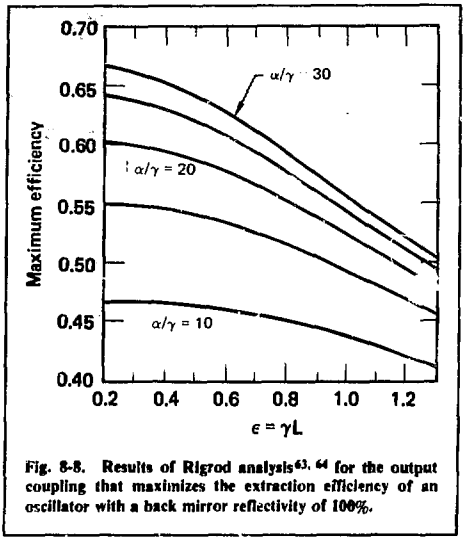

Fig. 8-8. Results of Rigrod analysis[63, 64] for the output coupling that maximizes the extraction efficiency of an oscillator with a back mirror reflectivity of 100%.

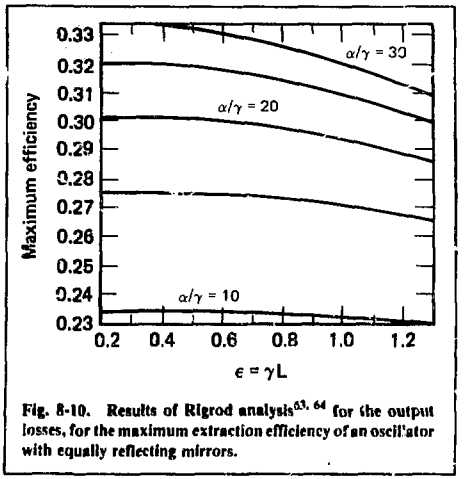

Fig. 8-10. Results of Rigrod analysis[63, 64] for the output losses, for the maximum extraction efficiency of an oscillator with equally reflecting mirrors.

The output coupling that maximizes the efficiency depends strongly on the ratio R_1/R_2. In the standard asymmetric configuration, R_1 varies from 0.9 to 1.0. In Figs. 8-8 and 8-9, the maximum efficiency and the optimum output coupling are shown for the asymmetric configuration. The graphs are parametric in α/γ, where η is an increasing function of α/γ and R_{opt} is a decreasing function thereof. In the symmetric configuration, the reflectivities are equal ($R_1 = R_2$). Then, the forward extraction efficiency is one-half of the total. The optimum parameters for this configuration are plotted in Figs. 8-10 and 8-11.

The transverse gain as a function of position may be used to define a maximum transverse dimension, as in the amplifier case. The same caveats with respect to other parasitics apply in the oscillator case, too.

Injection Locking of Plane Oscillators. The free-running oscillator gives a signal whose spectral width in steady state is given by the cavity parameters and by the temporal fluctuations in gain and

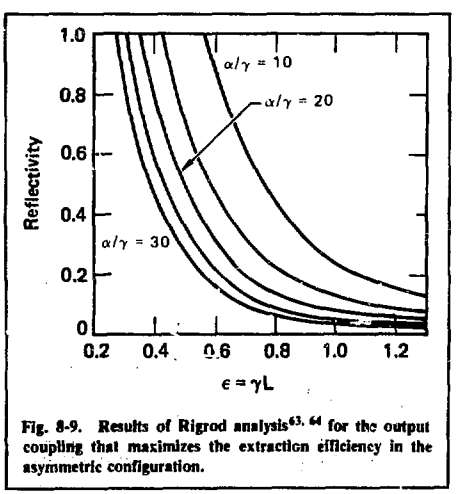

Fig. 8-9. Results of Rigrod analysis[63, 64] for the output coupling that maximizes the extraction efficiency in the asymmetric configuration.

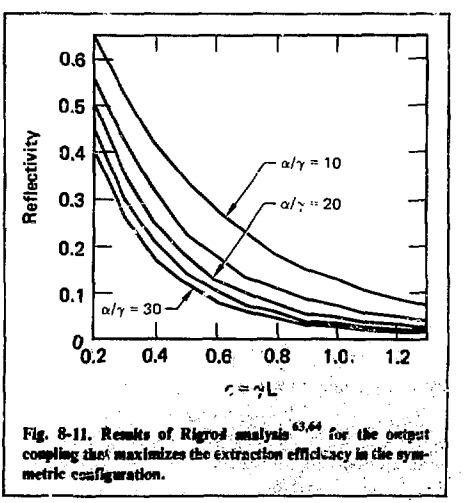

Fig. 8-11. Results of Rigrod analysis[63,64] for the output coupling that maximizes the extraction efficiency in the symmetric configuration.

loss in the medium. The time required for the spectrum to narrow to this state depends on the gain profile; media with flatter gain profiles take longer to reach steady state. In general, this time is much longer than the pulse length desired in fusion systems, and the line width of the oscillator must be controlled either by injection locking or by selective loss. If the injected signal spans many modes, line width control requires only that spontaneous oscillation at line center be suppressed. In short-pulse-length devices, this suppression requires that at all times the narrow-band, bright signal in the oscillator be stronger than the coupling of the broad-band source to the longitudinal parasitic modes. Thus, the injected signal fills the cavity before the medium is excited and is large enough to suppress all parasitic modes in the steady state limit. Otherwise, after a finite time, the oscillator will cease to be locked. Clearly, the steady-state injection locking intensity is an absolute limit, given the stated initial conditions, above which the oscillator is permanently locked. For intensities below the steady-state injection locking value, and the given initial conditions, there is a limit to the pulse length that may be used, which decreases as the injected intensity decreases.

For present purposes, the transverse parasitics may be ignored because we consider only *longitudinal* parasitic modes, which give limits on the injected intensity that are independent of the transverse dimension. For a given longitudinally locked oscillator, suppression of transverse oscillations implies a maximum transverse dimension, which may be determined from the solution of the longitudinal-locking equations.

If the gain line shape is $h(\nu)$, the narrow-band signal obeys the following equations:

$$\frac{1}{i^+}\frac{di^+}{dx} = -\frac{1}{i^-}\frac{di^-}{dx} = \sigma G\,[1 + \sigma(i^+ + i^-)]^{-1} - \epsilon_{in} \quad , \tag{50}$$

$$i^+(0) = R_1 i^-(0) + i_{in}(1 - R_1) \quad , \tag{51}$$

$$i^-(1) = R_2 i^+(1) \quad . \tag{52}$$

Here, $\sigma = h(\nu)/h(\nu_p)$, the ratios of gain at the injected frequency to the peak gain, and ϵ_{in} is the loss evaluated at the input frequency.

These equations assume that there are no interference effects at the input mirror R_1. The reflectivities are considered averages of the cavity response over a frequency interval that is large compared to the vacuum mode spacing. In a large oscillator, the empty cavity mode spacing is generally much less than the line width desired for subsequent Raman compression. Consequently, large refractive-index fluctuations that occur on a time scale comparable to the round trip time may couple the modes. It is possible that, even if a truly non-chromatic signal were injected, the output would have many modes because of this interaction. A strong coupling of this type implies that phase information is lost in less than one round trip. In turn, this implication suggests that conventional analyses of steady-state injection locking that depend critically on the phase information for mode definition and mode matching may not be applicable, especially in the ultraviolet portion of the spectrum. This possibility has led to the intensity analysis of injection-locking presented below. It is not yet known whether these conditions apply to the KrF medium or not. Because the mode spacing decreases with cavity length, the mode coupling is relatively stronger in larger cavities, and, ultimately, its applicability in fusion laser design will be determined by a comparison with experimental data from RAPIER and other systems.

If the modes are coupled strongly, the boundary condition at the input mirror is correctly given in Eq. (51). Otherwise, the condition is

$$e^+(0) = r_1 e^-(0)\,\beta + t_1 e_{in} \quad , \tag{53}$$

where the intensity $i = |e|^2$, and r_1 and t_1 are the complex reflectivity and transmissivity of the mirror, respectively. The coefficient β is $\exp(i\phi)$, where ϕ is the round-trip phase angle in the cavity for the particular injected frequency. For multimode injection, each injected mode leads to an equation like Eq. (53) but with different ϕ. These modes are coupled through the gain saturation in the oscillator, and the output spectrum is not linearly related to the input spectrum. In the following, the result for the strongly coupled mode, Eq. (51), is used. Further work on the case of the weakly coupled mode is planned.

The injection locking condition is

$$2\bar{g} + \ln(R_1 R_2) < 0 \quad , \tag{54}$$

where g is the maximum net gain within the gain bandwidth,

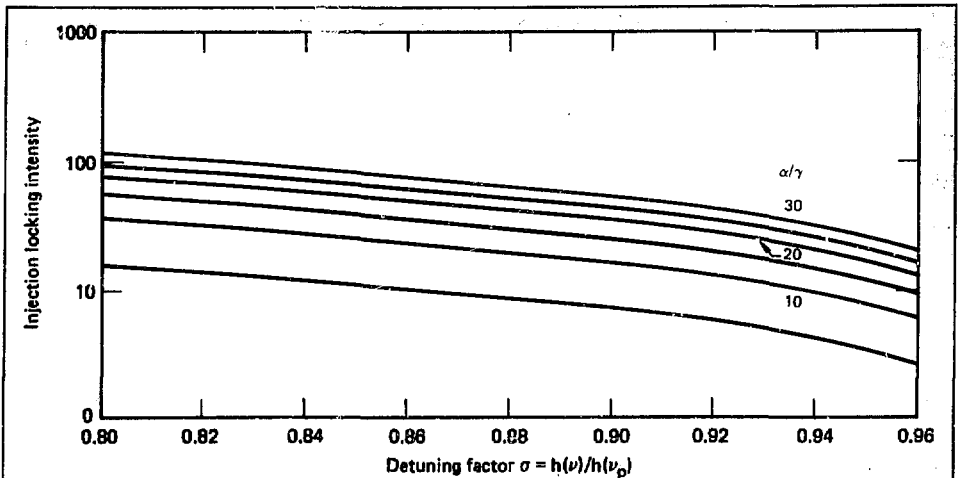

Fig. 8-12. Injection locking intensity off line center for L = 1, input mirror 95%, output mirror 10%, parametrically in α/γ. Only 5% of the locking intensity penetrates into the cavity in the plane mirror configuration.

$$\bar{g} = \mathrm{Max}_{\nu}\left[\sigma G_0 \int_0^1 \phi(x)\,dx - \epsilon\right]. \qquad (55)$$

The solution of these equations follows the previous analysis and is very similar to the Rigrod analysis. Figure 8-12 shows the injection-locking intensity for a plane oscillator with reflectivities of 95% and 1%, as a function of the detuning $\sigma = h(\nu)/h(\nu_p)$. The curves are parametric in α/γ, with γL held fixed at 1.1. The locking intensity is high, because only 5% of the injected signal passes through the input coupler into the cavity. However, $(1 - R_1)i_{lock}$ is much smaller than the circulating intensity in the cavity, especially close to line center where $\sigma \approx 1$. Consequently, injection locking and extraction efficiency calculations decouple, and the previous analysis may be used to evaluate the optimum output and input couplings under locked conditions also. The transverse dimension is constrained by the same equations that apply to the pure oscillator, again with the same reservations concerning model limitations.

Bidirectional Amplifier. The bidirectional amplifier is a mirrorless device that amplifies simultaneously two oppositely directed, overlapping pulses. The equations describing this device are the same as those for the oscillator, except that the boundary conditions contain the two input intensities. In this device, the gain loading is substantial throughout the whole gain region. Thus, the transverse parasitic gain and the ASE are small, comparable to the oscillator values. If the amplifier is operated symmetrically, the gain loading is smallest in the center (at a point equidistant from either end). Figure 8-13 plots this minimum loading as a function of input intensity for three values of

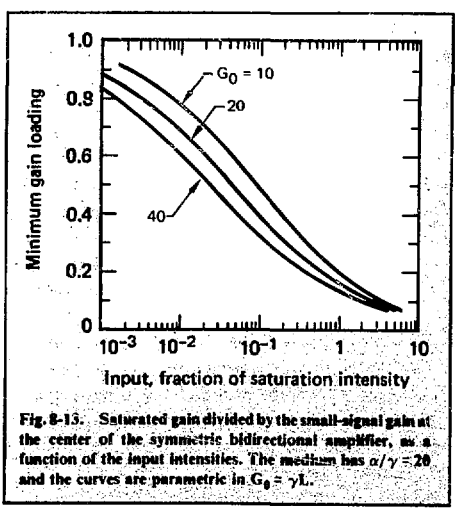

Fig. 8-13. Saturated gain divided by the small-signal gain at the center of the symmetric bidirectional amplifier, as a function of the input intensities. The medium has $\alpha/\gamma = 20$ and the curves are parametric in $G_0 = \gamma L$.

$\epsilon = \gamma L$ at $\alpha/\gamma = 20$. The noise intensity at either exit aperture is

$$i_n = \lambda \frac{\delta\Omega}{4\pi} P^{\sigma/2} , \qquad (56)$$

which, for a given power gain and aspect ratio, is smaller than the amplifier noise by the ratio $4P^{\sigma/2}$. Thus, for power gains greater than about 16, the bidirectional amplifier has less forward noise than does the unidirectional amplifier. The maximum transverse gain, however, is much less. The transverse gain in the center of the amplifier is

$$g_\perp = (G_0\phi_c - \epsilon)\, a/L , \qquad (57)$$

whereas for the unidirectional amplifier the minimal loading is $\phi^{-1} = 1 + i_{in}$, which is close to unity. Thus, using Fig. 8-13 as a guideline, we see that the bidirectional amplifier may be two to three times broader than is the unidirectional amplifier.

Conclusions. The properties of amplifiers and oscillators obtained in the steady state, quasi-one-dimensional limit form a partial basis for comparative analysis. The most important omissions are transient phenomena, possibly including bifurcation depending on the initial conditions, and oblique parasitics and whisper modes, which impact the transverse scaling and cavity design. Nonetheless, within the present approximation, several conclusions are already clear. In amplifiers, the maximum efficiency is achieved for an input intensity close to a saturation intensity. Thus, the power gain is of the order of $\alpha/2\gamma$. The unidirectional amplifier has a low gain loading at the input, leading to a strict limit on the transverse dimension. Increasing the transverse dimension allows the backward ASE to load the gain near the input, but this necessarily leads to a low extraction efficiency. The bidirectional amplifier controls the gain everywhere, but least effectively in the center of the amplifier. Thus, it tends to permit larger aspect ratios than does the unidirectional amplifier. Both amplifiers give comparable broadband components in the output that are small and that decrease as the point of measurement recedes from the exit aperture. Oscillators, on the other hand, may be injection-locked with small signals if the initial transient behavior is appropriately controlled. Thus, they allow higher power gains than do amplifiers. They are comparable in transverse properties to the bidirectional amplifier. The systems implications of these conclusions strongly favor oscillators as preamplifiers but appear to relegate the choice of a large power amplifier to other issues, such as multiplexing capability and propagation issues.

References

52. C. J. Buczek, R. J. Freiberg, and M. L. Skolnick, *Proc. IEEE* **61**, 1411 (1973).
53. R. Adler, *Proc. IEEE* **61**, 1380 (1973).
54. K. Kurokawa, *Proc. IEEE* **61**, 1386 (1973).
55. Q. H. F. Vrehen and A. J. Breimer, *Opt. Comm.* **4**, 416 (1972).
56. J. J. Turner, E. I. Moses, and C. L. Tang, *Appl. Phys. Lett.* **27**, 441 (1975).
57. U. Ganiel, A. Hardy, and D. Treves, *IEEE J. Quant. Electron.* **QE-11**, 881 (1975).
58. A. Yariv, *Optical Electronics* (Holt, Rinehart and Winston, New York, 1976), chs. 5 and 10.
59. H. Kogelnik and A. Yariv, *Proc. IEEE* **52**, 165 (1964).
60. L. W. Casperson, *J. Appl. Phys.* **48**, 256 (1977).
61. L. W. Casperson, *J. Appl. Phys.* **47**, 4555 (1976); **47**, 4563 (1976).
62. To compare with calculations of disk parasitics in storage lasers, where gain saturation is neglected, see J. B. Trenholme, NRL Memorandum Report 2480 (Jul. 1971); also Lawrence Livermore Laboratory, Livermore, Calif., reports UCRL-50021-73-1 and UCRL-50021-74; also D. C. Brown, S. D. Jacobs, and N. Nee, *Appl. Opt.* **2**, 211 (1978).
63. W. W. Rigrod, *J. Appl. Phys.* **34**, 2602 (1963); **36**, 2487 (1965).
64. W. W. Rigrod, *IEEE J. Quant. Electron.* **QE-14**, 377 (1978).

Author

D. Eimerl

8.3 Pulse-Compressor Laser Systems

Stimulated backward-wave Raman scattering has been recognized for some time as a potential means of generating short pulses for fusion applications.[65] The advent of efficient (>5%), long-pulse (>100-ns) ultraviolet lasers, the rare gas monohalides,[66] led to a reinvestigation of the utility of this technique in the context of advanced laser drivers.[66,67] The short wavelengths of efficient lasers, such as KrF (248.4 nm), increase the cross section for Raman scattering and allow a Raman amplifier to operate at near-atmospheric pressure with a reasonable gain coefficient and with a saturation fluence of about 1 J/cm^2. Of course, the ultimate point of interest is that target coupling may be enhanced by the short-wavelength radiation produced in a KrF-laser-driven Raman compressor.

The initial analysis of this pulse compression technique led to a thorough experimental and analytical study of its potential as an advanced-laser option. Measurements of small-signal backward-wave gain[67] and saturation effects[68] in gaseous methane have been reported in the literature as well as in last year's laser fusion annual report. A comprehensive review of this work has been given.[69] An analysis of the potential efficiency of Raman pulse-compressor systems and associated technological limitations has also been prepared.[70]

These studies have shown that:

- Raman pulse-compression factors of about 10, with efficiencies of about 60%, are possible.
- Nonsaturating losses limit the efficiently achievable intensities of KrF pump lasers to about 20 MW/cm^2.
- The hybrid combination of pulse-stacking schemes with Raman compression gives important technological advantages. Overall compression factors of 50 or more should be possible with compressor conversion efficiencies of 50% or more.
- Overall system efficiencies in excess of 3% appear possible.
- Improvements in Raman compressors or pumps could increase this overall efficiency.

Because of the favorable prognosis of Raman pulse-compressor/pulse-stacker hybrids, we mounted an increased effort in this area, including an analysis of alternative stacker–compressor geometries and scaling limitations for large-scale pulse compressors. Subsection 8.3.1 describes our initial work during 1978. We have continued theoretical studies pertaining to both KrF pumps and CH_4 Raman scatterers. Work on these topics is reported in §8.3.2 and 8.3.3. To experimentally assess and advance the technology associated with hybrid compression systems, a moderate-scale system test bed, called RAPIER, is currently under development. A progress report on this pulse-compressor test bed is given in §8.3.4.

References

65. A. J. Glass, *IEEE J. Quant. Electron.* **QE-3**, 516 (1967).
66. J. J. Ewing, *Physics Today* **31** (5), 32 (1978).
67. J. R. Murray, J. Goldhar, and A. Szoke, *Appl. Phys. Lett.* **32**, 551 (1978).
68. J. R. Murray, J. Goldhar, D. Eimerl, and A. Szoke, *Appl. Phys. Lett.* **33**, 399 (1978).
69. J. R. Murray, J. Goldhar, D. Eimerl, and A. Szoke, *IEEE J. Quant. Electron.* **QE-15**, 342 (1979).
70. J. J. Ewing, R. A. Haas, J. G. Swingle, E. V. George, and W. F. Krupke, *IEEE J. Quant. Electron.* **QE-15**, 368 (1979).

Author

J. J. Ewing

8.3.1 Potential Large-Scale Pulse Compressors

System Issues. We have evaluated three types of pulse compressors: pure Raman compressors, pure pulse stackers, and hybrid combinations of these two. Our analysis has shown that hybrid compressors offer a most attractive mix of the properties of each of these pure compression schemes. Hybrid compressors can have significantly larger compression ratios at high efficiency than can pure Raman compressors. Compression ratios of about 50 and overall system efficiencies in the range of 3 to 4% appear achievable.

In extending our analysis of these hybrid options, we have concentrated on the further elucidation of the following issues:

- Improvement of Raman-media extraction efficiencies by second-Stokes suppression techniques and alternate pulse-compressor geometries.
- Comparison of various hybrid architectures in terms of the important system parameters: the number of optical elements used to achieve a given compression ratio and the jitter and timing requirements of the system.
- Preliminary development of cost models to compare various pulse-stacking/Raman-compression hybrids.

We have found that a distributed two-photon absorber may be one attractive means of eliminating the second Stokes parasitic. This results in a larger value of the Raman-medium extraction efficiency at a fixed compression ratio. We have identified a two-pass architecture, using unequal Raman-medium gain lengths, which can increase Raman extraction efficiencies to about 80%. We have also analyzed conical Raman amplifiers and found them marginally more efficient than a constant-area Raman amplifier. This work is described in the following subsection.

To compare the various hybrid compression schemes more completely, we have now characterized their architectures in terms of important optical and electrical parameters. We have found substantial differences between stacker–compressors

and compressor–stackers in terms of jitter requirements, laser staging scenarios, and number of optical components. The stacker–compressor (sequentially extracted pump laser stacked in the Raman medium) yields the same efficiency for a given compression ratio as does a compressor–stacker (sequentially extracted Raman medium stacked on the target). However, jitter requirements, ASE standoff considerations, and the required number of mirrors favor the use of a compressor–stacker architecture. General considerations on jitter and number of mirrors are given later in this subsection. A tremendous simplification in terms of the number of mirrors utilized and a tremendous reduction in the number of optical beam lines facing the target results from the combined compression schemes. Preliminary cost-comparison studies have shown that the costs of optics and beam pointing and tracking systems are reasonable for hybrid compressors but excessive for pure pulse stackers of very high compression ratio (~50). Our cost models are in a preliminary stage and will be reported on further in next year's annual report.

Methods of Pulse Extraction from Raman Amplifiers at Higher Efficiencies. Suppressing the growth of second Stokes waves in a backward-wave Raman amplifier is one means of increasing the Raman-compression conversion efficiency. There are essentially two methods of suppressing the second Stokes parasitic: frequency selection or spatial quality selection. We first consider the frequency technique.

In general, frequency-selective absorbers are extremely specific in their application and require a high degree of frequency control to ensure that the frequency conditions are satisfied.[71-73] The absorber may be mixed in with the Raman medium if it is gaseous. Otherwise it must be placed in a solid host, which is located between stages in a Raman amplifier chain or which divides the Raman cell itself into several compartments. Liquid hosts may also be considered, in principle; they have the advantage of providing a natural cooling mechanism for the liquid container by flow. A gaseous absorber for use in a KrF/SF_6 compressor is xenon, which uses a narrow two-photon absorption line at $2\omega_s$. Analysis shows that the absorption coefficient is[71]

$$\alpha_{2S} = 7 \times 10^{-10}\ (0.3\ \mathrm{cm}^{-1}/\delta\nu)\ \mathrm{cm/W \cdot Torr\ Xe}\ , \quad (58)$$

where $S\nu$ is the second Stokes line width. This coefficient is large because the transition is bound–bound between narrow states. A peculiarity of two-photon absorption schemes is that they give a limit on the parasitic intensity, because the absorption is nonlinear in the intensity. In principle, this allows the achievable compression to increase without limit. For the specific system considered, the difficulties are the photoionization of the excited state of xenon and its tendency to form excimers at densities greater than about 25 Torr. The former is optical loss, and calculations show that this loss is small but noticeable. The excimer formation causes the absorption lines to broaden into bands, making the absorption no longer frequency-selective. It is not known whether these effects preclude the use of this system.

Other absorbers[74] are Er^{3+}, to be used with $XeCl/CH_4$ compressors, and Gd^{3+}, to be used with KrF/CD_4 compressors. The absorption cross section has been estimated at 10^{-19} cm^2, which requires a density of about 1 to 2 mole% in a typical solid host. The major considerations for the host are the nonlinear index of refraction, the absorption at other wavelengths, and the two-photon absorption. The obvious candidates are fluoroberyllate glasses and fluoride crystals.

A frequency-dispersive saturable absorber[73] may be used to suppress the second Stokes parasitic with little loss at the first Stokes frequency, if the second Stokes fluence is considerably less than the saturation fluence. The medium is inhomogeneous, and the saturation fluence at the first Stokes frequency is much less than the first Stokes fluence, which implies a cross section of about 10^{-15} cm^2. An electronic/vibrational transition can be used for suppression if the $V \rightarrow V$ and $V \rightarrow T$ rates are less than the desired pulse width. Then, saturation at the first Stokes frequency may coexist with lack of saturation at the second Stokes. The gas SO_2 seems to meet these requirements in the KrF/CH_4 compressor.

Methods based on spatial-quality selection rely on the large solid angle of the parasitic wave, which is expected on theoretical grounds. The theory of nonparaxial waves pumped by a large solid angle suggests that the solid angle of the parasitic is A/L^2, where A is the area of the Stokes beam and L is the length of the Raman cell. Thus, spatial filtering can reduce the parasitic intensity. Alternatively, distance filtering (allowing the waves to propagate a

long way) may be used to reduce parasitic intensity. The parasitic that remains within the solid angle of the Stokes wave after geometric filtering may be further reduced with a dispersive element, such as a prism or gratings. Scaling these dispersive elements presents formidable problems associated with surface figure and the nonlinear index of refraction. Fresnel prisms may circumvent this scaling problem.

The second Stokes limit, or the extraction efficiency, requires that the performance factor G_f/R be as large as possible. But G_f, the maximum tolerable gain exponent for the second Stokes wave, is limited in a chain configuration by the between-stage reduction in the second Stokes intensity. Ideally, the input to a compressor contains less second Stokes than is produced by spontaneous scattering. Thus, the between-stage reduction in the parasitic is ideally greater than about e^{-20}. Absorbers may be constructed with over 20 optical depths, although to do this with solid hosts may give rise to self-focusing problems. Geometrical methods, however, are limited by surface scatter and diffractive terms to suppressions of about 10^{-3}. Thus, several geometrical components are needed to reduce the intensity of the second Stokes by e^{-20}. In summary, although frequency selection appears more attractive than spatial-quality selection, its high specificity limits its applicability. Geometrical methods may be the only ones available for many systems, but they involve greater system complexity.

A second technique for improved Raman extraction efficiency is the conical Raman amplifier. The baseline conical amplifier is a compressor in which the pump and Stokes waves are not plane waves, but spherically converging and diverging, respectively. In other designs, the expansion or contraction is in one dimension only, or it may be more generally astigmatic. The advantage of the expanding geometry for the Stokes pulse is that it prevents the intensity from rising to a high value while, at the same time, allowing efficient energy extraction. As the Stokes fluence rises above the saturation fluence, it continues to extract efficiently, but the increase in total energy is countered by the increasing area, to give a slowly rising intensity. Since the second Stokes gain is an integral over the intensity, conical schemes have smaller parasitic gains than do plane or cylindrical designs. Figure 8-14 shows the decrease in the second Stokes gain with increasing cone angle. The curve labels are the

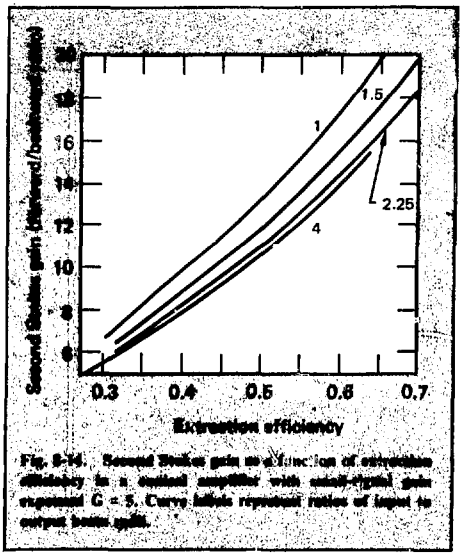

Fig. 8-14. Second Stokes gain as a function of extraction efficiency in a conical amplifier with small-signal gain exponent G = 5. Curve labels represent ratios of input to output beam radii.

ratios of the radii of the input and output Stokes beams. In this calculation, the pump pulse is flat, the input Stokes beam is Gaussian, and the transverse radial variations in intensity are neglected. The disadvantage of this scheme is the difficulty of multiplexing the pump, which is focusing down and is directed to the cell by mirrors at very large aperture. Fill factors are also worse in this arrangement, which presents only a marginal improvement in performance over plane or cylindrical designs.

Another technique for effective extraction from a Raman amplifier is to "recycle" the pump radiation into a second stage of Raman compression.[75] Since the first stage of Raman extraction depletes the back half of the pump pulse, one can recycle the pump radiation in a shorter cell, allowing operation at an effective *lower* compression ratio on the second pass. This has been shown analytically to give higher efficiency. Such a scheme is illustrated in Fig. 8-15. It makes use of the remaining pump energy, thereby increasing the overall device extraction efficiency. It provides an added benefit of high fluence gain by the judicious staging of Raman gains. Basically, the first cell and input Stokes fluence are so defined that most of the pump pulse is depleted at the exit of this cell, consistent with the

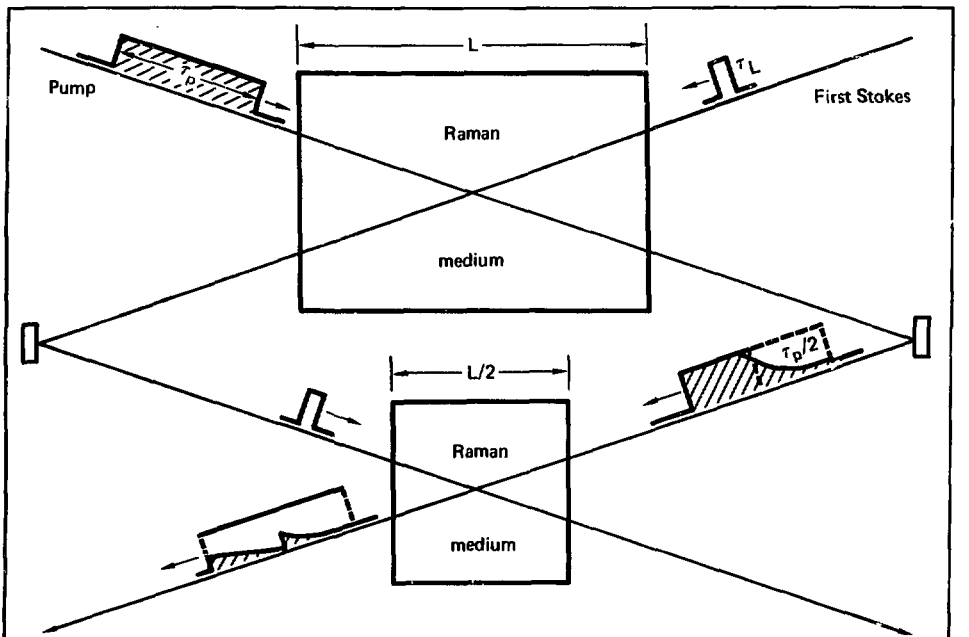

Fig. 8-15. Two-stage extraction process. This schematic shows the extraction of the rear portion of the pump in the long cell and the front portion in the shorter cell. The overall second-Stokes gain at a given efficiency is considerably smaller than that for single-stage compression.

second-Stokes G-integral limitations. The second-cell length and gain are specified so as to convert the remaining energy at high efficiency; this can be accomplished by reducing the effective compressor ratio. As an example, consider the case where $L_2 = L/2$, $G_1 = 10$, $G_2 = 5$, $\kappa_1 = 10$, and $\kappa_2 = 5$; then, the overall efficiency is given as

$$\eta = \eta_1 + (1 - \eta_1 - \epsilon)\eta_2 \ , \qquad (59)$$

where ϵ is the amount of pump energy, from the first compression, that is not utilized in the second cell. If the G integral can be reset to zero before entering the second cell, calculations[73] have shown that, for this case, overall extraction efficiencies of ~0.85 and fluence gains of ~600 can be achieved for a compression of $\kappa = 10$.

It is interesting to compare the backward-wave multipass architectures with a simple forward scheme. In the forward multiplexed scheme, a Stokes pulse copropagates with a pump pulse that is n times longer. Together, these pulses pass through the Raman cell several times. On the first pass, the Stokes pulse extracts that portion of the pump pulse which overlaps it. On the second pass, however, the Stokes pulse has been delayed with respect to the pump pulse, and it now overlaps a different portion, which it extracts. After passing through the cell n times, it has accessed every portion of the pump pulse. The major parasitics are the amplified spontaneous emission at the Stokes and second Stokes frequencies. The ASE at the Stokes frequency copropagates, approximately, with the pump pulse, and experiences a gain nG in n passes. Similarly, the second Stokes parasitic experiences a gain nGP/2, where P is the power multiplication and G is the gain exponent. Thus, the maximum power amplification is given by

$$P \lesssim 2g_f/nG \ , \qquad (60)$$

where g_f is the maximum tolerable gain. For G = 3 and n = 3, power gains of 4 seem feasible. Note that in this scheme the compression is n and that the major limitations on a multipass scheme such as this are refractive and figure losses in the optical train.

Comparisons of Hybrid Stacker-Compressors. The recirculating electrical power required in a laser-fusion power plant will decrease with increasing pump-laser efficiency. However, the capital costs are likely to be related to the number, quality, and complexity of the optical train as well as to the electrical power conditioning elements. One significant system comparison of these various pulse compressors is the total number of mirrors N required for a given power gain P/P_0. In Table 8-3, we list expressions for the figure of merit $N(P/P_0)^{-1}$ for several of the pulse compressors we have studied. Representative values of this figure of merit are also given for the specific case of n = 4 for the stacker systems. Equal numbers of pump and Raman media are assumed for this table. However, the analysis can be extended for cases of multiple pump beams per Raman aperture, with the same qualitative conclusions. We also assume that a stacking of n requires 2n optical elements and that each Raman compressor requires two optical elements.

The data in Table 8-3 show that pure Raman compressors and double compressors are most "mirror efficient." A stacker-compressor requires a somewhat larger number of mirrors than does a pure Raman compressor, but it makes considerably better use of mirrors than does a pure KrF stacker. Another important point is that sequential extraction of both a pump and a Raman medium (e.g., a stacker-compressor-stacker) can yield an order-of-magnitude greater power gain per mirror than can a pure pulse stacker. In general, it is a much more effective use of optical components to sequentially extract two media in series than it is to simply double the number of mirrors and extractions of the pump.

Table 8-3. Relative numbers of mirrors required for various pulse compressors, in terms of a figure of merit $N(P/P_0)^{-1}$, where N is the number of mirrors and P/P_0 is the power gain. For each case, the analytical expression for the figure of merit is given as well as a typical value for it. Lower values correspond to fewer required mirrors.

	Figure of merit, $N(P/P_0)^{-1}$	
Type of compressor	**Expression**	**Typical value**
Pure pump stacker	$\frac{2}{\eta_0}$	2.2[a]
Pure Raman compressor	$\frac{2}{\eta_R \kappa}$	0.4[b]
Stacker–compressor or compressor–stacker	$\frac{2n+2}{n}\left(\eta_0 \eta_R \kappa\right)^{-1}$	0.55 (n = 4)[c]
Double compressor[d]	$\left(\frac{2}{\eta_R \kappa}\right)^2$	0.16
Stacker–compressor–stacker	$\frac{2(n_1+n_2)}{n_1 n_2}\left(\eta_0^2 \eta_R \kappa\right)^{-1}$	0.24 ($n_1 = n_2 = 4$)
Compressor–stacker–compressor[d]	$\frac{2n+4}{n}\left[\eta_0^2\left(\eta_R \kappa\right)^2\right]^{-1}$	0.15 (n = 4)

[a] η_0 taken as 90%.

[b] $\eta_R \kappa$ taken as 5.

[c] n = number of beams sequentially extracting a medium.

[d] Three-color system: λ_{pump}, λ_{Stokes}, and $\lambda_{second\ Stokes}$.

Table 8-4 lists relevant formulas for the case of multiple pump beams exciting each Raman amplifier, the case most likely to be encountered in power-plant-size systems. For this table, m is the number of pump apertures combined in each Raman medium, and only systems with a single stage of backward-wave Raman compression are considered. The conclusion to be drawn from Table 8-4 is qualitatively similar to that from Table 8-3: Raman compressors, and hybrids based on them, utilize fewer total mirrors to achieve the same power gains. Sequential extraction of two media (the stacker–compressor–stacker) utilizes about an order-of-magnitude fewer mirrors than does a pure stacker for large numbers of pump beams. A distinction between stacker–compressors and compressor–stackers now becomes apparent. Sequentially extracting the Raman medium rather than the m pump lasers yields a power gain per mirror that is larger by the ratio $(nm + 1)/(n + m)$. Thus, for a large number of pumps combined in the Raman medium, the compressor–stacker is less mirror-intensive. A final point of comparison with respect to optics is the total number of mirrors required to transport the beams to the target. The mirrors that transport the pump laser radiation to the Raman cell may be of significantly lower optical quality than the mirrors transporting the laser energy that ultimately must impact the target. Thus, the optical train of a pure pulse stacker needs to be of an intrinsically higher quality than most of the mirrors in the stacker–compressor family. The total number of mirrors that face, or are imaged to, the target in a pure stacker is also larger than that for any of the members of the stacker–compressor family. This is a result of the amplifier intensity limitations caused by nonsaturating losses in the pump lasers.

Jitter is a basic factor that may strongly influence the choice of a compression scenario to achieve a desired final-pulse length. The high-gain pump laser or amplifier must be efficiently extracted during the gain excitation pulse, to suppress broadband, nonfocusable, amplified spontaneous emission. Thus, the extraction pulse or the first of a sequence of extraction pulses from a preamplifier must fill the amplifier during the rise time of the e-beam pump. For large-scale short-pulse devices, inductance considerations typically limit the pump deposition rise time to about 5 ns or longer. Electron beam jitter of about this value has also been obtained. One can increase the allowable jitter of

Table 8-4. Relative numbers of mirrors required by various pulse compressors when multiple pump beams excite each Raman amplifier, expressed in terms of the figure of merit $N(P/P_0)^{-1}$. For each case, the analytical expression for the figure of merit is given as well as the limit value for large m (m = number of pump apertures combined in each Raman medium).

	Figure of merit, $N(P/P_0)^{-1}$	
Type of compressor	Expression	Large-m limit[a]
Pure pump stacker	$\frac{2nm}{n\eta_0}$	2.2m
Pure Raman compressor	$\frac{2(m+2)}{\eta_R{}^{\kappa}}$	0.4 m
Stacker–compressor	$\frac{2(nm+1)}{n\eta_0}\,\frac{1}{\eta_R{}^{\kappa}}$	0.44m
Compressor–stacker	$\frac{2(m+n)}{n\eta_0}\,\frac{1}{\eta_R{}^{\kappa}}$	$0.44\frac{m}{n}$
Stacker–compressor–stacker	$\frac{2(nm+n_R)}{n+n_R}\left(\frac{1}{\eta_0}\right)^2\frac{1}{\eta_R{}^{\kappa}}$	0.25m (for $n = n_R$)

[a] Taking $\eta_0 = 0.9$, $\eta_R{}^{\kappa} = 5$.

the amplifier gain relative to extracting pulses in the sequence by injecting a sequence of pulses that "overfill" the medium (i.e., inject a sequence of pulses whose total pulse duration exceeds the sum of amplifier gain duration and relative time jitters). Stacking then yields the shortened pulse. The power gain for the overfilled amplifier is related to the effective number of pulses actually amplified rather than to the total number of pulses injected.

A second jitter consideration arises in the case of backward-wave Raman amplifiers. The leading edges of the pump beam and extraction pulses must meet at a fixed place and time. If the entire Raman oscillator-amplifier chain is driven by the output from the last KrF pump laser, the jitter of the pump relative to the Stokes extraction pulse in the final amplifier is zero, because accurate timing is ensured by appropriately adjusting propagation distances. If, however, the Raman master oscillators and low-energy power amplifiers are not driven from the final pump laser, the relative jitter of the first Stokes wave (and its pumps) and the final pump becomes important. A relationship can be derived that couples the relative jitter of Stokes and pump beams to the Raman pump-pulse duration and the spatial-temporal overlap of Stokes pump and Raman active medium. For a 90% temporal fill factor, one finds the maximum allowable jitter to be $t = \tau_p/20$. This jitter specification can be relaxed by increasing the Raman medium's length or by overfilling the Raman medium with multiple Stokes pulses. Increasing the Raman medium's length leads, however, to increased second-Stokes parasitic generation.

For the two simplest and nominally similar hybrid compression architectures (stacker-compressors and compressor-stackers), jitter considerations strongly favor sequentially extracting the Raman medium rather than the pump medium, to achieve the same final-pulse compression, especially for system output pulses shorter than about 10 ns. For a simplified example, a 90% temporal fill factor in the Raman medium of a stacker-compressor system, using a pump with duration τ_p extracted by n beams, and pumping a backward-wave Raman amplifier extracted by one Stokes pulse, requires a relative jitter no greater than $(1/n)(\tau_p/20)$. If, instead, a single pump pulse of duration τ_p is used to pump a Raman compressor extracted by n beams, the relative jitter need only be within $\tau_p/20$. Moreover, by using more extracting pulses in the Raman medium, the allowable jitter can be increased even further.

References

71. D. Eimerl, *KrF/Xe BTRA's*, LLL internal memorandum TDA-77-145 (1977).
72. D. Eimerl, *The Absorbing Subject of Xenon*, LLL internal memorandum TDA-77-143 (1977).
73. D. Eimerl and E. V. George, *Selective Absorption Techniques for Second Stokes Wave Suppression in Raman Compressors*, LLL Patent Disclosure IL-6568 (1979).
74. W. F. Krupke, *Er^+ Doped Glass for Second Stokes Suppression in an XeCl/CH_4 Raman Compressor System*, LLL internal memorandum (1978).
75. D. Eimerl and E. V. George, *Double Cell Raman Compressor for Increased Laser Efficiency*, LLL Patent Disclosure IL-6551 (1979).

Authors

D. Eimerl
J. J. Ewing

Major Contributor

E. V. George

8.3.2 Raman Medium Physics

Theoretical Structure Calculations on Methane. The methane molecule presently serves as the Raman scatterer of choice for a backward-wave Raman pulse compressor. Accordingly, we have conducted a theoretical study on methane to improve our understanding of its electronic spectra, to compute the Raman gain from first principles, and to estimate losses from two-photon absorption. Methane exhibits continuous absorption spectra with no structure that can be associated with bound excited states (see Fig. 8-16).[76,77] Our calculations show that the excited states of CH_4 are Rydberg in nature, predicting the excitation energies given in Table 8-5. These calculations were carried out with

Table 8-5. Calculated configurations and excitation energies for the low-lying Rydberg states of CH_4.

Configuration	Excitation energy, eV
$2a_1^2\,2a_1^2\,t_2^6$	0.0
$1a_1^2\,2a_1^2\,t_2^5\,3sa_1$	9.4
$1a_1^2\,2a_1^2\,t_2^5\,3p_xt_2$	10.5
$1a_1^2\,2a_1^2\,t_2^5\,3p_zt_2$	10.7
$1a_1^2\,2a_1^2\,t_2^5\,4sa_1$	11.5

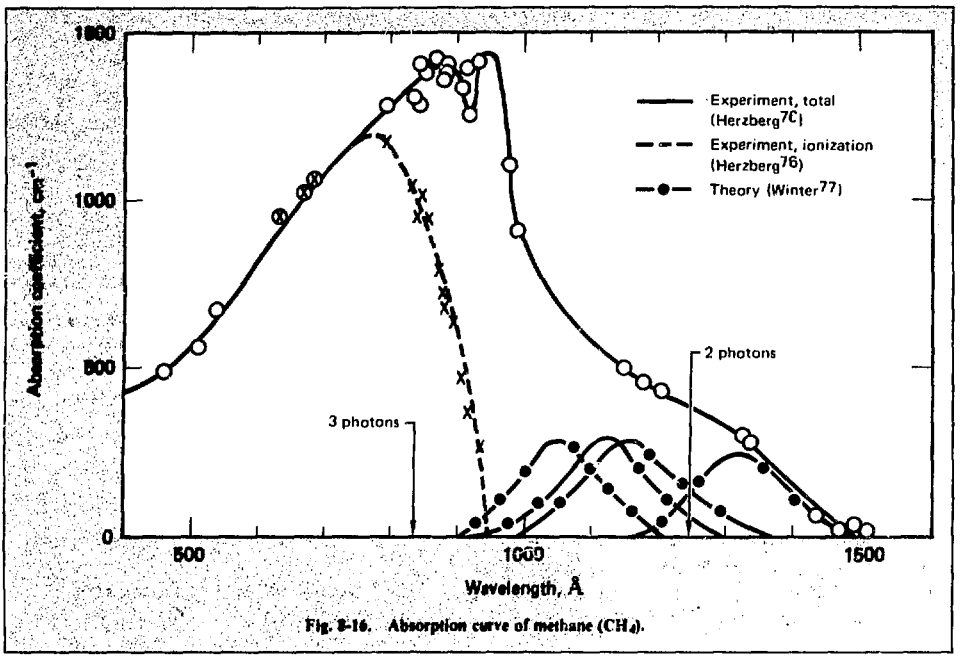

Fig. 8-16. Absorption curve of methane (CH_4).

the Improved Virtual Orbital (IVO) method and therefore may be in error by 1 to 5%. More accurate configuration-interaction calculations are in progress.

Using the IVO wave functions, we have also calculated the transition moments, both as a function of the principal quantum number of the Rydberg orbital and as a function of the symmetric-stretch vibrational coordinate. These quantities are required in order to calculate the gain and two-photon-absorption cross sections. Figure 8-17 shows the variation of the square of the transition moment for the nsa_1 series with the vibrational coordinate. We can see that, for highly excited levels, the transition moment is insensitive to the change of nuclear geometry, and in each case the curves are nearly linear. The variation of the transition moment with respect to principal quantum number n, for the equilibrium nuclear geometry of CH_4, is shown in Fig. 8-18. The curve closely follows a $1/n^3$ dependence for the higher members of the Rydberg series. This allows us to carry out a complete summation over intermediate states in the gain formula by extrapolation. The complete

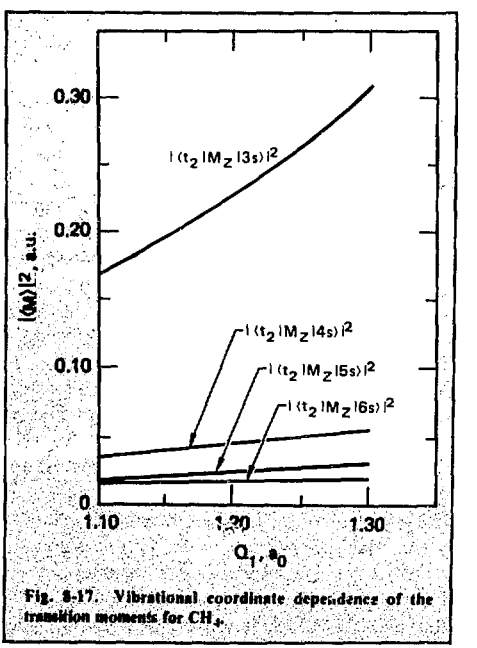

Fig. 8-17. Vibrational coordinate dependence of the transition moments for CH_4.

calculations are still in progress; however, using the calculated transition moments, we have been able to estimate the ratio of Raman gain and two-photon absorption coefficients at the KrF wavelength. We have taken the width of the Q-branch of CH_4 as 0.3 cm^{-1} and the bandwidth for two-photon absorption as 5000 cm^{-1}. Combining these data with transition moments, we estimate the gain-to-loss ratio to be about 10^{-3}. Our more accurate calculations will attempt to refine this estimate.

Pulse Shape Effects in Raman Compressors. As discussed in last year's annual report, the generation of radiation at the second Stokes frequency limits the extraction efficiency of Raman amplifiers. This limit is expressible as a function of the gain, efficiency, and pulse shape of the Stokes pulse:

$$F_S(G, \eta) \leqslant Z \equiv G_f/R\kappa \quad , \tag{61}$$

where Z is the performance quotient. The pulse-shape dependence of F_S is quite marked and is related to the distortion of the backward-wave Stokes pulse as it propagates through the cell. The front of the pulse steepens in a manner typical of a saturating amplifier. Thus, the peak of the Stokes pulse moves toward the front of the pulse and in fact moves faster than light. The pulse width also changes in a fashion depending on the input pulse shape and the degree of saturation. The net effect on the second Stokes gain is to simulate a dispersive medium in which the parasitic sees a pump pulse that is overtaking it. In this analogy, the gain at any point in the parasitic wave is given by an integral over that portion of the pump wave which it sees. In general, the maximum gain is minimized for a large relative velocity. In the compressor, this implies that the maximum parasitic gain, g_m = Max g(t), is minimized for large pulse distortion. Thus, by injecting a Stokes pulse that is positively skewed (forward-leaning), the achievable compression is reduced because such pulses distort the least. On the other hand, negatively skewed pulses distort the most and may increase the achievable compression, over equivalent Gaussian pulse shapes of the same FWHM, by as much as 20 to 40%. Figure 8-19 shows three pulse shapes that were used to

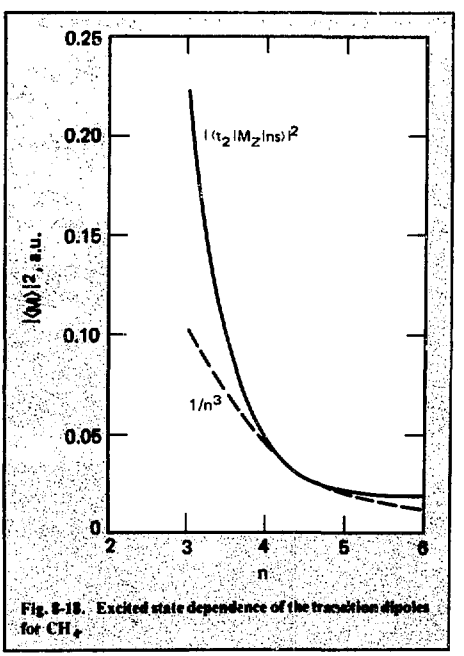

Fig. 8-18. Excited state dependence of the transition dipoles for CH_4.

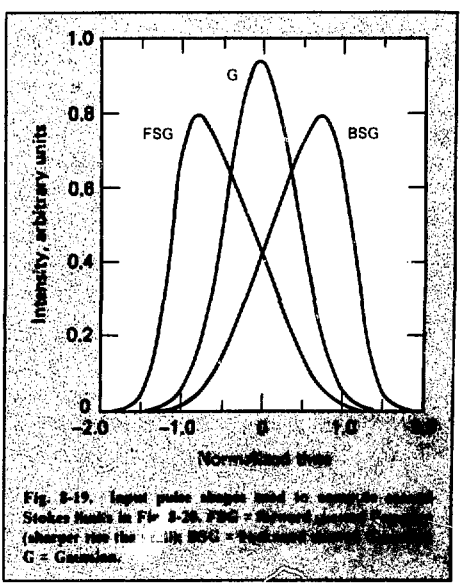

Fig. 8-19. Input pulse shapes used to examine optimum Stokes pulse shapes in Fig. 8-20. FSG = forward-skewed Gaussian (sharper rise than fall); BSG = backward-skewed Gaussian; G = Gaussian.

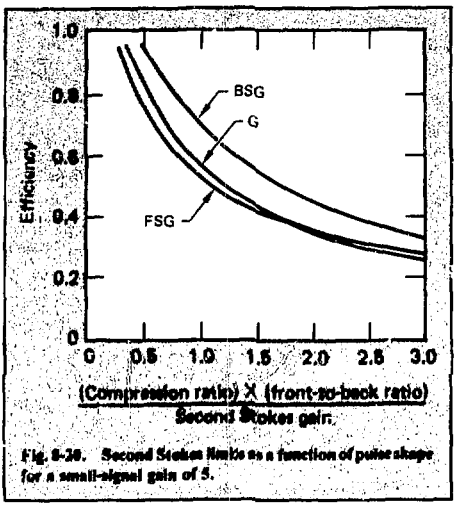

Fig. 8-20. Second Stokes limits as a function of pulse shape for a small-signal gain of 5.

recalculate the curves of achievable efficiency vs compression shown in Fig. 8-20. Apart from ambiguities associated with the definition of pulse width for skewed pulses, it is clear that there is considerable advantage to active pulse shaping.

What is the optimal pulse shape in the fusion context? In general, sharp rise times are undesirable; they lead to spiking and either subsequent hole-burning caused by second Stokes production or reduced efficiency. Consequently, several consecutive efficient amplifications appear to be unfeasible. The optimal injection pulse is negatively skewed, *but such pulses tend to increase in FWHM* during amplification. Negatively skewed pulses seem to be favored for efficient target coupling. This final-pulse shape could be achieved by pulse stacking rather than by active pulse shaping, allowing efficient amplification at the optimal shape for compressor performance.

The optimal pulse shape of a given total width is easily computed for arbitrary pump (i.e., KrF) pulse shapes. The Frantz–Nodvik theory predicts that the parasitic gain at the point x in the Stokes pulse is

$$g_{2S}(x) = R\frac{\partial}{\partial x}\int dy \ln\left\{\Phi(x) + \exp[-Gh(y)]\right\} , \quad (62)$$

where the saturation function is

$$\Phi(x) = -1 + \exp\left[S^{-1}\int_{-\infty}^{x} dx' I_S^{in}(x')\right] \quad (63)$$

and the pump pulse shape is

$$I_p^{in} h(y) = \int_{-\infty}^{y} dy' I_p^{in}(y') . \quad (64)$$

The problem is to minimize the maximum value of $g_{2S}(x)$, subject to the following conditions on Φ:

$$\Phi(x) = 0 \text{ for } x \leq 0 \ , \Phi(x) = \Phi \text{ for } x \geq \tau_S , \quad (65a)$$

$$\Phi = (e^{G\eta} - 1)/(e^{G} - e^{G\eta}) , \quad (65b)$$

where η is the extraction efficiency, held fixed. Now

$$\int_{G}^{\tau_S} dx\, g_{2S}(x) = R\int dy \ln\left[1 + \Phi e^{Gh(y)}\right] . \quad (66)$$

The problem reduces to minimizing the maximum value of $g_{2S}(x)$, subject to this integral condition. The solution is obviously

$$g_{2S}(x) = \text{constant} = g . \quad (67)$$

Thus, the optimal pulse shape is to be unfolded from the following implicit equation for $\Phi(x)$:

$$\frac{gx}{R\tau_p} = \int \frac{dy}{\tau_p} \ln\left\{1 + \Phi(x)\exp[Gh(y)]\right\} . \quad (68)$$

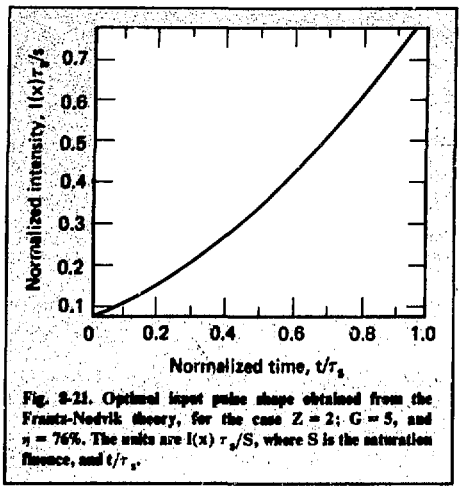

Fig. 8-21. Optimal input pulse shape obtained from the Frantz-Nodvik theory, for the case Z = 2; G = 5, and η = 76%. The units are I(x) τ_s/S, where S is the saturation fluence, and t/τ_s.

Figures 8-21 and 8-22 display the input pulse shape and output pulse shape, respectively, for a flat pump pulse obtained this way. The backward gain for this case is 5 and the performance quotient Z = 2; the extraction efficiency is 76%.

Of course, this is not to say that such pulses can be obtained in practice, where the effects of transiency and electro-optic switching response times influence the leading and trailing edges. However, the Frantz-Nodvik predictions obtained here may be taken as excellent guidelines for pulse shape optimization, representing an ideal case.

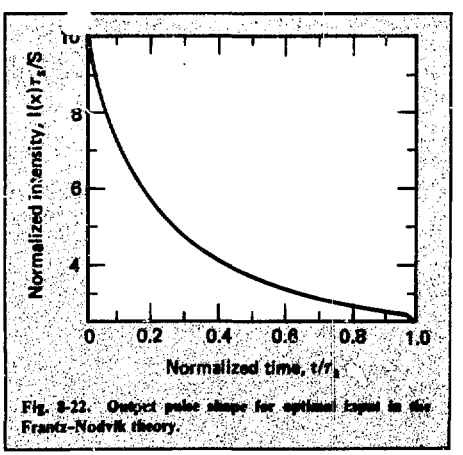

Fig. 8-22. Output pulse shape for optimal input in the Frantz-Nodvik theory.

Spatial and Temporal Inhomogeneities in Raman Amplifiers. Within the context of the Frantz–Nodvik theory, the gain in the backward amplifier is

$$G = J_p/S \quad . \tag{69}$$

To the extent that this expression is independent of the pump fluctuations, the backward amplifier is insensitive to them. A similar argument holds for the Stokes input fluctuations. On the other hand, if the fluctuations are rapid enough to cause the bandwidth to increase beyond the Raman line width, the gain drops and the pump components with frequencies that couple to the Stokes wave through the wings of the Raman line are not extracted efficiently. This is the familiar bandwidth limit, $\Delta\nu_p < \Delta\nu_R$.

If the inhomogeneity is random, then it will average out; if it is systematic, then different parts of the Stokes wave may experience different gains, leading to diffractive losses. Figure 8-23 illustrates this point. For a randomly inhomogeneous pump wave, the intensity seen by the Stokes wave varies along a ray in the Stokes wave. But when the pump wave intensity is integrated along many Stokes rays, the resulting integral varies among the Stokes rays by significantly less than the peak-to-valley variation in the pump. Specifically, the variation is reduced by t_c/t_p, where t_c is the pump correlation time along the Stokes rays. This approximation holds only for $t_c > T_2$, namely, for narrow-band pumping. It indicates that, in general, it is desirable to have t_c short, but not shorter than T_2. For a systematically inhomogeneous pump, this averaging does not occur. The variation in the small-signal gain exponent along a Stokes ray is the same as that of the pump.

For a forward Stokes ray copropagating with the pump wave, the small-signal gain exponent along the ray varies by proportionately as much as the pump intensity. Thus, temporal inhomogeneities increase the forward Stokes gain, increasing the forward loss, for both the random and systematic cases. Consequently, the desirable situation with regard to inhomogeneities finds the pump correlation time $t_c \approx nT_2$, where n is 2 to 5, and finds only random spatial inhomogeneities on the

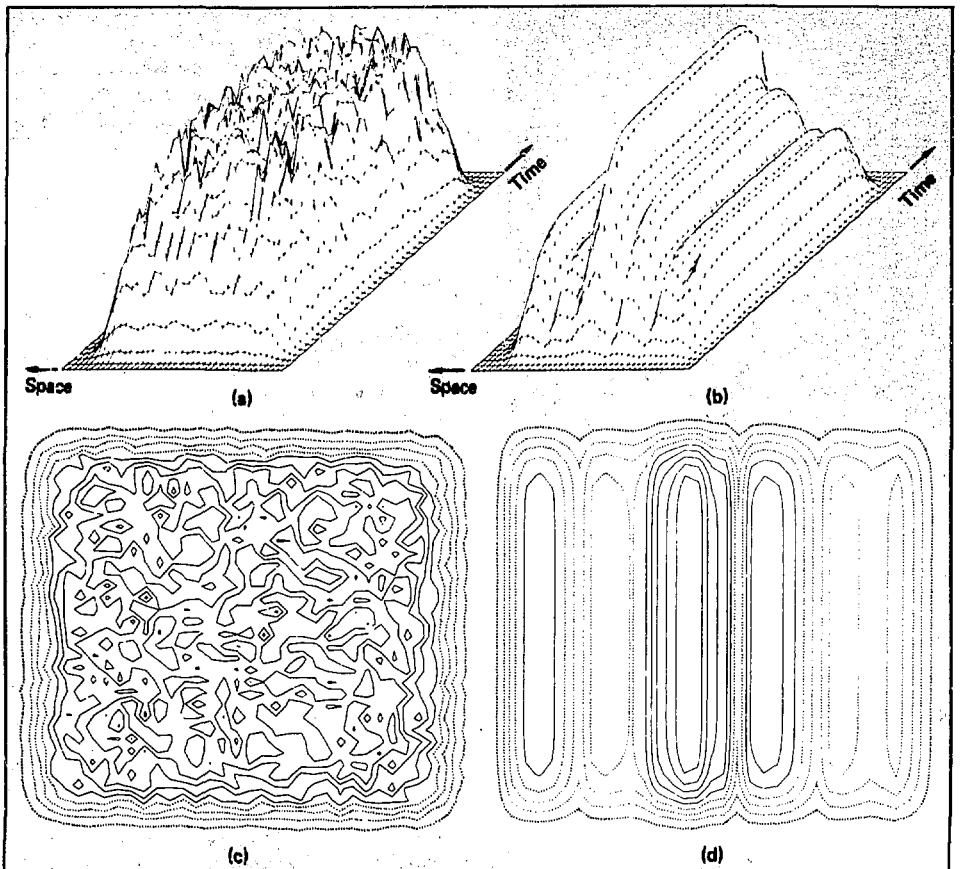

Fig. 8-23. Pump inhomogeneities. (a) Random pump inhomogeneities, which average out under narrow-band conditions. (b) Systematic pump inhomogeneities, which may lead to diffractive losses if sufficiently large. (c) Contour plot of (a). (d) Contour plot of (b).

pump wave. The desired transverse correlation length of the pump wave is determined by the angle between the pump and Stokes waves. In RAPIER, it must be larger than ~3 mm and considerably smaller than the transverse beam dimension.

An interesting effect associated with a pump wave structure containing a few well-defined modes is that the Stokes wave may diffract in a manner reminiscent of holography and phase conjugation experiments. The interference pattern must remain for several nanoseconds to have an effect; this is very unlikely in the KrF/CH_4 compressor.

References

76. G. Herzberg, *Electronic Spectra and Electronic Structure of Polyatomic Molecules*, vol. III of *Molecular Spectra and Molecular Structure* (Van Nostrand Reinhold, New York, 1966), p. 527.

77. N. Winter, Lawrence Livermore Laboratory, Livermore, Calif., private communication (Apr. 1978).

Authors

N. Winter

D. Eimerl

8.3.3 Group IVa Lasers

Modeling and Scaling the KrF Laser Medium. To date, high-power KrF lasers have operated in the 500-ns-to-1-μs regime with intrinsic medium efficiencies (i.e., laser energy extracted from the medium, divided by total energy deposited in the medium) of 9 to 10%.[78-82] These lasers have been operated in the oscillator configuration, producing 100 to 300 J of output energy.[78-83] Supporting KrF laser kinetic studies[78-81] have also addressed the 500-ns-to-1-μs regime of operation and have been quite successful in predicting laser performance characteristics. Our calculations with the KrF laser kinetics code[84] also compare favorably with experimental data obtained from these long-pulse, e-beam-excited systems. For example, AVCO reported[78,79] KrF laser experiments in which a 0.2%-F_2/4%-Kr/95.8%-Ar mixture at 1.7-atm pressure was excited for 600 ns by a 250-kV, 11.5-A/cm^2 e-beam; the measured intrinsic laser efficiency was 9%, with 70% oscillator output coupling. Our laser-media kinetics code[84] described in §2.3 predicts an efficiency of 9.2% for this device, which is well within uncertainties in deposition and reaction rates.

For KrF pulse-compressor systems,[85] the KrF pump laser will likely be operated at pulse lengths longer than 100 ns because of e-beam technology limits and shorter than 500 ns to minimize the total pulse compression required in the system. When the kinetic models that have been proven successful in analyzing long-pulse devices are used to evaluate KrF laser performance in this high-pump-power-density, short-pulse regime, they predict that the efficiency and maximum output intensity of the device increase. However, there are several kinetic processes that become more significant in this regime and, thus, may affect the predictions. These processes include the formation, vibrational relaxation, and collisional mixing and quenching of the B, C, and D states of the KrF molecule.

For example, in the short-pulse regime, the high e-beam pump power densities, 0.3 to 1 MW/cm^3, produce secondary electron densities in the range of 10^{15} to 10^{16} cm^{-3}. Under these circumstances, electron quenching of KrF excited states becomes a potentially serious problem, as illustrated by the parametric calculations presented in Fig. 8-24. These calculations were performed with our laser kinetics code[84] described in §2.3. Figure 8-24 shows the axial variation of the intrinsic medium efficiency and laser beam intensity, for a KrF amplifier containing a 0.3%-F_2/6%-Kr/93.7%-Ar mixture at 1-atm pressure. The e-beam pump power density was varied from 0.3 to 1 MW/cm^3. Pumping at 1 MW/cm^3 corresponds approximately to two-sided excitation with e-beam current densities of 100 A/cm^2 for 100 ns and 30% capture of the electron beam energy in the laser volume, conditions that are appropriate for square laser geometries and no guiding magnetic fields. The laser input intensity to the amplifier was held constant at 2 MW/cm^2. The calculations assume that the B and C states are fully mixed by collisional processes.

These results show a strong sensitivity to pump power density and electron quenching. In the absence of electron quenching, the highest efficiency and output flux occur at the highest pumping power considered, 1 MW/cm^3. However, when the electron-quenching rate constant is 10^{-7} cm^3/s and 3×10^{-7} cm^3/s, the highest efficiency is achieved at the lower pumping power density of 0.3 MW/cm^3. Electron quenching processes change both the gain and saturation characteristics of the amplifier. The ratio of net small-signal gain (g_0) to loss (γ), g_0/γ, is altered at high pump-power densities, changing the extraction efficiency of the amplifier.[85]

Although the magnitudes of the electron-quenching rate constants for KrF are not presently known, values for XeF have recently been reported.[86,87] These values vary from 2×10^{-8} cm^3/s (Ref. 86) to 2.8×10^{-7} cm^3/s (Ref. 87). Clearly, the uncertainty is quite significant. According to the results presented in Fig. 8-24, if the KrF electron-quenching rate constant lies in the upper end of this range, amplifier performance will be significantly affected. At present, our calculations indicate that, because of uncertainties in the kinetics of high pump-power densities, the intrinsic efficiencies of the KrF laser amplifiers for pulse compressor applications will be in the 10 to 15% range. Under these circumstances, maximum output fluxes will be 10 to 30 MW/cm^2. The pressure dependence of amplifier performance is shown in Fig. 8-25. These results indicate that optimal operation is expected to occur in the pressure range of 1 to 2 atm.

Figure 8-26 shows a plot based on computer simulation of the characteristic loss length γ^{-1}, small-signal gain coefficient, and gain-to-loss ratio for an atmospheric-pressure KrF laser, graphed as a function of volumetric power deposition. The beam

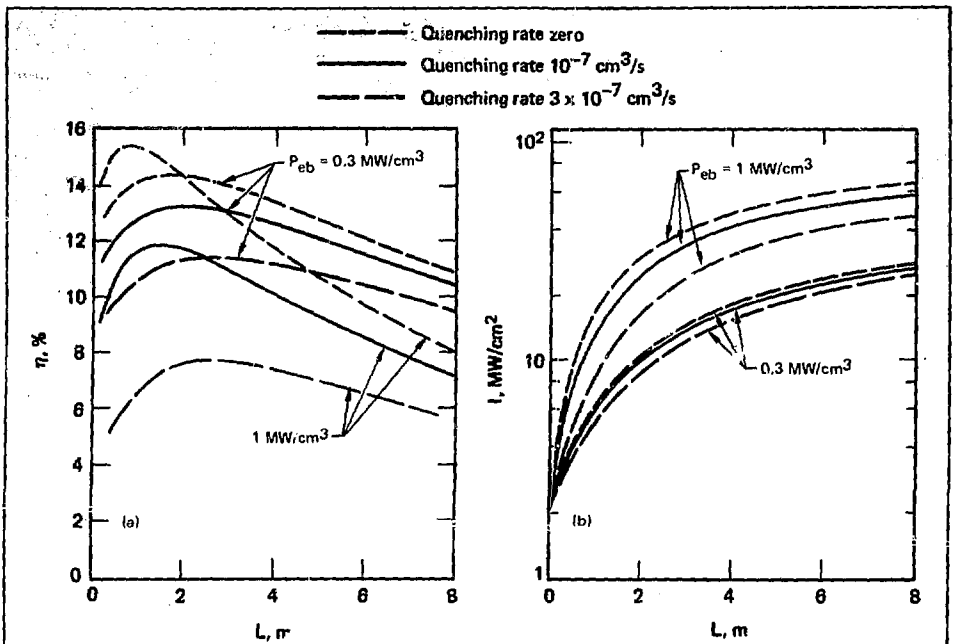

Fig. 8-24. Calculated axial variation of (a) intrinsic medium efficiency η, and (b) laser beam intensity, for a KrF amplifier containing a mixture of 0.3% F_2/6% Kr/93.7% Ar at 1-atm pressure. Two e-beam pump power densities are assumed: 0.3 and 1 MW/cm^3. The curves for each pump power density are parametric in the electron-quenching rate constant. Performance clearly degrades as the electron-quenching rate constant increases.

current densities that can be utilized to achieve these deposition rates are also shown, assuming two-sided excitation and efficient beam utilization. For cold-cathode e-guns, the maximum time during which power may be deposited in the gas scales is $J_{cb}^{-1/2}$ because of diode closure.[88] This time is also shown in the figure for the case of 20% growth in the deposition rate in the gas driving the pulse, assuming diode closure velocities of 3 cm/μs at high current densities and 2 cm/μs at low current densities. Use of magnetic guide fields may allow one to achieve higher beam current densities for longer pulse durations than those shown in Fig. 8-26. On the basis of this figure, it is clear that e-beam-pumped KrF amplifier systems of interest for large-scale pulse compressors should operate at high pump-power densities, $J_{eb} \approx 50$ A/cm^2. For these conditions, extraction efficiencies of 50% or more can be achieved with amplifier lengths of 1 to 2 m. Pump pulse durations in the range of 100 to 300 ns would be used. In addition, corresponding output fluxes could be in the range of 10 to 30 MW/cm^2, assuming that no deleterious kinetic effects arise at high deposition rates.

The laser intensity that can be drawn from the KrF medium at an extraction efficiency of 50% is roughly proportional to the gain-to-loss ratio, which scales approximately as $J_{eb}^{1/2}$. Thus, higher intensity operation should be possible at higher deposition rates. Figure 8-27 shows how the achievable intensity and fluence at 50% extraction efficiency for an e-beam-pumped KrF laser varies as a function of pulse length. The pulse duration is assumed as the maximum allowed by 20% diode closure. Thus, the deposition rate decreases as τ_p is increased. The plot shows that because the diode closure time scales as $J_{eb}^{-1/2}$ while intensity scales as $J_{eb}^{1/2}$, such amplifiers should be approximately constant-fluence devices. Consequently, for energy-intensive devices such as those that would make up

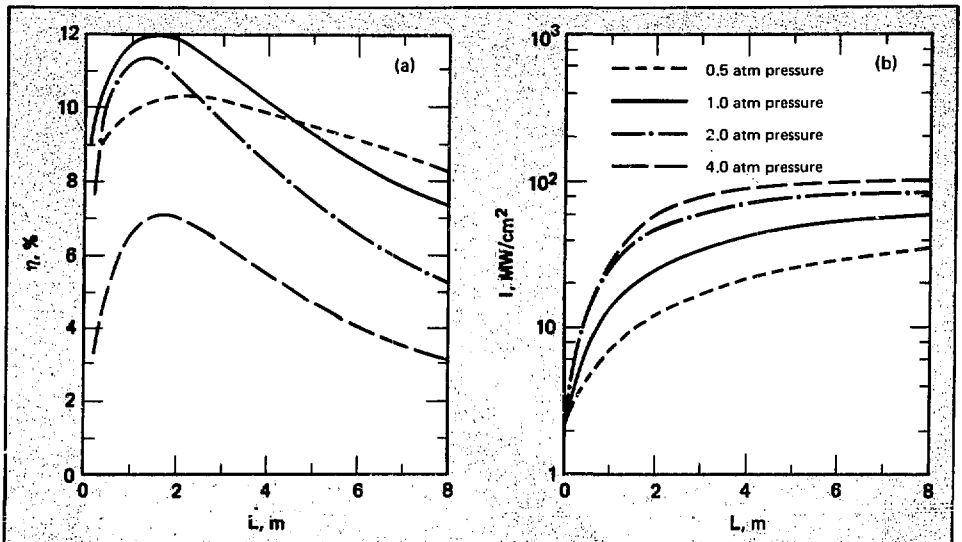

Fig. 8-25. Calculated axial variation of (a) intrinsic medium efficiency η, and (b) laser beam intensity, for a KrF amplifier containing a mixture of 0.3% F_2/6% Kr/93.7% Ar at four different pressures for an e-beam pump power density of 1 MW/cm³ · atm.

a 200-TW, 10-ns power-plant driver system, and for which the anticipated net pulse compressions are expected to be modest, technology considerations may favor pump pulses longer than 200 ns. However, for systems requiring high intensities and short pulse durations (a 1-TW, 1-ns device, for example), pulse compression and pulsed power technology tradeoffs may force one to work at shorter excitation pulses and at the highest possible intensity.

Note that any technique that reduces or eliminates diode closure in generating the e-beam (magnetic fields or hot cathodes, for example) will allow the high deposition rates associated with short pulses to be maintained for longer pulse durations, ultimately being limited by foil heating and depletion of F_2 in the medium.[89,90] In this case, the fluence that could be achieved would increase as τ_p rather than remaining roughly constant. Energy-intensive devices would then favor longer pump pulses. Ultimately, depletion of F_2 limits the extractable fluence. Assuming large-scale devices with extraction efficiencies of 50%, and allowing depletion of F_2 to one-half its initial value, one finds that typical laser mixtures are limited to extractable energy densities of about 15 J/litre. For the laser gain lengths anticipated, 2 to 3 m, this energy density value limits achievable fluence to about 4 J/cm² or 40 kJ/m².

Figure 8-27 shows that KrF amplifiers yielding 20-30 kJ/m² of pump aperture can be anticipated. The size of any individual aperture is constrained in a number of ways. One limit on transverse dimensions is the onset of parasitic depumping and superfluorescence in the transverse dimensions. This problem can be alleviated by use of input fields in excess of the saturation intensity and by paying careful attention to minimizing reflectivity of the laser walls (e-beam foils). Assuming amplification from an input of about 2 saturation intensities to about 20 saturation intensities, and assuming small-signal gain coefficients of 10 to 20/m, one can see that transverse dimensions of about 1 m are not unreasonable.

At lower deposition rates and gain coefficients, the gain in the medium should be easier to control. Detailed analysis of this phenomenon, and experimental demonstration of efficient narrow-band extraction in the presence of large transverse gains, are clearly important activities for the future. The use of electron beams to pump a KrF amplifier scaled to a "gain control" limit will require some control of the self-pinching of the e-beam in the

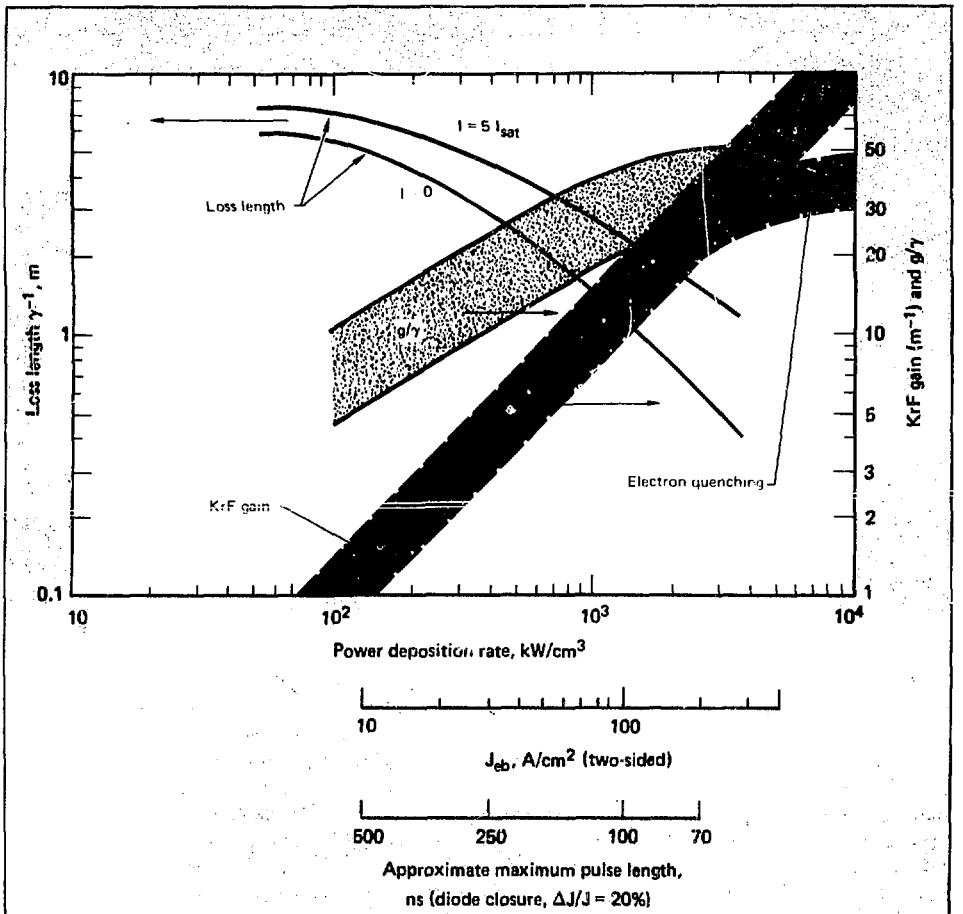

Fig. 8-26. Dependence of KrF laser performance parameters on e-beam volumetric pump power and current density. The loss length γ^{-1} increases with cavity/amplifier flux because of depletion of Kr_2F^*. At high deposition rates, estimated to be about 1 MW/cm^3, electron quenching decreases the gain from that otherwise expected. Pressure is 1 atm.

diode. This control can be achieved with magnetic guide fields, the use of multiple diodes per side of the amplifier (diode modularization), or some combination of both. Electron beam pinch most significantly impacts the short-pulse-duration, high-current-density systems, since the achievable e-beam height per module scales as $J_{eb}^{-1/2}$, in the absence of guide fields. Detailed trade-offs of the optimum-pinch-control technique remain to be determined. Preliminary estimates suggest that KrF amplifiers of about 0.5-m^2 output aperture should be realizable, yielding single-aperture energies of about 10 to 15 kJ.

References

78. M. Rokni, J. A. Mangano, J. H. Jacob, and J. C. Hsia, *IEEE J. Quant. Electron.* QE-14, 464 (1978).
79. J. C. Hsia, J. H. Jacob, J. A. Mangano, and M. Rokni, *One Meter KrF Laser System*, AVCO Semiannual Rept., Aug. 23, 1976-Feb. 22, 1977, for DARPA.

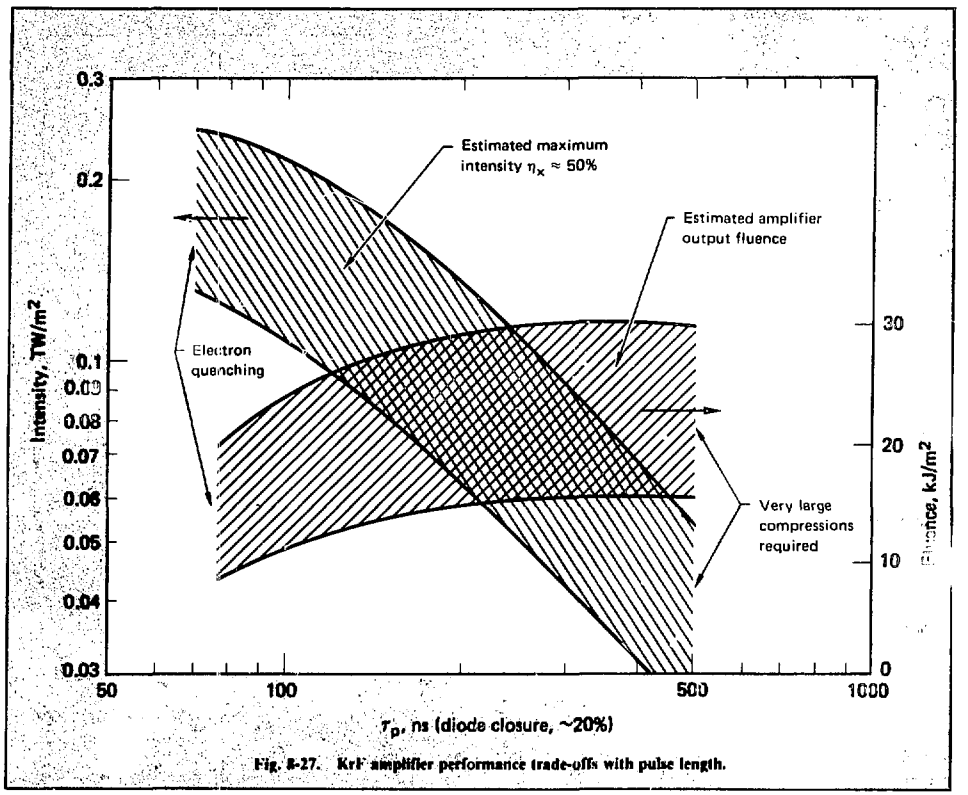

Fig. 8-27. KrF amplifier performance trade-offs with pulse length.

80. J. H. Jacob and J. A. Mangano, *Appl. Phys Lett.* **28**, 724 (1976).
81. W. B. Lacina and D. B. Cohn, *Appl. Phys. Lett.* **32**, 106 (1976).
82. R. O. Hunter, Western Research, San Diego, Calif., private communication (1978).
83. J. M. Hoffman, A. K. Hayes, and G. C. Tisone, *Appl. Phys. Lett.* **28**, 538 (1976).
84. R. A. Haas, W. L. Morgan, R. D. Franklin, and J. Harvey, *Laser Fusion Annual Report—1977*, Lawrence Livermore Laboratory, Calif., UCRL-50021-77 (1978), §6.2.1; see also §2.3 of this report.
85. J. J. Ewing, R. A. Haas, J. C. Swingle, E. V. George, and W. F. Krupke, *IEEE J. Quant. Electron.* **QE-15**, 368 (1979).
86. L. A. Newman, "Kinetic Operation of the XeF* Waveguide Laser Excited by a Capacitively Coupled Discharge," Proc. 31st Annual Gaseous Electronics Conference, Oct. 17-20, 1978, *Bull. Amer. Phys. Soc.* (to be published).
87. D. W. Trainor, M. Rokni, J. H. Jacob, and J. A. Mangano, "Temperature Effects on the Quenching Kinetics of XeF* in E-beam Pumped Ne/Xe/F_2 Mixtures," Proc. 31st Annual Gaseous Electronics Conference, *Bull. Amer. Phys. Soc.* (to be published).
88. J. D. Daugherty, "Electron Beam Ionized Lasers," in *Principles of Laser Plasmas*, G. Bekefi, Ed. (John Wiley & Sons, New York, 1976), pp. 369-419.
89. W. L. Nighan, *Appl. Phys. Lett.* **32**, 297 (1978).
90. W. L. Nighan, *Appl. Phys. Lett.* **32**, 424 (1978).

Author	Major Contributors
R. A. Haas	J. J. Ewing
	W. L. Morgan
	J. Harvey

KrF Fluorescence Spectra. Our experience in operating KrF discharge lasers under conditions providing for narrow-band output radiation suggests that the spectral gain profile behaves homogeneously. To understand these observations and to help provide a basis for predicting spectral

gain saturation of excimers under deficiency excitation conditions, we have studied the dependence of the KrF $III_{1/2} \rightarrow I_{1/2}$ fluorescence emission on the rotational excitation of the upper state. The rotational quantum number was fixed at J = 0, 30, 60, and 120, and the A-coefficient for bound-free emission was computed for the first three vibrational levels. The potential energy curves of Dunning and Hay[91] were used. The total intensity for each choice of J is plotted in Fig. 8-28. Note that, for a temperature of 450 K, the average rotational-level population of KrF has its maximum at J = 30. The curves for J = 0, 30, and 60 are similar; however, the emission for J = 120 is considerably less structured. The appearance is similar to that of the low pressure spectra of Golde and Thrush[92] and Velazco and Setser,[93] indicating that the low pressure spectra likely have a large degree of rotational excitation.

An important question is the effect of rotational excitation on the spectral homogeneity of the laser transition. The rotational effects enter primarily by adding a repulsive $J(J + 1)/2R^2$ term to the potential energy of the nuclei. For low values of J, the ground-state potential curve is parallel to the excited-state curve in the Franck–Condon region, and the contributions to the fluorescence from individual vibrational levels peak essentially at a common wavelength. For large values of J, the ground state is more repulsive in the Franck–Condon region, and the contributions from the low-lying vibrational levels do not overlap as well.

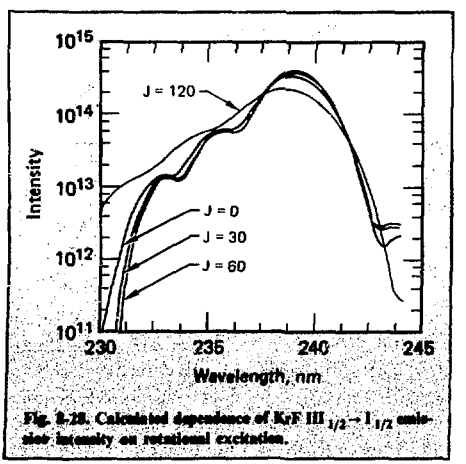

Fig. 8-28. Calculated dependence of KrF $III_{1/2} \rightarrow I_{1/2}$ emission intensity on rotational excitation.

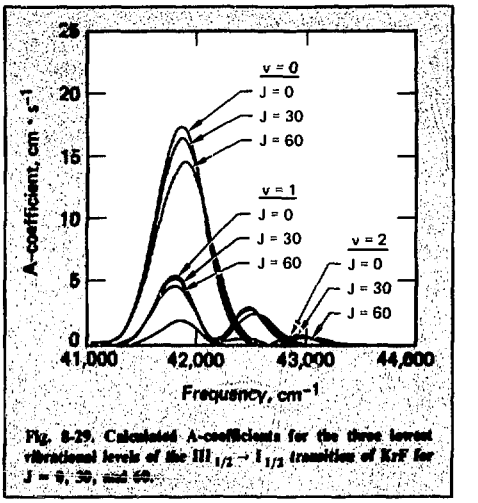

Fig. 8-29. Calculated A-coefficients for the three lowest vibrational levels of the $III_{1/2} \rightarrow I_{1/2}$ transition of KrF for J = 0, 30, and 60.

However, as the calculated A-coefficients in Fig. 8-29 illustrate, the transition remains largely homogeneous for reasonable values of J.

References

91. T. H. Dunning and P. J. Hay, *J. Chem. Phys.* **69**, 134 (1978).
92. M. F. Golde and B. A. Thrush, *Chem. Phys. Lett.* **29**, 486 (1974).
93. J. E. Velazco and D. W. Setser, *J. Chem. Phys.* **62**, 1990 (1975).

Author

N. Winter

8.3.4 RAPIER Pulse-Compressor Test Bed

The design and construction of the RAPIER pulse-compressor test bed were initiated in 1978. RAPIER, an acronym for *Raman amplifier pumped by intensified excimer radiation*, will significantly extend our research capabilities for studying Raman pulse-compression techniques. The devices developed for this system will be used to:

- Extend Raman compression/extraction measurements to the larger apertures, and lower Raman-scatterer densities that scaling studies show will be required for large-scale devices.
- Develop the technologies associated with hybrid pulse-stacking/Raman-compression schemes.

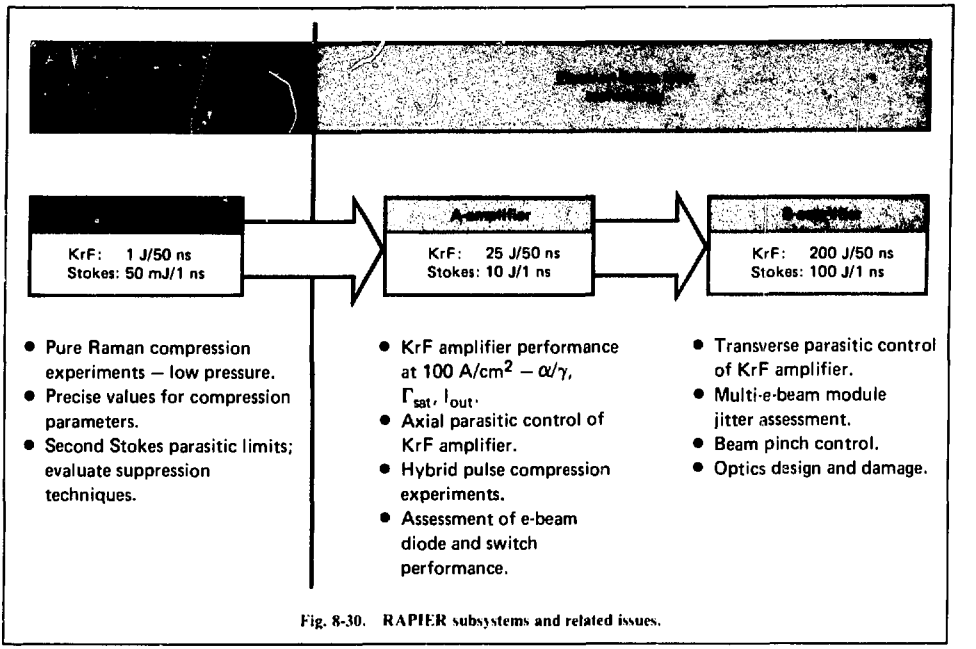

Fig. 8-30. RAPIER subsystems and related issues.

• Gain an understanding of the scaling limitations of pump lasers operating in the power excitation and pulse duration ranges of interest for fusion applications.

A major objective is to demonstrate efficient hybrid pulse compression with compression factors in excess of 30, while evaluating the important physics, technology, and scaling issues that bear on these hybrid systems. To attain this objective, the system is being constructed so that experiments can be performed at successively higher levels of KrF pump energy. An array of discharge-excited KrF lasers has been designed, fabricated, and tested to provide about 1 J of narrow-bandwidth excimer radiation in a 30-ns pulse with high beam quality. This array will serve as a front end for driving larger KrF amplifiers, and it will also provide pump energy to conduct pure Raman compression studies at the joule level.

For hybrid compressor experiments at the nominal 10-J level, we have designed an e-beam-pumped KrF laser amplifier capable of producing 25 J in 50-ns pulses. This device, called the A-amplifier, has been constructed and is about to begin testing and service as a laser. KrF pump radiation from the front-end subsystem will be linked to the A-amplifier to study some aspects of controlling and scaling KrF amplifiers and to provide quality radiation for compressor experiments. Ultimately, the output of the A-amplifier will be coupled to a larger e-beam-driven laser amplifier capable of producing 200 J of output. This amplifier, called the B-amplifier, is in the design phase.

The issues to be addressed by the major RAPIER subsystems are summarized in Fig. 8-30. The following subsections describe the 1978 progress in developing and integrating the components of this system as a research and development facility. An overall layout of the system, to be used for pulse compression experiments at the 10-J level during 1979, is shown in Fig. 8-31.

Author

J. J. Ewing

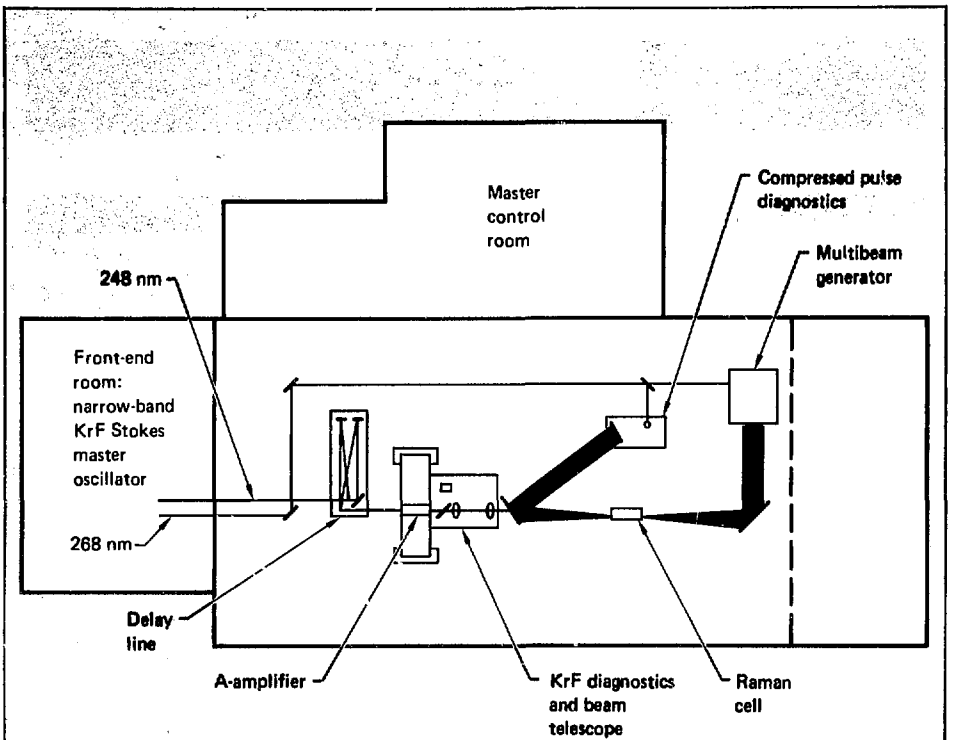

Fig. 8-31. Layout of RAPIER compressor-stacker experiments.

Front-End Subsystem. The RAPIER front-end subsystem consists of several double-discharge rare-gas-halide (RGH) laser gain media and Raman gas cells. The system will serve two purposes: (1) to investigate a variety of basic physics issues concerning the backward-wave Raman pulse compression technique, and (2) to deliver pump pulses of high spectral and spatial quality for frequency-locking the larger e-beam-excited KrF amplifiers, as well as tailored Stokes pulses to be used with the larger Raman cells. In 1978, our efforts concentrated on the design, fabrication, and testing of the system, along with the generation of KrF laser pump pulses at 248 nm and about 1 J. This coherent source will drive Raman oscillator/amplifier chains operating at the first Stokes frequency for the Q branch of the ν_1 mode in CH_4 at 268 nm. In this subsection, we discuss the performance features of the front end and give an outline of some experiments to be undertaken with this facility.

A general layout of the RAPIER front end is given in Fig. 8-32. A photograph of the completed facility is shown in Fig. 8-33. Narrow-band (~0.15-cm^{-1}) 248-nm radiation of about 150 mJ in a 20-ns pulse is generated in a master-oscillator/regenerative-amplifier (MORA), denoted in Fig. 8-32 as α_0 and α_1. The MORA output is passed through a spatial filter and double-passed through two larger amplifiers, denoted as β amplifiers, to produce a line-narrowed KrF laser pulse of about 1 J. The two-pass operation can be utilized as shown to extract the maximum possible energy from the 50-ns-long β_0 and β_1 gain media, by amplifying the 20-ns-long MORA pulse. Inherent inductance differences between the α and larger β devices are responsible for the difference in gain

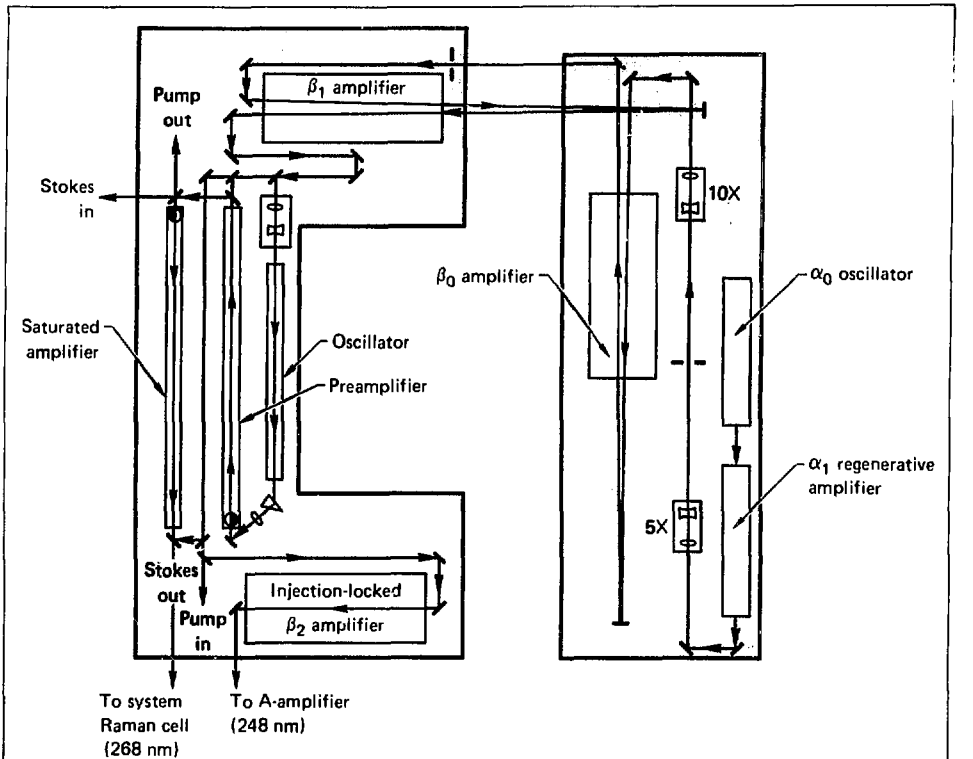

Fig. 8-32. General layout of the RAPIER front-end facility. The KrF discharge-laser medium will produce about 1-J pump pulses at 248 nm with line width ≈ 0.15 cm^{-1}. An alternate system architecture is described in the text.

pulse widths. Separate studies, using the β sources with stable oscillator configurations, resulted in reliable individual energy outputs of about 0.6 J. We have also evaluated an injection-locking architecture, as an alternative to that shown in Fig. 8-32, in which the MORA pulse is injected into an unstable resonator cavity for the β_0 amplifier. To date, these tests have shown line-narrowed outputs with pulse widths of about 30 ns and energies in excess of 500 mJ. Additional amplification is available by single-pass extraction of the β_1 amplifier, shown on the upper part of the C-shaped table in Fig. 8-32. Preliminary nonoptimized total output energies of 950 mJ in 30 ns have been measured, using the MORA β_0 injection-locked, β_1 single-pass layout. Selection of the final experimental configuration, from these two options, to generate the 1-J KrF Raman pump pulse will be dictated by relatively easy trade-offs of optical alignment and maintenance for pulsed power timing.

For the Raman pulse-compression experiments, the line-narrowed 1-J KrF laser pulse is split into three beams, which are directed into methane-filled Raman cells on the C-shaped table, as shown in Fig. 8-32. About 10 to 20% of the KrF pump energy is directed into the right-hand cell, which serves as the system Raman oscillator. The 268-nm coherent radiation is generated by forward scattering at the first Stokes frequency. A prism separates the 268-nm output from the KrF pump and higher-order Stokes beams. Two stages of backward-wave

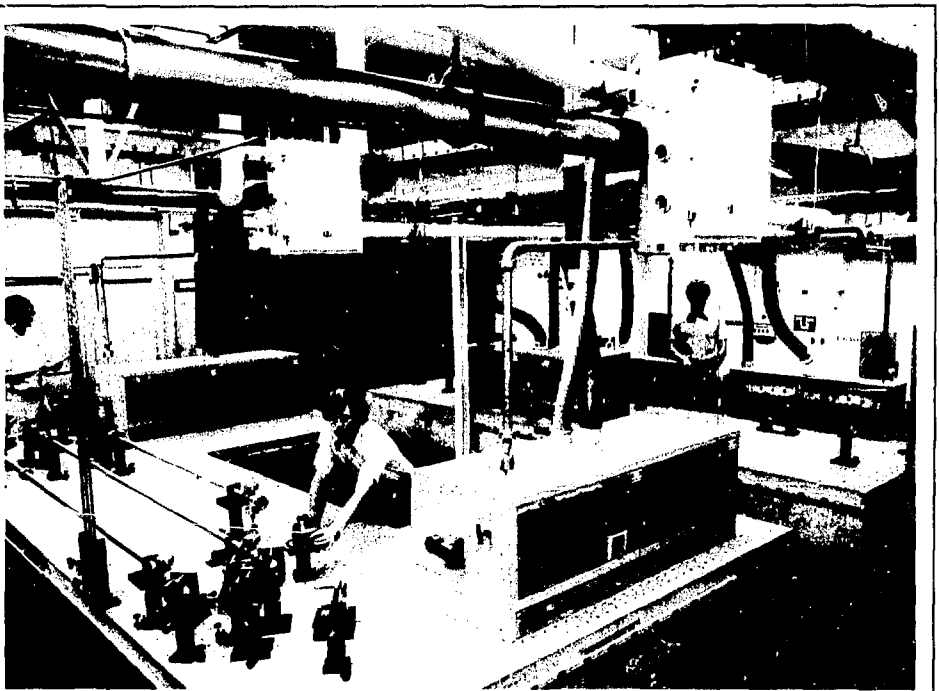

Fig. 8-33. Photograph of the completed RAPIER front-end facility.

Raman amplification and compression are then achieved in the other two Raman cells. (For optimal energy extraction from the Raman cells, future plans include time-tailoring the 268-nm pulse using established pulse-altering techniques.) The KrF and Raman beam lines are arranged so that the counter-propagating beams reach the methane cell boundaries at the same time. They are denoted in Fig. 8-32 by the two half-black, half-white circles.

For our initial studies, the 268-nm wave exits the middle preamplifier cell with a pulse width of about 3 ns, because of "geometrical pulse-shortening" caused by passage of the relatively long Stokes wave (20 or 30 ns, depending on the particular generation scheme selected for the 1-J pump) through a correspondingly long KrF pulse. The latter parts of this Stokes beam see reduced backward-Raman gain, because initial parts of the KrF pulse have already emerged from the small-signal middle cell. Finally, a dichroic mirror directs the Stokes pulse to the third Raman cell for additional, saturated, backward-wave amplification. About 50% of the initial 1-J KrF pump pulse is used in this saturated amplifier, and about half of it, i.e. $\gtrsim$250 mJ, will be converted into the "Stokes out" signal shown in Fig. 8-32.

A pulse width of about 1 ns is anticipated. The pulse width will be determined primarily by gain-steepening processes in the last Raman amplifier. The final Stokes output will be diagnosed in a variety of independent experimental studies. The KrF beam that injection-locks the KrF A-amplifier is produced by injection-locking the β_2 amplifier shown in Fig. 8-32, using a small fraction of the 1-J KrF pump beam that drives the Raman cells.

As indicated in Fig. 8-32, two types of double-discharge gain media are employed in the RAPIER front-end facility, designated either as α or β units. They represent the state of the art in RGH laser design and were developed and fabricated at LLL.[94]

The basic fast-pulse, RGH discharge laser approach is derived from fast-pulse CO_2 TEA laser designs and is described in the literature.[95] The α and β discharge media nominally produce about 0.1 and 1 J output energy, respectively, when operated as KrF lasers. Such discharge sources will be limited to no more than a few joules of available energy with apertures of several cm^2. However, their advantages of simplicity, ruggedness, and reliability make them preferred initial choices for front-end use.

For the α laser, the active gas mixture is preionized by ultraviolet radiation, from an array of resistor-ballasted spark pins, a few hundred nanoseconds before application of the main discharge voltage. The discharge volume of 0.5 × 2 × 100 cm^3 is excited by a pulse-forming circuit composed of barium titanate capacitors closely coupled to the laser body to reduce device inductance. The laser body is machined from Teflon to ensure fluorine compatibility and is equipped with CaF_2 Brewster-angle windows. The three-component laser gas mixture is set to pressures of about 1000 Torr; it consists of 0.4% F_2, 10% Kr, and with the balance He. When driven by a Marx bank circuit delivering a few joules at 60 kV, with the laser cavity formed by a high reflectance mirror and a quartz flat, this laser produced an output energy of 150 mJ in a 20-ns pulse.

The β amplifier shown in Fig. 8-34 is a geometrically scaled version of the unit. Its discharge volume is 1 × 4 × 100 cm^3, with the gain region surrounded by a glass envelope. The electrodes are secured by unique vacuum-tight metal supports passing through the glass envelope. The fast discharge required for uniform excitation of the gas is also obtained by pulse-charging an array of capacitors positioned along the discharge electrodes, which generate a 90-kV voltage pulse across the electrode structure. Ultraviolet preionization of the KrF laser medium for 800 ns, before application of the main discharge voltage, is provided by a series of sparks created along two parallel glass rods appropriately wrapped with small copper strips. At a total pressure of 1500 Torr, consisting of 0.2% F_2,

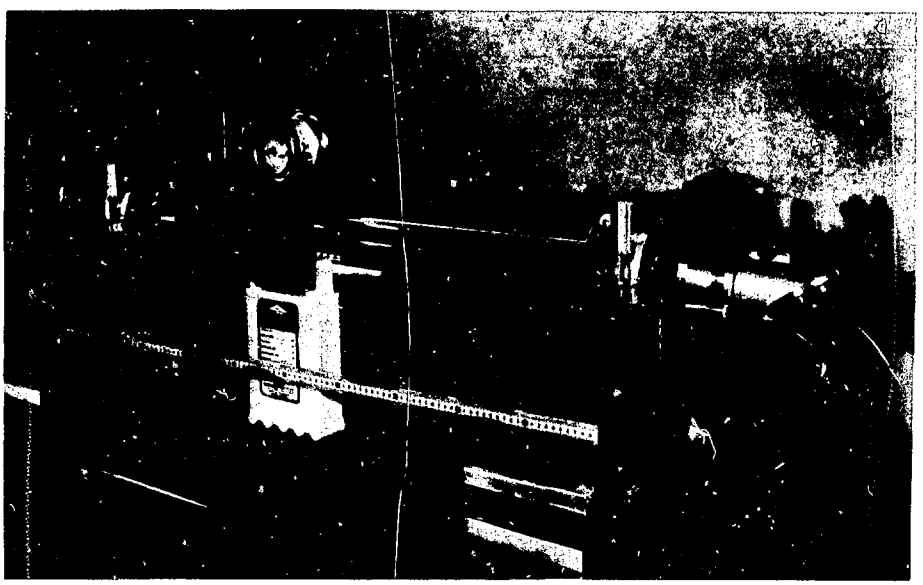

Fig. 8-34. Assembled β-size KrF discharge amplifier. Laser outputs of about 0.6 J in $\lesssim$50-ns-long pulses have been recorded with this unit. The main discharge energy is transferred from the 0.05-μF capacitor (in white) to the series of barium titanate capacitors (in red) that are close-coupled to the main discharge electrodes.

5% Kr, and the remainder He, about 0.6 J of KrF laser energy is extracted when the β amplifiers are outfitted with large-radius cavity mirrors having reflectivities of 98% and 4%.

Both the α and β devices are well engineered, compact and reliable. Successful operation of the scaled α amplifiers indicates that development of somewhat larger and more energetic amplifiers using discharge-excited RGH gain media may be possible. This ongoing effort is described in §8.5.3.

Provision of the pulsed electrical power for the RAPIER front-end gain media, shown in Fig. 8-32, represents a challenging electrical engineering exercise when considered in conjunction with the requirements of low-discharge time jitter ($\lesssim$1 ns), fast pulse rise times ($\lesssim$10 ns), and reliability of the various modularized electrical power units at voltage levels up to approximately 90 kV.

The laser system electronics are devices that convert commercially available low power to fast pulsed power, satisfying the needs of the α and β gain media. Figure 8-35 presents a block diagram of the major components comprising the RAPIER front-end electronics system. Line power is raised to voltages ranging from 25 to 90 kV in the various system elements. The units in the system provide energy storage and switching to time-integrate the line voltage into the proper high-voltage pulses. The five laser media present in the current system, i.e., α_0, α_1, β_0, β_1, and β_2, are represented by the shaded

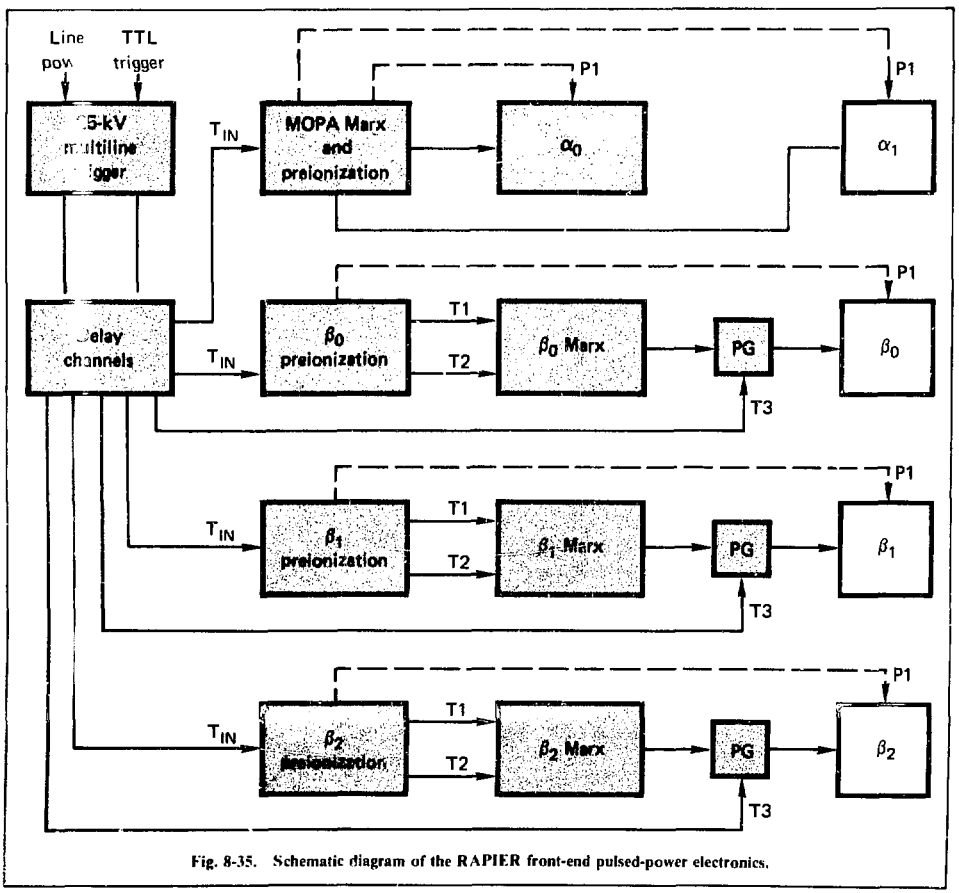

Fig. 8-35. Schematic diagram of the RAPIER front-end pulsed-power electronics.

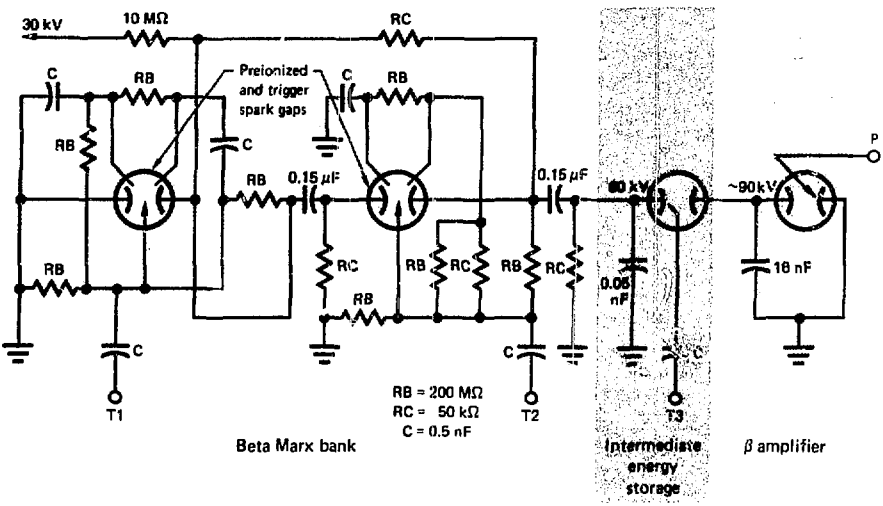

Fig. 8-36. Diagram detailing the pulsed-power circuitry for a representative β discharge amplifier. Discharge energies ~100 J are switched at ~ 90 kV with pulse rise times of 10 ns.

boxes in Fig. 8-35. Each gain medium has its energy supplied by functionally unique, but modularly similar, conditioning circuits.

Time synchronization of the system occurs at the 25-kV multiline trigger generator (MLT) and companion delay channels. The MLT provides a maximum of 12 trigger pulses synchronized to each other within 0.5 ns. The indicated delay chassis is used to fire each laser in the chain serially at the required times. In addition to the MLT, delay channels, and gain media, the system includes a dual-output Marx bank, three single-ended Marx banks, preionization units, and peaking gaps. All modules are interconnected through a network of interchangeable high-voltage connectors and cables. Additional electrical subsystems deal with data acquisition and total system control. Presently, these functions are performed manually in conjunction with shielded electrical cables and an 80-dB screen room. Future plans may incorporate automated system control and synchronized data-analysis techniques using minicomputers.

Figure 8-36 shows a schematic diagram for the pulsed power circuitry that delivers electrical energy to a single, representative β discharge amplifier. The two-stage Marx bank unit uses 0.15-μF capacitors that are initially de-charged to V = 30 kV, with no voltage appearing across the gain media. At this time, all the high-voltage spark gap switches are open and become midplane-biased at V/2 from the dc supply. Appropriate grounding and charging resistors, along with pulse isolation inductors, are utilized but are omitted from Fig. 8-36 for clarity of presentation. Next, the locations indicated as T1 and T2 receive trigger pulses from a preionization supply (not shown) that also helps generate a bath of ultraviolet light to ionize the active gas medium at the point designated as P, through the use of a series of fast sparks lasting about 800 ns. Upon application of the pulses at T1 and T2, the preionized, air-filled switches close, resulting in erection of the Marx bank voltage to 2 V or 60 kV at the 0.05-μF capacitor. To minimize losses and overall system inductance, five parallel high-voltage cables carry the Marx pulse to this intermediate storage capacitor. Final transfer of this energy proceeds at 90 kV to the 16-nF barium titanite capacitor assembly connected to the amplifier electrodes. The discharge energy can be transferred either by "overvoltaging" the preionized, air-filled spark gap at the 0.05-μF capacitor, or by command-triggering through application of a trigger pulse at T3 from the MLT

trigger unit. Similar circuitry energizes the discharges.

The use of pulsed, instead of static, powering of the discharge devices greatly reduces the size, weight, construction cost, and complexity of the driving electronics. An equivalent dc-charged device would require approximately three times the volume and would have to be encapsulated in oil or in a high-pressure gas atmosphere to prevent air breakdown. Thus, the fast-pulse methodology just described provides a straightforward means to apply discharge excitation energies at voltages very much in excess of the dc gas breakdown values.

Numerous basic research studies have been planned for the front-end facility, in addition to providing the tailored spectral, temporal, and spatial pulses at the 248-nm pump and 268-nm Stokes wavelengths required by successive stages of the RAPIER test bed. Included among these studies will be:

- Backward-wave Raman pulse compression experiments at the 1-J pump level, including generation of data at reduced methane pressures and increased apertures compared with earlier investigations.[96] Intensities in the near term will be more than 10 times greater than those for the prior work. The lower pressure tests will provide information on compressor properties that are more representative of scaled systems. The larger apertures of the RAPIER front end, compared with apertures previously used in Raman compression experiments, may enable us to verify the anticipated unimportance of off-axis parasitic processes, such as four-wave mixing, which can diminish the magnitude of the backward gain mechanisms. Such effects could not be suitably evaluated in the previous small-Fresnel-number experiments.
- Evaluation of the backward second-Stokes gain to help determine limiting values of backward first-Stokes intensity that can be accommodated in scaled Raman compressors.
- Methods to suppress the gain at the backward second-Stokes frequency by use of selective absorbers that would allow for propagation of significantly increased first-Stokes intensities.
- Alternatively, the evaluation of Raman pulse compression, using the first *and* higher-order Stokes frequencies. The resultant chromatic irradiation of fusion targets may appreciably enhance laser energy coupling and reduce the effect of competing processes such as stimulated, backward Brillouin scattering.

References

94. J. Goldhar and J. R. Murray, *Opt. Lett.* 1, 199 (1977).
95. R. Burnham and N. Djeu, *Appl. Phys. Lett.* **29**, 707 (1976); T. R. Loree, P. B. Scott, and R. C. Sze, in *Electronic Transition Lasers II*, L. E. Wilson, S. N. Suchard, and S. I. Steinfeld, Eds. (MIT Press, Cambridge, Mass., 1977), p. 35; R. C. Sze and T. R. Loree, *IEEE J. Quant. Electron.* **QE-14**, 944 (1979).
96. J. R. Murray, J. Goldhar, and A. Szoke, *Appl. Phys. Lett.* **32**, 551 (1978); J. R. Murray, J. Goldhar, D. Eimerl, and A. Szoke, *Appl. Phys. Lett.* **33**, 399 (1978).

Authors

R. Jacobs
S. Brown
R. Calliger

Major Contributors

J. Goldhar
J. Murray
R. Rapoport
J. Swingle
N. Nielsen

A-Amplifier. Preliminary analysis of various hybrid pulse-compression schemes (pulse stacking/Raman compression) indicates that a KrF beam energy of at least 25 J in a 50-ns pulse will be required to experimentally explore these system concepts. This level of KrF pulse energy is most readily achieved with excitation of the KrF medium by an electron beam. Moreover, this type of excitation will be required in all larger KrF pump systems. Therefore, we have initiated the development of such systems with the design of the e-beam-driven A-amplifier to provide the minimum required KrF pump radiation.

Additional technical requirements, in terms of command triggering and temporal jitter, are placed on the A-amplifier design for pulse-stacking experiments. The jitter of the laser system needs to be on the order of 1 ns for good temporal fill factors. To ensure reasonably constant laser pump intensity for Raman experiments, the rise time of the KrF laser (and, consequently, the rise time of the pulsed power driving this laser) should be a small fraction of the pulse length. Thus, we sought to build a device that would be triggerable with less than 1 ns jitter and have rise times of the order of 10 ns. Good geometric fill factors and ASE control of the KrF pump medium also imply an optical length for the overall system of about 10 times the length of the active medium, which is roughly 50 cm for the KrF laser and 200 cm for the Raman cell. This defines a

minimum room size for the experiments of about 20 m. Uniformity of KrF gain profile and corresponding laser intensity incident on the Raman medium imply a reasonably uniformly excited gas, which will be achieved with two-sided electron beam excitation. These considerations were folded together with previous short-pulse laser experience and KrF media modeling to define the aperture, gain length, operating pressure regimes, and power deposition rates required. Calculations of beam uniformity and efficiency of utilization had previously shown that media could be ionized uniformly within ±5% with a useful energy deposition efficiency of about 30% for a variety of rectangular shapes, without the use of beam-scatter-controlling magnetic fields.[97] We used these considerations to define a beam current density, beam voltage, and diode impedance requirement. The pulsed power system was then designed to meet these specifications.

A central issue to be resolved by planned A-amplifier KrF media experiments is the achievable intrinsic efficiency and the limiting intensity at 248 nm. The efficiency of the KrF medium in 1-m-gain-length, long-pulse (~300-ns), low-current-density devices has been well characterized to be 10%.[98] Efficiencies in excess of 10% for short gain lengths (10 to 20 cm) and 100 to 200-ns pulse durations have also been reported.[99,100] However, efficiencies of only 3 to 7% have been reported for various 50-ns devices.[101,102] Thus, an uncertainty of about a factor of two exists in the efficiency that one may reasonably expect from a short-pulse device such as the A-amplifier. For planning purposes, a conservative intrinsic efficiency of 5% was assumed. Thus, a 25-J output requires 500 J deposited in the active volume, or about 1600 J incident on the gas.

The second major consideration is the achievable intensity. Previous experiments have shown extracavity intensities in excess of 10 MW/cm^2. We chose a conservative design goal of 5 MW/cm^2. This goal implies a total aperture of 100 cm^2 for a 25-J, 500-MW pulse. Finally, the gain and gain length must be chosen to be consistent with the projected performance of 5 MW/cm^2, 5% intrinsic efficiency, and 25% excited-state extraction efficiency. For KrF at about 2-atm buffer pressure, this corresponds to an available-gain-length-times-gain product of 5. A length of 50 cm for the KrF medium and power deposition rates of about 2 MW/cm^3 are consistent with this gain coefficient and the medium's intrinsic efficiency. For a square 10-by-10-cm aperture and 2 atm of Ar buffer, this deposition rate is achieved with a nominal 300-keV, 100-A/cm^2 electron beam irradiating the gas from two sides. Table 8-6 summarizes the A-amplifier design parameters.

Four factors influenced our general approach in designing the e-beam system for the A-amplifier. Two separate e-beam machines were constructed to

Table 8-6. Specifications for the RAPIER A-amplifier.

• Performance goals	25-J narrow-band quality beam 50-60-ns pulse, low jitter
• Laser design	10-by-10-cm aperture 50-cm gain length 5-MW/cm^2 output intensity 2-MW/cm^3 pump power 5-10% medium efficiency 30-40% of pump e-beam in useful region 2-atm Ar/Kr/F_2 mixtures
• Pulsed power requirements	Current density:~100 A/cm^2, two-sided Beam voltage:~300 keV Beam area:50 × 10 cm^2
• Anticipated small-signal gains, losses	Gain:10-20% cm^{-1} Nonsaturating loss: 0.4% cm^{-1} Saturating loss:2% cm^{-1}

pump the medium from opposite sides to obtain the desired pumping uniformity. A water-dielectric pulse-forming line, charged by a Marx generator, was used to create the short pulse length. A triggered output switch was required to achieve precise timing. We selected a positively charged Blumlein configuration because of the relative accessibility of the output switch for triggering

The specification of the l[illegible] geometry (0 × 10 × 50 cm), operating pressure (2 atm Ar), pulse length (60 ns), output energy (25 J), and conversio[illegible] efficiency (5%) indirectly defines the design parameters for the e-beam system. However, an iterative, computer-assisted procedure coupled with experimental data is needed to translate these laser specificatio[illegible] into a detailed set of electrical and mechani[illegible]al designs.

One of the e-beam machines is shown in Fig. 8-37. The Marx generator is housed in the rectangular tank in the lower left portion of the picture. The cylinder directly above it contains components for coupling the trigger signal to the output switch. The longer cylinder extending to the right is the pulse-forming line, which ends in the evacuated diode chamber where the electron beam is formed. The beam passes through a metal foil window into the laser cell. A schematic of the machine (Fig. 8-38) [illegible]ntifies the individual components discussed [illegible]

[illegible]e laser [illegible] is made of aluminum, which passivates wh[illegible] exposed to the KrF gas mixture. The clear aperture transverse to the laser axis measures 10 × 10 cm and can be equipped with 1-cm-thick Suprasil I windows mounted at either Brewster's angle or near-normal incidence. The cell has five ports on the top and on the bottom for vacuum connections and diagnostics. The two remaining sides face the e-beam machines.

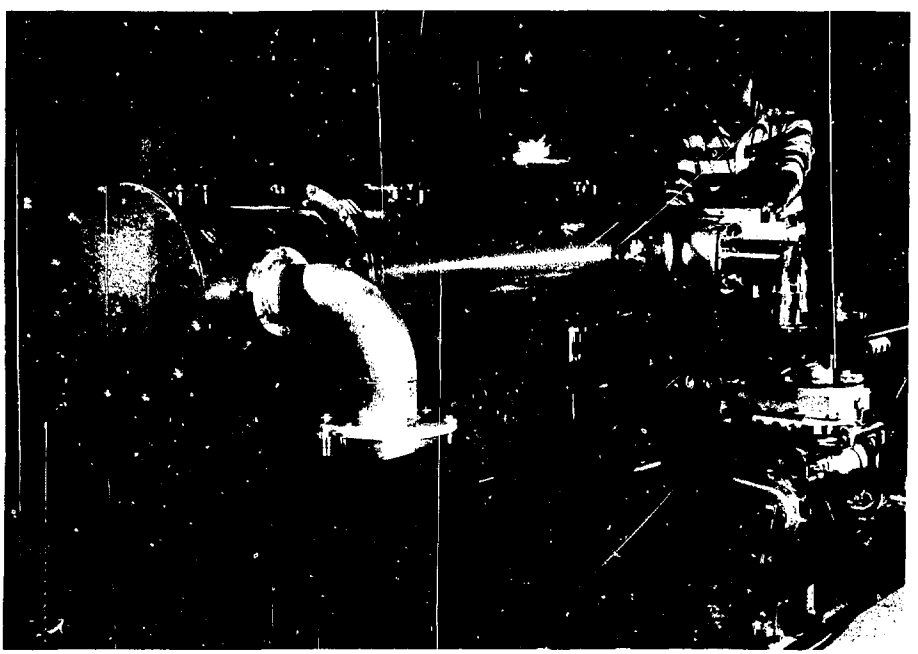

Fig. 8-37. A-amplifier e-beam machine.

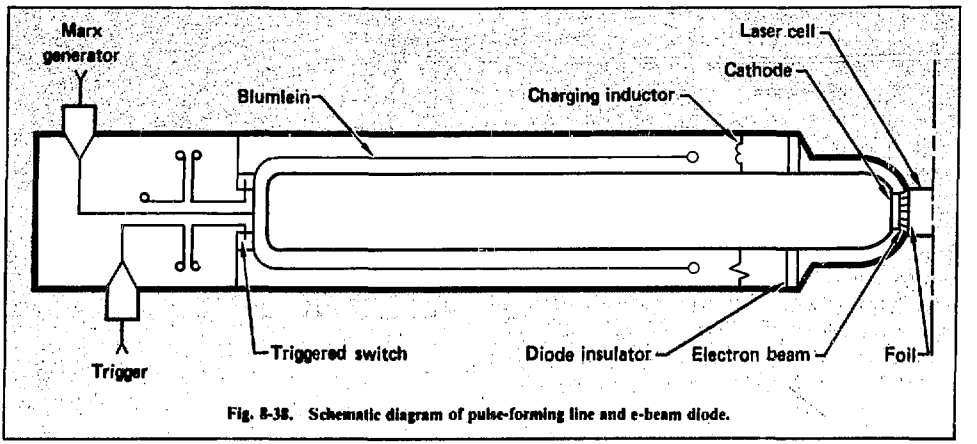

Fig. 8-38. Schematic diagram of pulse-forming line and e-beam diode.

A three-dimensional Monte Carlo computer simulation was performed to determine the magnitude and spatial distribution of energy deposited in the laser medium by the electron beams. A simulated 300-keV electron beam, 10 × 50 cm in area, was passed through a 13-μm Havar foil into a 10 × 10 × 70-cm volume filled with a mixture of 94% argon and 6% krypton gases at a total pressure of 2 atm. The calculation indicated that 32% of the energy incident on the foil is deposited in the gas. The pumping of the medium is uniform to 10% over most of the area transverse to the laser axis, as shown in Fig. 8-39. The laser conversion efficiency (5%) implies that 500 J must be deposited in the gas by the two electron beams, and thus each must supply 800 J incident on the foils.

The metal-foil e-beam windows must be thin enough to transmit 300-keV electrons but thick enough to support the differential pressure between the laser cell and the vacuum of the diode chamber. Havar, a cobalt alloy, was chosen because of its high strength (265 kpsi), good high-temperature properties, fluorine compatibility, and integrity at 13-μm thickness. Although the foil absorbs only 9% of the energy of each incident electron on the first pass, the total energy deposited in the foil may approach 30% as a result of electrons being backscattered by the gas, transmitted from the opposite beam, and reflected by electric fields in the diode after passing back through the foil from the cell. In spite of its exceptional strength, the foil cannot sustain the pressure differential over the entire beam area and therefore must be supported. This additional support is provided by a slotted plate with a geometrical transmission of 89%. One set of foil support plates made of nonmagnetic stainless steel permits operation at pressures up to 2 atm, and another set made of maraging steel permits operation up to 4 atm.

The electron beam is produced in vacuum by subjecting a cathode to an electric field of 200 kV/cm. The cathode is composed of multiple 80-μm-thick stainless steel foils, which are brazed and expanded to form hexagonal cells 0.3 cm across. Electron pinhole photographs indicate that field enhancement by this structure is sufficient to

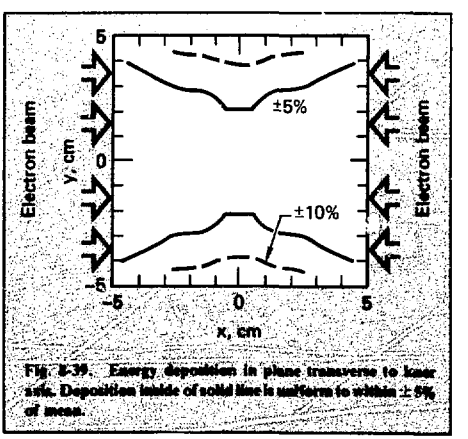

Fig. 8-39. Energy deposition in plane transverse to laser axis. Deposition inside of solid line is uniform to within ±5% of mean.

obtain three or four emission sites per cell, producing reasonably uniform illumination of the anode. To prevent the structure of the foil support from distorting the electric field in the diode and deflecting the beam electrons, the diode side is covered with a 13-μm-thick aluminized Kapton foil. The resulting beam-current density profile, as measured by a film dosimeter, is plotted in Fig. 8-40. The peak current density measured near the center of the beam is 120 A/cm^2. Unfortunately, the voltage produced across the diode during the charging of the pulse-forming line, combined with the field enhancement of the cathode, can lead to intense local emission that can puncture the cell foil. Control of this prepulse voltage is necessary for reliable operation.

The diode is separated from the water-filled pulse-forming line by a 5-cm-thick Lucite disk which, together with the surrounding metal surfaces, is shaped to produce an optimum geometry for voltage standoff. The pulse-forming line consists of three 1-m-long triaxial cylinders. The intermediate conductor is charged to +300 kV from the Marx generator, and the output pulse is produced when the outer and intermediate conductors are shorted together by the triggered output switch (see Fig. 8-38). The three conductors form two nested 2.5-Ω transmission lines, store 1100 J when charged to 300 kV, and produce a 300-kV, 5-Ω pulse at the diode. Output voltage and current pulse shapes are shown in Fig. 8-41. The inner conductor is held near ground potential during the charging of the line by the charging inductor. This inductor is in parallel with the diode load and is the principal cause of the voltage decline during the output pulse. To keep the prepulse voltage acceptably small, the charging inductor was reduced to about 1.3 μH and a 100-Ω resistor was placed in parallel with it. These two components draw about 200 J from the output pulse.

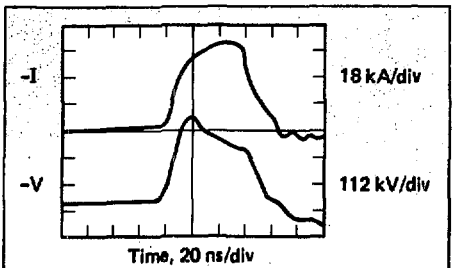

Fig. 8-41. Output pulse characteristics with e-beam.

The output switch must be triggered with low jitter and must contain more than one current-carrying channel if it is to produce an acceptable rise time. An annular switch with continuous stainless steel electrodes was chosen to meet these requirements. The switch electrodes have a mean diameter of 13 cm and a gap of 1 cm. The switch is pressurized with 100 psig of SF_6 gas and held together by eight 1-cm-diam nylon bolts. The outer Lucite insulator is 0.06 cm shorter than the inner insulator to accommodate the deflection of the switch assembly under pressure loading. A switch inductance of 15 nH is inferred from the rise time of the output pulse, and calculations indicate that at least three current channels are necessary to produce this inductance. The switch is triggered by a voltage pulse applied to a disk-shaped midplane electrode through an oil-insulated coupling capacitor. We used a trigger generator, producing a -150-kV pulse with a 10-ns rise time into a 50-Ω load, to determine the switch jitter. The resistive load was replaced by the output trigger circuit, and a series of 20 shots were fired. Neglecting one prefire, the standard deviation of the switch firing was 0.4 ns, as shown in Fig. 8-42.

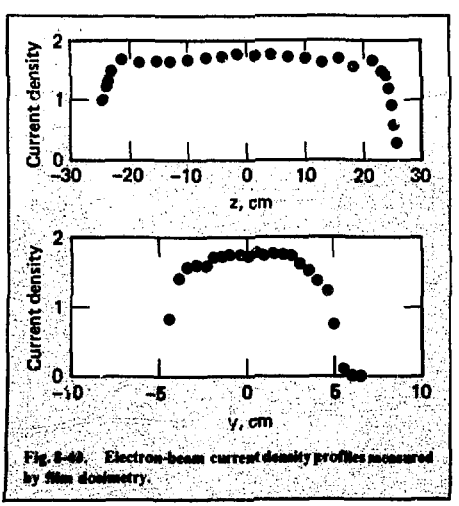

Fig. 8-40. Electron-beam current density profiles measured by film dosimetry.

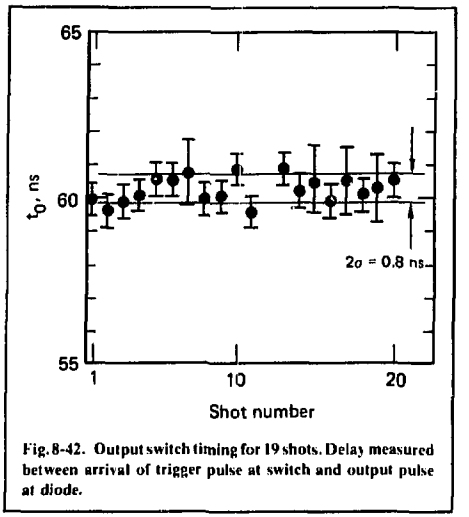

Fig. 8-42. Output switch timing for 19 shots. Delay measured between arrival of trigger pulse at switch and output pulse at diode.

The Blumlein is pulse-charged from a four-stage Marx generator operating at 100 kV per stage. The charging current is transferred from the Marx generator to the Blumlein by a short section of oil-filled coaxial cable and then through the center of the annular output switch. The Marx generator has an erected capacitance of 25 nF and stores a maximum of 2000 J. Inductance (8 μH) has been added to it, producing a 1-μs charging time to reduce prepulse.

Two of these e-beam generators have been assembled and tested. The switch of each electron beam was triggered simultaneously by a common untriggered switch. Outputs of the beams were measured with colorimeters and Faraday cups and were found to be the same to within 10%. Timing jitter between the two sides was $\lesssim$1 ns, which is consistent with the delay measured for the main switch. The energy deposited in the cell measured >1300 J, which is consistent with the design parameters of the system.

References

97. *Laser Program Annual Report—1976*, Lawrence Livermore Laboratory, Livermore, Calif., UCRL-50021-76, §6-11 (1977).
98. M. Rokni, J. A. Mangano, J. H. Jacob, and J. C. Hsia, *IEEE J. Quant. Electron.* **QE-14**, 464 (1978).
99. C. A. Brau and J. J. Ewing, *Electronic Transition Lasers*, J. I. Steinfeld, Ed. (MIT Press, Cambridge, Mass., 1976).
100. M. L. Bhaumik, R. S. Bradford, and E. R. Ault, *Appl. Phys. Lett.* **28**, 23 (1976).
101. J. M. Hoffman, A. K Hays, and G. C. Tisone, *Appl. Phys. Lett.* **28**, 538 (1976).
102. J. R. Murray and H. T. Powell, *Electronic Transition Lasers II*, L. E. Wilson, S. N. Suchard, and J. I. Steinfeld, Eds. (MIT Press, Cambridge, Mass., 1977), pp. 23-29.

Authors

J. J. Ewing
L. Schlitt
J. C. Swingle

8.4 Group VI Lasers

We continued experiments in 1978 to improve our understanding of the kinetics of excited sulfur and selenium atoms and to produce lasers based on their forbidden transitions. The background for this work is described in last year's annual report.[103] For a gain of 1% cm^{-1} on either the auroral line of sulfur and selenium or the transauroral line of selenium, the concentration of ^1S atoms must be about 2×10^{16} cm^{-3} (Ref. 104). This density approaches 1 Torr of the excited species (1 Torr equals 3.2×10^{16} molecules·cm^{-3}). To minimize line broadening as well as the index of refraction of the laser medium, we must produce this concentration of excited atoms in a buffer gas whose pressure is 1 atm or less. We have used photodissociation of OCS by 146-nm light and photodissociation of OCSe by 172-nm light to produce such concentrations of excited atoms.[105] For dissociation of these molecules at these wavelengths, the quantum yields for ^1S atom production have been measured to be near unity.[106,107] In our experiments, the OCS and OCSe concentrations were in many cases completely dissociated, that is bleached, by the incident vacuum ultraviolet (VUV) radiation.

Late in 1977, we discovered that free electrons can play a dramatic role in such photolysis experiments.[108] It is not obvious that free electrons should be present, since we have used only optical excitation. If present, however, electrons can rapidly deactivate the excited atoms through superelastic collisions. The energy of the electron is increased by the energy taken from the excited atom in such collisions. The hot electrons can then excite other atoms and may even create additional electrons[109] by exciting states above the ionization limit. The increased concentration of electrons

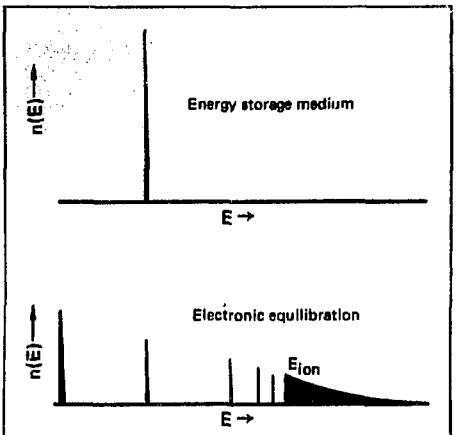

Fig. 8-43. Electron heating, followed by ionization and state-scrambling by electrons, tends to drive a high-energy-density laser medium toward electronic equilibration.

produced by ionization causes the energy scrambling among the electronic states to occur even faster. The overall tendency of the electron processes is to drive the medium toward a thermal equilibrium between the excited atomic populations and the electron energy distribution. This is shown schematically in Fig. 8-43.

We have found that this type of electronic collapse can occur in our proposed Group VI laser media in a time of 100 ns. We believe that deactivation by electrons is an important mechanism in any gas laser requiring a large concentration of electronic excited states. For lasers that are excited photolytically, this mechanism can be combated, as we shall discuss, by using a buffer gas that cools and attaches free electrons.[108,110] For lasers excited by either discharges or electron beams, this strategy cannot be used. Whether an electron-excited device can produce a large concentration in one excited electronic state with good efficiency seems questionable.

In our Group VI experiments (§8.4.1), we found that the initial concentration of electrons was quite significant. Free electrons were produced by photoionization of the ^1S atoms by the VUV radiation used for photolysis. Although this photoionization is spin-forbidden, the concentration of electrons produced at high fluence caused rapid deactivation of the ^1S atoms. We greatly reduced this quenching by using a buffer gas mixture of SF_6 with either N_2 or CO. The SF_6 molecules rapidly attached electrons having low kinetic energy; the N_2 or CO molecules cooled the electrons through vibrationally inelastic collisions, thereby enhancing their attachment rate. This cooling was necessary to offset the heating caused by ^1S atoms. After eliminating the ^1S deactivation by electrons, we found that quenching by heavy particles limited the energy storage time. For small fractional dissociation. ^1S deactivation by the parent molecules, OCS or OCSe, was dominant. Quenching of S(^1S) by OCS was slow; quenching of Se(^1S) by OCSe was quite fast. For bleaching conditions, the parent molecules were depleted, producing ^1S atoms, CO, and possibly other products such as ^1D or ^3P atoms. For such conditions, we found that the ^1S quenching was dominated by minority products plus the buildup of ^3P atoms. The S(^1S) and Se(^1S) decay times were quite similar for bleaching conditions.

Using an optimized buffer gas, we demonstrated a laser output of 5 mJ on the sulfur auroral line at 772.5 nm (Ref. 110), 16 mJ on the selenium auroral line at 776.8 nm, and 25 mJ on the selenium transauroral line at 488.7 nm. In all cases, the laser fluences within the cavity were adequate to extract the energy stored in ^1S atoms. A sketch of the experimental setup and a photograph showing the selenium transauroral laser in operation are shown in Fig. 8-44.

In §8.4.2, we describe calculations to determine the ^1S photoionization cross section, and we give a parametric formula for the photoelectron density vs photolysis fluence. We discuss estimates of the rate of superelastic ^1S quenching by scaling cross sections obtained from existing calculations on atomic oxygen. We then describe a simple model that predicts the steady-state electron temperature and demonstrates the effect of molecular buffer gases.[108] We also discuss the mechanism of ^1S quenching by ^3P atoms. In addition, we note that the products of Se(^1S) quenching by OCSe appear to be excited states of Se_2 and ground-state CO. Work performed by others[111] suggests it may be possible to reverse this kinetic process at high temperature and produce ^1S atoms by reaction of excited Se_2 molecules with CO. This process reversal may provide an alternative mechanism for ^1S atom production.

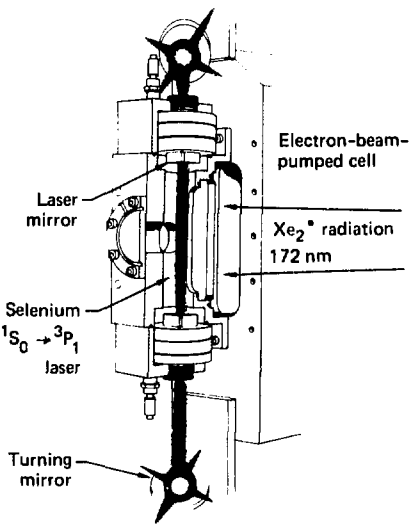

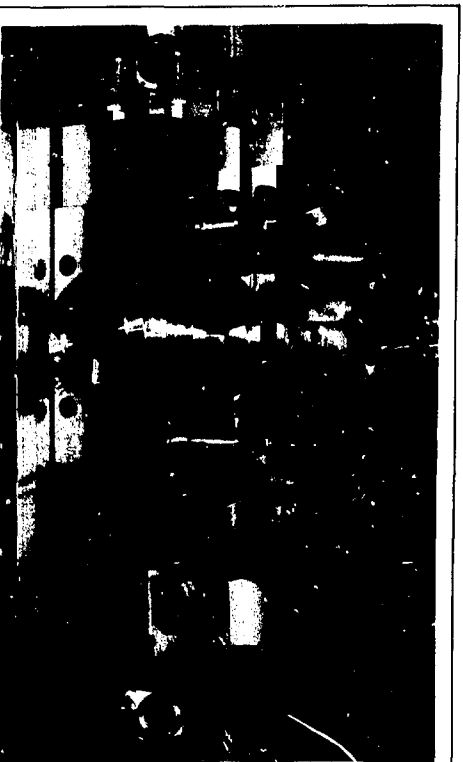

Fig. 8-44. Selenium transauroral laser.

In §8.4.3, we discuss time-dependent calculations of the ^1S density, electron density, and electron temperature appropriate to the experimental conditions. We also discuss calculations that show that the electron energy distribution can be quite non-Maxwellian in these superelastically heated plasmas. We compare rate coefficients obtained from a Maxwellian average with those obtained by an average over the self-consistent, non-Maxwellian distribution.

8.4.1 Laser and Kinetics Experiments

Sulfur Kinetics. We used krypton excimer radiation at 146 nm to photodissociate OCS and create a high density of $S(^1S)$ atoms. We excited the Kr_2^* source with a 50-ns-duration electron beam, delivering 50 kA at 1 MeV to a gas volume 50 cm long, 10 cm high, and 3 cm deep. Details of the experimental arrangement were described previously.[103] The end-coupled Kr_2^* output rapidly increased with fill pressure above 15 atm of Kr and exhibited a line-narrowing that is characteristic of amplified spontaneous emission. The spectrum half-width narrowed from 12 nm (FWHM) at low pressure to 1.5 nm at high pressure. The Kr_2^* superfluorescence lies within the spectral region of high quantum yield for $S(^1S)$ production by OCS photodissociation.[106] Because its absorption spectrum is highly structured in this region,[112] the saturation fluence for OCS dissociation by Kr_2^* radiation is not well defined. Simply using the absorption cross section at 146 nm (1.4×10^{-17} cm^2),

we calculated a saturation fluence of 100 mJ/cm^2. Hence, at our highest output fluence, most of the OCS in the first absorption depth should be dissociated to produce S(^{1}S).

Photolytic excitation was restricted to a channel, 0.8 cm wide by 1 cm deep, which ran along the 8-cm length of the VUV input window. Reentrant end windows terminated the channel, thus defining an 8 × 1 × 0.8-cm volume of gas that was uniformly illuminated by the VUV source. Fluorescence was viewed from one end of this volume by a photomultiplier-bandpass-filter combination and from the other end by a sensitive optical multichannel analyzer attached to a 0.3-m spectrometer. The viewing region of the photomultiplier was also restricted by apertures, to reduce signals caused by scattered light from the Kr_2^* source. We recorded kinetic data with oscillograms and in parallel with a transient digitizing system controlled by a minicomputer that provided semilogarithmic plots of fluorescence decays for immediate analysis.

The time dependence of fluorescence and time-integrated spectra is shown in Fig. 8-45 for a photolytic mixture of 1.5 Torr of OCS and 1000 Torr of Kr excited by various VUV fluences. We used the Kr buffer to increase the S($^1S_0 \rightarrow {}^1D_2$) fluorescence by collision-induced emission[113] to a level well above background. Because Kr has a small S(^{1}S) quenching coefficient, one may presume it does not significantly affect the S(^{1}S) decay. In Fig. 8-45(a), the fraction of OCS dissociated was small and, hence, the S(^{1}S) decay was determined from quenching by OCS and possible impurities in the starting mixture.[114] The blue-degraded spectral feature that peaks at the atomic line position is collision-induced $^1S_0 \rightarrow {}^1D_2$ emission.[115]

At higher VUV fluences, the S(^{1}S) decay time was greatly reduced and Kr emission lines appeared in the spectrum as shown in Fig. 8-45(b). We interpret the fast initial quenching of S(^{1}S) to be caused by superelastic collisions with free electrons, which then become sufficiently hot to excite the Kr buffer. We confirmed this hypothesis by using an Ar buffer, which then produced Ar emission lines. The indiscriminate excitation of the buffer suggests the presence of hot electrons, which clearly dominate the time dependence and emission spectrum at higher input fluence, as shown in Fig. 8-45(c). Because both the Kr and Ar emission lines lie within the transmission band of the filter, we could not determine the exact time dependence of S(^{1}S) from these data. The large initial spike was predominantly rare-gas emission.

Emission from the rare-gas buffer disappeared with the addition of molecular gases, which can either cool or attach free electrons. We have limited our attention to N_2, CF_4, and SF_6 because of their small absorption at the photolysis wavelength and their small S(^{1}S) quenching coefficients. The data in Fig. 8-45(d) show the effect of adding 25 Torr of SF_6 and 25 Torr of N_2 to the photolytic mixture for the same pump fluence, as in Fig. 8-45(c). The Kr lines are gone and the S(^{1}S) atoms are relatively long-lived, indicating a substantial reduction of the electron density. Addition of merely 5 Torr of SF_6 was adequate to produce the same effect. The data shown are for the SF_6/N_2 mixture, to correspond to laser experiments decribed below. Addition of either N_2 or CF_4 alone in pressures of 25 Torr or more also eliminated the atomic emission lines. However, the initial quenching rate of the S(^{1}S) atoms was still quite rapid. This suggests that quenching by the initial photoelectrons can be quite significant, even though the electrons remain cool and multiplication does not occur.

We believe that no significant concentrations of free electrons were present in the mixtures with SF_6. In Fig. 8-46, the initial quenching rate of S(^{1}S) observed for a mixture containing 1.5 Torr OCS, 5 Torr SF_6, and 1000 Torr Kr is plotted against the initial S(^{1}S) amplitude, which was varied by changing the input fluence. The initial quenching rate increased almost linearly with the S(^{1}S) amplitude. This increase is consistent with deactivation caused by a product of the photolysis. A logarithmic plot of the overall fluorescence decay vs time (Fig. 8-47) shows that the S(^{1}S) decay was nonexponential. The decay rate speeds up by approximately a factor of two as the plot goes from short times after the photolysis to long times. This speedup suggests quenching at late times by a secondarily produced species. Sulfur ground-state atoms are an obvious candidate for a species whose population grows in time.

In a simple picture, we assume that the photodissociation produces only CO and sulfur atoms in either the ^{1}S, ^{1}D, or ^{3}P states. The ^{1}D atoms are rapidly deactivated to ^{3}P. The S(^{1}S) quenching by CO is known to be slow. Self-quenching (^{1}S by ^{1}S) does not appear to be sizable, because the observed decay rates speed up rather than slow down in time. By elimination of possible

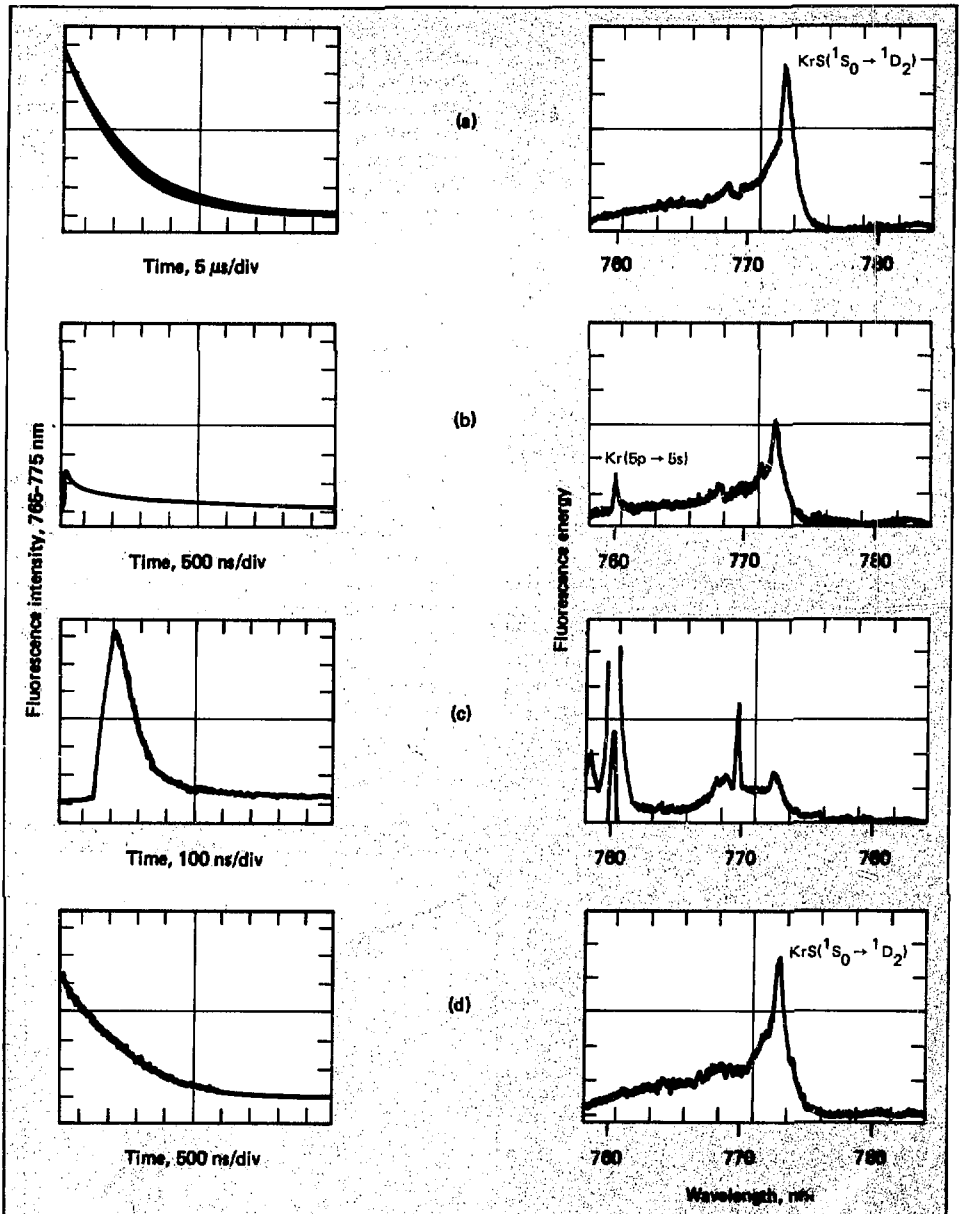

Fig. 8-45. Fluorescence time dependence and integrated emission spectra near the $S(^1S_0 \rightarrow {}^1D_2)$ line, from a mixture of 1.5 Torr CCl_4 and 1000 Torr Kr excited by Kr_2^* fluence of approximately (a) 6 mJ/cm^2, (b) 70 mJ/cm^2, (c) 150 mJ/cm^2, and (d) 150 mJ/cm^2. The mixture in (d) contains, in addition, 25 Torr SF_6 and 25 Torr N_2. The relative scales of the fluorescence intensities are (a) 1, (b) 20, (c) 20, and (d) 25. The amplitude scales of the fluorescence spectra are constant.

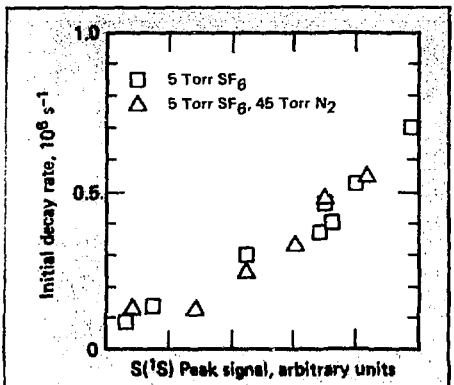

Fig. 8-46. The initial decay rate of $S(^1S)$ vs the $S(^1S)$ peak signal for an OCS pressure of 1.5 Torr. The peak $S(^1S)$ signal was varied by changing the VUV input fluence.

candidates, we conclude that the observed quencher must be $S(^3P)$. The speedup factor in the decay rate would suggest that roughly equal amounts of $S(^1S)$ and $S(^3P)$ are initially produced. Assuming that the final quenching rate is entirely caused by $S(^3P)$ and that the OCS is completely dissociated gives a quenching coefficient of 3×10^{-11} $cm^3 \cdot s^{-1}$. This value is 50% larger than a measurement of the analogous quenching rate for oxygen.[116] If, however, the OCS dissociated to O plus CS with even a small probability (~0.1),[117] the interpretation that equal amounts of $S(^1S)$ and $S(^3P)$ are initially produced could be incorrect. Presuming that the $S(^1S)$ quenching by O, or by CS, or by both is rapid compared to quenching by ^3P atoms, we find that a factor-of-2 speedup ir the decay rate could be consistent with a much higher $S(^1S)$ quantum yield (~0.9). Unfortunately, the correct interpretation is not clear.

Sulfur Laser. In laser experiments, we utilized a 12-cm optical cavity formed by two 1-m-radius-of-curvature mirrors mounted inside the photolytic cell. The channel defining the excitation region restricted the excited laser volume to 6.5 cm^3. We measured the transmission of the mirrors at 772.5 nm to be 0.17% and believe their absorption-plus-scattering loss was at least this large. We evacuated the photolytic cell within seconds, following photolysis, to reduce sulfur deposition on the mirrors. This procedure made it possible to observe many laser shots between mirror cleanings. We measured intensity from one end of the laser using a calibrated vacuum photodiode and neutral density filters. We cross-checked this intensity against the

Fig. 8-47. Logarithm of the $S(^1S)$ signal vs time for the data shown in Fig. 8-45(d). The fluorescence shows a speedup of the instantaneous decay time from 1.4 μs initially to about 0.5 μs at late times.

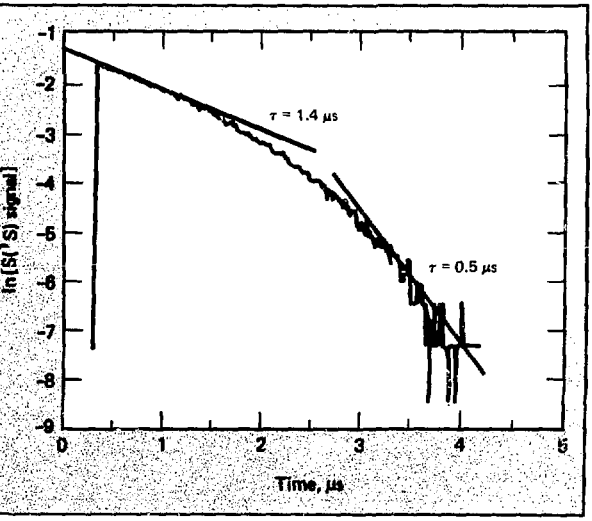

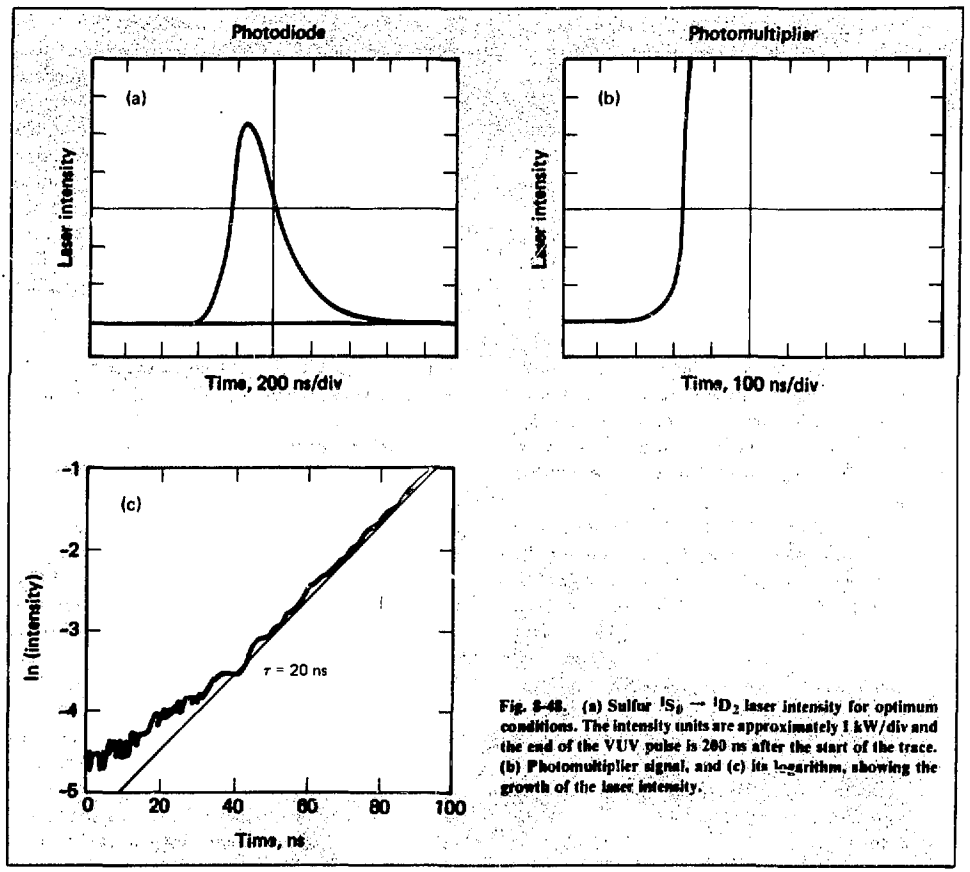

Fig. 8-48. (a) Sulfur $^1S_0 \rightarrow {}^1D_2$ laser intensity for optimum conditions. The intensity units are approximately 1 kW/div and the end of the VUV pulse is 200 ns after the start of the trace. (b) Photomultiplier signal, and (c) its logarithm, showing the growth of the laser intensity.

output energy from the opposite end, using a calorimeter calibrated by the National Bureau of Standards.

The performance of the S($^1S_0 \rightarrow {}^1D_2$) laser was extremely sensitive to the choice of buffer gas. Time dependence of laser emission under optimum conditions is shown in Fig. 8-48(a). The output beam profile matched the 0.8 × 1-cm cross section of the excited gas volume. Total output from both ends was 12 kW with an energy of 5 mJ for a photolytic mixture of 1.5 Torr OCS, 25 Torr SF_6, and 25 Torr N_2 excited by a VUV fluence of 150 mJ/cm^2. The laser output for this mixture exceeded that of mixtures of OCS with either pure SF_6, pure N_2, or pure CF_4 by at least two orders of magnitude, and it exceeded the output with SF_6/Kr, SF_6/CF_4, or CF_4/N_2 (equal parts) by a factor of 10. The OCS pressure, total buffer pressure, and VUV fluence were held constant for these comparisons. Differences between the various mixtures were even more apparent at higher VUV fluence, where only the OCS/SF_6/N_2 mixture produced laser oscillation. We believe that the sensitivity of the laser to these variations was exaggerated by its closeness to threshold.

We believe the superior laser results with the SF_6/N_2 buffer can be attributed to a greater efficiency for electron removal. The N_2 cools the electrons, thereby enhancing their attachment to SF_6, which has its peak attachment rate at low electron temperature.[118] Electron attachment by CF_4 (Ref. 119) is presumably less effective because it has

a smaller attachment rate than SF_6. However, we did not always find differences in the fluorescence behavior of these mixtures that corresponded to their differences in laser performance. Although SF_6 was much more effective than CF_4 in reducing electron effects such as Kr emission lines, the fluorescence decays with SF_6 and SF_6/N_2 buffers were not noticeably different. We speculate that the presence of 1000 Torr of Kr, which was necessary to produce adequate fluorescence signs, affected the electron kinetics.

Addition of more than 100 Torr of buffer gas seriously reduced laser performance. A similar reduction was also found by adding He to a typical laser mixture. These results suggest that line broadening reduces the gain cross section for pressures above 100 Torr. This conclusion is consistent with a collisional broadening coefficient that is gas-kinetic.

For the optimized laser output, there was significant depletion of the $S(^1S)$ population by the laser field. Saturation of the medium is expected, because the fluence seen by an $S(^1S)$ atom inside the cavity (i.e., the output fluence divided by the mirror reflectivity, $\sim 3.7\ J/cm^2$) exceeded the calculated saturation fluence[104] for the $^1S_0 \rightarrow {}^1D_2$ transition ($h\sigma/\sigma \approx 0.6\ J/cm^2$). The maximum possible laser energy at 772.5 nm was 80 mJ for our conditions, calculated by assuming 1.5 Torr of $S(^1S)$ and an active volume of 6.5 cm^3. However, the fluorescence data in Fig. 8-45(d) suggest that only 60% of the initially produced $S(^1S)$ atoms were available after the 700-ns buildup time of the laser. Hence, the measured laser output (5 mJ) represents about 10% of the maximum energy (48 mJ) that was theoretically possible at the laser peak. We do not know either the exact fraction of OCS dissociation or the laser energy lost to mirror absorption and scatter. We believe it is conservative to assume that the mirror losses were at least as large as their transmission, 0.17%. Then, the total laser output, adjusted for kinetic decay and mirror loss, implies that an energy density of at least 2.5 J/litre was stored in the laser transition immediately following photolysis.

We used the initial rate of laser intensity rise as measured by the photomultiplier [Fig. 8-48(b)] to determine the net gain. The data acquisition system computed the logarithm of the signal, as shown in Fig. 8-48(c). According to this plot, the initial exponentiation time was 20 ns, implying a net gain of 2% per pass. For optimum conditions, we determined a net gain of 2.5% per pass. The stimulated-emission cross section of the $S(^1S_0 \rightarrow {}^1D_2)$ line was previously calculated[104] to be $4.5 \times 10^{-19}\ cm^2$ on the basis of a theoretical radiative lifetime[120] and a Doppler line width. If we assume 20% conversion of OCS to $S(^1S)$, which is consistent with the measured output energy, the gain in the medium should initially be 3.5% per pass, in good agreement with the experiment. The gain cross section may be slightly reduced because of the increase in Doppler width caused by photolysis heating. We were unsuccessful in producing laser oscillation of the $^1S_0 \rightarrow {}^3P_1$ transition, which has a calculated gain cross section[103] 15 times smaller than that of the $^1S_0 \rightarrow {}^1D_2$ transition.

Selenium Kinetics. Xenon excimer radiation at 172 nm was used to photodissociate OCSe and create a high concentration of $Se(^1S)$ atoms. As we have shown previously,[103] either broad-band Xe_2^* fluorescence or gain-narrowed superfluorescence are excellent matches to the absorption band that produces $Se(^1S)$.[107] Like OCS, the OCSe absorption spectrum has considerable structure, so that its saturation fluence for dissociation is not well defined. At 172 nm, the absorption cross section[107] is about $10^{-16}\ cm^2$, giving a saturation fluence of 12 mJ. Hence, it was experimentally much easier to bleach OCSe with Xe_2^* radiation than to bleach OCS with Kr_2^* radiation. The Xe_2^* superfluorescence was also much less sensitive to impurities and reliably gave fluences above the bleaching level for many shots. Hence, we were able to obtain more detailed information for OCSe bleaching than for OCS bleaching.

We typically studied the $Se(^1S)$ decay in mixtures of OCSe with 500 Torr of Xe and other gases such as SF_6, N_2, and CO. Complete mixing at this pressure required letting the mixture sit for several hours in a storage bottle. Xenon provided collision-induced fluorescence of the $Se(^1S_0 \rightarrow {}^1D_2)$ line which, at 500 Torr of Xe, was much stronger than background signals. For these conditions, we observed the complete time history of $Se(^1S)$, even during the photolysis pulse.

Figure 8-49(a) shows the time dependence of $Se(^1S)$ that we observed at 0.3 Torr OCSe and at a Xe_2^* fluence of $6\ mJ/cm^2$. The rise of the $Se(^1S)$ signal corresponds to the duration of the VUV photolysis pulse, which was about 100 ns at the low Xe pressure required to produce this low fluence.

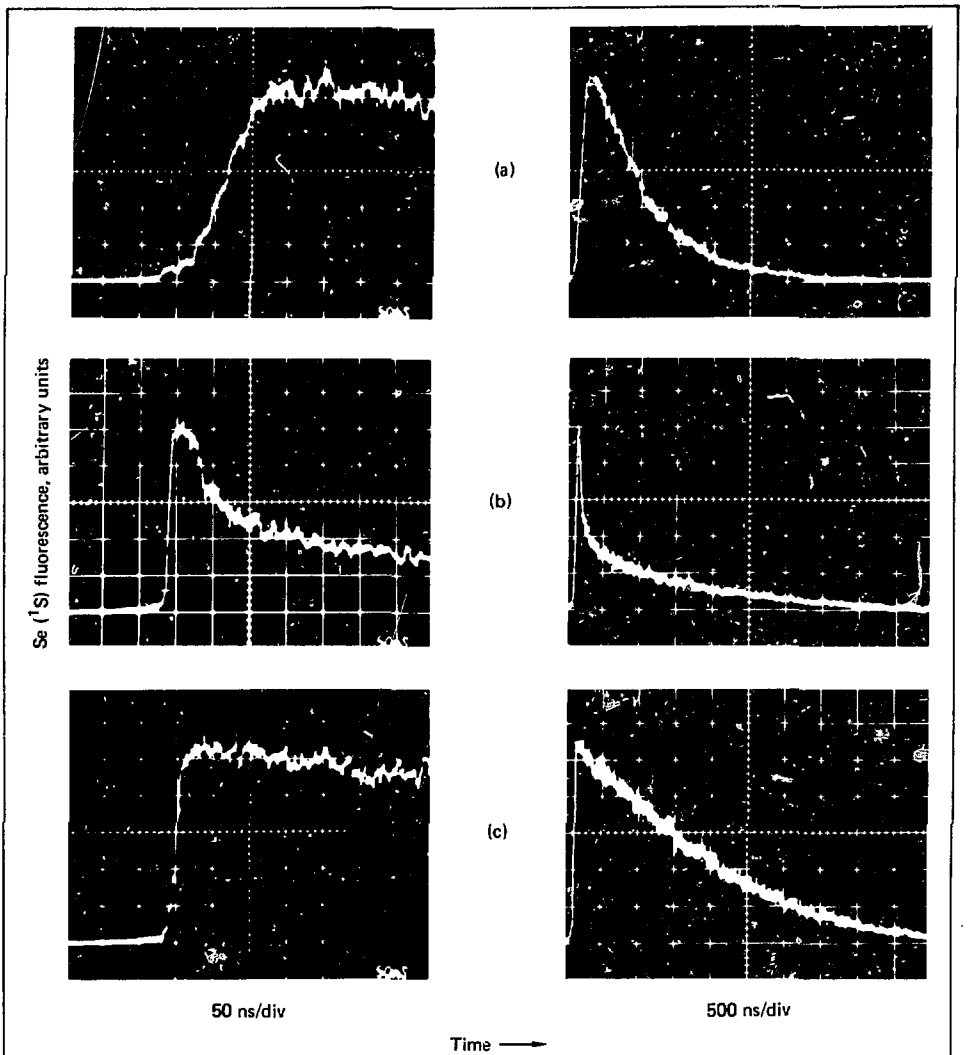

Fig. 8-49. Time dependence of Se(^{1}S). following photolysis of a mixture of 0.3 Torr OCSe and 500 Torr Xe by a Xe_2^* fluence of (a) 6 mJ/cm^2, (b) 100 mJ/cm^2, and (c) 100 mJ/cm^2. The mixture in (c) contains, additionally, 5 Torr of SF_6, which eliminates the rapid quenching caused by electrons.

Because only a small fraction of the OCSe was dissociated, the Se(^{1}S) decay was simply caused by OCSe. The decay has an exponential time constant of 750 ns, corresponding to a quenching coefficient of 1.4×10^{-10} cm$^3 \cdot$s^{-1}, in good agreement with previous measurements.[12]

Figure 8-49(b) shows the Se(^{1}S) time dependence at an input fluence of 100 mJ/cm^2, well above the bleaching fluence. The peak of the Se(^{1}S) signal occurs in about 20 ns, compared to the 50-ns duration of the VUV pulse. This 20 ns corresponds to the time required for bleaching. We believe the rapid decay of Se(^{1}S) during the next 50 ns is caused by electron quenching. Electron recombination occurs rapidly enough to allow some remaining Se(^{1}S) to decay on a long time scale. (At slightly higher input fluence, the Se(^{1}S) atoms are completely removed during the initial, rapid-quenching period.) The Se(^{1}S) fluorescence signals were unaffected by lines from excited Xe, the nearest of which was observed around 763 nm.

Figure 8-49(c) shows the Se(^{1}S) time dependence for the same conditions as in Fig. 8-49(b), except for the addition of 5 Torr of SF_6 to the photolytic mixture. The rapid component in the Se(^{1}S) decay was eliminated. Addition of more SF_6, up to 50 Torr, had no further effect on the observed signal. Also, addition of either CO or N_2 to the mixture with SF_6 produced no significant change. The addition of large concentrations (greater than 100 Torr) of CO alone reduced the rapid initial quenching much like small concentrations of SF_6 did. Because electron attachment is not significant for CO, we believe its major effect at high concentrations was to speed electron recombination.

In Fig. 8-49(c), on the 500-ns time scale, one may observe that the Se(^{1}S) decay time was considerably longer than it was at low VUV fluence, Fig. 8-49(a). This lengthening of the decay time was caused by bleaching, which then reduced quenching caused by OCSe. What prevented the Se(^{1}S) decay time from being even longer is not immediately clear. Plotting the logarithm of the Se(^{1}S) signal vs time, we found that, like S(^{1}S) decays, the Se(^{1}S) decay was nonexponential, speeding up in time. The instantaneous decay time in Fig. 8-49(c) varies from about 2.8 μs at short times to 1.3 μs at long times. We again argue that this speedup was caused by the buildup of ^{3}P atoms. Simply assuming that the late-time decay was caused by 0.3 Torr of Se(^{3}P), we computed a Se(^{1}S) quenching coefficient of 8×10^{-12} cm$^3 \cdot$s^{-1}. Thus, despite the disparity between the ^{1}S quenching rates by the parent molecules in sulfur and selenium experiments, the time decays of the ^{1}S atoms under bleaching conditions are quite similar. By bleaching OCS, the ^{1}S decay time shortens; by bleaching OCSe, it lengthens. We believe the limiting quenchers in both cases are ^{3}P atoms.

We simulated the conditions appropriate for a large-aperture amplifier by studying the Se(^{1}S) kinetics at fluences greatly above the bleaching fluence. We studied standard mixtures of OCSe with 5 Torr of SF_6 (for electron attachment) and 500 Torr of Xe (for collision-induced emission). Figure 8-50(a) shows the peak Se(^{1}S) signal vs input fluence for the cases of 0.32 Torr of OCSe and 1.0 Torr of OCSe. (The amplitudes at 0.32 Torr are multiplied by a factor of 3 to normalize the effect of OCSe pressure.) The VUV fluence, plotted along the x axis, was measured with the carbon calorimeter at the opposite end of the VUV cell. Because of the pinholes, the photomultiplier viewed a conical volume, which was about 0.5 cm in diameter and centered 0.5 cm from the entrance window. Without bleaching, the absorption depth of the Xe_2^* radiation is about 1 cm at 0.32 Torr of OCSe and 0.3 cm at 1.0 Torr. The graph demonstrates that a larger fluence is required at 1.0 Torr, compared to 0.32 Torr, to bleach through the optically thick OCSe and to maximize the Se(^{1}S) density in the viewing region. The decline in the peak amplitudes at very high fluence may be caused by direct photoionization loss of Se(^{1}S) atoms. The empirical bleaching fluence appears to be about 25 mJ/cm^2.

In Figure 8-50(b), we show the decay time to one-half amplitude for the same conditions as in Fig. 8-50(a). We plot the one-half time rather than some other decay parameter because, as we have explained, the shape of the decay curves changes with bleaching. The decay time lengthens from its value at very low fluences because of OCSe bleaching. It then reaches some maximum value and declines at very high fluence. The reason for this decline is uncertain. It may be caused by the Se(^{1}S) being quenched by Se(^{3}P) atoms that result from Se^+ recombination with SF_6^-. It is significant that the peak Se(^{1}S) signal and the decay time vary in a complementary fashion.

Selenium Laser. We performed selenium laser experiments in the same manner as we performed the sulfur laser experiments. We optimized the laser

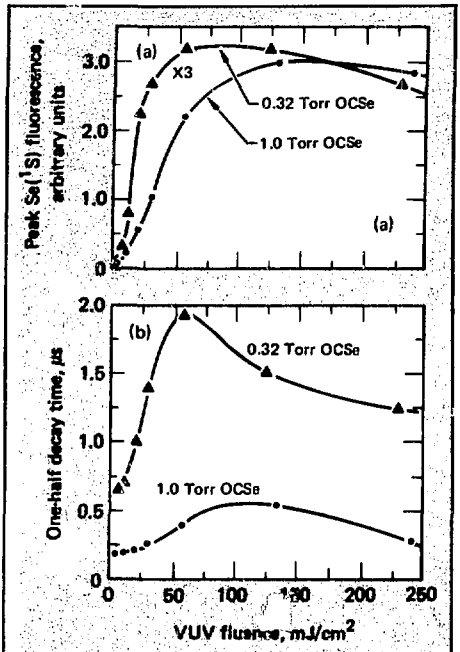

Fig. 8-50. (a) Peak Se(^{1}S) signal vs VUV input fluence for mixtures of 5 Torr SF_6 and 500 Torr Xe with 0.32 Torr OCSe and 1.0 Torr OCSe. The amplitudes for the 0.32-Torr OCSe data are multiplied by a factor of 3 for convenient comparison. The calibration of the VUV fluence is reliable to about a factor of two. (b) One-half decay time of the Se(^{1}S) signal for the same conditions as (a).

output energy at a fixed OCSe pressure of 1 Torr by varying the mirror transmission, the gas mixture, and the VUV fluence. For the 488.7-nm selenium transauroral laser, we obtained the best results with laser mirrors having 0.9% transmission, a mixture of 1 Torr OCSe, 5 Torr SF_6, and 50 Torr CO, and a Xe_2^* input fluence of 100 mJ/cm^2. Figure 8-51 shows the time dependence of the laser output for these conditions. The maximum laser intensity occurred 190 ns after the end of the photolysis pulse. Total output energy from both ends was 25 mJ (4 J/litre), and peak output power was 250 kW. The internal cavity power was 30 MW/cm^2; the internal energy fluence was 3 J/cm^2. This was adequate to saturate the energy stored in Se(^{1}S). [The saturation energy of the Se($^1S_0 \rightarrow {}^3P_1$) transition is approximately 1 J/cm^2.[104]] The laser mirrors were optically damaged by repeated shots at the maximum output energy.

We photographed the laser beam profile by focusing the camera on a translucent disk mounted at the output window surface. Figure 8-52 shows the beam profile as seen in reflection from a turning mirror that defines the elliptical outline seen in the picture. The beam profile was uniform over the rectangular cross section (0.8 × 1 cm) of the photolyzed volume, implying complete bleaching. Thus, the laser volume was well defined, and equaled 6.5 cm^3.

The measured laser output was 30% of the maximum possible output energy, 85 mJ, corresponding to one 488.7-nm laser photon for each

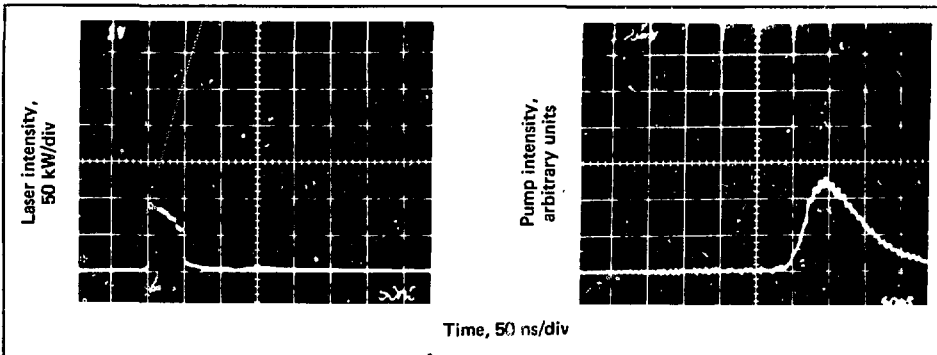

Fig. 8-51. Selenium $^1S_0 \rightarrow {}^3P_1$ laser intensity and the Xe_2^* pump intensity vs time. A mixture of 1.0 Torr OCSe, 5 Torr SF_6, and 50 Torr CO was photolyzed by a Xe_2^* fluence of 100 mJ/cm^2. The peak laser power (0.25 MW total from both ends) occurs about 190 ns after the end of the photolysis pulse.

Fig. 8-52. Beam cross section of Se($^1S_0 \rightarrow {}^3P_1$) laser.

OCSe molecule in the excited volume at 1 Torr pressure. To infer the initial Se(^{1}S) density, we must adjust the laser output for quenching that occurred during the laser buildup, for energy lost to mirror absorption and scatter, and for any remnant energy left in the excited volume. Quenching accounted for a 15% loss of Se(^{1}S) [see Fig. 8-50(b)], and we estimated that the mirror loss was about one-half of the mirror transmission. We assumed that the laser extraction was complete over the excited volume. Applying these corrections, we find that the indicated Se(^{1}S) yield under bleaching conditions was slightly greater than 0.5. Although we should also correct for the small loss caused by photoionization, our ^{1}S yield was clearly less than the quantum yield of unity measured by Black and co-workers.[107] However, a yield of 0.5 agrees well with the interpretation of the kinetic decay data, namely that the speedup in the Se(^{1}S) decay was caused by a factor-of-two change in the Se(^{3}P) density.

If one assumes a Se(^{1}S) concentration of 0.5 Torr, the single-pass gain in 8 cm should be 6% if the lines of the various Se isotopes are completely separated and should be 12% if they are exactly aligned.[104] The experiments suggest the single-pass gain was near 5%. This small gain could be explained either by isotopic effects or by an error in the spontaneous lifetime that was used[104] to compute the gain cross section.

We studied the performance of the Se($^1S_0 \rightarrow {}^3P_1$) laser with variations in the buffer gas and the VUV input fluence. Because the selenium laser was well above threshold, the effect of these variations was much less drastic than for the laser experiments on the sulfur auroral line. We found that SF_6 buffer gas was always required to produce significant laser

intensity; however, the choice of the other buffer gas was not critical. A mixture of 5-Torr SF_6/50-Torr He produced 25% of the optimum output obtained using SF_6/CO. Buffers of pure SF_6 and SF_6/N_2 produced outputs of about 60% of the SF_6/CO results. Also, the 5/50 ratio of SF_6 and CO was not critical; 50/50 mixtures produced comparable results. The laser output declined slightly at high VUV fluence, similar to the falloff in fluorescence [Fig. 8-50(a)].

We also obtained brief results for the Se($^1S_0 \rightarrow {}^1D_2$) auroral line at 777.0 nm. For output mirrors having 0.6% transmission, the auroral line output was 16 mJ for the same conditions, giving optimum performance of the transauroral line. Again, this energy was 30% of the maximum possible: 54 mJ at this wavelength. The gain of the selenium auroral line was slightly smaller than the gain of the transauroral line.

References

103. *Laser Program Annual Report—1977*, Lawrence Livermore Laboratory, Livermore, Calif., UCRL-50021-77, §7 (1978).
104. J. R. Murray and C. K. Rhodes, *J. Appl. Phys.* **47**, 5041 (1976).
105. H. T. Powell and J. J. Ewing, *Appl. Phys. Lett.* **33**, 165 (1978).
106. G. Black, R. L. Sharpless, T. G. Slanger, and D. C. Lorentz, *J. Chem. Phys.* **62**, 4274 (1975).
107. G. Black, R. L. Sharpless, and T. G. Slanger, *J. Chem. Phys.* **64**, 3985 (1976).
108. H. T. Powell and A. U. Hazi, *Chem. Phys. Lett.* **59**, 71 (1978).
109. T. J. McIlrath and T. B. Lucatorto, *Phys. Rev. Lett.* **38**, 1390 (1977).
110. H. T. Powell, D. Prosnitz, and B. R. Schleicher, *Appl. Phys. Lett.* **34**, 571 (1979).
111. M. C. Gower, A. J. Kearsley, and C. E. Webb, Oxford University, private communication (1978).
112. J. W. Rabalais, J. M. McDonald, V. Scherr, and S. P. McGlynn, *Chem. Rev.* **71**, 73 (1971)
113. G. Black, R. L. Sharpless, and T. G. Slanger, *J. Chem. Phys.* **63**, 4551 (1975).
114. O. J. Dunn, S. V. Filseth, and R. A. Young, *J. Chem. Phys.* **59**, 2892 (1973).
115. G. Black, R. L. Sharpless, and T. G. Slanger, *J. Chem. Phys.* **69**, 794 (1978).
116. T. G. Slanger and G. Black, *J. Chem. Phys.* **64**, 3763 (1976)
117. R. B. Klemm, S. Glicker, and L. J. Stief, *Chem. Phys. Lett.* **33**, 512 (1975).
118. L. G. Christophorou, D. L. McCorkle, and J. G. Carter, *J. Chem. Phys.* **54**, 253 (1971).
119. M. M. Bibby, B. J. Toubeliz, and G. Carter, *Electron. Lett.* **1**, 50 (1965).
120. S. J. Czyzak and T. K. Krueger, *Mon. Not. R. Astron. Soc.* **126**, 177 (1963).
121. G. Black, R. L. Sharpless, and T. G. Slanger, *J. Chem. Phys.* **64**, 3993 (1976).

Authors	Major Contributor
H. T. Powell	B. R. Schleicher
D. Prosnitz	

8.4.2 Theory of Kinetic Processes

Photoionization. Previous experiments on the Xe_2^*/OCSe system and subsequent theoretical analysis have demonstrated that the photoionization of S(^{1}S) and Se(^{1}S) by the rare-gas-excimer pump photons can lead to high concentrations of electrons in the laser mixture.[122,123] When high pump fluences are employed, the electrons rapidly deactivate the ^{1}S excited state, resulting in unacceptably short storage times unless molecular buffers are used.

Figure 8-53 shows schematically the various photoabsorption processes from the ^{1}S state that are energetically possible. As discussed previously,[122] photoionization of S(^{1}S) or Se(^{1}S) by the rare-gas-excimer pumps can lead only to the lowest, $^4S^o$, states of the corresponding ions. This process is spin-forbidden in LS-coupling because of the $\Delta S = 0$ selection rule for electric dipole transitions. However, the ^{1}S photoionization cross section is finite because of the spin-orbit coupling between the ^{1}S and ^{3}P states of the (p^4) configuration and between the $^4S^o$ and $^2P^o$ states of the corresponding (p^3) configuration of the positive ion. In addition, contributions from various autoionizing states must be considered, since the measured photoionization spectrum[124] for S(^{3}P) shows numerous autoionizing features in the energy region of interest above the $^4S^o$ threshold. Autoionization contributes considerable structure to the photoionization spectrum.

Previously, we have used a simple model to estimate the ^{1}S photoionization cross sections and obtained the following results[122]: for S(^{1}S) at 146 nm, $\sigma_i = 1.9 \times 10^{-20}$ cm^2; for Se(^{1}S) at 172 nm, $\sigma_i = 2.5 \times 10^{-19}$ cm^2. These values must be considered lower limits, since our model neglected spin-orbit coupling among the states of the resulting positive ions. More recently, two other independent studies have produced larger cross sections for S(^{1}S) at 146 nm. An ab initio configuration-interaction calculation by Weiss[125] gave $\sigma_i = 2$ to 8×10^{-20} cm^2, whereas the semiempirical calculation of McGuire[126] yielded

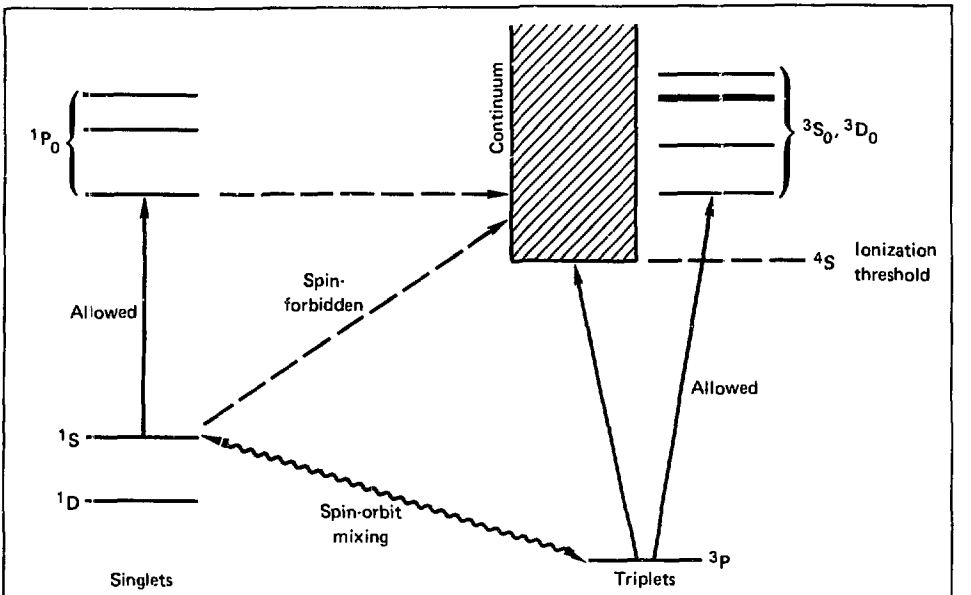

Fig. 8-53. Schematic energy level diagram showing the relevant states for the photoionization of S(^{1}S) and Se(^{1}S). The allowed and forbidden transitions for LS-coupled states in the electric dipole approximation are also shown.

a much larger value of 0.4 to 1.0 × 10^{-18} cm^2 for S(^{1}S). Thus, there appears to be a factor of 10 to 50 discrepancy between the results of McGuire and those obtained by Weiss and by us. In the case of Se(^{1}S), the theoretical situation is more satisfactory, as McGuire's calculation predicts $\sigma_i = 2 \times 10^{-19}$ cm^2 at 172 nm, which is fortuitously close to our value.

In view of the uncertainties in the computed ^{1}S photoionization cross sections, it is useful to consider the production of photoelectrons in more general terms. The density of photoelectrons produced at a given pump fluence ϕ is determined by the relative magnitudes of the cross sections for photoionization of the ^{1}S atom σ_i and photodissociation of the fuel (OCS or OCSe) σ_a. Solving the rate equations for the fuel, ^{1}S excited states, and photoelectron densities gives[123]

$$\frac{n_e}{N_0} = \left(\sigma_a - \sigma_i\right)^{-1} \left\{\sigma_a[1 - \exp(-\phi/\phi_i)] - \sigma_i[1 - \exp(-\phi/\phi_a)]\right\} , \quad (70)$$

where n_e is the photoelectron density and N_0 is the initial fuel density. The saturation fluences ($h\nu/\sigma$) for ^{1}S photoionization and fuel dissociation are given by ϕ_i and ϕ_a, respectively. Figure 8-54 shows the normalized electron density n_e/N_0 vs normalized fluence ϕ/ϕ_a for several values of σ_i/σ_a. When the photoionization cross section is much smaller than the photodissociation cross section ($\sigma_i << \sigma_a$) and $\phi >> \phi_a$, Eq. (70) reduces to the expected result: $n_e/N_0 = \phi/\phi_i$, i.e., in this regime the photoelectron density is proportional to pump fluence.

In our selenium experiments, pump fluences of up to 250 mJ/cm^2 ($\phi/\phi_a \approx 10$) were employed. Under these conditions, a photoionization cross section of 2 to 10 × 10^{-19} cm^2 ($\sigma_i/\sigma_a \approx 0.2$ to 1 × 10^{-2}) would imply a fractional ionization of 3 to 16% for Se(^{1}S). Figure 8-54 clearly shows that if σ_i were much larger than the current estimate, or if very high pump fluences ($\phi/\phi_a > 10$) were used, a significant fraction of the Se(^{1}S) population would be lost directly by ionization. Even if the fractional ionization is only a few percent, the density of the

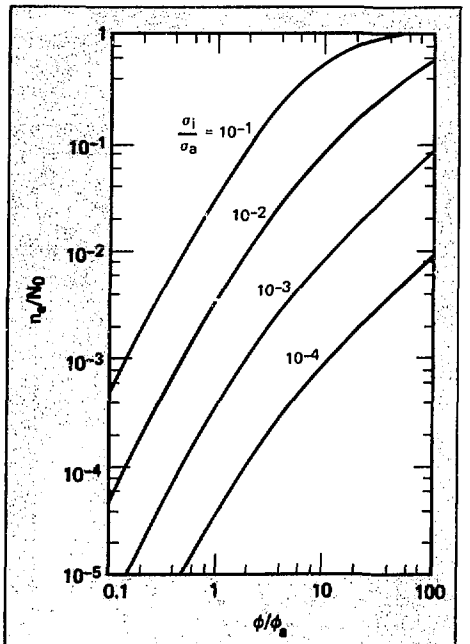

Fig. 8-54. Calculated photoelectron density normalized to the fuel density vs photolytic fluence normalized to the saturation fluence of dissociation, for several ratios of the cross sections for ^1S photoionization and fuel absorption.

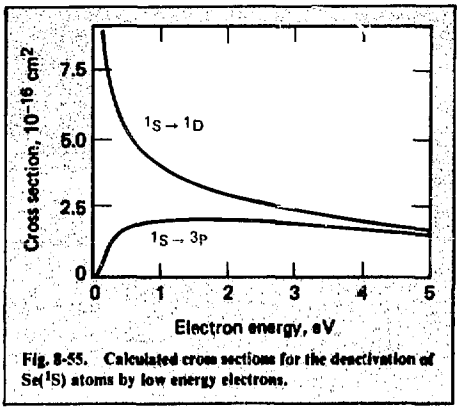

Fig. 8-55. Calculated cross sections for the deactivation of Se(^1S) atoms by low energy electrons.

resulting photoelectrons will be sufficiently large for electron collision processes to be important.

Quenching by Electrons. With low-energy electrons, there are two types of collisions that can depopulate the ^1S upper laser level: superelastic deactivation to the ^3P and ^1D levels and excitation to higher excited states, including the ionization continuum. To determine the quenching rate coefficients for S(^1S) and Se(^1S), we have estimated[123] the cross sections for $^1S \rightarrow {}^1D$ and $^1S \rightarrow {}^3P$ deexcitations, using previously calculated values for oxygen[127,128] and using the expected energy dependences at threshold.[129] The magnitudes for oxygen were scaled by factors of two and four for S and Se, respectively, to account for the larger atomic sizes of S and Se. Figure 8-55 shows the resulting superelastic cross sections for Se(^1S). Note that the $^1S \rightarrow {}^1D$ cross section is infinite at threshold, and that this leads to a finite zero-temperature limit of the quenching rate coefficient when the cross sections are averaged over a presumed Boltzmann distribution of electrons. The resulting superelastic rate coefficients are shown in Fig. 8-56(a).

We have also attempted to estimate the rate of depopulating the ^1S state by electron-impact ionization. Theoretical impact-ionization cross sections for sulfur[130] were scaled by a factor of two for selenium and then averaged over a Boltzmann distribution to obtain the rate coefficient shown in Fig. 8-56(a). As expected, at low electron temperatures the superelastic processes dominate over ionization, and presumably over excitation as well, by several orders of magnitude. Because the photoelectrons produced by the pump radiation are "cold" ($T_e < 1$ eV), depopulation of the ^1S excited states proceeds initially via quenching to the lower ^3P and ^1D levels in both sulfur and selenium. For the conditions of Fig. 8-49(b) ($\phi_i/\phi_a \approx 4$, OCSe $\approx 10^{16}$ cm^{-3}) and the estimated range of Se photoionization cross sections ($\sigma_i/\sigma_a \approx 0.2$ to 1×10^{-2}), the predicted electron density from Fig. 8-54 is 0.6 to 3×10^{14} cm^{-3}. This leads to a predicted Se(^1S) quenching time of 800 to 150 ns. The initial quenching time of about 100 ns in Fig. 8-49(b) supports the higher photoionization cross section ($\sigma_i \approx 10^{-18}$ cm^2), or a larger superelastic quenching rate, or both.

Electron-impact ionization of the gas mixture may provide additional electrons. Superelastic collisions with the ^1S atoms rapidly heat the electrons. As the electron temperature increases, the impact-ionization rate coefficients also increase drastically as shown in Fig. 8-56(a) for the case of Xe. If one

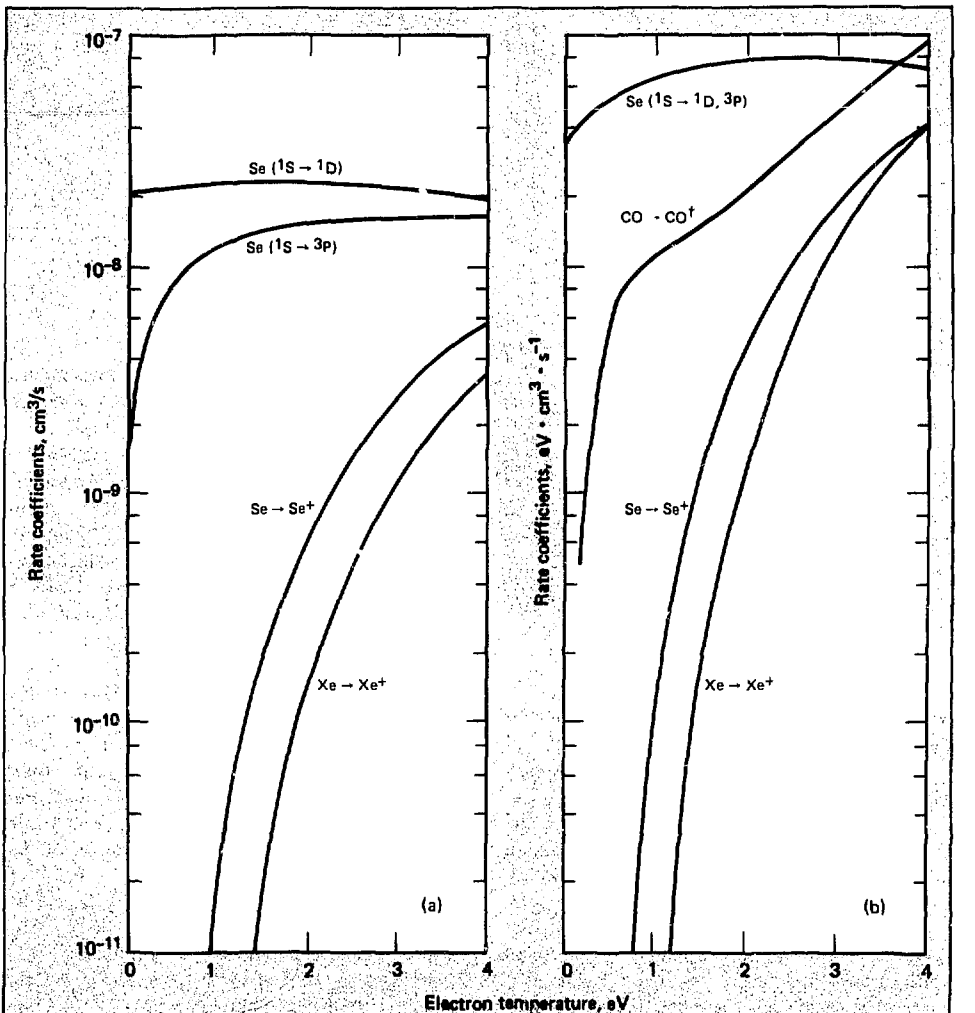

Fig. 8-56. *(a) Calculated rate coefficients as a function of electron temperature for quenching of Se(¹S) by electrons to ¹D and ³P, and for impact ionization of Se(¹S) and Xe. (b) Calculated rate coefficients for electron heating by superelastic collisions with Se(¹S) and for electron cooling by excitation of CO and ionization of Se(¹S) and Xe.*

...gas, excitation and ionization must cool the electrons. To estimate the steady-state electron temperature and to assess the importance of electron multiplication, we have evaluated the various heating and cooling rates by weighting each rate coefficient by the associated change in the electron energy. We show the resulting rates (in $eV \cdot cm^3 \cdot s^{-1}$) in Fig. 8-56(b) for heating by Se(^{1}S), and for cooling by CO vibrational excitation,[131] Se(^{1}S) ionization, and Xe ionization.

The difference between the electron heating and cooling rates gives the rate of change of the energy density of the electron gas. Because these rates are large, a Se(^{1}S) density of 10^{16} cm^{-3} rapidly drives the electron temperature to a steady state level where the superelastic heating (approximately 0.3 eV/ns) is balanced by energy lost in exciting and ionizing the Xe bath and the remnant CO. Assuming that the superelastic energy input is balanced, at steady state, by ionization cooling alone, we obtain the following expression for the maximum rate of electron production:

$$\frac{dn_e}{dt} = k_{eff}\, n_{Se(^1S)}\, n_e \,. \qquad (71)$$

The effective rate coefficient k_{eff} is simply the superelastic heating coefficient divided by the ionization potential of the dominant species. Equation (71) predicts that a Se(^{1}S) concentration of 10^{16} cm^{-3} in Xe gives an electron exponentiation time between 15 and 40 ns, depending on electron temperature. The actual ionization rate is probably lower because of other cooling mechanisms, such as accumulation of excited-state populations, spontaneous radiation, and heavy-particle quenching.

Experiments on both Kr_2^*/OCS and Xe_2^*/OCSe systems have shown that adding molecular buffer gases to the fuel mixture significantly increases the ^{1}S storage time and makes lasing possible. The effect of molecular buffers on the electron temperature can be evaluated in the steady-state temperature model. The curves in Fig. 8-56(b) imply that for a mixture of 1 Torr Se(^{1}S) and 50 Torr CO, a balance between heating and cooling occurs at about 0.25 eV. At this temperature, electron-impact excitation and ionization of the medium should be negligible, in agreement with the experimental observations.

Although cooling by molecular buffers can prevent rapid ^{1}S deactivation caused by electron multiplication, it does not remove quenching by the initial photoelectrons. Furthermore, since the excimer pumps Kr_2^* and Xe_2^* produce cold photoelectrons, a molecular buffer with a large attachment cross section at low electron energy, e.g., SF_6 (Ref. 132), must be used to remove the electrons. Other attaching gases, such as CO, CO_2, or CF_4, are less effective because of their high attachment thresholds, or smaller cross sections, or both. The measured temperature dependence of the attachment rate for SF_6 (Ref. 133) indicates that electrons are removed most efficiently at low electron temperature ($T_e < 0.5$ eV). To optimize the effect of the molecular buffers, one must choose the mixture so that, if necessary, the photoelectrons are cooled rapidly and then attached to SF_6. Some differences in the effects of various mixtures that we have observed for sulfur and selenium may be attributable to the different temperatures of the photoelectrons in these two cases. In OCS pumped by Kr_2^* near 146 nm, photoelectrons are ejected with an energy of 0.8 to 0.9 eV, whereas in OCSe pumped by Xe_2^* near 172 nm, they are ejected with 0.2 to 0.3 eV. Consequently, less cooling of the electrons that result from the ionization of Se(^{1}S) is required for efficient attachment to SF_6.

Quenching by Heavy Particles. When the deactivation of ^{1}S atoms by electrons is minimized, the storage times are determined primarily by heavy-particle quenching. For our experimental conditions, several possible quenchers need to be considered: the parent molecules OCS or OCSe, CO that is produced by the photolysis, ^{1}S atoms themselves, and "minority" products such as ^{1}D or ^{3}P atoms. The ^{1}S quenching rates of the additives that were selected for electron cooling and attachment (N_2, CO, CF_4, and SF_6) are slow. However, quenching by secondary products from these additives, such as negative ions and vibrationally excited molecules, also needs to be considered.

The rate coefficients for deactivating S(^{1}S) and Se(^{1}S) by their parent molecules OCS and OCSe are 4×10^{-13} and 1.6×10^{-10} cm$^3 \cdot$s^{-1}, respectively.[134,135] Thus, at low photolysis fluences, quenching by the parent is slow for S(^{1}S) and quite fast for Se(^{1}S). At high fluences, however, the parent molecules are completely bleached so that other species must be responsible for the observed storage

times. The deactivation of ^1S atoms by CO molecules can also be ruled out, as the measured rate constants are small, less than 3.5×10^{-16} $cm^3 \cdot s^{-1}$, for both sulfur[134] and selenium.[135]

Earlier it was suggested that self-quenching of the ^1S atoms may be important at high excited densities. However, independent theoretical calculations[122,136] of the relevant $^1\Sigma_g^+$ potential energy curves of S_2 uncover no favorable curve crossings. The 7-$^1\Sigma_g^+$ state of S_2, which correlates with $S(^1S) + S(^1S)$ at large internuclear separations, is crossed only by the $^3\Sigma_g^-$ and $^3\pi_g$ ion pairs in the energetically accessible regions.[136] Thus, the magnitude of ^1S self-quenching is determined mainly by spin-orbit coupling between these states. In addition, the 6-$^1\Sigma_g^+$ state arising from $S(^1S) + S(^1D)$ does not cross the $^3\Sigma_g^-$ ion-pair and $^3\pi_g$ ion-pair states, so that the collisional quenching by this mechanism must occur in several steps. The calculated spin-orbit-coupling matrix element[136] connecting the $^3\pi_g$ and 7-$^1\Sigma_g^+$ states is only about 0.4 cm^{-1} at the crossing (~10 bohr), and it probably leads to a self-quenching rate coefficient much less than 10^{-12} $cm^3 \cdot s^{-1}$. Consequently, we have concluded that self-quenching of ^1S atoms does not play a significant role.

The detailed mechanism for dissociating OCS and OCSe, at 146 nm and 172 nm respectively, is not well understood, and no products other than ^1S atoms and CO ($X\ ^1\Sigma_g^+$) have been identified with certainty. However, it is likely that some fraction of the photodissociation (>0.1) produces ^1D or ^3P atoms. Collisional decay of the ^1D atoms, and eventually the ^1S atoms, produces ^3P atoms. Hence, this species must be considered as a potential quencher of the excited atoms. Ab initio calculations[136] of the potential energy curves of S_2 indicate two favorable crossings at energies accessible in thermal collisions. The 5-$^3\pi_g$ state arising from $S(^3P) + S(^1S)$ crosses the fourth and fifth $^1\Sigma_g^+$ states, both correlating with $S(^1D) + S(^1D)$, near 5 to 6 bohr. As in the case of ^1S self-quenching, collisional transfer between these states can occur only because of spin-orbit coupling. The magnitude of this interaction has been calculated[136] to be 15 to 20 cm^{-1} for the 5 $^1\Sigma_g^+$ state. We have used this value in the Landau-Zener theory and obtained a $S(^3P) \rightarrow S(^1S)$ deactivation rate coefficient of 1×10^{-12} $cm^3 \cdot s^{-1}$ because of the 5 $^3\pi_g \rightarrow 5\ ^1\Sigma_g^+$ crossing alone. This rate appears to be too small to explain the $S(^1S)$ quenching coefficient inferred in our experiments. However, the contributions of other curve crossings have not been included because of the lack of relevant coupling-matrix elements. In addition, the magnitude of the spin-orbit interaction between these S_2 states varies drastically with internuclear distance,[136] and, consequently, small errors in the predicted crossings may lead to significant changes in the predicted quenching rates. At present, no definitive conclusions can be reached in this regard, and additional studies of ^1S quenching by ^3P atoms are clearly needed.

Finally, we comment briefly on the interesting observation[137] of $Se(^1S)$ production in experiments where a mixture of hot (~400°C) selenium vapor and CO was irradiated by 193-nm light from an ArF laser. The presence of $Se(^1S)$ was detected by observation of a long-lived (100-μs) and narrow-band emission corresponding to the $^1S_0 \rightarrow {}^3P_1$ transauroral line. The $Se(^1S)$ excited-state density was estimated to be of the order 10^{15} cm^{-3}. Gower and co-workers[137] suggested that $Se(^1S)$ atoms are produced by the 193-nm photolysis of OCSe, which is formed in a reaction between CO and hot selenium vapor. They argued that the quantum yield curve of OCSe was shifted to longer wavelengths because of the high temperatures, allowing significant production of $Se(^1S)$ by 193-nm radiation. This hypothesis, however, disagrees with other observations,[138] which indicate that direct vibrational heating of OCSe does not significantly increase the quantum yield of $Se(^1S)$ at 193 nm.

We have considered this problem and arrived at a different interpretation. It is known that saturated selenium vapor at low temperature is dominated by polymeric species[139] such as Se_5 and Se_8. It is quite likely that 193-nm radiation from ArF photodissociates these molecules efficiently, leading to a variety of products including various excited states of Se_2. We propose that the metastable states of Se_2 product can react with CO to produce $Se(^1S)$. This hypothesis is supported by the fact that the rapid quenching of $Se(^1S)$ by OCSe leads to CO and Se_2^* (Refs. 135, 140):

$$Se(^1S) + OCSe \rightarrow Se_2^* + CO \quad . \tag{72}$$

The radiative lifetime of this excited state of Se_2^* is about 3 μs.[138] When Gower and co-workers[137] excited hot selenium vapor at 193 nm, they found a spectrum and time decay similar to those observed

from Se(^{1}S) quenching by OCSe [Eq. (72)]. By introducing CO (pressure >10 Torr), they found the fluorescence changed from broad-band Se_2 emission with 2-μs decay to narrow-band emission to Se(^{1}S) emission with slow decay. Thus, it appears plausible that, for sufficiently long-lived Se_2^* excited states, the reaction of Eq. (72) could be reversed, at elevated temperatures, by adding CO to yield high densities of Se(^{1}S). Such a mechanism for producing Se(^{1}S) has the potential advantage of requiring only 193-nm radiation, which cannot photoionize the resulting excited atoms. Because little is known about Se_2 excited states other than the well known B $^3\Sigma_u^-$ state, additional experimental and theoretical investigations of this problem seem worthwhile.

References

122. *Laser Program Annual Report—1977*, Lawrence Livermore Laboratory, Livermore, Calif., UCRL-50021-77, §7 (1978).
123. H. T. Powell and A. U. Hazi, *Chem. Phys. Lett.* **59**, 71 (1978).
124. G. Tondello, *Astrophys. J.* **172**, 771 (1972).
125. A. Weiss, National Bureau of Standards, private communication (1978).
126. E. J. McGuire, *Photoionization of the $(np)^4$ $^1S_0$ Term of the Group VI Atom Via Autoionization Levels*, Sandia Laboratories, Albuquerque, N. Mex., Report SAND-78-1379J (1978).
127. L. D. Thomas and R. K. Nesbet, *Phys. Rev. A* **11**, 170 (1975).
128. M. Le Dourneuf, *Unified Treatment of the State of Electron-Atom Collision System by the Method of Core Polarization*, Ph.D. Thesis, Pierre and Marie Curie University, Paris (1976).
129. L. D. Thomas and R. K. Nesbet, *Phys. Rev. A* **12**, 1729 (1975).
130. G. Peach, *J. Phys. B* **4**, 1670 (1971).
131. J. Land, supplemental data memo to Joint Institute for Laboratory Astrophysics (JILA) Publication No. 1660 (1977), and *J. Appl. Phys.* **49**, 5716 (1978).
132. D. Spence and G. J. Schulz, *J. Chem. Phys.* **58**, 1800 (1973).
133. L. G. Christophorou, D. L. McCorkle, and J. G. Carter, *J. Chem. Phys.* **54**, 253 (1971).
134. O. J. Dunn, S. V. Filseth, and R. A. Young, *J. Chem. Phys.* **59**, 2892 (1973).
135. G. Black, R. L. Sharpless, and T. G. Slanger, *J. Chem. Phys.* **64**, 3993 (1976).
136. R. P. Saxon, *Theoretical Studies of Diatomic Laser Candidates*, SRI International Report MP78-105 (1978).
137. M. C. Gower, A. J. Kearsley, and C. E. Webb, private communication.
138. W. K. Bischel, SRI, International, Menlo Park, Calif., private communication (1978).
139. J. Berkowitz and W. A. Chupka, *J. Chem. Phys.* **48**, 5473 (1968).
140. G. Black, R. L. Sharpless, and T. G. Slanger, *J. Chem. Phys.* **64**, 3985 (1976).

Author	Major Contributors
A. U. Hazi	H. T. Powell
	N. W. Winter

8.4.3 Laser and Kinetics Modeling

Recent experiments suggest that photoelectron production, heating, and multiplication are important for pump fluences and excited state densities of interest in Group VI lasers. Furthermore, we have found that photoelectron effects can be suppressed and ^{1}S lifetimes significantly increased under these conditions, by the addition of molecular species that dissipate electron energy by inelastic collisions and remove electrons by attachment. We have constructed a simple model of Se(^{1}S) experiments with OCSe/CO/Xe mixtures, to illustrate the possible kinetic behavior caused by a buffer gas that cools but does not strongly attach electrons. The significant processes included in this model are summarized in Table 8-7. Unfortunately, for many of these processes, accurate kinetic data are not available; therefore, the present model is only qualitative and approximate.

We have used the model to explore two approaches to the Se laser kinetics problem. In the first approach, we assumed the electron distribution function to be Maxwellian with temperature T_e and the CO vibrational population to be Boltzmann with temperature T_v. We neglected electron interactions with OCSe. The dynamics of this system were governed by a set of continuity and energy equations describing particle gain and loss processes and energy flow between the translational and vibrational degrees of freedom of the gas medium.[148] In the second approach, we assessed the approximations made assuming a Maxwellian electron distribution function by solving the electron Boltzmann equation for the fractional ionization and excited state populations predicted by the kinetics calculations.

Figure 8-57 shows the calculated local kinetic behavior of two OCSe/CO/Xe mixtures with initial partial pressures (in Torr) of 1/0/250 [Fig. 8-57(a)] and 1/40/250 [Fig. 8-57(b)]. The pump intensity was 2 MW/cm^2 for 50 ns, corresponding to conditions achieved in the experiments discussed in §8.3.1. At this fluence, the medium is fully bleached and 3×10^{16} cm^{-3} (nearly 1 Torr) of Se(^{1}S) atoms are initially produced. In the mixture with no initial CO [Fig. 8-57(a)], 1 Torr of CO is produced by

Table 8-7. Significant collision processes included in Se kinetics model.

	Reference
Pump photoabsorption processes	
$OCSe \rightarrow Se(^1S) + CO$	1×10^{-16} cm^2 (Ref. 141)
$Se(^1S) \rightarrow Se^+ + e$	2.5×10^{-19} cm^2 (Ref. 142)
Excited state processes	
$Se(^1D) + Xe \rightarrow Se(^3P) + Xe$	2×10^{-10} cm$^3 \cdot$ s^{-1} (estimate)
$Se(^1D) + CO \rightarrow Se(^3P) + CO$	2×10^{-10} cm$^3 \cdot$ s^{-1} (estimate)
$Se(^1S) + OCSe \rightarrow Se_2^* + CO$	1.6×10^{-10} cm$^3 \cdot$ s^{-1} (Ref. 143)
Electron collision processes	
$Se(^1S) + e \rightarrow Se(^1D, {}^3P) + e$	Figs. 8-55, 8-56
$Xe + e \rightarrow Xe^+ + 2e$ $CO(v) + e \rightleftarrows CO(v') + e$ $CO + e \rightarrow CO^+ + e$	Fig. 8-56 (Refs. 144, 145)
Recombination processes	
$Se^+CO + M \rightarrow SeCO^+ + M$	10^{-31} cm$^6 \cdot$ s^{-1} (Ref. 142)
$SeCO^+ + e \rightarrow Se + CO$	10^{-17} cm$^3 \cdot$ s^{-1} (Ref. 142)
$Xe^+ + 2Xe \rightarrow Xe_2^+ + Xe$	2×10^{-31} cm$^6 \cdot$ s^{-1} (Ref. 146)
$Xe_2^+ + e \rightarrow Xe^{**} + Xe$	2.7×10^{-7} cm$^3 \cdot$ s^{-1} (Ref. 147)

photodissociation of OCSe. This CO concentration is ineffective in controlling the electron temperature, which rapidly rises to about 1.3 eV. The CO vibrational temperature equilibrates with the electron temperature by electron inelastic and superelastic collisions. Since the CO vibration-to-translation relaxation time is very slow,[149] the electron temperature remains high and decays slowly because of inelastic collisions with other species. At the predicted electron temperature, the electron

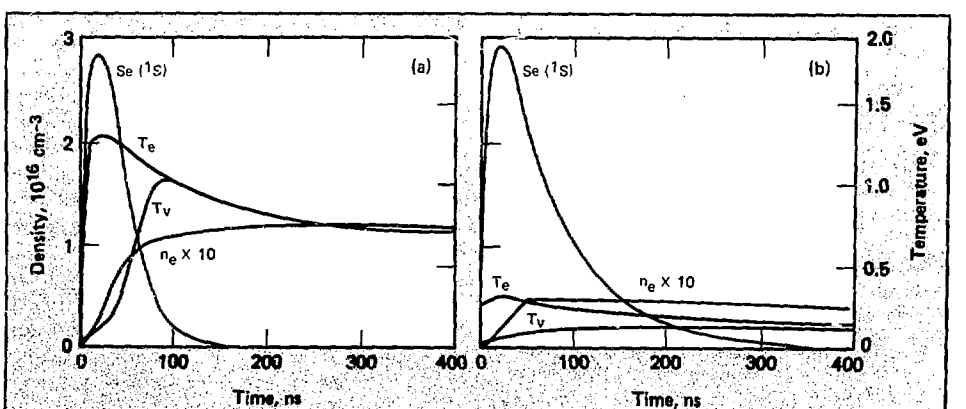

Fig. 8-57. (a) Se(^{1}S) density, electron temperature Te, CO vibrational temperature T_v, and electron density n_e vs time computed from the kinetic model. An OCSe/Xe mixture of 1/250 Torr was photolyzed by 100 mJ/cm^2 at 172 nm in a 50-ns pulse. (b) Computed kinetic behavior for the same conditions as (a) except for the addition of 40 Torr CO to the photolytic mixture. Electron multiplication has been eliminated in this case.

density rises because of impact ionization to a density of about 10^{15} cm^{-3}. The electrons rapidly quench the Se(^{1}S) excited-state density. Figure 8-57(b) indicates that when 40 Torr of CO are added, the electron temperature and density are constrained to smaller values. This constraint gives longer Se(^{1}S) lifetimes by eliminating electron multiplication. These simple kinetics calculations agree qualitatively with the experimental data presented in §8.3.1. We have not analyzed the case of an attaching buffer gas (such as SF_6), but we expect that the remnant quenching in Fig. 8-57(b), caused by the initial photoelectrons, would be eliminated.

To assess the significance of non-Maxwellian electron kinetics, we calculated the electron distribution functions by solving the electron Boltzmann equation. The results of the kinetic modeling (Fig. 8-57) indicate that, for the experimental conditions, the fractional ionization of the medium varies in the 10^{-6}-to-10^{-4} range. Figure 8-58 shows calculated electron distribution functions for two Se(^{1}S)/CO/Xe mixtures. Complete photodissociation of the OCSe is assumed in these calculations. The results presented in Fig. 8-58 clearly show that electron distributions in these media are highly non-Maxwellian and sensitive to

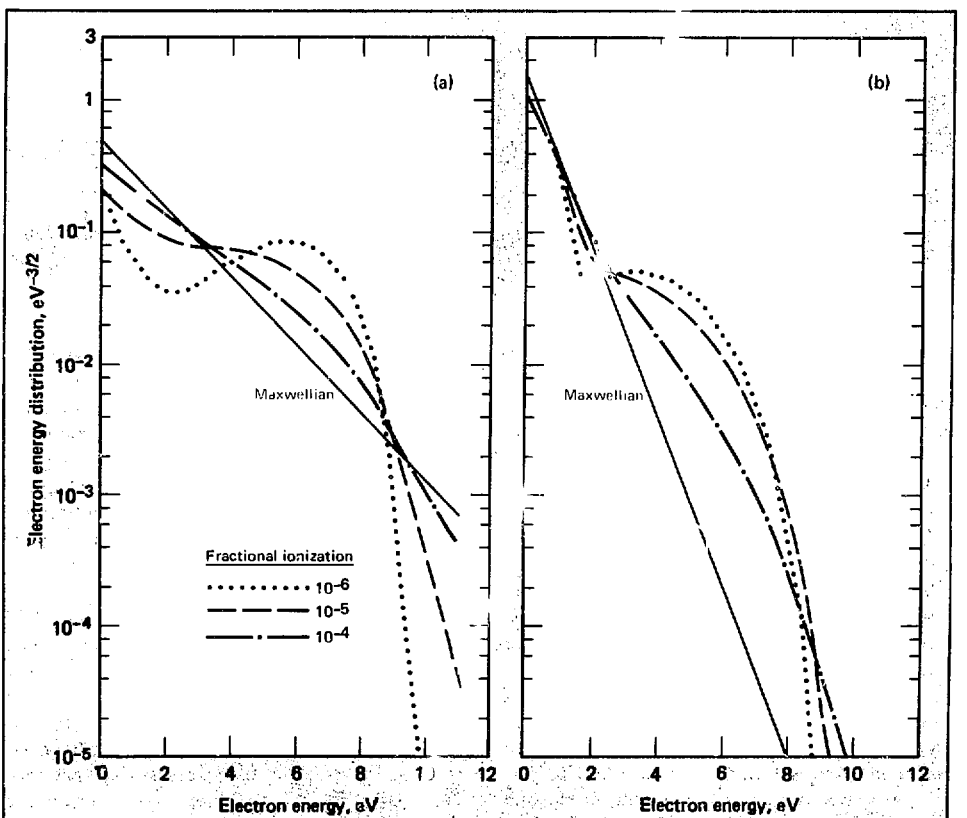

Fig. 8-58. (a) Electron energy distribution computed from the Boltzmann code for an Se(^{1}S)/CO/Xe mixture of 1/1/250 Torr and various fractional ionizations. A Maxwellian distribution is approached only at high electron density. (b) Computed distributions for Se(^{1}S)/CO/Xe mixture of 1/10/250 Torr.

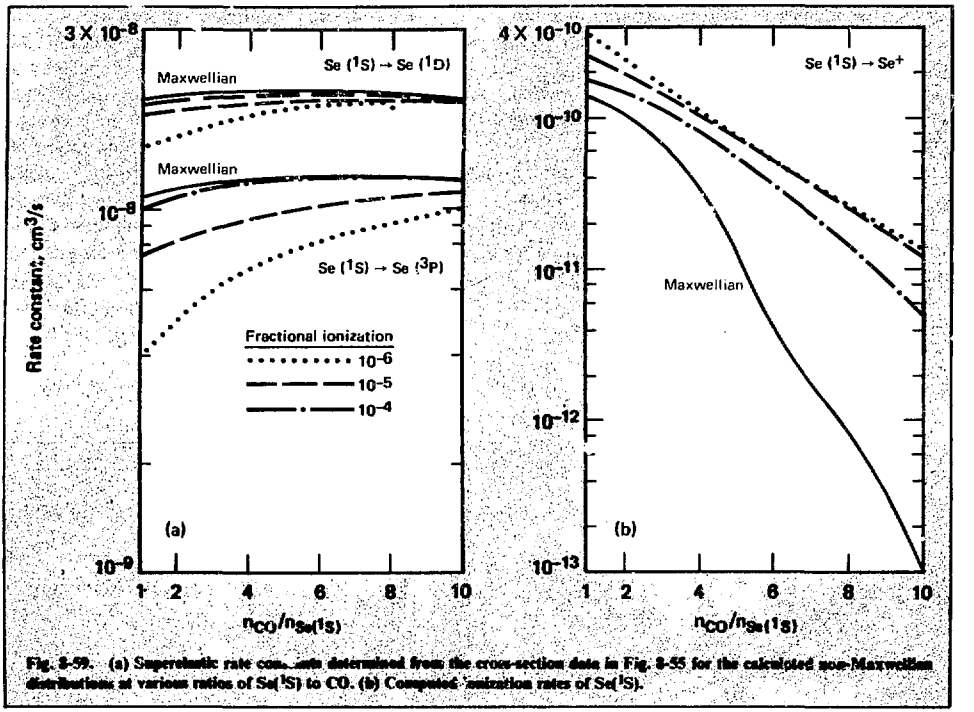

Fig. 8-59. (a) Superelastic rate constants determined from the cross-section data in Fig. 8-55 for the calculated non-Maxwellian distributions at various ratios of Se(^{1}S) to CO. (b) Computed ionization rates of Se(^{1}S).

fractional ionization. The well in the distributions in the 1-to-3-eV energy interval is caused by CO vibrational excitation. The corresponding peak in the 4-to-8-eV energy range is caused by electron heating by superelastic collisions with Se(^{1}S). In this energy interval, CO vibrational excitation is ineffective in dissipating excess electron energy. Figure 8-59 shows the effect of non-Maxwellian electron distributions on Se(^{1}S) deexcitation and ionization rate constants, respectively, for fractional ionization and CO/Se(^{1}S) ratios of experimental interest. The predicted rate constants only approach those calculated for a Maxwellian distribution at the highest values of fractional ionization. The rate constants for other electron-collision processes may also differ substantially from those calculated assuming a Maxwellian electron distribution.

In summary, we have found that the electron distributions are generally non-Maxwellian. Thus, rate constants for electron collision processes are sensitive to fractional ionization ($>10^{-6}$), relative CO concentration ($n_{CO}/n_{OCSe} > 1$), CO vibrational temperature, and fractional Xe electronic excitation ($n^*/n > 10^{-5}$). Non-Maxwellian electron effects must be included to achieve satisfactory agreement between modeling and experiments. The modeling supports the hypothesis that electron heating and multiplication can lead to rapid quenching of Se(^{1}S). Addition of an electron-cooling buffer, such as CO, can prevent electron multiplication; however, it does not eliminate ^{1}S quenching by the initial photoelectrons.

In practical applications, the magnitude of ^{1}S photoionization may limit laser-aperture scaling, even if the electrons produced are rapidly removed. Because the ^{1}S atoms are produced by propagation of a photodissociation wave across the laser amplifier, the direct loss of ^{1}S atoms by photoionization can be serious at the pump-radiation entrance boundary. The ^{1}S atoms at this boundary are bathed in intense pump radiation for virtually the entire amplifier pumping time. Figure 8-60 shows the fractional loss, caused by photoionization of ^{1}S atoms near the window, vs the width of aperture

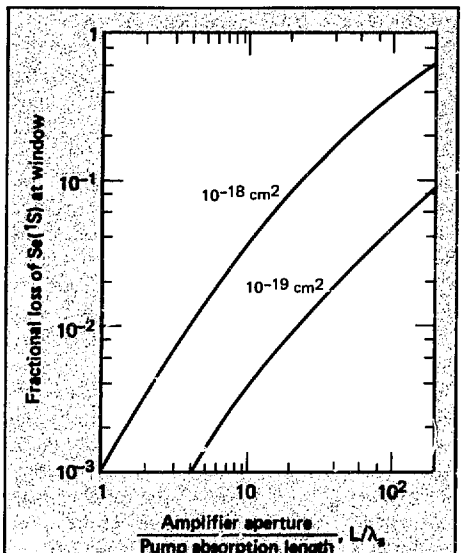

Fig. 8-60. Fractional loss by photoionization of Se(1S) at the input window, produced by bleaching an aperture of given width by two-sided irradiation. Curves for Se(1S) photoionization cross sections of 10^{-19} and 10^{-18} cm^2 are shown.

that is bleached by two-sided pumping. At an OCSe density of 10^{16} cm^{-3}, the absorption length (e^{-1}) is about 1 cm. If we limit the fractional loss near the window to 0.2 (i.e., 0.1 average across the aperture), the maximum width that can be pumped with a 10^{-18}-cm^2 photoionization cross section is 40 cm. However, the allowable width exceeds 1 m with a 10^{-19}-cm^2 cross section. Hence, if the ^{1}S photoionization cross section is as large as 10^{-18} cm^2, it poses a serious limitation to scaling these lasers to very large sizes.

References

141. G. Black, R. L. Sharpless, and T. G. Slanger, *J. Chem. Phys.* **64**, 3985 (1976).
142. H. T. Powell and A. U. Hazi, *Chem. Phys. Lett.* **59**, 71 (1978).
143. G. Black, R. L. Sharpless, and T. G. Slanger, *J. Chem. Phys.* **64**, 3993 (1976).
144. G. Peach, *J. Phys. B* **4**, 1670 (1971).
145. J. Land, supplemental data memo to Joint Institute for Laboratory Astrophysics (JILA) Publication No. 1660 (1977), and *J. Appl. Phys.* **49**, 5716 (1978).
146. A. P. Vitolo and H. J. Oskam, *Phys. Rev. A* **8**, 1860 (1973).
147. Y. J. Shiu, M. A. Biondi, and D. P. Siphor, *Phys. Rev. A* **15**, 494 (1977).
148. R. A. Haas, *Phys. Rev. A* **8**, 1017 (1973).
149. R. C. Millikan and D. R. White, *J. Chem. Phys.* **39**, 3209 (1963).

Author	Major Contributors
R. A. Haas	R. D. Franklin
	W. L. Morgan

8.5 Advanced Research and Technology

There is a continuing need for small-scale theoretical and experimental investigations of new techniques and candidates that might permit the construction of fusion lasers of higher efficiency and greater simplicity than the current lasers described above. These investigations include the identification of:

- New and more efficient pump sources for the conversion of electrical or chemical energy to light.
- New storage media or compression techniques with superior characteristics.
- New theoretical techniques to analyze existing or proposed laser systems.
- New technology to improve the engineering and performance of fusion lasers.

During the past year, we have pursued several research projects that show interesting possibilities for advances in these areas. The ionic-charge-transfer bands discussed in the following subsection (8.5.1) are candidates for an efficient new class of pump sources somewhat related to the efficient, ion-pair radiating states in the rare gas halides. The resonant Raman processes discussed in §8.5.2 may permit Raman compression with higher intensity gain than will the off-resonant vibrational scatterers discussed in §8.2 and 8.3. Subsection 8.5.3 discusses experiments aimed at understanding the limits to scaling RGH discharge lasers, and §8.5.4 and 8.5.5 cover advances in theoretical techniques that are generally applicable to the analysis of all the advanced lasers discussed here.

8.5.1 Ionic-Charge-Transfer Pump Sources

The chief cause of inefficiency in current laser-pump sources is the lack of efficiency in the conversion of electrical energy to light output. Therefore, we have a continuing interest in radiative transitions

with the potential for more efficient conversion of electrical excitation to fluorescence or laser output than exhibited by current pump sources.

A class of transitions that may be useful as efficient pump sources are ionic-charge-transfer bands in low-pressure, electron-beam-excited gases. We have begun a study of these charge-transfer bands in rare gases to improve our understanding of their properties and kinetics. The potential curves were obtained theoretically, and the emission spectra and high pressure kinetics were studied using a short-pulse electron gun.

The spectra of almost all combinations of heteronuclear rare-gas ions have been identified by Tanaka et al.,[150] who observed bands corresponding to charge-transfer transitions that can be symbolized by $X^+Y \rightarrow XY^+$. The low-lying states of the mixed ions correlate to the ionic ground-state multiplets of the constituent ions X^+ and Y^+, and the transition energy corresponds roughly to the difference beteen their ionization potentials.

Using the LAMP[151] short-pulse (25-ns), high-repetition-rate (50-Hz), 80-keV electron gun, we studied the spectrum (and its time dependence) of Ar/Xe mixtures in the vicinity of 330 nm (Ref. 152) and of Kr/Xe mixtures in the vicinity of 490 nm. In both mixtures, a strong band is seen that resembles the shape of the RGH emission bands (see also Tanaka et al., Ref. 150); indeed, such a spectrum is expected. The spectra of both the rare gas halides and the mixed noble gas ions represent charge-transfer transitions and thus have a large radiative rate. However, there are several differences. In the rare gas halides, the upper curve is ionic and is deeply bound because of the Coulomb attraction, while the lower state is repulsive. In the mixed rare-gas ions, this strong Coulomb attraction is absent. For example, the upper curves of Kr^+Xe are slightly attractive because of a charge-induced dipole force $-\alpha/R^4$, while the lower curves, corresponding to $KrXe^+$, may have significant binding (0.2 to 0.5 eV). The similarity of the spectrum of mixed noble gas ions to that of a bound-free excimer, RGH-type transition results from the great displacement of the potential minima of the upper and lower states. Therefore, the emission goes to very high vibrational states of the ground state, terminating on a nearly flat potential curve.

The physical basis of our picture can be seen in Fig. 8-61. On the left side of the figure we show our

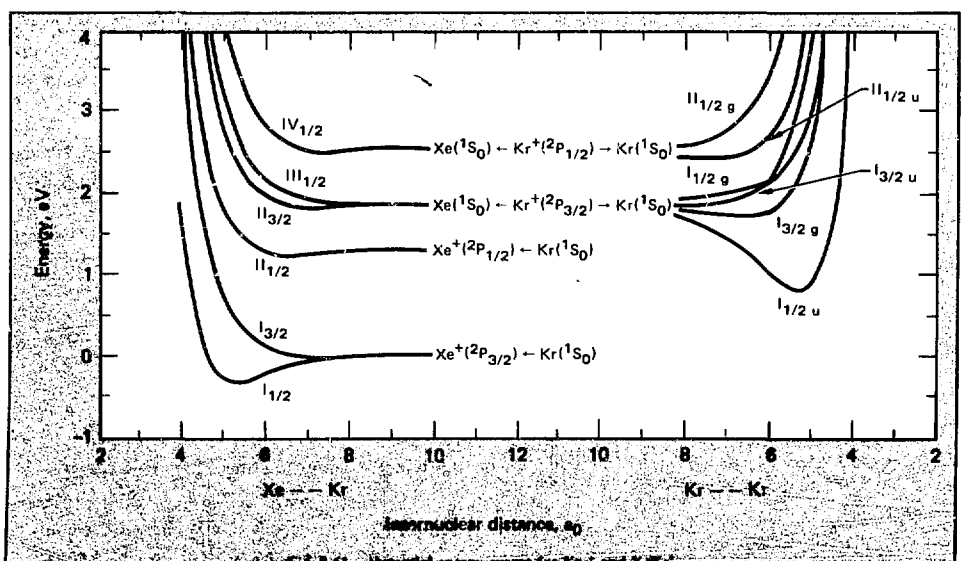

Fig. 8-61. Potential energy curves for Xe_2^+ and $XeKr^+$.

estimated potential-energy curves for $XeKr^+$; on the right, the potential energy curves for Kr_2^+ calculated by Wadt[153] are reproduced. It is clear that the ground-state $Kr^+(^2P_{3/2})$ ion can recombine with the Kr in the strongly attractive $I_{1/2u}$ state and hence is rapidly deactivated. The upper-state $Kr^+(^2P_{1/2})$ can form the slightly attractive $IV_{1/2}$ states of $XeKr^+$ or the more repulsive $II_{1/2u}$ and $II_{1/2g}$ states of Kr_2^+. The formation of the excited $XeKr^+$ state leads to the observed radiation.

Our kinetic studies show that the formation of the upper-state Kr^+Xe is directly from Kr^+, which in turn is produced by electron impact from Kr. One of the two spin-orbit-split doublets, the lower $Kr^+(^2P_{3/2})$ state, is quickly deactivated, while the other one, $Kr^+(^2P_{1/2})$, stores energy for some time (τ_{deact} = 70 ns at 2 atm), losing energy mostly by collisional deactivation.

There are several interesting consequences to our studies. First, the $Kr^+(^2P_{1/2})$ and other analogous states, $Ar^+(^2P_{1/2})$ and $Xe^+(^2P_{1/2})$, are quite long-lived and thus keep the electron density high even in pure gases. The influence of these species on rare gas laser performance needs to be studied. Second, in pure gases, there is a population inversion between the $^2P_{1/2}$ and $^2P_{3/2}$ states (the latter being deactivated via molecular ion formation and dissociative recombination), and laser action can be expected. Also, the depopulation of the $^2P_{1/2}$ state by stimulated emission could better the performance of the rare gas excimer lasers both by "force feeding" the excimer state and by the disappearance of a possibly absorbing molecule (the collisional complex formed from the $^2P_{1/2}$ ion). Third, population inversion can be expected on the $Kr^+Xe \rightarrow KrXe^+$ transition and analogous transitions.

There are possibilities of analogous systems in the rare-gas-alkali ions. One promising example is the $(NaXe)^+$ ion. The upper state Xe^+Na is populated directly from Xe^+, and since Xe has both higher ionization energy *and* higher stopping power than Na, kinetic processes favoring population inversion are expected even in a 50/50 Xe/Na mixture. Our calculations show that the upper state is bound by 0.3 eV, while the lower state has only a charge-induced dipole ($-\alpha/R^4$) minimum, since both Xe and Na^+ have closed electronic shells. The transition is expected to fall at 170 nm, and the efficiency could be comparable to the Xe_2^* excimer laser, which emits at that wavelength. This transition is therefore an interesting potential pump source for the Se(^{1}S) laser using OCSe photodissociation, which is discussed in §8.4.

References

150. Y. Tanaka, K. Yoshino, and D. E. Freeman, *J. Chem. Phys.* **62**, 4484 (1975).
151. *Laser Program Annual Report—1975*, Lawrence Livermore Laboratory, Livermore, Calif., UCRL-50021-75 (1976), p. 495.
152. A preliminary account of those studies was given at the 30th Gaseous Electronics Conference, Palo Alto, Calif. (1977).
153. W. K. Wadt, *J. Chem. Phys.* **68**, 402 (1978).

Authors

A. Szoke
N. Winter
H. Powell

8.5.2 Near-Resonant Raman Processes

Metal Vapor Systems for Compressors. A Raman process that is close to resonance with an intermediate state can reduce the gain for the backward second-Stokes process, which is the most important limit on the intensity gain in a Raman compressor. The scatterer should have a large Stokes shift and a sharp intermediate state to avoid single-photon absorption of the pump in the wings of the intermediate level. These conditions are most easily satisfied for electronic Raman scattering in atoms, with the liability that the appropriate atoms are metals and semimetals that require high temperatures to get the desired vapor densities.

Figure 8-62 shows a possible candidate for a near-resonant KrF compressor operating in atomic calcium. The KrF pump photon lies 1433 cm^{-1} below the $4s6p\,^1P_1$ state, which serves as a near-resonant intermediate state. The most desirable Raman transition is the transition of highest quantum efficiency ν_s, which terminates on the $4s3d\,^1D_2$ state and gives a Stokes wavelength of 532 nm. There are other possibly competing Raman transitions ν_s' and ν_s'', as well as the possibility of resonance-enhanced two-photon photoionization, and these competing processes must be understood.

Large-scale configuration-interaction calculations were completed for the $(4sns)\,^1S$, $(4snp)\,^1P^o$, and $(4snd)\,^1D$ states of Ca. The wave functions, which contained up to 550 space-spin configurations, were chosen to describe both the correlation of the two valence electrons and the dynamic polarization of the 3s and 3p orbitals of the M-shell.

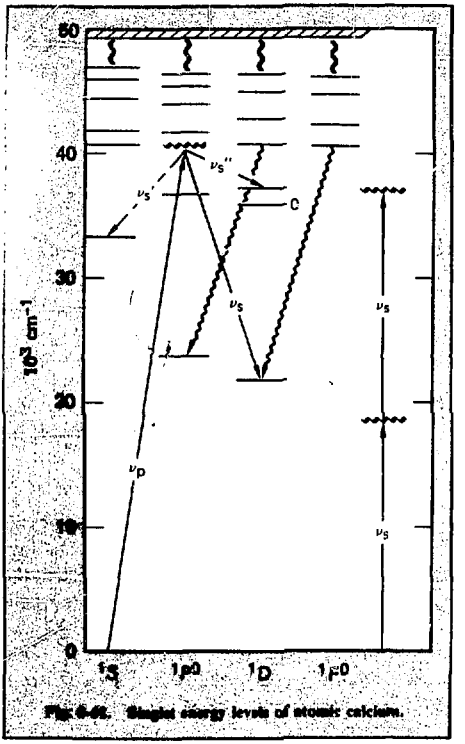

Fig. 8-62. Singlet energy levels of atomic calcium.

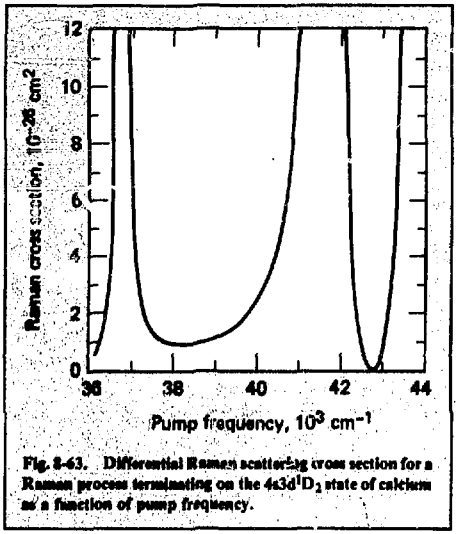

Fig. 8-63. Differential Raman scattering cross section for a Raman process terminating on the $4s3d^1D_2$ state of calcium as a function of pump frequency.

Using the calculated one-photon transition moments and the experimental transition energies, we have evaluated the Raman cross section and the gain coefficient as functions of laser frequency for both the main transition $(4s^2)^1S \rightarrow (4s3d)^1D$ and the possible parasitic transitions $(4s^2)^1S \rightarrow (4s5s)^1S$ and $(4s^2)^1S \rightarrow (4s4d)^1D$. As Fig. 8-63 shows, the Raman cross section for $(4s^2)^1S \rightarrow (4s3d)^1D$ at KrF pump energy (40 300 cm^{-1}) is larger than our earlier estimates, which neglected M-shell polarization, but is still about a factor of three less than initial crude estimates,[154] which neglected all states other than $4s6p^1P_1$. Figure 8-64 compares the gain γ in cm/W for the transitions ν_s, ν_s', and ν_s'' as a function of pump wavelength for a calcium density of 10^{16} cm^{-3} (vapor pressure of Ca at 820°C). The ν_s' parasitic is predicted to have a gain roughly equal to that of the ν_s, which is probably tolerable in a compressor. The forward saturation energy at this particle density is predicted to be 0.13 J/cm^2, giving a backward saturation energy of about 0.5 J/cm^2 with a KrF pump of 0.1-cm^{-1} line width. Restricting the pump intensity to 12 MW/cm^2 to avoid ground state depletion,[154] one would now predict that a calcium compressor at this density would accept a 400-ns pump pulse at about 5 J/cm^2, which is more favorable than initial estimates.[154] However, experiments at LLL and AVCO,[155] which attempted to

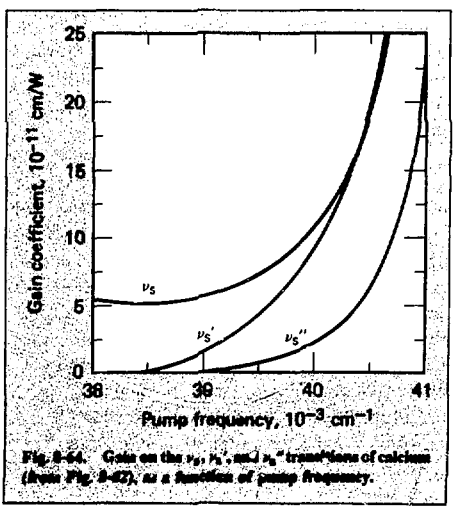

Fig. 8-64. Gain on the ν_s, ν_s', and ν_s'' transitions of calcium (from Fig. 8-62), as a function of pump frequency.

observe superfluorescent forward Raman scattering at 532 nm, have been unsuccessful to date. It is not yet clear whether this result stemmed from experimental difficulties with the hot vapor cells, from superfluorescence on the infrared transitions ν_s' and ν_s'', or from other problems such as two-photon photoionization in the intense focused KrF beams. A resolution of this issue requires more careful experiments, which are in progress.

Several other atoms have been proposed for use in a KrF compressor. Thallium has an energy defect of 1765 cm^{-1} for KrF pumping with a Stokes wavelength of 308 nm; however, it has been shown[156] that a competing 1650-nm transition has far higher gain, in agreement with our theoretical estimate that the infrared gain should be a few hundred times higher. Thallium could be useful at other wavelengths, and experiments to study the physics of near-resonant Raman scattering in this atom are discussed in the next subsection. There are other potential atomic candidates for KrF compressors, such as antimony and bismuth; however, only crude estimates are possible for these atoms, since the line strengths are poorly known. Both of these materials also have a significant dimer concentration in the vapor phase, and these dimers may have interfering absorption or stimulated scattering. Further study is planned to resolve these issues.

References

154. J. R. Murray, J. Goldhar, D. Eimerl, and A. Szoke, *IEEE J. Quant. Electron.* **QE-15**, 342 (1979)
155. D. W. Trainor and S. A. Mani, *Appl. Phys. Lett.* (to be published).
156. N. Djeu, Naval Research Laboratory, Washington, D.C., private communication (1978).

Authors

J. R. Murray
A. Szoke
A. Hazi
T. Rescigno
D. Eimerl
J. Goldhar

Theory of Raman Scattering Driven By Noisy Fields. As pointed out in §8.2.3, an incoherent, noisy, or multifrequency field causes a large forward-to-backward ratio of the Raman gain. The gain caused by a noisy multicolored field becomes especially interesting when the field is close to resonance with an intermediate level, where one expects a transition from a Raman to an optically pumped amplifier.

The theoretical problem is quite complicated, especially if the fields are strong. All calculations were carried out for a single three-level atom, depicted schematically in Fig. 8-65. The driving field is near resonance with the (0,1) level pair and can be "strong" (saturating). We calculate the susceptibility for a weak monochromatic field applied near resonance with the (1,2) level pair. The stochastic pump field, $\mathcal{E}(t) = \mathcal{E}_0 \exp[-i\phi(t)]$, is modeled as a field of constant amplitude $\mathcal{E}_0$ that undergoes a "phase diffusion," a Markov process, giving $\langle\langle \exp[i\phi(t') - i\phi(t)] \rangle\rangle = \exp[-\lambda(t' - t)]$, $t' > t$, corresponding to a Lorentzian spectrum. The resulting complex gain (susceptibility) formula is

$$\beta_0(\nu) = \frac{\nu N}{2\hbar c} |\mu_{12}|^2 \, G(i\nu) \, ,$$

$$G(s) = \frac{(\lambda + s + k'_{02})(n_1 - n_2) + \dfrac{\Omega_0^2}{4} \dfrac{k_{10} + k_{12}}{\lambda + i\Delta + k'_{10}} \dfrac{1}{f}}{(s - i\Delta + k'_{12})(\lambda + s + k'_{02}) + \dfrac{\Omega_0^2}{4}} \, , \qquad (73)$$

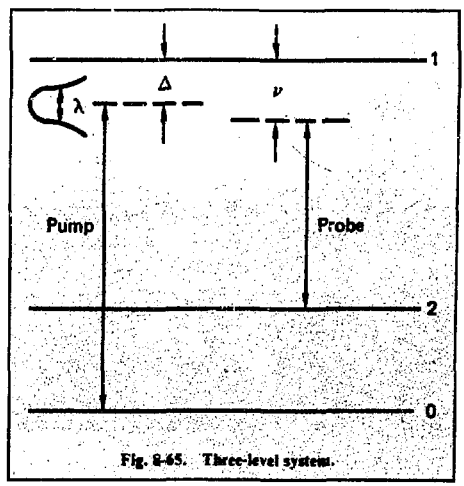

Fig. 8-65. Three-level system.

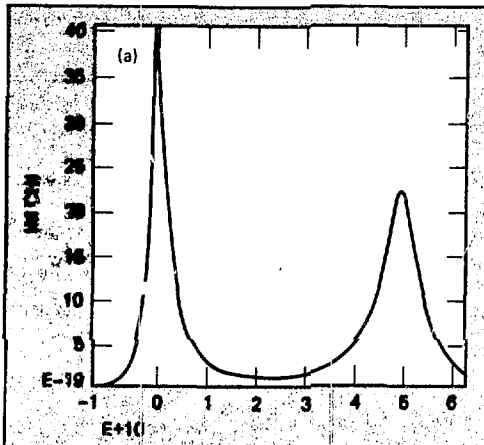

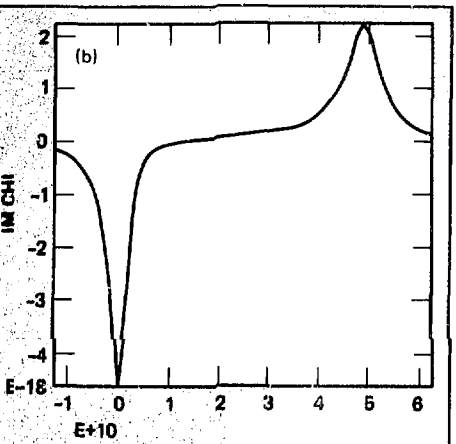

D	PARAMETERS IN FREQUENCY UNITS		
DETUN	5.000E+10	K10	5.000E+08
WIDTH	3.000E+09	K12	5.000E+08
RABI	1.000E+07	K20	7.000E+08
VDOP	3.000E+04	K02	0.
OME01	1.000E+15	K10P	2.500E+08
OME12	8.000E+14	K12P	2.000E+09
		K02P	1.500E+09

D	PARAMETERS IN FREQUENCY UNITS		
DETUN	5.000E+10	K10	5.000E+08
WIDTH	3.000E+09	K12	5.000E+08
RABI	1.000E+07	K20	5.000E+08
VDOP	3.000E+04	K02	0.
OME01	1.000E+15	K10P	2.500E+08
OME12	0.000E+14	K12P	2.000E+09
		K02P	1.500E+09

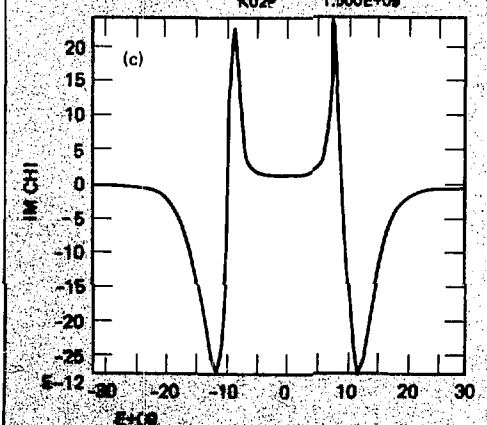

D	PARAMETERS IN FREQUENCY UNITS		
DETUN	0.	K10	5.000E+08
WIDTH	3.000E+09	K12	5.000E+08
RABI	1.000E+10	K20	4.000E+08
VDOP	3.000E+05	K02	0.
OME01	1.000E+15	K10P	2.500E+08
OME12	8.000E+14	K12P	7.500E+08
		K02P	2.500E+08

Fig. 8-66. Gain calculations in Doppler-broadened three-level system for parallel incident and amplified fields.

where

$$n_1 - n_2 = \frac{1}{f}\left[P\left(1 - \frac{k_{12}}{k_{20}}\right) - \left(k_{10} + k_{12} + P\right)\frac{k_{02}}{k_{20}}\right],$$

$$f = (k_{10} + k_{12})\left(1 + \frac{k_{02}}{k_{20}}\right) + P\left(2 + \frac{k_{12} + k_{02}}{k_{20}}\right),$$

$$P = \frac{\Omega_0^2}{2}\,\frac{\lambda + k'_{10}}{\left(\lambda + k'_{10}\right)^2 + \Delta^2},$$

$$\Omega_0^2 = |\mu_{01}|^2 \mathcal{E}_0^2,$$

and k_{ij} is the relaxation rate from level i to level j. This is a T_1 rate, which includes collisional and radiative relaxation. The corresponding off-diagonal (T_2) relaxation rate is k_{ij}, and the matrix element is μ_{ij}. The total density of atoms is N, and the center of the driving field is detuned by Δ from resonance with $0 \rightarrow 1$. The first term is the result of "optical pumping" into the intermediate level 1 by the Lorentzian tail of the input field. It peaks on resonance: $\Delta = 0$, and $\nu = \Delta$. The second, Raman, term has two parts: the Raman resonance at $\nu = 0$, and a contribution that subtracts from the optical pumping (peaking again at $s = \Delta$) and comes from the Raman effect populating the final level, level 2.

In the limit $\lambda \rightarrow 0$, the formula reduces to one derived by Mollow[157] for a monochromatic field.

We evaluated the equation on the computer and also integrated it over a Doppler distribution for parallel incident and probe fields. Three sample calculations (a, b, and c) are shown in Fig. 8-66.

We are presently extending the calculations for a Gaussian random field of arbitrary spectrum.

Reference

157. B. R. Mollow, *Phys. Rev. A* 8, 1949 (1973).

Authors

A. Szoke
J. Cooper (JILA)
C. R. Willis (Boston Univ.)

8.5.3 RGH Discharge Laser Technology

Because the RGH discharge lasers have become important laboratory tools, there is strong interest in the development of more powerful and reliable devices of this type. Also, the frequency control and the mode quality, which are obtainable only in an oscillator–amplifier system, are required for many RGH laser applications. In 1978, we progressed in both these areas. We constructed and tested several high-power state-of-the-art discharge lasers, and we developed electrical circuits for reliable synchronization of two discharges for an oscillator–amplifier laser system.

Because of the short duration of the laser pulses, the main difficulty that we encountered in operating a reliable oscillator–amplifier system was in the synchronization of the two discharges. When rugged spark gaps were used as the electrical power switches, drifts and jitters of tens of nanoseconds were observed. To overcome this problem, we developed a special electrical circuit for driving two discharges for an oscillator–amplifier application. In this circuit, in spite of the jitter of individual triggered spark gaps, the relative timing of the two discharges remains reproducible and easily adjustable. The system is rugged and requires minimum maintenance.

Figure 8-67 shows the layout of the oscillator–amplifier system. The electrical schematic for the entire system is shown in Fig. 8-68.

A two-stage Marx bank, which provides power for the amplifier, has a common spark gap with the oscillator pulser. The common gap is triggered about 50 ns after the other Marx-bank spark gap. This assures synchronization between the pulse going to the oscillator and the one going to intermediate storage for the amplifier. A self-triggered overvoltaged spark gap then switches the power from the intermediate stage to the peaking capacitors of the amplifier. The delay is adjustable by varying the pressure in the self-triggered spark gap and by changing the value of the intermediate storage capacitor. The delay gap is pretriggered

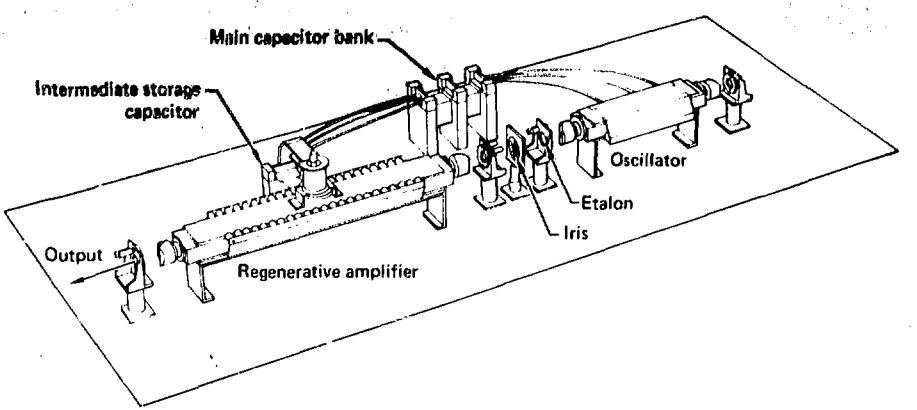

Fig. 8-67. RGH discharge oscillator-amplifier system.

(basically ultraviolet-preionized) and thus the breakdown occurs at a well-defined voltage, in this application adding less than 1 ns of jitter to the system.

The use of an intermediate storage stage also increases the power input to the laser by reducing the inductance of the driver and allowing operation at higher voltages. The laser amplifier shown in Fig. 8-67 has an interelectrode separation of 3 cm, provides uniform preionization from beneath a screen electrode, and generates 400 mJ of KrF radiation in a nearly diffraction-limited mode.

To find the limitations to scalability of a simple RGH discharge laser, we constructed a larger discharge device and the more powerful electrical pulser needed to drive it. Figure 8-69 shows the device, known as SP-III; its electrical system is shown schematically in Fig. 8-70.

The laser body is machined from PVC plastic and coated on the inside with a Kel-F grease to protect the plastic from the fluorine. The top electrode is solid aluminum, while the bottom one is shaped from a fine stainless steel screen with greater than 50% transparency. Three flash rods, located under the screen electrode, provide the preionization for the main discharge. Suprasil Brewster windows are used for the laser. The laser cavity consists of a maximum-reflectivity 10-m-radius-of-curvature mirror and an uncoated quartz flat as the output coupler. The high voltage pulser, used to power the main discharge consists of a 0.05-μF capacitor, is enclosed in a metal can for low inductance and pulse-charged by a two-stage Marx bank to 120 kV. A pretriggered spark gap (EGG 15-B pressurized to 30 psi of air) fires at proper voltage and is used to pulse-charge the $BaTiO_3$ peaking capacitors. The voltage across the laser reaches 100 to 200 kV, depending on the pressure and composition of the gas inside.

For a given operating pressure (above 1000 Torr), the best results were obtained when the laser was filled with 1000 Torr of our standard premix

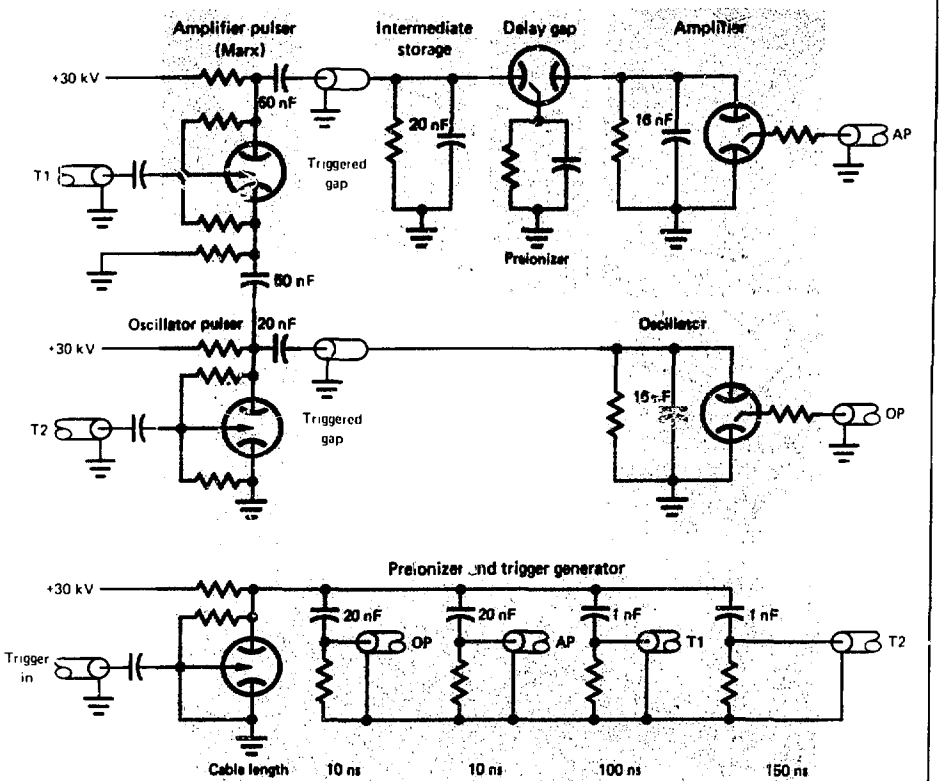

Fig. 8-68. Electrical circuit for the oscillator-amplifier KrF discharge laser.

(3 F_2/100 Kr/900 He) and then pressurized further with pure helium. Figure 8-71 shows the plot of output energy vs pressure in the laser as helium is added to the mix. At first, the output rises; then it levels off at about 45 psia. Typical output pulse energy in this regime is 0.9 to 1.0 J in a 25-ns pulse. The overall efficiency of this laser is quite poor because of impedance mismatches in the pulser; however, an estimate of the efficiency, considering only the energy of the $BaTiO_3$ capacitors as the input energy, yields approximately 1%, which is comparable to that of other discharge KrF lasers. The beam dimensions are 1.5 × 4.5 cm, and the longer dimension is limited by the aperture of the optics used. The obtainable length should be on the order of electrode separation, which is 6 cm.

We measured power density in the center of the beam by observing the laser output through a slit of known dimensions. Figure 8-72 shows a plot of the center power density vs the total output energy. The graph shows a linear dependence, which means there is no significant change in the beam profile with increasing power output. This linear dependence also means that at the highest powers

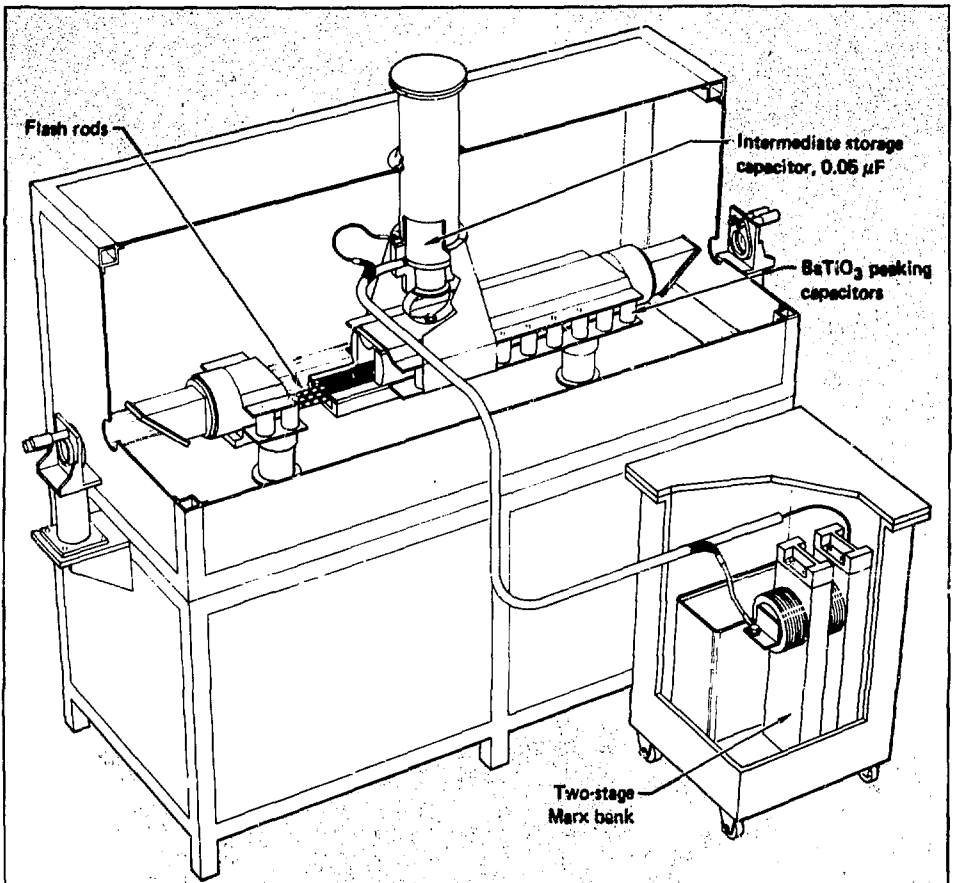

Fig. 8-69. SP-III high-power RGH discharge laser.

achieved here (9 MW/cm^2) there was no evidence of flux limit by such effects as unsaturable losses. Thus, discharge lasers longer than 100 cm may be built without loss of efficiency.

Measurements of laser performance were also made with larger peaking capacitors. As some of the 0.6-nF capacitors were replaced with 2.0-nF capacitors, the output energy began to decline and the output beam showed strong striations. The spacing between the stripes coincided with the grid size of the screen of the lower electrode. Apparently, the larger peaking capacitors result in too slow a voltage rise time between the electrodes, and some sort of prebreakdown instability has enough time to grow. To overcome this problem, one could install a low-inductance switch (such as a rail gap) in series with the peaking capacitors. Experiments using this approach are described in recent publications.[158,159] Another possibility is to use e-beam initiation of the discharge, described in §10.6.5 of this report. Either of these approaches may be used to further extend the output power and energy capabilities of a discharge-driven KrF laser.

In conclusion, we have demonstrated that a simple ultraviolet-preionized laser is capable of output power as high as 40 MW. However, we also

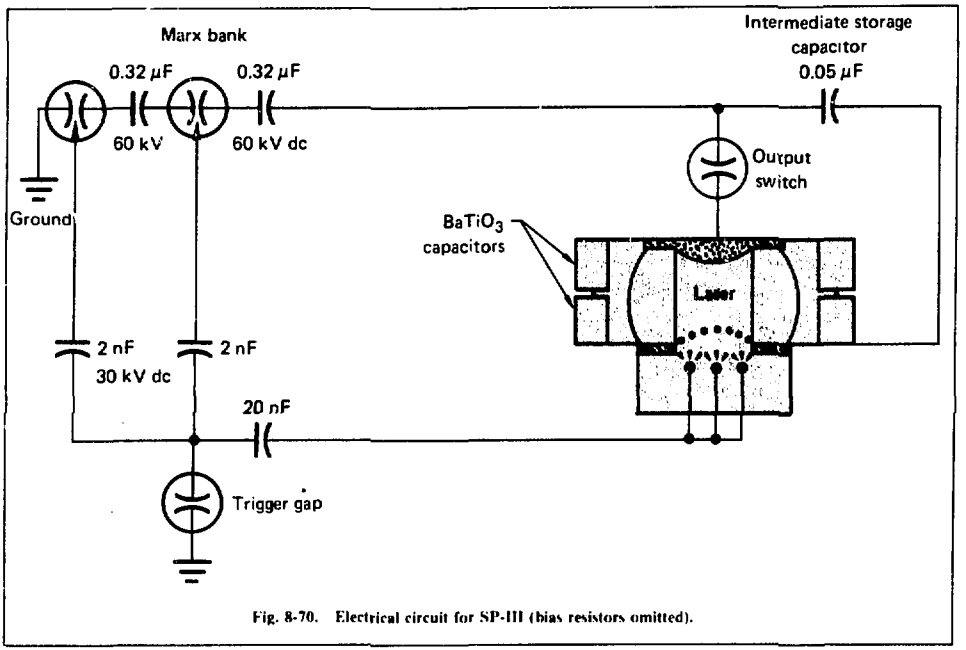

Fig. 8-70. Electrical circuit for SP-III (bias resistors omitted).

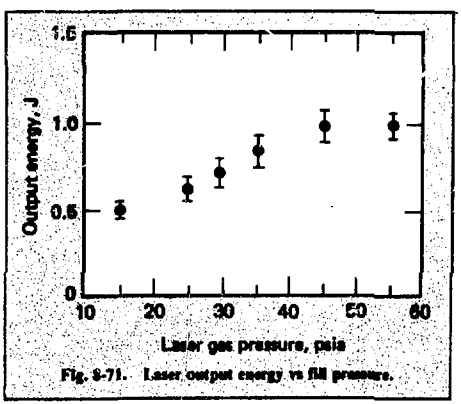

Fig. 8-71. Laser output energy vs fill pressure.

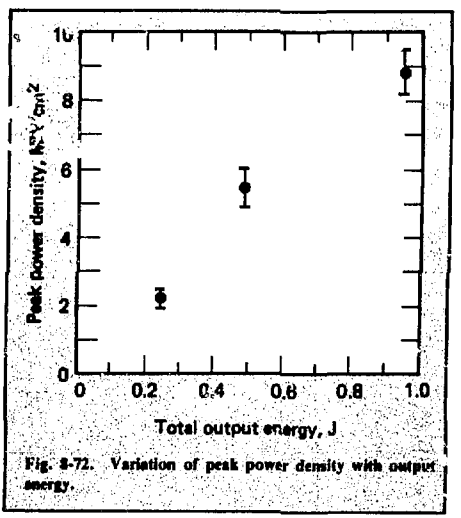

Fig. 8-72. Variation of peak power density with output energy.

came to the conclusion that further increase of the output power will require a more complex driver circuit for the discharge.

References

158. J. I. Levatter and R. S. Bradford, Jr., *Appl. Phys Lett.* 33, 742 (1978)
159. W. J. Sargeant, A. J. Alcock, and K. E. Leopold, *Appl. Phys. Lett.* 36, 635 (1977).

Authors

J. Goldhar
W. R. Rapoport

8.5.4 Advances in the Theory of Photoionization of Small Molecules

Among the various properties of the electronic continuum of small molecules, cross sections for photoionization are important in a wide range of practical applications. Nevertheless, until quite recently, these processes have resisted any systematic attempt at theoretical investigation, largely because of the enormous computational difficulty in obtaining continuum wave functions when noncentral and nonlocal molecular fields are involved. Consequently, much theoretical effort in the past few years has been directed at the development of methods that can provide the relevant cross sections without a detailed solution of the appropriate molecular wave equation.

The Stieltjes-Tchebycheff (ST) moment-theory technique[160] has emerged as one of the most promising approaches for ab initio investigation of molecular photoionization. During 1978, we undertook a variety of systematic ST studies, including calculations of the cross sections for photoionization in the outer shells of Ar_2^+ (Ref. 161), F_2 (Ref. 162), H_2CO (Ref. 163), H_2O, and HCN, and in the K-shell (an inner shell) of N_2 (Ref. 164). The theoretical details of the ST technique were discussed in the 1976 annual report and will not be repeated here. The key feature of the method, which has made such rapid progress possible, is its reliance on a finite number of transition energies and oscillator strengths that can be calculated in Hilbert space. In addition, since finite point-group and electron-exchange symmetries are basic ingredients of the standard bound-state technology that is used to implement the method, we can avoid many of the simplifying approximations needed in other techniques, such as the use of one-center expansions, additive atomic approximations, and local exchange potentials.

The studies undertaken at Livermore, together with similar investigations carried out elsewhere, have repeatedly pointed out the strikingly nonatomic features that are found in molecular photoabsorption, most notably the ubiquitous appearance of broad-shape resonances in photoionization cross sections. Such behavior is readily apparent in the photoionization cross sections of F_2 (Ref. 162) and H_2CO (Ref. 163), which are shown in Figs. 8-73 and 8-74, respectively. Examination of the dominant excitations in the resonance regions of these molecules and other first-row diatomics has enabled us to systematically classify these resonances in terms of compact σ^* and π^* orbitals.

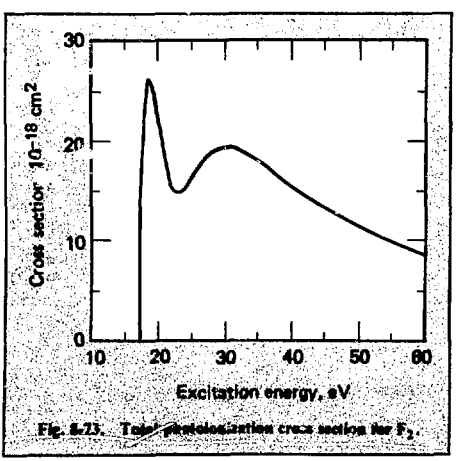

Fig. 8-73. Total photoionization cross section for F_2.

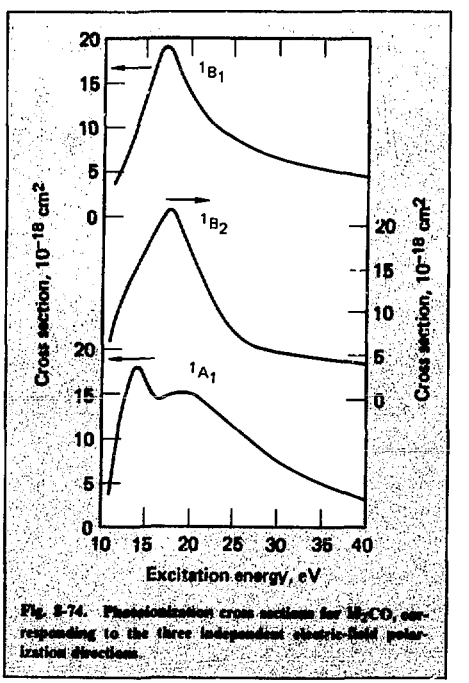

Fig. 8-74. Photoionization cross sections for H_2CO, corresponding to the three independent electric-field polarization directions.

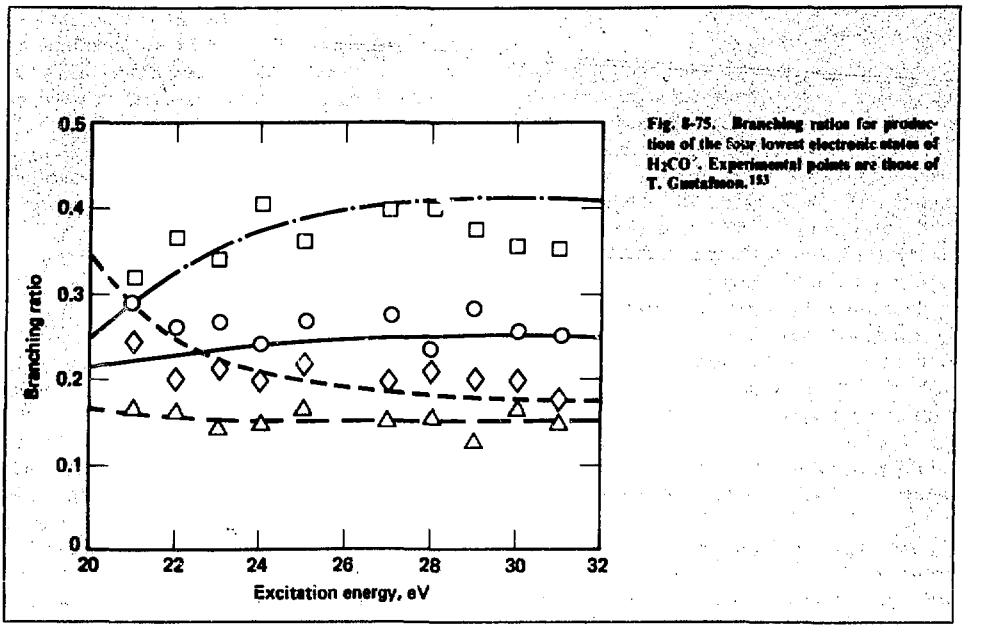

Fig. 8-75. Branching ratios for production of the four lowest electronic states of H_2CO^+. Experimental points are those of T. Gustafsson.[153]

In many cases, we have been able to evaluate not only total photoionization cross sections but also partial cross sections for production of molecular ions in specific electronic states. An example is given in Fig. 8-75, where we show the branching ratios in H_2CO photoionization to the four lowest ionic channels and a comparison with experimental values.[165] Such calculations assume a frozen-core model for the photoionization process and photoejection of an electron from a specific molecular orbital. Such "static-exchange" calculations have proved quite reliable in a variety of cases involving closed-shell molecules, but more elaborate configuration-interaction calculations are required when dealing with open-shell, or excited-state molecular species, or both. Our study of the photoionization of Ar_2^* (Ref. 161) is an example of such a case.

Another case in which the frozen-core model breaks down is in inner-shell photoionization, where orbital relaxation following ionization or excitation can be substantial. Moreover, since this process takes place deep inside the molecular core in an effectively "atomic" environment, it is often necessary to localize the inner-shell excitation on a particular atomic center to obtain good results. For homonuclear diatomics, this means abandoning the conventional g,u symmetry at the molecular orbital level. By carrying out broken-symmetry configuration-interaction calculations on N_2 (Ref. 164), we were able to clarify the nature of the 400-eV $^1\Pi_{g,u}$ resonance states that occur just below the K-edge.

References

160. P. W. Langhoff, "Stieltjes-Tchebycheff Moment-Theory Approach to Molecular Photoionization Studies," in *Electron-Molecule and Photon-Molecule Collisions*, T. Rescigno, V. McKoy, and B. Schneider, Eds. (Plenum, New York, 1979).
161. T. N. Rescigno, A. U. Hazi, and A. E. Orel, *J. Chem. Phys.* **68**, 5283 (1978).
162. T. N. Rescigno, V. McKoy, and P. Langhoff, *J. Chem. Phys.* (to be published).
163. T. N. Rescigno, A. E. Orel, V. McKoy, and P. W. Langhoff, *J. Chem. Phys.* **69**, 4689 (1978).
164. T. N. Rescigno and P. W. Langhoff, *Chem. Phys. Lett.* **51**, 65 (1977); T. N. Rescigno and A. E. Orel, *J. Chem. Phys.* **70**, 3390 (1979).
165. T. Gustafsson, Xerox Corporation, Palo Alto, Calif., private communication (1978).

Author

T. Rescigno

8.5.5 Advances in the Theory of Autoionization

Resonant autoionizing states of molecules and autodetaching states of molecular negative ions play crucial roles in many collision processes involving low-energy electrons, e.g., in dissociative attachment, dissociative recombination, and Penning ionization.[166] In discharge or e-beam-pumped lasers, such processes may constitute important steps in the kinetic pathway to forming the upper laser level. For instance, in rare gas fluoride lasers, the dissociative attachment of electrons to F_2 is the dominant mechanism for forming F^- ions.[167] In rare gas excimer lasers, the dissociative recombination of electrons with molecular ions, e.g., Xe_2^+ or Xe_3^+, leads to rapid formation of atomic and molecular excited states.[168] Thus, quantitative descriptions of molecular resonance phenomena are required for constructing kinetic models of these gas lasers. lasers.

Although the formal theory[166] of resonant scattering of electrons from molecules has been developed during the past 15 years, there have been very few ab initio studies of autoionizing resonances, even in diatomic molecules. The main reason for this has been the lack of practical methods for calculating the decay lifetimes τ of molecular resonances within the Born–Oppenheimer approximation.

During 1978, we developed two new approaches, the Stieltjes-imaging method[169,170] and the complex-basis-function technique,[171,172] for calculating the resonance parameters of autoionizing states. We implemented the Stieltjes moment-theory technique, which has been used extensively for calculating accurate molecular photoionization cross sections,[173] for molecular resonances. During the year, we used this method to study several well-known resonances of complex atoms,[169] e.g., He^- or Mg^-, and of diatomic molecules,[170] e.g., $H_2^{2\Sigma_u^+}$ and N_2^-. The complex-basis-function technique[171] is an extension of the complex-coordinate method,[174] designed to make the method practical for treating resonance states with more than two electrons. We demonstrated the utility of this approach by calculating the resonance energy and width of the $^2P^o$ shape resonance of Be^-.[171] In addition, we made significant progress in implementing the method for molecular resonances.[172]

The Stieltjes moment-theory technique is based on the "golden-rule" definition of the resonance width Γ, which is inversely proportional to the decay lifetime, i.e., $\Gamma = \hbar/\tau$. Direct application of the golden-rule formula to molecular resonances is difficult because of the complexities involved in determining the background continuum into which the resonance decays. When the electron-target interaction is anisotropic and nonlocal, as in the case of molecules, the computation of electron-scattering wave functions is an arduous task. The present method avoids the explicit construction of molecular continuum orbitals by utilizing well-established, bound-state techniques for approximating both the resonance state and the scattering continuum. Stieltjes moment-theory techniques, developed earlier for molecular photoionization studies,[173] are used to extract the correctly normalized width Γ from the computed discrete representation of the nonresonant background. Because the method uses square-integrable basis functions exclusively, its implementation requires only existing atomic and molecular structure codes. Many-electron effects, such as correlation and polarization, are easily incorporated into the calculation of the width through standard configuration-interaction techniques. Once the resonance width has been determined, the energy of the resonance can be computed by a straightforward evaluation of the required principal-value integral.

To demonstrate the utility of the Stieltjes-imaging technique, we calculated[170] the widths of several, doubly excited autoionizing states of He, the well-known 19.3-eV ^2S resonance of He^-, and the $^2P^o$ shape resonance of Mg^-. In all of these cases, our computed resonance parameters agree closely with the values obtained using other methods. We also applied the method to several core-excited, Feshbach-type resonances in the $e + H_2^+$ system and the well-known $^2\Pi_g$ shape resonance of N_2^- (Ref. 165). Our study of the $^1\Sigma_u^+$ and $^1\Pi_u$ autoionizing states of H_2 has shown that simple approximations, such as describing the ejected electron with undistorted Coulomb waves, may yield incorrect resonance widths. The computed energy and width of the $^2\Pi_g$ resonance of N_2^-, as functions of internuclear distance, are shown in Fig. 8-76. These results, obtained with a frozen-core static-exchange potential, agree reasonably well with the results of other very recent calculations.

The method of complex coordinates or basis functions[174] is based on a mathematical description

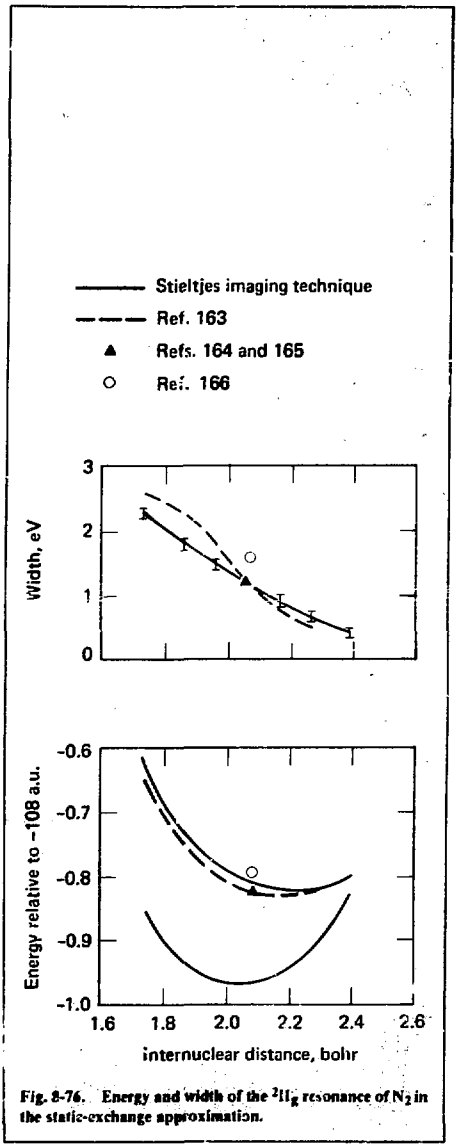

Fig. 8-76. Energy and width of the $^2\Pi_g$ resonance of N_2 in the static-exchange approximation.

of a resonance as a state with complex energy $E_{res} - i\Gamma/2$, at which the scattering amplitude is infinite. The real part of the complex energy gives the resonance position, and twice the imaginary part of the complex energy is the decay width. The resonance wave funtion is expanded in terms of complex basis functions, and the many-electron Hamiltonian is diagonalized to yield the complex resonance energy directly. In the original complex-coordinate method,[174] the basis functions were constructed by using the coordinate transformation $r \rightarrow re^{-i\theta}$ for each electron. Although this method yielded good results for autoionizing states in two-electron atoms, e.g., He**, its applications to complex atoms suffered from slow convergence. Our analysis of the theoretical foundations of the method has shown that convergence can be greatly enhanced by allowing only functions referring to the active, valence electrons to become complex, while keeping the basis functions for the core electrons real.

We implemented the modified complex-basis-function technique by using a separable expansion for the many-electron Hamiltonian, and we demonstrated its utility in several applications to model problems.[171] Calculations on the $^2P^o$ shape resonance of Be^- yielded 0.73 eV and 1.1 eV for the position and width, respectively. These values are consistent with estimates derived from calculated p-wave phase shifts, using effective range theory. The behavior of the complex eigenvalue of this resonance as a function of the transformation angle θ is shown in Fig. 8-77. The stationary points associated with the curve correspond to the complex resonance energy $E_{res} - i\Gamma/2$.

Direct application of the complex-coordinate transformation to molecular problems is impractical because it would require abandoning the Born-Oppenheimer separation of electronic and nuclear motions.[174] We have achieved a breakthrough in this area by using complex basis functions constructed from standard Gaussian functions, e.g., $e^{-\alpha r^2}$, in which the scale parameters α have been transformed: $\alpha \rightarrow \alpha e^{-i2\theta}$. The fact that this transformation leaves the bound states of a molecule unchanged has been verified by computations on H_2^+ (Ref. 172). Application of the method to a shape resonance in an anisotropic model potential yielded resonance parameters in excellent accord with the values obtained from a separable-potential T-matrix calculation.[172] These results suggest that further investigation of the complex-basis-function method and its application to molecular resonance phenomena will be worthwhile.

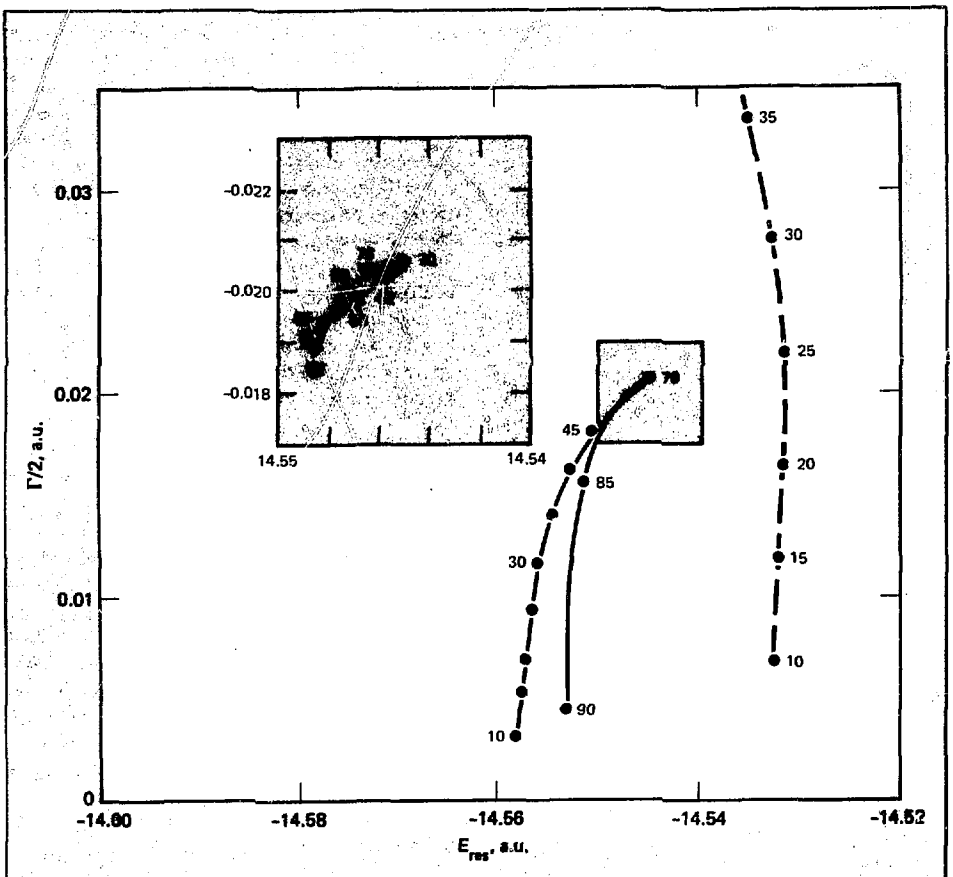

Fig. 8-77. Complex eigenvalues, $E_{res} - i\Gamma/2$, of Be^-, as a function of transformation angle θ. Solid line represents $(1s^2\,2s^2\,2p)\ ^2P_0$ resonance, dashed line a $^2P_0$ scattering solution. The number next to each data point indicates the value of θ.

References

166. J. N. Bardsley, *Rev. Mod. Phys.* (to be published, 1979).
167. J. J. Ewing, *Phys. Today* 31, 32 (1978).
168. M. A. Biondi, "Recombination," in *Principles of Laser Plasmas*, G. Bekefi, Ed. (Wiley, New York, 1976).
169. A. U. Hazi, *J. Phys. B* 11, L259 (1978).
170. A. U. Hazi, "Stieltjes-Moment-Theory Technique for Calculating Resonance Widths," in *Electron-Molecule and Photon-Molecule Collisions*, T. N. Rescigno, V. McKoy, and B. Schneider, Eds. (Plenum, New York, 1979).
171. T. N. Rescigno, C. W. McCurdy, and A. E. Orel, *Phys. Rev. A* 17, 1931 (1978).
172. C. W. McCurdy and T. N. Rescigno, *Phys. Rev. Lett.* 41, 1364 (1978).
173. P. W. Langhoff, "Stieltjes-Tchebycheff Moment-Theory Approach to Molecular Photoionization Studies," in *Electron-Molecule and Photon-Molecule Collisions*, T. N. Rescigno, V. McKoy, and B. Schneider, Eds. (Plenum, New York, 1979).
174. C. W. McCurdy, "Progress Toward the Application of Complex Coordinate and Complex Basis Function Techniques to Molecular Resonance Calculations," in *Electron-Molecule and Photon-Molecule Collisions*, T. N. Rescigno, V. McKoy, and B. Schneider, Eds. (Plenum, New York, 1979).

Authors

A. U. Hazi
T. N. Rescigno

SECTION 9

CONTENTS

SECTION 9

ENERGY AND MILITARY APPLICATIONS

9.1 Introduction

Our goal is to foresee the opportunities and problems in the engineering development of inertial confinement fusion (ICF). Our studies form a bridge between the current physics research program and such ICF users as the energy utilities and the military. A power plant that produces electricity is a familiar example of an energy application. An example of a military application might be a simulation facility to test the response of satellite components to x rays and neutrons similar to the radiation from a nuclear weapon detonation. We have set three primary objectives:

- To identify the most promising ICF applications.
- To formulate programs for the required technological development.
- To provide management information necessary to direct program resources toward yielding maximum benefit in the shortest time.

Conceptual design studies of power plants and test facilities are one of our more useful tools for early detection of potential technical problems. We assess emerging new technologies and work with the energy industry on their engineering and commercialization. We can save precious developmental resources through design innovations that shorten the required developmental time. Finally, we work closely with industry to realistically and economically plan the required technological development programs and strategies.

In this section, we report the results of two major studies: a conceptual design of a laser fusion power plant for electricity generation, and an assessment of fissile-fuel production for conventional nuclear reactors in a hybrid fusion–fission reactor. In each case, the fusion reactor functions as an energy converter in which small pellets containing deuterium and tritium are injected into the chamber at the rate of one to ten per second and illuminated by high-energy laser beams. The pellets are compressed to high densities and heated to temperatures of millions of degrees, conditions that are sufficient to ignite a thermonuclear reaction. The reaction releases hundreds of times more energy than that of the laser beams.

Energy from the reaction is released in the form of neutrons, x rays, and energetic pellet debris. To convert this energy, which is released in repetitive pulses, into useable form, we surround the chamber with a blanket that absorbs the energy yet survives the radiation. For electricity production we use a liquid-lithium blanket that captures the energy in the form of heat, which can then be transferred to a steam cycle. For fissile-fuel production, we capture the neutrons in a blanket of fuel rods containing fertile elements, which are transmuted to fissile elements that can fuel another reactor.

The first study is the conceptual design of a 1050-MW_e power plant, which is a collaboration between LLL and a team of university and industrial contractors. Project responsibilities are as follows:

- Lawrence Livermore Laboratory: Overall energy conversion design, optics, fluid mechanics, system integration, environmental aspects.
- Energy Technology Engineering Center (run by Rockwell International for the Department of Energy): Liquid-metals systems, corrosion, heat transfer, tritium.
- Rockwell International, Energy Systems Group: Chamber engineering, thermal and stress analysis, material selection.
- Bechtel National, Inc.: Heat transfer systems, steam cycle, safety, building layout and costing.
- Colorado School of Mines: Corrosion of steels by lithium.
- University of California–Davis: Stability of liquid jets.

Cooperation of team members has provided a study that is balanced between the innovative concepts required for fusion systems and the engineering experience gained from building fission reactors and components.

The energy conversion concept of the study calls for a dense array of lithium jets to be injected into a laser fusion target chamber between each

pulse. The lithium forms an effective 1-m-thick blanket between the fusion pellet and the first structural steel wall. This design requires no first-wall replacement for the life of the power plant and allows the use of available materials and techniques. It is called the High Yield Lithium Injection Fusion Energy (HYLIFE) concept.

When this study began, we intentionally chose a very high gain to determine the design constraints and considerations for high-yield pulsed-energy conversion systems. We now consider this combination of pellet gain and driver energy to be optimistic in terms of theoretical pellet performance.

Section 9.2 is a report of the results of this design study. It describes the approach and design philosophy, the chamber design, heat transfer analysis, and steam and electricity generation. The vital questions of optical survivability and pellet injection and tracking are also treated. Because we place as high a priority on public acceptance as on economic competitiveness, we devote a subsection to safety and environmental features of the HYLIFE concept. Technological development issues are summarized at the end of each subsection.

The HYLIFE design is conservative and constructible with near-term advanced fission technology. Therefore, we foresee no major obstacles to commercial electric power generation by ICF once scientific feasibility is demonstrated.

Although we devoted most of our resources to the HYLIFE study, we also completed neutronic studies of several innovative ^{232}Th and ^{238}U–^{232}Th blanket designs for fusion–fission hybrid reactors, as reported in §9.3. We studied compound blankets consisting of both fast and thermal fission portions to take maximum advantage of energy and neutron multiplication in added performance. The support ratio, defined as the number of burner reactors that can be fueled by a fusion–fission hybrid having the same thermal power, was calculated to be between 6 and 30, depending on the many combinations of fuel cycle, blanket design, and type of burner reactor. These high support ratios imply that the cost of electricity in a scenario that combines hybrids with conventional light-water reactors (LWR's) is insensitive to the cost of the hybrid. Because hybrid costs might be high (2.5 to 3 times that of a LWR) and are quite uncertain, this insensitivity favors hybrid development.

Both the electricity producing and fissile-fuel producing power plants appear to be feasible in terms of both the net energy they produce and the technology needed to build them. Our challenge is to intelligently plan and implement the requisite engineering development to ensure that the promise is realized.

Author

M. J. Monsler

9.2 Conceptual Design of a Laser Fusion Power Plant

9.2.1 Introduction

Our Energy Options. Demand for electricity in the next century is so uncertain that recent studies do not attempt to forecast beyond 1990.[1] If future electricity demands can be economically met in an environmentally and politically acceptable manner, then electricity will continue to be an ideal form of energy for homes and industry and will grow in importance for transportation. It is clean in end use, distributable, and can be made exceptionally reliable through use of interconnected grids.

Planners must look past near-term reduced demand forecasts, which can be met by a combination of oil- and coal-fired boilers and uranium-fueled light water reactors (LWR's), to an era of diminishing fossil and fissile resources coupled with the growing electrical demands of high-technology economies. Even if solar heating and cooling, supplemented by local electrical generation from wind machines, etc., are used widely, the role of central generation of electricity to provide power to urban areas and industry is likely to continue.[2]

Useful criteria for judging long-term energy sources are:

- Environmental acceptability.
- Economic competitiveness.
- Operational inexhaustibility.

To these we might add the ever present political constraints of assured security of the energy supply and freedom from such misuse as terrorism and weapons proliferation.

Only three long-term energy sources now exist—fusion energy, solar energy, and fission breeder energy. Each should be pursued through the developmental stage to properly evaluate its relative

merits and costs. None is without problems. For example, solar energy falls on the earth at no cost, but its diffuse and intermittent nature leads to collection and storage problems. Solving them, say by placing collectors in space and beaming the power to earth, may result in environmental and safety problems.

Ironically, solar technology has been found to be the most wasteful of nonrenewable resources of the three options because it requires so much material and energy for the mining and manufacture of components.[3,4] Measured in man-days lost per unit of net energy output (counting both occupational and public risk), solar-thermal electric power is apparently quite risky to human health.[5] A solar-thermal system has been calculated to have one-third the risk to health compared with a coal-based system but 70 times the risk of a nuclear system, again because of the huge requirement for mining, smelting, manufacture, and transportation of materials.

The fission breeder derives its inexhaustibility from its ability to breed fissile fuel from fertile feedstock while providing thermal power. Thus, the breeder eliminates the need for additional mining and enrichment beyond the initial loading of the reactor core. Unfortunately, fission product poisons build up so fast that the nuclear fuel elements must be reprocessed frequently. Demonstration of commercial feasibility is being held up in the United States pending resolution of political problems involving the risk of nuclear proliferation and the acceptability of reprocessing and waste disposal. Current estimates place the capital cost of a liquid-metal, fast-breeder reactor (LMFBR) at about twice that of an LWR, in constant dollars. The fuel cycle cost is also likely to be higher than that of an LWR, an unfortunate irony for an inexhaustible energy source.

Fusion energy is hard to evaluate in terms of cost because, unlike solar energy and fission breeder energy, the technical feasibility of generating useful net power has yet to be demonstrated. As a result, the configuration of a commercial fusion reactor of either the magnetic or inertial type is both sketchy and conceptual compared to solar-thermal or fission breeder devices.

Yet, the promise of fusion is relatively clear. We can envision capturing the energy source of the sun in a power plant on earth, in a concentrated and continuously available form, thereby solving the problems of solar energy. Burning a small amount of deuterium, which is available at low cost from water, this "captured sun" should have a negligible fuel cycle cost and be free from geopolitical fuel constraints. It should be a more acceptable neighbor to the consuming public than a fission power plant with its potential radiological hazards and the need to store its waste for millions of years.

A fusion power plant would be free from the air pollution of coal-fired plants and could potentially save thousands of lives by eliminating coal mining and transportation accidents. On the other hand, we must master the control of tritium within a fusion power plant to minimize leakage rates and the chances for inadvertent releases. The self-contained fuel cycle possible with fusion power will obviate the safety, diversion, and proliferation concerns about the transportation of nuclear materials. Finally, the growth of fusion power in some sense substitutes factors we have in increasing supply (innovation, high technology, and industrial productivity) for things that are nonrenewable and in diminishing supply (fossil and fissile fuels).

The HYLIFE Design Approach. Despite its advantages, fusion power will not be developed easily, nor be absolutely clean, nor result in electricity "too cheap to meter." The purpose of conceptual design studies such as the one reported here is to identify potential technical difficulties and to assess the economic and social costs, which we seek to minimize through early understanding and innovation. We seek to identify an attractive conceptual configuration of a fusion power plant to take advantage of the potential of fusion energy while pointing out a direction of minimum developmental effort to achieve that potential. The primary output of this study is not the design itself; rather, it is the sum of the innovations produced in response to the issues uncovered.

We established the following objectives at the start of the study:

- Point design. Perform a consistent point design of a power plant for the generation of baseload electricity, with an output near 1000 MW_e to allow comparisons to current technology.
- Performance. Assume that the technical feasibility of laser fusion will be demonstrated in the mid-1980's as now envisioned. Assume that projected fusion pellet gain as a function of input energy is on the high side of what is now calculated.

- Separability. Take advantage of the separability of the ICF driver system and energy converter system to ease engineering constraints.
- Environment and safety. Weigh public acceptability as heavily as economics in any design trade-offs.
- Materials. Reject the quest for exotic materials to withstand the fusion radiation. Modify the flux and energy spectra of radiation with damage-proof, reestablishable fluids. Use conventional materials when possible.
- Long life. Strive for operation for full 30-yr lifetime with no replacement of damaged first walls or radioactive structure.
- Minimize developmental time. Design within straightforward extrapolations of fission-reactor state of the art to shorten the time between a demonstration of technical feasibility and commercialization.

These objectives proved to be quite restrictive. They have led to a plant design that is remarkably similar to an LMFBR of the SUPERPHENIX-type now being built in France, particularly with regard to liquid-metal technology and containment building philosophy. We may have been unnecessarily conservative in both emphasizing near-term technology and requiring full service life. As a result, projected capital cost is high, while the hidden developmental costs are low. On the other hand, we do meet our goals of using common materials and minimizing induced structural radioactivity.

The HYLIFE Concept. The objectives stated above were used in previous studies[6,7] as selection criteria for the most promising concept for a laser fusion energy conversion chamber. The lithium waterfall concept,[8,9] in which a neutron blanket of lithium is placed inside the first structural wall, best satisfied the objectives of no first-wall replacement, no exotic materials, and minimum technological development. The general concept is not new. Its progenitors include a number of liquid-wall[10–13] and fluid-rain[14–15] concepts. The HYLIFE concept solves many of the problems uncovered in these exploratory studies.

The HYLIFE design[16] is the second iteration of the general concept, the first being a 380-MW_e power plant.[8] The present 20-man-yr study, a team effort, has resulted in an energy conversion chamber that is simple in design. Conceptually, it can operate without damage with very high yields of several thousand megajoules for up to a few times a second. The chamber operating conditions chosen, 2700 MJ at 1 Hz, provide 1055 MW_e when coupled with a superheated steam-electrical generation facility.

Simple in concept, the chamber configuration is basically a steel chamber in which a blanket of liquid lithium shields the steel wall from the neutron and x-ray energy. The pellet is injected horizontally into the center of the chamber and ignited by two opposing clusters of horizontal laser beams. Figure 9-1 is a schematic of the HYLIFE chamber. A lithium energy-conversion blanket, consisting of a dense array of 20-cm-diameter jets, is injected into the chamber between each laser pulse. The array provides an effective blanket thickness of 1 m between the fusion pellet and the first structural steel wall. The pellet and laser beams are injected through a specially arranged corridor in the array of jets.

The lithium blanket reduces the 14-MeV neutron flux from the pellet by a factor of 100 or more. Thus, a cylindrical first wall having a 5-m radius could operate 21 full-power years (30 yr at 70% availability) at an integrated neutron flux of 0.32 MW/m^2. The wall fluence without the lithium protection would be 5.7 MW/m^2; hence, the power density within the reactor vessel is high, approaching that of a fission reactor. A common low-alloy ferritic steel (2.25% chrome–1% molybdenum) is used throughout. The tritium breeding ratio is controllable between 1.0 and 1.7.

The fluid configuration in the chamber is an hexagonal array (0.5 packing fraction) of 20-cm-diameter lithium jets. The array effectively isolates the chamber from the shock of the fusion pulse and minimizes the wall stress from the impact of lithium. High-pressure blowoff gas, which results from x-ray and debris deposition in the lithium, merely blows through the array of jets, like wind through trees. The force of the volumetric expansion of lithium, which results from neutron absorption, is primarily taken up in liquid–liquid interactions of colliding jets. Finally, the enormous area of the fluid at a relatively cold temperature (500°C) acts as an effective condensation pump. Thus, mechanical vacuum pumping of hot plasma is not needed.

Table 9-1 summarizes the quantitative characteristics of the HYLIFE power plant. The plant requires 16 liquid-metal pumps to inject the lithium at 4.4 m/s into the 5-m-radius chamber. The primary

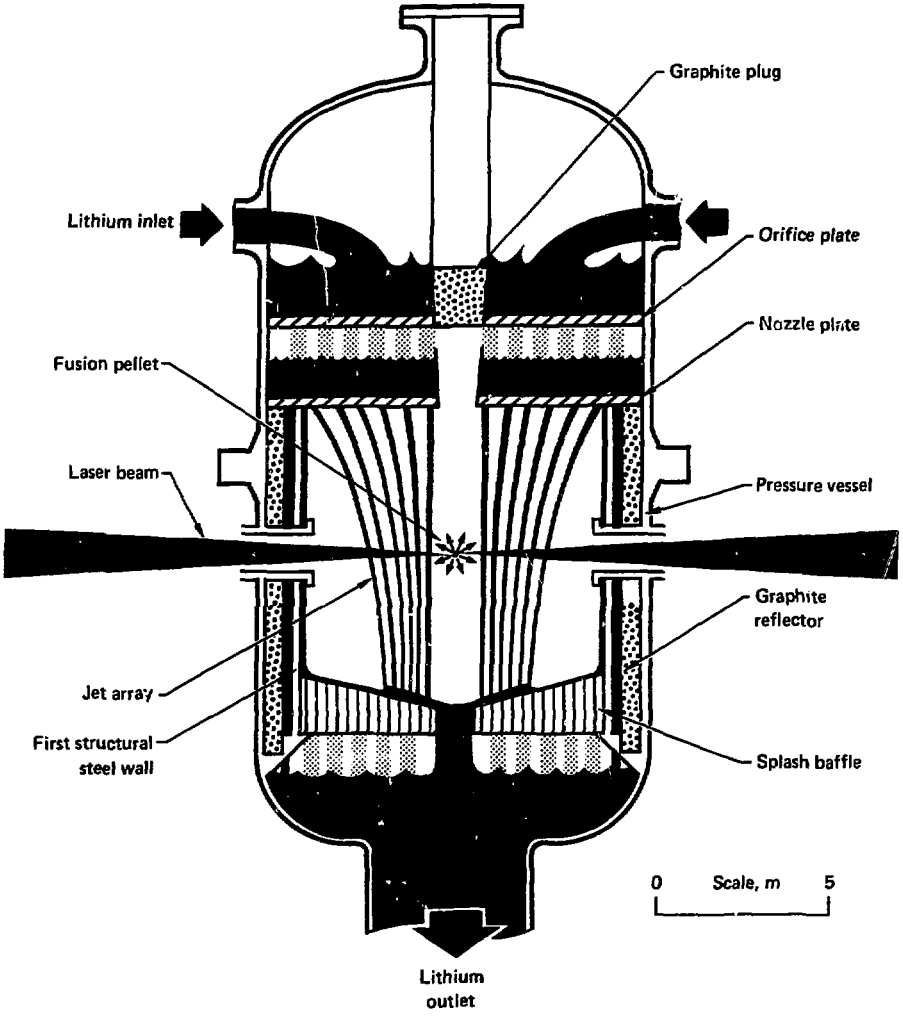

Fig. 9-1. Schematic of the High Yield Lithium Fusion Energy (HYLIFE) chamber.

Table 9-1. Summary of HYLIFE power plant characteristics.

System parameters	
Fusion power	2700 MW_t
Gross thermal power	3215 MW_t
Gross electric power	1255 MW_e
Net electric power	1060 MW_e
Net electrical efficiency	33%
Laser and pellet parameters	
Beam energy	3 MJ
Pellet gain	900
Yield	2700 MJ
Pulse repetition rate	1 Hz
Laser efficiency	3%
Power consumption	100 MW_e
Energy conversion chamber	
Height	8 m
Radius	5 m
Material	2.25 Cr-1.0 Mo
Neutron flux at midplane:	
With lithium	0.32 MW/m^2
Without lithium	5.76 MW/m^2
Number of jets	300
Jet diameter at midplane	0.2 m
Velocity at midplane	9.9 m/s
Lithium flow rate	93.3 m/s
Packing fraction of jets	0.5
Effective blanket thickness	1 m
Tritium breeding ratio	1.7
Lithium temperature (av)	500°C
Effective temp rise/pulse	13°C

lithium-recirculation pumping power is 20 MW_e, only 1.6% of the gross electric power. A conceptual drawing of a HYLIFE power plant, cut away to show the relationship of the chamber, heat transfer loops, laser mirrors, etc., is shown in Fig. 9-2.

Figure 9-3 is a power flow diagram of the power plant. A low fraction (16%) of total recirculated power can be attained with a high gain pellet, even with an advanced laser having low electrical efficiency. In conjunction with an intermediate sodium loop, the saturated steam cycle that we selected provides a gross electrical power of 1250 MW_e at a gross electrical efficiency of 39%. The net electrical power is 1055 MW_e, resulting in a net electrical efficiency of 33%.

Combination of the following features should lead to an economically attractive power plant:

- Low recirculation power.
- High power density.
- Use of common steels.
- Low-temperature operation.
- No first-wall replacement.
- Standard liquid-metal pumping techniques.

Environmentally, a savings of radioactive waste greater than a factor of 200 is possible for two reasons: the lithium protection reduces the induced activation in the wall by over a factor of 20 (Ci or kg); and the first wall will not have to be replaced 10 to 15 times during the useful life. Finally, if isotopically tailored Mo is used to manufacture the steel, we may be able to reuse the steel structure after 20 yr.

References

1. Energy Information Administration, "Projections of Energy Supply and Demand and Their Impacts," *Annual Report to Congress, Vol.II*, Washington, D.C., DOE/ETA-0036/2 (1977).
2. A. B. Lovins, *Soft Energy Paths: Toward a Durable Peace* (Ballinger Publishing Co., Cambridge, Mass., 1977).
3. S. Baron, "Solar Energy—Will it Conserve our Nonrenewable Resources?" in *Trans. of the Am. Nucl. Soc. 1978 Winter Mtg.*
4. T. L. Carr, "Electricity Options for the Future (Where 'Soft' Becomes Hard!)," in *Trans. of the Am. Nucl. Soc. 1978 Winter Mtg.*
5. H. Inhaber, "Is Solar Power Riskier than Nuclear?" in *Trans. of the Am. Nucl. Soc. 1978 Winter Mtg.*
6. W. R. Meier and J. A. Maniscalco, "Reactor Concepts for Laser Fusion," in *Proc. of Am. Inst. of Chem. Engineers, Nov. 13-17, 1977.*
7. J. A. Maniscalco, W. R. Meier, and M. J. Monsler, "Design Studies of a Laser Fusion Power Plant," in *Proc. of IAEA Workshop on Fusion Reactor Design, Oct., 1977, Madison, Wis.*
8. J. Maniscalco, J. Blink, R. Buntzen, J. Hovingh, W. Meier, M. Monsler, and P. Walker, *Civilian Applications of Laser Fusion*, Lawrence Livermore Laboratory, Livermore, Calif., UCRL-52349 (1977).
9. J. A. Maniscalco, W. R. Meier, and M. J. Monsler, *Conceptual Design of a Laser Fusion Power Plant*, Lawrence Livermore Laboratory, Livermore, Calif., UCRL-79652 (1977).
10. N. C. Christofilos, *A Design for a High Power Density Astron Reactor*, Lawrence Berkeley Laboratory, Berkeley, Calif., UCID-15731 (1970).
11. A. P. Fraas, *The Blascon—An Exploding Pellet Fusion Reactor*, Oak Ridge National Laboratory, Oak Ridge, Tenn., ORNL-TM-3231 (1971).

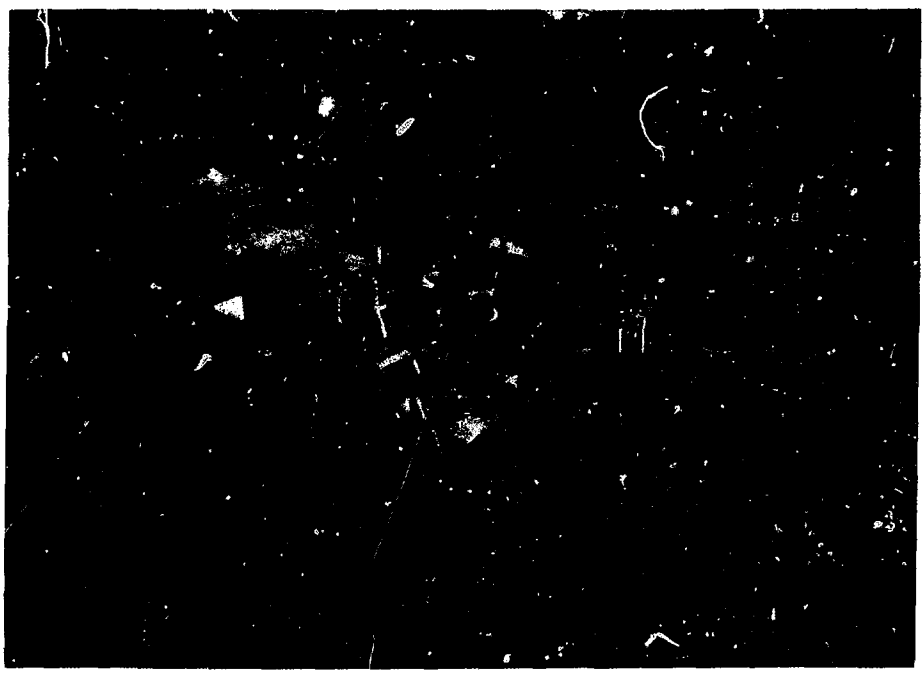

Fig. 9-2. Conceptual drawing of a HYLIFE power plant.

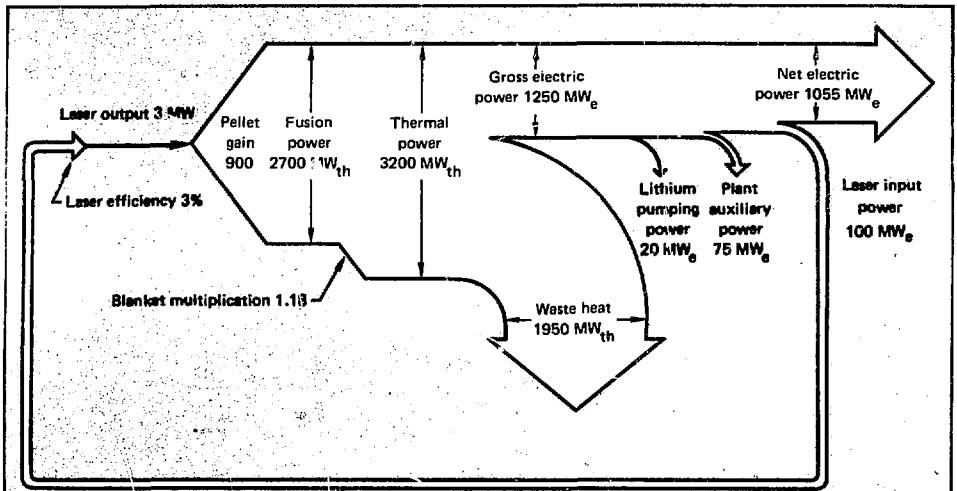

Fig. 9-3. Power flow diagram for HYLIFE power plant.

12. A. P. Fraas, "Conceptual Design of a Series of Laser Fusion Power Plants of 100 to 3000 MW$_e$," presented at *The 9th Intersociety Energy Conversion Engineering Conference, San Francisco, Calif., Aug., 1974.*
13. J. R. Powell, O. Lazareth, and J. Fillo, *A Liquid Wall Boiler and Moderator (BAM) for Heavy Ion-Pellet Fusion Reactors*, Brookhaven National Laboratory, Upton, N.Y., BNL-50744 (1977).
14. R. J. Burke, *Outline for a Large Pulse Electron-Beam-Ignited Fusion Reactor*, Argonne National Laboratory, Argonne, Ill., CTR/TM-31 (1974).
15. W. Seifreitz, in *Trans. of Am. Nucl. Soc.* **21**, (1975), p. 18.
16. M. Monsler, J. Maniscalco, J. Blink, J. Hovingh, W. Meier, and P. Walker, "Electric Power from Laser Fusion: The HYLIFE Concept," in *Proc. of IECEC Conf., Aug., 1978, San Diego, Calif.*.

Author

M. J. Monsler

9.2.2 Lithium Blanket Configuration

Introduction. The fundamental feature of our energy conversion concept is a blanket of liquid lithium that surrounds the laser-initiated fusion energy pulse inside a compact, high-power-density chamber. The blanket primarily shields the chamber structures from the damaging effects of fusion radiation. It absorbs the x rays and debris that would otherwise ablate a solid material. It also attenuates and moderates the neutron flux enough that even the first structural wall will last for the 30-yr life of the proposed power plant.

We call the region of flowing lithium a blanket because it is where the kinetic energy of the fusion products is converted to thermal energy. Placement of the energy conversion blanket inside the first structural wall is an important concept in the design of fusion reactors. A portion of the lithium flow is circulated through heat exchangers as the primary coolant. Therefore, we want as much energy as practical to be deposited directly in the flowing lithium. In this way, the heat load and cyclic thermal stress to the chamber structures can be reduced.

The flowing lithium blanket performs two other significant functions. It breeds the tritium required to fuel the DT pellets. As much tritium must be produced as the system consumes, a constraint that is easily met. It also serves as a vacuum pump for the chamber, condensing the lithium vaporized by each fusion energy pulse.

Thus, the flowing lithium serves as:

- A radiation shield for the chamber structures.
- An energy conversion and removal medium.
- The fertile material for tritium breeding.
- A vacuum pump.

Its effectiveness in performing each function depends on the blanket configuration. The configuration also must be stable, must be reestablishable between pulses, and must allow laser beams to reach the pellet at the center of the chamber.

Several potential blanket configurations perform the required functions and meet the various constraints. We find, however, that the blanket configuration also strongly influences the design of the first structural wall and even the rest of the plant. The response of the lithium blanket to the pulsed energy deposition is discussed in §9.2.3. In some configurations, the lithium strikes the first structural wall at high velocities and induces high dynamic stresses, which we want to avoid. The total flow rate required to circulate and maintain the lithium blanket is a function of its configuration. A low flow rate reduces both the number of large liquid-metal pumps required and the size of the containment building.

Annular Blanket. The simplest configuration is formed by injecting lithium downward through an annular nozzle at the top of the chamber. The flow forms a hollow cylindrical blanket around the pellet, as shown in cross section in Fig. 9-4(a). The

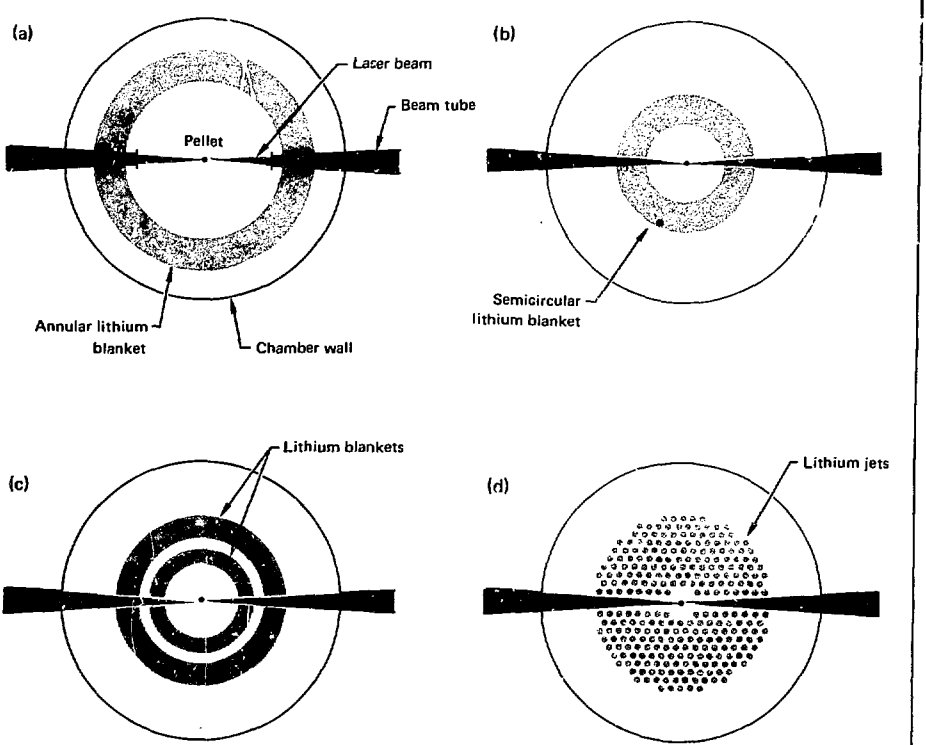

Fig. 9-4. Four lithium blanket configurations: (a) annular; (b) semicircular; (c) multiple semicircular; and (d) jet array.

blanket thickness decreases continuously with vertical distance from the nozzle as the fluid is accelerated by gravity. The shortest path for neutrons through lithium is just slightly below a horizontal midplane through the pellet. Because the first structural wall is closest to the pellet at this midplane, it is where the wall receives the highest radiation flux. Therefore, we use the midplane conditions to specify the chamber design. There is uniform azimuthal shielding because the blanket thickness is constant at a given vertical position.

Experiments with water at the University of California–Davis (UC–Davis) have shown that this flow configuration can be established and is stable over lengths corresponding to many times the chamber height.[17] Figure 9-5 shows the annular flow pattern in one such experiment.

One principal disadvantage of this configuration is that beam tubes must penetrate the flowing lithium to allow the laser beams to reach the pellet. This presents two basic problems. One is that the beam tubes are directly exposed to the intense fusion radiation. The minimum distance from the pellet to the beam tubes is set by the allowable radiation damage and heat flux levels for the tube material. This in turn determines the minimum inner radius of the lithium annulus. The minimum flow rate is also fixed by the tube position because the flow rate for an annular blanket of a given thickness decreases with decreasing radius. Thus, the beam tubes become a design limiting feature.

The second problem is that the beam tubes split the lithium blanket and form large inverted V-shaped openings below the tubes. UC–Davis

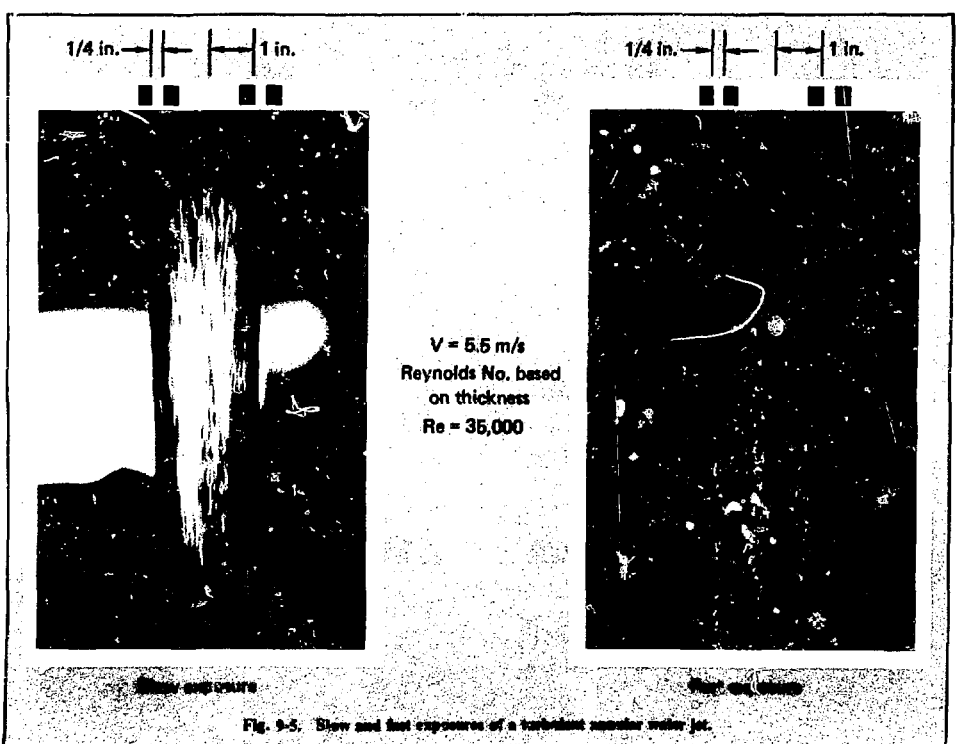

Fig. 9-5. Slow and fast exposures of a turbulent annular water jet.

researchers have experimentally demonstrated this behavior using both circular and aerodynamically shaped tubes. Significant additional flow is needed to protect the first structural wall near these openings.

Another principal disadvantage of this configuration is that its response to the fusion energy pulse results in an unacceptably high dynamic load on the first structural wall. Three basic factors contribute to the acceleration of the fluid. First, a high pressure builds up inside the annulus as lithium is vaporized off the inner surface. This pressure accelerates the annular blanket radially outward. Second, as a result of the short-range energy deposition, lithium is ablated off the inner surface, which sends a pressure wave radially outward. When the pressure wave reflects off of the outer surface of the blanket, lithium is spalled off toward the wall. Third, the sudden deposition of neutron energy causes the lithium to disassemble in all directions. Part of the blanket accelerates toward the wall.

Semicircular Blanket. Dividing the annular blanket into two semicircular blankets [Fig. 9-4(b)] alleviates some of the above problems. Because the laser beams can now penetrate through the openings between the two halves, no beam tubes are needed. Also, the inner radius of the blanket can be made small to reduce the flow rate. Some lithium vapor can vent through the openings and thus reduce the fluid acceleration due to pressure buildup in the central region. Unfortunately, too much fluid is still accelerated into the chamber wall as a result of the spallation and neutron energy deposition.

Multiple Semicircular Blankets. The semicircular blankets can each be divided into an inner and outer blanket [Fig. 9-4(c)]. The lithium spall resulting from the short-range radiation comes off the outer surface of the inner blanket and strikes the outer blanket instead of the chamber wall. Also, the neutron-induced motion causes the two blankets to collide with each other while only the outer half of the outer blanket moves unimpeded to the wall. Thus, much of the induced fluid kinetic energy is dissipated in fluid–fluid collisions.

Jet Array. Continued segmentation of the lithium blanket, to provide more channels for venting the central region and more layers to increase the amount of energy dissipated in fluid–fluid impacts, leads to the blanket configuration shown in Fig. 9-4(d). The lithium blanket consists of many individual jets arranged in a hexagonal-close-packed (HCP) array within a more or less annular envelope. Channels are left for beam entry.

While the jet array results in some azimuthal variation in blanket thickness and requires a more complicated nozzle design, it has some significant advantages over the other configurations. It provides many channels for venting the vaporized lithium and presents a large surface area of liquid to recondense vapor and lower the chamber pressure. The vapor is condensed so quickly that additional vacuum pumps are not required. The array also absorbs much of the imparted kinetic energy in fluid–fluid impacts. These effects combine to minimize the dynamic stress in the chamber wall.

The jet array is used for the HYLIFE design. It adequately protects the chamber structures from radiation damage, absorbs nearly all of the system energy, breeds more tritium than the system burns, and operates as an efficient vacuum pump. The jets are stable against breakup over the length of the chamber, and they are injected fast enough to reestablish between pulses. Most importantly, the configuration minimizes the stress to the chamber wall and allows beam entry without the use of beam tubes.

HYLIFE Blanket Configuration. The HYLIFE lithium blanket consists of 300 jets requiring a flow rate of 93.3 m^3/s. Their position at the chamber midplane is shown in Fig. 9-6. Nearly all jets are arranged in an HCP array within a more or less annular envelope around the pellet. Twenty of the jets form the laser beam apertures. The nominal midplane parameters are listed in Table 9-2. The thickness of the jet array is 2 m and the packing fraction (the ratio of the lithium cross-sectional area to total area) in this region is 0.5. Thus, the lithium blanket provides the equivalent of 1 m of shielding to the blanket structures. These parameters were selected based on neutronic considerations discussed in this section and on blanket response considerations discussed in §9.2.3.

Nozzle Plate. The jets are injected through a nozzle plate at the top of the 8-m-high chamber. The plate contains a hexagonal array of injector nozzles set nearly vertically at the inner edge and gradually slanting to ~45° at the outermost row. Dimensions of the nozzles are shown in Fig. 9-7. The entrance diameter and triangular pitch are the same and equal 0.45 m. The exit diameter D is

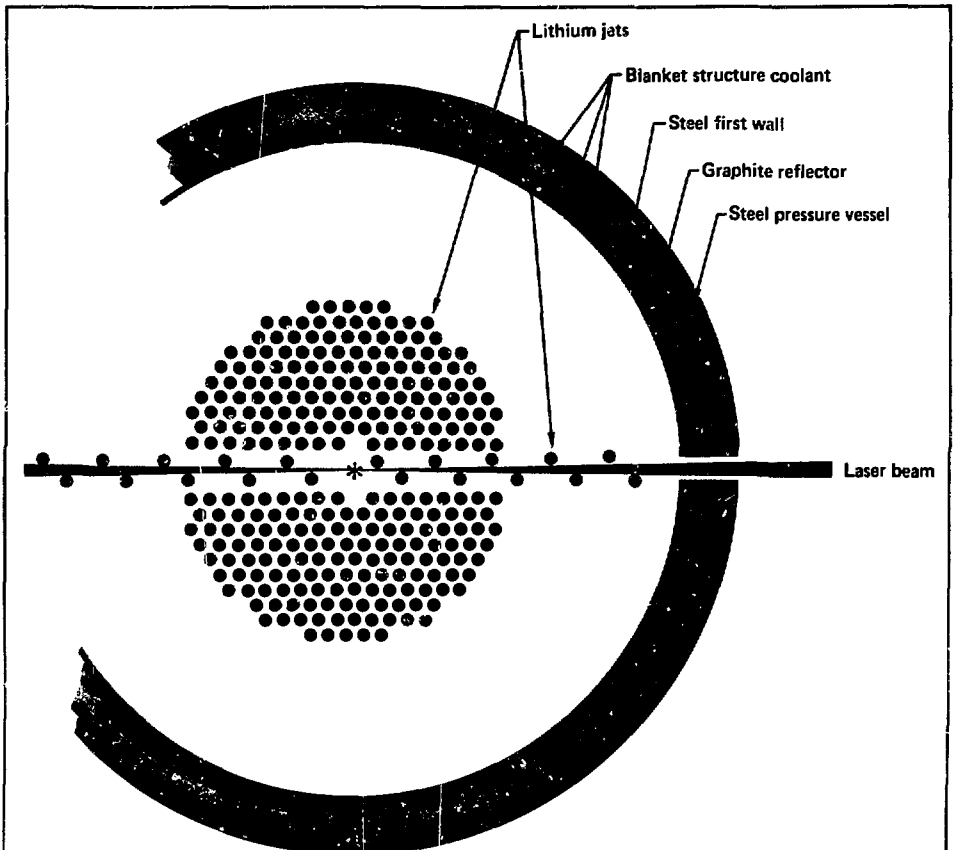

Fig. 9-6. Cross section of HYLIFE chamber.

Table 9-2. Parameters of jet array at midplane.

Annulus inner radius	0.5 m
Annulus outer radius	2.5 m
Jet diameter	0.2 m
Number of jets	300
Packing fraction	0.5
Jet speed	9.9 m/s
Flow rate	93.3 m^3/s

0.30 m and the plate thickness L is 0.40 m. The nozzle L/D of 1.33 is slightly less than the ASME design, which calls for an L/D of 1.6.

Because the maximum exit packing fraction with this nozzle design is 40%, the outer rows are focused toward the center of the chamber. By directing the jets radially inward, we obtain a higher packing fraction at lower elevations even though the jet diameter is continuously decreasing. At the chamber midplane, for example, the packing fraction is 0.5 while the jet diameter has decreased to 0.2 m (a 44.4% reduction in cross-sectional area of the jet).

To simplify the manufacture of the nozzle plate, we assume that each nozzle has a circular cross section in the plane perpendicular to its flow direction. Nozzles that are slanted to the vertical

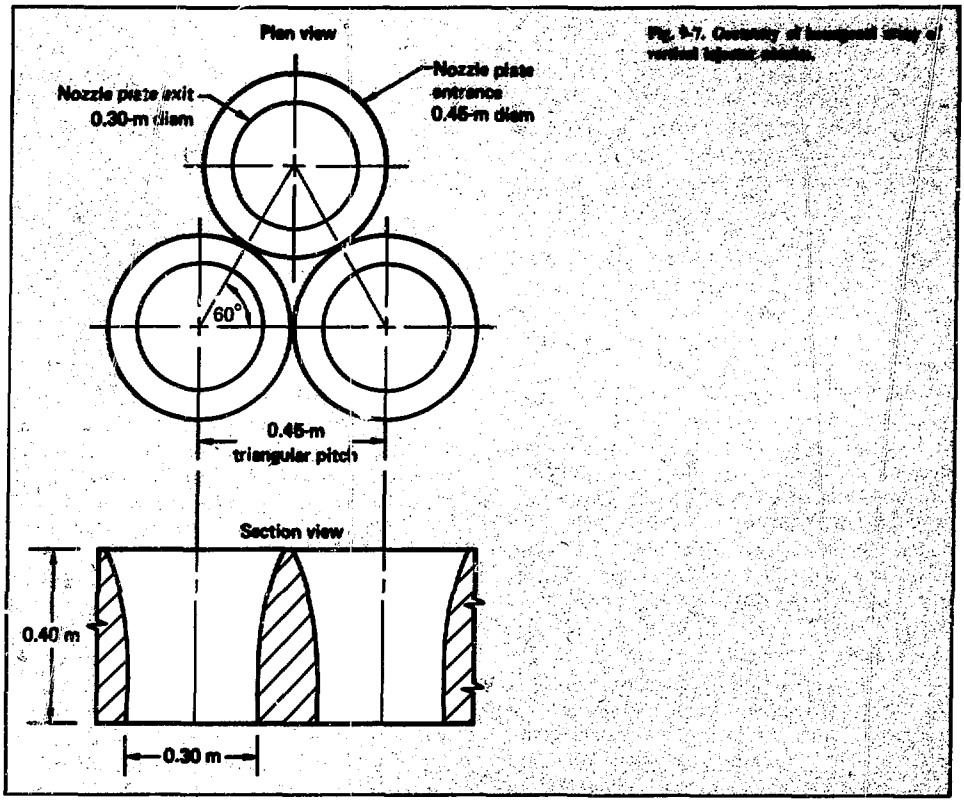

then have elliptical openings at the plate entrance and exit, which prevents the outer nozzles from being arranged in the normal HCP configuration. The net effect is that, for a given number of jets, the radial position of the outermost nozzles is larger than if all the jets were directed vertically downward.

All jets have the same injection speed, which is determined by the height of the lithium pool above the nozzle plate. The required speed is calculated by an iterative process based on the velocity requirements and position of the outermost jets.

First, the minimum vertical component of the velocity is fixed at 3.1 m/s to meet the constraint that the jets must reach the bottom of the 8-m-high chamber within the interpulse time of 1 s. The radial position of the outermost jets is then estimated and the horizontal velocity component is calculated so that the radius of the outer edge of the array is 2.5 m at the midplane. Knowing the two velocity components, we calculate the maximum injection angle that is required by the outermost jets. We can then calculate how much the array must be displaced from the normal HCP configuration and, thus, estimate a new outer-jet radius. Using this method, we find that the nozzle array extends to a radius of 4.5 m, the required injection speed is 4.4 m/s, and the maximum injection angle is 45°.

A sheet of lithium flows down the inner surface of the chamber wall to provide cooling, added shielding, and erosion protection. This sheet is 0.05-m thick at the midplane and requires a total

flow rate of 15.5 m^3/s. It is fed from the same reservoir that supplies the jets.

Beam Aperture/Neutron Stop. We use a set of 20 crisscrossing lithium jets to establish a flow pattern that allows the beams to reach the pellet unobstructed while leaving no area of the chamber wall unprotected. Ten jets are crossed over each beam, five to each side, in a direction perpendicular to the beam plane to form a gothic archway of lithium. (The beam plane is the vertical plane through the pellet and centerline of the two beams.) This archway protects the nozzle plate and part of the chamber wall above the beam while forming a narrow passageway for the beam.

A triangular region of the wall above the beam and a rectangular strip below the beam are not shielded from neutrons by the crossing jets. These areas of the chamber wall are therefore removed. Lithium flows through a ducting system located between the inner chamber wall and the outer vessel wall to fill these areas as illustrated in Fig. 9-8. Lithium enters the ducting from the same pool that feeds all the jets. A stream 0.4-m thick and 1.5-m high is directed to cross over the beam in a direction perpendicular to the beam plane and is then redirected to enter the chamber below the beam. Thus, the chamber wall has a long narrow opening while the opening in the outer vessel wall is only slightly larger than the laser beam at that point. A flow rate of ~2.7 m^3/s is required above each beam.

Figure 9-9 illustrates the beam aperture/neutron stop formed by the flowing lithium. Only two of the ten jets are shown. The jet speed is 4.4 m/s, and diameter at the nozzle plate is 0.3 m. These values are the same as those for the other jets in the blanket array. Note that the cross section of the cluster of laser beams is a vertically orientated rectangle. The beam converges to the pellet from an 8-m × 2-m mirror array located 60 m away. All crossing jet nozzles are displaced 0.2 m from the beam plane.

The injection angle θ, required for a jet to cross over the laser beam without intersecting it, increases with the radial position of the crossing jet. The outermost jet, which crosses the beam plane 4.5 m from the chamber centerline, requires an injection angle of 9.5°. At the position of the chamber wall (r = 5 m), the projection of the open triangular space above the beam is 1.5-m high and the projection of the open rectangular space below the beam is 0.32-m wide at the bottom of the beam. The parameters given here include a design allowance for a possible variation in the injection head of ±10%. Also, the jets crossing near the center of the chamber do not interfere with the jets in the blanket array until they are below the beam. With this flow configuration, no bare metal is exposed to the fusion radiation in the region of the beam apertures.

Injector Assembly. Lithium is delivered to the nozzle plate and the other flow channels (15 m^3/s is channeled between the chamber wall and the outer vessel wall) through the injector assembly illustrated in Fig. 9-10. The total flow of 129 m^3/s enters the top of the chamber through 16 inlet pipes. The lithium pours downward through baffles into an upper pool. The baffles reduce sloshing of the lithium while providing for lateral flow. This is accomplished by using a coarse hexagonal-shaped honeycomb structure. It is placed so that its lower edge ends above the top of the orifice plate. Its sides are perforated to allow flow between adjacent vertical flow passages.

The orifice plate and pool of lithium it supports isolate the circulating pumps from pressure pulses in the fusion chamber. The orifice plate uniformly meters the flow of lithium to the injection pool above the nozzle plate. The flow baffles above the nozzle plate serve three purposes:

- To inhibit wave formation and turbulence caused by the rain of lithium from the orifice plate above.
- To distribute the liquid evenly over the nozzle plate entrance.
- To provide a flow L/D ≥5 to reduce the turbulence at the nozzle entrance.

The hole in the center of the nozzle permits pressure equalization between the chamber and the nozzle plate pool. A replaceable graphite plug is positioned above the hole in the nozzle plate, where it is directly exposed to the fusion radiation. Additional information on the injector assembly is provided in Ref. 18.

Jet Stability. Understanding the fluid dynamics of the lithium blanket is of prime importance to the HYLIFE concept. We are analyzing the problem on both theoretical[19-21] and experimental fronts.[17] Our studies address the following topics:

- Stability of the liquid-lithium jet.
- Effects of the pulse energy on the jet.
- Reassembly between pulses.
- Condensation of the lithium vapor.

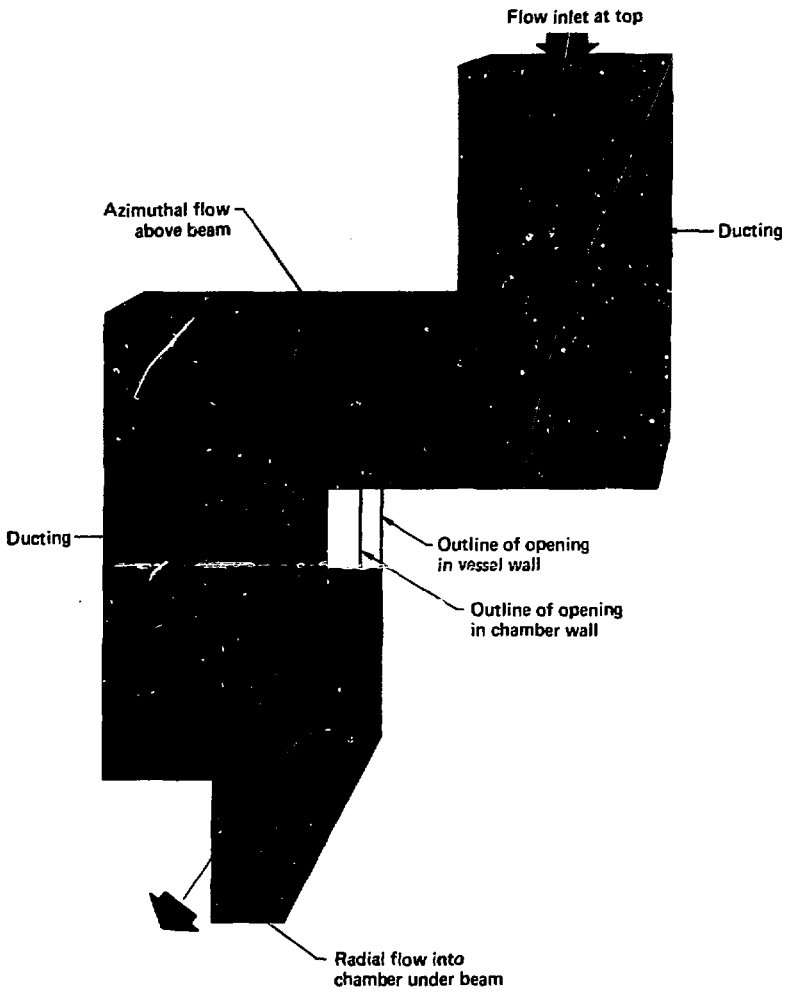

Fig. 9-8. Lithium flow configuration to fill areas not protected by crossing lithium jets.

Fig. 9-9. Beam aperture and neutron stop formed by flowing lithium.

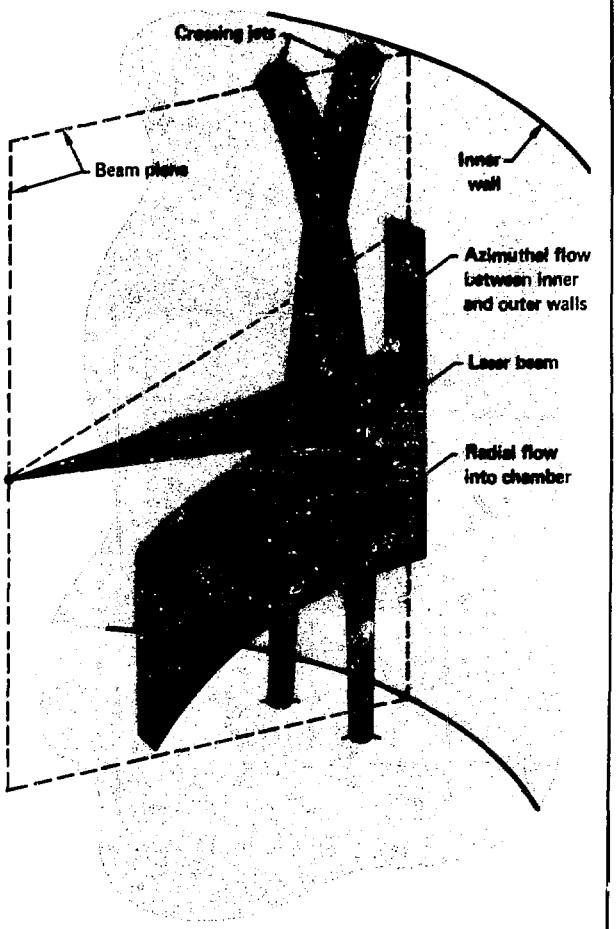

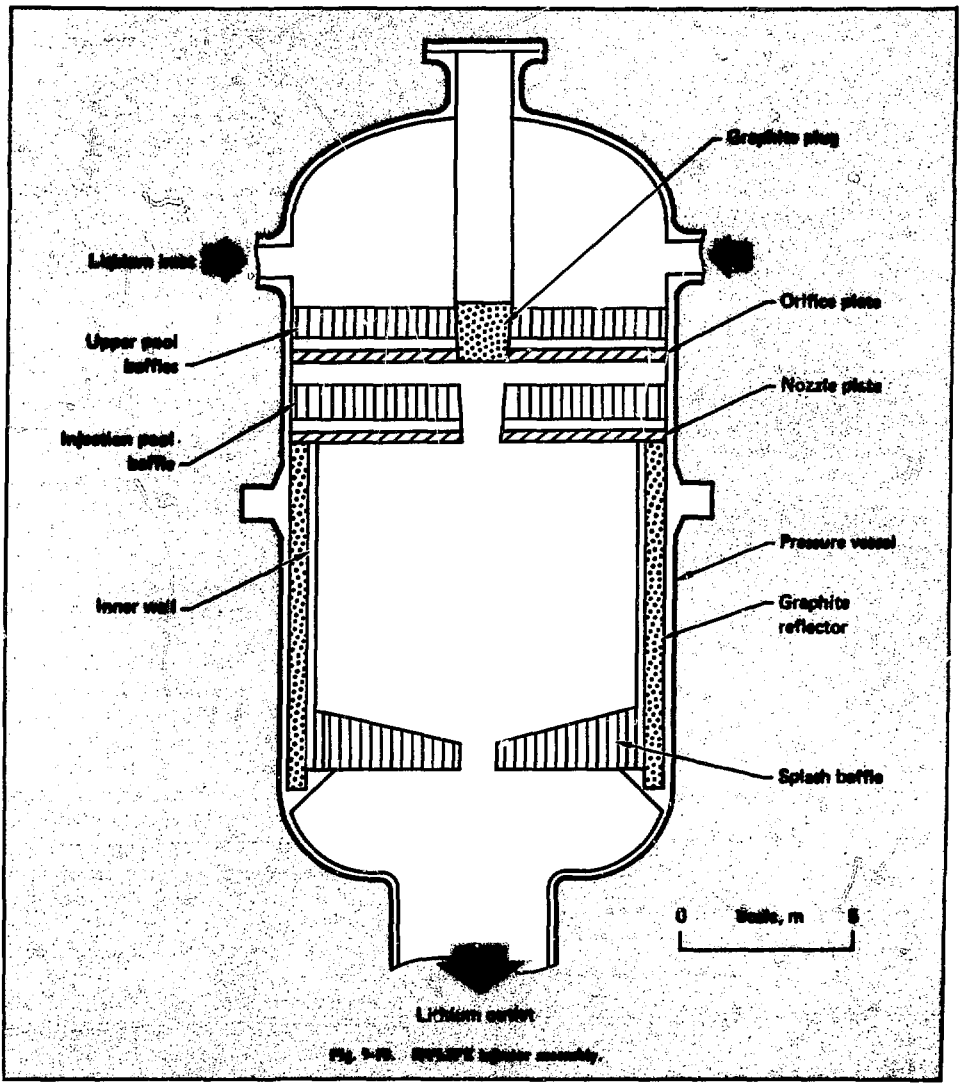
Graphite plug
Lithium inlet
Orifice plate
Upper pool baffles
Nozzle plate
Injection pool baffle
Pressure vessel
Inner wall
Graphite reflector
Splash baffle
0
Scale, m
5
Lithium outlet

Fig. 9-10. [illegible]

turbulent jet breakup, we can estimate the intact jet length based on the work of Phinney[23] and Kusui.[24] For Weber numbers (ratio of inertial to surface tension forces, $We = \rho V^2 D/\sigma$) greater than 625, Kusui proposes a correlation of the intact length as follows:

$$\frac{L}{D} \approx 55 + 1.085\,(We)^{0.5} .$$

Phinney's results and Kusui's correlation (Fig. 9-11) agree closely for small-diameter jets. Using Kusui's correlation with the HYLIFE jet parameters (ρ = 485 kg/m^3, V = 4.4 m/s, D = 0.3, σ = 0.35 N/m) gives an intact length of ~46 m, far larger than the chamber height of 8 m.

Experimenters at UC-Davis have investigated the stability of planar water sheet jets and annular jets.[17] They are now experimenting with the cylindrical jets proposed for HYLIFE. With sheet jets, any finite disturbance in the planar surface creates a local pressure gradient caused by the velocity differences in the gas flowing around the disturbance

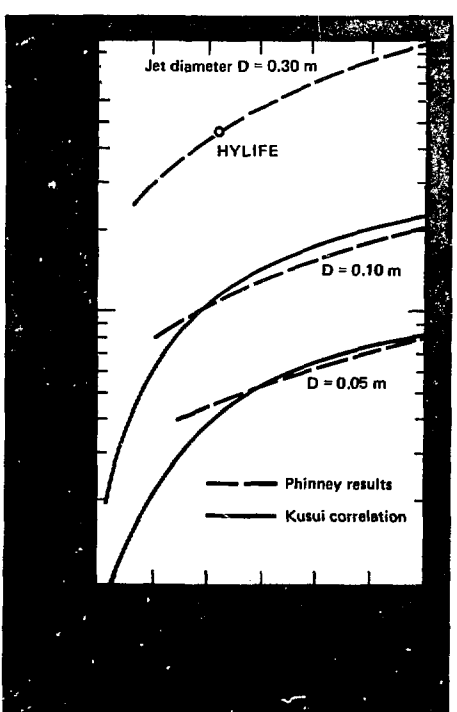

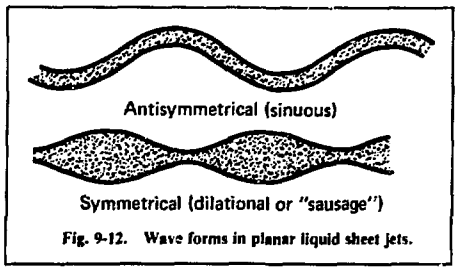

Fig. 9-12. Wave forms in planar liquid sheet jets.

(as seen from a reference frame moving with the liquid jet). In the absence of other forces, the disturbance grows with distance from the nozzle.

If the fusion pulse causes ringing of the nozzle plate, the jet may receive a sinusoidal disturbance. If the resulting sheet jet is unstable, it takes the form of a periodic wave that grows with distance from the nozzle. Figure 9-12 shows the two types of wave form that occur. They are antisymmetrical (sinuous) and symmetrical (dilational or "sausage" shaped).

For both wave forms, aerodynamic forces are destabilizing. For the antisymmetrical wave, surface tension forces are also destabilizing. In general, both wave forms exist on a fluid sheet as a superposition, but the antisymmetrical wave dominates the symmetrical wave in both size and growth rate. Therefore, only the antisymmetrical wave form is considered significant.

The UC-Davis experiments emphasized jet breakup caused by wave growth. Experiments using water sheet jets of Reynolds numbers up to Re = 1.3 × 10^4 revealed two main causes of wave growth: (1) aerodynamic effects of the sheet waves flowing through the still air; and (2) initial transverse momentum effects, i.e., the initial transverse velocity imparted to the fluid by a vibrating nozzle. Breakup caused by mechanisms other than wave growth were also observed and analyzed qualitatively. Theoretical predictions of the wave growth were compared to measurements of the actual wave growth.

The following parameters were used in the experiments: (1) frequencies of nozzle vibration of 20 to 500 Hz; (2) vibration amplitudes of 0 to 2 mm; (3) sheet thicknesses of 2.5 and 7.9 mm; and (4) ambient pressures of 0.20, 0.67, and 1.0 atm. Results showed the measured wave amplitudes decreased to as little as 1/100 of the value in 1.0-atm air as ambient pressure was reduced. The aerodynamic effects became negligible compared to initial

transverse momentum effects at the lowest pressure (0.20 atm).

At all flow conditions, breakup caused by wave growth was not observed, even when the wave amplitude grew to 10 times the initial sheet thickness. Theory and the above experimental results indicate a negligible aerodynamic wave growth for the proposed lithium jet in the low pressure (<0.1 Torr) chamber. Thus, any wave growth would probably result strictly from the initial transverse momentum effects, which are analogous to an oscillatory steering of a garden hose nozzle.

Other experiments, performed with struts placed through the sheet jets, revealed splashing of fluid at the leading edge, or splitting of the flow beneath the trailing edge, or both. The struts modeled the laser tubes penetrating the lithium sheet. These experiments strongly support the elimination of beam tubes.

Experimental and theoretical studies were performed on the convergence length of sheet jets. Convergence length is defined as the distance from the nozzle to the point where the edges meet after being pulled together by surface tension. Similar studies were done on hollow annular jets. Both theories and all experimental results indicate a convergence length on the order of 1000 times the sheet width or annulus radius for the proposed laser fusion flow conditions. Clearly, the normal steady effects of gravity and surface tension should not compromise the uniformity of blanket protection.

Nuclear Performance. The flowing lithium serves as an energy conversion blanket, a radiation shield for the chamber structures, and as the tritium breeding medium. We did one-dimensional (1-D) neutronics studies to determine how nuclear performance varies with blanket thickness. We used the TARTNP Monte Carlo[25] neutronics code to determine several reactor system parameters, including:

- Spatial energy deposition profile.
- Total energy deposition per DT fusion event.
- Helium production and atomic displacement rates in the chamber wall.
- Tritium breeding ratio.

The effect of compressed fuel upon pellet output has been included in all neutronics, materials damage, and activation calculations presented in this report. A 14.1-MeV fusion neutron source is uniformly distributed throughout a DT fuel region that has a compressed density-radius product ρR of 3.0 g/cm^2. The neutron spectrum of this pellet is shown in Fig. 9-13, as is the spectrum after 1 m of lithium. The absolute numbers correspond to the flux at a distance of 5 m from the fusion pellet.

Radiation Damage. Damage to the first structural wall is evaluated in terms of the helium production rate and the atomic displacement rate. Both rates are time-integrated and do not represent the instantaneous rate at the time of the fusion pulse. The rates are expressed per unit equivalent neutron wall loading to facilitate comparison with other fusion concepts. The equivalent neutron wall loading is defined as

$$\phi_n = 0.8\,(P_{TN})/4\pi R^2 \ ,$$

where P_{TN} is the thermonuclear power (yield × repetition rate) in MW, and R is the chamber wall radius in m. At the midplane of the HYLIFE chamber, ϕ_n = 6.9 MW/m^2 (P_{TN} = 2700 MW, r = 5.0 m). Recall that the minimum path length for neutrons from the pellet is in the midplane. Details of the calculations are given in Ref. 26.

Figure 9-14 shows the reduction in the helium production rate realized by protecting the chamber wall by a region of lithium. The production rate is measured in atomic parts per million (appm) of He per yr per MW/m^2 of equivalent neutron wall loading. Note that the nickel content of Type-316 stainless steel results in a helium production rate that is about twice that of ferritic steel.

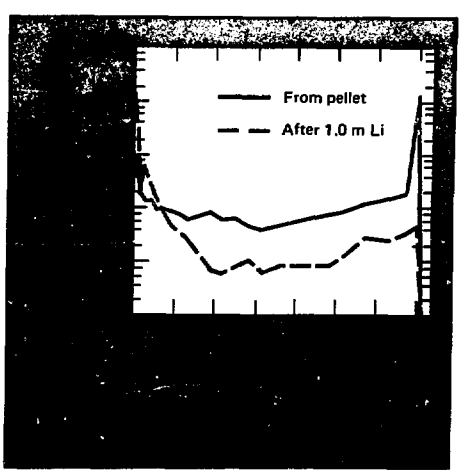

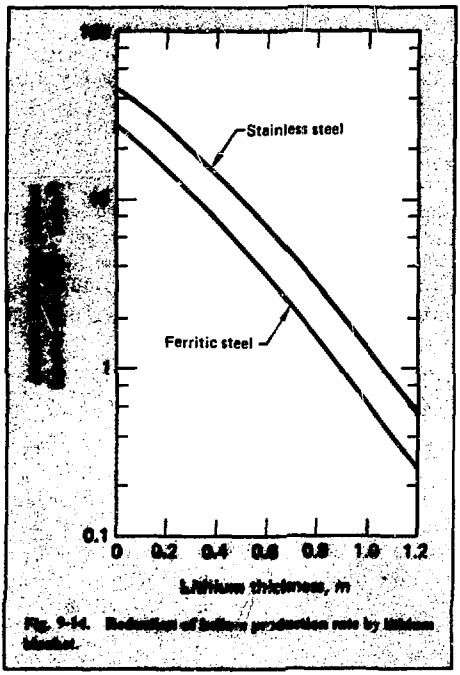

helium. Current design minimums for uniform elongation in the LMFBR program range from 0.2 to 0.5%. Helium production, therefore, does not appear to be a limiting factor for the HYLIFE design.

The effectiveness of the lithium blanket in reducing the displacement damage rate in iron is shown in Fig. 9-15. For 1 m of protection, the dpa rate is reduced to ~0.5 displacements per atom (dpa) per MW·yr/m^2. For the ferritic wall at ϕ_n = 6.9 MW/m^2, the total accumulated displacement damage after 21 full-power years is 73 dpa. The result for the stainless steel is 77 dpa total.

Radiation-induced swelling is generally assumed to be a linear function of dpa after some incubation dpa. Ion irradiation experiments of ferritic alloys indicate that they resist swelling better than Type-316 SS. Experiments with high-Cr ferritic alloys EM12 (9% Cr) and HT9 (12% Cr) showed 0.7% and 1.8% swelling after 80 dpa at their peak swelling temperatures of 550°C and 500°C,

The production rate in the ferritic wall protected by 1 m of lithium is 0.6 appm per MW·yr/m^2 or 4.1 appm per year for our reference case at 6.9 MW/m^2. Over a 30-yr operating life at 70% capacity factor, the accumulated helium concentration is less than 90 appm. For the stainless steel wall the value is 190 appm helium.

Atomics International studied the effects of helium on the tensile properties of alloys by irradiating miniature tensile specimens with alpha particles. Austenitic samples with low helium concentrations (40 appm) lost ductility more rapidly with increasing temperature than did ferritic steels with the same helium content.[27,28] Twenty percent cold-worked Type-316 stainless steel (SS) was irradiated and tensile-tested at 575°C. It retained a total uniform elongation of 1.5% while containing 2030 appm helium.[29]

If the superior ductility retention of a ferritic steel can be extrapolated to a high helium regime, then we can expect ferritic steels to retain at least 2% elongation at 500°C with greater than 2000 appm

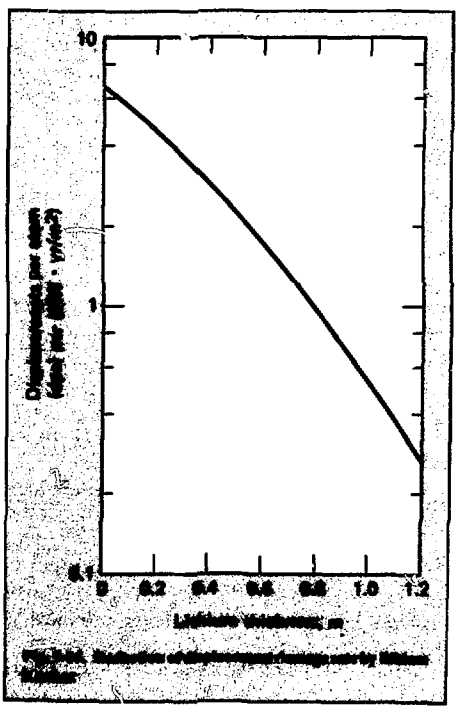

respectively.[30] However, neutron irradiation temperatures generally correlate to an ion irradiation temperature that is about 100°C higher. Therefore, we expect little swelling in either of these alloys under our system conditions of neutron irradiation at 500°C because little swelling occurs at 600°C during ion irradiation.

There is also evidence that swelling increases with increasing Cr content up to a point. Thus, the 2.25 Cr–1.0 Mo alloy considered for our design would exhibit even less swelling under the same condition. The alloy showed only 0.8% swelling after 115 dpa at 550°C.[30]

E\ ·0% cold-worked Type-316 SS, which is more ell. g-resistant than annealed stainless steel ·ows a swelling rate that is 4 to 6 times that of · itic alloys HT9 and EM12. From the correlati· ·n Ref. 28, 20% cold-worked Type-316 SS would have ~4% swelling from the 77 dpa expected after 30 yr in the HYLIFE chamber. A maximum of 10% swelling has previously been suggested as an end-of-life damage limit for Tokamaks.[31] Thus, even stainless steel could be used in our system with these radiation damage limitations.

Radiation Damage Limits. Radiation damage limits have not been made for ferritic steels, but the limited data suggest that they are less susceptible to the effects of neutron radiation than are the austenitic stainless steels. As a conservative estimate of damage limits for ferritic steels, we adopt the limits that have been suggested for Type-316 SS. Reference 31 suggests an accumulation limit of 500 appm-He for Type-316 SS at an operating temperature of 500°C.[32] Assuming a dpa-induced swelling limit of 10%, the correlation in Ref. 28 gives a displacement damage limit of 165 dpa. To avoid replacing the chamber wall in the HYLIFE converter, we want the radiation damage levels to remain below these limits for 21 full-power years (30 yr at 70% capacity factor) of operation. For a given lithium blanket thickness, damage rates are proportional to the fusion power and inversely proportional to the square of the chamber wall radius.

Figure 9-16 is a plot of the allowable fusion power (yield × repetition rate) vs chamber radius based on the damage limits of 500 appm-He accumulation and 165 dpa. The damage rates are for ferritic steel with 1 m of lithium protection. The figure also shows the steady thermal stress limit in a 3.5-cm-thick wall caused by nuclear heating. Thus, consideration of radiation damage would allow the

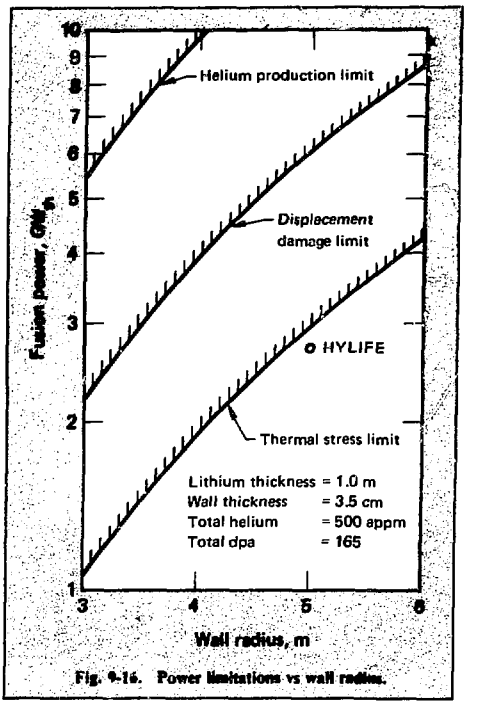

Fig. 9-16. Power limitations vs wall radius.

chamber wall radius to be as small as 3.3 m, but stress considerations force us to a larger chamber.

Energy Deposition. Figure 9-17 shows how neutron-induced energy deposition varies with the lithium blanket thickness for different zones. For a given thickness, a spatial energy deposition profile can be constructed from these curves. The curve labeled "Total" is the sum of the other three curves plus the energy leakage.

Note that neutrons deposit 2.1 MeV or 15% of their original 14.1-MeV energy in the pellet on the average. This energy plus the 3.5-MeV alpha particle energy accounts for 32% of the pellet energy and is delivered to the lithium blanket in the form of x rays and debris. Exoergic neutron reactions with blanket materials (primarily ^{6}Li) result in a net energy gain for the system. We define the system energy multiplication M_S as the total energy deposited in the system (neutron plus alpha) divided by 17.6 MeV. About 95% of the total system energy is deposited directly in a 1-m-thick lithium blanket.

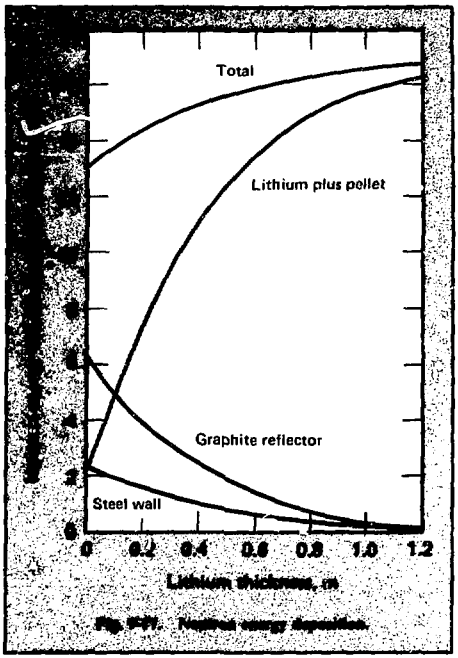

A two-dimensional (2-D) neutronics model (Fig. 9-18) is used for an accurate analysis of the system energy deposition and tritium breeding performance.[33] A total of 20.7 MeV is deposited in the system per DT fusion reaction. This represents an M_S of 20.7/17.6 = 1.176. This value times the thermonuclear power of 2700 MW (yield × repetition rate) gives a fusion chamber thermal power output of 3175 MW_t. Additional heat from the liquid-metal pumps raises the plant thermal power to 3212 MW_t.

Of the 20.7 MeV per fusion reaction, 19.2 MeV are deposited in lithium in the chamber (zones 2, 4, 16 of Fig. 9-18). Although this is 93% of the total energy deposited in the system, the mixed-mean temperature rise of the lithium is only 13.4 K per pulse. Thus, the lithium blanket, which circulates at nearly constant temperature, helps to decrease both the heat load and cyclic thermal stresses on the chamber's structural components. Only a small fraction of the circulating lithium is diverted to heat exchangers where thermal energy is removed.

An additional 0.7 MeV is deposited in the remaining lithium zones in the vessel (zones 6, 8, 11, 14, 18). Therefore, 96% of the total system energy is deposited directly in the liquid lithium.

The small fraction of total energy that does reach the chamber wall will induce a thermal stress distribution. Figure 9-19 shows the energy deposited per cm^3 of steel averaged over the wall thickness at the chamber midplane. For a given wall thickness, the specific energy deposition varies in both the radial and vertical directions. A 10-cm-thick wall, for example, has a neutronic heat load at the midplane that decreases nearly linearly from 5.5 J/cm^3 at the inner edge of the wall (r = 5.0 m) to 2.0 J/cm^3 at the outer edge (r = 5.1 m). The average heat load for the entire 8-m-high cylindrical wall is 2.6 J/cm^3.

In the HYLIFE design the chamber wall is cooled on both sides by flowing liquid lithium. The calculated temperature profiles and thermal stress distributions are discussed in detail in §9.2.3.

Uniformity of Coverage. Because the protective lithium blanket is composed of a large number of individual jets, there is an azimuthal variation in the blanket thickness. Figure 9-20 shows the straight-line path length through an HCP array of 0.20-m-diameter lithium jets as a function of azimuthal angle in the horizontal midplane. This angle is measured from the vertical plane through the laser beams. For this plot, one row of jets was removed to provide a path for the beams. Thus, the lithium thickness is zero at zero degrees. The jets are arranged within an annular envelope with an inner radius of ~0.5 m and an outer radius of ~2.5 m. The mean lithium thickness of 1.0 m equals the packing fraction (0.5) times the thickness of the annular envelope.

As Fig. 9-20 shows, the lithium thickness is within ±0.1 m of the mean at most angles. Some variations can be reduced by rearranging jets within the array. For example, an outer jet at 60° could be removed and used to provide additional thickness at 30°. The variation about the mean decreases as we decrease the jet diameter and increase the number of jets. However, large jets are more stable than small jets. In the compromise between a completely uniform blanket thickness and improved jet stability, we give jet stability priority.

The fusion neutrons will not follow straight lines from the pellet. Rather, they will undergo several collisions and scattering interactions with

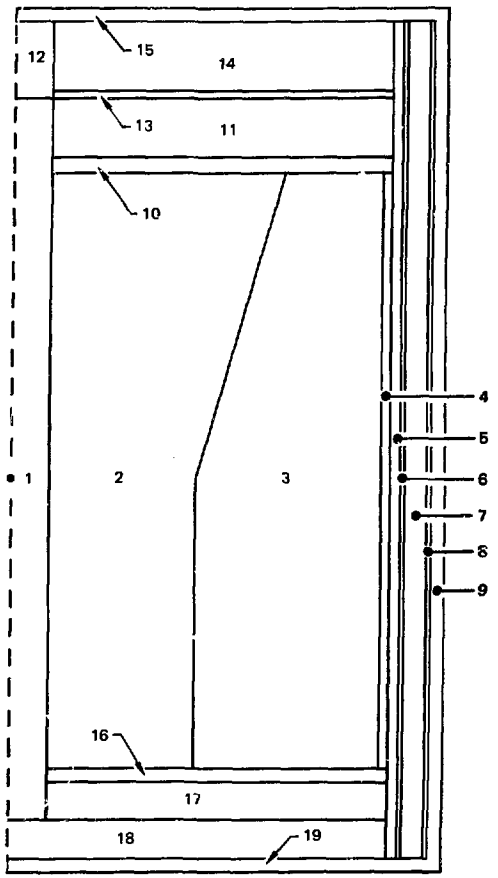

Zone number	Description
1	Central region, lithium (Li) vapor
2	Jet array, Li at half density
3	Outer region Li vapor
4	Sheet fall coolant, Li
5	First structural (or chamber) wall, ferritic steel (FS)
6	Wall coolant, Li
7	Graphite reflector
8	Coolant and shield, Li
9, 15, 19	Vessel wall, FS
10	Nozzle plate, FS
11	Injection head pool, Li
12	Graphite plug
13	Orifice plate, FS
14	Inlet collect region, Li
16	Lithium
17	Splash baffle, FS
18	Outlet collection region, Li

Fig. 9-13. Two-dimensional neutronics model of HYLIFE.

lithium. Scattering allows for path lengths through lithium that are even shorter than the straight-line path lengths. It also tends to smooth the azimuthal fluence variation at the chamber wall as a result of minor variations in flux distribution from pulse to pulse at any given point on the wall.

Even if we assume the radiation damage to be a function of the straight-line thickness through the lithium blanket, we find that the differential variation of damage in the azimuthal direction is approximately the same as the differential variation in the radial direction. Radial variation results from attenuation of the high energy flux by the steel itself. We also conducted three-dimensional (3-D) neutronics calculations to determine whether neutron streaming between rows of jets was a problem. There was some variation in flux, but it was of the same order as the standard deviation.

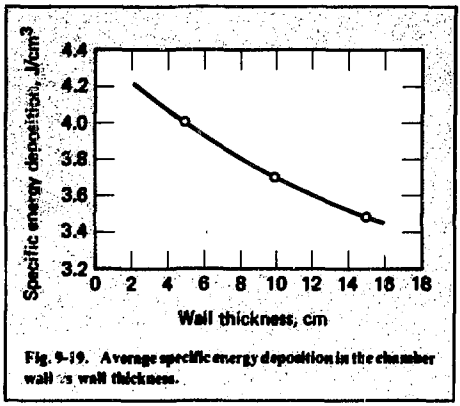

Fig. 9-19. Average specific energy deposition in the chamber wall vs wall thickness.

Thus, the jet array does not provide a completely uniform blanket of protection for the chamber wall, but we believe that the flux and radiation damage distributions will be essentially the same as those for a uniform blanket.

Tritium Breeding. The lithium blanket is the source of tritium needed for the fusion fuel. Tritium is bred from either isotope of natural lithium (7.4% ^{6}Li and 92.6% ^{7}Li) by the following neutron reactions:

$$^6\text{Li} + \text{n} \rightarrow {}^4\text{He} + \text{T} + 4.8\ \text{MeV}$$
$$^7\text{Li} + \text{n} \rightarrow {}^4\text{He} + \text{T} + \text{n} - 2.5\ \text{MeV}\ .$$

As shown in Fig. 9-21, the ^{7}Li reaction has a threshold of approximately 4 MeV. This reaction is

Fig. 9-20. Azimuthal variation in lithium blanket thickness.

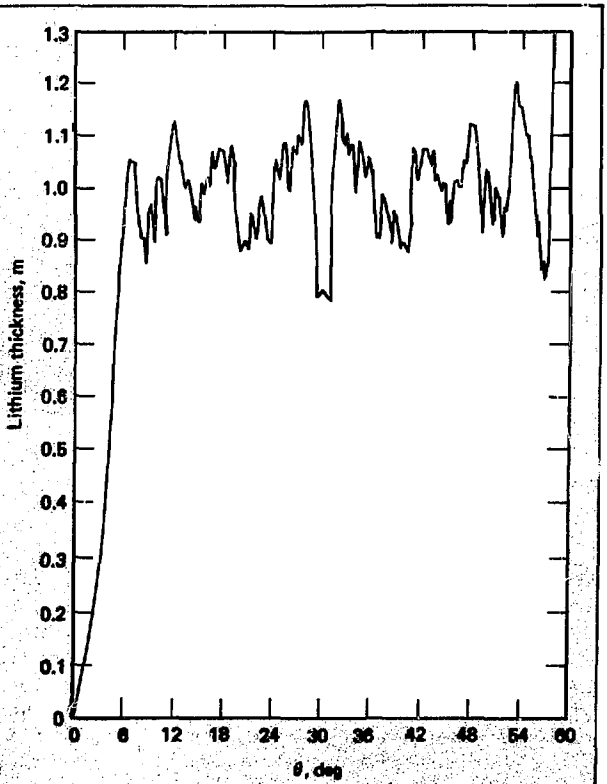

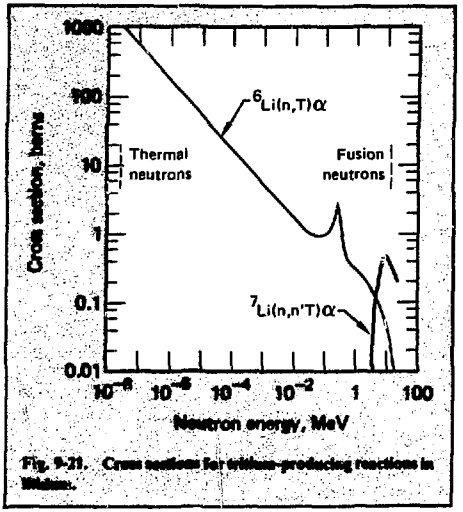

Fig. 9-21. Cross sections for tritium-producing reactions in lithium.

important since it produces a T atom and a low-energy neutron that can breed more tritium with ^{6}Li. The HYLIFE blanket configuration exposes lithium to the high-energy neutron flux from the fusion pellet. Thus, the number of ^{7}Li(n,n'T)α reactions is maximized. The thick lithium blanket also thermalizes and absorbs many neutrons in tritium-producing reactions with ^{6}Li.

The graphite reflector provides further thermalization and reflects neutrons back into the interior lithium zones. Any neutrons leaking out the graphite region are absorbed in the lithium zone between the graphite and outer pressure vessel wall. This outermost lithium zone serves as a coolant for graphite and vessel wall and as a shield. Thus, the HYLIFE configuration tends to maximize the tritium breeding ratio. The results of the 2-D neutronics calculations indicate a total tritium breeding ratio (TBR) of 1.74, with 0.68 T/n coming from ^{7}Li reactions.

Because the power plant only requires a TBR of 1.0 to maintain a self-sufficient fuel cycle, excess tritium will be recovered from the liquid lithium. It may be used to fuel other types of DT fusion reactors, D–^{3}He fusion reactors (tritium decays to ^{3}He), fusion–fission hybrids, synthetic fuel producers, actinide burners, or propulsion systems. If, however, a market for excess tritium does not develop, there are modifications that can be made to the HYLIFE concept to reduce the TBR while maintaining its important features. Little can be done to decrease the contribution to the TBR from ^{7}Li, but one or more of the following modifications can reduce the number of ^{6}Li(n,T)α reactions:

- Introduce a neutron poison in the lithium stream to compete for thermal neutrons.
- Limit the thickness of the lithium blanket.
- Prevent neutrons from reflecting back into lithium zones.
- Reduce the concentration of ^{6}Li in natural lithium.

A detailed discussion of these options is given in Ref. 34. We conclude that the most attractive modifications, if required, are to reduce the concentration of ^{6}Li to ~0.3% and to replace the graphite reflector with a boron carbide zone. The number of ^{6}Li reactions in the lithium blanket is reduced, and leakage neutrons are captured in ^{10}B instead of in ^{6}Li. This approach allows us to maintain a 1-m blanket thickness, reduce the TBR to ~1.0, and keep the coolant chemistry uncomplicated.

The economic penalty for using isotopically tailored lithium is expected to be small. Because ^{7}Li is the major isotope of lithium, the throughput of the separation process is very high and the cost is dominated by the cost of the feed material. Therefore, the cost of separated ^{7}Li is only incrementally higher than that of natural lithium. One disadvantage of this approach is that the thermal flux to the chamber wall is increased.

Conclusions. In terms of nuclear performance, the unique feature of the HYLIFE design is that the energy absorbing blanket region is inside the first structural wall. Because 93% of the system energy is deposited in the lithium within the vacuum chamber, radiation damage of the chamber is essentially eliminated as a design constraint. Such designs result in high blanket-energy multiplication factors and high tritium breeding ratios. Ferritic steels, which show high resistance to lithium corrosion, appear to have little susceptibility to radiation damage.

The HYLIFE lithium blanket configuration breeds tritium in a controllable fashion. It is stable and reestablishable, and it allows the laser beams to reach the pellet without beam tubes. A highly segmented flowing lithium blanket (the configuration calculated to be most favorable in reducing impact stress to the chamber wall) can be created with an array of cylindrical jets, which provides acceptable neutronic protection.

Technological Development. The lithium injection assembly and resulting fluid dynamics of the HYLIFE lithium blanket require further technological development. We need to study the injection nozzle itself through experiments on an array of HCP circular jets with realistic nozzle parameters. These experiments should produce high Reynolds numbers through both high-velocity flow and large-diameter nozzles. The injection head should be supplied by a pool of fluid as is proposed for the HYLIFE design.

In such an experiment, we would quantify real nozzle effects and investigate their dependence on parameters such as packing fraction, entrance length/diameter ratio, and height of the lithium pool. We would like to determine, for example, whether a uniform head of lithium can be maintained over a nozzle plate that has a very high ratio of flow area to total area (i.e., packing fraction ~0.8).

We must also investigate the reestablishment of chamber conditions after each pulse. We can divide this investigation into two subcategories: reestablishment of the lithium blanket configuration and condensation of the vaporized lithium. Both processes depend on the blanket configuration after the fusion energy pulse. We consider the reestablishment issue to be more a question of the exact length of time required than a question of whether or not the chamber conditions reestablish.

Finally, we need to investigate further the beam aperture/neutron stop. We propose a crossing jet configuration with added horizontal flow streams at the chamber wall for the HYLIFE design, but we believe that innovation is still needed. We must also do detailed 3-D calculations of neutron streaming out the beam ports.

References

17. R. K. Takahasi, *Experimental Investigation of the Stability of Liquid Sheet Jets*, M.S. thesis, Department of Mechanical Engineering, University of California, Davis, Calif., (1978).
18. M. Goodman, D. Kramer, A. B. Martin, and W. B. Thomson, *Conceptual Design Study of the HYLIFE Lithium Waterfall Laser Fusion Chamber*, Energy System Group, Rockwell International Corp., Canoga Park, Calif. (1978).
19. S. Kang, *The Lithium Fall Reactor Concept—The Question of Jet Stability, with Recommendations for Further Experiments*, Lawrence Livermore Laboratory, Livermore, Calif., UCRL-52531 (1978).
20. S. Kang, *Viscous Effects on a Turbulent Jet Near Nozzle Exit*, Lawrence Livermore Laboratory, Livermore, Calif., UCRL-81826 (1979).
21. L. A. Glenn and D. A. Young, *Dynamic Loading of the Structural Wall in a Lithium Fall Fusion Reactor*, Lawrence Livermore Laboratory, Livermore, Calif., UCRL-82125 (1978).
22. N. Dombrowski and R. D. Fraser, "A Photographic Investigation into the Disintegration of Liquid Sheets," *Philos. Trans. R. Soc. Lond.* A 247, 101 (1954).
23. R. E. Phinney, "Breakup of a Turbulent Liquid Jet in a Low-Pressure Atmosphere," *AIChE J.* 21 (5), 996 (1975).
24. T. Kusui, "Liquid Jet Flow into Still Gas," *Bull. JSME* 11 (48), 1084 (1968).
25. E. F. Plechaty and J. R. Kimlinger, *TARTNP: A Coupled Neutron-Photon Monte Carlo Transport Code*, Lawrence Livermore Laboratory, Livermore, Calif., UCRL-50400, Vol. 14 (1976).
26. W. R. Meier and W. B. Thomson, *Conceptual Design Considerations and Neutronics of Lithium Fall Laser Fusion Target Chambers*, Lawrence Livermore Laboratory, Livermore, Calif., UCRL-80782 (1978).
27. D. Kramer, K. R. Gass, and H. G. Pard, "Helium Embrittlement of a Ferritic Stainless Steel," *Trans. Met. Soc. AIME* 245, 1909 (1969).
28. D. Kramer, K. R. Gass, C. G. Rhodes, and A. G. Pard, "Helium Embrittlement of Type-316 Stainless Steel," *J. Iron Steel Inst.* 207, 1141 (1969).
29. E. E. Bloom et al., "Temperature and Fluence Limits for a Type-316 Stainless Steel CTR First Wall," *Nuc. Tech.* 31 (1976).
30. F. A. Smidt, Jr., "Swelling Behavior of Commercial Ferritic Alloys, EM-12 and HT-9, as Assessed by Heavy-Ion Bombardment," in *Irradiation Effects on the Microstructure and Properties of Metals*, ASTM STP 611 (1976).
31. G. L. Kulcinski et al., "Radiation Damage Limitations in the Design of the Wisconsin Tokamak Fusion Reactor," *Nuc. Tech.* 22, 20 (1974).
32. H. I. Avci and G. L. Kulcinski, *The Effect of a Liquid ISSEC on Radiation Damage Parameters in Laser Fusion Reactor First Walls*, University of Wisconsin, UWFDM-205 (1977).
33. W. R. Meier, "Two-Dimensional Neutronic Studies of the HYLIFE Converter" (to be published).
34. W. R. Meier, "Control of Tritium Breeding in the HYLIFE Converter" (to be published).

Author

W. R. Meier

Major Contributors

N. J. Hoffman
M. W. McDowell
(Energy Technology Engineering Center)

R. K. Takakasi
M. Hoffman
(UC-Davis)

S. W. Kang (LLL)

M. Goodman, D. Kramer, A. B. Martin, W. B. Thomson
(Energy Systems Group, Rockwell International)

9.2.3 Blanket Response

Because it will determine the lifetime of the chamber structure, the response of the first-wall blanket to the pulsed fusion energy deposition is a critical factor in the structural design of an energy conversion chamber.

General Response. The response of a continuum to internal energy deposition depends on both temporal-spatial deposition profiles and on the thermal and physical properties of the continuum. We consider first the effects of the temporal-spatial deposition profiles by assuming that a pulse of energy is deposited in the form

$$q'''(x) = q_0''' \exp(-\mu x) \ , \qquad (1)$$

where q_0''' is the energy deposition in the surface layer of the continuum, and μ is the energy attenuation coefficient through the continuum. We define the characteristic thermal time of the energy deposition in the continuum as the ratio of the energy storage in the distance μ^{-1} to the rate of heat conduction across the distance μ^{-1}, or

$$\tau_T = (\mu^2\alpha)^{-1} \ ,$$

where α is the thermal diffusivity of the continuum. We also define the characteristic mechanical response time that results from energy deposition in the continuum as the time required for a disturbance to propagate the distance μ^{-1}, or

$$\tau_m = (\mu c)^{-1} \ ,$$

where c is the wave velocity in the continuum.

Two cases are of special importance for inertial fusion. These cases are

$$\tau < \tau_m \ll \tau_T \qquad \text{(Case I)}$$

and

$$\tau_m \ll \tau_T \approx \tau \ . \qquad \text{(Case II)}$$

For Case I, the time variation effects produced by heat conduction are small compared to those produced by the pressure wave. Because the energy is deposited in a short time, the initial temperature rise and pressure rise can be estimated by simple models,

$$\Delta T(x) = \frac{q'''(x)}{\rho C_v} \qquad (2)$$

and

$$\Delta p(x) = \Gamma q'''(x) \ , \qquad (3)$$

where $q'''(x)$ is the energy deposition at position x in the continuum, and ρ, C_v and Γ are the density, specific heat at constant volume, and Grüneisen constant, respectively, of the continuum. Approximate theories of uncoupled dynamic thermoelasticity and viscoelasticity can then be used to determine the moving stress pulse produced by the energy deposition.

For energy deposition times that are long compared to the thermal characteristic time (which is long compared to mechanical characteristic time, Case II), the stress can be determined by quasi-static thermoelastic or viscoelastic theory. The temperature history can be determined using classical diffusion theory.

Several parameters should be minimized to reduce the temperature rise and pressure rise per fusion pulse. The amplitude of the temperature pulse can be minimized by minimizing the ratio of the energy attenuation coefficient to the specific heat at constant volume μ/C_v. The amplitude of the pressure pulse can be minimized by minimizing the product of the Grüneisen constant and the energy attenuation coefficient $\Gamma\mu$. Generally, for fusion products this involves using materials of low atomic number.

If the pressure cannot relieve itself because the deposition time is too short, a relief wave moves into the continuum from the surface. If the continuum is a solid, and if the tensile strength is exceeded, the surface will spall with a velocity

$$v(x) = \frac{1}{2\rho c\delta} \int_{2x}^{2(x+\delta)} \Delta P(x')dx' \ , \qquad (4)$$

where c is the acoustic velocity of the material, δ is the thickness of the spalled region, and $\Delta P(x')$ is given by Eq. (3). The thickness of the spall region is determined from

$$\Delta p\,[2(x+\delta)] = \Delta p(2x) - \sigma_c \quad , \tag{5}$$

where σ_c is the tensile strength of the material. For a liquid with essentially no tensile strength, the velocity of the spalled material at any position x is given by

$$v(x) = \lim_{\delta \to 0} \left[\frac{1}{2\rho c \delta} \int_{2x}^{2(x+\delta)} \Delta P(x')dx' \right] . \tag{6}$$

HYLIFE Fusion Events. The fusion yield selected for the HYLIFE converter is 2700 MJ. The DT fusion reactions in the compressed pellet ($\rho R_{fuel} \simeq 3$) release about 80% of their energy as 14.1-MeV neutrons and 20% as 3.5-MeV alpha particles. However, the alpha particle energy and some of the neutron energy is attenuated and absorbed in the compressed pellet. Of the 2700 MJ produced by DT reactions, 35 MJ are lost due to endoergic neutron reactions in the pellet, 1800 MJ escape the target as neutrons, and the remaining 865 MJ escape as x rays plus energetic pellet debris. The x rays include a hard component generated from the hot burning pellet and soft components radiated from the cooling debris as it expands.

The geometry for our 1-D Monte Carlo neutronics calculations using the TARTNP code[35] is shown in Fig. 9-22. The x-ray deposition profile was calculated using the BUCKLE code,[36] and the debris deposition was determined analytically using previously described methods.[37] The neutron energy and the hard component of the x rays are deposited throughout the thickness of the blanket. The soft x-ray and pellet debris energies are deposited in a thin region of the inner surface of the blanket.

Energy flow in the chamber is shown in Fig. 9-23. The neutron plus gamma ray energy is increased by 27% in the reactor primarily through the exoergic ^{6}Li-neutron capture reaction. The blanket absorbs 92% of the neutron plus gamma energy. Of the total 3156 MJ$_t$, 94% is absorbed by the blanket, 6% is absorbed in the walls and reflector, and only about 0.01% leaks from the reactor vessel.

Macroscopic Response. Because the energy deposition time of the x rays and neutrons is short compared to the characteristic times, the response of the blanket to energy deposition can be estimated using the methods of Case I described above. The deposition time of the pellet debris is long compared to the characteristic times. Hence, analysis of blanket response to debris energy can be estimated using the methods of Case II.

X rays arrive first at the blanket. Hard x rays have low specific energy, hence little effect on the motion of the blanket. The range of soft x rays in the blanket is short relative to the neutrons. The short range results in high specific energies and associated high pressures at the inner surface of the blanket. The analytic model for estimating spall velocity, Eq. (6), does not apply here because the material properties vary over the large pressure gradient in the thin deposition region. The large pressure gradients cause the pressure wave to form a shock wave that moves through the blanket. However, the relief wave from the front surface travels faster than the shock wave. As a result, the pressure wave is highly attenuated by the time it reaches the back surface of the blanket.

Because of the large pressure gradients, the response of the fall to x rays is calculated using codes such as CHART-D[38,39] or AFTON.[40,41] Adequate representation of the x-ray energy deposition in the fall requires fine zoning if CHART-D is used. This results in excessively long computational times. We solved the zoning problem by using the variable zoning option of AFTON, in which the problem initially has fine zones in the deposition region and coarse zones elsewhere. As time progresses, the zones are resized so that fine zoning is always present in the region of the moving pressure pulse.

The neutrons arrive at the blanket after the x rays. Neutron energy is deposited throughout the fall since the mean free path for 14-MeV neutrons in lithium is long. Therefore, the pressure rise in the lithium is small because the specific energy is small. The blanket disassembles into the cavity from the front surface with a relief wave moving into the blanket at about the acoustic velocity of the material.[42] The velocity of the material spalled into the chamber is essentially that given by Eq. (6) for the appropriate energy deposition profile. Momentum from the spalled lithium causes the back surface of the blanket to move toward the structure with a velocity profile that is the mirror image of the

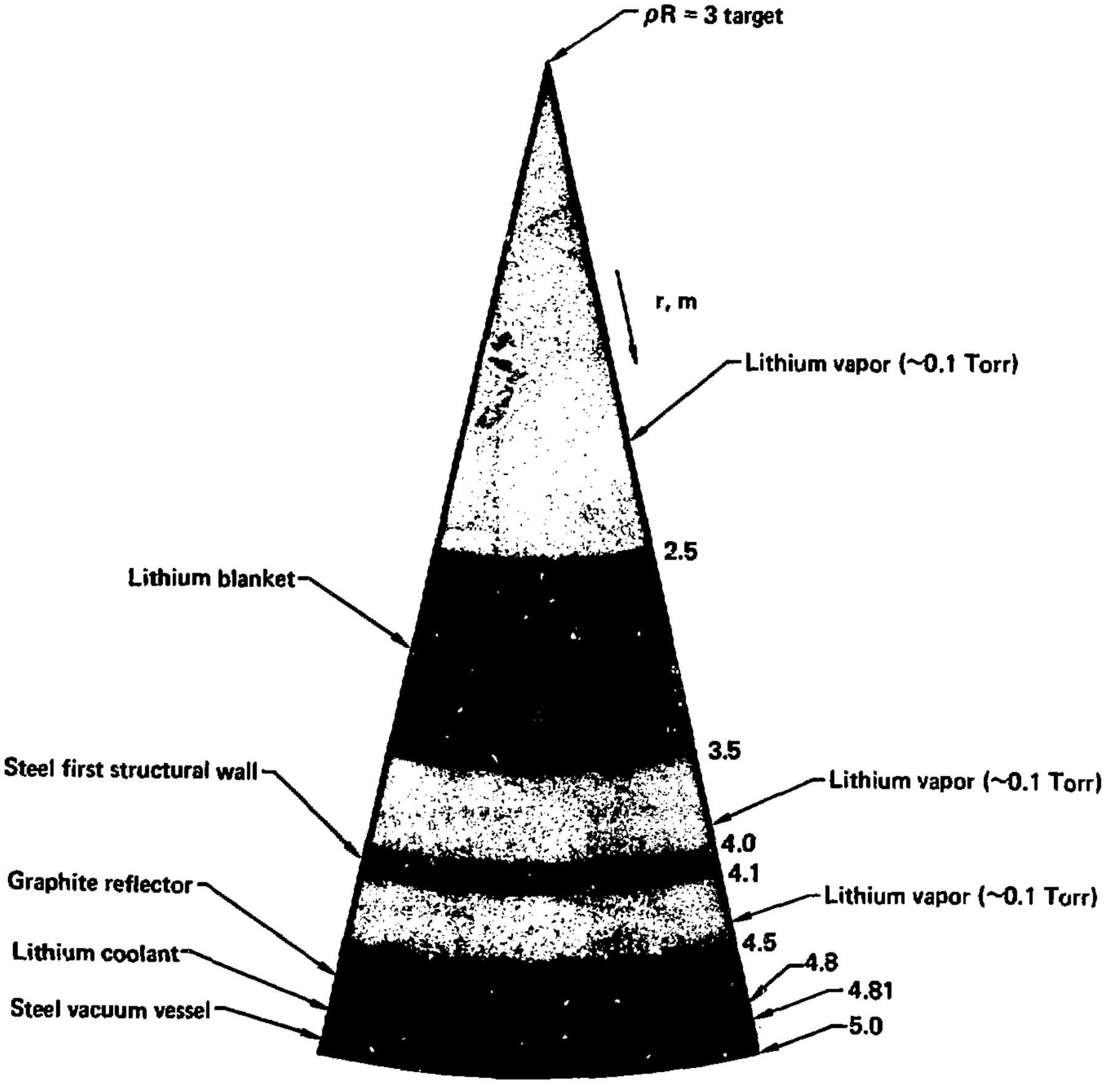

Fig. 9-22. Typical blanket geometry for the lithium blanket concept.

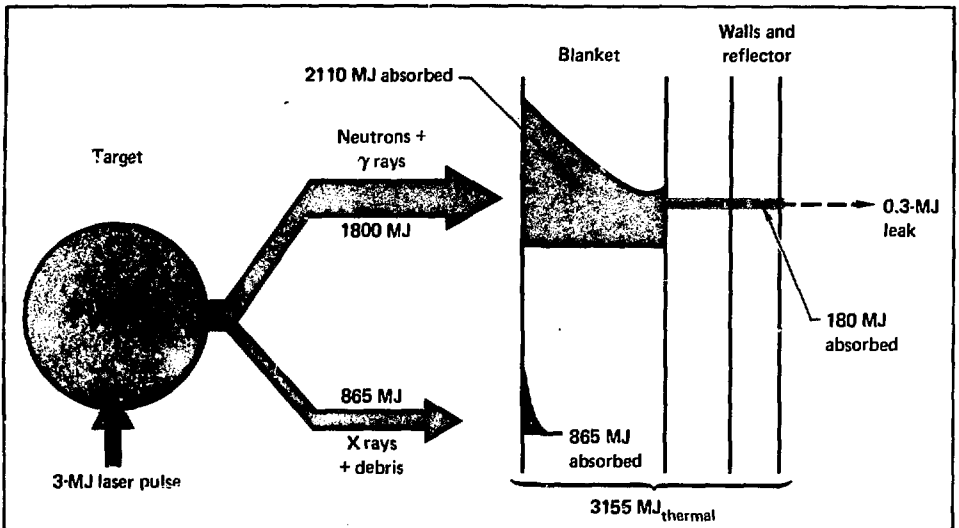

Fig. 9-23. Energy flow in the reactor chamber.

Kinetics of the Blanket. There are two sources of motion for the blanket. One is the rapid volumetric energy deposition that disassembles the blanket into vapor and drops having velocities normal to the surface. The other is the pressure of the gas vaporized from the inner surface of the blanket by the soft x rays. Heated by the pellet debris, the vapor pushes outward on the blanket in a way that is a function of the blanket design.

We considered two different blanket designs. The early design used a lithium fall.[43-45] The current design uses an array of lithium jets.[46] The qualitative and quantitative responses of the jet array are described below.

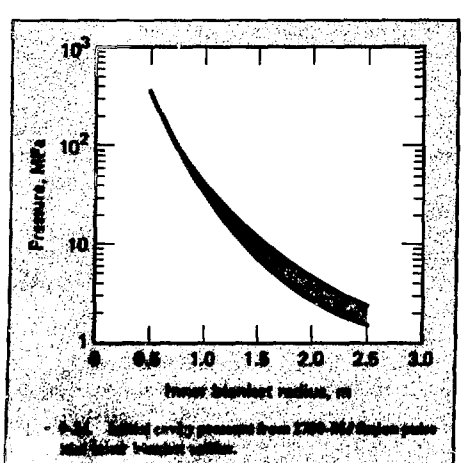

Lithium Jet Array. A cross section of the HYLIFE converter chamber (Fig. 9-6 of §9.2.2) shows the lithium jet array.[46] Figure 9-25(a) depicts the jet array converter at 10 ns after a fusion pulse. The soft portion of the x-ray pulse energy has been absorbed near the inner edge of the jets with "line of sight" to the fusion event. The resulting high energy density in the thin region has vaporized some of the liquid. Hot gas moves normal to the line-of-sight surface of the jet.

Figure 9-25(b) depicts the converter at 25 μs. Expanding hot vapor radiates energy to the jets, producing more two-phase material that moves into the center of the cavity. The relief wave from the neutron energy deposited in the jets has moved from the surface to the center of the jets. Thus, the jets are now a mixture of liquid and vapor expanding outward normal to their surfaces.

A depiction at 50 μs is shown in Fig. 9-25(c). Hot cavity vapor moves through the jets that are

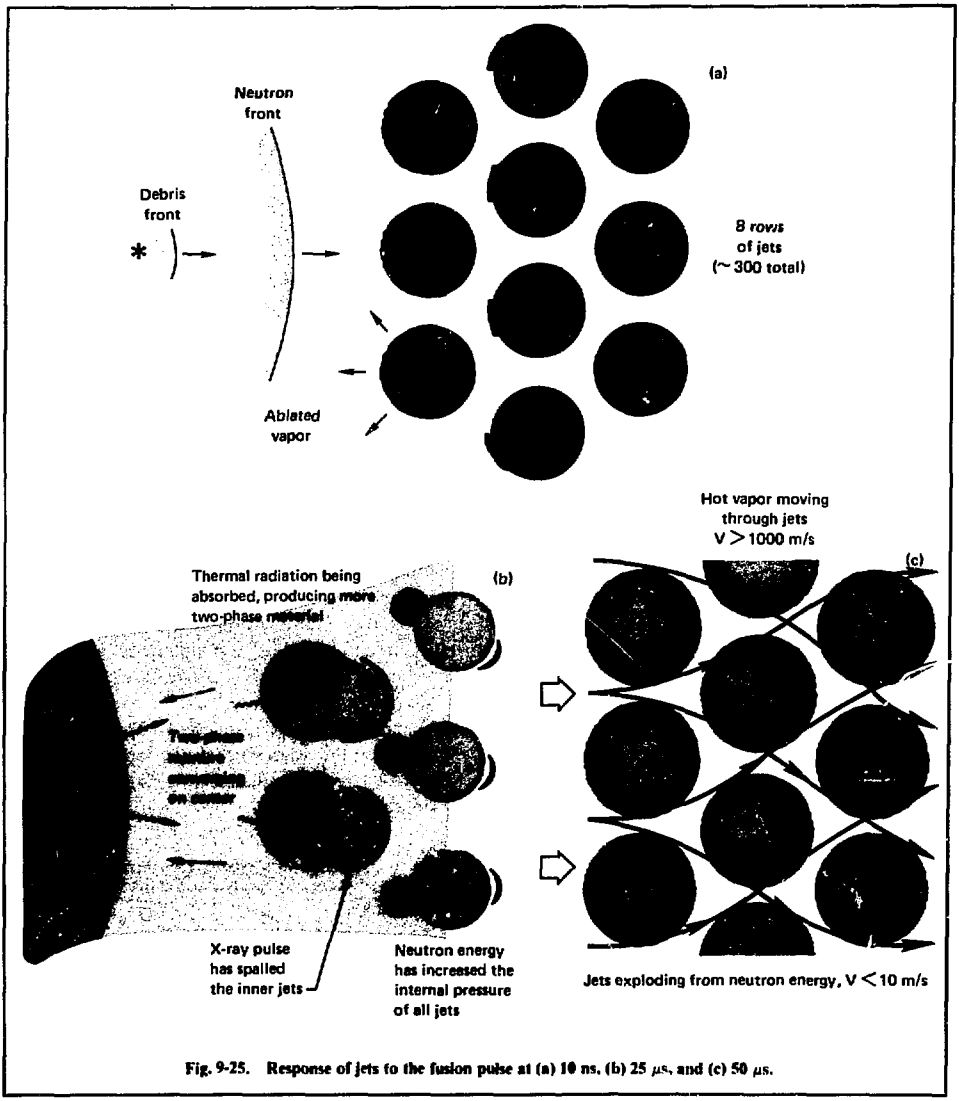

Fig. 9-25. Response of jets to the fusion pulse at (a) 10 ns, (b) 25 μs, and (c) 50 μs.

now a liquid-vapor mixture. The jets are then set in motion in an outward normal direction to the cavity center by the drag of the vapor on the jets. Because the inner rows of jets have a higher velocity than that of the outer rows, the jets will coalesce into a slug of material moving outward. This slug will have a lower terminal velocity than the slug of a liquid fall because of the gas venting through the jet array.

The momentum of the jet array is given by[47]

$$(mv)_{total} = 6.94\, gYC_D \left(\frac{\sqrt{\gamma}}{\gamma - 1}\right) \times \left[\frac{\sqrt{T}}{C_\ell (T_{vp} - T_i) + h_{\ell g} + C_{vg}(T - T_{vp})}\right] \times \left(\frac{\sqrt{\phi}}{1 - 0.8247\sqrt{\phi}}\right) \sum_{i=1}^{N} \left(1 + \frac{R_j}{R_i}\right) , \quad (7)$$

where

- g = fraction of x-ray and debris energy coupled to the cavity vapor,
- Y = fusion event x-ray and debris energy yield,
- γ = specific heat ratio of the cavity vapor,
- C_ℓ = specific heat of the liquid,
- $h_{\ell g}$ = heat of vaporization of the liquid at T_{vp},
- C_{vg} = specific heat at constant volume of the cavity vapor,
- T_{vp} = liquid temperature corresponding to a specific vapor pressure,
- T_i = bulk liquid temperature,
- T = cavity vapor temperature,
- R_j = radius of jets,
- R_i = radial position of *ith* row of jets,
- ϕ = jet packing fraction in the array,
- N = number of rows of jets in the array,
- C_D = drag coefficient.

We used the following values to simplify the equation: a 2700-MJ fusion event with 32% of the yield in x rays and debris energy; lithium jets at an initial temperature of 773 K; initial lithium vapor pressure of 0.1 Torr; and a packing fraction of 0.5. Equation (7) then becomes

$$(mv)_{total} = 4.6 \times 10^4\, g\, C_D \sum_{i=1}^{N} \left(1 + \frac{R_j}{R_i}\right) \text{ kg} \cdot \text{m/s} . \quad (8)$$

For 8 rows of 0.2-m-diameter jets, the total momentum becomes

$$(mv)_{total} = 4 \times 10^5\, g\, C_D \text{ kg} \cdot \text{m/s} . \quad (9)$$

Energy transfer from the hot cavity gas as a function of time is shown in Fig. 9-26. The gas loses more than half its energy in 20 μs, assuming that it is optically thin. Thus, for this case in which

$$g \simeq 1 - 0.5 = 0.5 ,$$

the drag coefficient of the hot lithium cavity gas over the jets is given by[48]

$$C_D \approx 0.2\, D_j^{-1/4} ,$$

where D_j is the jet diameter in m. This expression assumes that the jets remain as a single-phase liquid continuum with a pitch-to-diameter ratio of 1.35. We also assume that the flow of the cavity vapor is subsonic through the jet array by virtue of the formation of a detached standing shock wave on the inner side of the array.

We combined the expressions for the drag coefficient and the energy coupling to get a total momentum of 6.2×10^4 kg·m/s for a 2700-MJ fusion event in an array of 0.2-m-diameter jets located 0.5 m radially from the event. The space-time diagram for the response of the jet array is shown in Fig. 9-27. The jets coalesce into a slug 3 m from the fusion event.

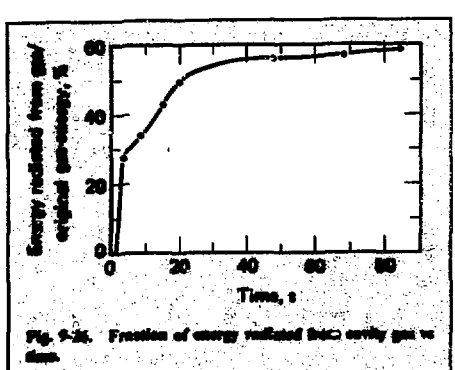

Fig. 9-26. Fraction of energy radiated from cavity gas vs time.

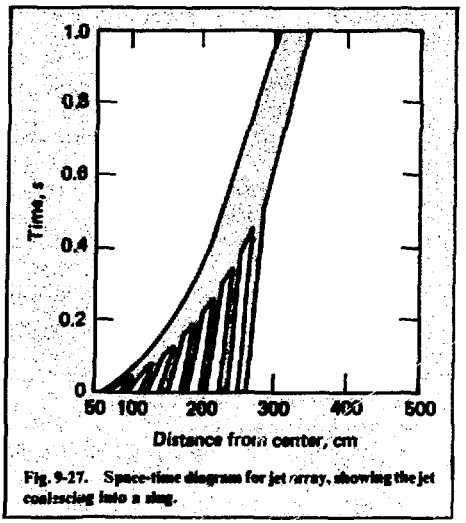

Fig. 9-27. Space-time diagram for jet array, showing the jet coalescing into a slug.

Future work on the response of the jet array should consider a range of fusion energies and initial radii for the first jet row. In addition, the effect of the highly time-dependent flow conditions in jet drag should be investigated. Finally, because the array disassembles into a noncontinuous two-phase flow by the time the cavity gas starts to vent through the first row of jets, interaction of the flowing cavity gas with the droplets should be considered. These droplets will certainly improve the transfer of heat from the cavity gas, but they will also increase the effective drag of the fluid columns.

Conclusions. The jet array appears to lead to less induced momentum in the outward normal direction than does the previously considered lithium fall. Partial venting of the high-temperature cavity gas through the array is primarily responsible for this reduction. However, we need to model better the jet array response to the flow of the cavity gas. Response of the blanket to a fusion pulse is a complex thermohydrodynamic problem that requires an extensive and balanced experimental and analytical program for its solution.

References

35. E. Plechaty and J. Kimlinger, *TARTNP: A Coupled Neutron-Photon Monte Carlo Transport Code*, Lawrence Livermore Laboratory, Livermore, Calif., UCRL-50400, Vol. 14 (1976).
36. R. K. Cole, Jr., *BUCKL: A Program for Rapid Calculation of X-Ray Deposition*, Sandia Corp., SC-RR-69-855 (1970).
37. J. Hovingh and S. L. Thomson, "Energy Deposition from Microexplosion Particle Debris in the First Wall of an Inertially-Confined Fusion Reactor," in *Proc. 7th Symp. on Eng. Problems of Fusion Research*, Vol. I, 162 (1977).
38. S. L. Thompson, *Improvements in the CHART D Energy Flow Hydrodynamic Code V: 1972/73 Modifications*, Sandia Laboratories, SLA-73-0477 (1973).
39. S. L. Thompson and H. S. Lauson, *Improvements in the CHART D Radiation Hydrodynamic Code II: A Revised Program*, Sandia Laboratories, SC-RR-71-0713 (1972).
40. J. Trulio and K. Trigger, *Numerical Solution of the One-Dimensional Hydrodynamic Equations in an Arbitrary Time-Dependent Coordinate System*, Lawrence Livermore Laboratory, Livermore, Calif., UCRL-6522 (1961).
41. L. A. Glenn, *AFTON Revisited—An Improved Algorithm for Numerical Solution of Initial Value Problems in Continuum Mechanics*, Lawrence Livermore Laboratory, Livermore, Calif., UCRL-52512 (1978).
42. I. O. Bohachevsky, "Inertial Confinement Fusion Reactor Cavity Phenomena," in *Proc. of the 3rd Topical Mtg. on the Tech. of Controlled Nuclear Fusion, Santa Fe, New Mexico* (1978).
43. J. A. Maniscalco and W. R. Meier, "Liquid Lithium 'Waterfall' Inertial Confinement Reactor Concept," *Trans. ANS 1977 Summer Mtg., N.Y.*, (1977), p. 62.
44. W. R. Meier and W. B. Thomson, "Conceptual Design and Neutronics of Lithium Waterfall Laser Fusion Target Chambers," in *Proc. of the 3rd Topical Mtg. on the Tech. of Controlled Nuclear Fusion, Santa Fe, New Mexico* (1978).
45. J. Hovingh, J. Blink, and L. Glenn, "Response of a Lithium Fall to an Inertially Confined Fusion Microexplosion," in *Proc. of the 3rd Topical Mtg. on the Technology of Controlled Nuclear Fusion, Santa Fe, New Mexico* (1978).
46. M. Monsler, J. Maniscalco, J. Blink, J. Hovingh, W. Meier, and P. Walker, "Electric Power from Laser Fusion: The HYLIFE Concept," in *Proc. of the 13th Intersociety Energy Conversion Eng. Conf., San Diego, Calif.* (1978), p. 2164.
47. J. Blink, *Wall Loading of the HYLIFE Chamber*, Lawrence Livermore Laboratory, Livermore, Calif., Internal Memorandum SS&A 78-141 (Sept. 21, 1978).
48. J. Hovingh, *Row-wise Effective Drag Coefficient of Jets in the HYLIFE Converter*, Lawrence Livermore Laboratory, Livermore, Calif., Internal Memorandum SS&A 79-16 (Jan. 29, 1979).

Authors

J. Hovingh
J. Blink

9.2.4 Materials Considerations

Materials exposed to the flowing liquid lithium and to the pulsed radiation are subjected to mechanical and thermal loads, liquid-lithium corrosion, radiation damage, and synergistic effects. Materials must retain adequate strength, ductility, and dimensional stability under cyclic stresses while exposed to the degrading effects of molten lithium and radiation. They should also be easy to fabricate, be low cost, and make limited use of scarce or imported elements.

Austenitic vs Ferritic Steels. We considered only commercially available materials with an eye to avoiding a developmental program that would be needed to certify a new material. We compared two general categories of steel: austenitic stainless steels and ferritic steels.

The austenitic stainless steels (SS) such as Type-316 and Type-304 are stronger than the ferritic steels. Moreover, most radiation damage studies have been done with Type-316 SS. Major disadvantages of austenitic stainless steels arise from the fact that they contain ~10% nickel. Liquid lithium leaches nickel from the metal surface. This process weakens the steel and results in the transport of nickel throughout the system. Exposed to a neutron flux, nickel activates to form ^{58}Co and ^{60}Co. These radioactive isotopes will then be present in the chamber walls, the flowing lithium, and the heat exchangers.

Because nickel has a higher cross section for helium producing (n, α) reactions than does iron, the rate of helium production in Type-316 SS for the HYLIFE design is about twice that in a low-alloy ferritic steel. Austenitic stainless steels need 2 to 10 times more chromium than do ferritic steels. This is an important resource consideration since there are no US sources of chromium.

Ferritic steels offer several other potential advantages compared to austenitic SS. They appear to be more resistant to both helium embrittlement and void swelling induced by displacement damage.[49–52] They exhibit less dissolution attack in lithium but may require a Nb microalloy or heat treatment to stabilize against grain boundary corrosion.[53–54] They also result in less activation and cost less.

We selected the low-alloy ferritic steel 2.25 Cr–1.0 Mo for the HYLIFE design. This steel is used extensively in the United States for heat exchangers and steam generators; the version stabilized with Nb is used in Europe and Japan in both fossil and nuclear systems.

Radiation Effects. A comparison of the radiation damage in ferritic steels and austenitic SS is discussed in §9.2.2. Neutron activation of the different types of steel is covered in §9.2.9.

Lithium Corrosion. Corrosion in liquid lithium is one of the most important materials problems that must be solved for the HYLIFE design. Although corrosion in liquid lithium is similar to that in liquid sodium, lithium is generally considered more corrosive than sodium.[55] The principal types of corrosion include[56]:

- Simple dissolution.
- Temperature-gradient mass transfer.
- Concentration-gradient or dissimilar metal mass transfer.
- Intergranular penetration.
- Impurity reactions.
- Alloying between liquid metal and solid metal.

The following variables can influence the type and severity of lithium corrosion on specified container materials[56]:

- Temperature and temperature gradients.
- Cyclic temperature fluctuation.
- Flow characteristics.
- Impurity levels in the liquid metal and the material.
- Ratio of metal surface area to liquid volume.
- Material surface condition, including grain size, finish, etc.
- Number of materials in contact with the same liquid metal.
- Stress and stress gradients.
- Heat treatment.

A detailed overview of lithium corrosion is given in Refs. 53 and 54. The general trends in lithium corrosion of ferrous alloys are discussed below along with comments on how they apply to the HYLIFE design, which uses 2.25 Cr–1.0 Mo.

High temperature, temperature gradients, and chemical activity gradients promote dissolution and mass transport.[56–61] At the maximum lithium temperature in the HYLIFE design (500°C), corrosion rates of 2.25 Cr–1.0 Mo are low. The main temperature gradient occurs in the intermediate heat exchanger (IHX) where the temperature of the primary lithium drops from 500 to 340°C. The fusion chamber operates at essentially a constant 500°C. Chemical activity gradients are minimized by using 2.25 Cr–1.0 Mo for all components and piping throughout the lithium-flow system.

Corrosion rates increase with the nickel content of the alloy.[53,62] We eliminate this concern by using nickel-free 2.25 Cr–1.0 Mo.

Nitrogen seems to be the most troublesome impurity in lithium and results in accelerated corrosion.[63–66] Nitrogen levels above ~500 appm in lithium can lead to severe grain boundary attack of

both ferritic and austenitic stainless steels. To prevent this attack, the lithium will be purified when it is first loaded into the system. Once operation begins, the lithium is never exposed to the atmosphere, which is the principal source of nitrogen. Nitrogen impurities that enter the lithium from the steel pipes will also be removed during early operation. Nitrogen monitoring will be required during plant operation, but we expect nitrogen levels to remain low.

Carbon impurities also accelerate corrosion rates.[67,68] In some cases, chromium ions in the steel tend to diffuse to the grain boundaries and form chromium carbides. The carbides may then react with lithium and promote cracking along the grain boundaries. To prevent cracking, extra-low-carbon steels or grades stabilized with minor additions of titanium or niobium may be required. The stabilizing additives tend to tie up most of the carbon and, thus, prevent the formation of chromium carbide. Low-chromium steels are less susceptible to this effect.

Chromium depletion in stainless steels may lead to nickel dissolution from the chromium-depleted (nickel-rich) regions adjacent to grain boundaries.[69,70] This effect is unimportant with 2.25 Cr–1.0 Mo. With austenitic steels, the effect can be minimized by using stabilizing additives or heat treating the metal to move Cr from inside the grains to the depleted regions.

Stresses and flow increase corrosion rate.[71–75] We must allow for these unavoidable influences in the HYLIFE system, which uses liquid lithium.

We are supporting experiments on lithium corrosion at the Colorado School of Mines (CSM).[76] In the first year of testing, specimens of both unstabilized 2.25 Cr–1.0 Mo and Type-304 SS were exposed to 500°C static lithium. Two types of coupons were used. Welded and bent metal strips were used to identify potential joining problems and to enable evaluation of the influence of complex stress states. Thin rectangular sheets were used to determine the rate of material weight loss as a function of the impurity content of the liquid lithium. These preliminary studies were designed to reveal catastrophic effects and also to help define parameters for further study. Although their results are not directly applicable to flowing-lithium systems, these experiments are an important precursor to the design of flowing-lithium test loops.

The results confirmed that ferritic steels show good corrosion resistance and dramatically illustrated the need for low nitrogen levels in the lithium. Figure 9-28 shows the weight loss for 2.25 Cr–1.0 Mo as a function of time and nitrogen concentration. The corrosion rate increased sharply when the nitrogen concentration was increased from its initial level of ~0.05% (500 appm) to ~0.4% (4000 appm).

Analysis of the spot-welded specimens of unstabilized 2.25 Cr–1.0 Mo showed that the welds caused crystals of iron to grow adjacent to the boundary between the weld and base metal. One case of severe penetration in the fusion zone of the weld was also observed. No explanation of the cause is yet available.

The CSM researchers also noted the importance of heat treatment on the structure of ferritic steels. One typical structure is a mixture of body-centered-cubic (BCC) crystals with masses of alternating lamellae of iron carbide and BCC plates. Another structure is composed of BCC crystals interspersed with spheres of carbides. Each structure may behave differently with respect to lithium compatibility.

Tests with 304-SS showed much less grain boundary attack than was expected based on tests of Type-304L, a low-carbon stainless steel. The corrosion rate increased rapidly with increased nitrogen levels.

Debris from the fusion pellets will introduce impurities into the liquid lithium of the HYLIFE

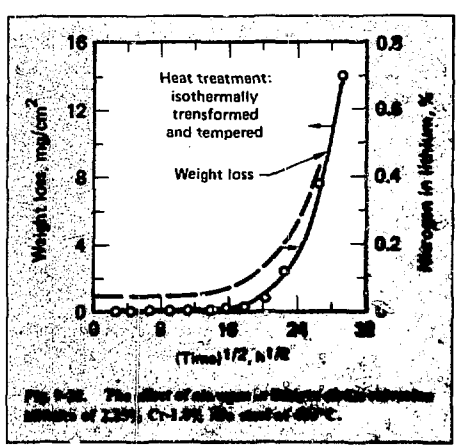

plant. The CSM researchers are continuing tests on lithium compatibility; for example, tests with 304-SS in lithium contaminated with lead showed an increase in the corrosion rate. They are evaluating various heat treatments of unstabilized 2.25 Cr–1.0 Mo and 2.25 Cr–1.0 Mo stabilized with Nb. The tests will show the effects of lead-contaminated lithium at 500°C with low nitrogen concentrations (<400 appm).

Conclusions. We now believe that 2.25 Cr–1.0 Mo, a low-alloy ferritic steel, is the most attractive steel for the HYLIFE chamber. The ferritic steels have shown good resistance to lithium corrosion at the temperatures of interest. At low nitrogen concentrations, 2.25 Cr–1.0 Mo can likely give the desired service life of 30 yr.[54] The low chromium content of this steel is an advantage in terms of corrosion resistance, resource use, cost, and possibly even resistance to radiation-induced swelling. The lack of nickel makes this material more resistant to corrosion and results in less neutron activation.

Technological Development. Unfortunately, the data base from which we must draw our conclusions about radiation damage and lithium corrosion—the two key areas of technological development required for materials—is meager. We hope to do the following:

- Study the time-integrated damage effects of neutrons on ferritic steels in existing fast-fission-reactor test facilities.
- Plan new materials test facilities to quantify the effects of pulsed radiation. (Instantaneous damage rates are up to 10^8 times the time-integrated rates.[77])
- Quantify the effects of flowing liquid lithium on candidate materials. Research must proceed from static testing and thermal loops to systems that reasonably simulate operating conditions, such as pumped loops containing stressed specimens.
- Consider the synergistic effects of radiation, corrosion, and fatigue.

References

49. D. Kramer, K. R. Garr, and H. G. Pard, "Helium Embrittlement of a Ferritic Stainless Steel," *Trans. Met. Soc., AIME* **245**, 1909 (1969).
50. D. Kramer, K. R. Garr, C G. Rhodes, and A. G. Pard, "Helium Embrittlement of Type-316 Stainless Steel," *J. Iron Steel Inst* **207**, 1141 (1969).
51. E. E. Bloom et al., "Temperature and Fluence Limits for a Type-316 Stainless Steel CTR First Wall," *Nuc. Tech.* **31**, (1976).
52. F. A. Smidt, Jr., "Swelling Behavior of Commercial Ferritic Alloys, EM-12 and HT-9, as Assessed by Heavy Ion Bombardment," *Irradiation Effects on the Microstructure and Properties of Metals*, ASTM, STP 611, pp. 227-241 (1976).
53. J. E. Selle and D. L. Olson, "Lithium Compatibility Research-Status and Requirement for Ferrous Materials," *Materials Considerations in Liquid Metal Systems in Power Generation*, National Association of Corrosion Engineers (1978).
54. J. E. Selle, "Corrosion of Iron Based Alloys by Lithium," in *Proc. of the Int. Conf. on Liquid Metal Tech. in Energy Production*, Champion, Pa., CONF-760503-P2 453 (1976).
55. E. E. Hoffman and W. D. Manly, "Comparison of Sodium, Lithium, and Lead as Heat Transfer Media from a Corrosion Standpoint," presented at the *Nuclear Engineering and Science Congress, Cleveland, Ohio, Dec. 12–16, 1955*, Preprint 74.
56. W. D. Manly, "Fundamentals of Liquid-Metal Corrosion," *Corrosion* **12** (7), 46 (1956).
57. J. E. Cunningham, *Resistance of Metallic Materials to Corrosion Attack by High Temperature Lithium*, Oak Ridge National Laboratory, Oak Ridge, Tenn., CF-51-71-135 (1951; declassified with deletions 1957).
58. R. B. Day and A. DeS. Brasunas, *Testing and Examination of Thermal Convection Loops Operated with Lithium and Lead*, Oak Ridge National Laboratory, Oak Ridge, Tenn., Y-F31-4 (1951).
59. M. H. Boyer, *Information on the Resistance of Materials to Attack by Molten Lithium*, California Research and Development Co., Livermore, Calif., CRD-T2C-33 (1951).
60. H. G. Elrod, Jr., R. R. Fouse, and P. B. Richards, *Erosion and Heat Transfer with Molten Lithium: Final Report*, Babcock and Wilcox Co., Lynchburg, Va., Report 5217 (1951).
61. E. E. Hoffman, *Corrosion of Materials by Lithium at Elevated Temperatures*, Oak Ridge National Laboratory, Oak Ridge, Tenn., ORNL-2674 (1959).
62. M. S. Freed and K. J. Kelley, *Corrosion of Columbium and Other Structural Alloys in High Temperature Lithium*, Pratt and Whitney Aircraft Div., United Aircraft Corporation, Middletown, Conn., PWAC-355 (1961).
63. J. M. McKee, *Effect of Nitrogen on Corrosion by Lithium*, Nuclear Development Corporation of America, White Plains, N.Y., NDA-40 (1957).
64. R. J. Schlager, R. A. Patteron, D. L. Olson, and W. L. Bradley, "Stainless Steel Weight Loss in Nitrogen Contaminented Liquid Lithium," *Nucl. Tech.* **29**, 94 (1976).
65. R. A. Patterson, R. J. Schlager, and D. L. Olson, "Lithium Grain Boundary Penetration of 304L Stainless Steel," *J. Nucl. Mat* **57**, 312 (1975).
66. J. A. Reeves, D. L. Olson, and W. L. Bradley, "Grain Boundary Penetration Kinetics of Nitrided Type 304L Stainless Steel," *Nucl. Tech.* **30**, 385 (1976).
67. H. G. Edler, *The Corrosion of Metals in Molten Lithium*, Aerojet Engineering Corp., Azusa, Calif., RTM-69 (1950) (title U, report SRD).
68. R. Anderson and H. Stephe, *Progress Report on Materials Tested in Lithium*, Fairchild Engine and Aircraft Corp., NEPA Div., Oak Ridge, Tenn., NEPA-1652 (1950).
69. H. W. Leavenworth and D. P. Gregory, "Mass Transfer of Type 316 Stainless Steel by Lithium," *Corrosion* **18**(2), 43t (1962).
70. S. Forster, "Closed Helium-Turbine Cycle with a Fusion Reactor," *Mech. Eng.* **13** (1973).

71. W. N. Gill, R. P. Vanek, R. V. Jelinek, and C. S. Grove, Jr., "Mass Transfer in Liquid Lithium Systems," *AIChE J.* 6(1), 139 (1960).
72. M. S. Goikhman et al., "Corrosion Failure of 1Kh18N9T in Liquid Lithium," *Sov. Mater. Sci.* (English Translation) 4(6), 491 (1968).
73. W. Jordan, W. L. Bradley, and D. L. Olson, "Liquid Lithium Penetration of Stressed Armco Iron," *Nucl. Tech.* 29, 209 (1976).
74. V. V. Popovich et al. "The Effect of Lithium on the Mechanical Characteristics of Austenitic Stainless Steels," *Sov. Mater. Sci.* (English Translation) 5(4), 345 (1969).
75. T. A. Whipple, D. L. Olson, W. L. Bradley, and D. K. Matlock, "Corrosion and Mechanical Behavior of Iron in Liquid Lithium," *Nucl. Tech.* 39, 75 (1978).
76. G. R. Edwards and D. L. Olson, *Corrosion Screening Test for Lithium Containment Alloys*, Colorado School of Mines, Golden, Colo. (Sept., 1978).
77. G. L. Kulcinski, *Progress in Materials Research for Fusion Reactors*, University of Wisconsin, Madison, Wis., UWFDM-228 (1977).

Authors

W. R. Meier

Major Contributors

G. Edwards
D. Olson
(Colorado School of Mines)

D. Kramer
(Energy Systems Group, Rockwell International)

N. Hoffman
(Energy Technology Engineering Center)

9.2.5 Chamber Design

We have wide latitude in specifying the geometry of the HYLIFE converter chamber (Fig. 9-29). The primary consideration is the protection of the first structural wall. We must also consider the roles of the energy converter (as power plant, fissile-fuel producer, etc.) as well as manufacturing and remote handling constraints.

The chamber of a HYLIFE-type converter must serve both as a vacuum vessel between the atmosphere and the fusion cavity and as a container of the effects of the fusion pulse on the liquid blanket.

We selected a cylindrical double-wall geometry for the energy converter for the following two reasons:

- To provide for ease of fabrication and access to inner components for repair.
- To separate the function of withstanding the inward, steady compressive load from withstanding the outward, pulsed, tensile load.

The HYLIFE chamber has a metal inner liner to withstand the reaction forces from the lithium impact (see §9.2.3). Hence, the outer chamber needs to perform solely as a vacuum vessel. The inner liner can be easily removed through the top of the chamber in the event of catastrophic failure. The HYLIFE converter also contains splash baffles and orifice plates to reduce the transmission of the pressure pulse to the pumps and external flow circuits. The pressure pulse results from deposition of the neutron energy in the lithium blanket. These orifice plates and baffles can also be removed through the top of the chamber.

This subsection is primarily a discussion of the response of the chamber inner liner to the fusion pulse, because we have identified this to be the dominant design constraint.

There are two sources of stress in the inner liner: impact of the moving lithium blanket, and thermal stress from deposition of neutron energy in the liner. Estimates of the two stresses, given below, are combined in a model that estimates the synergistic effects.

Lithium Impact Stress. The equation of motion of a thin cylindrical shell responding to a square pressure pulse is[78]

$$\ddot{u} + \omega^2 u = \frac{P(t)}{\rho\delta} \ , \quad \omega = \frac{1}{R}\sqrt{\frac{E}{\rho}} \ , \tag{10}$$

where u is the shell displacement, R is the radius of the shell, E and ρ are the elastic modulus and density of the shell material respectively, and δ is the shell thickness. If

$$P(t) = \begin{cases} P_0, & t < \tau \\ 0, & t > \tau \ , \end{cases}$$

then the solution to Eq. (10) is

$$u(t) = \begin{cases} A\cos\omega t + B\sin\omega t + \dfrac{P_0}{\rho\delta\omega^2} & , t \leqslant \tau \\ C\cos\omega t + D\sin\omega t & , t \geqslant \tau \ . \end{cases} \tag{11}$$

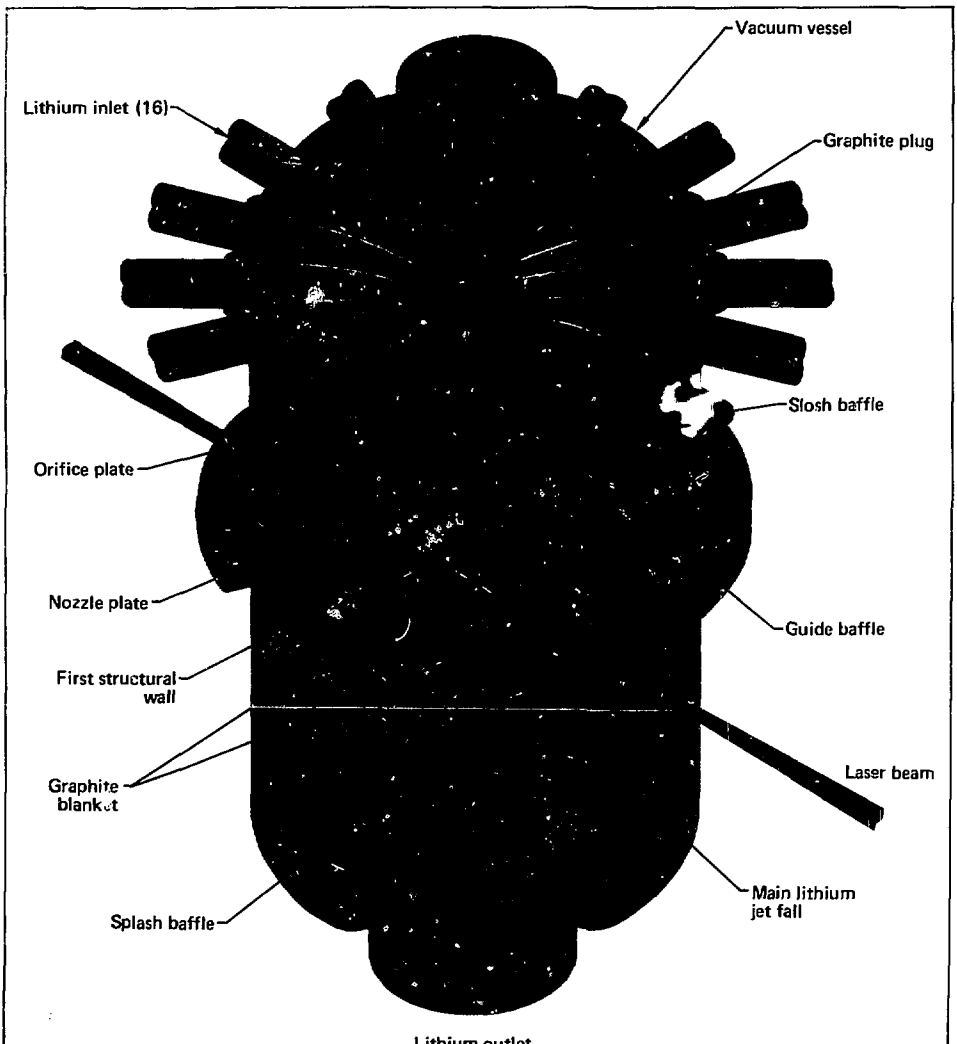

Fig. 9-29. Laser fusion HYLIFE converter chamber.

Using the initial conditions, $u(0) = 0$ and $\dot{u}(0) = 0$, and matching displacement and velocity at $t = \tau$, we obtain

$$\left.\begin{aligned} u(t) &= \frac{P_0}{\rho\delta\omega^2}\,(1 - \cos\omega t) \\ \dot{u}(t) &= \frac{P_0}{\rho\delta\omega}\,\sin\omega t \end{aligned}\right\} \quad t \leqslant \tau \ , \tag{12}$$

$$\left.\begin{aligned} u(t) &= \frac{P_0}{\rho\delta\omega^2}\,[\cos\omega(t-\tau) - \cos\omega t] \\ \dot{u}(t) &= \frac{P_0}{\rho\delta\omega}\,[\sin\omega t - \sin\omega(t-\tau)] \end{aligned}\right\} \quad t \geqslant \tau \ . \tag{13}$$

The stress in the shell is given by

$$\sigma(t) = \frac{E}{R}\,u(t) \ . \tag{14}$$

Thus, the stress at the end of the pulse is[79]

$$\sigma(\tau) = P_0\left(\frac{R}{\delta}\right)(1 - \cos\omega\tau) \ . \tag{15}$$

The maximum hoop stress occurs at turnaround when $\dot{u}(t) = 0$ or $\sin\omega t = \sin\omega(t - \tau)$. This maximum stress is[80]

$$\sigma_{max} = P_0\left(\frac{R}{\delta}\right)\sqrt{2(1 - \cos\omega\tau)} \ . \tag{16}$$

For an impulsive impact with interaction time much less than the wall-response time, $\sin\omega\tau \approx \omega\tau$, and Eqs. (15) and (16) reduce to

$$\sigma(\tau) = \frac{1}{2}\left(\frac{E}{\rho R\delta}\right)P_0\tau^2 \ , \tag{15a}$$

$$\sigma_{max} = \left(\frac{1}{\delta}\,\frac{\sqrt{E}}{\rho}\right)P_0\tau \ . \tag{16a}$$

The pressure from the liquid colliding with the shell is

$$P_0 = \rho_\ell\, c_\ell\, v \ ,$$

where v, c_ℓ, and ρ_ℓ are the velocity, acoustic velocity, and density of the liquid, respectively. The pulse time width is

$$\tau = f\,\frac{w}{c_\ell} \ ,$$

where w is the thickness of the liquid region striking the shell, and

$$f = \begin{cases} 1 & \text{if fluid sticks to wall} \\ 2 & \text{if fluid bounces elastically from the wall} \end{cases} .$$

Thus,

$$P_0\tau = f\,\rho_\ell\, vw = f\,\frac{mv}{A} \ , \tag{17}$$

where m/A is the mass of liquid per unit area.

Equations (15) to (17) describe the stress in the shell. We investigated the stress in an array of lithium jets.

Jet-Array Stress. We assumed that a 2700-MJ fusion pulse was contained in a 5-m-radius chamber protected by an array of liquid jets having a thickness equivalent to 1 m. The peak dynamic stress in the chamber liner from the impact of the jet array is[78]

$$\sigma_{max}\delta = \frac{f\,mv}{2\pi Rh}\,\frac{\sqrt{E}}{\rho} \ ,$$

where R is the chamber radius and h is the chamber height. Using the results for the array momentum from §9.2.3, and the properties of steel,

$$\sigma_{max}\delta = 50\,\frac{f}{Rh} \ .$$

For a liner radius of 5 m and a chamber height of 8 m, the peak product of hoop stress times wall thickness, in MPa·m, is

$$\sigma_{max}\delta = 1.25\ f$$

for a 2700-MJ fusion pulse. Because

$$1 \leqslant f \leqslant 2 \ ,$$

we chose a value of f of 1.5, which gives a peak product of about 1.8 MPa·m, roughly 50 times less than that for a continuous annulus of liquid.

Stress from Neutron-Energy Deposition. Absorption of neutron energy in the first structural wall, which is cooled on both surfaces, will produce a temperature distribution that, in turn, will induce a thermal stress distribution. The internal heat source calculated using the TARTNP Monte Carlo neutronics–photonics code[81] in spherical geometry is shown in §9.2.2. Previous time-dependent TARTNP calculations[82] show the deposition time to be of order ~1 μs.

A steady-state periodic solution was found for the wall cooled on both surfaces with internal energy generation.[83] The temperature rise during heating (~0.8 K) is spatially uniform and negligible compared to the temperature profile in the wall. Thus, a steady-state analysis using the appropriate time-averaged energy deposition is valid because

$$\tau \ll \theta \ ,$$

$$\frac{h\alpha\tau}{K\delta} \ll 1 \ ,$$

$$\frac{\alpha\tau}{\delta^2} \ll 1 \ ,$$

where

τ and θ are the heating and cycle times, respectively,

K is the thermal conductivity,

α is the thermal diffusivity,

h is the convective heat transfer coefficient,

δ is the wall thickness.

For a spatially uniform internal heat source, and for cooling of both the inner and outer surfaces, the solution of the steady-state energy equation in cylindrical geometry is

$$T(r) = -\frac{Qr^2}{4K} + \left(\frac{K_1K_6 - K_2K_5}{K_1K_4 + K_2K_3}\right)\ln r + \frac{K_3K_6 + K_4K_5}{K_1K_4 - K_2K_3} \ , \qquad (18)$$

where

$$K_1 = \frac{h_a a}{K} \ , \quad K_2 = \frac{h_b b}{K} \ ,$$

$$K_3 = 1 - K_1 \ln a \ , \quad K_4 = 1 + K_2 \ln b \ ,$$

$$K_5 = \frac{Qa^2}{4K}(K_1 - 2) + T_a \ , \quad K_6 = \frac{Qb^2}{4K}(K_2 + 2) + T_b \ ,$$

and a and b are the inner and outer coordinates of the slab, respectively.

Q is the time-averaged volumetric heat rate, and subscripts a and b refer to the inner and outer coordinates.

The elastic thermal stress is given by

$$\sigma_{zz}(r) = \frac{\bar{\alpha}E}{1-\nu}\left\{\frac{Q}{8K}(2r^2 - b^2 - a^2) + \left(\frac{K_1K_6 - K_2K_5}{K_1K_4 + K_2K_3}\right) \times \left[\left(\frac{1}{b^2 - a^2}\right)\left(a^2 \ln\frac{r}{a} + b^2 \ln\frac{b}{r}\right) - \frac{1}{2}\right]\right\} \ ,$$

$$\sigma_{rr}(r) = \frac{\bar{\alpha}E}{1-\nu}\left\{\frac{Q}{16K}\left[\left(\frac{ab}{r}\right)^2 - a^2 - b^2 + r^2\right] + \left(\frac{K_1K_6 - K_2K_5}{K_1K_4 + K_2K_3}\right)\left(\frac{1}{2(b^2 - a^2)}\right) \times \left[a^2 \ln\frac{r}{a} + b^2 \ln\frac{b}{r} - \left(\frac{ab}{r}\right)^2 \ln\frac{b}{a}\right]\right\} , \qquad (19)$$

$$\sigma_{\theta\theta}(r) = \sigma_{zz}(r) - \sigma_{rr}(r) \ ,$$

where $\bar{\alpha}$ is the linear coefficient of thermal expansion, E is the modulus of elasticity, and ν is Poisson's ratio.

Temperature profiles for three wall thicknesses are shown in Fig. 9-30 and thermal stresses are shown in Fig. 9-31. The azimuthal and axial stresses are indistinquishable. The peak thermal stress is plotted as a function of wall thickness in Fig. 9-32. These numerical results are for 2700-MJ fusion pulses at 1 Hz, equal inner and outer convective coefficients of 14.7 kW/m²·K, and equal fluid temperatures. The inner radius a is 5 m.

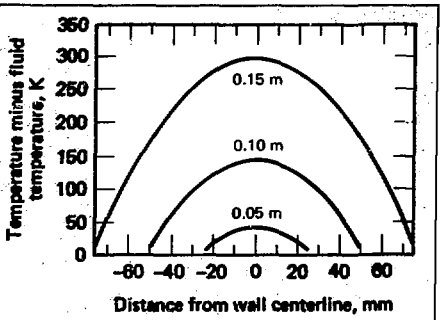

Fig. 9-30. Temperature profiles for neutron energy deposition in a first structural steel wall 5 m from the fusion pulse, for three wall thicknesses.

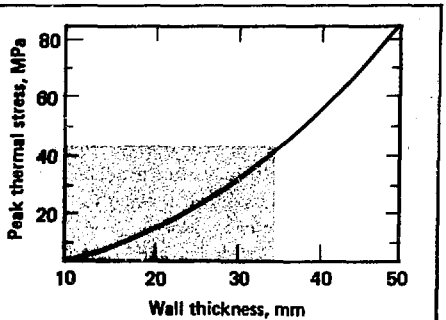

Fig. 9-32. Peak thermal stress vs wall thickness. Peak tensile stresses occur at the surfaces.

An additional thermal stress results from the sudden temporal deposition of energy in the wall. It can be estimated by means described in §9.2.3. This transient thermal stress is about 4 MPa, which is negligible compared to the stresses calculated from Eq. (19).

Synergism of Wall Stresses. The first structural wall of the fusion energy converter is subject to both steady and dynamic stresses. Thermal stress, which results partly from spatial temperature gradients caused by neutron energy deposition, dominates the steady stress. Secondary photons that emerge from

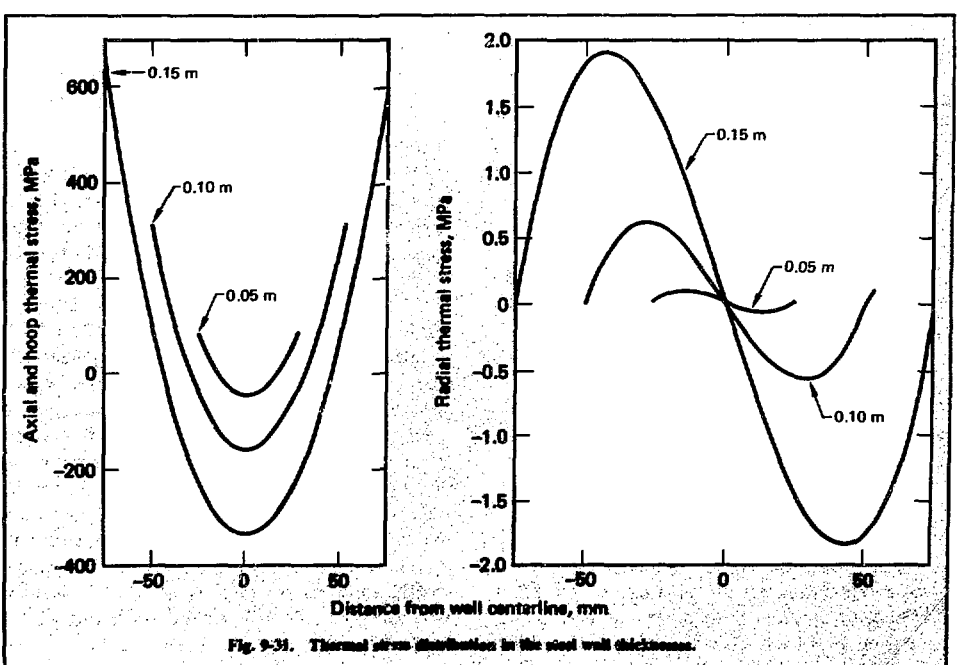

Fig. 9-31. Thermal stress distribution in the steel wall thicknesses.

the lithium blanket also contribute to the thermal stress.

The major dynamic stress is the response of the structure to the impact of the lithium. A minor part of the dynamic stress is the pressure rise from the sudden deposition of neutron energy. However, this pressure rise is small because the temperature rise in a single pulse is negligible compared to the steady temperature profile in the wall.

To determine the design adequacy of the first structural wall, we must calculate a combined loading by adding a mean stress to an alternating stress. The Soderberg law is an empirical law that relates the allowable stress to the alternating fatigue strength and the static yield strength for a given steady stress.[84] This law is

$$\frac{\sigma_a}{S} \leq 1 - \frac{\sigma_m}{S_y} , \tag{20}$$

where

σ_a = allowable alternating stress,
σ_m = mean stress,
S_y = yield strength,
S = alternating fatigue strength.

The Soderberg limit is an additional constraint. We must also meet the failure criteria[85] on mean stress,

$$\sigma_m \leq S_a , \tag{21}$$

where S_a is the allowable stress for 10^5 h at 800 K. We now identify the mean and alternating stress limits as follows:

[redacted]mal stress,

[redacted]o (ASTM 387, [redacted]00 K, we have

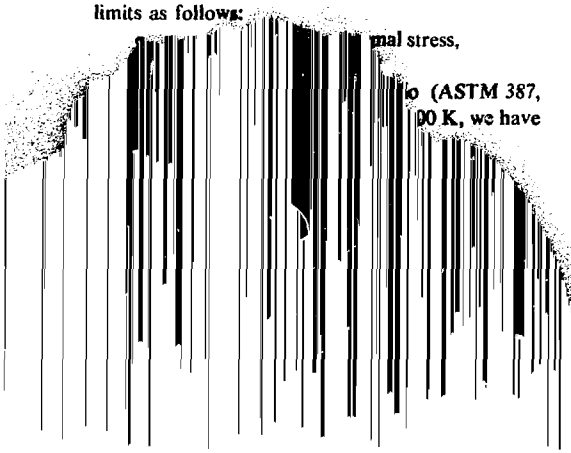

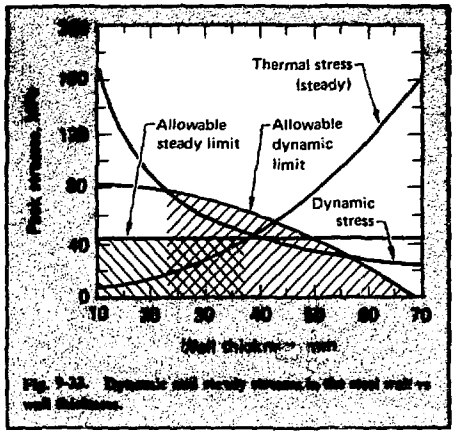

[redacted]

36 mm (Fig. 9-31). To satisfy the dynamic stress consideration (Soderberg's law), the thickness must be between 23 and 54 mm. To satisfy both the static and dynamic stress constaints, the thickness must be between 23 and 36 mm. Because the uncertainty for the dynamic stress is much larger than that for the steady stress, we chose a 35-mm-thick wall.

Chamber Top and Bottom. The top and bottom of the chamber are protected from neutron damage by a splash baffle and nozzle plates. These "high-impedance" plates partially hold up the lithium flow for protection, but they are porous enough to allow partial relief of the pressure buildup in the chamber from vaporized lithium. The lithium flowing freely through the lithium pipes and splash baffle will not transmit pressure pulses to the circulation pumps. We have yet to design in detail the splash baffle and nozzle plate and to determine the loads and stresses.

Other Design Considerations. To design a viable energy converter, we must consider such problems as the fabricability of its components, the assembly of the components into the converter, and the periodic inspection and maintenance of the components to ensure surprise-free operation with a minimum of unscheduled shutdowns. We must also consider disassembly of the components for repair, replacement, or decommissioning of the converter. We plan to use inexpensive, easily fabricated materials in the HYLIFE converter so that it can be assembled or disassembled as easily as the innards of a coffee pot. The 2.25 Cr–1.0 Mo ferritic steel is easily fabricated into the shapes required for the HYLIFE converter.

The HYLIFE converter parts are easily assembled in the following order:

- Graphite blanket.
- First structural wall.
- *Splash baffle.*
- Nozzle plate.
- Orifice plate.

These components rest freely on supports provided in the chamber. The required tolerances are undemanding. The lithium inlet pipes are welded to the vessel, and then the top cap is welded on to the vessel. Disassembly requires cutting the welds and removing the components in the reverse of the assembly procedure.

Inspection and maintenance of the converter components must be performed remotely. The flanged opening in the top cap can be opened during scheduled shutdowns for this purpose. For further discussion of remote inspection and maintenance, see §9.2.9.

Conclusions. The chamber design for the HYLIFE converter allows for easy fabrication, assembly, inspection, and maintenance. Our present calculations call for a 35-mm-thick, 5-m-radius first structural wall made of ferritic steel. The wall will be protected by a 2-m-thick annular array of 0.2-m-diameter lithium jets. With a packing fraction of 0.5 for the jet array, the first wall can survive for 30 yr as the primary structure containing the 2700-MJ, 1-Hz fusion energy pulses.

References

78. J. Blink, *Wall Loading of the HYLIFE Chamber*, Lawrence Livermore Laboratory, Livermore, Calif., Internal Memorandum SS&A 78-141 (Sept. 21, 1978).
79. J. Hovingh, J. Blink, and L. Glenn, "Response of a Lithium Fall to an Inertially Confined Fusion Microexplosion," in *Proc. 3rd Topical Mtg. on Technology of Controlled Nuclear Fusion, Santa Fe, N. Mex.* (1978).
80. J. Hovingh, J. Blink, and L. Glenn, "Response of the Laser Fusion HYLIFE Reactor Chamber to the Fusion Microexplosion," *Trans. Am. Nucl. Soc.* 30, 22 (1978).
81. E. Plechaty and J. Kimlinger, *TARTNP: A Coupled Neutron-Photon Monte Carlo Transport Code*, Lawrence Livermore Laboratory, Livermore, Calif., UCRL-50400, Vol. 14 (1976).
82. J. Blink and P. Walker, *Recent TARTNP Run*, Lawrence Livermore Laboratory, Livermore, Calif., Internal Memorandum SS&A 78-021 (Feb. 1, 1978).
83. J. Hovingh and J. Blink, *Thermal Stress in the HYLIFE First Structural Wall*, Lawrence Livermore Laboratory, Livermore, Calif., Internal Memorandum SS&A 78-154 (Oct. 16, 1978).
84. P. G. Forrest, *Fatigue of Metals, 94*, (Pergamon Press, Oxford, 1962).
85. J. Hovingh, *First Structural Wall Stresses*, Lawrence Livermore Laboratory, Livermore, Calif., Internal Memorandum SS&A 78-172 (Nov. 2, 1978).
86. Rockwell International Corp., *Conceptual Design Study of the HYLIFE Lithium Waterfall Laser Fusion Chamber*, FY78 Annual Report to LLL, Appendix B (1978).

Authors	Major Contributors
J. Hovingh	M. Goodman, D. Kramer
J. A. Blink	A. B. Martin,
	and W. B. Thomson
	(Energy Systems Group,
	Rockwell International)

9.2.6 Liquid-Metal Circulation System

As described in §9.2.2, liquid lithium is used to shield the chamber from the fusion radiation, to remove the heat from the chamber and transfer it to the power-conversion cycle, and to breed tritium to fuel the system. In this subsection, we describe the circuits of flowing liquid metal required for each of these functions. Additional information can be found in Refs. 87 and 88.

Protective Lithium Blanket. The total flow rate of the protective lithium-blanket circuit is 129 m^3/s. As Table 9-3 shows, most of this flow is in the array of lithium jets. Other contributions to the total flow within the chamber are as follows:

- Sheet flow on the inside surface of the chamber wall to provide cooling and added radiation protection.
- Cooling flow between the chamber wall and steel-clad-graphite reflector.
- Flow between the reflector and the vessel wall to both remove heat and to minimize thermal neutron leakage.

Table 9-3. Circulating lithium flow rates, m^3/s.

Jet array[a]	93.3
Sheet flow on chamber wall	15.5
Beam apertures[b]	5.4
Chamber wall/reflector coolant[c]	7.0
Reflector/vessel wall coolant[d]	7.5
Total	128.7

[a] Includes jets that cross over beams to form part of beam aperture.

[b] Flow crossing horizontally above and below beams.

[c] Channel between first structural wall and graphite reflector.

[d] Channel between reflector and outer vessel wall; also serves as a neutron shield.

The lithium-blanket circulation system consists of 16 individual loops that bring lithium from the bottom to the top of the HYLIFE vessel. Each loop consists of one pump and piping of 1.22-m (48-in.) internal diameter. Bellows relieve the stresses of thermal expansion in the piping. The loops are grouped into four cells of four loops each in conjunction with a primary heat transfer loop whose flow is diverted from the circulation loops. We chose 16 pumps for the following reasons:

- To keep the pumps a manufacturable size, yet retain the cost advantages of scale.
- To allow the pumps to be clustered closely around the reaction vessel.
- To be devisable by four to coordinate with the four heat transfer loops.

The piping size was chosen to provide a flow velocity near 6 m/s; it is actually 6.9 m/s. Although a higher velocity would allow us to reduce the lithium inventory by using smaller, less expensive pipes, we limit velocity to minimize erosion over the 30-yr plant life.

Figure 9-34 shows how the 16 pumps are arranged around the fusion chamber, and Fig. 9-35, an elevation, shows two of the loops.

There is a vertical distance of 16.2 m between the top surface of the lithium pool at the bottom of the vessel and the horizontal centerline of the pipes that bring the lithium back into the top of the vessel. The pump must supply this head as well as friction losses in the lines and exit losses around the circuit. The total pump head required is approximately 23.5 m.

Because we deem gas pressurization unfeasible, the suction side of the pumps requires a minimum head that must be provided by an actual height of lithium. Losses on the suction side necessitate an even greater height of lithium than the theoretical value needed to prevent cavitation. A total of 5.8 m of lithium is needed between the top surface of the lower pool to the centerline of the pipes bringing the lithium into the suction side of the mechanical pumps. Thus, the centerline-to-centerline distance from pump inlet up to reaction-vessel inlet is 22 m.

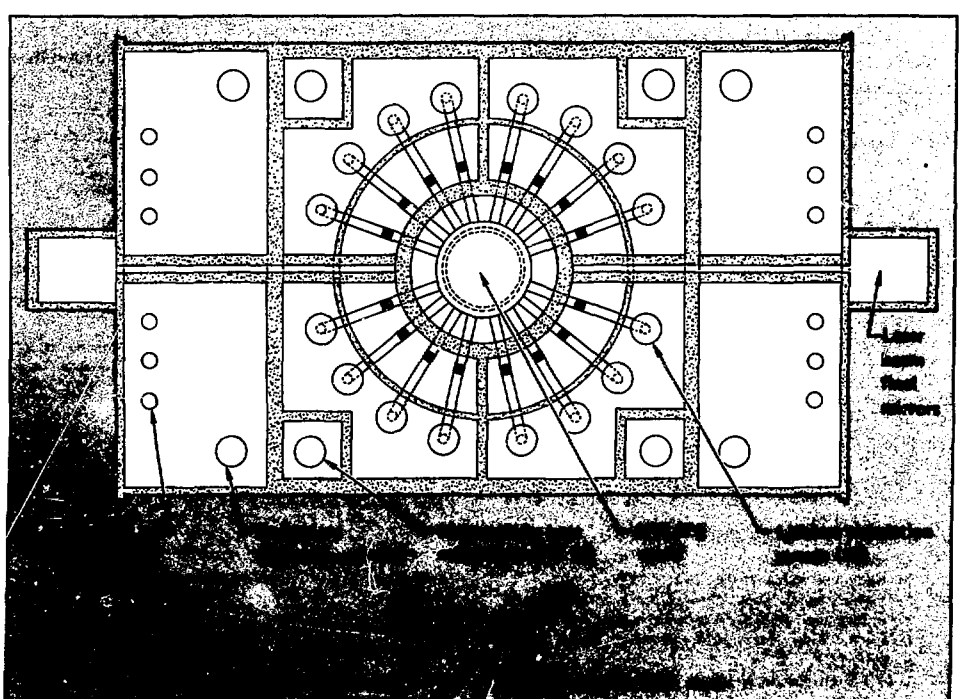

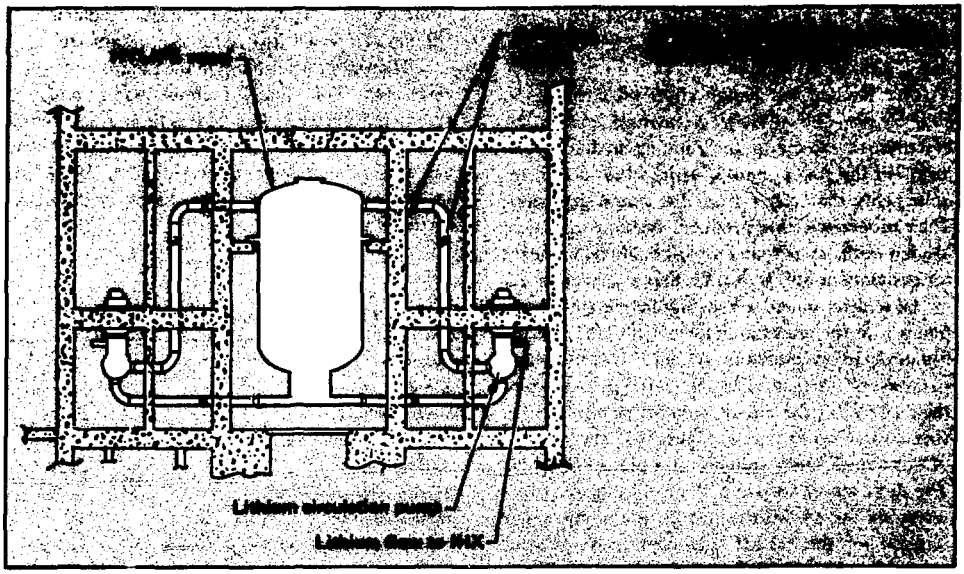

Definition of Terms. We will define three terms that describe the pump characteristics before explaining our selection of a pump design. These terms are specific speed N_s, suction specific speed S_s, and net positive suction head NPSH.

Specific speed is used to describe a mechanical pump in terms of impeller shape. Numerically, the specific speed relates to the pump rpm N, the flow rate Q in gpm, and the developed head H in ft, by the formula $N_s = N\sqrt{Q}/H^{3/4}$. The highest efficiency impeller shape occurs at an N_s of approximately 2500. Higher N_s values mean smaller diameter impellers for a given head and capacity. Depending on S_s, there is a lower limit on N_s before impeller diameter becomes too large to be cast by a steel foundry in this century. The power used by the pumps increases markedly as N_s increases above 2500.

The pump suction specific speed is given by $S_s = N\sqrt{Q}/NPSH^{3/4}$. This formula is similar to that for N_s, except that it relates the pump rpm and flow rate to NPSH rather than to developed head. Like N_s, S_s relates to the geometry of the pump's rotating elements. Centrifugal pumps commonly have an S_s range between 8000 and 12,000. An axial pump may have an S_s of from 20,000 to 30,000. The higher the suction specific speed, the lower the required NPSH.

The NPSH is the absolute pressure, including dynamic head, in feet, at the pump inlet. An NPSH that is too low will cause pump cavitation, damage, and eventual failure. The plant must therefore be able to supply an NPSH to the recirculation pumps that will allow safe, cavitation-free pump operation for a long time. With a fixed head and capacity, the necessary NPSH is determined by N_s and S_s.

Pump Design. Our main pump-design objective was to minimize the plant lithium volume and thereby reduce the plant tritium inventory. Because the lithium circulation system accounts for about 75% of all the lithium in the plant, our design could have a significant impact. We also wanted to reduce the pump power requirements.

We considered only pump designs that were essentially conventional in their hydraulic design and fabricability. This meant limiting S_s to 12,000 or less and limiting the impeller diameter to 2.6 m. A larger S_s may be possible if advanced combined axial-centrifugal pumps can be developed. We limited the impeller diameter by requiring that the impeller be a

ferrous casting and by estimating that the largest such casting possible in the United States by the year 2000 will be ~2.6 m.

We focused our design effort on selecting N_s and S_s for the lithium circulation pump; N_s describes the shape of the rotating hydraulic elements in the pump, and S_s defines the suction requirements that result from the pump geometry. Their proper selection produces the least volume of lithium in the system and a reasonable requirement for pumping power, within the limitations imposed.

We determined the hydraulic design of the pump with the aid of a mathematical model of the lithium-blanket circulation system. We varied pump parameters (in particular, N_s and S_s) to examine their effect on the circuit volume, pump impeller size, and pumping power. Figure 9-36 shows a line of constant lithium volume on a plot of S_s vs N_s. The direction of variation of the parameters of interest are shown with respect to the pump design selected for the HYLIFE converter. We selected values for N_s of 2725 and for S_s of 11,000 to minimize the system volume. The pump diameter is ~2.6 m. Table 9-4 lists the pump parameters.

The volume of lithium in the pumps and piping associated with the lithium-blanket circulation system is ~1950 m^3. The total plant lithium volume is ~2700 m^3. About 500 m^3 of the additional 750 m^3 are within the vessel, and the remaining 250 m^3 are in the primary heat-transfer loops and tritium-recovery systems.

Table 9-4. Lithium pump parameters.

Flow rate	8.96 m^3/s
Speed	198 rpm
Developed head	23.5 m
Net positive suction head, NPSH	3.7 m
Specific speed, N_s	2725
Suction specific speed, S_s	11,000
Number of pumps	16
Total blanket circulation pumping power	19.9 MW_e

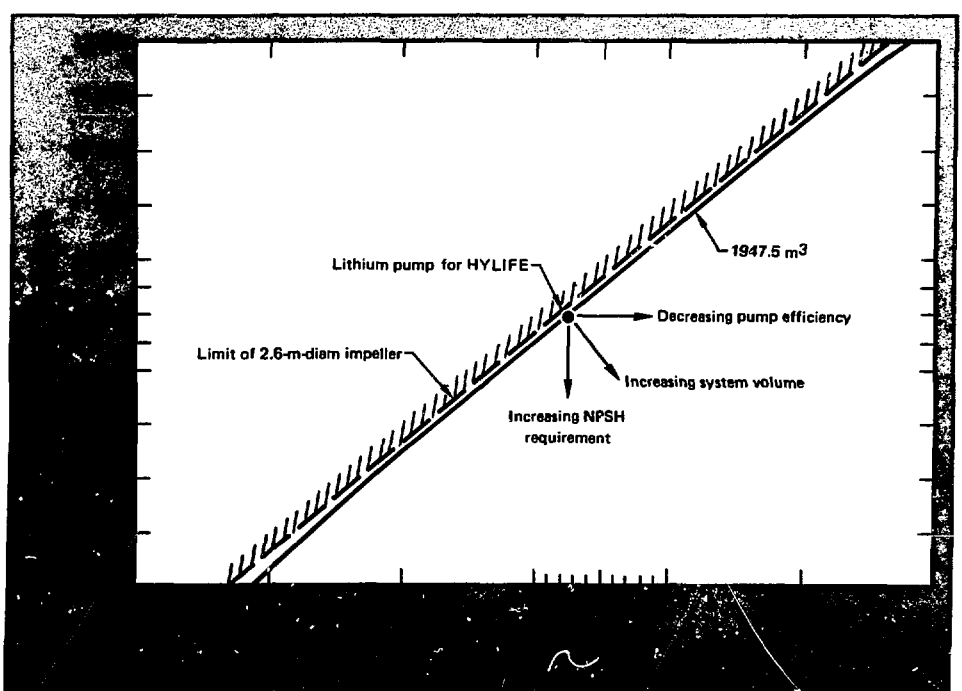

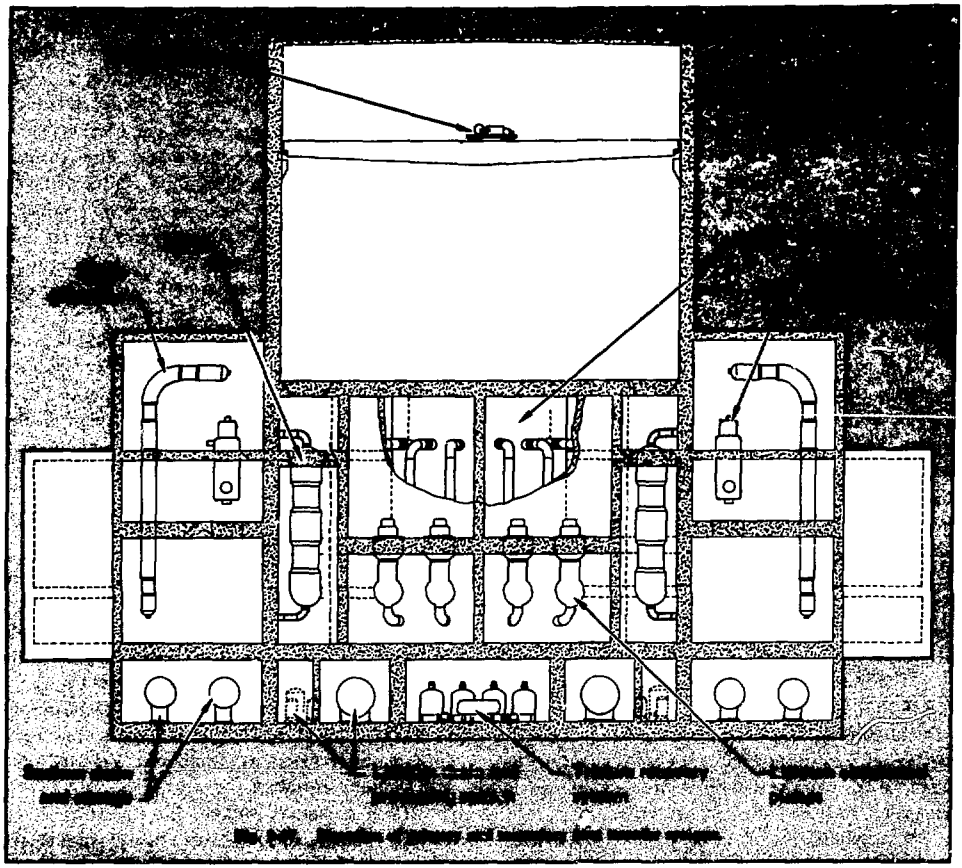

An important feature of the circuit is that the variable-speed pumps can maintain the total required flow rate (129 m^3/s) even in the event of a pump failure. Thus, repairs could be made without shutting the plant down.

Heat Transfer System. The heat transfer system (HTS) consists of three subsystems:

- A primary system that uses lithium to transfer heat from the reaction vessel to the secondary system.
- A secondary system that uses sodium to transfer heat from the primary system to the steam generators.
- A steam-and-feedwater system that functions as the actual power cycle (a superheated-steam Rankine cycle) for the production of electricity. (The generation of steam and electricity is discussed in §9.2.7.)

The locations of the HTS components are shown in Fig. 9-34 and in Fig. 9-37, an elevation.

The same pumps that circulate the lithium directly back into the HYLIFE vessel also circulate lithium through the primary HTS. A second-stage booster is added to the top of the basic pump discussed in the previous subsection. Of the 8.06 m^3/s of lithium that enter the bottom of each circulation

pump from the HYLIFE vessel, only 0.61 m^3/s enters the second stage of the pump.

The second stage provides the necessary additional head to circulate the lithium coolant through an intermediate heat exchanger (IHX) and back to the top of the vessel where it joins the lithium that is circulated directly. A total of 119.2 m^3/s of lithium at constant temperature (500°C) is directly recirculated to the top of the vessel while 9.8 m^3/s return at 340°C after passing through an IHX. The total additional pumping power required to circulate the primary lithium coolant is 4.0 MW_e.

The primary HTS consists of four loops, each with one IHX supplied by four lithium circulation pumps. Each loop (four pumps, one IHX) is totally independent except for the common flow path within the vessel. The pumps and IHX's are fixed components. Thermal expansions are accommodated by expansion joints (bellows) located in each major horizontal and vertical run of piping. We placed piping supports and seismic snubbers throughout the primary HTS in compliance with the ASME Boiler and Pressure Vessel Code, Section III, Class I.

The lithium flow within the pipes is limited to 9 m/s and is adjustable on a loop basis through variable-speed pumps. Leak detectors and electric heaters affixed to the pipes are encapsulated by the 30 cm of insulation that surrounds all the piping and components of the primary HTS.

The overall layout of the blanket circulation and primary HTS represents a simple, symmetric, and markedly compact design. The two factors that we considered most in establishing the basic layout were the locations of the lithium pumps and the primary shield wall. The primary lithium pumps are positioned on a 22-m radius from the reactor centerline. This arrangement accommodates the piping run required by the elbows and bellows located outboard of the primary shield wall and maintains a minimum of 1 m of access space between all adjacent components and the cell walls or both. The positioning of the primary shield wall provides an access annulus for the vessel and maintains a minimum of 1 m of wall between pipe penetrations to ensure structural integrity.

The positioning within the reactor containment building complies with standard practice in the design of existing liquid-metal systems. Such compliance is advantageous in that it allows the plethora of existing design data, developed for liquid-metal-cooled fission reactors, to be applied directly to the HYLIFE converter concept.

The secondary sodium loop is needed to reduce the radiological consequences of a reaction between liquid lithium and water that would result from a steam generator failure. The lithium in the primary coolant loop contains activated corrosion products, pellet debris, and radioactive tritium. The tritium that diffuses from the lithium to the sodium through the walls of the IHX is the only radioactive contaminant in the secondary coolant loop.

Sodium is used as the secondary fluid because it is easy to remove hydrogen isotopes from sodium by using cold traps. Tritium can be removed to a concentration of less than 1 ppm by weight in the circulating sodium. The diffusion of tritium into water is not a problem because the partial pressure of tritium above both cold-trapped liquids is about the same. The important consideration is the amount of tritium that would be within the liquid metal exposed to water in the event of a steam generator failure.

Another point in favor of sodium is the advanced technology of modular steam generators based on a sodium system. Large facilities for studying ways to handle sodium–water reactions are operating. To build similar facilities to study lithium–water reactions would take years of time and millions of dollars.

Each secondary sodium loop consists of an IHX, a sodium pump, and three hockey-stick steam generators. The sodium pumps are located in the hot leg between the IHX and the steam generators. The sodium hot- and cold-leg temperatures are 484°C and 316°C, respectively. The flow rate of each pump is ~4.5 m^3/s for a total of 18 m^3/s, and the total pumping power required for the secondary sodium HTS is 12.1 MW_e.

Tritium Recovery System. We selected a tritium recovery system based on a molten-salt (LiF–LiCl–LiBr) extraction process. This approach is being studied intensively at Argonne National Laboratory[89,90] with funds from magnetic fusion energy programs. The Argonne researchers have built a loop specifically to evaluate this concept.

In this process, lithium is routed from the hot leg (500°C) of the primary HTS to a mixer where it contacts the molten salt. The mixture is then allowed to separate in a settler, the tritium (and deuterium) having undergone exchange from the

lithium to the salt. The lithium is then rerouted through a surge tank back to the hot leg of the primary HTS. The molten salt is processed through an electrochemical cell in which the tritium is removed for transfer to the pellet manufacturing unit. The salt is recycled to the mixer. This relatively simple and compact system keeps the tritium concentration in the lithium at 1 ppm by weight by continuously processing approximately 0.12 m^3/s of lithium.

The system is divided into four identical basic processing units. Each unit contains a separate mixer-settler and electrochemical cell, and each is served by a common salt and lithium pump backed by a spare. Further redundancy is incorporated by having each unit designed with a 33% operating margin.

Lithium Storage and Processing. The system for storing and processing lithium drains and stores the plant lithium and maintains lithium purity levels commensurate with corrosion and nuclear-performance guidelines. The system is divided into four independent units, each serving a corresponding primary HTS. Each large drain tank is sized to accommodate a volume somewhat greater than 25% of the total lithium inventory. Few pumps, valves, heaters, flow meters, leak detectors, and little insulation are needed for the system.

Various trapping and exchange stages within the cell routinely process the lithium to remove impurities. The nature and size of these systems depend on the type and level of impurities in the lithium. We now expect the lithium to contain appreciable levels of Br, Cl, and F from the tritium recovery system, and an equally problematic amount of debris from the pellet. These impurities are highly corrosive and represent a potentially sizable source of radioactivity.

The tritium recovery system, the liquid-metal storage and processing system, and also the gas storage and processing systems are housed in the lower level of the reactor containment building as shown in the plan view of Fig. 9-38. Thus, all of the primary tritium-bearing systems are contained within a leak-tight barrier. The tritium system, gas systems, and each lithium-system quadrant are housed in independent and totally isolated cells. This arrangement provides an additional tritium barrier and limits the extent of a lithium spill. As shown in Fig. 9-38, the sodium drain tanks are also located in separate cells on the lower level.

Conclusions. Liquid-metal circulation systems comprise the bulk of the hardware within the HYLIFE power plant. The liquid-lithium flow systems consist of 16 liquid-lithium pumps with a combined capacity of 129 m^3/s. About 92% of this

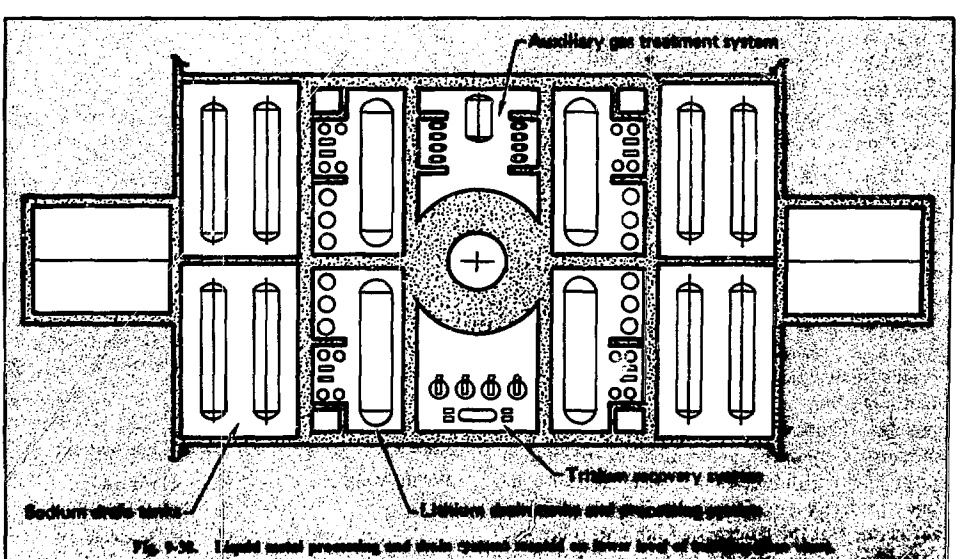

flow simply circulates from the bottom of the HYLIFE vessel to the top, to continuously replenish the lithium pools needed to establish the flowing protective lithium blanket within the fusion chamber. The remaining 8% is diverted and circulates through intermediate heat exchangers before returning to the top of the vessel. These two circuits require a combined total of 23.9 MW$_e$ of the plant's electric power production. There is also a liquid-lithium loop associated with the tritium recovery system, which is based on a molten-salt extraction process. A final lithium loop is required for the removal of other contaminants such as pellet debris, corrosion products, and elements from the salt extraction system.

Besides the liquid-lithium loops, an intermediate heat transfer loop with sodium as the working fluid is part of the plant design. This loop is primarily a radiation barrier between the primary lithium coolant and the steam generators.

All liquid-metal systems have been designed according to current standards and practices. The secondary sodium system is based on the technology developed for the LMFBR program.

Technological Issues. Many different components will have to be developed and tested for the liquid-metal systems of the laser fusion power plants. General categories include such items as valves, heat exchangers, instrumentation, pipe expansion joints, purification equipment, and pumps.

Valves are needed to modulate flow and to isolate lines. We are not now certain whether the valves used in sodium systems will be applicable to lithium systems.

Intermediate heat exchangers will transfer heat from a lithium primary loop to a sodium secondary loop. Because large surface areas are required for efficient heat transfer, the heat exchangers will be excellent pathways for the diffusion of tritium to the sodium or to the environment. We must understand tritium diffusion through these components to design a safe plant.

Instrumentation will be needed to monitor the plant. On-line measurements of flow rates, pressures, temperatures, liquid levels, and the amounts of impurities and tritium in the lithium and sodium are all necessary for plant control. The ability to detect impurities in the lithium is important because of the tendency of lithium to become more corrosive as impurity levels increase.

Pipe expansion joints are needed to eliminate large expansion loops. Because minimizing the amount of lithium in the plant is one of our goals, we need to minimize the volume of lithium in expansion loops. Reliable expansion joints for liquid-metal piping have not been developed yet.

We need to develop equipment to remove impurities and tritium from the liquid lithium. Cold trapping, which is conventional in sodium systems, will not be sufficient for a lithium system. Gettering with hot traps will also be needed to remove lithium impurities. The molten-salt tritium extraction process proposed for the HYLIFE plant is only in the earliest stages of study.

The design, fabrication, and testing of liquid-lithium pumps is an important area of technological development for the HYLIFE power plant concept or for any other fusion concept that uses flowing liquid lithium.

Much work has already been done in the development and testing of liquid-sodium system components for the LMFBR program. This experience provides a significant technology on liquid metals and a measure of the long developmental times required for liquid-metal system components. However, because lithium and sodium differ, we may be faced with new problems and obstacles. Furthermore the HYLIFE power plant needs liquid-metal systems that will not be studied as part of the LMFBR research and development effort.

References

87. N. J. Hoffman and M. W. McDowell, *1000 MW Net Electric Laser Fusion Plant System Study*, Energy Technology Engineering Center, Canoga Park, Calif. (1978).
88. *Conceptual Design Study of the HYLIFE Laser Fusion Facility*, Bechtel National, Inc., Research and Engineering, San Fransisco, Calif. (1978).
89. V. A. Maroni, R. D. Wolson, and G. E. Staahl, "Some Preliminary Considerations of a Molten Salt Extraction Process to Remove Tritium from Liquid Lithium Fusion Reactor Blankets," *Nucl. Tech.* 25, 83 (1975).
90. W. F. Calaway, "Electrochemical Extraction of Hydrogen from Molten LiF-LiCl-LiBr and its Application to Liquid-Lithium Fusion Reactor Blanket Processing," *Nucl. Tech.* 39, 63 (1978).

Author

W. R. Meier

Major Contributors

N. J. Hoffman
M. W. McDowell
(Energy Technology Engineering Center)

9.2.7 Steam and Electricity Generation

The primary purpose of the HYLIFE converter is the production of electricity in a central power station. Thus, we are interested in the energy transfer from the primary coolant to the steam cycle to the turbine-generators that produce electricity. We discuss below the thermodynamic cycles that we considered and describe the one that we selected.

Thermodynamic Cycles. The HYLIFE converter and power plant are designed to use near-term state-of-the-art technology. Thus, we have drawn heavily on current and near-term LMFBR technology. We investigated the two alternative steam-cycle conditions proposed for the Prototype Large Breeder Reactor (PLBR). These PLBR cycles include the saturated steam cycle proposed by the GE Bechtel team and the superheated steam cycle proposed by both the Atomics International/Burns and Roe team and the Westinghouse/Stone and Webster team.

In an evaluation of alternative PLBR steam cycles, Lewe et al.[91] identified the following consequences of the fundamental differences between a saturated steam cycle and a superheated steam cycle:

- Higher sodium and steam temperatures in the superheated steam cycle lead to a greater potential for creep fatigue damage in the steam generator and result in higher developmental risk.
- Higher steady-state, sodium-to-water temperature differences in the saturated steam cycle complicate the steam generator design, necessitating protection of the tubes in the sodium entrance region, prevention or accommodation of departure from nucleate boiling (DNB), and protection of the upper tube sheet.
- The design and development of turbine-generators differ in that the saturated steam cycle can use LWR turbines that have been, or will be, field tested in 1000-MW and 1350-MW sizes, while the superheated steam turbine requires development.
- Steam-generator water-side transients are more severe for the superheated steam cycle.
- Higher sodium temperatures increase the design difficulty of sodium-side components in the superheated steam cycle.
- Sodium-side transients are more severe in the saturated steam cycle.
- Thermal efficiency of the superheated steam cycle is greater; hence, there will be less heat rejection to the environment.
- The superheated steam cycle has a potential for growth through increasing temperature and pressure.

Lewe et al. made the following judgments:

- In terms of licensing, the cycles do not differ significantly.
- Differences in thermal efficiency and waste heat rejection must be balanced against the differences in the capital and operating costs.
- Alternative designs have not been sufficiently developed to permit a final judgment on relative capital and operating costs.
- Risk and reliability will be problems for the first few turbine-generators developed, but not for subsequent units.

Hoffman and McDowell performed energy balances for the HYLIFE-converter power plant based on both steam cycles.[92] For an increase of electrical conversion efficiency of ~11% (from 35% for the saturated steam cycle to 39% for the superheated steam cycle), the net plant efficiency increased ~15% (from 27.7% to 31.8%).

Based on the strong leverage of electrical conversion efficiency and net plant efficiency, we chose the superheated steam cycle for the HYLIFE-converter power plant. If we find that the lower availability and higher capital cost of the superheated steam cycle outweigh its efficiency advantage over the saturated steam cycle, we will reconsider our selection.

Heat Transport System. The heat transport system for the HYLIFE-converter power plant is made of three subsystems (Fig. 9-39).[91-93] The primary system uses lithium to transport the fusion energy to an intermediate heat exchanger (IHX). The secondary system uses sodium to transport energy from the lithium primary system to steam generators. The third system is the steam cycle that converts the thermal energy to electrical energy by a turbine-generator set. The primary and secondary systems are discussed more fully in §9.2.6.

The pump system that recirculates the lithium blanket and includes the primary heat transport system consists of four independent loops. Each loop contains four 8.66-m^3/s, two-stage, combined axial-centrifugal pumps and a 794-MW_t IHX. The pumps continuously circulate 92% of the primary lithium flow through the HYLIFE vessel through

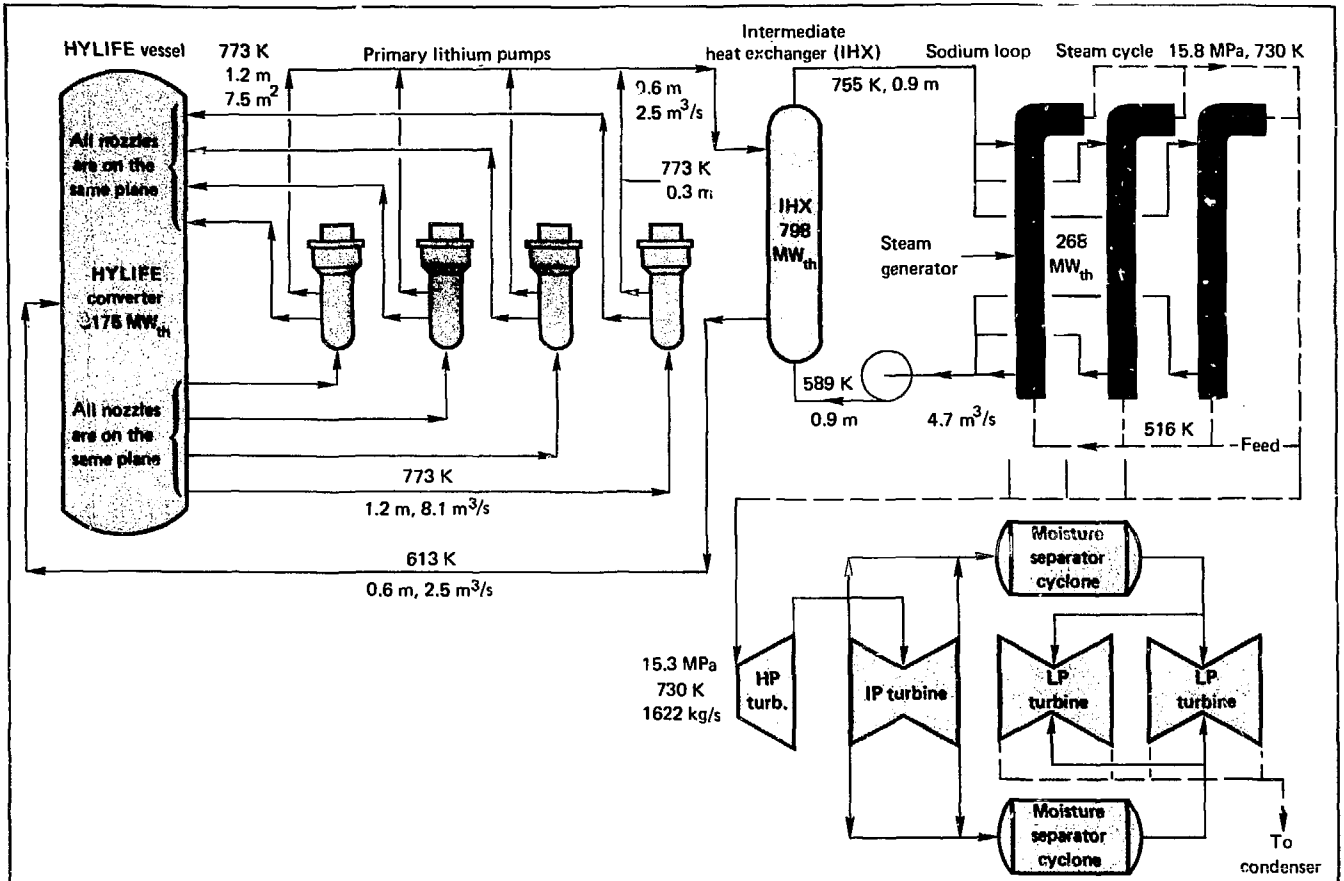

Fig. 9-39. Heat transport system for HYLIFE converter power plant. The lithium, sodium, and steam generator systems shown represent one of four loops. The steam cycle is adapted from the AI superheated cycle.

1.2-m-diameter recirculation piping. Expansion joints (bellows) in each vertical and horizontal run of piping accommodate thermal expansion. These bellows also reduce the space required for the primary piping, allowing for a small reactor containment building. The remaining 8% of lithium flow is routed at 773 K to the IHX through 0.6-m-diameter piping.

The IHX characteristics are given in Table 9-5. The exchangers are of the two-pass, tube-and-shell, counterflow type construction. They are made of 2.25 Cr–1.0 Mo steel and are mounted vertically in the reactor building.

The secondary heat transport system delivers sodium at 755 K to the steam generators through a conventional looped piping arrangement. The steam generators are divided into four independent and identical loops. The loops are operated in a parallel once-through mode, which allows a single module to serve as both an evaporator and superheater. Hot-leg sodium from the IHX is delivered uniformly to each of the three steam generators in a loop. The three cold-sodium return legs are manifolded into a common 0.9-m-diameter line.

Hot sodium enters the steam generator in the upper portion of the vertical section, 23 m from the bottom of the unit. The sodium is distributed around the annulus, passes downward, then exits 4.5 m above the bottom of the steam generator. The feed water enters at the bottom of the assembly and flows upward through the tube bundles where it is heated by the downward flow of sodium around the tubes. Superheated steam exits at the top of the steam generator.

Table 9-5. Characteristics of the intermediate heat exchangers (IHX) (Source: Ref. 93).

Number of loops	4
Number of IHX's per loop	1
Duty per IHX	794 MW_t
Type	2 pass, tube and shell, vertical
Surface area per IHX	6121 m^2
Number of tubes	5088
Tube diameter	25 mm
IHX material	2.25 Cr–1.0 Mo
Lithium flow rate	2.5 m^3/s
Lithium inlet temperature	773 K
Lithium exit temperature	613 K
Sodium flow rate	4.7 m^3/s
Sodium inlet temperature	589 K
Sodium exit temperature	755 K
Log mean temperature differences	20.9 K
Lithium pipe diameter	0.6 m
Sodium pipe diameter	0.9 m

Table 9-6. Steam generator characteristics (Source: Ref. 93).

Type	Hockey stick, shell and tube
Material	2.25 Cr–1.0 Mo steel
Number in plant	12 (3 per loop)
Duty/unit	265 MW_t
Surface area/unit	2370 m^2
Tube diameter	15.9 mm
Tube wall thickness	2.77 mm
Number of tubes/unit	2025

Fluid parameters	Sodium (shell side)	Water and steam (tube side)
Temperature in, K	755	516
Temperature out, K	589	730
Inlet pressure, MPa	1.14	16.2
Outlet pressure, MPa	.09	15.8
Flow/unit, kg/s	1255	405

Table 9-6 summarizes the parameters of the conceptual steam generator. The hockey-stick steam generators are scaled up from previous types designed by Atomics International. We chose them because they appear to represent a relatively simple, proven, and economical method of steam generation for large liquid-metal reactors. The differential tube-to-tube and tube-to-shell thermal expansion is accommodated by the offset-leg (hockey-stick) arrangement of the upper section. Each steam generator produces 265 MW_t of 730-K, 15.8-MPa superheated steam.

The superheated steam is delivered to a low-speed (1800 rpm), tandem compound, nonreheat type of turbine. No such turbines exist for the HYLIFE-converter power plant, but several turbines could be modified for the superheated steam cycle. As an example, we chose an Allis Chalmers design that has a 1.12-m last-stage blade (TC4F-44"LSB). The unit has four cylinders: a single-flow, high-pressure (HP), barrel-type cylinder; a double-flow, intermediate-pressure (IP) cylinder; and two double-flow low-pressure (LP) cylinders.

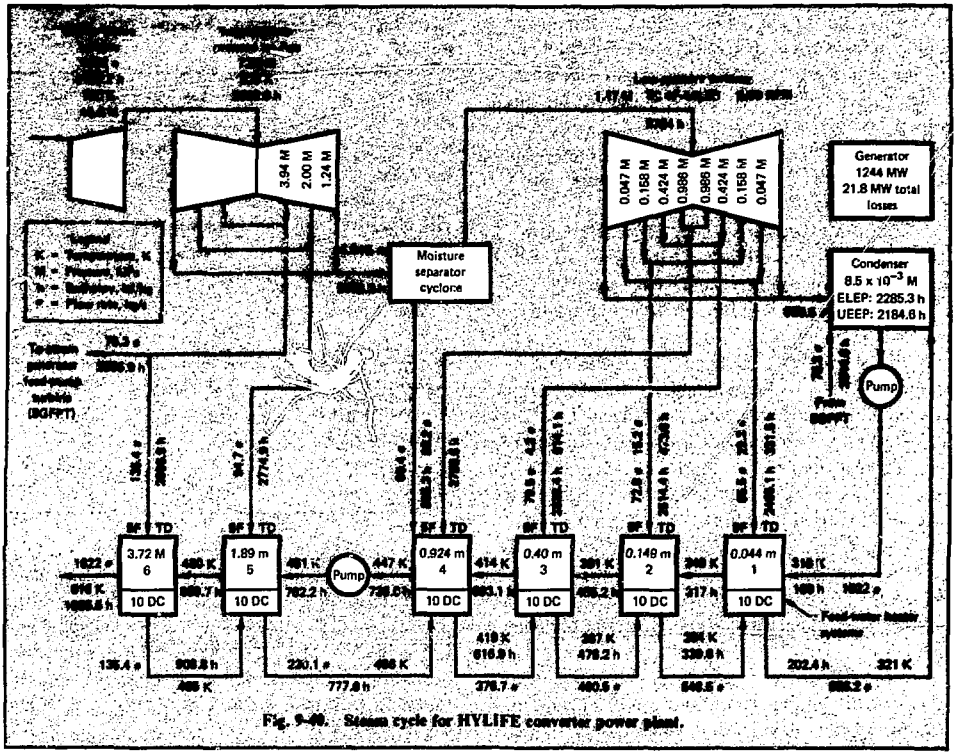

Fig. 9-40. Steam cycle for HYLIFE converter power plant.

Two moisture separation cyclones are located between the IP and LP cylinders to maintain a 1% moisture level at the LP inlet. The need for the cyclones is not definitely established at this time in LWR systems. The IP cylinders are modified versions of the existing LWR HP cylinders. The barrel-type HP element has been developed, but not completely designed for fabrication. The generator and exciter units are near-existing hardware and will require little or no modification for this application.

In general, we selected the 1800-rpm turbine because it is more efficient and operates under more stable conditions (higher availability) than a 3600-rpm turbine of the same capability.

The turbine-generator set produces 1244 MW_e, of which 194 MW_e supply the power requirements of the laser, pumps, and other auxiliary equipment. The net 1050 MW_e establish the net thermal efficiency of the HYLIFE power plant at 33%. Figure 9-40 shows details of the steam cycle, which we adopted from an Atomics International PLBR design.[94]

Conclusions. We must balance the risks of poor performance and reduced availability for turbine-generator sets developed for the superheated steam cycle against the inherent improvements in the efficiency and environmental impact of that cycle. Therefore, choice of the saturated steam cycle on the basis of present turbine-generator advantages may result in our abandoning technically and economically attractive alternative systems of superheated steam cycles in the future.

We selected the superheated steam cycle over the saturated steam cycle in the spirit of fusion energy being a relatively clean, abundant energy source. We plan to develop high efficiency plants with concomitant low heat rejection and, hence, low environmental impact.

References

91. C. K. Lewe, W. A. Maxwell, W. L. Partain, G. C. Rudy, E. A. Saltarelli, J. C. Scarborough, E. R. Schmidt, and Z. Zudans, *Evaluation of Alternative Steam Cycle Conditions for the Prototype Large Breeder Reactor*, NUS Corp., Rockville, Md., NUS-1883 (1977).
92. N. J. Hoffman and M. W. McDowell, *Liquid Metal Engineering Center Laser Fusion Quarterly Report, January to March, 1978*, Energy Technology Engineering Center, Canoga Park, Calif. (1978).
93. *Conceptual Design Study of the HYLIFE Lithium Waterfall Laser Fusion Facility*, Bechtel National, Inc., Research and Engineering, San Francisco, Calif. (1978).
94. *Liquid Metal Fast Breeder Reactor Conceptual Plant Design 1000 MW$_e$*, Atomics International, Canoga Park, Calif., FBR-77-3 (1977).

Author

J. Hovingh

Major Contributors

W. O. Allen, T. J. Wood, and S. Thomson (Bechtel National, Inc.)

9.2.8 Optical and Pellet-Injection Systems

The laser, pellet, and energy-converter subsystems must all be integrated for the successful operation of an Experimental Test Reactor, the first laser fusion system to use a repetitively pulsed laser. To achieve this integration, we must consider the following problems:

- Survivability of the final optical system.
- Protection against tritium migration and neutron streaming.
- Constraints on beam focusing.
- Performance limitations on the aiming and timing of laser beams and pellets.

Two separate aspects of these problems must be merged in the conceptual design. The first is a trade-off in the design of the optical focusing system to attain both long life and adequate focusing. Large f-number optics allow us to place the final mirrors far from the pellet, giving long mirror lifetimes.[95] Unfortunately, these optics also lead to large minimum focal-spot sizes and, if we are not careful, awkward design of the reactor containment vessel.

The second aspect involves the choice between active pellet-trajectory correction or active pointing of the high-energy laser beam or, perhaps, the use of both.[96] There are systematic and random errors in the delivery of both the pellet and laser pulse, in both space and time. In this subsection, we first examine the optical survivability issue, since it has the most impact on the configuration of the system. Then we address the error analysis of injecting a pellet and aiming a high-power laser beam.

Final Optical System. We envision the laser system to be physically separated from the fusion energy conversion system. The separate laser building can be built in half the time of a containment building, reducing capital cost. Separation provides increased accessibility and maintainability, at less total cost, but it necessitates windows in the energy-converter building to admit the laser beams and to prevent tritium migration. The final focusing configuration must be designed to freely transmit light in one direction while preventing the opposite migration of x rays, debris, neutrons, lithium vapor, and tritium.

Figure 9-41 is a schematic of the proposed final focusing system. The laser beams pass through the optical tunnel connecting the laser and energy conversion buildings and enter windows, which are the primary interface. The beams are then cylindrically focused through slits in a neutron shield.

Each of the 30 slits (one per laser beam) is a few millimeters wide by a meter long. The combination of a partial vacuum on each side of the slit and a line focus will keep intensities below breakdown threshold. Each slit in the shielding is in a separate, hydraulically activated safety gate, which may be closed quickly in case of window failure, or for normal shutdown. The final mirrors focus the beams onto the pellet at the center of the chamber.

Fusion products follow the reverse path of the laser beams. The neutrons, x rays, and debris are first apertured by the chamber's lithium blanket so that they do not strike the chamber structure directly. A set of replaceable baffles located in the beam tube near the entrance to the chamber catch lithium droplets, condense out lithium vapor, and further restrict the direct neutron beam to only that solid angle subtended by the final mirrors. The baffled region is vacuum-pumped to prevent lithium vapor, tritium, and other gases from migrating up the beam tube. Following the baffled region there is a safety gate, a heavy sliding door that may be closed to isolate the optical tunnel and hall of mirrors from the liquid-metal circulation system.

The region between the safety gate and the final mirrors is filled with low-pressure xenon gas, dense

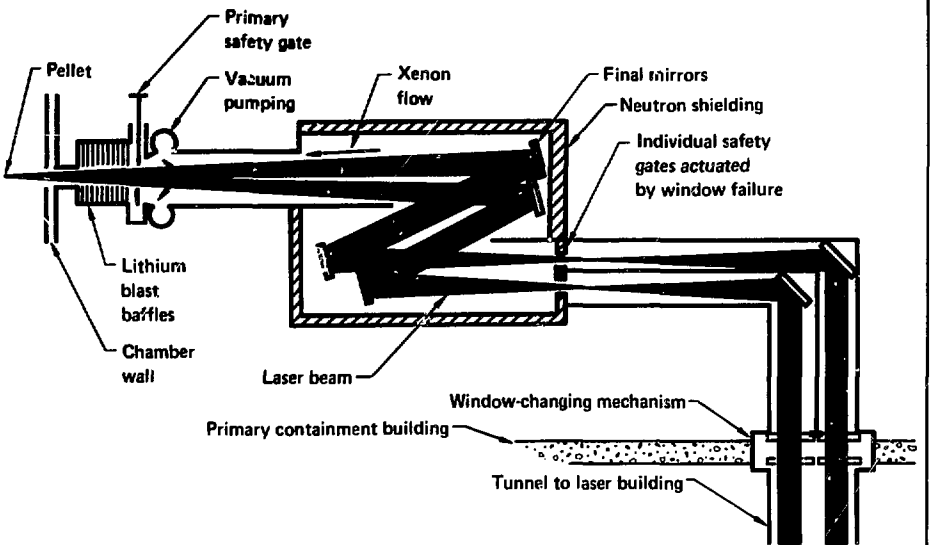

Fig. 9-41. Schematic of final laser focusing system.

enough to stop the debris and soft x rays that would otherwise damage the surface of the mirror. The neutrons and hard x rays penetrate deeply into the mirror substrate, causing insignificant volumetric heating. The neutron streaming and gamma scattering in the optical corridor[97] and mirror hall are effectively trapped inside because the slotted safety gates through which the beams pass are so small in area.[95,98] Further protected by another right-angle turn and a pressure balance, the window should not suffer significant radiation damage, activation, or physical damage.

There are three barriers against tritium leakage from the optical system:

- Tritium must pass the baffled region of the laser beam tube, where the vacuum pumping occurs, and migrate against the pressure gradient of counterflowing xenon gas.
- Tritium molecules have a small probability of finding and passing through the small laser beam slots.
- The window, probably made of quartz, is the final physical barrier against diffusion of tritium.

We have yet to quantify the small loss rate of tritium by this pathway.

Survivability of the Final Optics. We have identified the following techniques for protecting the final optics against various types of incident radiation:

- Solid angle reduction.
- A magnetic field to deflect ions.
- A replaceable transparent film.
- A transverse gas flow.
- A rotating shutter.
- A gas lens.
- Liquid-metal mirrors.

Only the solid angle reduction allowed by high f-number optics reduces the fluences of all components, neutrons, ions, x rays and neutral particles, and blast effects.

We combine high f-number optics to reduce the neutron flux with a gas, of high atomic number Z, to absorb x rays and debris. In the HYLIFE design, 30 laser beams are focused on a target from a distance of 60 m by an array of 1-m^2 mirrors. The fraction of total solid angle subtended by the mirrors, 6.6×10^{-4}, dramatically reduces the radiation flux.

A region of high-Z gas prevents the x rays and debris from striking the final optics. This gas stops the x rays by the photoelectric effect and thermalizes the debris through collisions. To some extent, these processes are already at work in the lithium vapor in the chamber. We can estimate the requirement using mean-free-path arguments.

Xenon is taken as an effective high-Z absorber, though almost any gas that is otherwise compatible could be used. We graphed the mean free path of x rays vs their energy in one atmosphere of xenon gas (Fig. 9-42), using data from the LLL library of photon cross sections.[99] We expect x rays throughout the 100-eV to 20-keV region of the spectrum. Softer x rays have short mean free paths in the gas and are readily absorbed in the lithium vapor.

From Fig. 9-42 we see that 0.2 cm·atm (1.52 m·Torr) of xenon will provide attenuation of one mean free path for 3-keV x rays. To obtain a factor of 100 reduction in x-ray intensity, we need to provide 4.6 mean free paths of gas, equivalent to 7 m·Torr of xenon. We also want to absorb the radiation over a long distance to prevent generation and effective transmission of shock waves. Hence, a 30-m section of the beam tube containing 0.25 Torr of xenon should be adequate. Any pressure disturbances created in this low-density gas are unlikely to have sufficient amplitude to affect the mirror.

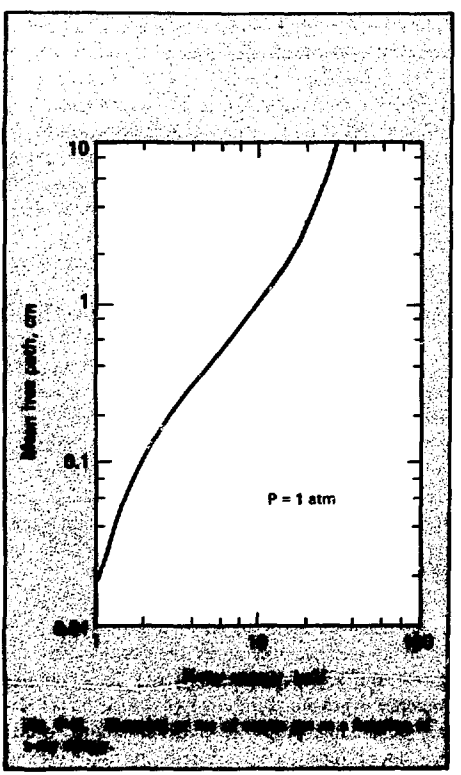

An additional benefit accrues from this scheme. The counterflowing gas isolates the cooled optical surface from the hot lithium vapor, which might otherwise tend to condense on the optical surface.

The laser intensities in this region are below 10^9 W/cm^2, safely clear of any breakdown thresholds in a 0.25-Torr gas.

Refracting vs Reflecting Optics. The optical damage limit, energy per pulse, wavelength, and size of the final laser amplifier aperture combine to dictate the total required area of the final mirrors or lenses. Assuming a 10-J/cm^2 damage threshold and 3 MJ of laser energy per pulse, a beam area of 30 m^2 is required. Both fabricability and radiation-damage considerations lead to a choice of mirrors over lenses.[95] It is now less costly to diamond-turn large mirror blanks on a lathe controlled by an interferometer than to cast and polish glass blanks of similar size for the same surface figure accuracy. Also, bulk neutron damage thresholds are generally lower in glasses than in metals. In all cases, we are more concerned about loss of optical performance due to changes that are radiation-induced, than we are about changes in strength, embrittlement, etc.

Depending on laser wavelength, the final mirror may have a high-reflectance coating. If the metal acts only as a substrate for a dielectric coating, absorptivity is irrelevant. However, in both coated and uncoated mirrors, high dimensional stability is required to maintain surface accuracy. Cooling readily handles both the volumetric mirror heating caused by the deposition of neutrons and hard x rays and the surface heating caused by absorbed laser radiation.[95]

We identified two mechanisms that could shorten the lifetimes of metal mirrors:[95,100]

- Increased optical distortion due to swelling from (n, α) helium production reactions in both uncoated and coated mirrors.
- Distortion and decreased damage threshold of high-reflectance coatings.

Nonuniform swelling of the metal substrate causes the surface distortion. The helium produced in (n, α) reactions migrates to form microscopic bubbles. These bubbles can cause surface distortion on the order of a wavelength of light, which degrades optical performance. No experimental data are available to demonstrate this postulated optical effect, but we can predict its onset based on volumetric swelling rates of neutron-irradiated materials.

At 60-m distance, the neutron flux is 0.042 MW/m^2. For a mirror temperature of 300 K, the volumetric swelling rate of any of the metals considered (Mo, Al, Cu, Ti) should be below 10^{-3}% per year. Estimating the linear deformation by $\Delta x/x = (\Delta V/V)/3$, and setting it equal to a maximum allowable distortion of $\lambda/8$ at $\lambda = 0.25\ \mu$m, we calculate a mirror lifetime of 10.6 yr, a favorable value.

The second postulated determinant of lifetime is the degradation of optical coatings. Little is known about dielectric coating performance in a 14-MeV neutron environment. Testing is required to gather this information. Fortunately, the use of high f-number optics eliminates the need for new and expensive test facilities. The neutron fluxes the mirrors will experience are 100 times less than those on a reactor first wall, and are, therefore, experimentally accessible much earlier. For example, the LLL Rotating Target Neutron Source (RTNS-II) produces a continuous source of 13- to 15-MeV neutrons at the rate of 4×10^{13} neutrons/s.[101] We could obtain a neutron flux of 0.18 MW/m^2 over a 1-in. witness sample, enough flux to accumulate a 1-yr dose for the HYLIFE design in 12 wk. Thus, we will soon be able to obtain superb data on radiation damage to optics without waiting for fusion test reactors. Only the question of the pulsed vs continuous irradiation will remain.

Pellet Injection and Tracking. The conceptual system for pellet injection and tracking that we identified for integration with the HYLIFE converter has some unique characteristics. Pellets are injected with a repeating gas gun positioned horizontally alongside a cluster of laser beams. No pellet trajectory correction is desired or required. Simple tracking of the target requires a low-power laser illuminator, an x-y position-sensing photodetector, and a trajectory prediction scheme. Two-degree-of-freedom (x-y) beam steering is preferred, without refocusing capability. Both the tracker and the adaptive mirror are placed in the laser building out of the radiation environment.

The clearest attack on this problem is to organize an error analysis around the following functions:

- Injection. The pellet may not go exactly where it was aimed or it may not arrive at the expected time.
- Tracking. The pellet may not be where it appears to be.
- Pointing. The beam may not go exactly where it is aimed.
- Focusability. The beam focal spot size is larger than ideal.

We considered space-time error contributions from (1) target position uncertainties caused by perturbations and tracking error, and (2) such deviations of the laser optical train from the ideal as misalignment, jitter, gas turbulence, mirror figure error, diffraction, and other limits on steering and focusing.

We chose a horizontal pellet injection scheme for our conceptual design. A pneumatic gas gun may have to stand off many tens of meters for radiation protection. It is awkward and costly to have an ~50-m appendage extending upward in the containment vessel when it is not necessary. If redundancy in target injection is required, a gas gun can be installed alongside each of the opposing beam paths. Gravity will cause the pellet to drop somewhat during its trajectory, but in a repeatable manner. Only the shot-to-shot variations are important.

The options and reasoning for the issue of trajectory control versus beam control are shown in Fig. 9-43 and explained in Ref. 96. We advocate the shaded sequence of steps in Fig. 9-43. This approach is based on the use of an adaptive pointing mirror, a membrane-like mirror surface driven by piezoelectric actuators or electrostatic forces.[102–104] These mirrors can be placed in the laser building, safely out of the radiation path.[105] They can even be placed in the small-diameter portion of the optical train before the largest laser amplifiers, so that they need only be ~10 cm in diameter rather than approximately 1 m.

Pellet Injection. We assume that the pellets are spherical, with diameter depending on yield. They have fairly critical tolerances on layer thickness and finish and are, perhaps, cryogenic. It is common practice in gas gun technology to encase the pellet in an expendable projectile called a sabot,[96] which provides protection against damage from handling,

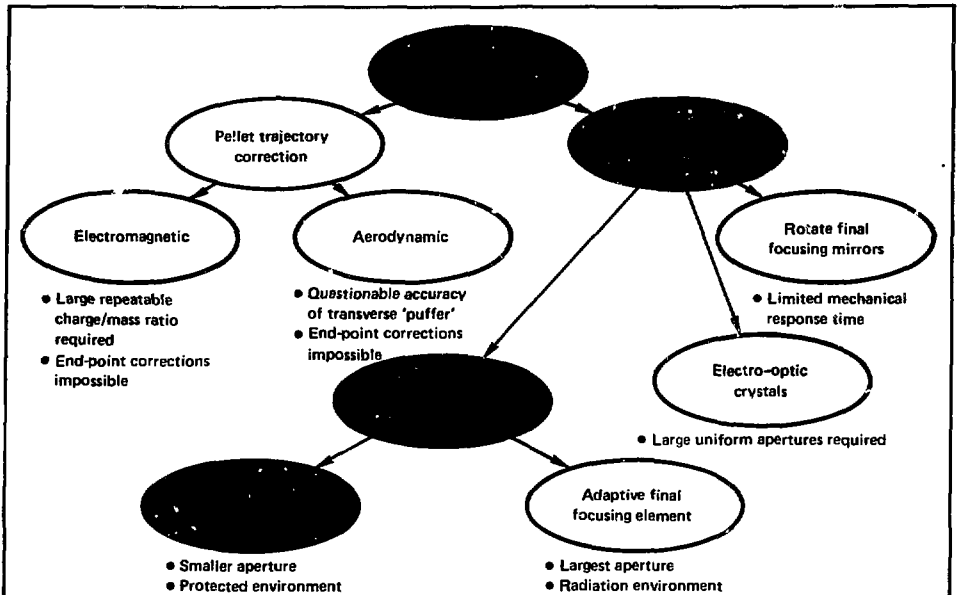

Fig. 9-43. Options for pellet trajectory correction vs beam pointing correction.

barrel friction, and rifling. The sabot insulates the pellet from detrimental heat transfer with the accelerating gas or the barrel. Figure 9-44 is a schematic of a pellet injection system.

We included a coast section of length L_C = 60 m between the gun shielding and the reactor first wall, primarily to reduce the x-ray and debris fluence per shot to low levels.

Several constraints interact to restrict operation to ranges of muzzle velocity, gun length, and acceleration. We can derive a lower limit on velocity because the pellet cannot enter the chamber until the last 10% or so of the interpulse time. This restriction allows the chamber to clear and reestablish chamber conditions. If ψ = pulse repetition frequency and R_W = the chamber wall radius, then these two constraints are written as

$$a \leqslant a_{max} \ , \quad v \geqslant 10\, R_w \psi \ .$$

The total time spent in acceleration and coast should not exceed the interpulse time. Otherwise, at least two pellets are in the gun at the same time. One pellet would then be exposed to radiation from the previous pellet fusion, a situation we can easily avoid by imposing the constraint

$$(2\ell_a/a)^{1/2} + L_c/v \leqslant \psi^{-1} \ ,$$

where ℓ_a and a are the acceleration length and acceleration, respectively. This constraint results in the curve that bounds the allowed operating region in Fig. 9-45. The velocity that is attained for a particular acceleration is shown by the operating line. The most favorable operating point is determined by the minimum velocity and acceleration allowed by the constraints. Actual maps are provided in Fig. 9-46 for pulse repetition frequencies of 1 and 10 Hz. We chose the nominal values shown in Table 9-7 to obtain long tracking times by minimizing velocity and to save space and money by minimizing acceleration length.

Note that the 10-Hz system requires almost 10 times the acceleration and velocity of the 1-Hz system, even though we have decreased the coasting distance to 20 m (a higher pulse rate would result in lower yield and would require less standoff distance) and increased the acceleration distance tenfold. Even so, the acceleration of 8990 g seems high.

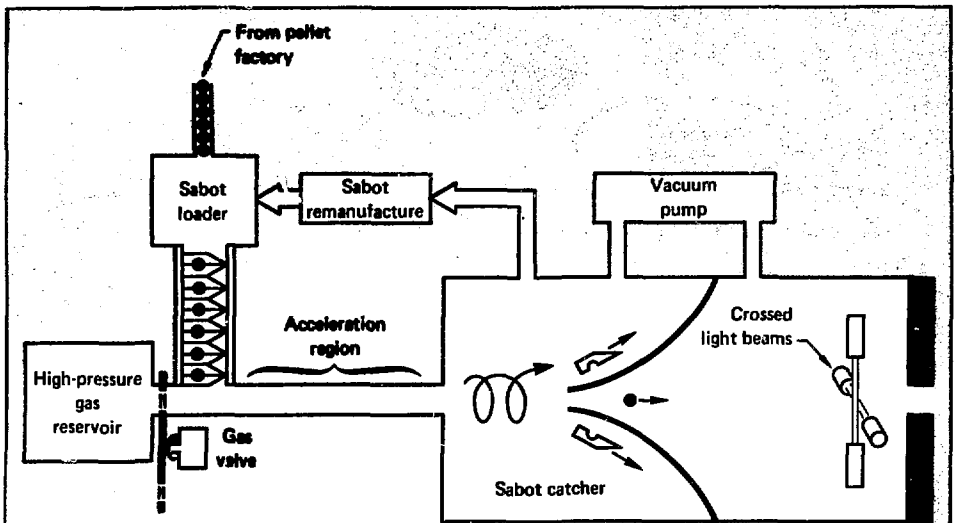

Fig. 9-44. Schematic of pneumatic pellet injection gun.

For comparison, a 0.30-caliber bullet experiences an acceleration of ~50,000 g, a home-run baseball ~1500 g. Unfortunately, we do not yet know the acceleration limit for a pellet to experience damage, but Devaney suggests 6000 g.[106,107] Thus, a 10-Hz system may be problematical within the given constraints.

We can easily estimate the sensitivity of the final position to errors in injection velocity. The pellet emplacement error in the vertical direction Δy due to errors in the nominal final velocity v is

$$\Delta y = \frac{g L_c^2}{v^2} \left(\frac{\Delta v}{v}\right).$$

We suppose that the pneumatic gun is accurate to 0.1% in velocity and then calculate a vertical position error of 8.6 mm for the 1-Hz case, and 24 μm for a 10-Hz case having greater velocity and shorter coast distance. We cannot control this error, but we can predict it by measuring the velocity at the muzzle. Coarse adjustment to a pointing mirror can be made during the entire coast period of the pellet.

Tracking. We must estimate both the position of the pellet and its arrival time to know where to point the beam and when to fire the laser oscillator. The pellet trajectory is tracked over time and a computer then fits the data to a model of the flight trajectory, using a Kalman filter or other scheme for real-time estimation and control.

Three methods of tracking have promise:

1. One tracker for all n beams.

2. A shared-aperture tracker-pointer system for each beam.

3. Same as method 2, plus an active target-designation system.

Method 1 is simplest, least expensive, and has the largest errors. Method 2 has an advantage in that it is far more immune to errors from beam self-alignment and mirror jitter, and it eliminates error from the relative misalignment between different beams. Method 3 provides even greater accuracy. The target designation system points a low-power test beam at the target through the optics of the high-energy laser (HEL) in a closed-loop strategy. Returns of the designator pulses from the pellet can assure us that the optics are indeed on target. Method 3 seems to be more expensive and sophisticated than necessary.

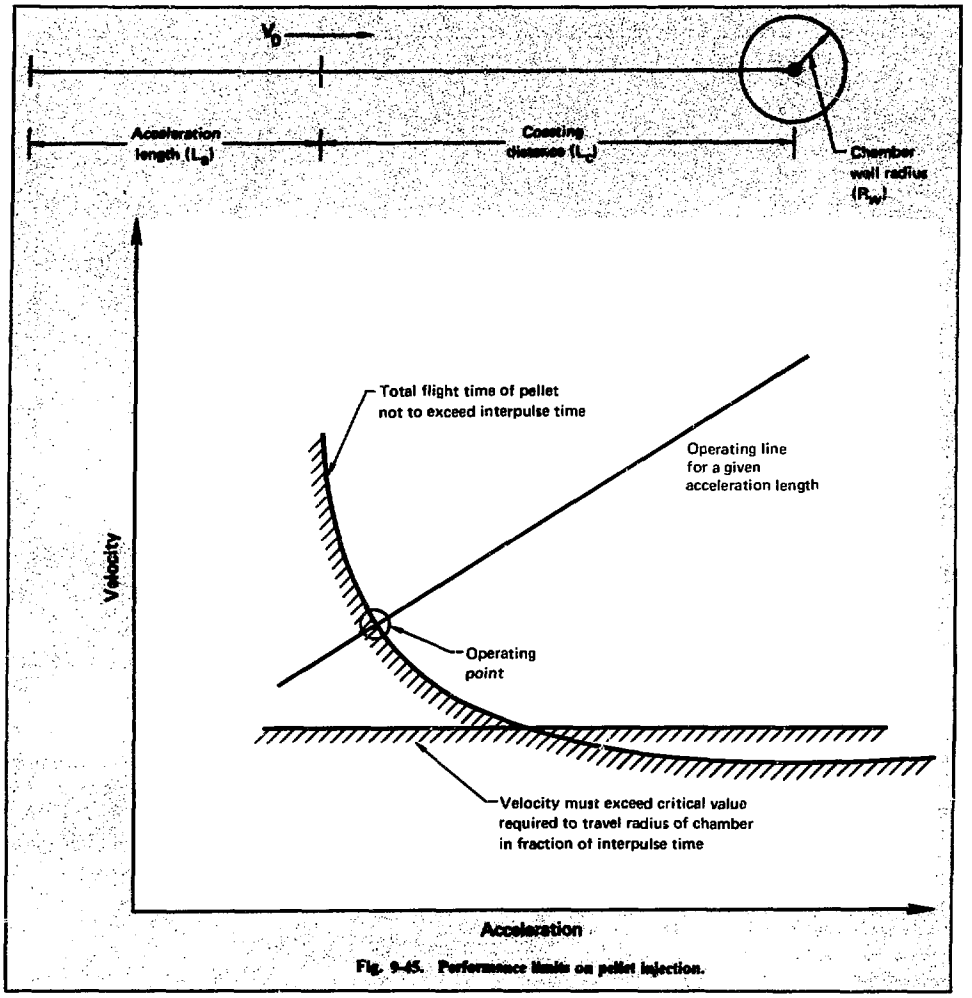

Fig. 9-45. Performance limits on pellet injection.

Method 2 is illustrated in Fig. 9-47. A tracker system is located in the laser building, away from the hostile reactor environment. During the last 2 to 5 m of its flight, the pellet is imaged onto a photodetector in the tracker. Because the HEL beam axis and the pellet trajectory are almost parallel, this is possible within a reasonable tracker field of view (FOV). The pellet is passively illuminated with a CW laser, so that the tracker sees a bright glint off the target. The laser illumination cone and tracker FOV can be closely matched. An example of a large (1.22 m) tracking telescope is discussed in Ref. 108.

The most attractive feature of this system is that the tracker optical path, with light rays emanating from the target, is the reverse of the HEL path. The paths share the same optics. The system is particularly insensitive to static or dynamic alignment errors. Because the rays share the same optical elements and path, an index-of-refraction gradient in a gas laser amplifier or angular mirror vibration will not cause errors. Each beam has a dedicated

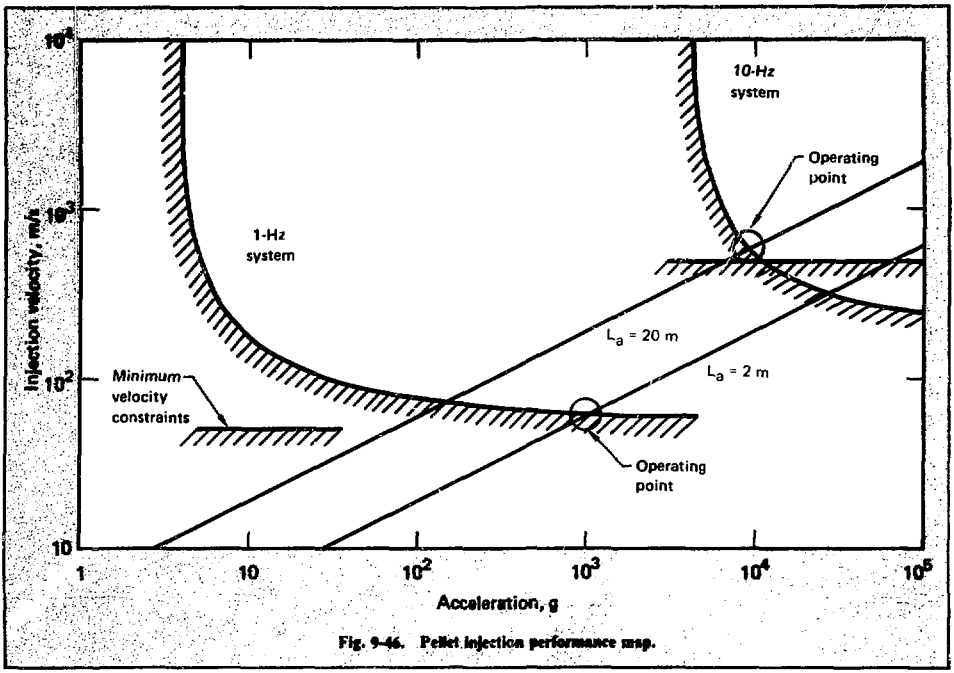

Fig. 9-46. Pellet injection performance map.

Table 9-7. Acceleration and coasting characteristics of pellet injections at pulse repetition rates ψ of 1 and 10 Hz.

Characteristic	ψ = 1 Hz	ψ = 10 Hz
Acceleration, g	1024	8990
Acceleration length, m	2	20
Acceleration time, ms	63	66
Final velocity, m/s	64	600
Coasting distance, m	60	20
Coasting time, ms	937	34

tracker and intrinsically follows any change in apparent target position.

Both the tracker and the pointer are placed ahead of the large laser amplifier in the small-diameter part of the beam. Assuming D and d to be the diameters of the large and small beams, respectively, the tracker sensitivity is enhanced by the magnification ratio (D/d) in this scheme. The error in the target plane $(\Delta r)_t$ is related to the minimum resolvable distance $(\Delta r)_d$ on the face of the photodetector through the ratio of the primary focal length to the detector focal length (Z_f/Z_d) and the magnification ratio, as follows:

$$(\Delta r)_t = \left(\frac{Z_f}{Z_d}\right)\left(\frac{d}{D}\right)(\Delta r)_d \ .$$

Using a magnification ratio of 10, focal lengths of Z_f = 50 m and Z_d = 0.3 m, and a readily achievable[109] detector resolution of $(\Delta r)_d = 3 \times 10^{-4}$ in., we obtain a typical tracker error in the target plane of $(\Delta r)_t = \pm 0.125$ mm. This is much smaller than the size of a pellet.

The effects of misalignment and slow vibrational jitter of the optics are irrelevant because of the shared path.

Pointing. The pointing mirror system can also be placed in the laser building ahead of the largest laser amplifiers where the beam is of small diameter, say 10 cm rather than 1 m. Such a 10-to-1 reduction

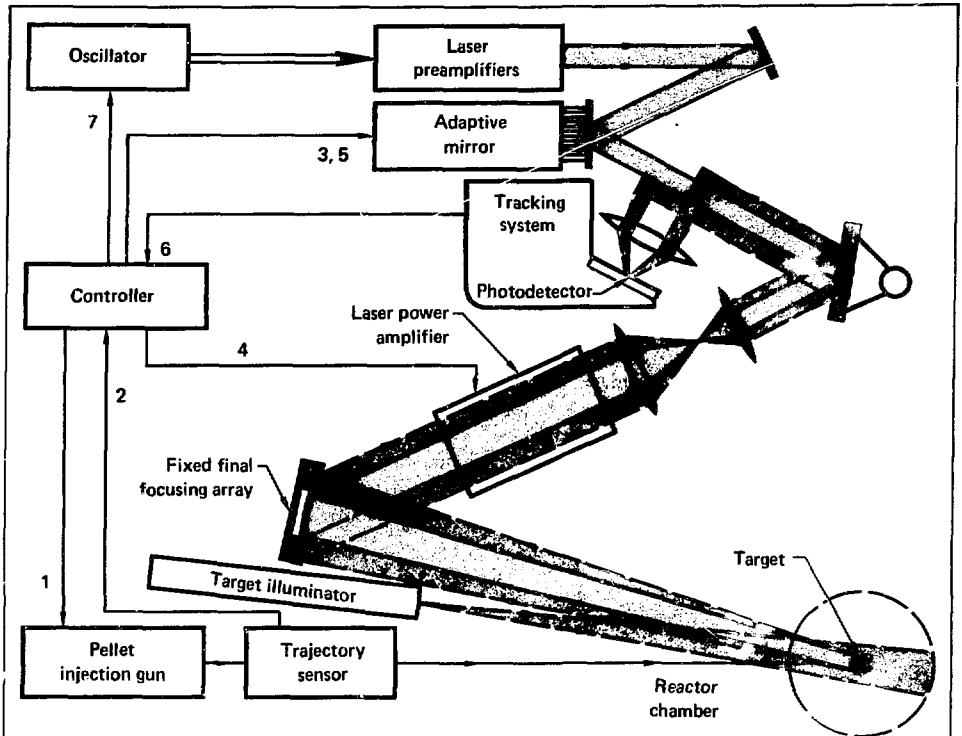

Fig. 9-47. *A shared-aperture tracker-pointer system. Numbers indicate order in which the controller communicates with each component.*

in the diameter of an active mirror reduces cost by a factor of ten. In addition, since an angular deviation from an ideal ray path is reduced by the magnification ratio when a parallel beam is increased in diameter, we can expect any pointing errors to be ten times smaller in the target plane. Two benefits accrue. The beam magnification helps increase tracking sensitivity and decrease the sensitivity to pointing errors. A disadvantage is that the maximum angular range of the adaptive pointing mirror is reduced.

Pointing can be done in two phases, using a coarse and a fine adjustment. Coarse pointing is performed during the relatively long coasting stage of the pellet trajectory, based on an estimate of the pellet final position and arrival time. The computer generates this estimate from a simple measurement of velocity at the end of the acceleration region of the gas gun. The angular velocities of the beam required in this phase are $\dot{\theta} \leq 5$ mrad/s, well within the state of the art.[110]

In the fine pointing stage, we remove the remaining errors detected during the tracking period while the pellet is in the chamber. Because both the required lateral movement in the target plane and the time allowed for performing corrections are much smaller during this phase, the angular velocities required of the mirror are no larger than before.

Deformable mirrors are not absolutely required. Movable mirrors, supported on two-degree-of-freedom gimbals, can also do the job at these low rotation rates. However, adaptive optics are likely to be part of any future gas laser system for use in

power plants because of their versatility in removing a wide variety of wave-front distortions. Pointing is a logical and desirable additional role for an active mirror.

The pointing errors are of two types: those due to misalignment and jitter of the optical elements between the tracker and pointer, and those due to the difference between the actual angle of the mirror and the intended angle. If the linear stroke of a piezoelectric transducer can be controlled to $\pm\Delta\ell$, then the error angle of the reflecting light ray is $(2\Delta\ell/d)$ and the error angle at the target plane is $2\Delta\ell/D$. Similarly, the error angle in the target plane due to a mirror jitter angle of θ_j would be $\pm 2\theta_j d/D$. If we assume that there are m independent mirrors between the tracker and the pointer, and sum the squares of the angle variances, the total error angle due to pointing is

$$\theta_p^2 = \left(\frac{2\Delta\ell}{D}\right)^2 + m\left(\frac{\theta_j d}{D}\right)^2 .$$

(The factor of m becomes m^2 only if the errors are correlated, as they would be in intensity-dependent optical-path distortions, for example.) Let us assume that $\Delta\ell/\ell = 0.01$ is the precision possible at the maximum stroke of $\ell = 15\ \mu$m. Furthermore, we assume mirror diameters of d = 10 cm and D = 1 m, a jitter angle of 5 μrad, and m = 3. The total pointing error is about one microradian. Thus, lateral error in the target plane is only 50 μm, a negligible amount. This insensitivity is primarily due to the system magnification.

Focusability. In any optical train, there are many sources of distortion that will cause the beam to diverge from the intended geometrical path. Some lead to unintended beam steering and others cause defocusing, but all stem from deviations of the optical path from the ideal. Some are the same from shot to shot, as is mirror figure error. Others, such as turbulence, are time-dependent. Turbulence is random, but boundary layers present a very organized disturbance. Thermal distortion of mirrors and thermal blooming in beam tubes are intensity-dependent. Some of the sources of degradation in focusability are:

- Large-scale random irregularities in steady flow.
- Small-scale turbulence.
- Thermal or momentum boundary layers.
- Acoustic waves generated by energy addition.
- Entropy disturbances in flow from acoustic interaction.
- Surface figure errors in mirrors.
- Thermal distortion of mirrors and solid windows.
- Aerodynamic windows.
- Thermal blooming in beam tubes.
- Neutron-damage-induced distortion of final focusing mirror.
- Breakdown in chamber gas.
- Diffraction.

We discuss here diffraction and both turbulence and acoustic waves in the gas laser amplifiers.

Diffraction limits the spot size of the laser beam in the focal plane to the minimum allowed by the wavelength and f-number of the primary focusing system. The angular deviation from the geometrical optics ray path is

$$\theta_D = \frac{1.2\lambda}{D} .$$

If there were no other degradations, the radius of the focal spot would be

$$r_0 = Z_f\theta_D = \frac{1.2\lambda Z_f}{D} .$$

Spatial variations of the index of refraction of the gas laser medium produce a degrading effect, expanding the minimum focal spot. The effect is similar to the distortions seen in looking across a hot road on a sunny day. The effect has two causes. One is the random turbulence and irregularities present in the gas wind-tunnel flow. The other is the regular pattern of acoustic waves remaining in the flow from the rapid energy addition of the previous pulse. We can estimate the average effect of these disturbances by using the following formulae fo angular deviations:

$$\theta_A = \left(\frac{\rho}{\rho_s}\right)(n-1)\frac{L}{D}\,b\left(\frac{\Delta\rho}{\rho}\right)_{acoustic} ,$$

$$\theta_T = \left(\frac{\rho}{\rho_s}\right)(n-1)\frac{2\sqrt{aL}}{D}\left(\frac{\Delta\rho}{\rho}\right)_{turbulent} ,$$

where

n = index of refraction of a gas at standard density,

ρ/ρ_s = ratio of average density to standard density,

L, D = length and diameter of region of gas,

$\Delta\rho/\rho$ = amplitude of fluctuation, peak to peak,

a = scale size of turbulence,

b = mode number of acoustic waves = $2D/\lambda$ acoustic.

For small variances from the geometric ray paths, we can obtain the expected defocusing angle by summing the variances. The expected spot size is then

$$r_s = Z_f \left(\theta_D^2 + \theta_A^2 + \theta_T^2\right)^{1/2}$$

$$= Z_f \left\{ \left(\frac{1.2\lambda}{D}\right)^2 + \left[\frac{\rho}{\rho_s}(n-1)\frac{L}{D}\right]^2 \times \left[b^2 \left(\frac{\Delta\rho}{\rho}\right)_A^2 + \frac{\Delta a}{L}\left(\frac{\Delta\rho}{\rho}\right)_T^2\right] \right\}^{1/2}.$$

Table 9-8 gives typical values of laser parameters for two gas lasers of interest, the CO_2 laser in the infrared and the KrF^*/CH_4 Raman pulse compressor laser in the ultraviolet.

Common parameters are the diameter D = 1 m, the turbulence scale size a ≈ 0.2 D, the mode number of the most important remaining acoustic wave b = 3, and the peak-to-peak fluctuation amplitude $(\Delta\rho/\rho)_A = (\Delta\rho/\rho)_T = 5 \times 10^{-4}$. The first two acoustic modes contribute primarily to pure steering and pure focusing, which can be easily corrected by the optical system.

Table 9-8. Laser parameters for calculation of focusability.

Parameter	CO_2	KrF^*/CH_4
Amplifier length, m	9 (triple pass)	15 (single pass)
Density, ρ/ρ_s	2.7	1.0
Index of refraction (n - 1)	1.7×10^{-4}	4.44×10^{-4}
Wavelength λ, m	10.6×10^{-6}	0.268×10^{-6}

Calculated spot diameters are 1.4 mm for λ = 10.6 μm and 1 mm for λ = 268 nm. The diffraction contribution, which dominates the CO_2 laser system, is negligible in the KrF^*/CH_4 laser system in which refractive contributions dominate. These results are discussed further below.

Integrated Injection and Tracking Errors. The two interrelated problems are:

- Allocation of interval durations needed for each activity, within the budget determined by interpulse time.
- Allocation of spatial errors accumulated in performing the individual activities, within the budget determined by pellet size.

Figure 9-48 summarizes the first problem for two pulse repetition rates, ψ = 1 and 10 Hz. The 1-Hz system accelerates the pellet to 64 m/s in 2 m at 10^3 g, while the 10-Hz system requires a velocity of 600 m/s and an acceleration of 9000 g. The available tracking times for the two systems are 78 ms and 8 ms, respectively.

The second problem, the allocation of spatial errors, has been studied for wavelengths of 10.6 μm and 268 nm, the longest and the shortest currently envisioned for fusion lasers. The envelope diameter of the expected spot size, including the errors in tracking, pointing, and focusing, was calculated as a function of the focal length of the primary mirror. For the parameters chosen, we found that a 60-m focal length system can have spot sizes less than 2 mm in diameter, quite compatible with plausible reactor pellet diameters.

Conclusions. We propose a conceptual design for a pellet-injection and final optical system, most of which is feasible within the state of the art. Although many other approaches are possible, we draw the following conclusions:

- A high f-number focusing system, consisting of two opposing clusters of laser beams, leads to low fluences of damaging radiation on the mirrors. It allows mirror lifetimes of greater than 1 yr, thereby not compromising the availability of the power plant.
- A low-pressure xenon-gas region in the beam tubes sufficiently protects the mirrors from surface damage without degrading the laser beam.
- Horizontal pellet injection is both feasible and desirable; sabots are recommended; accelerations and velocities required for the 1-Hz system are acceptable.

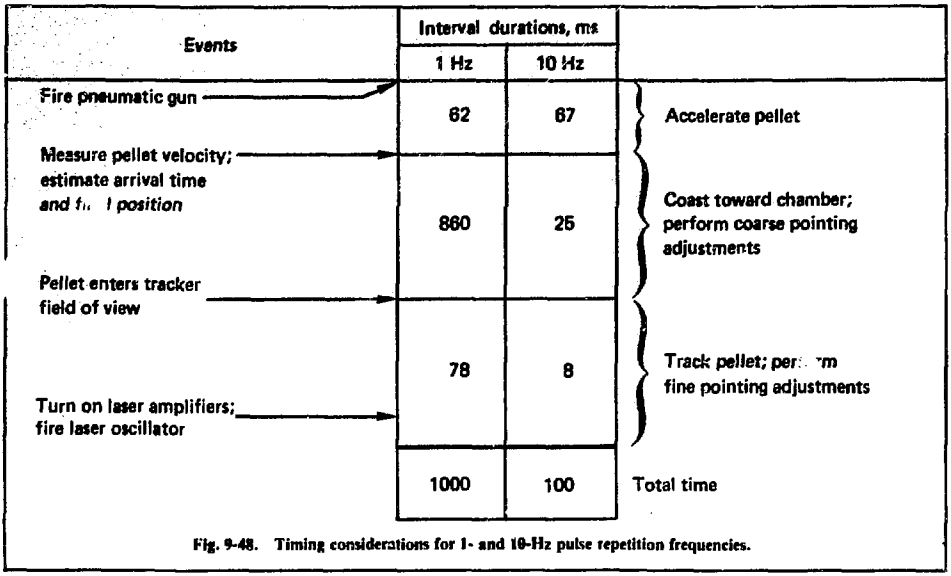

Fig. 9-48. Timing considerations for 1- and 10-Hz pulse repetition frequencies.

- Beam pointing can be performed in two phases: coarse pointing, performed during pellet coast to remove relatively large pellet emplacement errors caused by variations in muzzle velocity, and fine pointing, performed during the final tracking phase to remove small remaining errors.
- A shared-aperture tracking-and-pointing system, using the same optical train as the laser, is attractive since it eliminates a host of misalignment and vibration errors.
- Both tracker and pointer can be located in the laser building, away from the hostile radiation environment of the reactor. Adaptive optics are feasible and can be used in the small-diameter portion of the beam ahead of the final gas laser amplifiers.
- For primary focal lengths of 60 m, the spot diameter of all the errors is a small fraction of the pellet diameter for a 2700-MJ, 268-nm system.
- Pointing and tracking considerations favor laser fusion scenarios with high-yield pellets, low repetition rate, and short-wavelength lasers. In general, engineering a pellet-injection and beam-steering system will not impede the progress of laser fusion.

Technological Development. We need to:

- Develop and test high-reflectance mirror coatings and substrates tolerant to neutron irradiation.
- Develop optical system configurations to reduce neutron and tritium leakage outside the converter building to licensable levels.
- Demonstrate injection, tracking, and pointing at required performance levels in laboratory simulations.

As we have pointed out, a system can be tested now. It is the definition of acceptable regulatory standards for such items as containment penetrations for laser windows that is likely to be critical.

References

95. M. J. Monsler and J. A. Maniscalco, "Optical Design Considerations for Laser Fusion Reactors," *SPIE* **121**, *Optics in Adverse Environments* (1977), Bellingham, Wash.
96. M. J. Monsler, "Laser Fusion: An Assessment of Pellet Injection, Tracking and Beam Pointing," in *Proc. of the 3rd Topical ANS Mtg. on Fusion, Santa Fe, N. Mex., May 9-11, 1978.*
97. M. M. H. Ragheb and C. W. Maynard, *Calculated Neutron and Gamma Irradiation Response of Actively Cooled Mirrors for Laser Fusion Power Reactors*, University of Wisconsin, Madison, Wis., UWFDM-218 (1977).

98. J. E. Howard, *Beam Port Reduction Scheme for a Laser Fusion Reactor*, University of Wisconsin, Madison, Wis., UWFDM-244 (1978).
99. E. F. Plechaty, D. E. Cullen, and R. J. Howerton, *Tables and Graphs of Photon Interaction Cross Sections from 1.0 keV to 100 MeV Derived from the LLL Evaluated Nuclear Data Library*, Lawrence Livermore Laboratory, Livermore Calif., UCRL-50400, Vol. 6, Rev. 1 (1975).
100. M. Sparks and M. Guinan, "Radiation Damage and Heating of the First Mirror in Proposed Commercial Laser Fusion Systems," (to be published).
101. J. C. Davis et al., "Rotating Target Neutron Source II: Progress Report," in *Proc. of the 2nd Topical Mtg. Tech. of Contr. Nucl. Fusion, Richland, Wash., Sept. 21-23, 1976*, Conf-760935-P4, Vol. IV.
102. A. Buffington et al., "Correction of Atmospheric Distortion with an Image Sharpening Telescope," *J. Opt. Soc. Am.* 67 (3) (1977).
103. J. E. Pearson and S. Hansen, "Experimental Studies of a Deformable-Mirror Adaptive Optical System," *J. Opt. Soc. Am.* 67 (3) (1977).
104. R. P. Grosso and M. Yellin, "The Membrane Mirror as an Adaptive Optical Element," *J. Opt. Soc. Am.* 67 (3) (1977).
105. J. A. Maniscalco, W. R. Meier, and M. J. Monsler, *Design Studies of a Laser Fusion Power Plant*, Lawrence Livermore Laboratory, Livermore, Calif., UCRL-80081 (1977).
106. J. J. Devaney, *Injection of Laser Fusion Pellets*, Los Alamos Scientific Laboratory, Los Alamos, N. Mex., LA-7477-MS, Part I (1978).
107. R. G. Tomlinson et al., *Pellet and Laser Beam Space-Time Interaction System Study*, United Technologies, E. Hartford, Colo., UTRC-R78-954373-1 (1978).
108. Itek Corporation, *48 inch Aperture High Performance Tracking Telescope*, Lexington, Mass., technical bulletin.
109. United Detector Technology, Inc., Santa Monica, Calif., Reticon Corp., Sunnyvale, Calif., or Silicon Detector Corp., Newbury Park, Calif.; Photodetector sales brochures.
110. E. J. Nalos, "New Developments in Electromagnetic Energy Beaming," *Proc. of the IEEE* 66 (3) (1978).

Author

M. J. Monsler

9.2.9 Environmental and Safety Considerations

We integrated environmental and safety factors into all phases of the HYLIFE converter design from the onset of its development. Safety issues must be identified and quantified early in the evolving design, though it is difficult to do so. Environmental and safety considerations significantly influence such engineering choices as the selections of structural materials and methods to contain tritium.[111]

Environmental and safety issues are increasingly important to the government and the public. Many current problems in the nuclear fission industry are attributable to an overzealous advocacy of nuclear electric power generation in the late 1950's along with little early consideration of environmental issues.

Our task in the HYLIFE converter design study has been to adequately claim the realistic promises of the concept while beginning to identify problems and to suggest ways to solve them. We have addressed the following concerns:

- Choice of materials for minimum activation.
- Identification of source terms for shielding design.
- Requirements for remote maintenance systems.
- Incorporation of safety features in the design.
- Plant layout and isolation systems.

We discuss each concern in this subsection.

Induced Activation in Structural Materials. Two steels appear to offer a good combination of strength, compatibility with liquid lithium, and reasonably low activation when protected from the total output of the fusion pellet in the HYLIFE chamber. Type-316 stainless steel (SS) is a commonly used material in many large pressure-container structures. Several magnetic-fusion conceptual designs make use of Type-316 SS, notably the University of Wisconsin Tokamak system UWMAK-I.

Our original liquid-lithium waterfall concept for a laser fusion reactor called for Type-316 structural steel. We discovered, however, that the nickel in stainless steel presents two problems. Nickel is leached out of the outer layers of Type-316 SS during lithium corrosion. This process creates a ferritic layer that may shield the remainder of the steel from some further corrosion.[112] A greater problem is that nickel activates in fast-neutron reactions to produce isotopes of cobalt, which emit high-energy gamma rays and have relatively long half-lives.

These observations led us to consider ferritic 2.25 Cr–1.0 Mo as the HYLIFE structural steel. This ferritic alloy is presently ASME-approved for use in steam generator construction in nuclear power plants. It offers good resistance to lithium corrosion at temperatures up to 500°C and contains no nickel.

Figure 9-49 presents a comparison of radioisotopes produced in both Type-316 SS and 2.25 Cr–1.0 Mo ferritic steels. The isotopes are arranged in order of increasing half-life. The activity, in curies, of each isotope was computed based on 1 yr

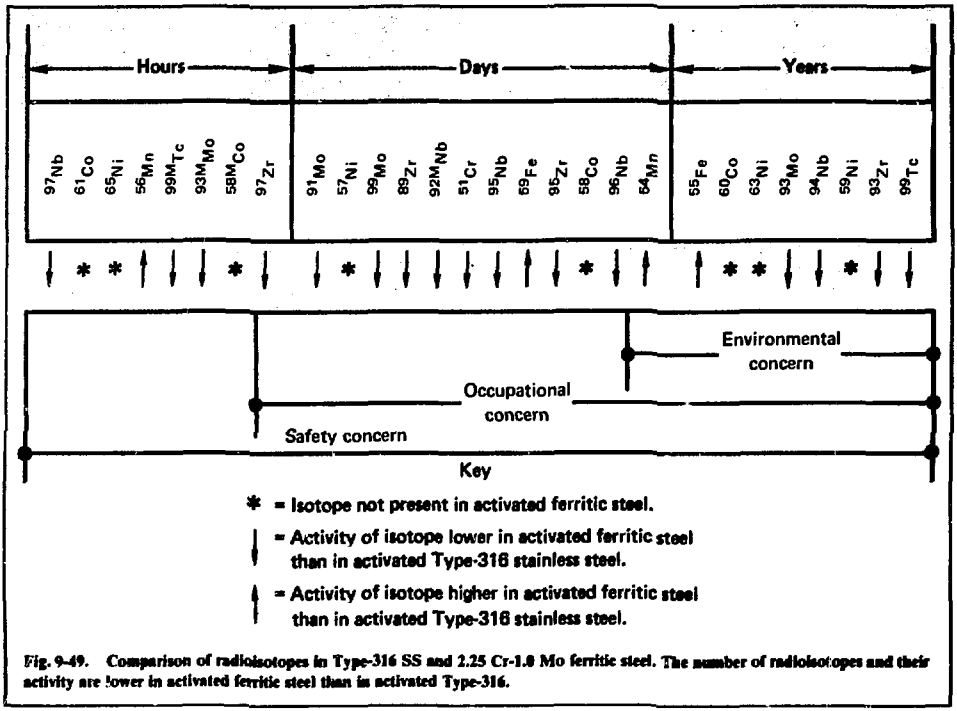

Fig. 9-49. Comparison of radioisotopes in Type-316 SS and 2.25 Cr-1.0 Mo ferritic steel. The number of radioisotopes and their activity are lower in activated ferritic steel than in activated Type-316.

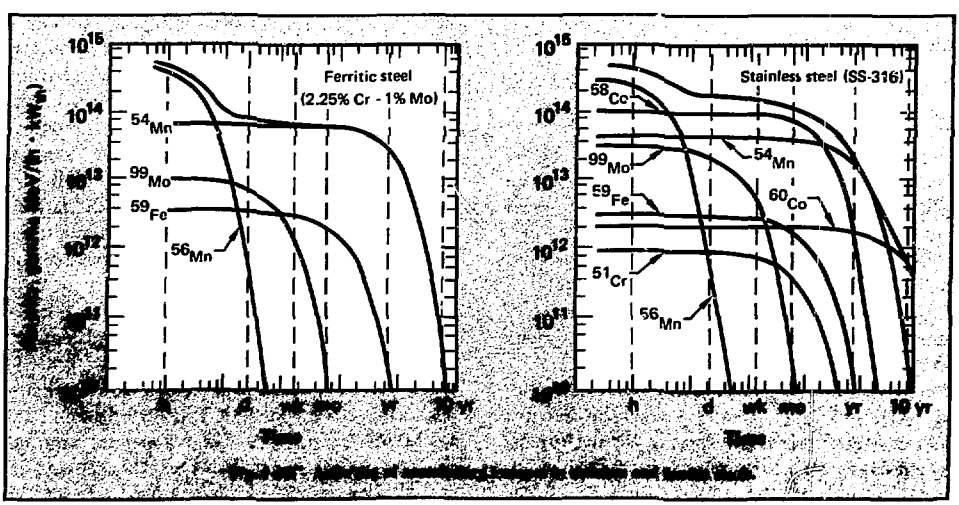

of operation in the HYLIFE chamber at 3176 MW_t.[111] Only those radioisotopes parented by iron are produced in increased amounts in ferritic steel compared to Type-316 SS.

Another parameter of interest in comparing activation in the two steels is their respective rates of gamma energy output. Figure 9-50 shows the gamma emission rates for significant isotopes in the two steels, and Fig. 9-51 compares the total emission rates. The data presented in the two figures were calculated for activation during 1 yr of full-power reactor operation. Throughout the important period for maintenance and inspection between 1 d and 1 mo after shutdown, ferritic steel emits approximately one-third as much gamma energy per hour as Type-316 SS. Beyond 8 yr after shutdown, the dominant gamma emitter in Type-316 SS is ^{60}Co (5.27-yr half-life, E_γ = 1.13 MeV and 1.33 MeV). In ferritic steel, ^{93}Mo (100-yr half-life, E_γ = 0.03 MeV) is dominant; it is not on the scale of Fig. 9-51 because of its low activity.

Once we selected 2.25 Cr-1.0 Mo ferritic steel as the structural material in the HYLIFE converter,[113] we were able to proceed with more detailed 2-D activation calculations to comprehensively define the source term in HYLIFE chamber steel for environmental and shielding applications.

We soon found that this material, when protected by a 1-m effective thickness of liquid lithium, activates even less than some exotic materials especially chosen to reduce the level of radioactivity in other fusion-reactor first-wall designs.[114]

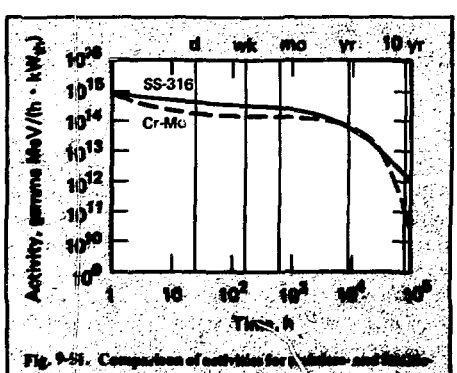

Fig. 9-51. Comparison of activities for [illegible] steel structures.

Figure 9-52 compares the activation of HYLIFE chamber steel to that of various magnetic-confinement first-wall structures after 2 yr of operation at a wall loading of 1.25 MW/m^2. For the period from shutdown to 2 wk, during which time much maintenance and inspection would be performed, the ferritic steel activity is greatly below any MFE structural material, including aluminum alloy. In the long term, HYLIFE chamber activity falls to a negligible level in approximately 1000 yr, as ^{93}Mo decays. As we show in a subsequent subsection, this time can be significantly reduced if one or more of the parent isotopes of ^{93}Mo is separated from the feed molybdenum used in the ferritic steel structure.

Activation in the ferritic steel structure is quite unevenly distributed. Figure 9-53 shows that over 93% of the induced radioactivity is produced in the zones of steel immediately adjacent to the lithium flow within the chamber. Because the average gamma ray emitted from radioisotopes in the activated ferritic steel has an energy of approximately 0.8 MeV, outlying layers of less activated material in the chamber will provide significant self-shielding. Remote systems will still be required for maintenance and inspection operations near or on the chamber exterior surfaces; however, the radiation environment encountered by such devices will be relatively benign, requiring, for example, little special protection for remote television cameras.

The same may not be true for electronic components inserted directly into the chamber center for inspection and servicing of the first-wall assembly. Figure 9-54 illustrates the gamma exposure rate at the HYLIFE chamber center after 1 yr of operation. The exposure rate will remain above 10 R/s to beyond 2 wk following shutdown. Similar curves follow for exposure rates 1 m from the chamber side and 1 m above the chamber top, with values scaled down by factors of 6.2 and 38.75, respectively, from the rates shown in Fig. 9-54.

The long-term radioactivity remaining in the structure after final shutdown is of concern from the standpoints of decommissioning and dismantling the reactor and reducing wastes that ultimately must be isolated from humans. Figure 9-55 shows exposure rates at the chamber center after a full service life of 30 yr at a 0.7 capacity factor. The activity of ^{54}Mo (E_γ = 0.835 MeV) falls off rapidly between 10 and 20 yr, but ^{93}Mo sustains an exposure rate greater than 10 mR/h to 800 yr after shutdown.

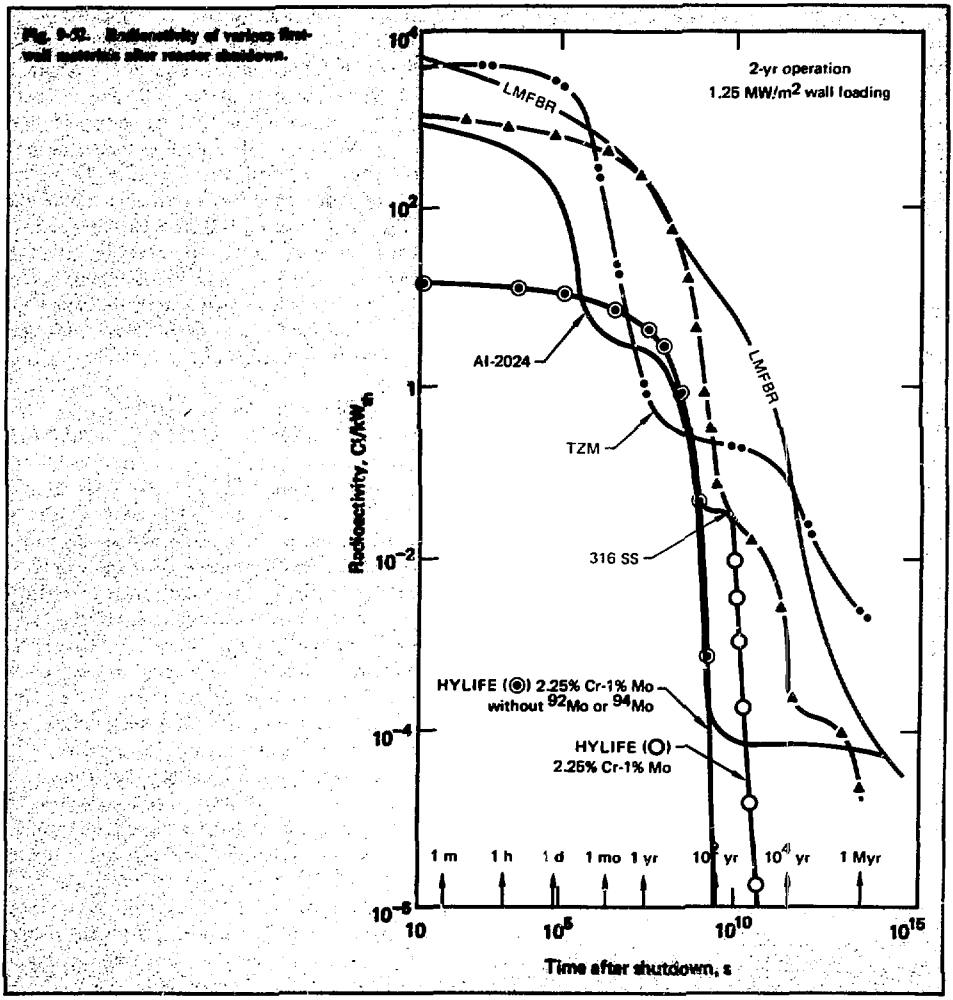

The scientific feasibility of laser isotope separation of molybdenum isotopes has been demonstrated in laboratory experiments.[115] If this or other processes prove economical with large feed quantities, removal of ^{92}Mo to two orders of magnitude below its natural abundance (14.8%) can move the 10-mR/h exposure rate point to less than 20 yr after shutdown. This is shown by the bottom curve in Fig. 9-55 for ^{93}Mo activity resulting only from fast neutron reactions in ^{94}Mo. This feature would greatly reduce the environmental impact of long-term radioactive wastes from nuclear fusion power production. It raises the engaging possibility of reprocessing reactor steels after brief cool-down times.

Shielding Source Term. We have completed calculations on the production and inventory of radioisotopes in the HYLIFE chamber, including decay times up to 50 yr after shutdown and production of radioactive daughters during decay. Some of

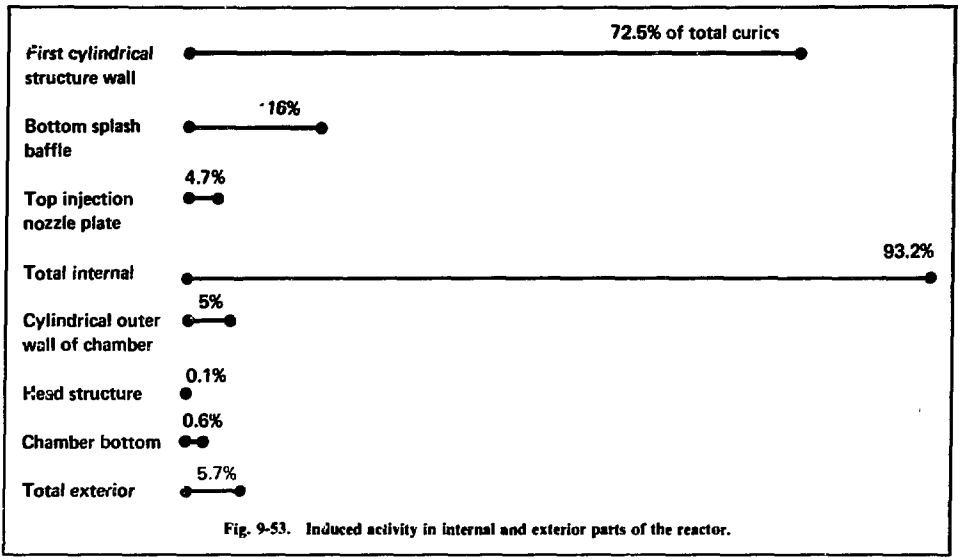

Fig. 9-53. Induced activity in internal and exterior parts of the reactor.

our results are used in the preceding analysis and in first-order bulk-shielding computations. Walls of Portland concrete (normal density, $\rho = 2.35$ g/cm^3) that are 2-m thick will reduce the exposure rate in the pump cells surrounding the HYLIFE chamber by a factor of 1.62×10^{11}, allowing contact maintenance if activity in the lithium flow, or from aggregated radioactive corrosion products, is sufficiently low.[114]

We also compiled spectral data for the neutron and gamma ray fluences at various points in the

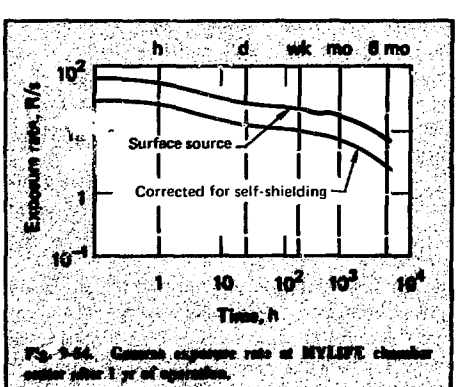

Fig. 9-54. Gamma exposure rate at HYLIFE chamber outer after 1 yr of operation.

HYLIFE chamber during operation. However, exposure rates during full-power operation have not yet been calculated, since such rates will be strongly dependent upon neutron and photon streaming in ducts and voids in the reactor and associated piping. More detailed design and analysis are required before further shielding computation is meaningful.

Remote Systems Requirements. Scheduled and unscheduled maintenance using remotely controlled systems may be required during both operation and shutdown on components located in high-radiation areas. Also, inspection of walls, piping flanges and welds, and other lithium loop components may require remote viewing techniques. We believe that many of the systems already in use in hot-cell or fission-reactor operations may be directly applicable in the HYLIFE power plant. Certainly, the ingenious systems designed for first-wall inspections in the much more hostile Tokamak environment could be used in HYLIFE with modification.

Regularly scheduled maintenance may be needed on

- Chamber head assembly and injection nozzles.
- Chamber interior and openings.
- Pellet injection apparatus.
- Laser beam tunnel components.
- Lithium cleanup traps.

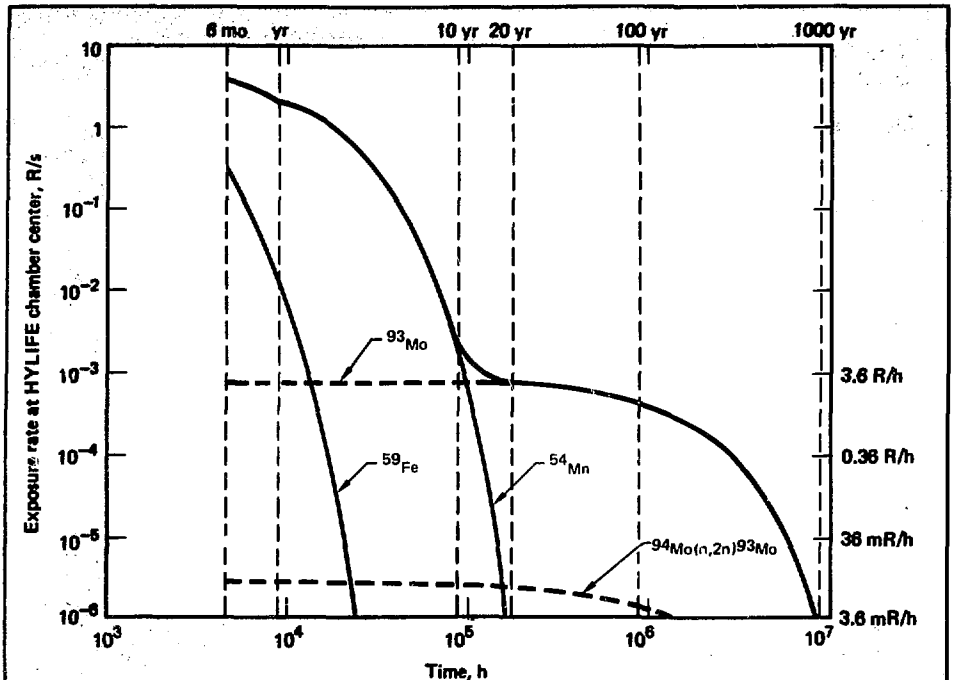

Fig. 9-55. Exposure rate for long times after shutdown following 30-yr operation at 0.7 capacity factor.

- Pumps, casings, and valves.
- Laser beam optics.

The reactor building is equipped with an overhead crane for head and major component handling. Operations using the crane will be performed either from a neighboring viewing room or by using remote television monitors. Another television system of great application might be a remotely controlled mobile cart with a boom-mounted, fully articulated television head and grappling mechanism. After the head or plug of the HYLIFE chamber is raised, such a device could be lowered into the chamber for visual inspection or maintenance.

Inspections during operation or while the HYLIFE chamber is shut down may be required on

- Piping, flanges, and welds.
- Interior wall of chamber.
- Injection plates and splash baffle.
- Beam tube coupling and blast baffles.
- Pellet injection tube.
- Pumps and valves.
- Components of tritium extraction facility.
- Lithium cleanup traps

Many of these areas will require remote viewing systems. We believe, however, that systems presently in use for LMFBR's and LWR's can be applied with little modification, since the layout of major components and the cell design of the HYLIFE converter building are similar to those of present reactors.

Safety Features. Many safety features are intrinsic to the design. We incorporated others to reduce both the possibility and consequences of an accident.

During operation of the reactor, isolation systems and comparted building construction ensure the ability to rapidly close off an accident area and thereby limit the spread of radiation or chemical hazards. These isolation features include

- Reactor containment building separated from the laser building.
- Separate pump, intermediate heat exchanger, and tritium processing cells.
- Fast-acting valves and narrow aperture windows in the final turning optics.
- Separate steam generator and turbine building.
- Isolated lithium storage and processing systems with drain tank capacity exceeding the volume of lithium in the plant.

Perhaps the most cogent isolation feature intrinsic to the HYLIFE power plant is simply the physical separation of the laser from the fusion reaction. This, combined with an ability to rapidly dump and store the primary lithium coolant, effectively separates energy-bearing systems from one another and from the main site of radioactivity, the HYLIFE chamber.

Liquid-lithium spills probably present the greatest accident consequences in the HYLIFE power plant design. When ignited and burned in air, lithium produces flame temperatures high enough (>2000°C) to melt the ferritic steel used in the plant. However, nitrogen or an inert gas such as helium or argon will either prevent ignition entirely or limit flame temperatures to below 1300°C.[116] The many characteristics and design safety features to limit lithium spill and fire hazards are described in the following excerpts from a Bechtel report[117]:

- Liquid-metal systems operate at low pressure relative to LWR's. Consequently, failure is less likely and, should it occur, would be less catastrophic.
- Systems containing lithium or sodium are designed and fabricated to the highest standards. Conservative design, in addition to system inspections, provide confidence that a large system break will not occur. If small cracks were to occur, they would be detected by instrumentation or inspection, and the system would be drained before leakage became significant.
- Should lithium or sodium leak into a space, the steel cell liners would prevent reactions with the water in the concrete. Because of conservative design, only a small amount of concrete would be exposed to react in the unlikely event of a cell liner crack.
- An atmosphere of helium in the chamber cell and argon in other areas containing lithium is maintained to prevent reactions with air in case of a leak. Backup "inerting" systems are available if primary systems fail.
- Systems are separated so that an accident in one area would not affect the entire plant.
- The actual amount of tritium associated with a hypothetical spill of lithium is a small portion of the total inventory of tritium in the plant. For example, if 10% of the lithium were spilled, this would release about 5% of the tritium in the plant. Based on exposure estimates by the Electric Power Research Institute, the tritium released would give an integrated dose of less than 2 rem over a 1-km^2 area adjacent to the plant.

Containment of Radioactivity. The presence of physical barriers to prevent the release and spread of radioactive isotopes is necessary both for normal operational safety and for environmental and public safety during an accident. We have included three barrier types within and around those areas bearing radioactivity and have provided for a fourth barrier, if needed, as follows:

- Primary reactor boundary.
- Compartmentalized cells in the vicinity of the reactor.
- Reactor containment building.
- Secondary containment (confinement).

The primary reactor boundary is the chamber itself, including the fast-acting valves for isolating the chamber from the tunnel complex extending out to the final turning optics. The laser tunnel is a vacuum vessel and will be designed to contain whatever tritium, activated pellet materials, and corrosion products and other isotopes present in the lithium vapor might be blown into the tunnel at each fusion pulse. A layout of the chamber and tunnel system portion of the reactor containment building (RCB) is shown in Fig. 9-34 (§9.2.6).

Figure 9-56 illustrates the cells in the RCB. The cells are bounded by concentric walls of concrete 2-m thick and by radial walls 1.5-m thick. Surfaces subject to contact with lithium in a spill, or those containing tritium, are lined with 0.635-cm-thick steel and insulation, as required. This cellular mode of design is also carried out in the tritium recovery and processing area, in pump and trap systems, and throughout the intermediate heat transfer loop.

Containment of all sources of radioactivity is provided within the overall RCB. The isolation valves in the final laser optics system are part of this barrier. Components and subsystems in the RCB include

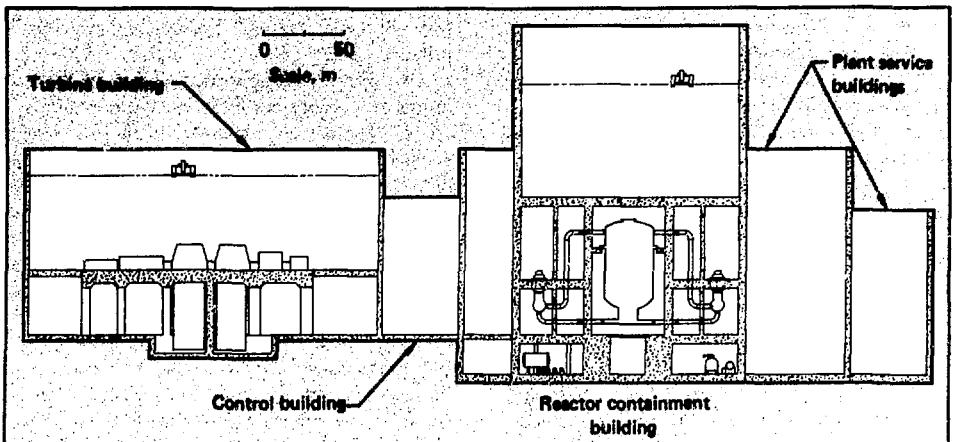

Fig. 9-56. Elevation of HYLIFE reactor facility.

- Chamber and laser tunnels.
- Pellet manufacturing facility and storage of pellets.
- Pellet injector.
- Tritium extraction, cleanup, and storage.
- Liquid-metal loops.
- Coolant cleanup traps and storage tanks.

Finally, we considered providing a secondary containment shell structure around the entire primary reactor containment building. The gap between the two barriers would be maintained at a negative pressure to prevent leakage to the environment of any radioisotopes or chemicals passing across the primary containment barrier. In fact, this additional protection may not be required. The overall radioactive hazard present in the HYLIFE converter is substantially lower than that of comparably-sized fission power plants or other fusion schemes. The decision whether to incorporate secondary containment will have to be made weighing the relatively low risk to the public, along with the soundness of the cellular and primary reactor containment structures.

Licensing Considerations. We compared HYLIFE power plant characteristics to the licensing requirements that are anticipated to be imposed on fusion power plants. Thorough design is required for preparation of the required Safety Analysis Report (SAR), and the report for the HYLIFE plant may differ in detail from present-day SAR's for fission plants. Nevertheless, it is helpful to consider the major licensing issues likely to appear. Because so much of the HYLIFE system is similar to LMFBR plants, a standard SAR for this type of liquid-metal-cooled reactor was used by Bechtel National, Inc., as a basis for a conceptual SAR for the HYLIFE plant.[117] Some of their findings are included in the following conclusions.

Conclusions. The HYLIFE design provides significant environmental and safety advantages when compared to present-day nuclear fission technology, or to most other concepts of magnetic or inertial fusion. These include:

- Induced activation in the structure and in pellet materials is relatively low and is manageable with existing techniques.
- Long-term radioactive waste is practically nonexistent.
- Areas requiring remote maintenance and inspection can be served with present-day systems for LMFBR in most cases.
- No large-scale replacement of activated structure is required for the entire service life of the plant.
- Energy-bearing systems are physically isolated from each other and from the activated structure.

Technological Development. Several issues remain to be resolved in achieving a full understanding of the HYLIFE environmental and safety characteristics. Experiments that can be conducted in the near future to resolve these issues include:

- Corrosion and transport of radioisotopes in a dynamic lithium loop, including spontaneous trapping phenomena.
- Solubility definition to establish levels of bromine from tritium removal to be expected in the coolant flow.
- Activation cross sections for bromine and debris in the coolant, and ferritic steel in the HYLIFE structure, to validate computer calculations.

Major technological development is needed for the following items:

- Tritium containment structure throughout the extraction, bottling, and pellet fabrication processes.
- Traps and cool-down storage facilities for removal of radioisotopes from the liquid-lithium flow.
- Specific remote systems for special applications such as chamber interior inspection and servicing.

References

111. P. Walker, "Environment and Safety Features of a Lawrence Livermore Laboratory Laser Fusion Reactor Design," in *Proc. 3rd ANS Topical Mtg. on the Tech. of Cont. Nucl. Fusion, Santa Fe, N. Mex., May 9-11, 1978.* Also, Lawrence Livermore Laboratory Report UCRL-80564.
112. J. Selle and D. Olson, "Lithium Compatibility Research—Status and Requirements for Ferrous Materials," *Materials Considerations in Liquid Metals Systems in Power Generation* (National Association of Corrosion Engineers, 1978).
113. M. Monsler et al., *Electric Power from Laser Fusion: The HYLIFE Concept*, Lawrence Livermore Laboratory, Livermore Calif., UCRL-81259 (1978).
114. P. Walker, *Remote Systems Requirements of the High Yield Lithium Injection Fusion Energy (HYLIFE) Converter Concept*, Lawrence Livermore Laboratory, Livermore, Calif., UCRL-81309 (1978).
115. S. D. Winter, Advanced Isotope Separation Systems Studies Group, Lawrence Livermore Laboratory, Livermore, Calif., personal communication (Feb., 1979).
116. D. Dube and M. Kazimi, *Analysis of Design Strategies for Mitigating the Consequences of Lithium Fire Within Containment of Controlled Thermonuclear Reactors*, Department of Nuclear Engineering, MIT, C bridge, Mass. (1978).
117. Bechtel National, Inc., *Conceptual Design Study of the HYLIFE Lithium Waterfall Laser Fusion Facility* (Nov., 1978).

Author

P. E. Walker

Major Contributors

S. Winter
H. Meldner
N. Hoffman
(Energy Technology and Engineering Center)

9.3 Fission–Fusion Hybrid Reactors

9.3.1 Introduction

We have been investigating the potential of laser-fusion-driven hybrid reactors at LLL for several years. Initially, neutronic studies[118,119] were used to identify attractive hybrid blanket configurations and to estimate an upper bound on their performance. More recent hybrid studies of engineering, environmental, and economic issues, as well as neutronic aspects, were carried out in collaboration with Bechtel Corp.[120-122] and Westinghouse Corp.[123]. In general, these studies confirmed the attractive features suggested by our neutronic studies.

Several other important features of laser-fusion-driven hybrids emerged from the more detailed engineering design studies. Most importantly, we found that these hybrids will cost at least twice as much as light water reactors (LWR's) and probably more than fission breeder reactors, but the cost of electricity is insensitive to the capital cost of a hybrid that provides fissile fuel for LWR's. The cost of electricity increases by only 20 to 40% when the capital cost of the hybrid ranges from two to three times that of an LWR.

We also conclude that fissile fuel production is the most attractive use of a fusion–fission hybrid. Simultaneous electricity production is desirable only because it makes the fuel product cheaper. A hybrid that produces fissile fuel results in system electricity costs lower than those of a power producer and more directly satisfies our energy needs.

The engineering design studies were based on hybrids that produce plutonium for use in LWR's. In 1978, we analyzed laser-fusion-driven hybrids that produce ^{233}U for consumption in modified

LWR's and in advanced converter reactors such as heavy water reactors (HWR's), spectral shift control reactors (SSCR's), or high-temperature gas reactors (HTGR's).[124,125] A ^{233}U-producing hybrid is attractive for two reasons: ^{233}U is a more efficient fuel than plutonium for thermal fission reactors, and the ^{233}U–thorium fuel cycle may be less vulnerable to proliferation than the uranium–plutonium fuel cycle.

The possibility of commercial nuclear power increasing the proliferation of nuclear weapons has led to an indefinite postponement of reprocessing and recycling of plutonium. The current national energy policy also calls for an intensive search for alternative reactors and nuclear fuel cycles that do not allow direct access to materials used in nuclear weapons. If reprocessing is not allowed, hybrids could still be used as power producers with throwaway fuel cycles.

Such hybrid power plants could be fueled with either thorium or depleted uranium, thus taking advantage of the energy multiplication characteristics of fuels that are abundant and cheap. Hybrid systems will be significantly more expensive than LWR's; therefore, electricity generated from hybrids that do not produce fissile fuel will cost substantially more than it does now. However, one advantage over an LWR's fuel cycle would remain: no uranium mining, milling, or enrichment would be required.

We estimate that a depleted uranium hybrid blanket could multiply fusion neutron energy more than 15-fold. Therefore, this power-producing hybrid could operate with fusion energy gains one-tenth that required for pure fusion power production. With fuel burnups of 30,000 MW·d/Mg, this system would increase the energy extracted from uranium in a throwaway fuel cycle by a factor of five.

Another nonreprocessing option is the fissile enrichment of depleted uranium fuel by irradiating it in a hybrid. The fuel would subsequently be used in an LWR. The feasibility of this approach depends primarily on the development of high-burnup fuel elements that could operate in both a hybrid and an LWR. Alternatively, the enriched hybrid fuel could be partially reprocessed without removing the fission products. The hybrid fuel would be declad, ground up, homogenized, and compacted into LWR fuel pins. All of these operations would be conducted at high cost in shielded hot cells. Either of these fissile-fuel-producing options could provide enough fuel for two LWR's of equivalent output power. This is a three-fold reduction in the fissile fueling capability available with full reprocessing.

All of the nonreprocessing options that we have considered produce fissile fuel less efficiently and generate more costly electricity than do the reprocessing options. The hybrid scheme we propose to prevent proliferation requires reprocessing, and it would work like the scheme proposed by Feiveson and Taylor[126] for a fission economy based on fast breeders and thermal converters. In this approach, thermal fission reactors would be supplied with ^{233}U that has been diluted with enough ^{238}U that it is no longer weapons grade material.

A fission-fuel-producing complex consisting of a fusion breeder, a fuel-reprocessing facility, and a fuel-fabricating facility would be located in a safeguarded area. The complex would provide denatured uranium to thermal burner reactors located outside secure areas. However, with ^{238}U in their fuel, the thermal reactors would produce some plutonium; therefore, their spent fuel must be removed and shipped back to the safeguarded fuel complex, where the plutonium can be removed. It would then be either burned in the fusion breeders or stored. The more thermal reactors that can be fueled from a ^{233}U-producing hybrid, the smaller the fraction of energy that must be generated in secure areas under government control.

Two attractive ^{233}U-producing blankets have been identified from neutronic scoping calculations and incorporated into the LLL/Bechtel[122] hybrid design. Incorporating these blankets into our existing engineering design allows us to evaluate the overall performance of laser-fusion-driven ^{233}U producers. In evaluating the two fusion breeders, we have estimated (1) the number of fission converter reactors (LWR's, SSCR's, HWR's, and HTGR's) they can fuel, (2) their capital cost, and (3) the cost of electricity in the combined fusion breeder–converter reactor scenario. We also investigated the sensitivity of electricity costs, in the combined scenarios, to fusion breeder capital costs and to whether the fusion breeder produces electricity.

9.3.2 Neutronic Scoping Studies

In our neutronic scoping studies, we sought a blanket configuration that maximizes ^{233}U production per unit of thermal energy while maintaining an

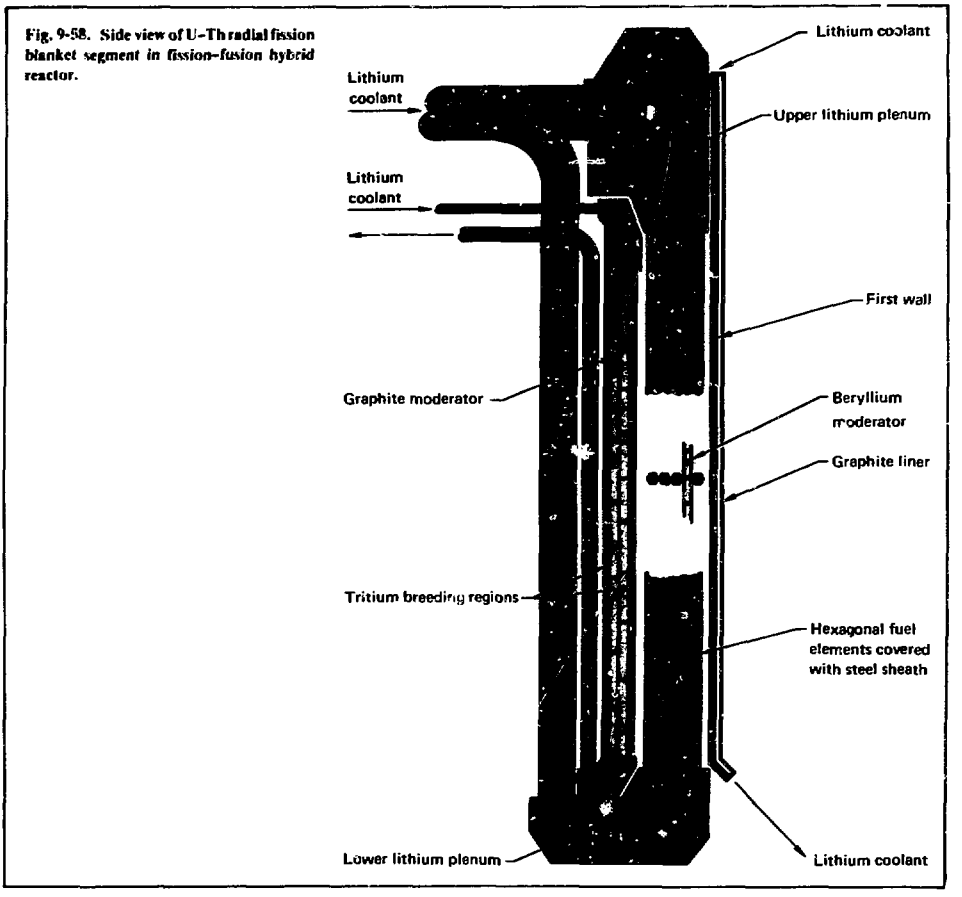

Fig. 9-58. Side view of U–Th radial fission blanket segment in fission–fusion hybrid reactor.

2300 and 3290 MW of thermal power, respectively. The higher energy multiplication of the U–Th blanket leads to a fusion breeder that produces twice as much net electricity (671 MW_e vs 335 MW_e). This excess electricity can be sold to reduce the price of the ^{233}U produced. However, this enhanced energy multiplication is gained at the expense of a 40% reduction in ^{233}U production per unit of thermal energy.

The ^{233}U production capabilities of both fusion breeders can be put in perspective by looking at the number of thermal burner reactors they can fuel. Figure 9-59 gives the number of equivalent thermal-power LWR's, SSCR's, HWR's, and HTGR's that each of the fusion breeders can fuel. The ^{233}U consumption rates for the LWR, SSCR, and HWR were obtained from Ref. 127. The consumption rate for the HTGR was based on a system with a conversion ratio of 0.85. We should also note that all consumption rates are for denatured uranium (12% ^{233}U).

The performance of the LLL/Bechtel hybrid should be compared to that of the ^{233}U-producing hybrids. The LLL/Bechtel hybrid produces 0.88 $kg/MW_t \cdot yr$ of ^{239}Pu—enough to fuel 6.25 LWR's, 7.73 SSR's, 10.0 HWR's, or 6.6 HTGR's of equivalent thermal power. It is also interesting to compare the ^{233}U production rates of the Th and

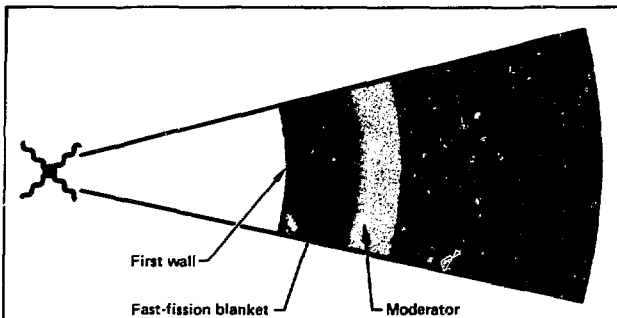

Fig. 9-57. Schematic of a ^{233}U-breeding hybrid blanket.

adequate tritium breeding ratio (TBR). Maximum fusion energy multiplication was an important, but secondary, objective. Specifically, we wanted a blanket design that produces more than 1 kg of ^{233}U per $MW_t \cdot yr$ of thermal energy, while maintaining a TBR greater than one and multiplying the fusion energy as much as four-fold.

We performed exploratory calculations using spherical coordinates, with the fission zone sandwiched between a sacrificial first wall and a tritium breeding region. We considered two ^{233}U-producing hybrid blankets: a thorium (Th) blanket and a uranium–thorium (U–Th) blanket.

Figure 9-57 is a schematic representation of the U–Th blanket, which consists of a uranium fast-fission zone surrounded by a moderator region and a Th blanket. We investigated the performance of both the Th and the U–Th blankets for various zone thicknesses, fission fuel types (metal or carbide), coolant types (sodium, lithium, or enriched lithium), and moderator types (beryllium or graphite). The volume fractions of fuel, coolant, and structure in the fission blankets were selected to be consistent with compositions used in the LLL/Bechtel hybrid. In all cases, a ferritic steel (2.25 Cr–1.0 Mo) was used as the structural material in the fuel cladding and blanket.

9.3.3 Two-Dimensional Calculations

We carried out 2-D calculations on the most attractive Th and U–Th blankets obtained from the spherical calculations. The blanket configurations were revised to closely approximate the engineering features and cylindrical geometry of the LLL/Bechtel hybrid. The fission blanket in these calculations is a 10-m-high cylindrical shell with an inner radius of 5.93 m. The first wall is a sacrificial liner of graphite blocks that are attached to, and supported by, a lithium-cooled molybdenum structure. Lithium-cooled tritium-breeding blankets are positioned in the top and bottom of the reactor and behind the radial fission blanket. The fission blankets selected for the 2-D calculations were a 35-cm-thick thorium blanket, cooled with natural lithium, and a U–Th blanket with a 5-cm-thick zone of uranium-metal fuel, cooled with enriched lithium (40% ^6Li by weight).

A side view of the U–Th radial fission blanket is shown in Fig. 9-58. The uranium fission zone is composed of one row of hexagonally shaped steel process tubes containing a 7-rod cluster of steel clad uranium-metal fuel pins. The moderator between the uranium and thorium zones is a 10-cm-thick region of beryllium. The thorium zone consists of three rows of steel process tubes containing a 19-rod cluster of steel clad thorium-metal fuel pins. In the Th blanket system, the uranium and beryllium zones were eliminated.

9.3.4 Analysis of Fusion Breeders

To evaluate and compare the Th and U–Th fusion breeders, we selected laser and target parameters that appear feasible in light of current technology. The selected parameters and the resulting performance of the two ^{233}U producers are presented in Table 9-9. In both designs, fusion targets producing 100 MJ of fusion energy are irradiated by a 1-MJ laser at 13 Hz. The 1300 MW_t of fusion power is multiplied by 1.77 in the Th blanket and by 2.53 in the U–Th blanket, yielding

Table 9-9. System performance of two laser-fusion-driven ^{233}U producers. (The 1-MJ, 13-Hz, 4-beam laser system is 3% efficient, and the pellet has a gain of 100 and a yield of 100 MJ.)

	Thorium	Uranium-thorium
Thermal power, MW_t	2300	3290
Thermonuclear power, MW_t	1300	1300
Plutonium production, $kg/MW_t \cdot yr$	0	0.61
^{233}U production, $kg/MW_t \cdot yr$	1.9	1.10
Gross electrical power, MW_e	828	1184
Laser input power, MW_e	433	433
Auxiliary power, MW_e	60	80
Net electrical power, MW_e	335	671
Recirculating power fraction	0.60	0.43
System efficiency	14.6%	20.4%
Av blanket energy multiplication	1.77	2.53
Av tritium breeding ratio	1.05	1.15
Av first-wall neutron flux, MW/m^2	2.35	2.35

U–Th blankets to those of an LMFBR. The production rates for oxide-, carbide-, and metal-fueled LMFBR's have been estimated at 0.077, 0.115, and 0.134 $kg/MW_t \cdot yr$, respectively.[127]

9.3.5 Cost Analysis

Capital cost estimates for Th and U–Th fusion breeders allow us to estimate both the cost of ^{233}U produced by these facilities and the cost of electricity from fission burner reactors that use the ^{233}U. Both blanket designs are similar to the LLL/Bechtel hybrid design; hence, their cost has been estimated by extrapolating from the most recent estimate for the reference blanket.[122] The cost per kW_t of the LLL/Bechtel hybrid without a laser or a target fabrication facility was shown to be approximately 1.75 times that of an LWR. Major differences between the LLL/Bechtel hybrid and the fusion breeders discussed here include the following:

- Lithium replaces sodium as a coolant in the fission zones of the ^{233}U producers.
- Ferritic steel replaces stainless steel as the structural and fuel-cladding material in the ^{233}U producers.
- The ^{233}U producers have lower blanket power densities for a given first-wall flux.
- The ^{233}U producers have less thermal power than the 4000-MW_t reference system.

The first two points should make the ^{233}U producers less expensive than the reference system, while the last two should make them more expensive. [The effects of less power output can be seen by noting that a 600-MW_e LWR costs approximately 45% more (per kW_t) than a 1200-MW_e LWR.] Accounting for all four points, we estimate the following capital cost ranges (per kW_t) for the Th and U–Th fusion breeders without lasers and target fabrication facilities.

- Th system cost: 1.7 to 2.2 × LWR cost.
- U–Th system cost: 1.5 to 2.0 × LWR cost.

The LWR we took as a reference costs \$284/kW_t in 1978 dollars. It was taken to be a 1200-MW_e plant, ordered in 1978 for delivery in 1987. This reference LWR produces electricity at 35.2 mills/kW·h with a 16% rate of return on capital, assuming operation and maintenance charges of 3.66 mills/kW_t·h and uranium costs of \$43/lb. With \$100/lb uranium, it will produce electricity for 40.1 mills/kW·h.

We have not done detailed cost studies on the laser system or target fabrication facility. If we allow \$400 million for the laser and \$100 million for the target fabrication facility, the cost range of the Th fusion breeder becomes 2.5 to 3.0 times that of the reference LWR. For the U–Th system the cost range becomes 2.0 to 2.5 times that of the reference LWR. The effect of these capital cost ranges on the cost of ^{233}U from the Th and U–Th fusion breeders is shown in Table 9-10. The cost of ^{233}U ranges from 65 to 80.9 \$/kg for the Th system and from 69.6 to 97.0 \$/kg for the U–Th system. The last entry in Table 9-10 gives an indication of how much the cost of ^{233}U increases when the excess electricity is not sold.

The cost of electricity from fission burner reactors that have been supplied with ^{233}U from the Th and U–Th fusion breeders is shown in Fig. 9-60. To determine the cost of electricity from the HWR and SSCR, relative to the LWR, we made the following estimates[128]: (1) the capital cost of the HWR was

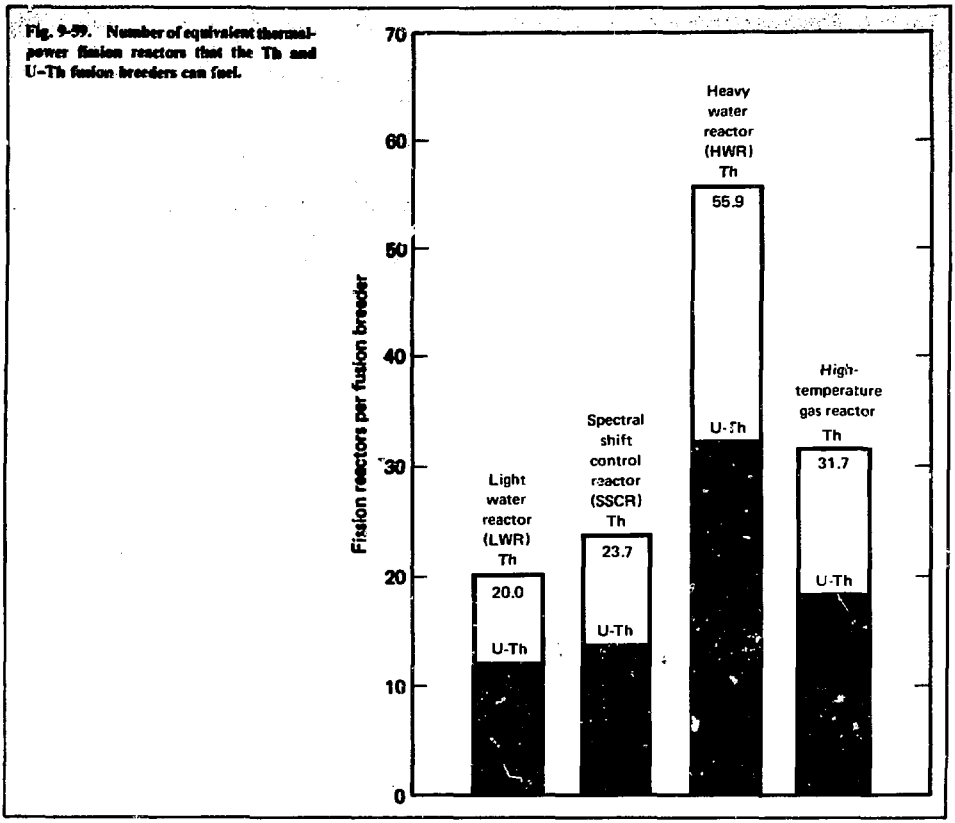

Table 9–10. Cost summary for the ^{233}U-producing fusion breeders.

Capital cost estimate	Thorium hybrid		Uranium–thorium hybrid	
	2.5 X LWR	3.0 X LWR	2.0 X LWR	2.5 X LWR
Revenues required for capital cost at 16% rate of return, $/kW·yr	114.2	137.0	92.5	115.2
Revenues required for fusion breeder fuel cycle,[a] $/kW·yr	12.1	12.1	12.1	12.1
Revenues from sale of electricity at 35 mills/kW·hr and 75% capacity factor, $/kW·yr	−33.5	−33.5	−46.9	−46.9
Cost of ^{233}U at 75% capacity factor, $/g	65.0	80.9	69.6	97.0
Cost of ^{233}U at 75% capacity factor with no revenues from electricity, $/g	88.4	104.3	126.1	153.5

[a]For thorium fuel, fabrication = $30/kg, reprocessing = $300/kg, burnup = 10 MW·d/kg.
For uranium fuel, fabrication = $30/kg, reprocessing = $170/kg, burnup = 6 MW·d/kg.

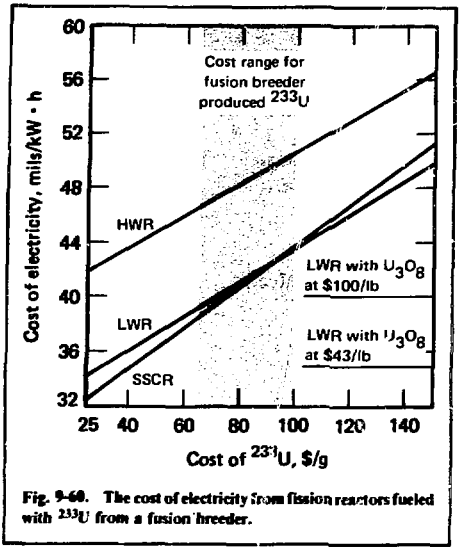

Fig. 9-60. The cost of electricity from fission reactors fueled with ^{233}U from a fusion breeder.

taken to be 15% higher than that of the reference LWR; with an additional cost of $160/kW$_e$ for heavy water, and (2) the capital cost of the SSCR was taken to be 5% higher than that of the reference LWR, with an additional cost of $40/kW$_e$ for the heavy water reactor inventory.

Finally, the contribution of the ^{233}U–Th fuel cycle to the cost of electricity for all the fission reactors has been estimated on the basis of the data in Table 9-11. The refabrication, spent-fuel shipping, and reprocessing costs were compiled and averaged from Refs. 127 and 129-131. The high refabrication and reprocessing costs for ^{233}U–Th fuels result from the need to remotely handle radioactive fuel in shielded facilities.

The results shown in Fig. 9-60 are encouraging. They indicate that thermal burner reactors fueled by fusion breeders can supply the world with reasonably priced electricity for hundreds of years. Assuming U^{233} prices of 65 to 100 $/g, LWR's and SSCR's produce electricity that costs from 38.5 to 44 mills/kW·h. This is only 10 to 25% higher than the cost of electricity from the reference LWR, with $43/lb uranium. Unfortunately, the HWR, with the best ^{233}U utilization (Fig. 9-59), produces electricity at higher cost than do the other two reactors: 46.5 to 51 mills/kW·h, when the price of ^{233}U ranges from

Table 9-11. Fuel cycle cost bases for thermal reactors using ^{233}U–Th fuels.

	Cost basis	Reactor type
Refabrication	$300/kg HM[a] $200/kg HM	LWR, SSCR HWR
Spent fuel shipping	$20/kg HM $15/kg HM	LWR, SSCR HWR
Reprocessing	$300/kg HM	LWR, SSCR, HWR
Plant capacity factor	75% 80%	LWR, SSCR, HWR
Fixed charge rate on capital	16%	
Present worth discount rate	10%	
Basic inflation rate	6%	

[a]Heavy metal.

65 to 100 $/g. We had expected the cost of electricity from HWR's to be more expensive at lower ^{233}U prices, but less sensitive to ^{233}U price increases. Instead, we found the HWR's better fuel utilization to be outweighed by higher fuel cycle costs (associated with the HWR's lower fuel burnup limits) and higher ^{233}U inventory requirements.

References

118. J. A. Maniscalco, "Fusion-Fission Hybrid Concepts for Laser-Induced Fusion," *Nuc. Tech.* **28**, 98 (1975).
119. A. G. Cook and J. A. Maniscalco, *^{233}U Breeding and Neutron Multiplying Blanket for Fusion Reactors*, Lawrence Livermore Laboratory, Livermore, Calif., UCRL-77284 (1975).
120. J. A. Maniscalco, *A Conceptual Design Study for a Laser Fusion Hybrid*, Lawrence Livermore Laboratory, Livermore, Calif., UCRL-78682 (1976).
121. L. F. Hansen and J. A. Maniscalco, *Neutronic Study of a Laser Fusion Hybrid Reactor Design*, Lawrence Livermore Laboratory, Livermore, Calif., UCRL-78069 (1976).
122. Bechtel Corporation, *Laser Fusion-Fission Reactor Systems Study*, Lawrence Livermore Laboratory, Livermore, Calif., UCRL-13796 (1977).
123. L. F. Hansen, R. R. Holman, and J. A. Maniscalco, "Scoping Studies of Blanket Designs for a Power-Generating Laser Fusion Hybrid Reactor," *Trans. Am. Nuc. Soc.* **26** (1977).
124. J. A. Maniscalco and L. F. Hansen, "New Initiatives in Laser Driven Fusion-Fission Energy Systems," in *Report on the 2nd MFE-Fusion-Fission Energy Systems Review Mtg.*, Lawrence Livermore Laboratory, Livermore, Calif., UCRL-81509 (1977).
125. J. A. Maniscalco, L. F. Hansen, and W. O. Allen, *Scoping Studies of a ^{233}U Breeding Fusion Fission Hybrid*, Lawrence Livermore Laboratory, Livermore, Calif., UCRL-80585 (1978).

126. H. A. Feiveson and T. B. Taylor, *Bull. of Atomic Scientists* **32**, 14 (1976).
127. Y. I. Chang et al., *Alternative Fuel Cycle Options: Performance Characteristics and Impact on Nuclear Power Growth*, Argonne National Laboratory, Argonne, Ill., ANL-77-70 (1977).
128. S. Strauch, Deputy Director, U.S. Department of Energy, Office of Fuel Cycle Evaluation, private communication (April, 1978).
129. Atomic Industrial Forum, *Reprocessing-Recycle Economics*, (Nov. 10, 1977).
130. P. R. Kasten et al., *Assessment of the Thorium Fuel Cycle in Power Reactors*, Oak Ridge National Laboratory, Oak Ridge, Tenn., ORNL-TM-5565 (1977).
131. N. L. Shapiro et al., *Assessment of Thorium Fuel Cycles in Pressurized Water Reactors*, Electric Power Research Institute, Palo Alto, Calif., EPRI NP-359 (1977).

Authors

J. A. Maniscalco
(now at Exxon Research and Engineering Co.)

L. F. Hansen

W. O. Allen
(Bechtel National, Inc.)

Major Contributor

W. R. Meier

SECTION 10

CONTENTS

SECTION 10

SELECTED HIGHLIGHTS OF ADVANCED ISOTOPE SEPARATION PROGRAM

10.1 Introduction

Laser isotope separation (LIS) involves a general class of photophysical and photochemical processes that center about the use of very monochromatic laser radiation to selectively isolate particular isotopes of atoms or isotopically substituted compounds. The isotope differences that are important for LIS are evident in the electronic and vibrational spectra of these species. They appear as slight shifts in the absorption spectra of atoms and molecules (typically 5 to 10 GHz for atomic uranium). Coherent laser sources are available with line widths (0.1-1.0 GHz) and frequency stabilities (typically 1-5 MHz) that can easily resolve these isotope shifts. Consequently, by the absorption of tuned laser radiation, it is easy to excite and preferentially ionize the isotope of interest.

It was this atomic vapor process that was used at LLL in early 1975 to demonstrate enrichment of macroscopic quantities of reactor grade uranium. Since the pioneering Morehouse Project, we have been evaluating the technology options and physics scaling laws for LIS processes that use the atomic vapor. Studies performed by LLL indicate that laser isotope separation of uranium, using the atomic vapor process, can reduce not only the capital and operating costs for primary enrichment plants, but can also provide an economic means of processing tails from the present gaseous diffusion plants and planned gas centrifuge plants.

The major advantages from such processes stem from a large (about 10 times) reduction in plant capital costs. Such costs dominate the present enrichment enterprise:

- Expansion of capacity, which permits more efficient tails stripping, is limited by plant capital costs.
- Enrichment services contracts would be controlled by the capital turnover rates, if existing technologies (gaseous diffusion, gas centrifuge) were used by the private sector.
- Uprating of installed plant capacity is currently capital-intensive.

The projected sharp reduction in plant capital costs gives uranium LIS high economic leverage, even if we realize no further gains in separative work unit costs (presently more than $100/SWU). Our program goal is to develop processes that can enrich uranium up to light water reactor (LWR) grade and also achieve efficient tails stripping with FY 1980 unit costs in the range $10 to $40/SWU.

Based on our projections of reduced power, capital, and operating costs for a large-scale LIS uranium enrichment facility, we have implemented an Advanced Isotope Separation (AIS) program. The main objectives that dictate the structure of our long-range AIS research and development plan are, first, to demonstrate the technology of an LIS reference process as soon as possible and, second, to assure that we meet the economic target of the LIS process by actively developing backup and advanced technology to complement the mainline technology, thus increasing the potential of the process to surpass the target.

Of the many feasible and economic options for subsystem development open to us, all use near-term technology and various subsystems. We have developed candidate designs for each option, most of which are interchangeable for integration into a final LIS process. The economic payoff is potentially high for several options. We are therefore keeping the options open, presently preferring not to single out any one set of subsystems for system integration. This approach reduces the residual risk and also increases the potential for achieving costs even lower than now projected.

The AIS program is structured in four major stages:

- Technology Evaluation (1978-80)—to determine basic process parameters and to establish component scaling relations.
- Component Development and Integration Demonstration (1980-84)—to scale process compo-

nents to final size and to integrate them into an operating system.

- Engineering Demonstration (1984-87)—to establish the operability, maintainability, and economic feasibility required for commitment to a full-scale production facility.
- Production Demonstration (1987-92)—to bring a full-scale plant on-line for commercial production.

The time schedules are tentative, reflecting the unpredictability of funding and national goals for nuclear power.

It should be emphasized that the key systems components for the atomic vapor processes advocated in this program already exist. In the past year, we have focused on research engineering of many subsystems with an eye toward initial scale-up. Our efforts generally have been quite successful, and we have followed our projected time schedules. Although many scientific and technical questions remain before engineering hardening and commercialization of the atomic vapor process can begin, we are encouraged by our continuing progress. Through an appropriate and timely allocation of resources, we believe all potential problems can be solved.

Detailed descriptions and reviews of developments in uranium LIS at LLL are given elsewhere.[1] In this section we present only a few selected highlights of the AIS program, representing some of the supporting research. An important theme of the experiments described here is that proved methods for generating a scientific data base for uranium have been successfully applied to related atomic and molecular systems. The purpose of such experiments is twofold:

- To create a body of information on which comparisons to uranium can be drawn to extend our predictive capabilities.
- To investigate economically attractive alternate applications of program technologies.

Section 10.2 describes experiments using laser techniques pioneered at LLL that have unraveled the excited state spectra of the atomic actinide neptunium (Np). In §10.3 we focus on experiments bearing on the role of laser excitation on reaction rates and dynamics in vapor-phase atom-...olecule collisions. In §10.4 we examine laser-induced unimolecular decomposition of important isotopic compounds in both solid and vapor states. Section 10.5 updates recent theoretical developments describing the behavior of atoms and molecules bathed in intense resonant or nearly resonant light fields. The results are important for modeling photophysical and photochemical systems of interest. Finally, in §10.6 we review some laser technology developments during the past year. These advances impact not only on the uranium LIS effort but also on those alternate applications of program technologies under study.

Reference

1. J. I. Davis and R. W. Davis, "Some Aspects of the Laser Isotope Separation Program at Lawrence Livermore Laboratory," in *Proc. of Annual Meeting of the American Institute of Chemical Engineers* (Chicago, Ill., Nov. 28-Dec. 2, 1976).

Authors

J. I. Davis
J. A. Paisner

10.2 Atomic Vapor Actinide Laser Spectroscopy—Neptunium

To investigate neptunium, we have used the laser spectroscopy techniques[2,3] developed to study uranium and the lanthanides. The first ionization potential (IP) of Np was determined by both the threshold of photoionization and the convergence of Rydberg series. Thresholds and Rydberg series were obtained from several different laser-populated excited levels. The Rydberg convergence values are the most accurate and yielded a value of 50,536(4) cm^{-1} [6.2657(5) eV] for the IP of Np.* This value is somewhat larger and much more accurate than the values obtained by surface ionization[4] [6.16(6) eV], by appearance potential[5] [6.1(1) eV], or from the $5f^5 7s^2$ to $5f^5 7s8s$ interval [6.19(12) eV].[6] The lifetimes of five levels were determined, and estimates of transition probabilities were made from emission intensities.[7] For the three-step excitation of the Rydberg series, it was necessary to determine new high-lying levels because none were known[8] in the required energy range.

*Numbers in parentheses give the uncertainty in the final digit.

10.2.1 Experimental

The experimental apparatus used has been described in detail.[3,9] In the experiments, an atomic beam of Np was irradiated sequentially in time by the output of two or three tunable pulsed dye lasers. These lasers stepwise-excited and photoionized the atoms (threshold detection) or populated bound Rydberg levels, which were field-ionized.

The Np beam was generated, using a resistively heated tungsten tube oven containing a single crystal tantalum crucible loaded with 0.5 g of pure ^{237}Np metal. Sufficient vapor density for our experiments was produced by heating the oven to 1900 K or less. Because of the vapor pressure relation between Np and NpO,[10] and because no quadrupole filtering was used in the field ionization experiment, it was necessary to eliminate NpO from the source by heating at about 1650 K for approximately 12 h. Because NpO can absorb at the laser wavelengths used, this procedure avoided background photoionization of the NpO.

10.2.2 Ionization Potential

We first determined the photoionization threshold because it is easy to recognize and it would give us an ionization potential accurate to 30 cm^{-1}. We used this potential to limit the region of search to find Rydberg series. For the threshold searches, we used two-step photoionization techniques. Our search range, determined by the uncertainties and variation in the reported[4–6] IP values, was about 2400 cm^{-1} or 430 Å. Figure 10-1 shows a photoionization threshold of Np marked by the onset of very strong dense autoionization features.

Autoionizing Rydberg series were sought but none were found because of the very dense autoionization structure from "valence" levels. To obtain Rydberg series in Np, it was necessary to apply ionization techniques[2] where the bound Rydberg levels were ionized by a pulsed electric field applied several microseconds (5 μs, in this case) after the last populating laser was fired. This postpopulation ionization allowed decay of the shorter-lived

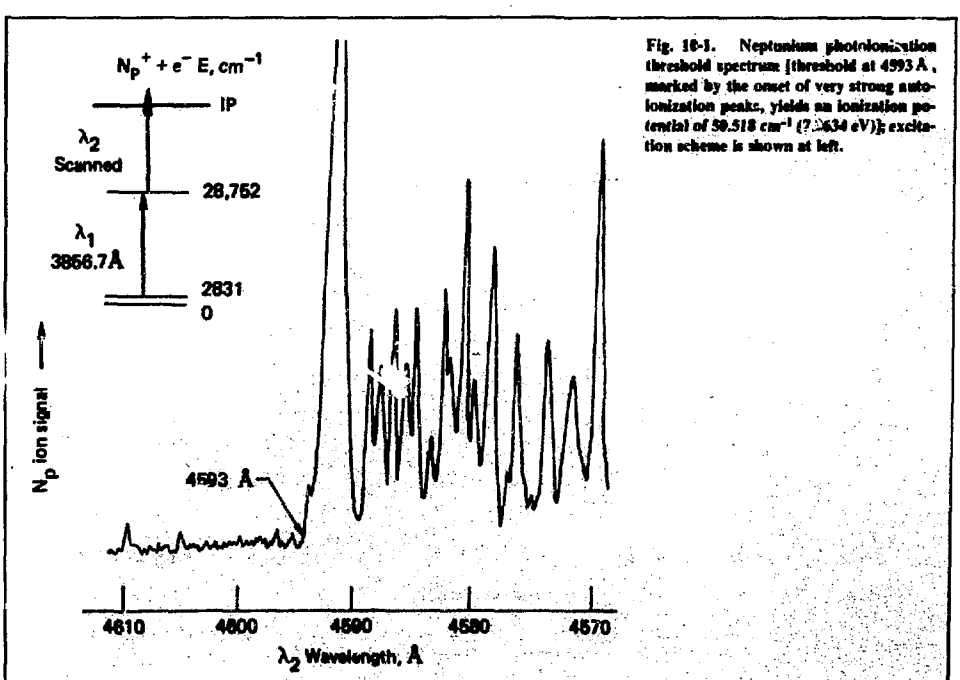

Fig. 10-1. Neptunium photoionization threshold spectrum [threshold at 4593 Å, marked by the onset of very strong autoionization peaks, yields an ionization potential of 50.518 cm^{-1} (?.634 eV)]; excitation scheme is shown at left.

Table 10–1. *First ionization potentials of neptunium determined by various techniques.*

Ionization potential, cm^{-1} [eV]	Method	Reference
49,685(480) [6.16(6)]	Surface ionization	4
49,200(610) [6.1(1)]	Appearance potential	5
49,930(970) [6.19(12)]	$f^5 7s^2$-$f^5 7s8s$ interval interpolated	6
49,950 [6.193]	Semiempirical	11
50,517(25)[a] [6.2633(30)[a]]	*Photoionization* threshold	This work
50,536(4) [6.2657(5)]	Rydberg series	This work

[a]Uncertainty based on observed differences between photoionization thresholds and Rydberg series limits in uranium and the lanthanides (Refs. 2 and 3).

valence states that would obscure the Rydberg series. Several series were obtained by this technique.

10.2.3 Results

The photoionization thresholds were obtained using two-step excitation schemes. Six thresholds from six different excited states of Np were determined. The values obtained varied from 50,514 to 50,521 cm^{-1} and yielded an average value of 50,517(6) cm^{-1} [6.2633(7) eV]. While the precision of the threshold value is very good, it is 19 cm^{-1} below the more accurate ionization potential obtained from Rydberg convergence limits (see Table 10-1). The same approximate difference (15 to 40 cm^{-1}) between the threshold value and the Rydberg convergence value was found for the lanthanides and for uranium. The difference is attributed to an

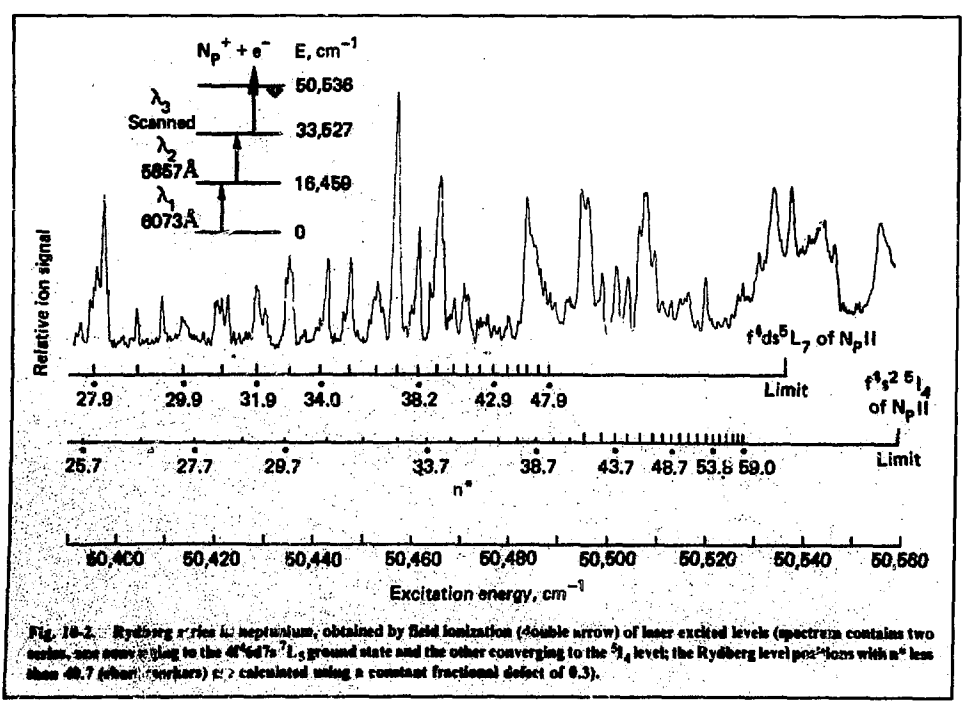

Fig. 10-2. Rydberg series in neptunium, obtained by field ionization (double arrow) of laser excited levels (spectrum contains two series, one converging to the $4f^46d7s\,^7L_5$ ground state and the other converging to the $^5I_4$ level; the Rydberg level positions with n* less than 49.7 (short vertical markers) are calculated using a constant fractional defect of 0.3).

unknown experimental parameter, such as electric fields from ion optics, intense laser radiation, and/or collisional effects.

Eight Rydberg convergence limits were obtained by three-step excitation techniques and one by two-step excitation. A three-step scan containing two Rydberg series is shown in Fig. 10-2. The excitation scheme is shown at the left. The 1.3-μs-wide field ionization pulse of 7000 V/cm was applied 5 μs after the laser 3 pulse. As indicated in the figure, one series converges to the $5f^4 6d7s^7L_5$ ground state of the ion while the other series converges to the $5f^4 7s^2\ ^5I_4$ level 24.27 cm^{-1} above the ground state.† For the latter series, the shorter markers are calculated positions, assuming that the fractional part of the quantum defect $(n - n^*)$ was constant at 0.3. This is the value obtained from the higher members (longer markers) of the series.

†We are indebted to J. Blaise, Laboratoire Aime Cotton, Orsay, France, and to M. Fred, Argonne National Laboratory, Argonne, Ill., for providing us with the unpublished low-lying energy levels of singly ionized Np.

As can be seen, these two series explain most of the observed features. In addition to the two limits at 0.00 and 24.47 cm^{-1}, Np has a third limit at 83.49 cm^{-1} above the ground state, so that many of the unexplained features in the scan could be Rydberg members converging to this limit. The next limits are more than 900 cm^{-1} away.

Values of n^* for the Np series were determined using the equation

$$n^* = [R/(\text{assumed level} - \text{level value})]^{1/2} . \qquad (1)$$

The variation in quantum defect $(n - n^*)$ vs n with change in assumed limi for the two series in Fig. 10-2 is shown in Figs. 10-3 and 10-4. The value of n is not necessarily the principal quantum number but a number chosen close to n^* to evaluate the variation in quantum defect. The series convergence limit (ionization potential) is taken as the assumed limit that gives the most constant quantum defect as a function of n for the high-quantum-number Rydberg levels.

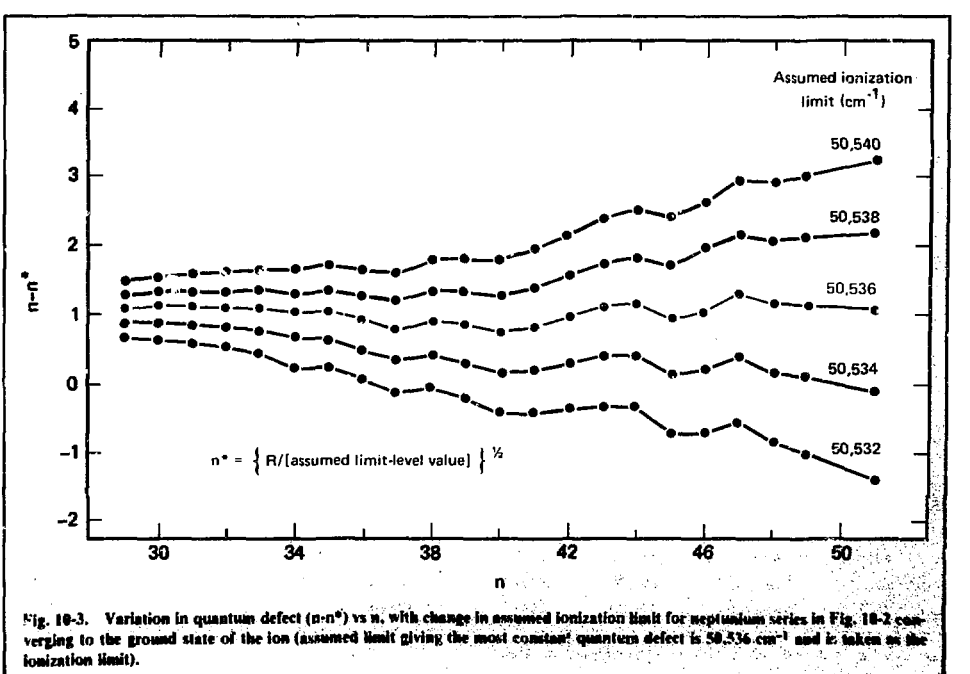

Fig. 10-3. Variation in quantum defect (n-n*) vs n, with change in assumed ionization limit for neptunium series in Fig. 10-2 converging to the ground state of the ion (assumed limit giving the most constant quantum defect is 50,536 cm^{-1} and is taken as the ionization limit).

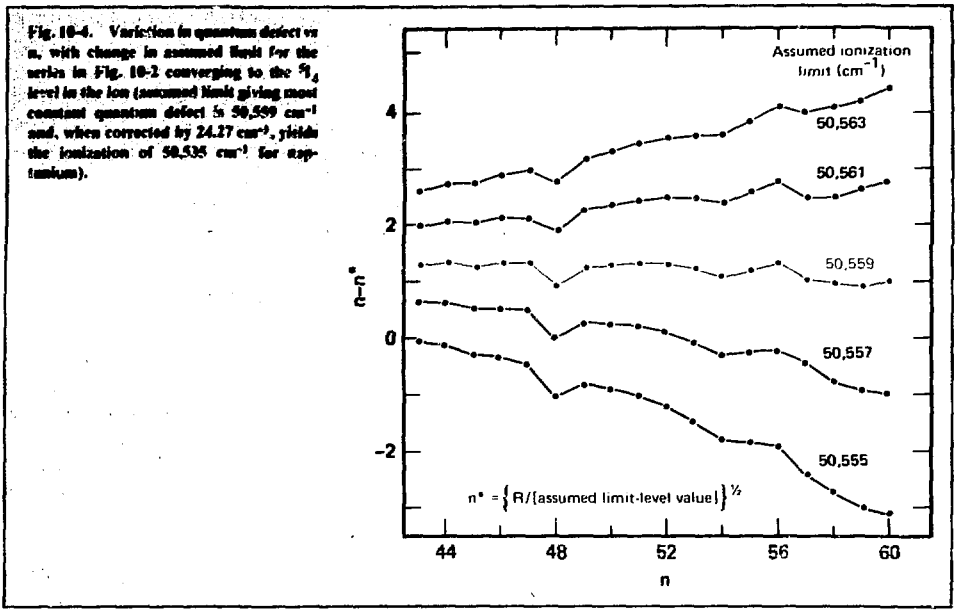

Fig. 10-4. Variation in quantum defect vs n, with change in assumed limit for the series in Fig. 10-2 converging to the $^6I_{\frac{1}{2}}$ level in the ion (assumed limit giving most constant quantum defect is 50,559 cm^{-1} and, when corrected by 24.27 cm^{-1}, yields the ionization of 50,535 cm^{-1} for neptunium).

For the three Rydberg series converging to the level in the ion 24.27 cm^{-1} above the ground state, the convergence limit was corrected by 24.3 cm^{-1} to yield the ionization potential.

By this method, three values of 50,535(4) cm^{-1}, five values of 50,536(4) cm^{-1}, and one value of 50,537(3) cm^{-1} were obtained from the nine observed Rydberg series. These yield a value of 50,536(4) cm^{-1} for the ionization potential of Np. The uncertainty is considerably larger than the standard deviation of the nine values and represents the estimated uncertainty in obtaining limits from the quantum defect plots (see Figs. 10-3 and 10-4).

Table 10-1 summarizes the ionization potential determinations for neptunium. Our values are higher but more accurate than the other experimental findings and the value obtained by Rajnak and Shore,[11] which was based on regularities in electron binding energies in $l^N s^M$ configurations. The ionization potential derived from Rydberg series is the most accurate value. The surface ionization[4] and appearance potential[5] values are lower than this

Table 10-2. Lifetimes of five excited states of neptunium and estimated branching ratios and transition probabilities.

Excited level,[a] cm^{-1}	Lifetime, ns	Transition,[a] cm^{-1} Odd	Even	Wavelength,[a] Å	Branching ratio,[b] B.P.	Transition probability, A, 10^6 s^{-1}
26,264.37	108 ± 10	0	26,264	3806.4	0.5 ± 0.2	4.2 ± 2
27,824.89	37 ± 3	2033	27,824	3876.2	0.7 ± 0.1	19 ± 3
28,752.40	40 ± 3	28,752	2831	3856.7	0.8 ± 0.1	20 ± 3
28,986.45	76 ± 5	28,986	2831	3822.2	0.9 ± 0.1	12 ± 1.4
29.023.76	288 ± 25	29,023	2831	3816.8	0.9 ± 0.1	3 ± 0.4

[a]Level energy, transition assignment, and wavelength from Ref. 7.

[b]Branching ratio estimated from intensities in Ref. 7.

value beyond the quoted uncertainties. Sugar's value,[6] obtained from interpolated f^n7s^2 to f^n7s8s intervals in the actinides, agrees within the uncertainties.

10.2.4 Lifetimes and Transition Probabilities

The lifetimes and new levels were determined using techniques explained in detail elsewhere.[2] Lifetimes were determined from plots of the natural logarithm of the ion signal vs delay time between the photoionizing laser pulse and the populating pulse.

Lifetimes of two even and three odd levels of Np are given in column 2 of Table 10-2. The transition and its wavelength are listed in columns 3 and 4. The branching ratios (B.R.) in column 5 were estimated from unpublished data of M. Fred et al.[7] These branching ratios were used with the equation:

$$A = B.R./\tau \ , \qquad (2)$$

to calculate the transition probabilities given in column 6. The uncertainties estimated for the branching ratios and the transition probabilities may be conservative. The uncertainties could be as large as 50% of the value.

10.2.5 New High-Lying Levels

New high-lying even and odd levels were found by multistep photoionization techniques. These new levels were determined during our search for three-step laser excitation of Rydberg levels. To obtain the levels, laser 1 was fixed at a known wavelength to populate an odd or even level in the range 16,000 to 19,000 cm^{-1}. Laser 2 was scanned over the desired wavelength range, and laser 3 was fixed at a wavelength to ionize any levels populated by scan laser 2. We found 37 even levels and 27 odd levels.

The high even levels of Np are reported in Table 10-3. Searches were made from three different levels. Their wavelengths, energies, and J's are the headings for columns 1, 2, and 3 of the table. Column 4 gives the average energy of the levels found. The estimated uncertainty in the level energy is less than 0.5 cm^{-1} when observed from two or more odd levels, and about 1 cm^{-1} when observed from only one level. Because the odd levels used have J values of 4.5 and 6.5, the selection rule $\Delta J = 0, \pm 1$ can be used to assign J values (see column 5). The only case where an unequivocal assignment can be made is for the value 5.5. Further searches from other levels could improve the J assignment.

High odd levels obtained in a search from the 19,373.87 cm^{-1}, J = 3.5 even level are listed in Table 10-4. They are uncertain by about 1 cm^{-1}. Their J value can be 2.5, 3.5, or 4.5.

These energy level searches are by no means a complete coverage of the energy ranges. They were performed to obtain levels for use in our three-step laser excitation studies. Six of the levels were used to search for Rydberg series.

References

2. L. R. Carlson, J. A. Paisner, E. F. Worden, S. A. Johnson, C. A. May, and R. W. Solarz, "Radiative Lifetimes, Absorption Cross Sections, and the Observation of High Lying Odd Levels of ^{238}U Using Multistep Laser Photoionization," *J. Opt. Soc. Am.* **66**, 846-853 (1976).
3. R. W. Solarz, C. A. May, L. R. Carlson, E. F. Worden, S. A. Johnson, J. A. Paisner, and L. J. Radziemski, "Detection of Rydberg States in Uranium Using Time-Resolved Stepwise Laser Photoionization," *Phys. Rev.* **A14**, 1129-1136 (1976), and E. F. Worden, R. W. Solarz, J. A. Paisner, and J. G. Conway, "First Ionization Potentials of Lanthanides by Laser Spectroscopy," *J. Opt. Soc. Am.* **68**, 52-61 (1978).
4. D. H. Smith and G. R. Hertel, "First Ionization Potentials of Th, Np and Pu by Surface Ionization," *J. Chem. Phys.* **51**, 3105-3107 (1969).
5. E. G. Rauh and R. J. Ackermann, "The First Ionization Potentials of Neptunium and Neptunium Monoxide," *J. Chem. Phys.* **62**, 1584 (1975).
6. J. Sugar, "Revised Ionization Energies of the Neutral Actinides," *J. Chem. Phys.* **60**, 4103 (1974).
7. M. Fred and F. S. Tomkins, Argonne National Laboratory, Argonne, Ill., and J. E. Blaise, P. Camus, and J. Berges, Laboratoire Aime Cotton, Orsay, France, *The Atomic Spectrum of Neptunium*, Argonne National Laboratory, Argonne, Ill., ANL-76-68 (1976).
8. M. Fred, F. S. Tomkins, J. E. Blaise, P. Camus, and J. Verges, "Term Analysis of Neutral Neptunium (Np I)," *J. Opt. Soc. Am.* **67**, 7-23 (1967).
9. *Laser Program Annual Report—1976*, Lawrence Livermore Laboratory, Livermore, Calif., UCRL 50021-76 (1977), pp. 8-11.
10. R. J. Ackermann and E. G. Rauh, "The Thermodynamics of Vaporization of Neptunium and Plutonium," *J. Chem. Thermodyn.* **7**, 211-218 (1975).
11. K. Rajnak and B. W. Shore, "Regularities in s-Electron Binding Energies in $l^N s^M$ Configurations," *J. Opt. Soc. Am.* **68**, 360-367 (1978).

Author E. F. Worden

Major Contributor J. G. Conway

Table 10–3. High even levels of neptunium observed from the three odd levels given as headings for the first three columns (excitation wavelength, energy, and J value).

λ_1 wavelength, A	6188.59	6120.49	6073.59		
Odd level, cm^{-1}	16,154.29	16,334.00	16,459.34		
Odd level, J	4.5	6.5	4.5		
	Observed level energy, cm^{-1}			Even level[a] energy, cm^{-1}	Even level, J
	_[b]	33,128.4	_[b]	33,128.4	5.5,6.5,7.5
	_[b]	33,162.7	_[b]	33,162.7	5.5,6.5,7.5
	_[b]	33,176.3	_[b]	33,176.3	5.5,6.5,7.5
	_[b]	33,273.8	_[b]	33,273.8	5.5,6.5,7.5
	33,364.6		_[b]	33,364.6	3.5,4.5
	33,367.7		_[b]	33,367.7	3.5,4.5
	33,372.5	33,372.2	33,371.7	33,372.2	5.5
	33,435.4	33,434.3		33,434.8	5.5
	33,445.3	33,445.0	33,445.0	33,445.1	5.5
		33,454.5		33,454.5	6.5,7.5
	33,476.0		33,476.3	33,476.2	3.5,4.5
		33,487.8		33,487.3	6.5,7.5
	33,491.1		33,491.7	33,491.4	3.5,4.5
	33,495.7	33,495.8	33,495.7	33,495.7	5.5
	33,527.7	33,527.6	33,527.7	33,527.7	5.5
		33,538.4		33,538.4	6.5,7.5
	33,548.5		33,548.1	33,548.3	3.5,4.5
	33,556.5			33,556.5	3.5,4.5
	33,569.6			33,569.6	3.5,4.5
	33,582.7	33,582.3	33,582.4	33,582.5	5.5
	33,584.0	33,585.2		33,584.6	5.5
		33,608.4		33,608.4	6.5,7.5
			33,634.2	33,634.2	3.5,4.5
			33,641.5	33,641.5	3.5,4.5
	33,652.7	33,652.7	33,652.5	33,652.6	5.5
	33,673.4	33,673.3	33,673.2	33,673.3	5.5
	_[b]	33,679.5		33,679.5	6.5,7.5
	_[b]		33,684.9	33,684.9	3.5,4.5
	_[b]	33,703.3	33,704.1	33,703.7	5.5
	_[b]		33,712.5	33,712.5	3.5,4.5
	_[b]		33,717.7	33,717.7	3.5,4.5
	_[b]		33,729.4	33,729.4	3.5,4.5
	_[b]	33,736.0	33,736.2	33,736.1	5.5
	_[b]		33,742.5	33,742.3	3.5,4.5
	_[b]		33,761.0	33,761.0	3.5,4.5
	_[b]	33,770.4	33,770.3	33,770.4	5.5
	_[b]	33,774.0		33,774.0	6.5,7.5

[a]The uncertainty is ±0.5 cm^{-1} for levels with two or more observed values and ±1 cm^{-1} for the others.

[b]No search made.

Table 10-4. High odd levels of Np obtained from the 19,373.87 cm^{-1}, J = 3 ? even level, populated by λ_1 at 6043.?? Å (2831-19, 373); the J of the upper levels observed could be 2.5, 3.5, or 4.5.

λ_2, Å	Level,[a] cm^{-1}	λ_2, Å	Level,[a] cm^{-1}
5939.95	36,204.4	5804.95	36,595.8
5926.35	36,243.0	5803.21	36,600.9
5896.15	36,329.4	5769.67	36,701.1
5890.00	36,347.1	5764.26	36,717.3
5874.97	36,390.5	5764.01	36,718.1
5861.74	36,428.9	5757.35	36,738.1
5849.38	36,465.0	5755.02	36,745.2
5846.52	36,473.3	5753.15	36,750.8
5844.35	36,479.7	5742.77	36,782.3
5831.24	36,518.1	5736.25	36,802.0
5827.39	36,529.4	5735.00	36,805.8
5819.69	36,552.2	5723.63	36,840.5
5806.88	36,590.1	5713.06	36,782.8
		5700.63	36,910.9

[a]Level uncertainty is about ±1 cm^{-1}.

10.3 Laser Photochemistry and Reaction Dynamics

Several studies in laser photochemistry and reaction dynamics are detailed in this section. The common theme of each experiment in the first three subsections is the use of a laser to initiate chemical reactions by placing one of the reagents in a specific internal energy state favorable to the ensuing chemical reaction. By studying the forms of internal energy that effectively initiate such reactions and by measuring the reaction rates as a function of quantum number (E', V'', J''), a more complete picture of the dynamics of reactions, particularly those taking place at high temperatures, can be obtained. It is possible that the understanding developed from such studies may eventually result in improvements in commercially significant high-temperature chemical syntheses. The final two subsections outline recent survey work on the chemical and scattering behavior of high-Z atoms. This work was carried out to gain a basic understanding of the chemistry of these systems, so that parallels or contrasts in their behavior with that of lighter atoms could be used to improve current, isotopically selective, photochemical reactions of interest to the AIS program.

10.3.1 Reactions of Laser-Excited Atoms with Halogenated Methanes

In last year's annual program report[12] we presented our preliminary results on the reactions of laser-excited alkaline earth atoms with hydrogen halides and halogenated methanes. The reactions of these polyatomics with ground-state alkaline earth atoms to form the diatomic product are exothermic by a considerable amount. However, in several instances, these reactions are apparently inhibited by large barriers along the reaction coordinate. These reactions hold great promise for isotopically selective photochemistry because:

- The reaction cross sections, when the reactants are placed on a potential surface conducive to chemical reaction, are normally very large ($\sim 100\ Å^2$) because of the harpoon-like reaction mechanism.[13]
- Reactions can be initiated by a modest expenditure of energy when compared with reactions that are endothermic from the ground state and that require substantial energy simply to bring the reactants to thermoneutrality.
- A wide variety of reagents is available that assures maximum flexibility in reagent selection.

In the following pages we report our results on reactions of this type. The focus of our studies has been to determine the role of the electronic state of the atomic reagent in the outcome of these reactions, and to determine the state-to-state distributions of energy in these reactions in order to fully understand the dynamics of the reactions studied. In the reactions reported here, we study in a systematic fashion, using the method of laser-induced fluorescence,[14] the effect of electronic excitation of the attacking metal atom on carbon-halogen bond rupture.

The exoergic reactions of metal atoms with halogenated methanes have played an important role in the study of reaction mechanisms. Following the initial molecular beam studies of Brooks[15] on the reaction of potassium with oriented CF_3I, a number of reports appeared that expanded on the course of reaction and subsequent deposition of available energy in systems of this type. Observations by Nazar, Polanyi, and Skrlac (H + NOCl

and H + ICl),[16] and more recently work by Smith, Whitehead, and Zare (Ba + CF_3I),[17] suggest that there are two basic modes of attack in reactions of this type. It has been shown that, depending on (1) the vertical electron affinity of the various halogenated methane reagents, (2) the dissociative behavior of their respective negative ion species, and (3) the change in geometry that can occur in the bonds of the leaving $CH_{4-n}X_n$ radical, vibrational excitation of the new MX bond can vary from being the dominant mode of energy disposal in the reaction to a relatively ineffective mode of energy deposition. Because the reactions of electronically excited atomic species may be greatly influenced by the large number of potential energy surfaces available to the reactants, it is of interest to see whether similar dynamics are observed on excited state surfaces; i.e., whether or not considerations similar to those just given can lead to predictive ability for energy deposition in excited state reactions.

Of added interest in these reactions is their potential to yield different chemical products. When the halogenated methane contains more than one type of halogen, reaction of either halogen with the attacking metal atom is exoergic, and each product channel's exoergicity is approximately equal to that of the others. While no evidence of branching to yield different diatomic products has been reported in reactions of this type from ground state reagents, it is of interest to see whether a similar pattern is maintained in the case of electronically excited atomic reagents.

The laser-induced fluorescence apparatus is identical to the apparatus described previously.[18] Briefly, the beam apparatus consists of a differentially pumped vacuum chamber with the atomic oven contained in one chamber. This chamber is normally evacuated to less than 10^{-6} Torr. The oven containing the metal is then heated resistively to a temperature sufficient to give an atomic number density of approximately 10^{11} atoms/cm^3 in the laser-induced fluorescence detection zone. The vapor issues through a slot separating the oven vacuum chamber from the static gas chamber, where the reactant gas is present at pressures ranging from 2×10^{-5} to 2×10^{-4} Torr. No vibrational relaxation of the metal halide products is observed under these conditions. A mass spectrometer, located in the static gas chamber, is used for on-line gas purity analysis.

We report the results of reactions with ground state ($^1S_0$) strontium and barium atoms and also laser excited strontium ($^3P_1$) and barium ($^3D_2$ and $^3D_1$). Laser excitation of strontium to the $^3P_1$ state at 14,504 cm^{-1} is performed with a flashlamp-pumped Oxazine 720 (Exciton Corporation) dye laser (Chromatix CMX-4) with a per pulse energy of approximately 1 MJ and a repetition rate of 10 pps. Laser excitation of barium to its $^3D_2$ and $^3D_1$ states from the ground $^1S_0$ electronic state is achieved by cascade or radiative pumping from the $^3P_1$ level at 12,636 cm^{-1}, which is excited by the output from an optical parametric oscillator (Chromatix Model 1026) having an approximate per pulse energy of 0.5 MJ and a pulse repetition rate of 10 pps. The $^3P_1$ state of barium has a radiative lifetime of 2.9 μs and decays with a large branching ratio into the ^3D manifold. Given the ratios of the lifetimes of the $^3P_1$ and ^3D states and the mean collision time of the atoms under the conditions reported here, the barium excited state reactions that we observe are predominantly from the $^3D_2$ and $^3D_1$ states at 9215 cm^{-1} and 9033 cm^{-1}, respectively.

The product, laser-induced fluorescence spectra were detected by monitoring laser excitation of the $X^2\Sigma$ states to either the $A^2\pi_{1/2,3/2}$, $B^2\Sigma^+$, or $C^2\pi_{1/2,3/2}$ excited electronic states. Figures 10-5 through 10-7 show typical excitation spectra (unnormalized fluorescence intensities vs exciting laser wavelength) for a few of the reactions studied. The resulting spectra are analyzed using standard methods[14] to determine the disposition of internal energy in the resulting product molecules.

Table 10-5 gives an overview of the reactions studied. Included in the table is the bond energy of the carbon–halogen bond of interest. The exothermicity of each reaction is also shown. In many of the reactions studied, the possibility existed that more than one diatomic metal halide product could be formed. For example, the reactions to form BaCl or BaF from CF_3Cl are reaction pathways that are approximately equally exoergic. However, in no case were we able to detect formation of a metal fluoride diatomic product. In all cases where more than one type of halogen was contained in the reagent molecule, the bond between the carbon atom and the heavier of the two halogens was always broken. This result is consistent with the known photodissociative behavior of these reactant species; namely, if the reactions are visualized as proceeding through an electron jump mechanism,

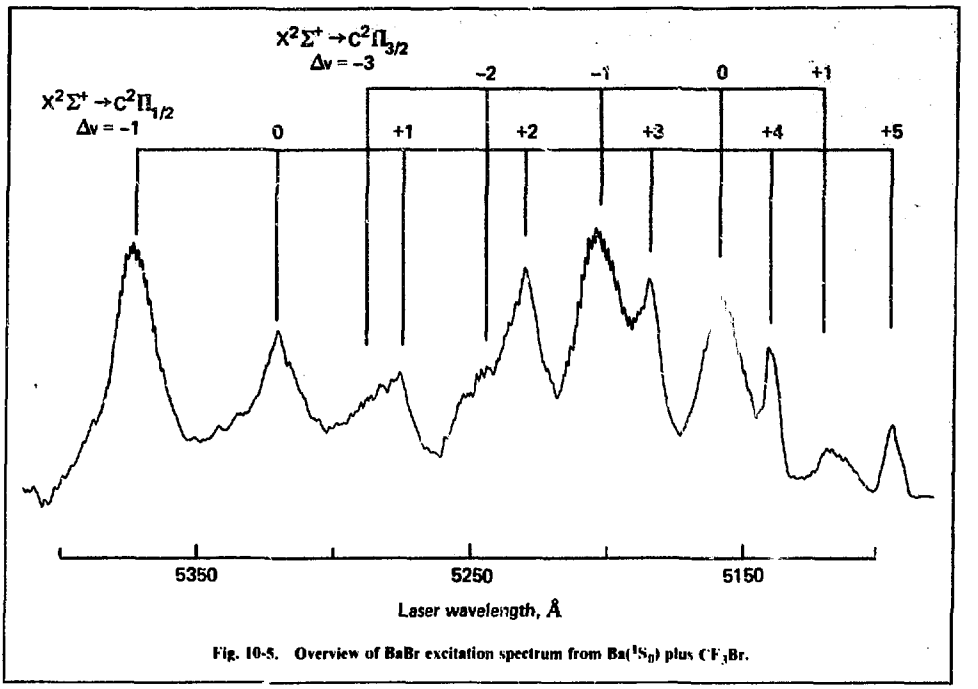

Fig. 10-5. Overview of BaBr excitation spectrum from Ba($^1S_0$) plus CF_3Br.

the added electron is inserted into an antibonding molecular orbital localized near the heaviest halogen, which in turn favors the kind of molecular decomposition observed.

Recent reports regarding the difference in reactivity of the $^3P_2$ and $^3P_0$ spin orbit states of mercury[19,20] make of interest similar studies of the relative reactivity of barium $^3D_2$ and $^3D_1$. Because these states are populated in our experiments by means of radiative cascade from the $^3P_1$ state, they are formed with a relative rate determined only by their statistical weights (verified experimentally by the intercepts of curves A and C in Fig. 10-8). The subsequent depletion of these states by the reactant gases can then be monitored by the use of a probe laser to connect the populated metastable ^3D states to a common higher-lying fluorescing state. When measurements of this type are made as a function of reactant gas pressure, the rate of depletion of the individual spin orbit states is an accurate monitor of the relative reactivity of the $^3D_2$ and $^3D_1$ states. We can eliminate the possibility that rapid intramultiplet relaxation equilibrates population with the ^3D manifo. before reaction takes place, because no detectable amount of $^3D_3$ state is seen in these experiments. Using this method of measurement, we have determined that the relative reactivity of the $^3D_2$ and $^3D_1$ states is identical to within 10% (see Fig. 10-8).

A full description of the reaction dynamics that emerge from these studies is given in Ref. 21. Briefly, we find that, when the dissociative behavior of the relevant negative polyatomic ion, the geometry change of the leaving radical in the reaction, and the route of approach of the attacking metal atoms are considered, qualitative predictions of internal energy excitation in the newly formed diatomic bond from ground state reagents have proven reasonably reliable. We find that these same concepts are reassuringly independent of the electronic state of the attacking atom, allowing one to predict qualitatively the partitioning of energy in the reactions of Ba(^3D) with CH_3Cl and CF_3Cl (see Tables 10-5 and 10-6). The observed relatively low (high) fraction of energy deposited into vibrational excitation of the BaCl product, from Ba(^3D)

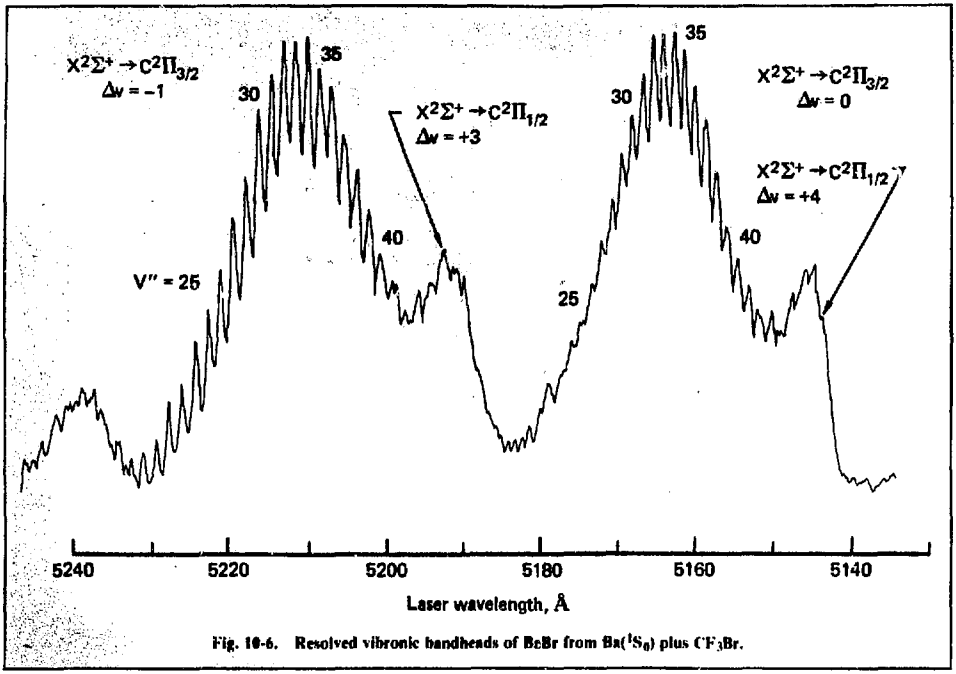

Fig. 10-6. Resolved vibronic bandheads of BaBr from $Ba(^1S_0)$ plus CF_3Br.

Table 10-5. Summary of reactions studied.[a,b]

Carbon-halide and (bond energy)	Alkaline earth atom and electronic state			
	$Ba(^1S)$	$Ba(^3D)$[c]	$Sr(^1S)$	$Sr(^3P)$
CH_3–F(108)	(35.6)[d]	(61.9)[d]	(24.0)[d]	(65.5)[d]
CH_3–Cl(81)	(25.9)[d]	BaCl(52.2)	(18.2)[d]	(59.7)[d]
CH_3–Br(70)	BaBr(19.1)	–[e]	SrBr(12.0)	–[e]
CCl_2F–Cl(73)	BaCl(37.6)	–[e]	–[e]	–[e]
CCl_3–Cl(70.4)	BaCl(40.9)	–[e]	SrCl(31.6)	–[e]
CF_3–F(125)	NR(21.1)	(47.7)[d]	(10.6)[d]	(52.1)[d]
CF_3–Cl(86.1)	NR(23.7)	BaCl(50.0)	(15.2)[d]	(56.7)[d]
CF_3–Br(70.6)	BaBr(20.3)	–[e]	SrBr(13.5)	–[e]

[a]Column one contains carbon–halogen bond energy of interest. Columns 2 through 5 contain the calculated reaction exothermicities, which include both the internal energy of the reactants and their mean relative kinetic energies. All values in parentheses are in kcal$/mole.

[b]All alkaline earth halide diatomic bond energies are taken from Ref. 22; carbon–halide bond energies are taken from Ref. 23.

[c]Exothermicity calculated from barium $^3D_2$ state.

[d]No reaction.

[e]Not studied.

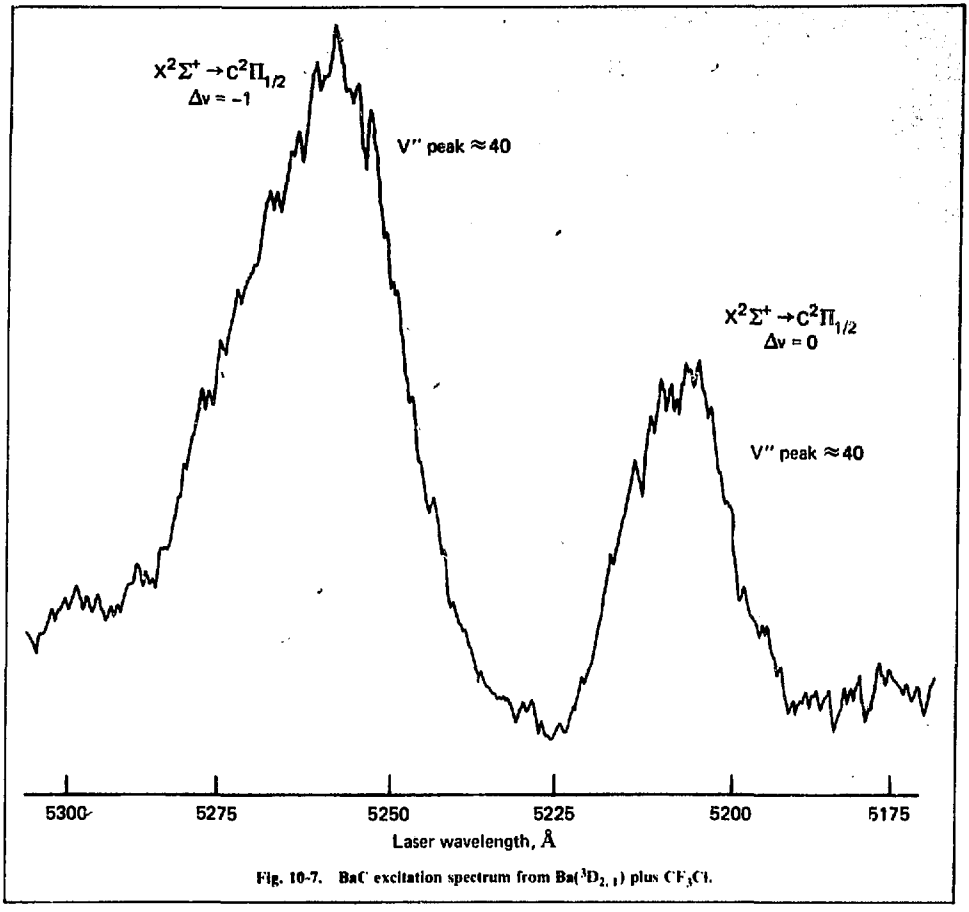

Fig. 10-7. BaCl excitation spectrum from $Ba(^3D_{2,1})$ plus CF_3Cl.

reacting with CH_3Cl (CF_3Cl), supports the contention that the nature of the reactant polyatomic is principally responsible for determining the internal energy distribution in the alkaline earth halide, and that it is to a large degree independent of the surface on which reaction occurs (see Table 10-6).

The differences in the reactivity of $Sr(^3P)$ and $Ba(^3D)$ with halogenated methanes are clearly surprising. While triplet barium is effective in breaking carbon-chlorine bonds in both CH_3Cl and CF_3Cl, triplet strontium is totally ineffective in this regard. Most simple models would predict the opposite of this experimental observation. For example, the ionization potential of $Sr(^3P_1)$ is lower than that of $Ba(^3D)$; one would therefore expect this lowering to facilitate the electron jump needed to initiate the chemical reactions. Furthermore, general rules, suggesting that the more exothermic the reaction the smaller the reaction barrier, also fail. It is the more exothermic reactions of CH_3Cl and CF_3Cl with $Sr(^3P)$ that do not proceed.

Still, the reaction of Ba with CH_3Cl and CF_3Cl by way of excitation of the $Ba(^3D)$ state is a striking demonstration of the ability to initiate chemistry by placing the reactants on a surface conducive to reaction. Clearly, the differences between Ba and Sr are not understood, and it is expected that additional data on reactions of this type will eventually lead to added knowledge of the influence of excited state surfaces (and their crossings) on the outcome of such chemical reactions.

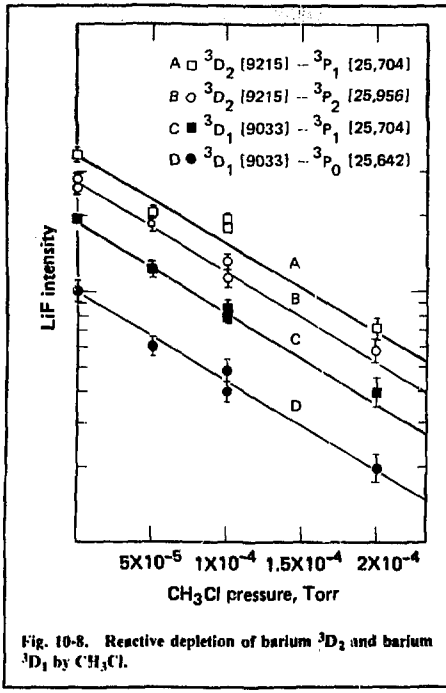

Fig. 10-8. Reactive depletion of barium $^3D_2$ and barium $^3D_1$ by CH_3Cl.

It has already been noted that the present results on the spin orbit states of barium, namely, that $^3D_2$ and $^3D_1$ react at effectively identical rates with certain halogenated methanes, are in contrast to recent results on Hg $^3P_2$ and $^3P_0$ reacting with diatomic chlorine[19] and bromine,[20] where the $^3P_2$ reactivity significantly exceeds that of $^3P_0$. In the present case, however, consideration of each spin orbit state of ^3D barium shows that each component undergoes an avoided crossing with the ion-pair states of the reactants; this is inferred from a surface picture developed earlier[18] in which the reactants acquired ionic character by adiabatic as opposed to diabatic mixing-in of ion-pair surface character. Consideration of each spin orbit state also shows that these crossings occurred at very nearly the same radius. It is therefore expected that each component would be equally effective in acquiring the ionic character necessary for initiating the chemical reaction. This acquisition is in contrast to the mercury reactions, in which it has been pointed out that $^3P_2$ and $^3P_1$, but not $^3P_0$, are subject to such crossings.[25]

Table 10-6. Fractional deposition of reaction energy into vibrational excitation of MX products for the reactions of Table 10-5 (in percent).

	Ba(^{1}S)	Ba(^{3}D)	Sr(^{1}S)	Sr(^{3}P)
CH_3Cl	–[a]	BaCl(34)	–[a]	–[a]
CH_3Br	BaBr(35)[b]	–[c]	SrBr(29)	–[c]
CCl_3F	BaCl(61)	–[c]	–[c]	–[c]
CCl_4	BaCl(72)[b]	–[c]	SrCl(59)	–[c]
CF_3Cl	–[a]	BaCl(61)	–[a]	–[a]
CF_3Br	BaBr(88)	–[c]	SrBr(79)	–[c]

[a]No reaction.

[b]The reactions of Ba(^{1}S) with CH_3Br and CCl_4 were also studied in Ref. 13 where f_v values were reported as 17 and 75, respectively. The discrepancy is due primarily to use by Rommel and Schultz of bond energies that differ from those used here. When the spectral data of Ref. 24 are used, and the bond energies of this report, f_v values become 29 and 72, respectively, in good agreement with our results.

[c]Not studied.

In conclusion, we have reported studies on the reactions of Ba (^{1}S and ^{3}D) and Sr (^{1}S and ^{3}P) with several different halogenated methanes. We have shown that, in certain cases, reactions with prohibitively large barriers in the ground or lowest reaction surface can be initiated by placement of the reactants on surfaces with diminished barriers. We have shown that internal energy distributions of the diatomic products formed on either ground or excited state surfaces are consistent with the current models for the dynamics of these types of reaction. Finally, we have shown that barium $^3D_2$ and $^3D_1$ react at similar rates with CF_3Cl and CH_3Cl, and that this reaction is consistent with a picture that takes into account the adiabatic crossings of the various spin orbit states with ion-pair surfaces along the reaction coordinate. It is hoped that extension of the studies, reported here, to metal atom systems of commercial significance will prove that photochemical isotope separation methods can become competitive with photophysical isotope separation techniques in properly designed systems.

10.3.2 Single-Photon Infrared Laser-Induced Photochemistry Facility

In conjunction with studies on the role of electronic excitation of chemical reactions, we have ini-

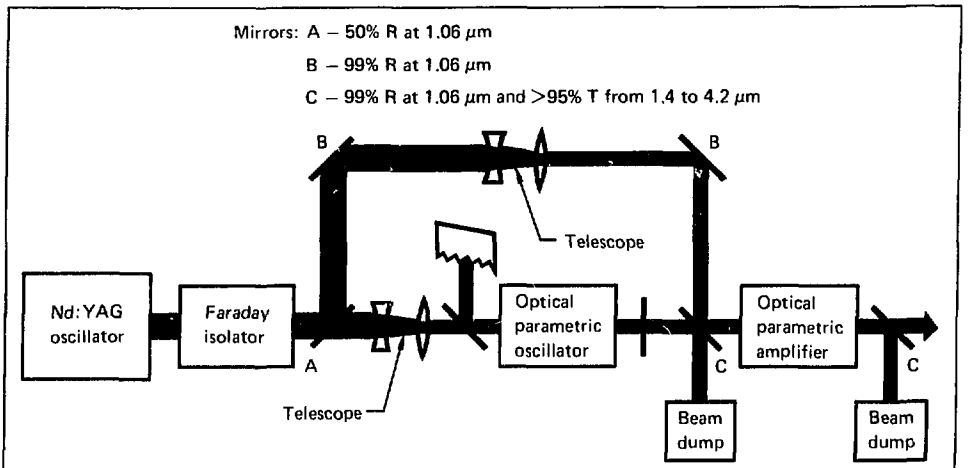

Fig. 10-9. High-power tunable optical parametric oscillator and amplifier system.

tiated a program to study systematically the effect of change of vibrational mode and quantum numbers on the course of chemical reaction. The principal aim here is to gain an understanding of the influence of vibrational energy (in particular, the differences between various types of intramolecular nuclear motions) in a simple system.

In recent years a number of methods have been developed for generating the high-power-tunable near-infrared radiation needed to pump these vibrational systems. While substantial progress has been made on methods such as frequency mixing and Raman scattering (see §10.6.3), the optical parametric oscillator (OPO) remains the method of choice in the generation of high spectral brightness radiation in the near infrared. In particular, the angle-tuned $LiNbO_3$ parametric oscillator, described by Byer and others,[26] is a simple and reliable tool for generating high-power radiation from 1.4 to 4.2 μm. An OPO based on the Byer design has been constructed for the purpose of infrared photochemistry experiments in our laboratory. This device is shown in Fig. 10-9. Amplifier performance has been described by Andreou.[27]

A critical parameter in the construction of high-average-power OPO's is the pulse length of the Q-switched Nd:YAG pump laser. It has been shown[26] that 20 ns is the optimum pulse length for operation of these devices. Unfortunately, commercially available pump lasers now generally provide much shorter pulse lengths, leading to reduced OPO efficiency and reduced per-pulse power. A 7-ns-pulse-length Nd:YAG laser, purchased from Quanta Ray (Model DCR-1), was used as the pump source. With this pulse length and a beam diameter of 3 mm, a threshold of approximately 30 mJ has been measured for the line-narrowed OPO (L-shaped cavity with a grating used as the dispersive device). The damage threshold has been measured to be 100 mJ/pulse under these conditions. As a result, the OPO can be operated in a reliable fashion at pump powers not exceeding three times threshold. While this means that an infrared energy of about 4 mJ/pulse can be obtained in an approximately 0 cm^{-1} line width near degeneracy (2.12 μm), the output energy rapidly decreases as the oscillator is tuned from degeneracy, because the threshold rises rapidly when $\omega_{signal} \neq \omega_{idler}$. Tuning of the idler wave to 2.7 μm has been achieved with a singly resonant oscillator having an output mirror that is 80% reflective at the higher gain signal wavelength. Thus, while the device is reliable with high power output near degeneracy, lengthening of the Nd:YAG pump pulse to $\tau > 12$ ns appears to be critical for full wavelength coverage. This modification of the pump laser and construction of a parametric amplifier are currently under way. It is anticipated that this modification will easily permit

tuning of the system with high average power from 1.4 to 4.2 μm.

A number of simple chemical systems have already been identified for the initial studies with this device. These systems are all slightly endothermic for unexcited reagent states and possess moderately strong infrared absorption features between 1.4 to 4.2 μm. Some of these systems are the reactions of aluminum with carbon dioxide, (101) and (04°1) combination bonds, strontium with various overtones of DF and HCl, strontium and barium with methyl chloride, ν_1 and ν_4, and various reactions of metal atoms with OCS.

References

12. *Laser Program Annual Report—1977*, Lawrence Livermore Laboratory, Livermore, Calif., UCRL-50021-77 (1978).
13. E. F. Gurnee and J. L. Magee, "Interchange of Charge Between Gaseous Molecules in Resonant and Near Resonant Processes," *J. Chem. Phys.* **26**, 1237 (1957).
14. H. W. Cruse, P. J. Dagdigian, and R. N. Zare, "Crossed-Beam Reactions of Barium with Hydrogen Halides," *Discuss. Faraday Soc.* **55**, 277 (1973).
15. P. R. Brooks, "Molecular Beam Reaction of K with Oriented CF_3I: Evidence for Harpooning?" *J. Chem. Phys.* **50**, 5031 (1969).
16. M. A. Nazar, J. C. Polanyi, and W. J. Skrlac, "Energy Distribution Among Reaction Products H + NOCl, H + ICl," *Chem. Phys. Lett.* **29**, 473 (1974).
17. G. P. Smith, J. C. Whitehead, and R. N. Zare, "Bimodal Distribution of BaI Vibrational States from the Reaction Ba + CF_3I," *J. Chem. Phys.* **67**, 4912 (1977).
18. R. W. Solarz, S. A. Johnson, and R. K. Preston, "The Deposition of Energy from Reactions of Laser Excited Atoms: Strontium $^3P_1$ with Hydrogen Halides," *Chem. Phys. Lett.* **29**, 473 (1974).
19. H. F. Krause, S. G. Johnson, S. Datz, and F. K. Schmidt-Bleek, "Crossed Molecular Beam Study of Excited Atom Reactions: Hg(6 $^3P_2$ with Cl_2 and Chlorinated Methane Molecules," *Chem. Phys. Lett.* **31**, 577 (1975).
20. S. Hayashi, T. M. Mayer, and R. B. Bernstein, "Crossed Molecular Beam Chemiluminescence Study of the Metastable Mercury Reaction: Hg ($^3P_0$) + Br_2 Hg Br (B) + Br*," *Chem. Phys. Lett.* **53**, 519 (1978).
21. R. W. Solarz and S. A. Johnson, "Laser Induced Fluorescence Studies of the Reactions of Barium (^1S, ^3D) and Strontium (^1S, ^3P) with Halogenated Methanes," *J. Chem. Phys.* (to be published).
22. P. D. Kleinschmidt and D. L. Hildenbrand, "Dissociation Energies of CaI, SrI, and BaI from High Temperature Mass Spectrometry," *J. Chem. Phys.* **68**, 2819 (1978).
23. B. deB. Darwent, *Bond Dissociation Energies in Simple Molecules*, National Bureau of Standards, Washington, D.C., Standards Reference Data Series No. 31 (1970).
24. M. Rommel and A. Schultz, "Laser Induced Fluorescence for the Reactions of Ba with ($CH_{4-n}X_n$)," *Ber. Bunsenges. Phys. Chem.* **81**, 139 (1977).
25. J. Muckerman, Brookhaven National Laboratory, Brookhaven, N.Y., private communication (1978).
26. R. L. Byer, R. L. Herbst, and R. N. Fleming, "A Broadly Tunable IR Source," in *Laser Spectroscopy*, S. Haroche et al., Eds., *Proc. 2nd Intern. Conf. Megeve, France* (Springer Verlag, 1975).
27. D. Andreou, "A $LiNbO_3$ Optical Parametric Amplifier," *Optics Commun.* **27**, 171 (1978).

Authors

R. Solarz
S. Johnson

10.3.3 Associative Ionization Reactions of Alkaline Earth Elements

Our motivations for studying associative ionization and other chemistry of excited states in alkaline earth elements include:

- Advances in Rydberg state chemistry.
- Wider knowledge of multiphoton ionization processes.
- Application of alkaline earth vapors for infrared lasers and detectors.
- Wider knowledge of excited-state–excited-state reactions.

Phenomena of the type we have observed in our studies may be important in any "high density" atomic vapor irradiated by resonant (multistep) laser radiation.

In last year's annual report,[28] we discussed the following reactions and mechanisms of laser excited states in strontium:

- Production of dimer ions by associative ionization of strontium Rydberg states with ground state atoms.
- Dimer ion production by excited-state–excited-state reactions.
- Destruction of high-lying Rydberg states by electron ionization in an avalanche mechanism under certain conditions.
- Two-photon transitions from Sr(5s 5p $^1P_1$) excited states to "core-excited" Sr(5p ns and 5p nd) autoionizing Rydberg states.

These were all new observations for an alkaline earth element. Associative ionization was known to occur in the noble gases[29] and alkali metals,[30] but it had not been established as occurring in the alkaline earths, although it had been assumed to take place.[31,32]

We have extended our studies of photo, collisional, and associative ionization in atomic

vapors to calcium and barium. (The reactions observed for these elements were similar to those for strontium, but there were some differences.)

The experimental techniques were identical to those used with strontium.[33,34] Briefly, a stream of atoms in a vacuum chamber was irradiated sequentially by two pulsed-dye lasers tuned to excite the atoms to high Rydberg states through resonant transitions. The atom densities in the interaction region were varied from about 10^{12} to 10^{14} atoms/cm^3 depending on the reaction being studied. Ion detection was used exclusively, and a quadrupole mass filter was employed to select either the atomic ion or dimer ion of the element under investigation. Rydberg states of the atoms were excited by the process

$$\mathrm{M}(\mathrm{ms}^2\,{}^1\mathrm{S}_0) \xrightarrow[\text{fixed}]{\lambda_1} \mathrm{M}(\mathrm{ms\,mp}\,{}^1\mathrm{P}_1) \xrightarrow[\text{variable}]{\lambda_2} \begin{matrix}\mathrm{M}(\mathrm{ms\,ns}\,{}^{1,3}\mathrm{S}) \\ \text{or} \\ \mathrm{M}(\mathrm{ms\,nd}\,{}^{1,3}\mathrm{D})\end{matrix} , \qquad (3)$$

where m is 3 for calcium and 5 for barium and $n \geq m$. For calcium, λ_1 was 4226.7 Å, and for barium, 5535.5 Å.

The associative ionization reactions

$$\mathrm{M}(\mathrm{ms\,nl}) + \mathrm{M}(\mathrm{ms}^2\,{}^1\mathrm{S}_0) \rightarrow \mathrm{M}_2^+ + \mathrm{e}^- , \qquad (4)$$

and

$$\mathrm{M}(\mathrm{ms\,mp}\,{}^1\mathrm{P}_1) + \mathrm{M}(\mathrm{ms\,mp}\,{}^1\mathrm{P}_1) \rightarrow \mathrm{M}_2^+ + \mathrm{e}^- , \qquad (5)$$

were observed under conditions of high atom density in the beam (stream). Dimer ion production by the excited-state–excited-state reaction (5) required considerably higher densities than from Rydberg states, reaction (4), when n for reaction (4) was large or greater than 12. At low n, the dimer ion signal from reaction (5)—single laser irradiation at λ_1—was relatively larger. For Sr, the signal from reaction (5) was equivalent to that from reaction (4)—$\lambda_1 + \lambda_2$ irradiation—and for Ba, it was larger. These observations can be explained by the decrease in production of dimer ions by reaction (4) at low n that results from the shorter lifetimes of these Rydberg states and the presumably smaller cross section for the reaction. In Ba, the measured lifetimes for 6s nd $^1D_2$ levels range from 20 ns at n = 8 to 226 ns at n = 12; they then increase to 580 ns at n = 17.[35]

The mechanism for reaction (5) is still unknown. The dimer ions could arise either directly from $^1P_1$ – $^1P_1$ collisions or indirectly from collisionally populated Rydberg states that subsequently associatively ionize. At present, we favor the latter mechanism.

The destruction of high-lying Rydberg states by the electron avalanche mechanism was found to occur in Ca and Ba. The mechanism involves the reaction

$$\mathrm{M}(\mathrm{ms\,nl}) + \mathrm{e}^- \rightarrow \mathrm{M}^+ + 2\,\mathrm{e}^- , \qquad (6)$$

where the initial electrons are produced by photoionization,

$$\mathrm{M}(\mathrm{ms\,nl}) \xrightarrow{\lambda_2} \mathrm{M}^+ + \mathrm{e}^-\,(2\ \mathrm{eV}) . \qquad (7)$$

The process results in a decrease in the dimer ion signal at line center as λ_2 is scanned across the $^1P_1$ to Rydberg state transition (see Fig. 10-10). It is more pronounced in Sr and Ba than in Ca because the photoionization cross section [reaction (5)] is greater for Sr and Ba. As seen in Fig. 10-10, decreasing the intensity of λ_2 reduces the avalanche process by decreasing the number of 2-eV electrons produced by photoionization [reaction (5)] so that a "normal" line shape results. The 4s 4p $^1P_1$→4s $23s\,^1S_0$ transition is normal in both scans because production of electrons by photoionization at this transition has not reached the critical value.

Two photon transitions were observed in Ca from the 4s 4p $^1P_1$ level to autoionizing levels of the 4p ns and 4p nd Rydberg series that converge to the 4p $^2P_{1/2}$ and the 4p $^2P_{3/2}$ levels of the ion. These transitions are two-photon, two-electron transitions that occur at high vapor densities near the resonant one-photon transitions from the 4s 4p $^1P_1$ level to bound Rydberg levels. They appear as satellite lines near the strong resonant transitions and were first observed in Sr.[34] We have observed these two-photon transitions in Ba, also.

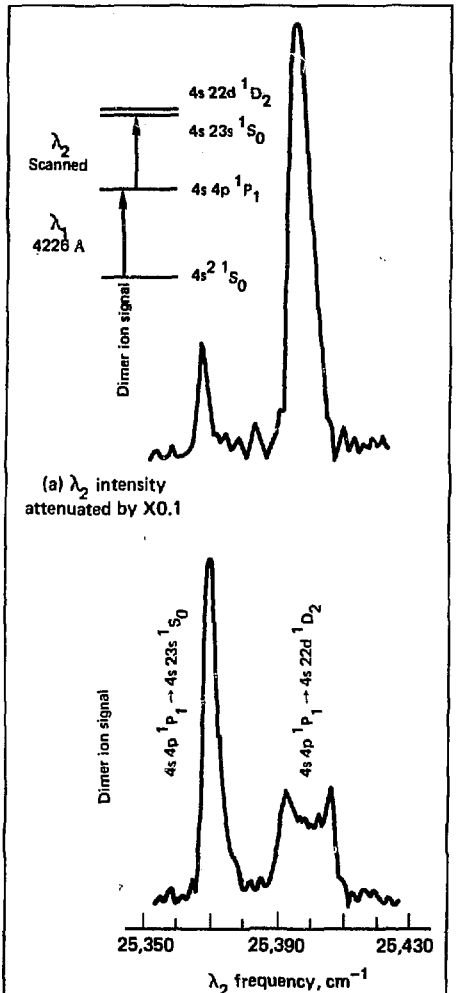

Fig. 10-10. Dimer ion signals in calcium vapor at two different intensities of laser 2. The excitation scheme is shown at the left. The dimer ion signal at the 4s 4p $^1P_1 \rightarrow$ 4s 22d $^1D_2$ transition is strongly affected by the intensity of laser 2. At high power the dimer ion signal is weaker at line center because the 4s 22d $^1D_2$ Rydberg levels are destroyed by an electron avalanche mechanism before they can undergo associative ionization (see text).

For an associative ionization reaction to occur, the excitation energy of the atom(s) plus the binding energy of the dimer ion formed must exceed the ionization potential (IP) of the metal atom. Thus, by determining the lowest Rydberg level that undergoes the associative ionization reaction, one can determine an energy value that the binding energy of the dimer ion formed must equal or exceed. Because of the relatively large energy interval (~0.2 eV) between Rydberg levels in the region defined by (IP – dimer ion binding energy) for the alkaline earths, an accurate value for the binding energy (dissociation energy) of the dimer cannot be obtained by this technique. Only the limit values given in Table 10-7 can be found. As indicated in the table, the dissociation energy of Ca_2^+ is at least 1.07 eV. This is in agreement with the value 1.04 eV calculated from theory by Liu and Olsen.[37]

Table 10-7. Binding energies of alkaline earth dimer ions.[a]

Element	Ionization potential[b]	Lowest Rydberg yielding[b] Dimers	Lowest Rydberg yielding[b] No dimers	Binding energy Greater than	Binding energy Less than
Ca	6.113	5.045	–[c]	1.068	–[c]
Sr	5.695	4.920	4.766	0.775	0.925
Ba	5.212	4.434	4.261	0.778	0.951

[a] All values in electron volts (eV).

[b] Ionization potentials and Rydberg level energies from Ref. 36.

[c] Not determined.

The binding energy for the Ca_2^+ ion is greater than that for Sr_2^+ or Ba_2^+, indicating that the binding energy is higher for the lighter alkaline earth elements. The dimer ions of the alkali metals are more stable for the lighter elements (Cs_2^+, 0.70 eV; Rb_2^+, 0.73 eV; K_2^+, 0.75 eV; Na_2^+, 1.01 eV; Li_2^+, 1.55 eV).[38] We plan experiments with Mg to confirm that this stability is true in the alkaline earths.

References

28. *Laser Program Annual Report—1977*, Lawrence Livermore Laboratory, Livermore, Calif., UCRL-50021-77 (1978).
29. J. A. Hornbeck and J. P. Molnar, "Mass Spectrometric Studies of Molecular Ions in the Noble Gases," *Phys. Rev.* **84**, 621 (1951).
30. F. L. Mohler and C. Boeckner, "Photoionization of Cesium by Line Absorption," *J. Res. NBS (US)* **5**, 51 (1930).
31. A. Fontijn, "Recent Progress in Chemi-Ionization Kinetics," *Pure Appl. Chem.* **39**, 287 (1974).
32. J. J. Wynne, IBM Thomas J. Watson Research Center, Yorktown Heights, N.Y., private communications (1977, 1978).

33. J. I. Davis and R. W. Davis, "Some Aspects of the Laser Isotope Separation Program at Lawrence Livermore Laboratory," in *Proc. of Annual Meeting of the American Institute of Chemical Engineers* (Chicago, Ill., Nov. 28-Dec. 2, 1976).
34. E. F. Worden, J. A. Paisner, and J. G. Conway, "Associative Ionization of Laser-Excited Rydberg States in Strontium Vapor," *J. Opt. Soc. Am.* **68**, 156 (1978).
35. D. Kaiser, P. Kulina, A.E. Livingston, H. H. Radloff, and S. Tudorache, "Lifetime Measurements of Rydberg States in the 6snd $^1D_2$-Series of Ba I," *Z. Phys.* **A285**, 111 (1978).
36. C. E. Moore, *Atomic Energy Levels*, National Bureau of Standards, Washington, D.C., National Standards Reference Data Services No. 35, I, II, III (1971).
37. *B. Liu and R. E. Olson*, "Potential Energies for Ca_2^+ : Cross Sections of Ca^+ and Rydberg Ca^{**} with Ca," *Phys. Rev.* **18**, 2498 (1978).
38. Y. T. Lee and B. H. Mahn, "Photosensitized Ionization in Alkali-Metal Vapors," *J. Phys. Chem.* **42**, 2893 (1965).

Author

E. F. Worden

Major Contributors

J. A. Paisner

J. G. Conway

10.3.4 Crossed Molecular Beam Studies—Uranium Ground-State Chemistry Survey

During the past year, we initiated an extensive study of the reactivity of uranium atoms in the gas phase. Such information is important in developing uranium photochemical isotope enrichment processes, i.e., those based on a laser selectively inducing chemical reaction. This study allows us to identify candidate systems for such processes, as well as to evaluate various proposed schemes for chemical separation of the photochemical products of photoinduced reactions from the unreacted uranium. Furthermore, an understanding of the dynamics of ground-state reactions is essential in interpreting results of excited-state experiments.

This section discusses the chemical properties of uranium with various oxidizers (both inorganic and organic) and mild halogenating agents. Uranium is regarded as an extremely reactive element; this perception is based on the properties of the solid and liquid phases, especially at high temperatures. Our results indicate that gaseous uranium exhibits a wide range of reactivity and that a number of reactions, although quite exothermic, proceed rather slowly. What is perhaps more important is that we find the pattern of reactivity of uranium remarkably similar to that of other heavy metals.

Conventional techniques for studying gas phase reactions are unsuitable for highly refractory elements. Such reactions, however, can be easily investigated in the molecular beam facility. A beam of the reagent intersects an atomic uranium beam; a rotating detector (a small quadrupole mass spectrometer with an electron-bombardment ionizer) then monitors reaction products as a function of scattering angle.

The mass-sensitive detector allows easy identification of the reaction products. Further, the measured angular scattering pattern yields important details about the dynamics of the reaction itself. The dynamics information of interest includes the reaction mechanism (the time scale of the interaction and the preferred directions into which the product is scattered), and the deposition of the reaction exothermicity in product vibration, translation, rotation, and electronic modes. Both of these factors determine the angular range where reaction products will be found. Such information on where to look is essential when searching for reaction products of a photoexcited beam. Typically, the density of excited uranium can be 10 to 100 times lower than the ground-state density (see §10.5.2), and a similar decrease in the product flux is expected.

Extraction of an absolute reaction cross section from relative reactive scattering measurements is not straightforward. First, the detector is confined to a single plane and cannot collect all of the scattered product. Second, an absolute rate measurement requires calibration of the cross beam intensity and very careful control of the beam geometry. We have developed such techniques for elastic scattering[39] and will apply them to reactive scattering in the near future. For the present, we estimate total reaction cross sections by comparison with the $U + O_2$ reaction, which has a reported cross section[40] of 18 $Å^2$.

A schematic of the apparatus as designed for ground-state chemistry is shown in Fig. 10-11. We operate the uranium source at 2500 to 2600 K and the gas source at approximately 360 K. The gas source backing pressure is set to 1 Torr for all gases studied; this typically gives rise to a 0.5 to 0.8% attenuation of the uranium beam, with only a moderate increase in the main chamber background pressure. The gas beam is chopped with a mechanical flag at a slow rate (0.2 Hz); the difference in count rate with the gas beam on and off is

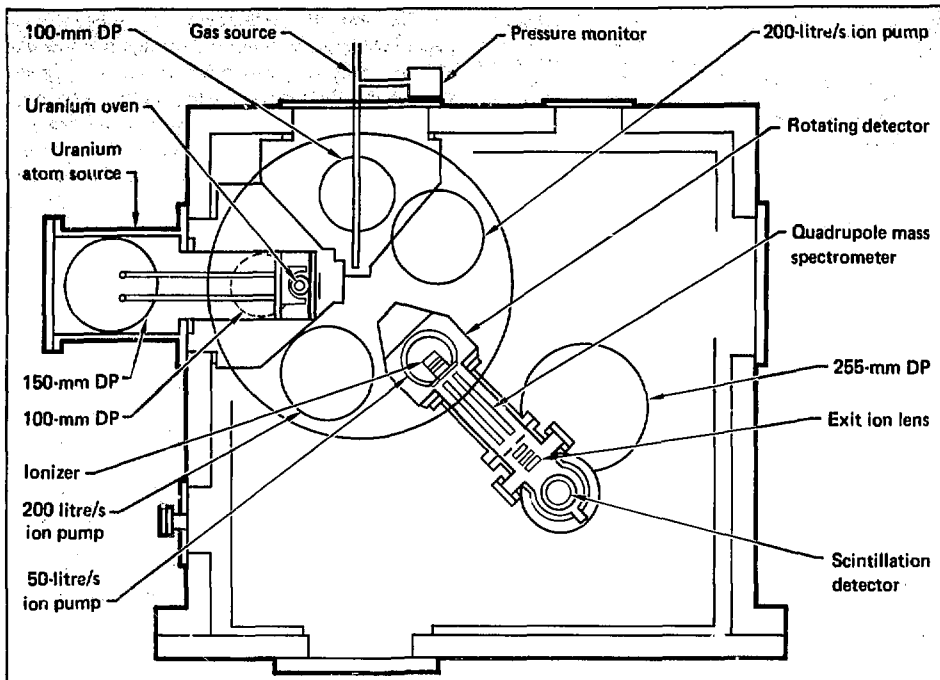

Fig. 10-11. Schematic of molecular beam facility configured for crossed molecular beam chemistry.

the reactive scattering signal. This signal is averaged for approximately 4 min before we proceed to a new angle. After four or five angles, we return to a standard reference angle (usually 10 deg LAB) to correct for long-term drifts in the beam intensities.

Inorganic Oxidizers. The first set of reactions studied involved diatomic and triatomic oxidizers (O_2, NO, CO_2, N_2O, NO_2, SO_2). In each case, the reaction producing UO was exothermic with $-\Delta H$ ranging from 32 kcal/mole (NO) to 143 kcal/mole (N_2O) (see Table 10-8). Large UO signals were observed for the reaction of U with O_2, NO, SO_2, and NO_2, and a full angular distribution for each reagent was measured. Plots of these distributions are found in Fig. 10-12. The dashed lines indicate the distribution of centroids (center-of-mass of the colliding pair); this distribution represents the scattering pattern that would be observed if the reagents did not separate after colliding. UO signals were approximately 30 times lower for U + N_2O and U + CO_2, and no attempt was made to measure the angular distribution of the UO product. After each distribution was completed, we calibrated the apparatus by running the U + O_2 reaction with the O_2 source pressure set equal to that of the oxidizer. This procedure makes each of the normalized scattering distributions absolute to within a *common* proportionality constant. For the present, we estimate total reactive cross sections from the ratio of the product intensity at 10. This procedure is crude at best, as it ignores both kinematic (differing oxidizer masses) and dynamic effects (different reaction mechanisms—see below); nevertheless, we estimate at most a moderate error (50%). Table 10-8 lists reaction cross sections relative to the U + O_2 cross section of 18 $Å^2$. We found reaction cross sections ranging from 35 $Å^2$ to less than 1 $Å^2$. These rates are not correlated with the electronic structure of the gas or with reaction exothermicity; for example, the reaction involving fission of the weakest oxidizer bond (N_2O) was very slow. Also, the SO_2 and CO_2 energetics were comparable, yet a large dif-

Table 10-8. Cross section for production of uranium oxide in reactions of uranium with selected inorganic oxidizers.

Oxidizer	Electronic state	Exothermicity,[a] kcal/mole	Cross section,[b] Å^2
NO	$^2\pi_{1/2}$	32	33
SO_2	$^1A_1$	51	9
CO_2	$^1\Sigma_g^+$	56	≤1
O_2	$^3\Sigma_g^-$	64	18
NO_2	$^2A_1$	110	12
N_2O	$^1\Sigma^+$	143	≤1

[a]Exothermicities calculated from bond strengths tabulated in Ref. 41.

[b]Estimate obtained from ratio of scattered intensity (see text).

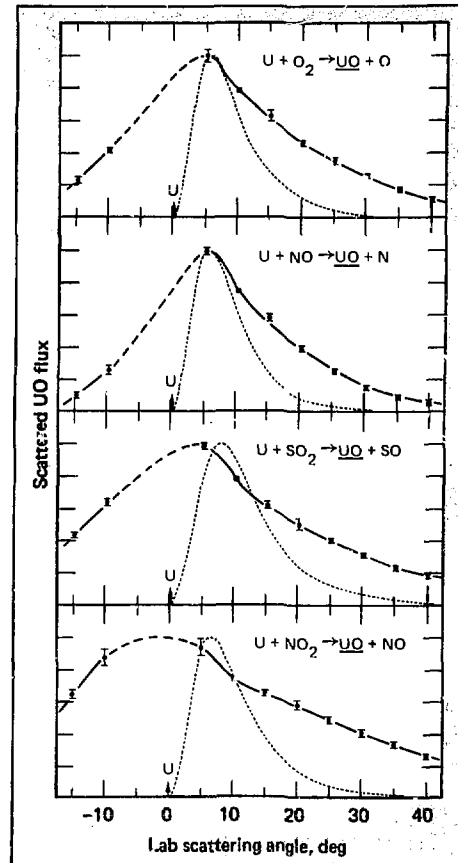

Fig. 10-12. Laboratory angular distribution for UO product from U + O_2, U + NO, U + NO_2, U + SO_2 reactions (dashed lines indicate the distribution of centroids; error bars represent ±1 standard deviation of the mean — error bars smaller than the size of the symbol are omitted).

ference in rates was observed. Details of the intermolecular interaction clearly play a major role in determining reaction rates in this set of simple and highly exothermic reactions.

In the case of reaction with NO and O_2, the UO product distribution peaked near the distribution of the centroids, indicating a long-lived collision complex. Furthermore, the angular distribution was not much wider than that of the centroids, suggesting that only a small fraction of the available energy was channeled into translation.

To confirm our observations about the dynamics in the U + O_2 reaction, we measured the velocity distribution of the scattered UO. A time-of-flight chopping wheel, installed at the detector entrance aperture, admitted a pulse of UO; the spectrum of arrival times was then recorded. For these sets of measurements, we replaced the effusive gas source with a high-pressure nozzle source to better define the O_2 velocity. A typical product velocity distribution is shown in Fig. 10-13 along with that for the uranium beam itself (nominal temperature, 2600 K). A rather complicated analysis is required to convert these spectra to a detailed plot of product intensity as a function of both angle and velocity. This analysis is under way and will be completed in the near future. Nevertheless, we can draw some qualitative conclusions. Both the scattered UO and U beam time-of-flight spectra peak around the same arrival times. The product distribution also appears narrower than that of the main beam. These two observations confirm that the reaction deposits little if any of the exothermicity in product translation.

The UO from the U + NO_2 reaction is forward-peaked, indicating a direct (i.e., instantaneous) reaction mechanism. The U + SO_2 reaction also appears to be forward-peaked; however, our inability to measure the UO product close to the U beam (where elastic scattering of a small UO contaminant in the beam masks reactively scattered

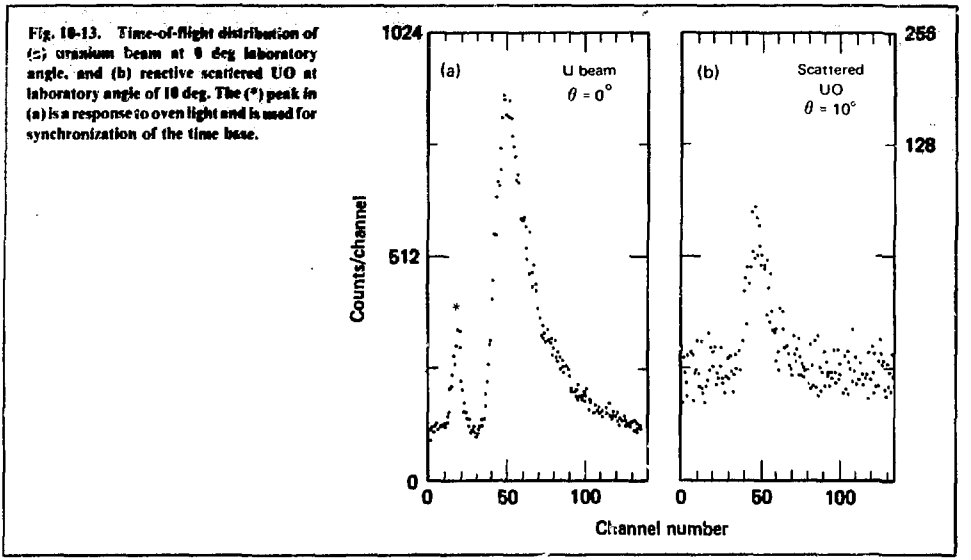

Fig. 10-13. Time-of-flight distribution of (a) uranium beam at 0 deg laboratory angle, and (b) reactive scattered UO at laboratory angle of 10 deg. The (*) peak in (a) is a response to oven light and is used for synchronization of the time base.

UO) makes this observation quite tentative. Both these systems exhibit the same inefficient channeling of the exothermicity into product translation. The observed deposition is consistent with the high density of electronic states in UO.

Organic Oxidizers. Because little is known about the reactions of metal atoms with organic molecules, we investigated the reactivity of uranium with two classes of organic oxidizers: alcohols (R–OH) and ketones ($R-\overset{O}{\overset{\|}{C}}-R$). Our prime motivation was to discover sufficiently inert reagents for possible use in photochemistry-based isotope separation processes.

The carbonyl bond strength in aldehydes and ketones is approximately 175 kcal/mole,[42] making reactions with U to yield UO barely exothermic. Fission of the C=O bond is also a rather uncommon reaction channel, and we expected uranium and ketones to be quite unreactive. We intersected beams of acetone and uranium and measured large scattered UO signals. Cross sections were extracted as before by calibration with U + O_2, and we estimated a reaction cross section of 33 $Å^2$. The angular distribution peaked around the centroids, inferring a long-lived complex. We suspect that the reaction involves rearrangement of the CH_3-C-CH_3 fragment to form a stable molecule, such as propene $CH_2=CH-CH_3$. Such a rearrangement would make the reaction more exothermic and could explain the high reactivity. We intend to test this hypothesis by measuring the reaction of uranium with formaldehyde where such rearrangement is impossible.

Recent laser-induced fluorescence studies[43] indicate that Group IIIB metals (Sc, Y, La) react with water and alcohols to form the oxide. Because the detection scheme is not sensitive to hydroxides, the relative yield of oxide and hydroxide is unknown. We crossed uranium with beams of water and small alcohols (CH_3OH and C_2H_5OH) to determine the major product. Because the masses of the possible products differ by only one atomic mass unit, separation of the two products requires great care. As we increased the resolution of the mass spectrometer, the apparent signal at the UOH mass decreased much more rapidly than the UO signal. We conclude that UO is the major and, most likely, the only product. Cross sections for these reactions, which are listed in Table 10-9, range from 4 $Å^2$ for methanol to 9 $Å^2$ for water.

Formation of the oxide in these reactions involves rupture of both the R–O and O–H bonds in the alcohol. A reaction mechanism in which uranium simply extracts the oxygen, leaving behind separate R and H fragments, is endothermic. This reaction must then involve simultaneous formation

Table 10-9. Cross sections for oxidation reactions with selected organic oxidizers.

Reaction	Exothermicity, kcal/mole	Cross section,[a] A^2
$U + CH_3COCH_3 \rightarrow UO + CH_3CCH_3$	10[b]	33-
$U + CH_3OH \rightarrow UO + CH_4$	93	4
$U + C_2H_5OH \rightarrow UO + C_2H_6$	93	6
$U + H_2O \rightarrow UO + H_2$	66	9

[a]Estimate obtained from ratio of scattered intensity (see text).
[b]Estimated.

Table 10-10. Relative cross sections for reactions of uranium with halogenated methanes.

Reaction	Relative cross section
(1) $U + CCl_4 \rightarrow UCl + CCl_3$	0.5
(2) $U + CH_3I \rightarrow UI + CH_3$	1.0
(3) $U + CF_3Br \rightarrow UBr + CF_3$	~0.2
(4) $U + CF_3Cl \rightarrow UCl + CF_3$	0.05
(5) $U + CF_4 \rightarrow UF + CF_3$	NR[a]

[a]NR = no reaction product observed.

of both R—H and U—O bonds and most likely proceeds through a long-lived complex. We observed the scattered UO to be peaked close to the centroids, consistent with the proposed mechanism.

The reactivity of both ketones and alcohols, for which we observed moderate to large cross sections despite rather complex rearrangements of the organic fragments, contrasted markedly with that of certain simple inorganic oxidizers exhibiting very low reactivity.

Halogenated Methanes. The reactions of a number of halogenated methanes (CH_3X, CF_3X, with X = F, Cl, Br, I) with various metals (Li,[44] Ba,[45,46] Sr,[45,46] Ca,[46] Sn[47]) have been well characterized. The reactivity of these substituted methanes decreases in the order X = I, Br, Cl, and F; one generally observes MI and MBr product but rarely any MCl or MF. In some cases excitation of the metal atom is effective in inducing reaction[45] (e.g., Ba + CF_3Cl, CH_3Cl). We reacted uranium with a set of halogenated methanes (CCl_4, CH_3I, CF_3Br, CF_3Cl, and CF_4) to determine whether uranium exhibits a similar pattern of reactivity.

Extraction of total reaction cross sections for these reactions is much more difficult than for reactions producing UO, because the sensitivity of the detector to UX relative to UO is unknown. Hence, we report only relative cross sections. Table 10-10 lists the reactions studied and estimates the relative cross sections. We observe a pattern of reactivity that is essentially identical to that for the Group IIA metals, i.e., the iodide is more reactive than the bromide. Some UCl is observed in reaction (4) of Table 10-10; however, the signal is just above the background noise level, and we consequently assign only an upper limit to the relative cross section. No UF is observed in reaction (5) even though the reaction is estimated to be approximately 30 kcal/mole exothermic, nor is any UF seen in reactions (3) and (4).

Angular distributions were measured for scattered UI and UCl from the first three reactions. The UI from the reaction with CH_3I, and UBr from the reaction with U + CF_3Br, are backward-peaked. The UCl from U + CCl_4 appears sideward-peaked. Again, these features are in qualitative agreement with those of the corresponding Ba and Sn reactions.

The bond strengths of the uranium halides are completely unknown, except for a reported value of 156 kcal/mole for the UF bond.[48] We can, however, use the product angular distribution and in particular a complete velocity-angle distribution to establish lower limits for these unknown bond strengths.

We found that the reactivity of uranium with Freons parallels that of a number of other metals. These systems may then offer some promise for isotopically selective photochemistry.

References

39. R. C. Stern and N. C. Lang, *Measurement of the U-Kr Momentum Transfer Cross Section Using Crossed Molecular Beams*, Lawrence Livermore Laboratory, Livermore, Calif., UCRL-81209 (1978).
40. W. L. Fite, H. H. Lo, and P. Irving, "Associative Ionization in U + O and U + O_2 Collisions," *J. Chem. Phys.* **60**, 1236 (1974).
41. *Handbook of Chemistry and Physics*, 58th ed. (CRC Press, Cleveland, Ohio, 1977), p. F-219.
42. S. W. Benson, "Bond Energies," *J. Chem. Ed.* **42**, 503 (1965).
43. K. Liu and J. M. Parson, "Mechanisms of Central O-atom Abstraction Reactions: A Molecular Beam, Laser Induced Fluorescence Study of Group IIIB + ROH Systems," *J. Chem. Phys.* **68**, 1794 (1978).

44. C. M. Sholeen and R. R. Herm, "Product Magnetic Deflection Slotted Disk Velocity Analysis Molecular Beam Kinetics Li + CH_3NO_2, CCl_4, and CH_3I," *J. Chem. Phys.* **65**, 5398 (1976).
45. R. W. Solarz and S. A. Johnson, *Laser Induced Fluorescence Studies of the Reactions of Barium and Strontium with Halogenated Methanes*, Lawrence Livermore Laboratory, Livermore, Calif., UCRL-81928 (1978).
46. S-M. Lin, C. A. Mims, and R. R. Herm, "Crossed-Beams Reactions of Barium, Strontium, and Calcium with Some Halides of Methane," *J. Phys. Chem.* **77**, 569 (1973).
47. T. P. Parr, R. Behrens, Jr., A. Freedman, and R. R. Herm, "Crossed Molecular Beam Kinetics: SnI and SnCl Recoil Velocity Spectra from Sn + CH_3I, n-C_3H_7I, and CCl_4 and a Lower Limit for D_0 (SnI)," *J. Chem. Phys.* **69**, 2795 (1978).
48. I. N. Godnev and A. S. Sverdlin, *Izv. Vysshikh Vchebn. Zavadenii, Khim. Tekhnol.* **9**, 40 (1966).

Author

Neil Lang

10.3.5 Scattering Theory—The Hg-K System

Numerous atomic properties, such as cross sections for atom-atom elastic scattering, rely for their determination upon the computation of curves (or surfaces) of potential energy of the transitory molecule, found during the collision, as a function of internuclear separation. Other properties, such as lifetimes and fluorescence spectra of excimers, require additional details not only of the energy but also of transition dipole moments as a function of internuclear distance. Traditional approaches to the computation of such molecular energies and dipole moments rest upon the Born-Oppenheimer approximation, which hypothesizes the electrons accommodating the instantaneous position of the various nuclei; the molecular properties then stem from *numerical solutions to the multielectron* Schrödinger equation (perhaps with relativistic corrections) at a succession of values for fixed internuclear separation.

This ab initio computation of molecular potential energy curves becomes progressively more time-consuming as the number of electrons increases, so that the theoretical prediction of the scattering of two heavy atoms is prohibitively expensive. For this reason various simple approximations have been employed over the years. Some of these have proven remarkably reliable in describing potentials between rare gas atoms, and so it is natural to hope for similar success for these models when applied to heavy open-shell atoms. To test this possibility, we chose the mercury-potassium system and carried out a succession of increasingly elaborate computations based on increasingly complicated models.

Some of the simplest ab initio models of intermolecular potentials rest on the assumption that there occurs *no rearrangement* or distortion of the electron density distribution when the atoms come together. One can then employ, for all internuclear distances, electron densities appropriate to free atoms. The classical electrostatic (coulomb) potential energy of the two overlapping frozen electron densities $\rho_1(r_1)$ and $\rho_2(r_2)$ is, for internuclear separation R,

$$V_{coul}(R) = \int dv_1 \int dv_2 \rho_1 \rho_2 \left(\frac{1}{R} + \frac{1}{r_{12}} - \frac{1}{r_1} - \frac{1}{r_2} \right).$$

Here, individual contributions express the repulsion between nuclei, the repulsion between electrons, and the attraction between each nucleus and the electrons.

To this classical electrostatic energy we must add quantum mechanical contributions: the zero-point kinetic energy $V_{kin}(R)$, the exchange energy $V_{exc}(R)$, and the correlation energy $V_{corr}(R)$. The simplest model for these corrections, the electron gas approximation, uses formulas appropriate to a uniform electron gas. This model permits us to compute the interaction energy:

$$V(R) = V_{coul}(R) + V_{kin}(R) + V_{exc}(R) + V_{corr}(R) ,$$

given the charge densities $\rho_A(r_A)$ and $\rho_B(r_B)$ for the electrons of atoms A and B about their respective nuclei.

One of the standard models for electron densities, the Thomas-Fermi Statistical Model, assumes that the electrons form a classical charge distribution. With the incorporation of an exchange energy, the model becomes the Thomas-Fermi-Dirac (TFD) Model. The electron density and, in turn, the potential V(R), are expressible in terms of the TFD function. Abrahamson has shown[49,50] that such potentials are well described by the Born-Mayer parameterization:

$$V(R) = Ce^{-bR} .$$

From Abrahamson's tables[51] of b and C values together with a combination rule, one can readily obtain potential energy curves for any pair of atoms.

The electron densities computed from TFD theory are inadequate in several respects: they terminate abruptly at finite distances, rather than fall exponentially as more realistic densities do, and they fail to describe atomic shell structure. Thus, it is natural to employ more realistic electron densities, such as those obtained from a self-consistent field (SCF) computation in place of TFD densities. Gordon and Kim[52] advocated this procedure and demonstrated that, when applied to interactions between closed-shell atoms, it predicted potentials in good agreement with empirical potentials.

To construct the free-atom electron densities, we solved the numerical Hartree–Fock (HF) equations using the code of R. Cowan (Los Alamos Scientific Laboratory). This code includes a relativistic correction for $l = 0$ orbitals; the correction has been shown to be important for heavy atoms. We used numerical tables of these electron densities, linearly interpolated, to construct numerical quadrature approximation to the necessary integrals. We verified that we could reproduce the tables of noble-gas potentials published by Gordon and Kim[52] as well as the mercury–mercury potential published by Pyper, Grant, and Gerber.[53]

The Thomas–Fermi–Dirac and Gordon–Kim models neglect all distortion of the electron clouds during a collision. At the opposite extreme, one can assume that the electrons instantaneously adjust to the current nuclear positions throughout the course of the collision. In this approach one must determine the energy of a diatomic molecule for a succession of fixed internuclear distances; the resulting function is the adiabatic potential.

Ideally, one would like to carry out a many-electron, multiconfiguration, relativistic self-consistent field calculation for each distance. Unfortunately, such a computation is beyond contemporary capabilities. Instead, we introduce a succession of approximations:

- We employ nonrelativistic wavefunctions. Pyper, Grant, and Gerber[53] have shown that relativistic corrections alter Hg–Hg Gordon–Kim potentials by only a few percent. Thus, we expect only a small error for this approximation.

- We represent the core electrons by an effective potential. We have used a single valence-electron effective-core potential (ECP) for potassium, determined by Topiol, Moskowitz, and Melius.[54] For mercury we have used two pe entials: a 2-electron potential (the 6s shell) by Basch, Newton, Jafri, Moskowitz, and Topiol[55] and a 12-electron potential (the 6s and 5d shells) by Hay, Wadt, Kahn, and Bobrowicz.[56]

In each case the potentials were obtained by a similar procedure: starting with a set of orbitals[57] that satisfy the isolated-atom Hartree–Fock equations, one constructs from the valence orbitals a nodeless linear combination—a pseudo-orbital. Then the effective core potential is constructed so as to yield the pseudo-orbital as a solution of the single-particle Schrödinger equation. Conventionally, one employs a different effective potential for each angular momentum; one expresses each of these as a superposition of Gaussian functions.

- Using the effective potentials to represent the effects of core electrons upon the two nuclei, we carry out single-configuration, Hartree–Fock, self-consistent field computations for the valence electrons.

In our ECP computations, the valence electrons (3 or 13 in number) move in a self-consistent molecular potential generated by the electrons themselves and by the effective cores. The energy as a function of internuclear separation (the molecular potential curve) includes coulomb repulsion between electrons, interaction between valence electrons and cores, as well as kinetic energy of valence electrons. But it treats the core–core interaction as the interaction between two nonoverlapping charge distributions (and, hence, as a point-charge interaction). This approximation must fail at small separation, where the cores overlap. To account for this effect, we computed the Gordon–Kim potential for the core electrons and, after removing the point-charge portion, added this correction to the previously computed ECP values. These corrections bring the ECP curves into agreement with the Gordon–Kim curve.

Figure 10-14 compares results of our computations using five models: (1) the Thomas–Fermi–Dirac potential constructed with Abrahamson's Born–Mayer parameterization (labeled A); (2) the Gordon–Kim model (labeled G); (3) and (4), two models in which potassium is represented by a single valence electron, and in which mercury is

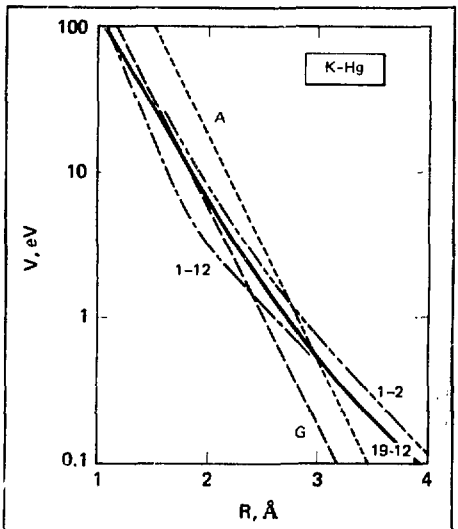

Ground states of potassium and mercury:

$^{19}K(^2S)$: $1s^2 \cdot 2s^2 2p^6 \cdot 3s^2 3p^6 \cdot 4s$

$^{80}Hg(^1S)$: $1s^2 \cdot 2s^2 2p^6 \cdot 3s^2 3p^6 \cdot 3d^{10} 4s^2 4p^6 \cdot 4d^{10} 5s^2 5p^6 \cdot 4f^{14} 5d^{10} 6s^2$

Fig. 10-14. Potential energy curves for potassium-mercury system, computed in various approximations: A: Thomas-Fermi-Dirac potential of Abrahamson; G: Gordon-Kim potential; 1-2: Effective-core SCF with 1 electron potassium, 2 electrons mercury in valence shells; 1-12: Effective-core SCF with 1 electron potassium, 12 electrons mercury in valence shells; 19-12: Effective-core SCF with (all) 19 electrons potassium, 12 electrons mercury in valence shells.

represented by 2 or 12 valence electrons moving in an effective core (labeled 1-2 and 1-12, respectively—these potentials include a Gordon–Kim correction for the core-core interaction); and (5) a calculation treating all 19 potassium electrons and 12 mercury electrons as a self-consistent field problem (labeled 19-12). One expects that this sequence of increasingly elaborate models should converge upon the true, theoretical, adiabatic diatomic potassium–mercury potential. Indeed, the curves of our less elaborate models do bracket the most refined 19-12 curve.

For internuclear separations smaller than about 2.5 Å (potential energies exceeding 1 eV), the simple Gordon–Kim model provides an excellent approximation to the potential energy; at larger separation it falls too rapidly and so underestimates the internuclear separation of the potential-well minimum. The very simple TFD potential overestimates (by some 10%) the separation distance for a given repulsive energy exceeding 1 eV and, like the Gordon–Kim model, underestimates the position of the well minimum. We conclude that the Gordon–Kim model adequately represents the repulsive portion of the interaction potential for energies exceeding 1 eV.

References

49. A. A. Abrahamson, "Repulsive Interaction Potentials Between Rare-Gas Atoms. Homonuclear Two-Center Systems," *Phys. Rev.* **130**, 693 (1963).
50. A. A. Abrahamson, "Born–Mayer-Type Interatomic Potential for Neutral Ground-State Atoms with Z = 2 to Z = 105," *Phys. Rev.* **178**, 78 (1969).
51. A. A. Abrahamson, "Repulsive Interaction Potentials Between Rare-Gas Atoms. Heteronuclear Two-Center Systems," *Phys. Rev.* **133**, A990 (1964).
52. R. Gordon and Y. S. Kim, "Theory for the Forces Between Closed-Shell Atoms and Molecules," *J. Chem. Phys.* **56**, 3122 (1972).
53. N. C. Pyper, I. P. Grant, and R. B. Gerber, "Relativistic Effects on Interactions Between Heavy Atoms: The Hg–Hg Potential," *Chem. Phys. Lett.* **49**, 479 (1977).
54. S. Topiol, J. W. Moskowitz, and C. F. Melius, "Atomic Coreless Hartree–Fock Pseudopotentials for Atoms K through Zn," *J. Chem. Phys.* **68**, 2364 (1978).
55. H. Basch, M. D. Newton, J. Jafri, J. W. Moskowitz, and S. Topiol, "Effective Core Potentials for the Cadmium and Mercury Atoms," *J. Chem. Phys.* **68**, 4005 (1978).
56. P. J. Hay, W. R. Wadt, L. R. Kahn, and F. Bobrowicz, "Ab-Initio Studies of AuH, AuCl, HgH, and $HgCl_2$ Using Relativistic Effective Core Potentials," *J. Chem. Phys.* **69**, 984 (1978).
57. A. J. H. Wachters, "Gaussian Basis Set for Molecular Wavefunctions Containing Third-Row Atoms," *J. Chem. Phys.* **52**, 1033 (1970).

Authors

B. Shore
N. Winter

10.4 Laser-Induced Unimolecular Decomposition Studies

This section includes two areas of study that have application to separation technology beyond present uranium laser isotope separation. One study explores the potential for separating lighter isotopes by the recently discovered technique of vapor phase, multiphoton infrared photodissociation.

The other study examines a long-standing problem in visible photodecomposition: the detailed nature of the photoreduction of uranyl compounds.

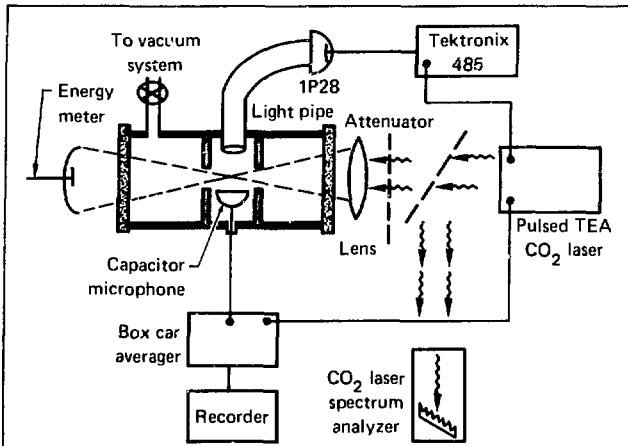

Fig. 10-15. Schematic diagram of apparatus for measurement of multiphoton absorption and luminescence of methylamine during CO_2 laser irradiation.

The investigation concentrates on crystalline uranyl compounds and has potential application in nuclear fuel reprocessing and isotope separation technology.

10.4.1 Laser Isotope Separation of ^{15}N–^{14}N

During the past year, we began an evaluation of applications of laser photochemistry for the potential enrichment of ^{15}N or ^{14}N isotopes. Our ultimate goal was to develop an economic and scalable ^{15}N or ^{14}N enrichment process, using well-engineered, efficient laser systems. There are two significant applications for enriched nitrogen isotopes: as a tracer in biology and agriculture, and in the synthesis of uranium nitride for potential use in liquid metal, fast breeder reactors.[58]

Current production of ^{15}N is about 1000 kg/yr, while the present enrichment cost for ^{15}N, by fractional distillation and chemical exchange techniques, is about $65,000/kg or about $1000/mole. The projected unit cost for a 300-Mt/yr plant, based on the chemical exchange and fractional distillation methods, is estimated to be $20,000/kg, providing that suitable reflux technology and cascade column performance are eventually demonstrated. After systematic (technological and economic) evaluation of the issues, we developed two photochemical schemes[59] that might be used for enriching ^{15}N or ^{14}N isotopes from industrial chemical feed stocks:

- Multiphoton dissociation of CH_3NH_2 (methylamine) by a pulsed CO_2 laser.
- Single photon dissociation of NO by a rare gas halide laser.

Recently, we began a small scale experimental effort to determine the feasibility and limitations of these proposed schemes. The overall concept of the infrared scheme is quite simple. Mixtures of CH_3NH_2/NO are irradiated with a tunable, pulsed CO_2 laser. After selective dissociation of CH_3 $^{15}NH_2$, the $^{15}NH_2$ radical is scavenged by the NO. The products of this reaction are known to be ^{15}NN and H_2O. The CH_3 radical might react with NO and form a CH_3NO molecule, or it might recombine to give C_2H_6. After laser radiation, molecular ^{15}NN is physically separated from the unreacted CH_3NH_2, NO, CH_3NO, and H_2O by fractional distillation at 77 K. We describe the results of the infrared photolysis experiments below.

In Fig. 10-15 we show a schematic of the experimental arrangement for the infrared multiphoton photolysis measurements. Irradiation of samples of methylamine was carried out with a pulsed CO_2 laser. The typical laser power at 9.6 μm was about 2 MW or 0.4 J in 200 ns (FWHM). For achieving high power densities in the reaction cell, a Ge lens was used. The power density at the focal point was about 2 GW/cm^2. Power density at the focal zone could be attenuated with Ge filters. The multiphoton absorption spectra of polyatomic molecules in a strong field were measured, using an optical acoustic cell designed and fabricated at LLL. We designed the acoustic detector and acoustic cavity carefully so that they would register

only the acoustic signals originating from the spatially limited region where the laser beam was focused. The visible luminescence emitted from the focal zone during and after laser irradiation was detected through a side window, using a 1P28 photomultiplier. The wavelength of the CO_2 laser was determined by a precalibrated spectrum analyzer. Gas pressure in the irradiation cell was monitored using a capacitance manometer.

During the opto-acoustic experiments, an infrared laser beam of known wavelength and intensity was directed into the spatially confined irradiation cell. The pulse energy absorbed by the molecules in the cell was rapidly degraded into heat via a vibrational-to-translational energy transfer process. The corresponding pressure changes were monitored by the capacitor microphone, whose signal was amplified and fed to the oscilloscope and recorder. The background acoustic signal associated with the molecular absorption at the unfocused zone or lower laser power region was attenuated by a pair of diaphragms with narrow apertures. The background signals were normally detected much later because of the finite transit time required for acoustic wave propagation in the cell.

We carried out the photolysis experiments in a similar stainless steel cell with the diaphragms removed. Sample pressures were typically 260 Pa or less. Following irradiation of the sample with up to 3000 laser pulses (10 to 15 min), we transferred the entire sample to a 10-cm-long absorption cell for infrared analysis. Using a Beckman IR-9 spectrophotometer, we determined the extent of the reaction by the changes of $CH_3{}^{14}NH_2$ or $CH_3{}^{15}NH_2$ absorption near 12.8 and 9.6 μm. After the infrared analysis, the irradiated sample was condensed at 77 K. The vapor pressure of noncondensibles was measured by a capacitance manometer. The chemical composition of the noncondensible gas was determined by means of a quadrupole mass spectrometer.

Matheson methylamine (98% purity) was purified by repeated distillations in a closed system from traps at −90 to −196°C. We generated nitrogen-15 methylamine by dropping an aqueous solution of nitrogen-15 methylamine hydrochloride on NaOH pellets in a T-necked flask. We transferred the $CH_3{}^{15}NH_2$ vapors through a condenser and collected them in a long-necked flask, surrounded by a dry ice-acetone bath. Residual water in $CH_3{}^{15}NH_2$ was removed by fractional distillation.

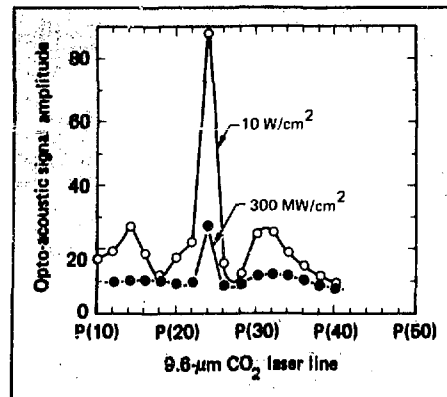

Fig. 10-16. Opto-acoustic data of methylamine $CH_3N^{14}H_2$ observed at various CO_2 laser line (10 Wcm^2 spectrophone data were obtained using a chopped cw CO_2 laser; data at 300 MW/cm^2 were obtained using a pulsed CO_2 laser; both sets of data are normalized to a common P(40) base line).

One of the necessary conditions for selective excitation or dissociation by the multiphoton process is the existence of an isotope shift in the spectral region of interest. Because the infrared spectrum of nitrogen-15 methylamine was not found in the literature, we made several measurements with the Beckman IR-9 spectrometer. The Q branch transition of the C-^{15}N stretching mode was found at 1031.5 cm^{-1}. We confirmed that the corresponding transition for the $CH_3{}^{14}NH_2$ molecule is 1044.0 cm^{-1} (Ref. 60). Thus, the vibrational isotope shift of methylamine in the 9.6-μm region is 12.5 ± 0.5 cm^{-1}.

To optimize the overlap between the CO_2 laser lines and the vibration-rotational transitions of $CH_3{}^{14}NH_2$ to $CH_3N^{15}H_2$ molecules, we measured the relative absorption intensities of the compounds, using the spectrophone and CO_2 laser described in Fig. 10-15. Figure 10-16 shows the spectrophone data of methylamine $CH_3{}^{14}NH_2$ observed at various CO_2 laser power densities. The low power spectrophone result was obtained with a continuous wave CO_2 laser. The laser beam was chopped at 10 Hz. Spectrophone data at higher power densities were obtained with a pulsed CO_2 laser. All spectrophone measurements were made in pure methylamine gas in the pressure range of 5 to

10 Torr. The P(24) laser line at 9.6 μm was found to match well with the Q branch transition of nitrogen-14 methylamine. At a laser power density of about 10 W/cm^2, the spectrophone signal induced by the P(24) line is roughly nine times higher than those signals induced by other laser lines of the same laser intensity. The contrast ratio of the spectrophone signal decreases to about 3 to 1 as the laser power density is increased to about 300 MW/cm^2. Similar measurements nitrogen-15 were made. However, no distinct strong spectrophone signal was observed; i.e., none of the CO_2 laser lines were found to match well with the vibration-rotational transitions of $CH_3{}^{15}NH_2$. In particular, at a power density of 300 MW/cm^2 and similar gas conditions, the P(24) spectrophone signal observed in the nitrogen-14 methylamine gas is roughly three times higher than that observed in the nitrogen-15 sample.

At a power density of 150 MW/cm^2 or higher, weak visible or ultraviolet luminescence was also observed during and after the excitation of the methylamines. The time history of the luminescence signal was monitored by the 1P28 photomultiplier. The luminescence signal appears to be composed of two distinct emission events. A fast rise and decay signal occurs almost instantaneously at the onset of the CO_2 laser pulse, and a slower decay signal lasts for 1 μs or longer. It is generally believed[61] that the instantaneous signal is due to emissions from the excited molecule or excited fragments formed in the intense infrared field. The longer component is due to emissions from hot molecules or radicals excited by the collisional energy transfer processes.

In principle, it is possible to use the luminescence intensity as an indirect measure of the extent of multiphoton absorption in gas. We made a luminescence intensity scan of a nitrogen-14 methylamine sample at various CO_2 laser frequencies. During these experiments the methylamine pressure was kept at 1 Torr, and the pulsed laser energy fluence was kept at about 62 J/cm^2. The luminescence intensity appeared to reach its peak as the laser was scanned to the region of the Q branch transition of methylamine. The luminescence intensity was also found to increase with increasing laser power density. We made no attempt to resolve spectroscopically the origin of these luminescences.

Because the P(24) laser line at 9.6 μm was found to match well with the Q branch transition of $CH_3{}^{14}NH_2$, we performed a series of photolysis experiments to enrich nitrogen-14 in isotopic mixtures. Table 10-11 lists the experimental conditions and gas compositions. Molecular NO was added as a scavenger for the released $NH_2^{\cdot}$ and $CH_3^{\cdot}$ radicals. The isotopic selectivity was determined from the diminution rate of each methylamine isotopic species,

$$S = \frac{\Delta}{\Delta}\frac{\left[CH_3{}^{14}NH_2\right]}{\left[CH_3{}^{15}NH_2\right]} \Big/ \frac{\left[CH_3{}^{14}NH_2\right]_0}{\left[CH_3{}^{15}NH_2\right]_0},$$

where $[CH_3NH_2]_0$'s are the initial mole fractions of methylamine in gas and $\Delta[CH_3NH_2]$'s are the

Table 10-11. Summary of experimental results.

Run	P, Torr $CH_3N^{14}H_2/CH_3N^{15}H_2$/NO,	Laser fluence, J/cm^2	Selectivity,[a]	9.6-μm transitions
1	0.8/0.8/3.2	60	1.4	P(24)
2	0.4/0.4/1.6	60	1.8	P(24)
3	0.4/0.4/1.6	30	1.2	P(24)
4	0.2/0.2/0.8	60	2.0	P(24)
5	0.4/0.4/1.6	60	1.2	P(32)
6	0.4/0.4/1.6	60	1.1	P(36)
7	0.4/0.4/1.5	60	1.0	P(6)
8	0.4/0.4/0	60	–[b]	P(24)

[a]The experimental uncertainty of these values is roughly ± 15%.

[b]No conversion.

changes in concentration of each species before and after laser irradiation. The results are also summarized in Table 10-11. Note that a maximum selectivity of 2 was obtained using the P(24) line. We observed smaller selectivity factors as the laser was detuned from this transition. Mass analysis of the irradiated sample frozen at 77 K indicated that molecular N_2 is the major volatile product. The threshold laser energy fluence for reaction was found to be roughly 30 J/cm^2. In the absence of a molecular scavenger, we found no change in chemical composition of the irradiated sample.

Based on the experimental findings, we believe that the primary multiphoton infrared dissociation channel for CH_3NH_2 is:

$$CH_3NH_2 \rightarrow CH_3^{\bullet} + NH_2^{\bullet} \qquad \Delta H = 79 \text{ kcal/mole} .$$

It is known that NH_2 radicals react rapidly with NO to yield molecular N_2, the major nitrogen-containing product:

$$NH_2^{\bullet} + NO \rightarrow N_2 + H_2O,$$

$$k = 8 \times 10^{-12} \text{ cm}^3\text{/molecule,s} \qquad \text{(see Ref. 62).}$$

where k is the reaction rate. The competing recombination reaction $CH_3^{\bullet} + NH_2^{\bullet} + M$ is slow compared to the scavenging reaction. In addition, cleavage of the CH_3–NH_2 bond is the lowest endothermic channel for dissociation. The other dissociation channels are:

$$CH_3NH_2 \rightarrow CH_3NH + H \qquad \Delta H = 96 \text{ kcal/mole}$$
$$\rightarrow CH_2NH_2 + H \qquad \Delta H = 102 \text{ kcal/mole} .$$

In the absence of NO, the lack of a measurable enrichment and the lack of any change in the chemical composition suggest that the three-body recombination rate of $CH_3 + NH_2 + M$ is considerably faster than either $CH_3 + CH_3 + M$ or $NH_2 + NH_2 + M$ reactions.

Based on these results, we propose the following set of steps for the overall processes:

$$CH_3{}^{14}NH_2 \xrightarrow{nh\nu} CH_3 + {}^{14}NH_2 \qquad n \geq 26,$$

selective excitation/dissociation

$$^{14}NH_2^{\bullet} + NO \rightarrow {}^{14}N_2 + H_2O$$

$$CH_3^{\bullet} + NO \xrightarrow{M} CH_3NO$$

$$CH_3{}^{14}NH_2^{\bullet} + CH_3{}^{15}NH_2 \rightarrow CH_3{}^{14}NH_2 + CH_3{}^{15}NH_2^{\bullet},$$

collisional energy transfer

$$^{14}NH_2 + CH_3{}^{15}NH_2 \rightarrow CH_3{}^{14}NH_2 + {}^{15}NH_2,$$

collisional radical exchange.

In general, the energy transfer and radical exchange reactions tend to decrease the selectivity of reaction. This decrease is consistent with our experimental findings in which the observed enrichment factor appears to be somewhat smaller than the spectroscopic selectivity, namely, 3 to 1.

Both the spectrophone and luminescence data seem to indicate a stronger absorption of infrared photons, because the laser was tuned to the Q branch transition of nitrogen-14 methylamine. This stronger absorption may be caused by two factors: a better matching of the laser and molecular vibrational frequencies, and a higher density of absorption lines of methylamine at the Q branch region. Because a similar effect was not observed in the nitrogen-15 sample, the second factor is probably not important. The relative intensities of the spectrophone signals observed in the methylamine sample of different nitrogen isotopes have also shed some light on the maximum enrichment factor that one can achieve with high intensity CO_2 laser radiation. For example, at the P(24) laser transition, the contrast of nitrogen-14 vs the nitrogen-15 spectrophone signal is roughly 3. The experimentally achieved enrichment factor was 50% of that expected.

Although the vibrational isotope shift of the CH_3–NH_2 stretch mode is sizable, the enrichment factors achieved from these photolysis experiments are quite small; this has probably resulted from the overlap of the vibrational-rotational lines of $CH_3{}^{14}NH_2$ and $CH_3{}^{15}NH_2$, because of power broadening under the intense infrared laser field. The ^{15}N isotope separation might also be achieved by multiphoton dissociation of other nitrogen-containing polyatomic molecules, such as N_2H_4, or other amines using molecular NO as a radical

scavenger. However, the enrichment factor will probably be small because of this limiting factor.

In summary, we have demonstrated a selective, multiphoton infrared chemical process for enriching ^{14}N in methylamine. An enrichment factor of two has been achieved from the irradiation of a $CH_3{}^{14}NH_2/CH_3{}^{15}NH_2/NO$ mixture, using the P(24) line of the 9.6-μm CO_2 laser. The threshold energy fluence for decomposing CH_3NH_2 to $CH_3^{\cdot}$ and $NH_2^{\cdot}$ radicals was roughly 30 J/cm^2. The radical scavenger NO appears to be essential for obtaining the selectivity in the photolysis. We believe ^{15}N enrichment could be directly achieved with a similar photochemical scheme, using a continuously tunable high-pressure CO_2 laser. Higher enrichment factors might be possible by dissociating methylamine, using a scheme incorporating pulses from two infrared lasers.[63]

References

58. V. J. Tennery, *Nitrogen-15 Enrichment and its Potential Use in Advanced LMFBR Mixed-Nitride Fuels*, Oak Ridge National Laboratory, Oak Ridge, Tenn., Rept. TM-5621 (1977).
59. H.L. Chen and J.W. Dubrin, *Isotope Separation of ^{15}N by Selective Photodissociation of CH_3NH_2 or NO*, UC LLL Patent Disclosure, Lawrence Livermore Laboratory, Livermore, Calif., Invention Case No. IL-6379 (1978).
60. A. P. Gray and R. C. Lord, "Rotation-Vibration Spectra of Methyl Amine and it's Deuterium Derivatives," *J. Chem. Phys.* **26**, 691 (1957).
61. V. N. Bagratashvili, I. N. Knyazen, V. S. Letokhov, and V. V. Lobko, "Resonance Excitation of C_2H_4 Molecule Luminescence by Pulsed High-Pressure Continuously Tunable CO_2 Laser," *Opt. Commun.* **14**, 426 (1975).
62. M. Gehring, K. Hoyermann, H. Schackle and J. Wolfrum, "Elementary Steps for the Formation and Destruction of Nitric Oxide in the Hydrogen-Nitrogen-Oxygen System," *14th Symp. of Combustion*, p. 99 (Pittsburgh, Pa., 1973).
63. R. V. Ambartzumian, Yu. A. Gorokhov, G. N. Markarov, A. A. Puretskii, and N. P. Furzikov, "Separation of Osmium Isotopes by Dissociation of the OsO_4 Molecule in a Two-Frequency Infrared Laser Field," *Sov. J. Quantum Electron.* **7**, 904 (1977).

Authors

H. L. Chen
C. Borzileri

10.4.2 Photochemistry of Crystalline Uranyl Compounds

Low-temperature crystalline uranyl (UO_2^{+2}) compounds were considered for uranium isotope separation during the Manhattan project. The spectra of two compounds taken at that time showed isotopic structure, but no photochemical activity on which to base a separation process was observed in the project's limited investigation. Such a process may still have considerable advantage over present gaseous methods. As a result, the photochemical as well as spectroscopic properties of uranyls have been investigated as part of the reaction dynamics research activities.

The spectroscopy and photochemistry of uranyl (UO_2^{+2}) compounds are subjects having extensive literatures dating back to the nineteenth century.[64,65] A large number of distinct salts have been synthesized with combinations of organic and inorganic anions and alkali and alkaline earth cations. These uranyl compounds all have a characteristic absorption in the visible region, which can be exceedingly rich in structure. In aqueous solutions, the lowest excited state of UO_2^{+2} has proven to be a powerful photochemical agent capable of oxidizing such diverse anions as I^-, $C_2O_4^{-2}$, and HCO_2^-, and any number of alcohols.

The understanding of both the spectroscopy and the photochemistry has proven to be an elusive objective; almost all the photochemistry has been done in solutions in which, as it appears, multiple reaction pathways have obscured the nature of the fundamental processes. Similarly, the spectroscopy has generally been solution work at elevated temperatures, where low resolution has reduced conclusions to educated guesses.

Notable exceptions exist that have concentrated the properties of crystalline compounds, particularly at low temperatures.[66] Here, the regular crystalline array yields a simplified spectrum and allows controlled studies of photochemical activity. However, only three crystalline uranyl compounds were reported to react photochemically,[64,67] each containing the formate (HCOO) ligand.

Undaunted, we set about to survey the photochemical and spectroscopic properties of a large number of uranyl crystals to determine the exact extent of crystalline photochemical behavior in uranyls. We discuss here some results of that search and one example of a detailed investigation into the photochemical behavior of a uranyl crystal: uranyl formate monohydrate.

Survey of Crystalline Uranyl Visible Photochemistry. The first report of photochemical activity of a crystalline uranyl compound was made by Muller in 1915 on uranyl formate monohydrate; scant development has occurred since. Only the sodium

Table 10-12. Survey of crystalline uranyl visible photochemistry.

	H_2O	Li^+	Na^+	K^+	Rb^+	Cs^+	NH_4^+	$(CH_3)_4N^+$	$Guan^+$
Formate	10	10	10	10	10	10	10	–	–
Lactate	10	10	10	10	–	–	–	–	–
Glycolate	10	–	10	–	–	–	–	–	–
Oxalate	1	3	3	1	–	–	3	–	5
Acetate	0	–	0	–	–	–	–	–	–
Nitrate	0	–	–	0	0	0	0	–	–
Chloride	0	–	–	0	–	0	0	0	–

and ammonium salts of the formate have been reported to be photoactive. The high lability of the hydrogen on the formate has been suggested as the key to the chemical activity in the solid state. We prepared a number of compounds that have labile hydrogen atoms on the ligands (the formate, lactate, and glycolates) and that have reported photochemical activity in solution (oxalates); also, we prepared a number of compounds whose virtues were due more to their clean spectra than to anticipated visible photochemistry.

The prepared crystals were illuminated in the visible by exposure to bright sunlight, and a rank order of activity was established. The results of this survey are summarized in Table 10-12, which displays a matrix of compounds formed by the intersection of the anion ligand row with the cation (or H_2O) column. The numbers represent a rough estimate of relative photochemical activity. Blanks appear where no compound was prepared. The survey uncovered a remarkably large number of active crystalline systems and demonstrates that, to a large degree, the photoactivity of a given reducing ligand is independent of the particular crystalline structure in which it is located.

Uranyl Formate Monohydrate [$UO_2(COOH)_2 H_2O$]. Uranyl formate monohydrate (referred to below as "the formate") is particularly interesting because of its photochemical activity. We have so far learned that fluorescence in the formate occurs from at least two excited states, and that the formate photochemistry, which proceeds with near unit quantum efficiency at room temperature, has extremely low quantum efficiency at 12 K.

A fluorescence spectrum of the formate with laser excitation at 4682.5 Å is given in Fig. 10-17. The regular repetition of groups of lines is characteristic of uranyl fluorescence spectra. The spacing (850 cm^{-1}) corresponds to the symmetric stretch vibration in the ground electronic state of the linear

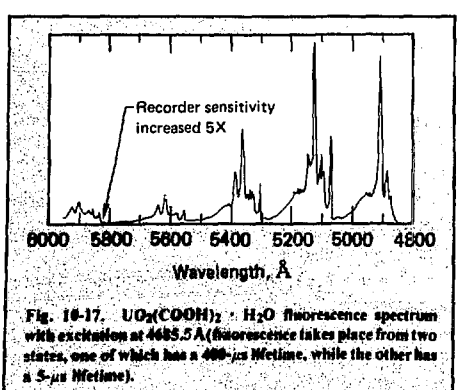

Fig. 10-17. $UO_2(COOH)_2 \cdot H_2O$ fluorescence spectrum with excitation at 4685.5 Å (fluorescence takes place from two states, one of which has a 400-μs lifetime, while the other has a 5-μs lifetime).

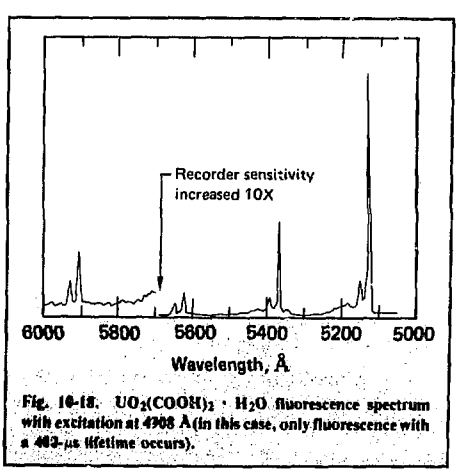

Fig. 10-18. $UO_2(COOH)_2 \cdot H_2O$ fluorescence spectrum with excitation at 4908 Å (in this case, only fluorescence with a 403-μs lifetime occurs).

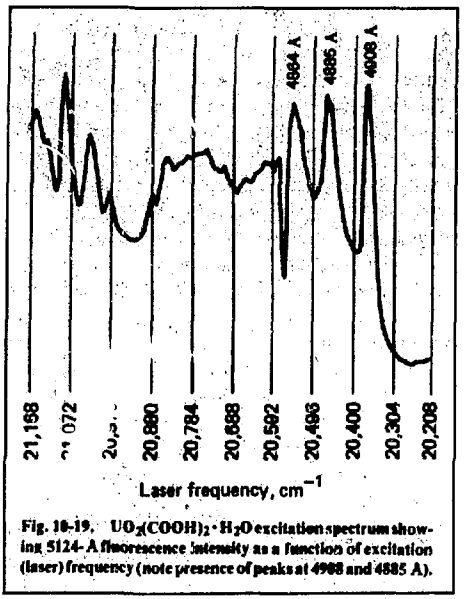

Fig. 10-19. $UO_2(COOH)_2 \cdot H_2O$ excitation spectrum showing 5124-Å fluorescence intensity as a function of excitation (laser) frequency (note presence of peaks at 4908 and 4885 Å).

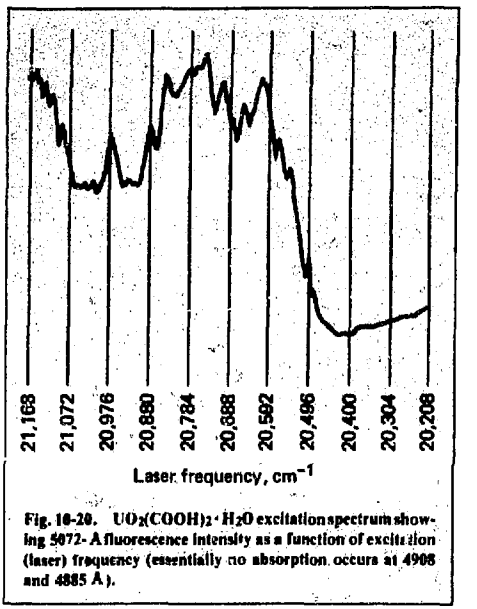

Fig. 10-20. $UO_2(COOH)_2 \cdot H_2O$ excitation spectrum showing 5072-Å fluorescence intensity as a function of excitation (laser) frequency (essentially no absorption occurs at 4908 and 4885 Å).

OUO^{+2} group. The spectrum of Fig. 10-17 should be compared to that of Fig. 10-18 in which the laser wavelength of 4908 Å corresponds to the longest wavelength that excites fluorescence. Note that the series of lines at 5072, 5304, 5557, 5833, and 6139 Å are entirely absent under long wavelength excitation.

The excited state that produces the series of lines beginning with 5072 Å is distinguished also by its lifetime. At 12 K, where all the fluorescence, excitation, and absorption spectra presented here were taken, it has a lifetime of 5 μs, compared to the 400-μs lifetime of other lines in the fluorescence spectrum.

Figure 10-19 shows the fluorescence intensity at 5124 Å (the second peak in the progression beginning with 4908 Å) as a function of excitation (laser) frequency. A sharp onset of fluorescence is observed at 20,375 cm^{-1} or 4908 Å. Because this frequency is observed both in excitation and in fluorescence (see Fig. 10-19), it corresponds to a pure electronic transition. In both absorption and fluorescence, therefore, vibronic progressions will be built on this origin (see Figs. 10-17 and 10-20).

Figure 10-20 shows a similar spectrum for production of fluorescence at 5072 Å. In this case, however, fluorescence does not begin until the laser frequency exceeds about 20,480 cm^{-1}. This spectrum indicates that significant exchange of energy among the fluorescing states does not occur until about 100 cm^{-1} above the 20,375 cm^{-1} origin.

An unusual aspect of the formate excitation spectrum of Fig. 10-19 is that the origin at 4908 Å and the peaks at 4885 and 4864 Å are of similar intensity. In the absorption spectrum of the formate that is given in Fig. 10-21, the absorption at 4864 Å is very much stronger than the absorption at the other wavelengths. This type of behavior could be explained by saturation of the absorption by the laser, but this does not seem to be the case because fluorescence intensity was observed to depend on laser intensity. A more likely explanation is that the 4864-Å absorbing state is coupled to one or more other states. The excitation spectrum of Fig. 10-20 shows that 4864-Å light does cause fluorescence at 5072 Å, while 4885- and 4908-Å absorption does not. Thus, part of the absorption at 4864 Å, which would otherwise lead to fluorescence at 5124 Å and related lines, is shunted over to the state that produces 5072 Å, etc., fluorescence. It is not clear at this point that coupling to this state alone is sufficient to explain the difference between absorption

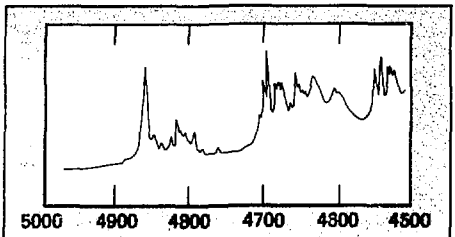

Fig. 10-21. $UO_2(COOH)_2 \cdot H_2O$ ground-state absorption spectrum (dominant feature on left end is at 4864 Å; comparison with excitation spectra indicates energy partitioning between two or more states follows absorption at 4864 Å, while at longer wavelength it does not).

and excitation spectra. We suspect, in fact, that a third state is also coupled to the 400-μs state, and that this state may be the one responsible for photochemistry.

The photodecomposition studies of the formate have been carried out at room temperature by previous workers,[67] and a two-step mechanism has been suggested to produce U(IV) from U(VI) in which the first step to produce U(V) is photochemical. The final products have been identified as UO(OH)(COOH) H_2O and CO_2. The intermediate products are in doubt, though formation of the COOH radical has been observed. No suggestions on how the charge transfer and decomposition take place from a molecular structure viewpoint have been made.

We have discovered in the following simple experiment that the photochemical activity of the formate is essentially nonexistent at 12 K, compared to its activity at room temperature. A crystal of the formate was irradiated for 4 h at room temperature with blue light filtered from a quartz-iodine lamp. The crystal turned from yellow to dark olive green. A similar crystal was irradiated under the same conditions except that the sample temperature was 12 K. The irradiation went on for 14 h without apparent change in the crystal color or other physical properties. Its absorption spectra before and after irradiation were identical. Apparently, sufficient lattice energy must be present to permit reorientation, or some other change, to take place in the excited molecular complex. Otherwise, decomposition does not occur.

This observation suggests that a photochemical quenching of fluorescence should occur as the temperature is raised from 12 K toward room temperature. Quenching of fluorescence is indeed observed: at 12 K, as already mentioned, the lifetime is 400 μs; at 40 K, it has dropped to 65 μs; and at 60 K it is 20 μs. A plot of the logarithm of the lifetime as a function of T^{-1} shows a straight line, implying that a thermal activation mechanism is responsible for quenching. The rate of quenching is, therefore, of the Arrhenius form $k = k_0 \exp(-E_a/kT)$. In this case the activation energy is $E_a = 100\ cm^{-1}$, and the infinite temperature limit on the rate of quenching is $k_0 = 7 \times 10^5$ s. We cannot yet identify the extent to which the quenching effect is due to photochemistry, because nonradiative relaxation can also be responsible. Thus, for example, at temperature 40 K, fluorescence at 5072 Å is observed with excitation at 4908 Å, indicating thermally induced radiationless energy transfer from the 400-μs state to the 5-μs state. This process must contribute to the quenching of fluorescence from the 400-μs state, but it is not yet clear to what extent. Experiments are in progress to determine the role of photochemistry in fluorescence quenching and to characterize the state(s) from which it originates.

References

64. E. Rabinowitch and R. L. Belford, *Spectroscopy and Photochemistry of Uranyl Compounds* (Macmillan, New York, 1964).
65. A. F. Bernhardt and C. G. Stevens, *Laser Isotope Separation Annual Report—1976*, Lawrence Livermore Laboratory, Livermore, Calif., UCRL-50040-76 (1977), (title U, report SRD), pp. 200-202; and C. G. Stevens and A. F. Bernhardt, Patent Disclosure—Invention Case No. IL-6212.
66. G. H. Dieke and A. B. F. Duncan, *Spectroscopic Properties of Uranium Compounds* (McGraw-Hill, New York, 1949).
67. B. Claudel et al., "Kinetic Modules Models in Solid State Photochemistry: Their Validity and Interpretation in the Case of Uranyl Formate Monohydrate," *J. Photochem.* **8**, 117 (1978).

Authors

A. F. Bernhardt
C. G. Stevens

10.5 Photon-Atom Dynamics

10.5.1 Theoretical Background

Continuing our support on the experimental development of efficient schemes for selectively exciting and subsequently ionizing atomic vapor sources, we have developed theoretical models implemented as computer codes that permit us to follow detailed time dependence of excitation and ionization; this allows us to predict the effects of modified operating conditions (e.g., choices of excitation transitions and laser intensities). By revealing the fundamental behavior of atoms exposed to brief intense fields, our codes allow us to examine the observable effects of coherent excitation. These studies are a natural outgrowth of the program reviewed in last year's annual report.[68] The following sections summarize some of our subsequent observations.

Basic Equations. Previous annual reports[68,69] have described the model that underlies our theoretical description of atomic vapor excitation and ionization by multiple resonantly tuned pulsed lasers. Because by design the laser-induced ionization occurs more rapidly than competing collisional or spontaneous emission processes, the dynamics of excitation follows laws of motion expressed by the time-dependent Schrödinger equation in the rotating wave approximation (RWA).[70] In this approximation, we parameterize the N-level atom dynamics by a set of N values for cumulative detunings Δ_n of laser frequencies away from Bohr frequencies, of N values for probability loss rates γ_n from individual levels, and of N – 1 values for the interaction energy between atomic transition dipole moments and laser electric fields, traditionally expressed as Rabi frequencies Ω_n. These parameters appear in the RWA Hamiltonian W governing the time dependence of complex-valued amplitudes $C_n(t)$,

$$i\frac{d}{dt}C_n(t) = \sum_m W_{nm}C_m(t) ,$$

whose absolute square yields the probability $P_n(t) = |C_n(t)^2|$ of finding an atom in state n. As we have previously pointed out,[68,71,72] the time-dependent Schrödinger equation has analytic solutions under special conditions. Consider an excitation flow through an unbranching chain-like succession of N adjacent linked levels (the N-level ladder); then, for particular choices of the N – 1 Rabi frequencies and resonant tuning of the N – 1 monochromatic exciting lasers, the probability amplitudes become expressible in terms of well-known special functions. Although such analytic solutions provide useful insight into the mechanism of coherent excitation, they do not provide a reliable quantitative description of experimental conditions. Such realistic modeling can be done only by direct numerical integration of the time-dependent equations of motion. For this purpose, we have developed computer codes capable of integrating the appropriate equations, of carrying out the needed statistical averages, and of displaying results in useful graphical form.

Computer Modeling. To illustrate the behavior of pulsed coherent excitation, Fig. 10-22 schematically depicts the excitation linkage of a hypothetical three-level atom. A pulsed laser is tuned to the resonance atomic frequency between the ground state (level 1) and an excited state (level 2). A second simultaneous pulsed laser is tuned to the frequency connecting level 2 with a third, autoionizing, level. Our codes permit flexibility in describing the time dependence of the laser pulses; for the following examples the pulse intensities follow a Gaussian envelope.

Because the vapor source has a distribution of thermal velocities leading to a distribution of Doppler-shifted detunings, we must average the numerical solutions over the Doppler detunings (an example of inhomogeneous relaxation) to obtain theoretical excitation populations. Figure 10-23(a) shows, for this example, the Doppler distribution of un-ionized atoms at a succession of times. We observe that the laser excitation preferentially removes atoms from the center portion of the distribution—atoms whose Doppler shifts do not appreciably exceed the peak value of the (time-varying) Rabi frequency. Figure 10-23(b) displays the (Doppler-averaged) probabilities for population at each of the three levels, together with the ionized fraction. Observe that the Doppler averaging has nearly eliminated evidence of the population oscillations that characterize individual solutions to the Schrödinger equation. Only a slight ripple gives evidence of the underlying coherence.

The three-level model neglects several characteristics of real atomic transitions. Many atomic

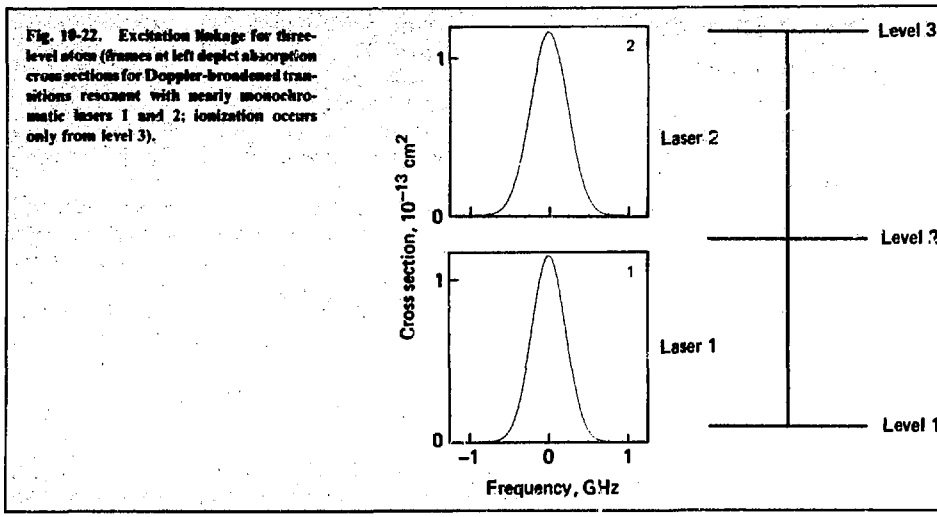

Fig. 10-22. Excitation linkage for three-level atom (frames at left depict absorption cross sections for Doppler-broadened transitions resonant with nearly monochromatic lasers 1 and 2; ionization occurs only from level 3).

ground states and most excited levels have an angular momentum associated with the electronic structure. A level whose angular momentum quantum number is J has 2J + 1 quantized possible orientations (each corresponding to a distinct magnetic sublevel) of the dipole transition moment in the laser electric field. Hence, there are 2J + 1 possible Rabi frequencies among the atomic ensemble.[68,73] Like the effect of Doppler-shift distributions, the distribution of orientations (or averages over magnetic sublevels) acts to average out the apparent population oscillations,[73] although for the example of Fig. 10-23 the resulting effect is insignificant.

A second, potentially more significant, extension of the three-level atom occurs when nuclear spin adds an additional angular momentum to the electronic angular momentum. The resultant total angular momentum F produces, through selection rules $\Delta F = +1, 0, -1$, a more complicated excitation than the simple three-level chain. Figure 10-24 shows the excitation linkage diagram for a hypothetical three-level atom whose electronic angular momenta $J = 5 \rightarrow 6 \rightarrow 7$ couple with a nuclear spin $I = 5/2$ to yield a range of values for the total angular momentum F. The linkages satisfy the selection rules $\Delta F = +1, 0, -1$. Because the hyperfine levels are not exactly degenerate (Fig. 10–24 exaggerates the assumed energy splitting), the absorption coefficient for each transition exhibits structure. The coefficient shown in Fig. 10-25(a) is a

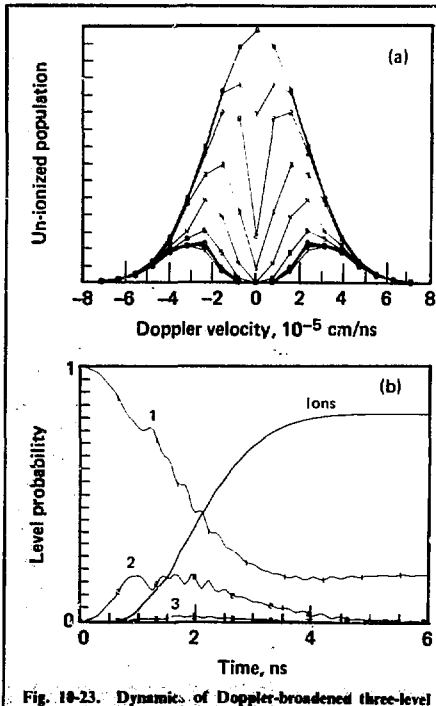

Fig. 10-23. Dynamics of Doppler-broadened three-level atom: (a) Doppler distribution of un-ionized atoms vs Doppler velocity; (b) probabilities P_n for population in levels n = 1, 2, and 3, and ionization probability averaged over Doppler distribution of detunings, as a function of time.

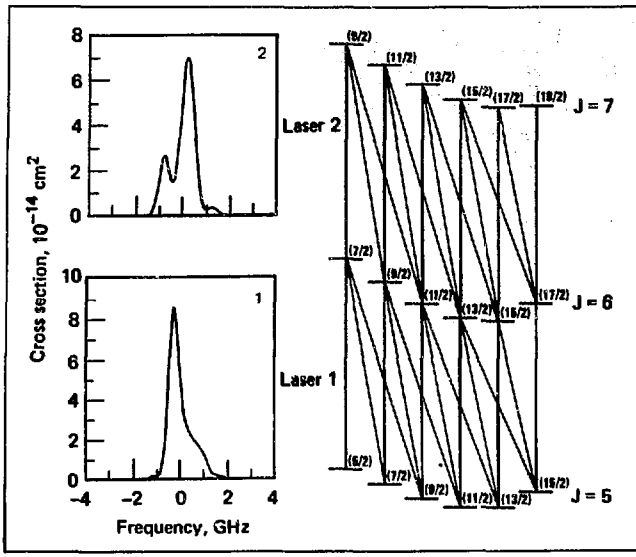

Fig. 10-24. Excitation linkage for hypothetical three-level atom with hyperfine structure appropriate to nuclear spin I = 5/2 in sequence of atomic angular momenta J = 5 → 6 → 7 (frames at left show absorption cross section for Doppler broadened hyperfine structure; ionization occurs equally from all sublevels of the J = 7 level).

superposition of independent Gaussian profiles centered at the various hyperfine component frequencies, with weights proportional to the transition strength of the component.

The addition of hyperfine structure to the model three-level atom produces the excitation probabilities shown in Fig. 10-25(b). Population oscillations remain observable as small fluctuations. The overall picture is qualitatively similar to Fig. 10-24, although ionization here is less complete; appreciable population remains trapped in relatively inaccessible sublevels. The portrayal of un-ionized Doppler distribution in Fig. 10-25(a) shows how hyperfine splitting can act as an inhomogeneous broadening mechanism by spreading out the resonant frequencies; we no longer see a narrow band of ionized atoms centered around zero detuning, but instead we see a much broader ionization profile.

The foregoing examples illustrate the numerical modeling results, which permit us to address a broad range of issues concerned with choosing laser characteristics to achieve optimum ionization.

Fitting Rate Equations to Excitation Dynamics. Although we expect the underlying dynamics of our pulsed excitation experiments to comply with the coherent Schrödinger equation, the introduction of statistical averages over magnetic sublevel populations and over Doppler shifts, taken with the hyperfine linkages, produces time-dependent excitation and ionization functions that appear qualitatively similar to those obtainable from rate equations. Statistical averages damp the oscillatory behavior typical of coherent excitation. Because integration of simple rate equations saves considerable computation time compared with the effort required to compute statistical averages over hyperfine linkages, we attempted to fit our computed results into the form of rate equations by determining empirical rate coefficients. However, we found that such rate equations would require time-dependent rate coefficients or, alternatively, several rate constants per transition. In general, using a single rate constant, we would underestimate the laser power required to produce a given amount of ionization, some of the numerous transitions between hyperfine sublevels of the atom are relatively weak and so act as bottlenecks in the population flow out of some levels. We conclude that rate equation approximations are not reliable predictors of our excitation experiments.

Limitations of Rate Equations. Traditional modeling of radiative-excitation dynamics, dealing with incoherent low-intensity excitation, has ap-

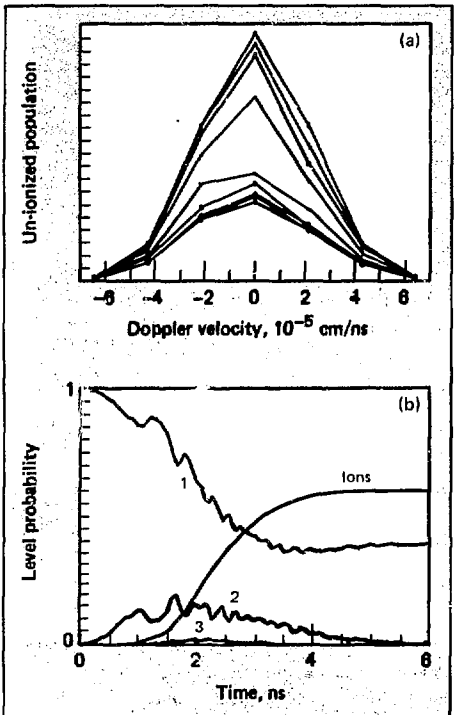

Fig. 10-25. Dynamics of Doppler-broadened three-level atom with hyperfine structure: (a) Doppler distribution of un-ionized atoms vs Doppler velocity; (b) probability P_n for population in levels N = 1, 2, and 3 and ionization probability averaged over Doppler distribution of detunings, as a function of time.

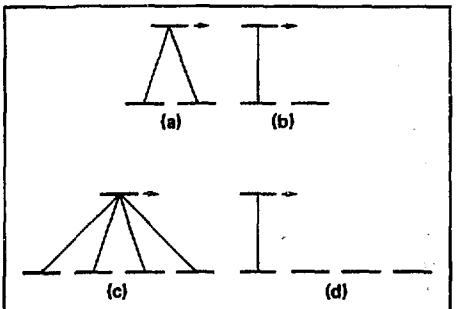

Fig. 10-26. Single-step excitation linkages of multiple levels to single ionizing upper level: (a) the lambda system, (b) equivalent system, (c) the N-leg system, and (d) equivalent system.

plied rate equations to the calculation of non-equilibrium populations. Predictions of such equations can differ dramatically from predictions of the Schrödinger equation. The following simple examples illustrate the qualitative differences that can occur between coherent and incoherent excitation.

As an example, we have previously learned[73,74] that, for a lossless N-level system with ladder-like excitation, the Schrödinger equation with equal Rabi frequencies predicts long-time average populations close to the rate-equation steady-state values of 1/N. The introduction of a small ionization loss from the final (Nth) level of the ladder does not alter the qualitative agreement between rate equations and the Schrödinger equation: all the population eventually ionizes.

However, we have also pointed out[66] a case in which rate equation analyses fail to predict, even qualitatively, the ionization process: in a coherently excited three-level ladder with loss from the middle level—the lambda system; see Fig. 10-26(a)—only half of the population can ionize. The rest remains locked in a coherent state. By contrast, the rate equations incorrectly predict complete ionization for the lambda system.

We can readily trace the failure of the rate equations in the lambda system to the importance of phase relationships in the dynamics. Indeed, a suitable redefinition of basis levels replaces the lambda system with the system of Fig. 10-26(b): a two-level ladder plus an isolated level.

The general N-leg system of Fig. 10-26(c) is similar: it is equivalent to N − 1 isolated levels and a two-level ladder, so that only 1/N of the population ionizes. Again, this result contrasts with a rate equation, which would predict eventual complete ionization. As with the lambda system, it is the phase relationships that permit the transformation from Fig. 10-26(c) to Fig. 10-26(d); they cause destructive interference between the excitation paths, thereby diminishing the excited state population.

The interferences prevent us from applying rate equations to excitation with crossed polarization, as illustrated in the case of excitation from a level with angular momentum J = 0 to a level with J = 1, and thence to J = 0 from whence ionization occurs. If we neglect degeneracy and regard the system as a three-level ladder—see Fig. 10-27(a)—then we expect all of the population to eventually ionize. This

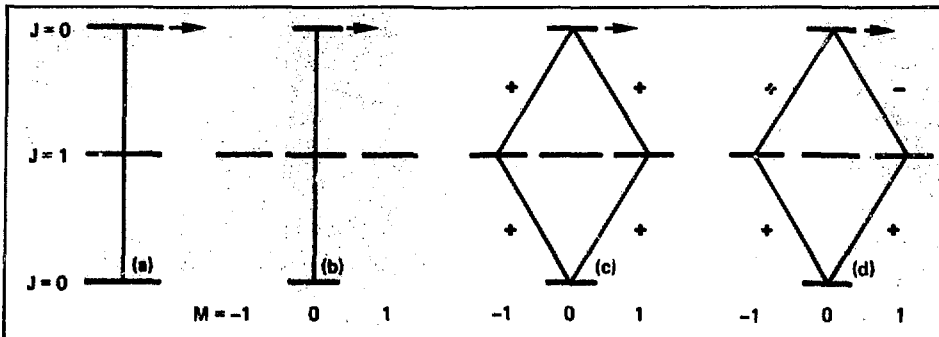

Fig. 10-27. Two-step excitation linkages: (a) three-level ladder; (b) J = 0 → 1 → 0 linkage for linear polarization; (c) linkage for helicity representation, linear polarization + signs indicate phases of Rabi frequencies, and (d) linkage for crossed-linear polarization.

is indeed the case when both lasers are linearly polarized along the same axis, but for other choices of polarization there may be no ionization at all. To understand this effect, consider the magnetic sublevel structure,[73] as shown in Fig. 10-27(b). Lines indicate the linkages appropriate to linear polarization with quantization along the polarization axis; the selection rule is $\Delta M = 0$. We see that in this representation the system comprises a three-level ladder with two extraneous unpopulated levels. All of the population eventually ionizes, as we expect from a rate equation.

These same results must, of course, occur in a helicity basis in which we express linear polarization as a superposition of right- and left-circular polarization (selection rules $\Delta M = +1$ and $\Delta M = -1$). Figure 10-27(c) shows these linkages with their phases. However, if we change one of the phases from + to –, the linkage represents crossed-linear polarization, Fig. 10-27(d). We now find that no excitation reaches the final J = 0 level, so that no ionization ever occurs. Destructive interference prevents this excitation. Rate equations, unable to distinguish between the linkages of Figs. 10-27(c) and 10-27(d), predict complete ionization in both cases.

The foregoing examples emphasize a fundamental limitation of rate equations. Whenever phases are important in the definition of a problem (as they are in closed loops or in crossed polarization), rate equations are not a reliable model of excitation dynamics.

Definition of Virtual Levels. The notion of "virtual level," as opposed to a "real level," occurs when we deal[75] with a nonresonant atomic (or molecular) excitation process—a process for which there is a mismatch (detuning) between the atomic energy difference E and the excitation energy h. The designations "real" and "virtual" actually refer to extreme cases of zero and large detunings, respectively. We found it interesting to examine in detail[76] the transition between these extremes and to identify the dividing line between the two cases, by examining a three-level atom excited by two monochromatic lasers. We let ionization occur from the third level and assumed that two-photon excitation to this ionizing level remained exactly resonant, while the single photon transition to level 2 could be detuned by an amount Δ.

From plots of the level probabilities $P_n(t)$ for various detunings, with the choice of equal Rabi frequencies for simplicity, we observed the gradual change from resonant three-level atom behavior when detuning was absent to regular two-level population oscillations bypassing level 2 when the detuning exceeded two Rabi frequencies. Figures 10-28 and 10-29 illustrate this effect. We have published a detailed illustrated account of this behavior.[76]

Calculation of Long-Time Average Populations. The resonant excitation of atoms by monochromatic lasers introduces several time constants:

- The Rabi frequencies, which set the time interval over which the atom can respond to the excitation.
- Relaxation rates, which set the time interval for loss of coherence.
- Ionization rates, which set the time scale for loss of probability.

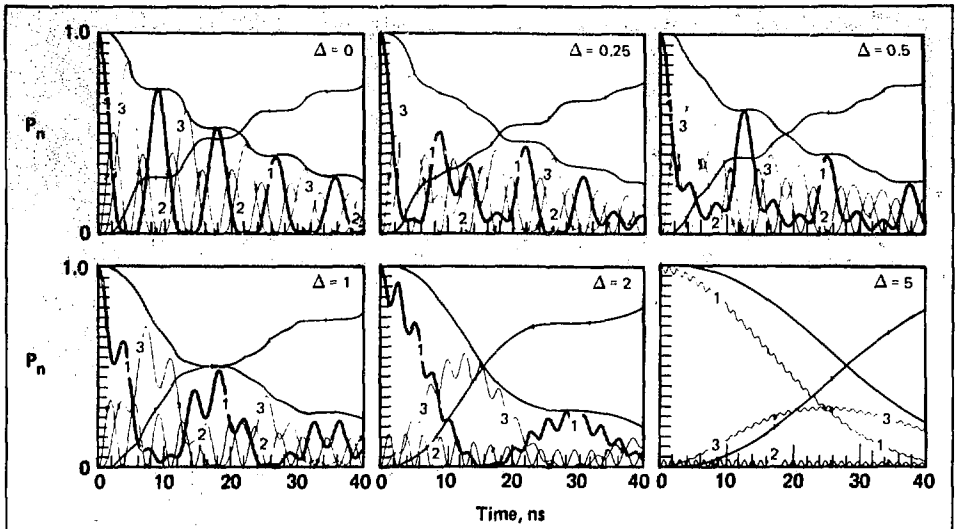

Fig. 10-28. Population probability P_n vs time for three-level ladder, with drain, for successively larger values of detuning of level 2 from resonance, while maintaining 2-photon resonance condition.

It may happen that observations take place over many Rabi cycles, yet still over a time interval in which there is little loss of coherence or of probability. Such observations probe time-averaged populations. These excitation populations, established in the absence of relaxation, can be very different from the steady state populations that rate equations predict. To predict the populations, one must determine, from solutions to the time-dependent Schrödinger equation, time averages of the probability $P_n(t)$ of finding level n excited. One may use the RWA Hamiltonian W to express the amplitude at time t in terms of the known initial amplitude,[68]

$$P_n(t) = \left| \sum_m < n \left| e^{-iWt} \right| m > C_m(0) \right|^2$$

One may then employ (right) eigenvectors $R_n(k)$ of W and (left) eigenvectors $L_n(k)$ of the transpose W^T to write:

$$P_n(t) = \sum_{k,k'} R_n(k)\, B(k)\, R_n(k')^*\, B(k')^* \times \exp\left[-i\,(Z_k - Z_{k'}^*)t\right] ,$$

where Z_k is the k'th eigenvalue of W and where:

$$B(k) = \sum_m L_m(k)\, C_m(0) ,$$

is the initial component of the kth eigenvector. If one now averages $P_n(t)$ over a long time compared with the characteristic times $1/Z_k$, the exponential time factor averages to zero unless $Z_k = Z_{k'}^*$. When the matrix W is nondegenerate, eigenvalue equality occurs only when k = k', and the long-time average can be obtained quite simply as the single sum[72]

$$\bar{P}_n = \sum_k \left| R_n(k)\, B(k) \right|^2$$

When degeneracies are present, as in problems of ellipitical polarization, one must introduce two modifications. First, one must explicitly bi-orthogonalize the degenerate eigenvectors. Second,

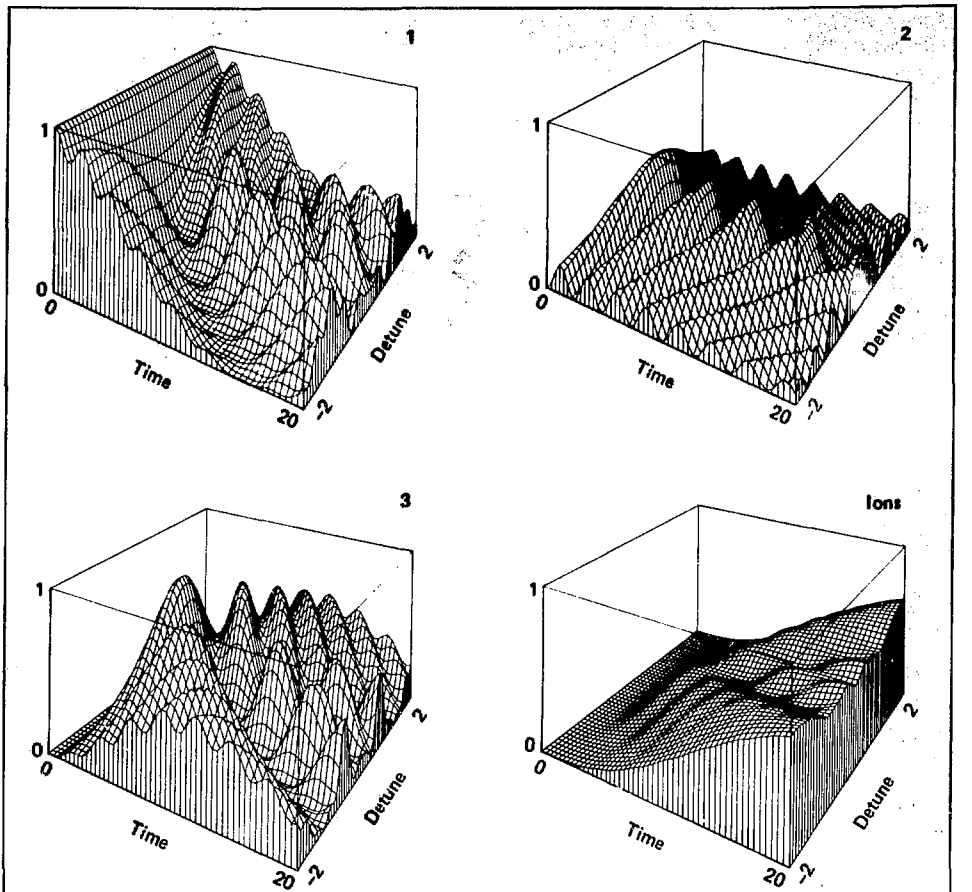

Fig. 10-29. Perspective view of excitation probabilities $P_n(t)$ for the three-level ladder of Fig. 10-28 as a function of time (in units of inverse Rabi frequency) and detuning in units of Rabi frequency.

one must replace the single sum by a double sum over degenerate eigenvectors:

$$\bar{P}_n = \sum_{k,k'} R_n(k)\, B(k)\, R_n(k')\, B(k')^*\, \delta\,(Z_k - Z_{k'}^*) \ .$$

We have incorporated these two modifications into the code BLOCHB and have verified that they are necessary and sufficient conditions to permit computation of long-time averages when degeneracies are present.

Relaxation Phenomena. The single Schrödinger equation fails to account for various relaxation processes that destroy coherence. In previously reported publications[68,77,78] we have discussed effects of collision-induced relaxation (as expressed through the Bloch equation) and of homogeneous broadening of absorption lines as treated by imaginary diagonal elements of the RWA Hamiltonian. Further inhomogeneous broadening occurs because different atoms reside in slightly different environments. The distribution of Doppler shifts comprises a significant source of inhomogeneous relaxation in

an atomic vapor, and we have published detailed examinations[79,80] of this effect upon excitation and ionization.

Fluctuations and Statistical Effects. Much of our modeling idealizes lasers as monochromatic electric fields. Real lasers do not have zero bandwidth, and we have therefore supported, through contract, studies of fluctuations and statistical effects in the excitation of atomic and molecular systems. Conventional perturbation methods assume the Rabi frequency to be much less than the laser bandwidth, contrary to conditions of interest to us. We have devised heuristic techniques[81,82] for treating fluctuations in both the phase and amplitude of the electric fields; also, we have obtained a general and exact algorithm[83] for incorporating the most commonly assumed phase noise (Gaussian, a short memory) into Bloch-operator or density-matrix equations of motion. The algorithm permits us to insert the laser bandwidth directly into fluctuation-averaged atomic equations as a parameter rather than a stochastic variate, thereby permitting more compact numerical modeling.

Light Propagation in Multilevel Absorbers. Traditional treatments of radiation propagation,[84] applicable to light of low intensity, express the incremental alteration of a propagating pulse through Beer's law of exponential attenuation. This treatment fails in the regime of coherent excitation: where Rabi frequencies are much larger than relaxation rates, one can observe dramatic pulse reshaping and self-induced transparency.[85-87] To study this regime, we are undertaking development of computer codes to integrate self-consistent dynamic equations for the electromagnetic field and the atomic vapor. The codes are based on Maxwell's field equations, rather than on the equation of radiative transfer, combined with the density matrix or Schrödinger equation, rather than with the rate equations or perturbation theory. Our studies deal with propagation of multiple-frequency pulses through multilevel Doppler-broadened systems.

References

68. "Photon Dynamics," *Laser Program Annual Report—1977*, Lawrence Livermore Laboratory, Livermore, Calif., UCRL-50021-77 (1978).
69. "Photon Dynamics," *Laser Program Annual Report—1976*, Lawrence Livermore Laboratory, Livermore, Calif., UCRL 50021-76 (1977).
70. B. W. Shore, "Dynamics of Multilevel Laser Excitation: Three-Level Atoms," *Phys. Rev.* **A15**, 1640 (1977).
71. B. W. Shore and J. H. Eberly, "Analytic Approximations in Multi-Level Excitation Theory," *Opt. Commun.* **24**, 83 (1978).
72. Z. Bialynicka-Birula, I. Bialynicki-Birula, J. H. Eberly, and B. W. Shore, "Coherent Dynamics of N-level Atoms and Molecules. II. Analytic Solutions," *Phys. Rev.* **A16**, 2048 (1977).
73. B. W. Shore, "Effects of Magnetic Sublevel Degeneracy on Rabi Oscillations," *Phys. Rev.* **A17**, 1739 (1978).
74. J. H. Eberly, B. W. Shore, Z. Bialynicka-Birula, and I. Bialynicki-Birula, "Coherent Dynamics of N-Level Atoms and Molecules. Numerical Experiments," *Phys. Rev.* **A16**, 2038 (1977).
75. P. W. Milonni and J. H. Eberly, "Temporal Coherence in Multiphoton Absorption. Far-Off Resonance Intermediate States," *J. Chem. Phys.* **68**, 1602 (1978).
76. B. W. Shore, "The Definition of Virtual Levels," *Am. J. Phys. (in publication).*
77. J. R. Ackerhalt and B. W. Shore, "Rate Equations Versus Bloch Equations in Multiphoton Ionization," *Phys. Rev.* **A16**, 277 (1977).
78. B. W. Shore and M. A. Johnson, "Coherence Versus Incoherence in Stepwise Laser Excitation," *J. Chem. Phys.* **68**, 5631 (1978).
79. J. R. Ackerhalt, J. H. Eberly, and B. W. Shore, "Statistical Broadening and Population Loss in Strongly Excited Three-Level Systems," *Phys. Rev.* A (1978).
80. J. H. Eberly, "Application of Extended Two-Level Model Theory to Doppler- Laser- and Collision-Broadened Bound-Bound Multiphoton Absorption," *J. Phys.* **B11**, L1 (1978).
81. J. H. Eberly and S. V. O'Neil, "Coherence Versus Incoherence: Time-Independent Rates for Resonant Multiphoton Ionization," *Phys. Rev. A (in publication).*
82. J. L. F. De Meijere and J. H. Eberly, "Rate of Resonant Two-Photon Ionization in the Presence of a Partially Coherent Radiation Field," *Phys. Rev.* **A17**, 1416 (1978).
83. K. Wodkiewicz, "Some Exact Solutions of Multiplicative Stochastic Processes," *J. Math. Phys.* **20**, 45 (1979).
84. S. Chandrasekhar, *Radiative Transfer* (Dover Publications, New York, 1960).
85. G. L. Lamb, "Analytical Descriptions of Ultrashort Optical Pulse Propagation in a Resonant Medium," *Rev. Mod. Phys.* **43**, 99 (1971).
86. A. Icsevgi and W. E. Lamb, Jr., "Propagation of Light Pulses in a Laser Amplifier," *Phys. Rev.* **185**, 517 (1969).
87. A. Kujawski and J. H. Eberly, "On Solutions Describing Self-Induced Transparency of Ultra-Short Pulses," in *Coherence and Quantum Optics*, L. Mandel and S. Wolf, Eds. (Plenum Press, New York, 1978).

Author

B. Shore

10.5.2 Experimental Investigations

Saturation Studies. In modeling coherent excitation of an N-level atom, the N – 1 separate Rabi frequencies are key parameters that provide the link between theory and experiment. Each of the Rabi frequencies is equal to the product of the resonant

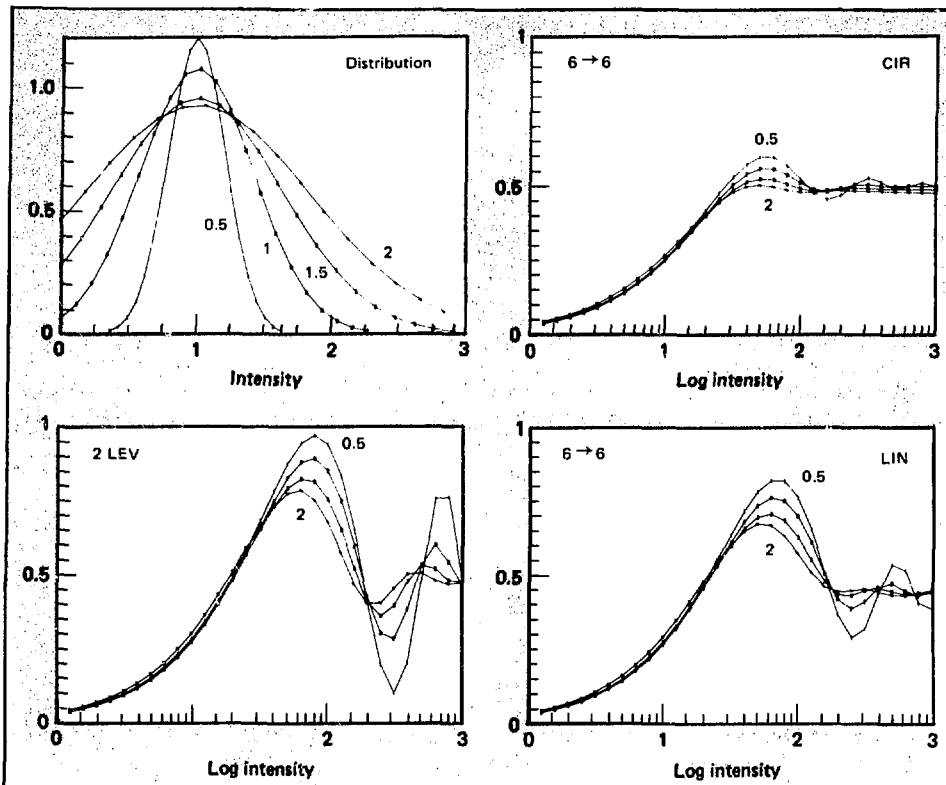

Fig. 10-30. Saturation curves for two-level atom for four assumed distributions of pulse-to-pulse intensity fluctuations, showing cases of transition J = 6→ 6 with circular polarization, J = 6 → 6 with linear polarization; and nondegenerate two-level atom.

or near-resonant laser electric field amplitude and transition dipole moment, divided by Planck's constant. Thus, accurate modeling requires accurate values of dipole moments. By measuring suitable indicators of excitation we can determine these moments.

We designed one such series of experiments to measure the removal of population from the atomic ground state through excitation by a pulsed pump laser. By plotting the removed fraction as a function of laser intensities we obtained a saturation curve, so called because the excited fraction appears to approach an asymptotic limiting value of 1/2 as the intensity grows large.

Applying rate equations, we predicted that excitation by a monochromatic pulse of duration T should produce, in a two-level system, the excited fraction $F = 1 - \exp(-2\Omega^2 T/\gamma)$, where Ω is the Rabi frequency and γ the appropriate width of the absorption line profile. By contrast, the Schrödinger equation predicts an oscillatory excited fraction $F = 1 - \cos(\Omega T)$. Various mechanisms, particularly the averaging over various dipole-moment orientations, over various Doppler shifts, and over pulse-to-pulse amplitude fluctuations, act to dampen the apparent Rabi oscillations, thereby producing a saturation curve similar to, though not identical with, the saturation curve predicted from a rate equation. Figure 10-30 illustrates the effects of these mechanisms by comparing saturation curves for a nondegenerate two-level atom with curves for $J = 6 \rightarrow 6$ transitions. In each case we show four curves, corresponding to four successively broader distributions of intensity fluctuations. The two-level

atom undergoes pronounced population oscillations, which remain clearly defined even in the presence of appreciable intensity fluctuations. The presence of angular momenta, with $2J + 1$ orientations, dampens the oscillations. Linearly polarized light, for the $J = 6 \rightarrow 6$ transition, also retains pronounced population oscillations. Circularly polarized light produces a wider range of Rabi frequencies for $J = 6 \rightarrow 6$, and hence the saturation curves for this polarization show little evidence of population oscillations.

We have measured excitation probability over a range of laser intensities to obtain saturation curves for selected uranium transitions. In principle, an accurate determination of laser intensity would permit us to determine, by comparing the saturation curve with theoretical models, the dipole transition strength. In practice, experimental results do not always provide clear distinction between model curves; it is difficult, therefore, to obtain accurate dipole moments with this technique.

AC Stark Effect. The population (Rabi) oscillations that play so dominant a part in the dynamics of coherent excitation manifest themselves in the frequency domain as spectral sidebands. The consequent splitting of absorption lines into two (or more) components separated by the Rabi frequencies—the dynamical or AC Stark effect (or optical Autler–Townes effect)—offers a possible means for determining transition strengths.[88,89] To observe this effect, we fixed a strong pump laser coincident with a transition between two levels 1 and 2 (with 1 the ground state or a populated excited state), and then we tuned a weaker probe laser to a second transition $2 \rightarrow 3$ leading to ionization from level 3. When we swept the frequency of the probe laser, we observed two peaks in the ion signal. This two-peak pattern is the AC Stark effect.

Previously this effect has been observed (through fluorescence) and reported in two-level systems of sodium atoms.[88,89] We have carried out the first observations, in uranium, of an element having large angular momentum ($J = 6$). The uranium system is not a two-level transition; rather, it is a statistical average over $2J + 1 = 13$ quantized orientations of two-level systems. This orientation average tends to wash out the conventional two-peaked pattern. Nevertheless, theory predicts, and experiments show, clearly resolved structure. Figure 10-31 shows experimental results taken at four successively increasing power levels. The frequency

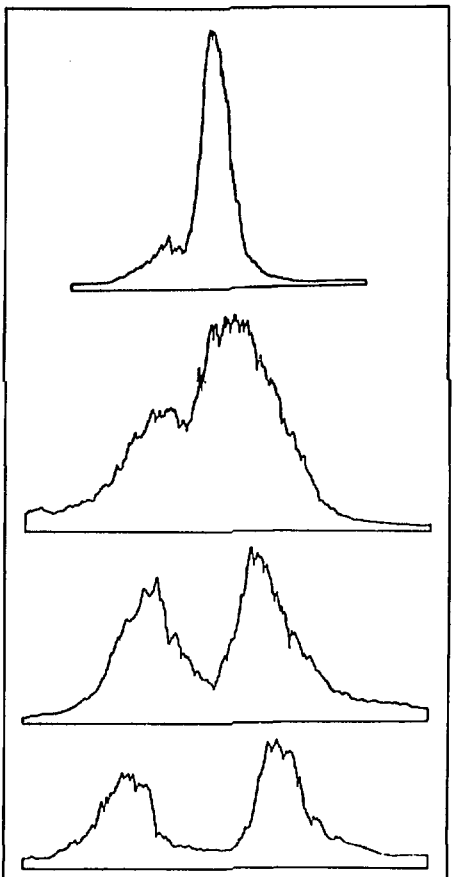

Fig. 10-31. Observed AC Stark effect in uranium: ionized fraction as a function of probe-laser detuning for four values of pump-laser intensity.

splitting between peaks increases as the pump laser is detuned from resonance; the smallest splitting (no detuning) is the effective Rabi frequency. As the pump is further detuned, the two peaks become asymmetric. This asymmetry offers a second possible measurement of the Rabi frequency, as various scientists have noted. Unfortunately, the asymmetry is sensitive to details of the time dependence. For square-pulse excitation at sufficiently short times (on a scale fixed by the ionization rate), the peaks are symmetric at any detuning. For longer times, the ratio of peak values approaches an asymptotic

limit. One expects this limiting ratio to be the square of the ratio of dressed-atom eigenvector components, because under steady-state conditions these are the system eigenstates. For a two-level atom, this limiting ratio R follows the formula

$$R = \left(x + \sqrt{x^2 - 1}\right)^2 ,$$

where x is the separation between peaks, measured in units of the Rabi frequency.

The experimental data only poorly fit this pattern. We have investigated some of the possible sources of this discrepancy. We have established that the theoretical pattern differs in detail between pump excitation by circularly polarized light and by linearly polarized light (assuming that the probe laser has the same polarization as the pump). We have verified that the pattern does not depend upon the relative phase of circular polarization between pump and probe (e.g., right–right or right–left).

Because the results are so sensitive to time dependence (under excitation conditions wherein one does not reach the asymptotic peak ratio), it appears that the peak asymmetry does not provide a useful diagnostic tool. Indeed, if the pulse rises sufficiently slowly, the asymmetry gives a measure of the rise time.

References

88. J. L. Picqué and J. Pinard, "Direct Observation of the Autler-Townes Effect in the Optical Range," *J. Phys.* **B9**, L77 (1976).
89. H. R. Gray, and C. R. Stroud, Jr., "Autler-Townes Effect in Double Optical Resonance," *Opt. Commun.* **25**, 359 (1978).

Authors

B. Shore
M. Johnson
L. Hackel

10.5.3 Fluorescence Probing of Laser Pumping

For the past year the AIS Collision Physics Group has been studying photochemical reactions of uranium atoms. This research aims to demonstrate a uranium-atom, photochemical, isotope separation process.[90] Our experiments consist of passing a collimated beam of uranium vapor through a beam of reagent, simultaneously irradiating the beam intersection region with laser light. The three beams (uranium, reagent, and lasers) intersect orthogonally, as depicted in Fig. 10-32. We employ a pair of cw dye lasers, propagating colinearly. The superposed lasers are gently focused in one dimension with a 2- to 3-deg convergence angle, which matches the divergence angle of the uranium beam. Thus each atom encounters, during its flight through the irradiation zone, Doppler-shifted monochromatic light at its resonance frequency. The two lasers are polarized in orthogonal planes, a consequence of our beam combiner. The lasers sequentially pump the uranium atoms from the ground level (level 1, with J = 6) to an excited level 2 (J = 6) and then to a reactive level 3 (J = 5). Figure 10-33 illustrates the excitation linkage and also indicates losses by radiative decay to metastable levels.

The 1977 Laser Program Annual Report (§9.4.3)[91] described the molecular beam apparatus and the lasers, as well as the unique electronic system that locks two lasers within a few MHz of their respective line centers.[90]

Our experiments do not observe details of time-dependent reaction dynamics. Rather, the flux I_i of reaction products from level i depends upon the combination

$$I_i = n_1 n_2 V v \sigma_i \bar{P}_i ,$$

where n_1 and n_2 are the particle densities of the two colliding beams, V is the scattering volume, v is the relative velocity of the reactants, and $\bar{P}_i$ is the time-averaged probability of population in level i during the time T when uranium atoms reside in volume V. We see that to determine σ_i—the object of our experiment—we must determine, in addition to incident particle fluxes and the interaction volume, both the reaction product flux and the average excitation probabilities. Absolute measurements of number densities pose challenging problems. We circumvented these difficulties by comparing reaction fluxes to flux $\hat{I}$ from a ground-level reaction of a known cross section. We then needed only to measure the relative fluxes of the two processes, $I_i/\hat{I}$, and the relative populations $\hat{P}/\bar{P}_i$:

$$\sigma_i = \hat{\sigma} (I_i/\hat{I}) (\hat{P}/\bar{P}_i) .$$

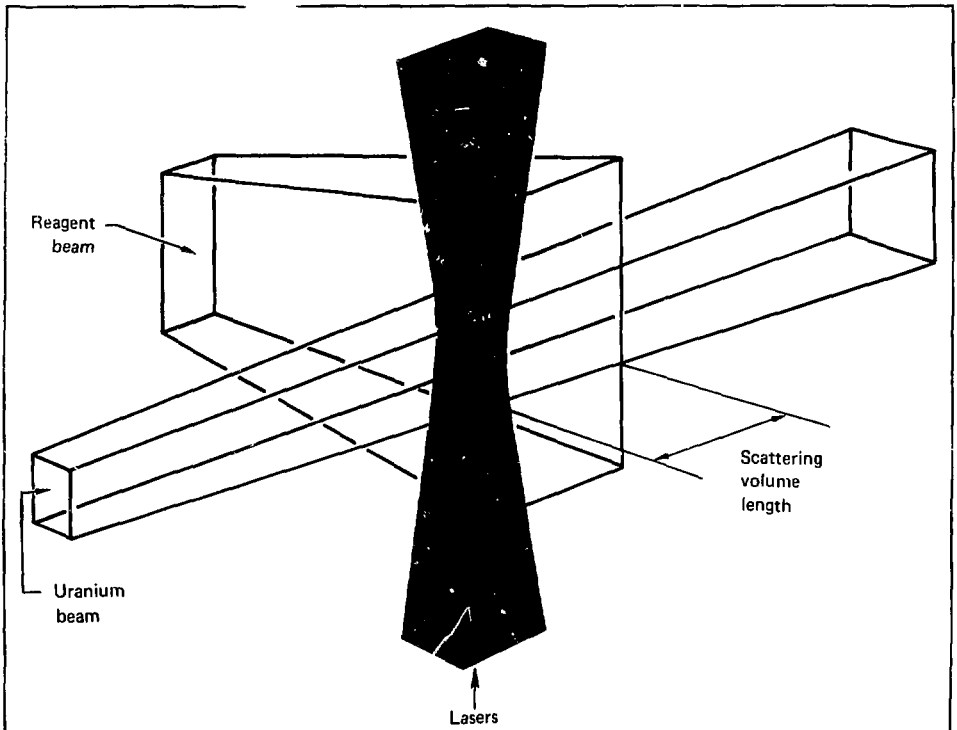

Fig. 10-32. Laser irradiation geometry.

We determine average populations by monitoring fluorescence from levels 2 and 3. The expression for fluorescence counting rate

$$F_i = G A_i n_1 V \bar{P}_i$$

involves a geometric collection efficiency factor G and the spontaneous decay rate A_i for level i.

In the absence of laser excitation, reactions are rare and the ground level P_1 is very close to unity. Laser-excited levels radiatively decay to nonreacting metastable states. When appreciable population becomes so trapped, as is the case for uranium, the sum of the $\bar{P}_i$ from laser-connected levels is appreciably less than unity. The measured flux is correspondingly small, adding to the difficulty of the experiment.

It is notoriously difficult to determine, from observed count rates, the number density of radiating atoms—i.e., to measure the geometric factor G. To circumvent these difficulties, we would prefer to deal with ratios of relative count rates. Our experiments provided one such relative measurement: the dip in level-2 fluorescence count rate when the second laser was turned on, as compared with the value when only laser 1 was present. It then became the task of theory to relate this observed fluorescence dip to population averages $\bar{P}_i$.

Theory addresses population averages P_i by providing detailed histories of time-dependent level probabilities $P_i(t)$, which can then be averaged over the duration T of uranium exposure to reagent:

$$\bar{P}_i = \frac{1}{T} \int_0^T dt\, P_i(t) \ .$$

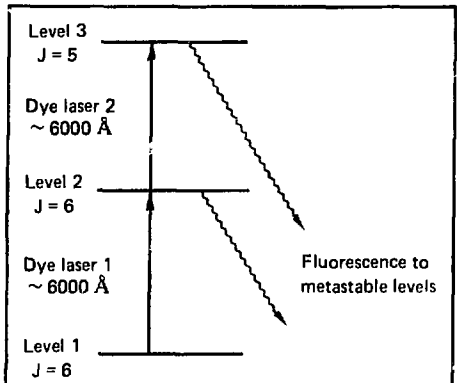

Fig. 10-33. Schematic of two-laser excitation of uranium atoms.

During the first portion $(0,\tau)$ of the reacting time (0,T) the uranium experiences laser excitation; subsequently, the excited populations decay exponentially in time because of radiative transitions. We have examined several models, of increasing sophistication, to predict the time-dependent probabilities.

For our simplest models, we considered stationary atoms irradiated by monochromatic light for a time interval that is sufficiently long for the atomic populations to approach steady state time-averaged values, yet short enough for negligible population loss to occur through spontaneous decay. During the transitions of interest, there is a small probability (14% or less) that the decays repopulate the levels of the excitation ladder. Such decays produce optical pumping, whereas the major portions of the decays to metastable levels act as probability drains.

The very simplest model assumes that the atom is a three-level system whose dynamics follows the prediction of rate equations. Then, in the equilibrium steady state, all populations of laser-connected levels equalize. When only laser 1 acts, the populations equalize between two levels, whereas when both lasers act, all three levels equalize. Thus this model predicts a fluorescence dip of 33%.

As a slight refinement of the elementary rate equation model, we note that each level has an angular momentum J and consequently has $2J + 1$ magnetic sublevels. When we excite the sequence $J = 6 \rightarrow 6 \rightarrow 5$, using linearly polarized light, with both lasers polarized in the same direction, the system comprises 13 separate independent excitation ladders, as indicated in Fig. 10-34. Simple accounting then gives a fluorescence dip of 28%.

Application of rate equations to this problem provides an extremely simple procedure for computing the P_j values. However, the premises upon which the equations rest are not valid: rate equations apply when relaxation (through collisional phase interruption, for example) or incoherence (as can occur with broad-band excitation) dominate the coherent stimulated emission and absorption. Furthermore, rate equations cannot correctly treat the phase relationships essential for modeling

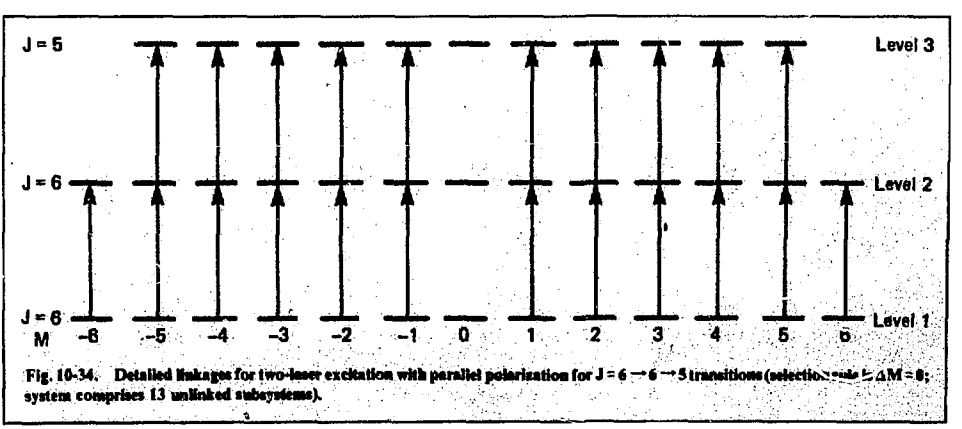

Fig. 10-34. Detailed linkages for two-laser excitation with parallel polarization for $J = 6 \rightarrow 6 \rightarrow 5$ transitions (selection rule: $\Delta M = 0$; system comprises 13 unlinked subsystems).

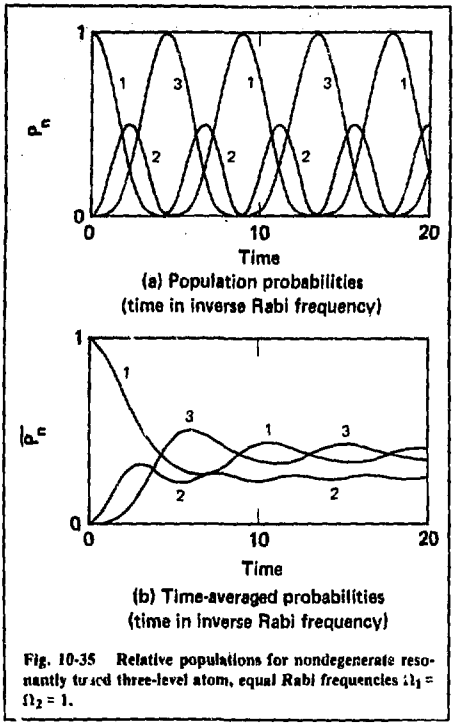

Fig. 10-35 Relative populations for nondegenerate resonantly tuned three-level atom, equal Rabi frequencies $\Omega_1 = \Omega_2 = 1$.

crossed polarization (see §10.5.1). We must instead solve the RWA Schrödinger equation to obtain the time-dependent probabilities. Unlike solutions to the rate equations, solutions to the lossless Schrödinger equation do not approach stationary time-independent values; rather, they continue to oscillate indefinitely with periods fixed by the values of the Rabi frequencies. Nevertheless, the time-averaged probabilities P_i approach asymptotic values within two oscillation periods (see Fig. 10-35).

We estimate that a typical uranium atom undergoes between 5 and 20 population oscillations during transit of the laser beam. Thus infinite-time averages (see §10.5.1) provide a satisfactory estimate of Schrödinger-equation population averages in the absence of decay. Employing such averages, we predict, for the three-level atom with equal Rabi frequencies, a fluorescence dip of 50% (contrasted with the rate equation dip of 33%). A model with magnetic sublevels and crossed polarization (see Fig. 10-36) yields a dip of 46% (parallel polarization yields a dip of 52%, contrasted with the rate equation results of 28%).

Because of the geometry of our intersecting beams, the uranium atoms continue to react after they have emerged from the laser beam. Thus, the integral defining time averages $\bar{P}_i$ must extend well beyond the time when the laser stimulation governs the dynamics: into time when populations simply decay exponentially. Almost all atoms decay during this irradiation-free flight, which endures for several lifetimes. Correction for this decay diminishes predicted excited-state population averages by roughly an order of magnitude.

The assumption of monochromatic radiation fails to treat correctly the variation in amplitude and frequency of the laser field encountered by an

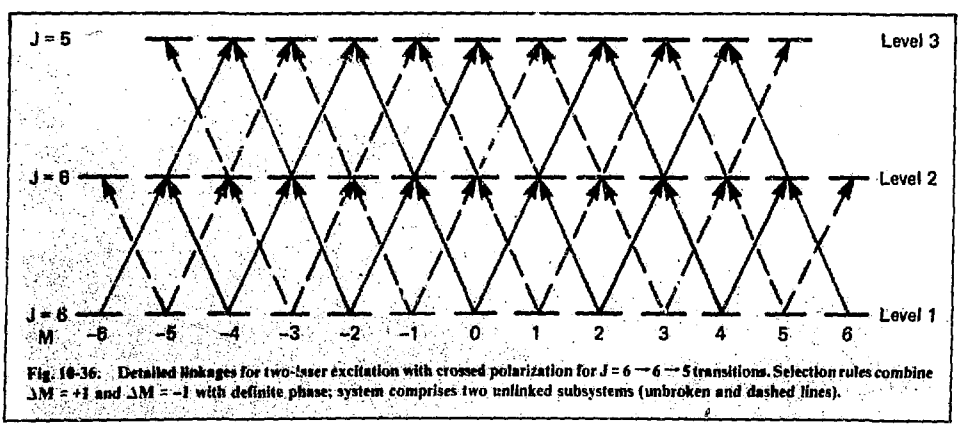

Fig. 10-36. Detailed linkages for two-laser excitation with crossed polarization for $J = 6 \rightarrow 6 \rightarrow 5$ transitions. Selection rules combine $\Delta M = +1$ and $\Delta M = -1$ with definite phase; system comprises two unlinked subsystems (unbroken and dashed lines).

atom traversing a focused beam. For a typical laser operating in the TEM_{00} mode, the spatial profile of intensity follows a Gaussian pattern; this spatial distribution leads to a Gaussian-profile time-dependent Rabi frequency as atoms move steadily across the beam. Such pulses, rising over several population oscillations, produce adiabatic-following population dynamics that can differ dramatically from results for fixed-amplitude square pulses (smoother pulse shapes tend to return all of the population to the ground state).

Finally, we note that an atom traversing a diverging radiation beam encounters a time-varying carrier frequency, as it encounters the full range of wave vectors. This frequency chirping can profoundly affect the population dynamics (chirped pulses tend to leave populations in excited states). Figure 10-37(b) shows population histories for a chirped Gaussian pulse, appropriate to modeling a fluorescing three-level atom (including magnetic sublevels and parallel polarization). Figure 10-37(a) depicts the populations in the absence of chirping (i.e., for a plane-parallel laser beam of Gaussian profile).

Realistic modeling must include an average over Doppler speeds and a distribution over paths in the diverging atomic beam, each of which meets a slightly different field history.

Table 10-13 compares some of the results for a few of the models we have studied. The differences among these various models are striking. Furthermore, our most refined model indicates an ap-

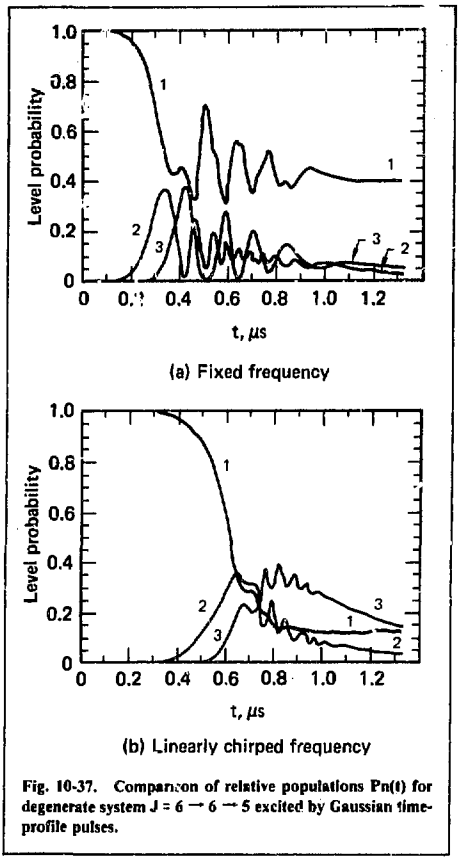

Fig. 10-37. Comparison of relative populations Pn(t) for degenerate system J = 6 → 6 → 5 excited by Gaussian time-profile pulses.

Table 10-13. Calculated average populations.

Model	$\bar{P}_i$ Level 1	$\bar{P}_i$ Level 2	$\bar{P}_i$ Level 3	FD, %	$(\bar{P}_3/FD) \times 10^3$
3-level	0.310	0.0386	–		– 1 laser –
rate equation	0.196	0.0249	0.0301	35	0.86
Sublevel	0.346	0.0366	–		– 1 laser –
rate equation	0.253	0.0257	0.0240	30	0.80
Sublevel Schrödinger equation	0.346	0.0366	–		– 1 laser –
	0.421	0.0191	0.0200	48	0.42
Sublevel Schrödinger equation,	0.346	0.0366	–		– 1 laser –
cross polarized	0.323	0.0201	0.0267	45	0.59
Sublevel Schrödinger equation, with Gaussian					
pulse and decay	0.257	0.0442	–		– 1 laser –
No chirp	0.430	0.0209	0.0197	53	0.37
Chirp	0.202	0.0494	–		– 1 laser –
	0.213	0.0217	0.0402	56	0.72

preciable sensitivity of the predicted fluorescence dip to details of the dynamics and, in turn, to a detailed description of the laser-beam profile. We conclude that the fluorescence dip is not a reliable indicator of population. However, our modeling studies have given us valuable new insights into the mechanisms of laser excitation and into the difficulties of monitoring excited state populations.

References

90. R. C. Stern and N. C. Lang, *Measurement of U-Kr Momentum Transfer Cross Sections Using Crossed Molecular Beams*, Lawrence Livermore Laboratory, Livermore, Calif., UCRL-81209 (1978), to be published in the *J. Chem. Phys.* (1979)
91. "Photon Dynamics," *Laser Program Annual Report—1977*, Lawrence Livermore Laboratory, Livermore, Calif., UCRL-50021-77 (1978).

Authors

B. Shore
N. Lang
R. Stern

10.5.4 Deflection of Atoms in Resonant Radiation

The use of a resonant electromagnetic wave, or a combination of resonant and static fields, to deflect a beam of neutral atoms has been the subject of renewed interest since the advent of higher-power tunable lasers. A potential application of laser deflection is to the problems of laser isotope separation.

Several methods of photodeflection have been proposed,[92-97] some of which have been demonstrated experimentally.[98-102] Most of these methods require an interaction time that is long compared to the natural lifetime of the excited atoms. This requirement makes the practical application of these methods impossible in many cases, because an atom excited by the resonant radiation makes transitions to metastable states, which are not affected by the applied field.[100] Such transitions remove atoms from the interaction cycle, and little or no deflection is produced. The purpose of this section is to show that, in a strong resonant standing wave, significant atomic deflections can occur in a time less than the spontaneous lifetime of the excited atom, and hence the problem of transitions to metastable levels is circumvented by the speed of the process.

When an atomic beam is irradiated by a strong resonant electromagnetic wave, absorption-emission processes proceed at two distinct rates. Photons are absorbed from and emitted into the applied field at the induced rate Ω, and occasionally photons are spontaneously emitted, in random directions, at the spontaneous rate γ. Deflection or scattering of the atomic beam results when momentum is transferred from the field to the atoms, and the rate of momentum transfer depends on the nature of the applied field.

If the applied field consists of a single plane wave, momentum is transferred to the atoms at the spontaneous rate γ. This momentum transfer (i.e., radiation pressure) proceeds at the spontaneous rate, because absorption followed by induced emission into the same field mode involves no net transfer of momentum, while absorption followed by spontaneous emission transfers an average of one quantum of momentum for each spontaneous event (isotropic spontaneous emission does not carry away the momentum acquired by the atom through absorption).

If the applied field is composed of two or more plane waves, an atom can absorb a photon from one of the plane waves, and induced emission can cause that photon to be emitted into a different plane wave, with a resultant transfer of momentum at the induced rate Ω. Because the induced rate may exceed the spontaneous rate by many orders of magnitude in a strong applied field, it is expected that deflection processes operating at the induced rate will be more efficient and more rapid than processes operating at the spontaneous rate. In the following subsections we will show that momentum transfer in a standing wave proceeds at the induced rate, a feature of the interaction that gives rise to the rapid deflection mentioned above.

Theory. The Hamiltonian for an atom in a classically prescribed electromagnetic field, in the dipole approximation, takes the form

$$H = P^2/2M + H_0 - \underline{\mu} \cdot \underline{E}(\underline{R},t) , \qquad (8)$$

where $P_2/2M$ is the kinetic energy associated with the center-of-mass momentum $\underline{P}$, H_0 is the Hamiltonian for the internal motion of the atom, $\underline{\mu}$ is the dipole moment operator, and $\underline{E}(\underline{R},t)$ is the electric field evaluated at the center-of-mass position $\underline{R}$. Consider the motion of a two-level atom

with energy levels E_1 and E_2 in a monochromatic standing wave $\underline{E}(x,t) = \hat{\epsilon}\mathscr{E}(\underline{x})\cos t$. Here the amplitude $\mathscr{E}(\underline{x})$ will be a solution of the time-independent wave equation $\nabla_2 \mathscr{E} + (\omega/c)^2 \mathscr{E} = 0$. Let $\psi_1(\underline{x})$ and $\psi_2(\underline{x})$ be the amplitudes of the atom that is located at position $\underline{x}$ and occupies energy levels E_1 and E_2, respectively. Then it follows from Eq. (8) that the Schrödinger equation for the two-component wave function is

$$i\hbar\frac{\partial\psi_1}{\partial t} = \frac{\hbar^2}{2M}\nabla^2\psi_1 + E_1\psi_1 - \mu\mathscr{E}(\underline{x})\cos\omega t\,\psi_2 ,$$

$$i\hbar\frac{\partial\psi_2}{\partial t} = -\frac{\hbar^2}{2M}\nabla^2\psi_2 + E_2\psi_2 - \mu\mathscr{E}(\underline{x})\cos\omega t\,\psi_1 . \qquad (9)$$

where $\mu = (\sim \underline{\mu}\cdot\hat{\epsilon}\,2)$ is the transition dipole moment. In the case of exact resonance, $\omega = (E_2 - E_1)/\hbar$, the substitution $\psi_1 = C_1\exp -iE_1t/\hbar$, $\psi_2 = C_2\exp -iE_2t/\hbar$ and a rotating wave approximation (i.e., neglect of nonessential terms that oscillate at twice the optical frequency) put Eq. (9) in the form:

$$i\hbar\frac{\partial C_1}{\partial t} = \frac{\hbar^2}{2M}\nabla^2 C_1 - \frac{1}{2}\mu\mathscr{E}(\underline{x})C_2 ,$$

$$i\hbar\frac{\partial C_2}{\partial t} = -\frac{\hbar^2}{2M}\nabla^2 C_2 - \frac{1}{2}\mu\mathscr{E}(\underline{x})C_1 . \qquad (10)$$

Equation (10) is decoupled by the unitary transformation:

$$u_+ = 2^{-1/2}(C_1 - C_2) ,$$

$$u_- = 2^{-1/2}(C_1 + C_2) . \qquad (11)$$

The equations of motion for $u_\pm(\underline{x})$ are:

$$i\hbar\frac{\partial u_\pm}{\partial t} = -\frac{\hbar^2}{2M}\nabla^2 u_\pm \pm \frac{1}{2}\mu\mathscr{E}(\underline{x})u_\pm , \qquad (12)$$

and the probability density for the position of the atom, $P(\underline{x}) = |\psi_1(\underline{x})|^2 + |\psi_2(\underline{x})|^2$, becomes:

$$P(\underline{x}) = |u_+(\underline{x})|^2 + |u_-(\underline{x})|^2 . \qquad (13)$$

Equation (12) states that the wave functions $u_\pm$ propagate independently of one another, and Eq. (13) shows that there is no spatial interference between these waves. An atom initially in the ground state ($C_2 = 0$) has an equal probability of being in one or the other of the waves $u_\pm$, and Eq. (12) implies that these probabilities are time-independent. The waves $u_\pm$ each satisfy a simple time-dependent Schrödinger equation but with potential energies $V_\pm(\underline{x}) = \pm(1/2)\mu\mathscr{E}(\underline{x})$ of opposite sign. Therefore, the forces acting on atoms in the two waves are in opposite directions, and it follows that the amplitude gradient of the resonant radiation will split a narrow atomic beam into two components, in much the same way as the magnetic field gradient split an atomic beam in the Stern–Gerlach experiment.

If the atomic wave function is initially a plane wave propagating in the positive z direction, and this wave traverses a standing wave

$$\underline{E}(x,t) = \begin{cases} 2(8\pi I/c)^{1/2}\hat{\epsilon}\cos kx\cos\omega t & \text{for } 0 \leqslant Z \leqslant L \\ 0 & \text{otherwise} , \end{cases} \qquad (14)$$

one finds that the transverse momentum density is given by:

$$W(P_x,t) = \sum_{n=-\infty}^{\infty} J_n^2(\Omega t)\,\delta(P_x - n\hbar k) , \qquad (15)$$

where $\Omega = \mu(8\pi I/c)^{1/2}/\hbar$, and t is the interaction time.[103] Equation (15) states that the probability $P_m(t)$ that the atom has acquired transverse momentum $n\hbar K$ ($n = 0, \pm1, \pm2, \ldots$) is:

$$P_n(t) = J_n^2(\Omega t) . \qquad (16)$$

In cases of practical interest, Ωt is a large number. For $|n| < \Omega t$, the probability $J^2(\Omega t)$ is not a monotonic function of n but tends to increase with $|n|$ and has maximum near $|n| = \Omega t$. For $|n| > \Omega t$, $J_n^2(\Omega t)$ decreases rapidly to zero as $|n|$ increases.

In view of Eq. (16), the maximum deflection is $\theta_{max} \approx \hbar k\, \Omega t/P_z$. This result shows quite clearly that momentum is transferred to the atom at the induced rate Ω. The deflection geometry is illustrated in Fig. 10-38.

It is interesting to note that Eq. (15) is formally identical to the equation for Fraunhofer diffraction of a plane wave by a sinusoidal phase grating. In effect, the atomic beam is diffracted by the periodic amplitude [$\mathscr{E}(x) \propto \cos kx$] of the standing wave, and the deflection angles $\theta_n = n\hbar k/P_z$ are precisely what one would expect on the basis of the optical analogy, if the atomic beam is regarded as a wave of wavelength equal to the de Broglie wavelength $\lambda_0 = h/P_z$.

Numerical Example. If the atoms issue from an oven at temperature T, $P_z \approx (2MkT)^{1/2}$ and $V_z \approx (2kT/M)^{1/2}$ (here k is Boltzmann's constant). The rms deflection is:

$$\theta_{rms} = \hbar\omega\Omega t_{max}/2^{1/2}\, c\, P_z$$
$$= (\hbar\Omega/2^{3/2}kT)^{1/2} \quad . \tag{17}$$

Consider a mildly refractory, moderately massive atom with a strong visible absorption. Let

$$T = 1000\ K, \qquad M = 1.6 \times 10^{-22} g$$
$$\mu = \langle 1|\underline{\mu}\cdot\hat{\epsilon}|2\rangle = 4D, \qquad \omega = 3 \times 10^{15}\ s^{-1} \tag{18}$$

Then, for $I = 2.5 \times 10^6\ W/cm^2$ in the interaction region, we calculate

$$t_{max} = 6.2 \times 10^{-9}\ s$$
$$\theta_{rms} = 3.9 \times 10^{-2}\ rad = 2.2\ deg \quad . \tag{19}$$

Thus, a 2-deg deflection is obtained for our "typical" atom in a field of $2.5 \times 10^6\ W/cm^2$. The interaction time required for this deflection is less than the natural lifetime of the transition ($\tau_1 \approx 5 \times 10^{-8}$ s).

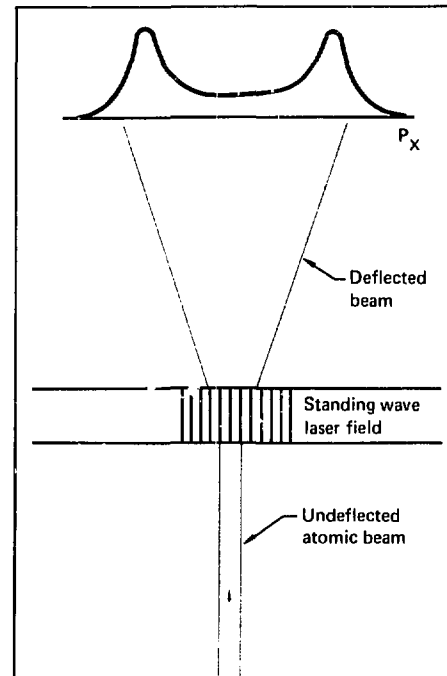

Fig. 10-38. Distribution of deflected atoms.

References

92. R. Frish, *Z. Physik* **86**, 42 (1933).
93. A. Ashkin, "Atomic-Beam Deflection by Resonance-Radiation Pressure," *Phys. Rev. Lett.* **25**, 1321 (1970).
94. P. L. Kelley, N. M. Kroll, and C. K. Rhodes, "Isotope Separation Involving Photo-Induced Changes in the Electric and Magnetic Properties of Molecules and Atoms," *Opt. Commun.* **16**, 172 (1976).
95. M. H. Mittleman, K. Rubin, R. H. Callender, and J. I. Gersten, "Deflection of Laser-Excited Atoms by an Electric Field," *Phys. Rev.* **16**, 583 (1977).
96. I. Nebenzahl and A. Szoke, "Deflection of Atomic Beams by Resonance Radiation Using Stimulated Emission," *Appl. Phys. Lett.* **25**, 636 (1974).
97. A. P. Kazantesev, "The Acceleration of Atoms by Light," *Sov. Phys. JETP* **39**, 784 (1974).
98. A. F. Bernhardt, D. E. Duerrer, J. R. Simpson, and L. L. Wood, "Isotope Separation by Laser Deflection of an Atomic Beam," *Appl. Phys. Lett.* **25**, 617 (1974).
99. A. F. Bernhardt, "Isotope Separation by Laser Deflection of an Atomic Beam," *Appl. Phys.* **34**, 19 (1976).
100. A. F. Bernhardt, D. E. Duerre, J. R. Simpson, and L. L. Wood, "Multifrequency Radiation Pressure Laser, Isotope Separation," *Opt. Commun.* **16** 169 (1976).
101. J. L. Picque' and J. L. Vialle, "Atomic-Beam Deflection and Broadening by Recoils due to Photon Absorption or Emission," *Opt. Commun.* **5**, 402 (1972).

Fig. 10-39. ArF laser experiment (laser output from unstable resonator scraper mirror in upper right is directed toward diagnostics including Fabry-Perot interferometer, photodiode, and 1.0-m spectrometer equipped with a 500-channel multichannel analyzer).

102. R. Schieder, H. Walther, and L. Woste, "Atomic Beam Deflection by the Light of a Tunable Dye Laser," *Opt. Commun.* 5, 337 (1972).

103. R. J. Cook and A. F. Bernhardt, "Deflection of Atoms by a Resonant Standing Electromagnetic Wave," *Phys. Rev.* 18, 2533 (1978).

Authors

R. Cook

A. Bernhardt

10.6 Laser Technology Developments

10.6.1 Line-Narrowed ArF Laser Oscillator

Recent developments in rare gas halide (RGH) laser technology have demonstrated these systems to be efficient (~1%) high-energy (~1 J/litre atm), broad-band (~300 cm^{-1}) sources of ultraviolet. The ultimate utility of RGH laser systems in spectroscopic applications or as pump sources for Raman lasers depends on achieving line-narrowed, tunable output. We have conducted experiments on ArF lasers that have demonstrated continuously tunable output over 320 wave numbers from 1928 to 1940 Å with a line width of 0.25 wave numbers. The ArF laser can be used directly or as a master oscillator for a Raman laser pump. Because Raman scattering may be used to access a wider spectral region than ArF lasers alone, issues associated with Raman lasers have been analyzed and will be discussed in the next subsection.

The experimental laser facility is shown in Fig. 10-39. The ArF laser output from the unstable-resonator scraper mirror (upper right) is shown directed toward diagnostics. The laser discharge volume is 0.4 × 2.0 × 100 cm and is ultraviolet-preionized by a double row of 40 spark plugs. The

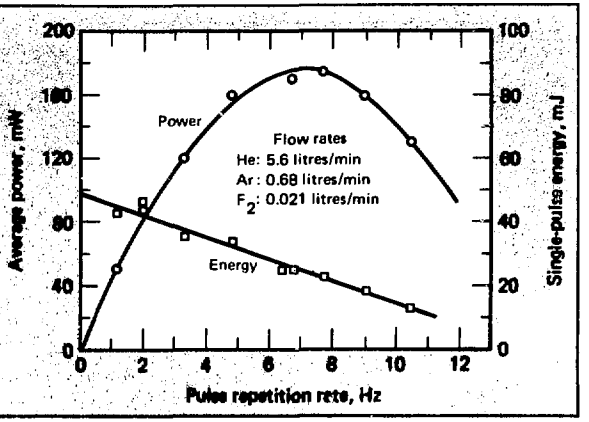

laser gas flow system combines fluorine, argon, and a helium buffer in the optimum ratio (1:40:360) and is capable of a longitudinal flow of 30 litre/min, allowing continuous 10-Hz operation of the laser. The average power and single-pulse energy are shown in Fig. 10-40 as a function of pulse repetition rate. These data were taken with a flat-flat stable resonator without line-narrowing optics.

Line-narrowing and tuning experiments were completed with the half-symmetric unstable resonator[104] illustrated in Fig. 10-41. The hole in the scraper mirror is elliptical so that the optical mode will more closely match the 4.0 × 20-mm gain cross section. The optical cavity and beam paths to all diagnostics are purged with nitrogen to prevent oxygen absorption. The coarse ArF tuning and narrowing can be accomplished by either gratings or prisms. Dispersion in quartz prisms at 1930 Å is comparable to that produced by eschelle gratings in high order (m = 30), although ultraviolet-grade quartz prisms are preferred for their lower optical losses.

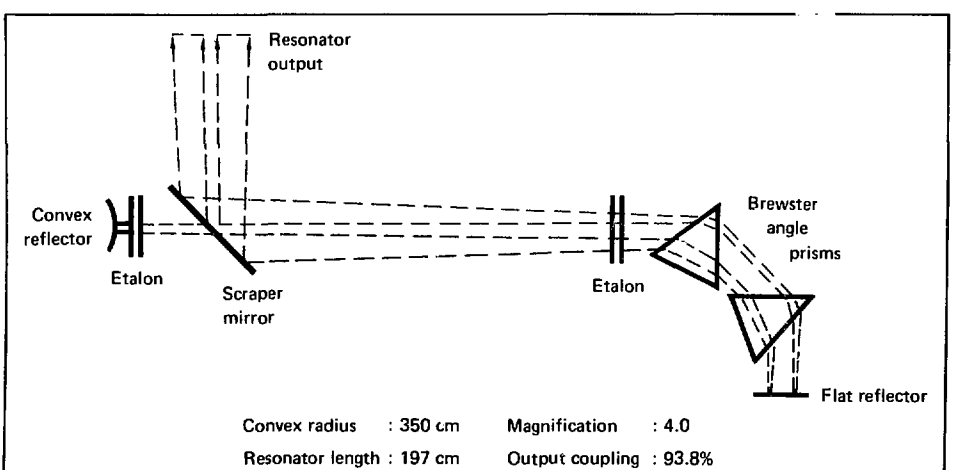

Fig. 10-41. Half-symmetric unstable resonator with frequency selective optics (hole in scraper mirror is elliptical so that optical mode will more closely match the 4.0 × 20-mm gain medium).

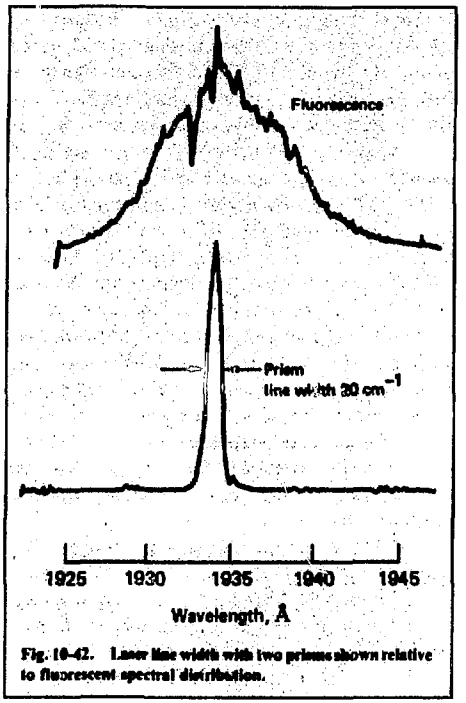

Fig. 10-42. Laser line width with two prisms shown relative to fluorescent spectral distribution.

The two quartz prisms reduced the line width to 20 cm^{-1} from the 240 cm^{-1} (FWHM) fluorescence bandwidth, as shown in Fig. 10-42. These spectra were recorded in the film plane of a 1.0-m spectrometer with an optical multichannel analyzer. The spectrometer resolution was 5.0 cm^{-1}. Both etalons

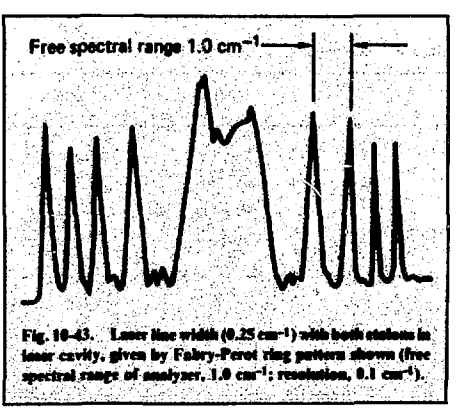

Fig. 10-43. Laser line width (0.25 cm^{-1}) with both etalons in laser cavity, given by Fabry-Perot ring pattern shown (free spectral range of analyzer, 1.0 cm^{-1}; resolution, 0.1 cm^{-1}).

are air-spaced with a variable super-Invar gap, are piezoelectrically tuned, and have a reflectivity finesse of 10. The etalon surfaces are matched to $\lambda/70$ at 1930 Å, ensuring an overall finesse given by the reflectivity (73.5%).

Because etalon peak transmission T is a strong function of the dielectric coating loss L and the mirror reflectivity R, where $T = 1 - (L/1 - R)^2$, two low-finesse etalons were used instead of one with a higher finesse. Losses for these etalons were between 1 and 2% at 1930 Å, implying an overall transmission of 79% for both. The free spectral range is 25 cm^{-1} for the etalon near the prisms and 2.5 cm^{-1} for the etalon near the scraper mirror (Fig. 10-41). The laser line widths were measured with a third analyzer etalon. The ring pattern was recorded with a linear, optical multichannel analyzer. With two prisms and the 25-cm^{-1} etalon in the cavity, the line width is 1.0 cm^{-1}. With both prisms and both etalons the laser line width is 0.25 cm^{-1}, as shown by the ring pattern in Fig. 10-43. These results are summarized in Table 10-14 along with the laser energy for each line width. The fact that the laser energy drops by only a factor of 16 when the line width is reduced by a factor of 80 is consistent with the homogeneous nature of the bound-free ArF laser transition.

The tuning range of the ArF laser was also investigated. At a line width of 0.25 cm^{-1}, the output was continuously tunable over 320 cm^{-1} from 1928 to 1940 Å. The intensity variation of the laser output over this tuning range closely resembles the fluorescence intensity distribution shown in Fig. 10-42. At 2.7 Hz, the laser energy is 540 μJ at 1933 Å and 10 μJ at the band edges. The strong absorption feature at 1932 Å can be observed while tuning. However, at gas exchange rates that are 10 times higher that those relevant for Fig. 10-42, this absorption is just barely discernable while tuning

Table 10-14. Line width and energy characteristics of ArF laser at 1933 Å.

	Line width (FWHM), cm^{-1}	Single-pulse energy, mJ @ 2.7 Hz
Fluorescence	240	–
Two prisms	20	8.6
+25 cm^{-1} etalon	1.0	3.8
+2.5 cm^{-1} etalon	0.25	0.54

the laser and is considerably reduced in the fluorescent spectra, indicating that it is caused by long-lived contaminants generated in the laser discharge.

These experiments have demonstrated ArF lasers with sufficiently high pulse energy (0.54 mJ), tuning range (320 cm^{-1}), line width (0.25 cm^{-1}), and repetition rate (1 to 10 Hz) to be a useful spectroscopic tool. The amplified output of this system can also be used to investigate Raman conversion to other frequencies in the VUV.

10.6.2 ArF-Pumped Raman Laser Analysis

For several reasons, Raman lasers are very attractive devices for shifting the ArF frequency to other spectral regions. Raman lasers can have high conversion efficiencies (~50%), they can be scaled very easily with laser pump power, and they can be very compact devices at the pump energies of interest here. The analytical details supporting these conclusions are outlined below.

The theory of Raman scattering has been developed by many authors.[105] In the small signal limit, the Stokes intensity I_s grows exponentially as

$$I_s(l) = I_s(O) \exp(g_s I_L l) , \qquad (20)$$

where I_L is the intensity of the pump and l is the length of the medium. The gain coefficient is given by

$$g_s = \frac{2N}{\pi h n^2 (\tilde{\nu}_L - \tilde{\nu}_R)^3 (\delta\tilde{\nu}_R + \delta\tilde{\nu}_L)} \left(\frac{d\sigma}{d\Omega}\right)_{||} . \qquad (21)$$

In this equation, N is the number density, h is Planck's constant, n is the refractive index, $\tilde{\nu}_L$ is the pump laser frequency, $\tilde{\nu}_R$ is the Raman frequency shift, $\delta\tilde{\nu}_R$ and $\delta\tilde{\nu}_L$ are the Raman and laser line widths, respectively (all frequencies expressed as wave numbers), and $(d\sigma d\Omega)_{||}$ is the total spontaneous scattering cross section for light polarized parallel to the plane-polarized incident light. Table 10-15 lists the properties of several Raman laser candidates. The gains are extrapolated to λ = 193 nm from the experimentally determined values in the visible spectral region. The gain listings assume the laser line width is much narrower than the Raman line width. In fact, to achieve maximum gain, this is a requirement for the ArF pump laser. A laser bandwidth of 0.1 cm^{-1} will be sufficiently narrow for most scatterers listed in Table 10-15 for which data are available. Notable exceptions are LN_2 and H_2 (which has a narrow, pressure-dependent line width).

Since overall laser efficiency is strongly influenced by the Raman amplifier, a detailed model is useful for assessing the utility of Raman frequency conversion. The rate equations for forward Raman scattering provide the basis for the amplifier modeling. Following the formalism of von der Linde, Maier, and Kaiser,[105] one obtains for forward Raman amplification

$$\frac{n_L}{c}\frac{\partial I_L}{\partial t} + \frac{\partial I_L}{\partial z} = -\frac{\omega_s}{\omega_L} g_s I_s I_L - \alpha I_L , \qquad (22)$$

and

$$\frac{n_s}{c}\frac{\partial I_s}{\partial t} + \frac{\partial I_s}{\partial z} = g_s I_s I_L - \alpha I_s . \qquad (23)$$

Table 10-15. Properties of selected Raman scatterers.

	H_2	CH_4	LN_2	CO_2
Raman frequency shift, cm^{-1}	4155	2916	2327	1388
Shifted ArF frequency, cm^{-1}	47,560	48,800	49,390	50,330
Raman line width, cm^{-1}	0.01–0.07	0.34	0.067	~0.5–1.0
Gain coefficient, cm/MW (at 193 nm[a])	1.1×10^{-2}	2.4×10^{-4}P(atm)	0.12	$\sim 10^{-5}$P(atm)

[a]Scaled from data in visible region according to:

$$g \sim \frac{(\nu_L - \nu_R)}{(\nu_a - \nu_L)^2 (\nu_a + \nu_L)^2} , \text{ where } \nu_a \text{ is the closest ultraviolet absorption line.}$$

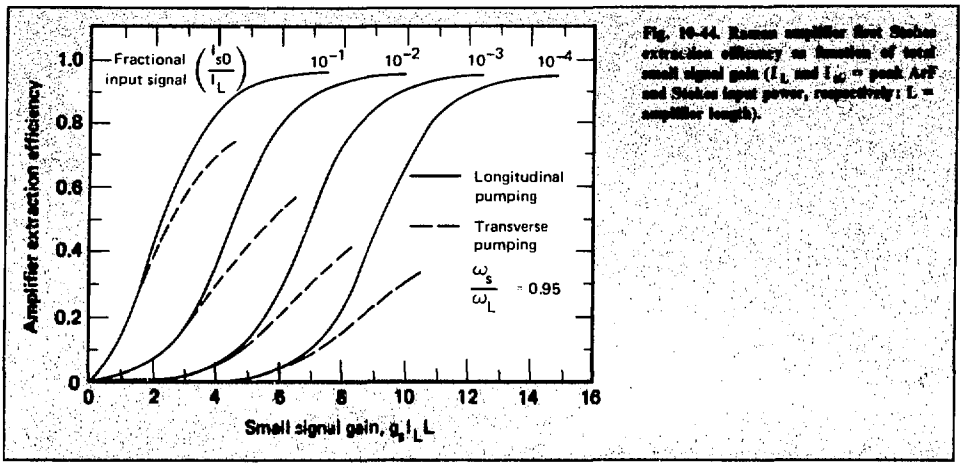

Fig. 10-44. Raman amplifier first Stokes extraction efficiency as function of total small signal gain (I_L and I_{s0} = peak ArF and Stokes input power, respectively; L = amplifier length).

In these equations, I_L is the pump laser intensity, I_s is the first Stokes intensity, n_L and n_s ($n_L \approx n_s$) are the indices of refraction, c is the velocity of light, and α is the absorption coefficient. Backward scattering is ignored because the amplifier will be driven strongly in the forward direction by the input oscillator signal. Higher-order Stokes components including anti-Stokes components are also neglected. This neglect is justified if the pump laser intensity is no greater than that required for efficient first Stokes conversion. In any real amplifier these higher order components will be present, but their effect on overall device performance can be minimized by careful design. A further simplification can be made if the pump laser pulse length is long enough. The time to reach steady state is given by $t_s = 2/c\delta\bar{\nu}$ and is 10 to 1000 ps for scatterers of interest. Because ArF pulse lengths are typically 20 to 40 ns, the steady state solution is valid.

Longitudinal and transverse pump geometries have been analyzed in detail. In longitudinal pumping, the Stokes oscillator signal and ArF pump beam are focused colinearly into the same mode volume within the amplifier. A quartz prism has enough dispersion to allow combination of the two wavelengths into one colinear beam. In the transverse geometry, the pump beam is focused into the amplifier from both sides to maximize intensity uniformity. The input signal is focused to match the pumped volume. For high-prf operation, the Stokes medium flows transverse to the beams. The calculated extraction efficiency for these two configurations is shown in Fig. 10-44. The analysis is based on Eqs. (22) and (23) under steady state conditions. The Stokes and pump beams are assumed to be spatially uniform in the plane perpendicular to the propagation direction. For a fixed fractional-input signal (I_{s0}/I_L), the first Stokes extraction efficiency depends only on the total small signal gain $g_s I_L L$, where I_{s0} and I_L are the peak Stokes and ArF input power, respectively, and L is the amplifier length. The value of $\omega_s/\omega_L = 0.95$ is typical of N_2 and CH_4. It is clear from Fig. 10-44 that, for the same gain and Stokes input intensity, longitudinal pumping is more efficient. However, the difference in efficiency is smaller at higher Stokes inputs.

The advantages of transverse over longitudinal pumping are that, for the same pump intensity, the beam dimension along the medium flow direction is significantly smaller, and, for a given prf and medium clearing ratio, the velocity required for transverse pumping is smaller. In addition, parametric coupling of the pump and first Stokes to generate higher order Stokes components cannot occur in a transverse geometry.

The dimensions of both longitudinally and transversely pumped Raman amplifiers can be quite small for the pulse energies of interest. The amplifier beam diameter d is dictated by the optical damage limit $\epsilon_D(J/cm^2)$ if one desires to minimize

the amplifier length at a fixed extraction efficiency. For longitudinal pumping with an output Stokes pulse energy, E_{s1},

$$d = \left(\frac{4E_{s1}}{\pi \epsilon_D k_{s1}}\right)^{1/2} \tag{24}$$

The amplifier length is given by

$$L = \frac{\chi(k_{s1})\tau_p}{g_s \epsilon_D} , \tag{25}$$

where (k_{s1}) is the total small signal gain required to achieve the desired extraction efficiency k_{s1} and γ_p is the laser pulse length. Similarly, for transverse pumping, the height, width, and length are given, respectively, by:

$$h = \frac{g_s E_{s1}}{\tau_p k_{s1} \chi(k_{s1})} \tag{26}$$

$$d = \frac{\tau_p k_{s1} \chi(k_{s1})}{g_s \epsilon_D} . \tag{27}$$

$$L = \frac{\tau_p \chi(k_{s1})}{2 g_s \epsilon_D} . \tag{28}$$

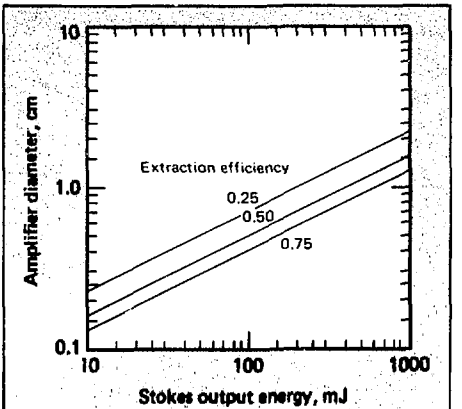

Fig. 10-45. Longitudinal Raman amplifier beam diameter vs first Stokes output energy (required energies are typically 100 mJ, implying beam diameters of ~ 0.5 cm).

The diameter scaling relationship for the longitudinal case—Eq. (24)—is illustrated in Fig. 10-45. The optical damage limit for quartz at 193 nm was taken as 1 J/cm^2. The ArF pulse length, typical of ultraviolet-preionized discharge devices, is 30 ns. The beam diameter is shown as a function of the required Stokes output energy. Shown in Fig. 10-46 is the amplifier length as a function of small signal gain at the damage limit (33 MW/cm^2). Small signal gains for representative scatterers are also indicated. The amplifier length is limited by output beam quality requirements. The output phase variation $\Delta\phi/2\pi$ for a density variation $\Delta\rho/\rho$ is given for gaseous media (nonturbulent flow) by

Table 10-16. Raman amplifier characteristics.

ArF pump energy	600 mJ
First stokes energy	300 mJ
Power gain	50
Extraction efficiency	50%
Dimensions:	

Scatterer	Longitudinal		Transverse		
	D, cm	L, cm	H, cm	D, cm	L, cm
LN_2	0.87	1.1	0.35	0.71	0.72
H_2,CH_4(50 atm)	0.87	12.5	0.35	7.9	7.9
CO_2(50 atm)	0.87	280	Too small for pump beam quality		

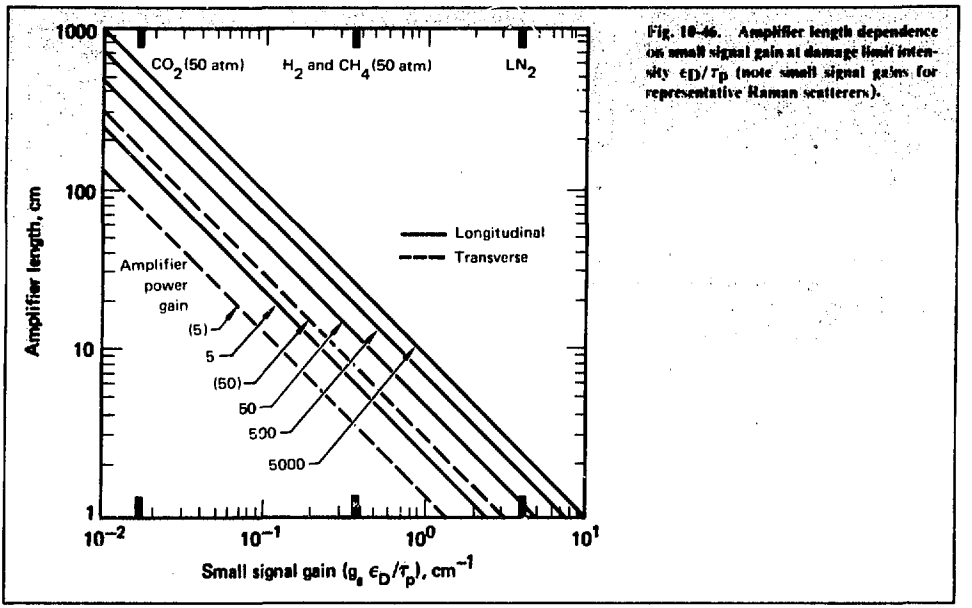

Fig. 10-46. Amplifier length dependence on small signal gain at damage limit intensity ϵ_D/τ_p (note small signal gains for representative Raman scatterers).

$$\frac{\Delta\phi}{2\pi} = (n_0 - 1)(\rho/\rho_0)\frac{\Delta\rho}{\rho}\frac{L}{\lambda}, \qquad (29)$$

where n_0 is the refractive index at density ρ_0. For gases such as methane and CO_2, $(n_0 - 1) \approx 4 \times 10^{-4}$ and, at 50 atm, $\Delta\phi/2\pi \approx 1.2$ L(cm) for a $\Delta\rho/\rho$ of 10^{-3}. CO_2 at a power gain of 50 can have serious beam quality problems ($\Delta\phi/2\pi \approx 200$). However, for turbulent flow, the phase distortion is reduced by a factor $(\Omega/L)^{1/2}$, where Ω is the characteristic scale of the turbulence. If Ω is approximated by the pump beam diameter (flow channel width), the phase distortion is reasonable even for low-gain systems such as CO_2.

Scaling transversely pumped Raman amplifiers is similar to the longitudinal case discussed above. As an example, amplifier characteristics for both longitudinal and transverse geometries are given in Table 10-16. The ArF pump energy was taken as 600 mJ and the amplifier extraction efficiency as 50%. Note that, in the high and moderately high-gain Raman systems, the amplifiers are very compact devices.

This analysis has shown that Raman scattering can efficiently convert (50%) the ArF laser output to other spectral regions where the tuning range (320 cm^{-1}) may be utilized. In addition, Raman amplifiers can be relatively compact devices (1 × 10 cm) and can yield pulse energies in excess of 100 mJ.

References

104. A. E. Siegman, "Unstable Optical Resonators for Laser Applications," *Proc. IEEE* **52**, 227 (1965).

105. D. von der Linde, M. Maier, and W. Kaiser, "Quantitative Investigations for the Stimulated Raman Effect Using Subnanosecond Light Pulses," *Phys. Rev.* **178**, 11 (1969).

Author

S. R. Hargrove

10.6.3 Tunable Vibrational Ultraviolet Generation by Raman Scattering in H_2

Last year in the atomic spectroscopy facility, we embarked on an experimental program to develop a tunable coherent light source to attain wavelengths below 2200 Å for spectroscopy and photochemistry applications (see §10.2 through 10.4). We have investigated and developed a remarkably simple and versatile method based on anti-Stokes Raman scattering (SRS) in molecular

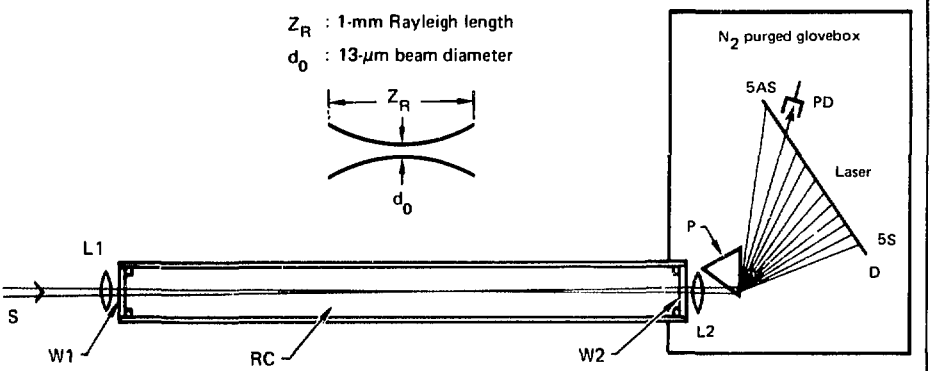

S: 1-cm diameter collimated 2660 Å pump radiation

L1: 50-cm Suprasil prism W1: 10-mm Suprasil prism P: 60-deg; Suprasil prism

5AS: 5 anti-Stokes components

L2: 20 cm MgF_2 W2: 10 mm MgF_2 5S: 5 Stokes components

RC: 100- X 4-cm Raman cell containing 446 kPa of H_2

D: Fluorescent screen

PD: Pyroelectric detector

Fig. 10-47. Schematic of anti-Stokes Raman generator.

hydrogen vapor. Using this process, we have successfully generated wavelengths to 1713 Å. To our knowledge this is the shortest wavelength ever generated by vibrational Raman scattering. We believe that, by extending the method described below, tunability to 1300 Å may be possible.

The usual method for generating tunable ultraviolet is second-harmonic generation and optical mixing in nonlinear birefringent crystals. Although these crystals can be transparent to below 1750 Å,[106,107] their birefringence limits phase matching to considerably longer wavelengths. The shortest wavelength reported in any nonlinear crystal by optical mixing has been 1850 Å in potassium pentaborate (KPB) and, by second-harmonic generation, 2160 Å in deuterated potassium pentaborate (D-KPB).[108] However, KPB and D-KPB are extremely difficult to work with, owing to their very small nonlinear coefficients $d[d_{31}(KPB) = 1/10\ d_{36}(ADP)]$.[109] The practical lower limit for tunable nonlinear generation is 2220 Å, corresponding to the optical mixing of the second harmonic of a tunable dye lased at 2805 Å with the fundamental of Nd:YAG at 1.064 μm.[110] Until rediscovery of anti-Stokes SRS in H_2, there were no viable alternatives for generating continuously tunable light to wavelengths below 2200 Å.[111]

Stimulated Raman scattering was extensively studied in the earliest days of quantum electronics.[112,113] With the advent of tunable light sources in the infrared and powerful lasers in the ultraviolet, SRS has recently experienced a second renaissance.[113-115] The process we have used to extend the tuning range of visible dye lasers was actually first investigated over a decade ago, using ruby (6943 Å) and Nd:YAG (1.06 μm) radiation by Duardo and Johnson.[112] However, it seems to have been overlooked even after the subsequent development of tunable dye lasers, probably due to lack of sufficient dye laser powers and to poor beam qualities.

Our initial studies on anti-Stokes SRS were performed with the fourth harmonic output at 2660 Å from a Nd:YAG laser, using the experimental geometry shown in Fig. 10-47. With this arrange-

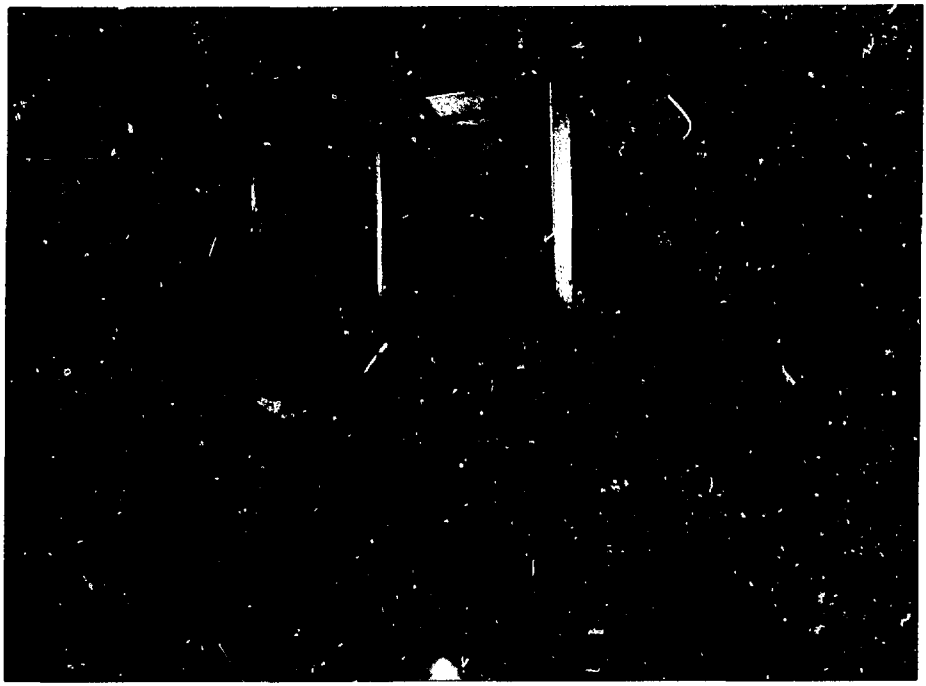

Fig. 10-48. Raman generator output.

ment we have generated, quite easily, at least five anti-Stokes (AS) and five Stokes (S) components under modest pumping conditions. The 5AS wave occurs at 1713 Å. The 6AS wave occurs at 1599 Å and, if present, would be totally absorbed by the Suprasil dispersing prism used.

Thresholds for 4AS and 5AS generation were less than 2 mJ (in a 5-ns pulse) under the conditions shown in Fig. 10-47: 446 kPa of H_2, focal spot diameter approximately 13 μm. With 15 mJ of pump energy we have measured more than 150 μJ at 1844 Å (4AS) and about 5 μJ at 1713 Å (5AS). Figure 10-48 shows the beams exiting the Raman cell and dispersed by the 60-deg prism.

Once the threshold for first Stokes is reached, all higher-order components appear to light simultaneously (i.e., at the same pump intensity). This suggests that the higher-order Raman processes are parametric. This is not surprising since the intensity at the focus of the pump is of the order 10^{12} W/cm^2, assuming no pump depletion or self-defocusing. That the process is parametric is confirmed at higher hydrogen pressures (>1.0 MPa) where steep cone angles develop for the higher-order Stokes radiation because of increased optical dispersion. These angles increase and eventually exceed the original diffraction angles of the focused beams.

We have observed pump depletions greater than 75%. The energy partitioning favors the low-order Stokes and anti-Stokes, but a reasonable efficiency is achieved in the higher orders (~1% energy in 4AS).

Using a commercially available dye laser pumped by the doubled output of the Nd:YAG laser, we have obtained similar results. With the dye laser operating at 5600 Å, we have observed 8AS (1956 Å) to 2S (1.048 μm); with its second harmonic at 2800 Å, we have observed 4AS (1911 Å) to 6S (9279 Å). We did not attempt to observe longer-wavelength Stokes. We were prohibited from observing shorter-wavelength anti-Stokes by the quality

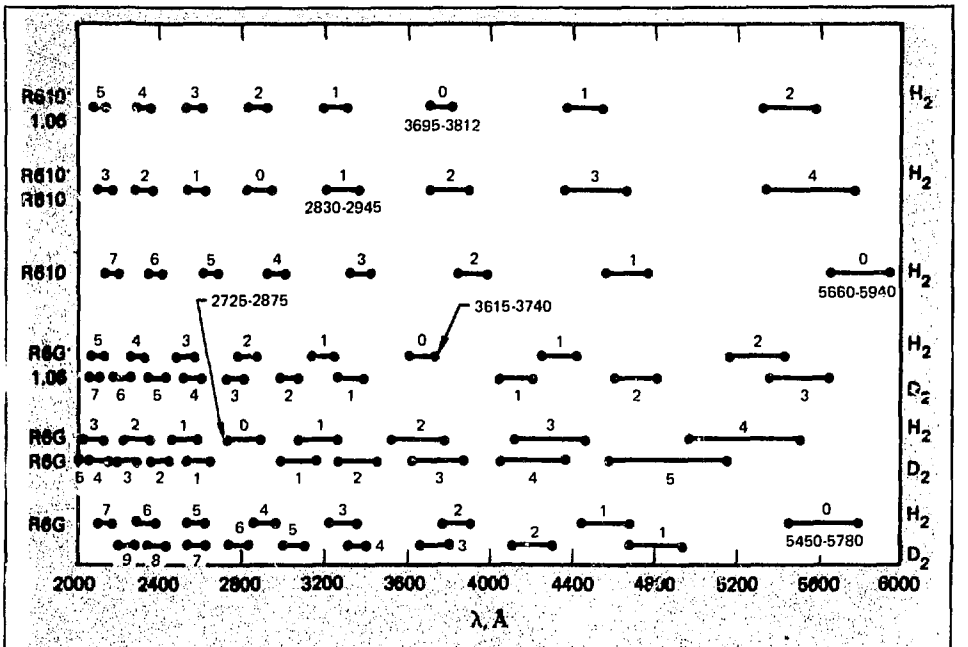

Fig. 10-49. Stokes Raman scattering in spectral coverage 2000 to 6000 Å, using Rhodamine 6G (R6G) and Rhodamine 610 dye laser; fundamental, doubled and 1.06-μm mixed pump radiation tuning ranges are as shown (numbers above each bar indicate Stokes or anti-Stokes order; for R6G, scattering in $D_2 - \upsilon_R = 2991\ cm^{-1}$ — is also shown).

o the output window (Homosil quartz) used in these experiments. The threshold and power conversion efficiencies with the 2800-Å pump were similar to those obtained with the fourth harmonic of Nd:YAG at 2660 Å. We measured about 25 μJ at 8 nS (1956 Å) for 65-mJ input (~5 ns) at 5600 Å.

Although we have not yet made an exhaustive parametric study, we have investigated some important properties of these high-order Raman processes. Because Raman processes are purely parametric, the spectral line width of the anti-Stokes and Stokes emission should approach that of the pump[116] independent of the Raman line width. As a result, optical resolutions $\Delta\lambda/\lambda$ of 10^{-5} to 10^{-6} are not only possible but routinely obtained at these wavelengths using the anti-Stokes SRS method. Furthermore, because the Raman process is purely vibrational [Q(1) mode], the scattered radiation is linearly polarized with the pump. Circular polarization of the pump induces rotational Raman components [S(1) and S(0) modes] and reduces the conversion efficiency of the vibrational Raman lines. We believe that the beams are close to diffraction-limited. We attribute this to the diffraction-limited pump, the tight focusing in the experiment, and the low hydrogen pressures (<500 kPa) at which we operated the cell.

It is useful to note that, with the output powers available from commercial dye lasers, tremendous spectral coverage can be achieved using SRS with only a few dyes. In fact, with Rh6G alone, essentially the whole spectrum to below 1750 Å can be spanned, as shown in Figs. 10-49 and 10-50.

We believe that this SRS method, besides being an extremely versatile spectroscopy tool, will find immediate applications in both photochemistry and quantum electronics. For example, the excellent spectral and spatial properties of the scattered radiation make an anti-Stokes generation device an ideal signal source for injection-locking short-wavelength excimer lasers. In addition, since SRS gain increases with pump frequency, the parametric

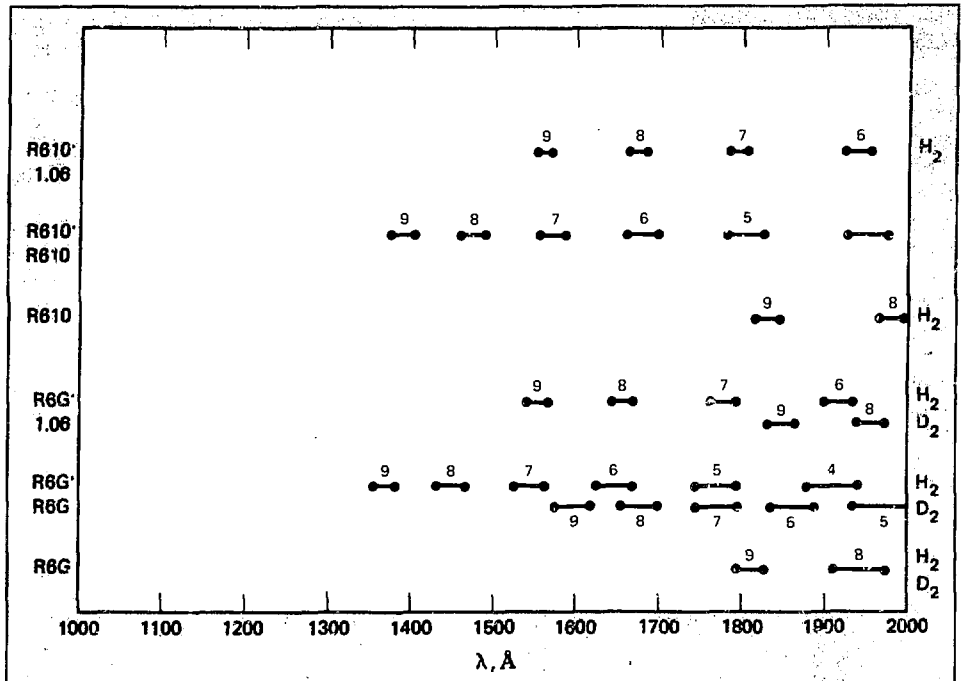

Fig. 10-50. Anti-Stokes spectral coverage below 2000 Å, using tuning ranges available from Rhodamine 6G and Rhodamine 610 dye lasers.

processes will have progressively lower thresholds at shorter wavelengths despite increased dispersion and potential gas breakdown problems. The ultimate limit may be the absorption edge of H_2 (~1100 Å). We believe tunable output to 1300 Å may be possible, using an ArF-laser-based system,[117] because the 5AS(6AS) of the 1933-Å output of ArF would occur at 1379 Å (1304 Å). A tunable device at these wavelengths would open up new vistas in photochemistry and materials research.

References

106. W. L. Smith, "KDP and ADP Transmission in the Vacuum Ultraviolet," *Appl. Opt.* **16**, 1978 (1977).
107. J. A. Paisner, M. L. Spaeth, D. C. Gerstenberger, and I. W. Ruderman, "Generation of Tunable Radiation below 2000 Å by Phase Matched Sum-Frequency Mixing in $KB_5O_8 \cdot 4H_2O$," *Appl. Phys. Lett.* **32**, 476 (1978).
108. R. E. Stickel and F. B. Dunning, "Generation of Tunable Coherent Vacuum UV Radiation in KB5," *Appl. Opt.* **17**, 981 (1978).
109. H. J. Dewey, "Second Harmonic Generation in $KB_5O_8 \cdot 4H_2O$ from 217.1 to 315.0 nm," *IEEE J. Quantum Electron.* QE-12, 303 (1976).
110. R. Herbst, Quanta Ray Corporation, private communication (1978).
111. V. Wilke and W. Schmidt, "Tunable UV-Radiation by Stimulated Raman Scattering in Hydrogen," *Appl. Phys.* **16**, 151 (1978)
112. J. A. Duardo, F. M. Johnson, and L. J. Jugent, "Some New Aspects in Stimulated Raman Scattering from Hydrogen Gas," *IEEE J. Quantum Electron.*, **QE-4**, 397 (1968).
113. R. L. Byer and W. R. Trutna, "16-μm Generation by CO_2-Pumped Rotational Raman Scattering in H_2," *Opt. Lett.* **3**, 144 (1978).
114. P. Rabinowitz, A. Stein, R. Breckman, and A. Kaldor, "Stimulated Rotational Raman Scattering from Para-H_2 Pumped by a CO_2 TEA Laser," *Opt. Lett.* **3**, 147 (1978).
115. T. R. Loree, R. C. Sze, and D. L. Baker, "Efficient Raman Shifting of ArF and KrF Laser Wavelength," *Appl. Phys. Lett.* **31**, 37 (1977).
116. J. Murray, Lawrence Livermore Laboratory, Livermore, Calif., private communication (1978).
117. J. J. Ewing, Lawrence Livermore Laboratory, Livermore, Calif., private communication (1978).

Authors

J. A. Paisner
S. R. Hargrove

10.6.4 Closed Cycle Operation of Rare Gas Halide Lasers

Discharge-excited rare gas halide (RGH) lasers have the potential for high average powers at high pulse repetition frequencies (prf's) by operation with transverse gas flow. For practical operation, these lasers must employ closed-loop gas flow with minimal gas makeup. One of the greatest uncertainties associated with such a system is the lifetime of a gas fill. Initial data from a modified CO_2 gas transport laser operated by Fahlen[118] indicated that the gas degradation problem was severe, limiting operation at 1 kHz to a few minutes' duration. To carefully assess this issue as well as other high prf phenomena at modest power levels, we built a high-purity closed-cycle-flow ultraviolet-preionized discharge laser system designated as the closed cycle test bed (CCTB). To our knowledge, this system is the first closed-cycle-flow, high-prf laser specifically designed for operation with the rare gas halides.

Flow Loop. The flow loop, shown in Fig. 10-51, is made entirely of materials that either passivate or do not react with F_2. The flow ducts are fabricated from type 304 stainless steel, with Viton O-ring seals. Gas circulation is driven by a tube-axial fan (nominal 600 cfm, 300 litre/s). The 3/4-hp, 11,000-rpm motor is enclosed in an O-ring-sealed housing through which the propeller shaft extends. Isolation of the motor and its bearings from the laser gas is achieved with two shaft seals: a metal-bellows-operated O-ring static seal and a gas-buffered dynamic seal. The laser gas mixture is cooled by a nominal 10-kW thermal capacity tube and fin heat exchanger, which also serves as a flow-conditioning device. Coolant for the heat exchanger is provided by a temperature-controlled recirculating chiller. A

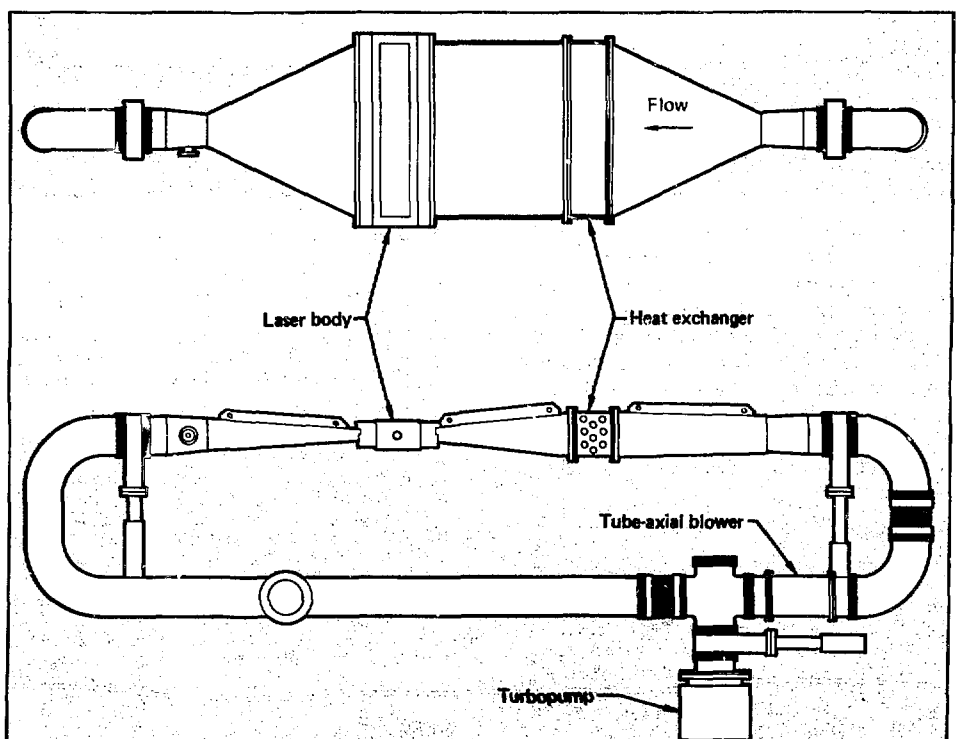

Fig. 10-51. Flow loop for closed cycle test bed laser (overall length, 3 m; internal volume, 200 litres).

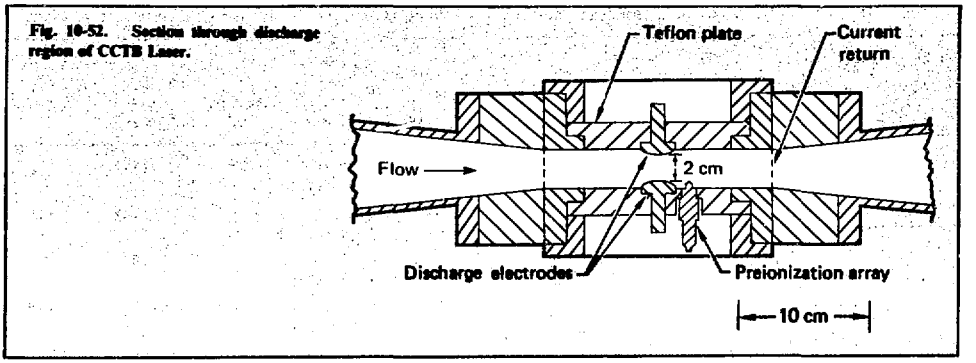

Fig. 10-52. Section through discharge region of CCTB Laser.

turbomolecular vacuum pump is used to evacuate the loop to a base pressure less than 2×10^{-6} Torr.

A cross section of the laser head is shown in Fig. 10-52. The aluminum discharge electrodes are 60 cm long and are separated by 2 cm. An ultraviolet-preionization arc array, comprising 34 modified automotive spark plugs, is located downstream of the electrodes. The discharge current is returned through the flow by two sets of wire grids. The gas flow field between the electrodes has been measured with an array of pitot-static probes. These measurements gave an average flow speed of ~20 m/s with a maximum variation of ±4%.

Discharge Excitation Circuit. Both the main discharge and ultraviolet preionization discharge are thyratron-driven. The main discharge excitation pulser is shown schematically in Fig. 10-53. This circuit is switched by two ceramic hydrogen thyratrons (EG&G HY-53) connected in parallel and mounted in coaxial housings through which cooling oil circulates. The circuit is connected to a command charge pulser and protected by a thyratron inverse diode circuit. Custom low-dissipation mica capacitors are used as the energy storage elements. The operating parameters for the discharge circuit, with a typical RGH gas fill, are summarized in Table 10-17. The preionization array is driven by a

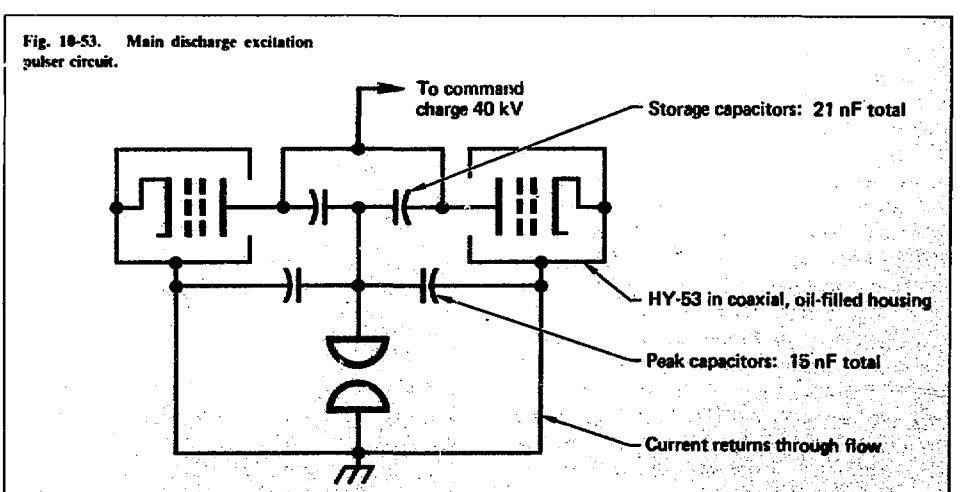

Fig. 10-53. Main discharge excitation pulser circuit.

Table 10-17. Discharge circuit characteristics.

Charging voltage	40 kV
Energy stored	15 J
Thyratron current pulse (each tube)	6-kA peak 100-ns FWHM
Discharge current pulse	20-kA peak 25-ns FWHM
Laser pulse	20-ns FWHM

10-nF capacitor, which is LC-charged to 20 kV and switched by a thyratron into a set of 5-m-long cables individually connected to the spark plugs. The synchronization of the main discharge tubes and their timing relative to the preionization circuit are controlled by nanosecond-resolution digital delay generators.

Closed Cycle Test Bed Operational Characteristics. Assembly of the closed cycle test bed (CCTB) flow loop was completed in August 1978 with installation of the fan. Work on the system through the next three months centered on increasing the power dissipation capability and reliability of the excitation circuits and performing an initial characterization of the laser behavior. By year's end, continuous hour-long operation at 250 Hz and brief operation to 600 Hz had been achieved. By then the laser had been run with the four rare gas halides of interest (ArF, 193 nm; KrF, 249 nm; XeCl, 308 nm; and XeF, 351 nm), and the prf dependence of the laser pulse energy and the gas lifetime had been investigated. The maximum average power obtained was 23 W, with XeCl. The longest sustained laser operation was more than 11 W for 2-1/2 h, again with XeCl.

The initial laser performance characteristics are summarized in Table 10-18, which lists the optimum gas mixture, the maximum pulse energy and average power, and the typical gas fill half-life for the four RGH's. Data for XeF are shown for the two fluorine donors F_2 and NF_3. These results were obtained with a stable resonator, using ultraviolet-grade synthetic fused-silica optics. The output coupler transmission was generally 70%, except with KrF for which an uncoated flat was used. Fused-silica windows have allowed the maximum laser energies; however, CaF_2 and sapphire windows have been found more resistant to laser and chemical surface damage.

Table 10-18. Summary of CCTB laser performance.

System	Mixture (partial pressures), Torr	Energy, mJ	Average power, W (Hz)	Gas life, h
KrF	F_2, Kr, He 2.5/150/1350	80	13 (250)	2
ArF	F_2, Ar, He 2.5/150/1150	47	7 (400)	0.25
XeF	F_2, Xe, He 3.5/15/1280	34	5 (200)	0.5
	NF_3, Xe, He 2/10/1250	39	4.5 (200)	0.25
XeCl	HCl, Xe, He 3.5/70/1230	48	23 (600)	>2

The measured prf dependences of the laser pulse energies for the four RGH's are exhibited in Fig. 10-54. With the notable exception of XeCl, the laser energy decreases monotonically with increasing prf. Near the maximum prf, the degradation for each case is presumably due to flow limitations; note that, at 500 Hz, the discharge clearing ratio—the ratio of the gas flow volume between successive pulses to the discharge volume—is approximately equal to 3. At lower prf 's the mechanisms for decrease, or increase in the case of XeCl, are uncertain.

Several diagnostic experiments have been performed to investigate these observations, including observing the recovery of the optical transmission of the active volume following a discharge pulse,

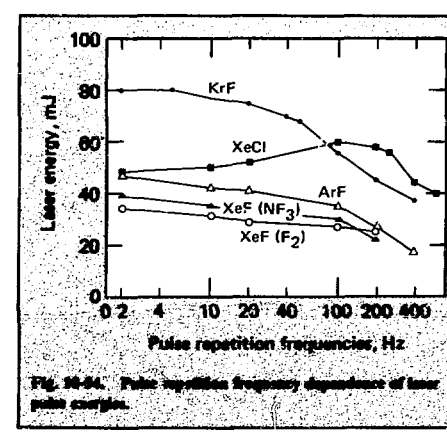

Fig. 10-54. Pulse repetition frequency dependence of laser pulse energies.

monitoring the performance of the excitation circuits at varying prf 's, and running bursts of pulses to determine the time required for the degradation to occur. Initial results indicate that the degradation cannot be attributed to vibration of the optics, to acoustic disturbances in the medium, to varying excitation conditions, or to discharge-created chemical species. In the case of XeCl, one may speculate that the increase is due to the beneficial effect of the photolysis of discharge-produced Cl_2 yielding HCl by absorption of 308-nm fluorescence or laser radiation, as has been discussed by Sze and Scott.[119]

If one runs the laser at a constant prf, its power, after turn-on transients, typically decays in time at a fairly constant rate until it approaches threshold. As apparent from Table 10-18, the gas lifetime characteristics of the four systems vary greatly. Our results are consistent with the characteristics of typical static-fill low-prf devices and are presumably determined by the systems' sensitivity to contaminants that degrade discharge stability or efficiency, or absorb laser radiation. It has been suggested that the very long lifetime of XeCl mixtures is aided by the photolysis of Cl_2, as mentioned above.[119] To improve the gas lifetime, it will be necessary to identify the contaminant species and, more important, their sources. For this purpose, an on-line sampling quadrupole mass analyzer system will be added to the flow loop for use beginning in early 1979.

References

118. T. S. Fahlen, *Final Report on Task 2 of Phase II of USERDA Contract No. EY-76-C-03-1245* (1977).
119. R. S. Sze and P. B. Scott, *Appl. Phys. Lett.* **33**, 419-20 (1978).

Authors

J. Miller
J. Davin
J. Swingle

10.6.5 E-Beam-Switched Discharge Rare Gas Halide Lasers

Rare gas halide lasers are of interest for several LIS and fusion applications. In particular, the short wavelength and high efficiency make these lasers possible sources for driving laser fusion power plants. Two primary technologies have been used to excite RGH lasers[120-123]: preionized discharge,[124] and electron beams.[125-127] In the former, excitation of the laser volume is obtained by applying a high-voltage pulse to a pair of electrodes. Preionization of the discharge volume by some external source before application of the high voltage has been found necessary in generating a diffuse discharge. Ultraviolet radiation is the usual source. In electron beam excitation, the power input to the laser volume is generated by passage of a high-energy electron beam through the laser output volume. Some enhancement of the laser output can be obtained from application of an electric field, but the primary power input comes from the electron beam.

Over the past few years, we have been investigating hybrid excitation techniques involving both electron beams and electrical discharges.[128] Early work in this area was mainly concerned with studies of laser kinetics. The combination of electron beam and discharge provided a stable source for such experiments. It became evident, however, that operation in this regime may have significant technological advantages over either discharge or electron beam excitation alone for some applications. Operation in this hybrid regime is referred to as the electron-beam-switched discharge (EBSD).

The electrical circuits for the EBSD are similar to the usual circuits used for discharge excitation. The discharge is generated between a pair of electrodes driven by a low-inductance pulsed power supply. In most cases this power supply consists of an array of capacitors tightly coupled to the electrodes along their length. These capacitors are charged by a second pulsed power supply, which may have higher inductance and which contains the main electrical switches.

The main differences between the preionized discharges and the EBSD lie in the timing and magnitude of the various electrical inputs to the discharge. These inputs are compared in Fig. 10-55. For preionized discharges, there is initially no voltage across the electrodes. Before application of the voltage, the laser volume is preionized with ultraviolet radiation or a weak electron beam. The preionization produces an electron density of 10^8 to 10^{10} cm^{-3} between the electrodes. A few tenths of a microsecond after the preionization pulse, the main electrode voltage is applied. The rise time of this voltage must be rapid, since the discharge breaks down as the voltage rises. Thus, the only energy deposited in the discharge is that stored in the primary capacitors before breakdown. Breakdown times are generally 10 to 100 ns. One consequence of

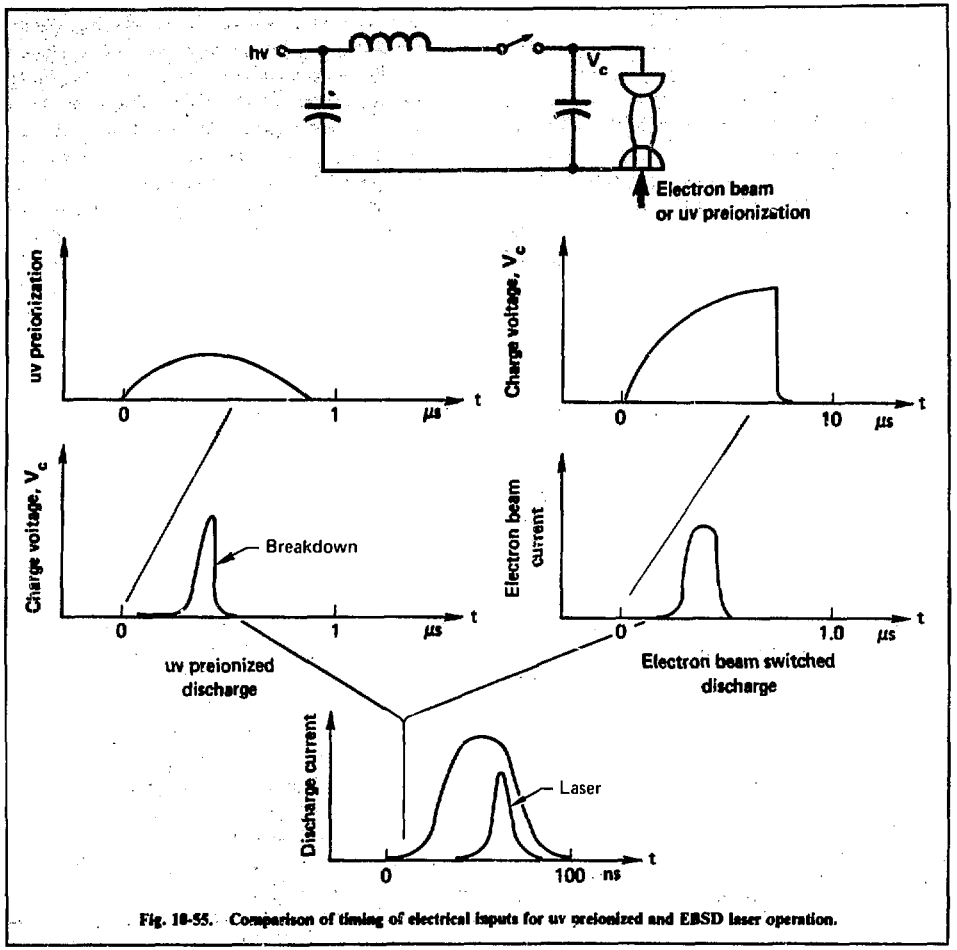

Fig. 10-55. Comparison of timing of electrical inputs for uv preionized and EBSD laser operation.

the requirement for rapid charging is that the switch in the secondary circuit transfers all the input energy at high peak power. A typical preionized discharge requires a 100-MW power input in 100 ns. This high power is debilitating to switches, particularly when the equipment is operating at high repetition rates.

For the EBSD, the corresponding electrical inputs are as shown on the right in Fig. 10-55. In this case the discharge volume is not preionized. The charging of the primary capacitors takes place relatively slowly over a period of several microseconds. The applied voltage is maintained low enough to preclude breakdown over this period. At the desired time, an electron beam pulse of short duration is applied to the volume to initiate the discharge. The intensity of the electron beam required to initiate the EBSD is substantively higher than that needed for preionization. Electron beam current densities greater than approximately 0.1 A/cm^2 are required, corresponding to an electron density of approximately 10^{12} cm^{-3}. After breakdown, the subsequent phases of the discharge are similar for both preionized and EBSD operation. The discharge current and voltage are determined by the discharge kinetics and the characteristics of the external power supply.

The primary advantage of the electron-beam-switched discharge is reduction of the peak power handled by the switches. Pulse charging in 10 μs rather than in 100 ns significantly reduces the peak power. This advantage would not be so important if the fast pulse switching problems were merely transferred to the electron beam system. Fortunately, the electron beam power required to switch the discharge is substantively smaller than the peak discharge power input, and the electron beam of sufficient intensity can be generated by several different techniques.

Experimental Setup. The operation of the EBSD has been investigated using a small commercial electron beam source. This device has a nominal output of 15 A/cm[6] at 250 kV with a pulse width of 100 ns over a 1- × 35-cm aperture. For the EBSD experiments, the current density of the electron beam could be reduced to less than 0.1 A/cm^2 by use of screens over the electron beam foil. The resulting beam was collimated before it entered the discharge cell. The pulse shape could be modified to some extent by adding pulse-forming networks in series with the diode.

The discharge cell was a modified ultraviolet-preionized laser body made from a single block of Teflon. The electrodes were 35 cm long with a 2.25-cm separation. The electron beam entered the cell through a screen over one electrode. The primary power supply was made up of 30 barium titanate capacitors with a nominal capacitance of 460 pF each. These capacitors were arrayed along both sides of the electrodes to reduce the inductance to a minimum. Larger mica capacitors in a similar configuration were used for some experiments. The primary capacitors were pulse-charged from an external source in times from 1 to 10 μs to voltages up to 40 kV. Direct-current charging of the capacitors was also used. The gas for the experiments was premixed to the desired composition.

Laser Characteristics. Lasing was observed in the EBSD in ArF, KrF, XeF, and XeCl. Most experiments were performed with KrF. The laser cavity consisted of a full reflector and a 70% output coupler, both with a 5-m radius of curvature. The mirror separation was 80 cm. The laser cell was closed with Brewster windows of CaF_2, and the path length in the gas was 60 cm. Laser output, as a function of total pressure for KrF as a function of gas mixture, is shown in Fig. 10-56. The optimal mixture was 0.3% F_2, 12% Kr, and the remainder either Ar or He at a total pressure of 700 Torr. The lower curves for the EBSD were taken with an unoptimized optical cavity. The maximum output was nominally 150 mJ. For comparison, measurements are shown in Fig. 10-56 for an ultraviolet-preionized discharge of similar volume, power supply, and optical cavity. The buffer gas was He rather than Ar, and the F_2 fractional concentration in the mixture was the same. However, the laser performance was generally found similar for both discharges. Laser pulse lengths were also similar, about 20 ns in each case.

The variation of laser output with electron beam current density under similar conditions is shown in Fig. 10-57. The laser output for the EBSD was insensitive to the magnitude of the electron beam current density above 0.25 A/cm^2, while below this value the laser output decreased and the amplitude became erratic. Laser output was observed, however, at current densities as low as 0.1 A/cm^2. Above 10 A/cm^2, the electron beam began to contribute significantly to the power input to the laser gas. The rise time of the electron beam current was 50 ns, but an increase to 100 ns did not significantly affect the laser performance. The laser output increased with operating voltage. Maximum voltage was limited to 40 kV by the onset of arcing outside the laser body. The output was also insensitive to the pulse charging time, provided the discharge was initiated before the system spontaneously arced.

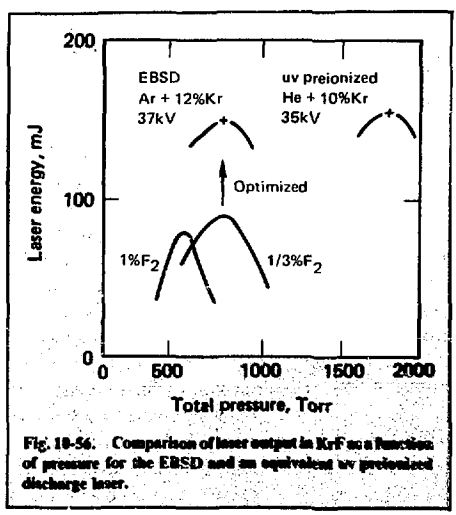

Fig. 10-56. Comparison of laser output in KrF as a function of pressure for the EBSD and an equivalent uv preionized discharge laser.

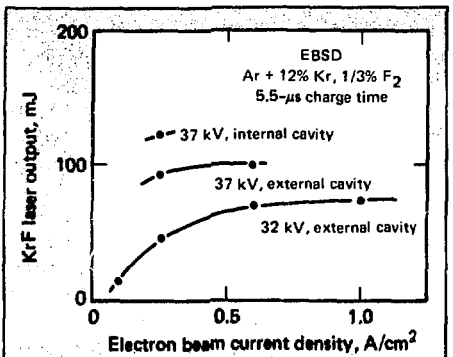

Fig. 10-57. Variation of KrF laser output as a function of electron beam current density for several supply voltages and optical cavity configurations.

Laser operation with Ar as a buffer gas was one of the interesting characteristics of the EBSD. Such operation is not possible with preionized discharges; the discharge constricts immediately into an arc. The actual laser performance, however, was not particularly sensitive to the different buffer gases. This performance suggests that the processes limiting the laser efficiency to approximately 1% are not associated with the production kinetics.

Discharge Characteristics. As with the laser output, the gross electrical characteristics of the EBSD are similar to the preionized discharge. During the main current pulse, the voltage drops rapidly as the current rises. The peak current and rise time are determined primarily by the external power supply. In both discharges there is a tendency to form a constricted arc at times late in the discharge. This tendency is aggravated by attempts to increase the energy input to the discharge.

The peak discharge current is a function of initial charge voltage for operation in the EBSD mode. Two operating regimes are observed. At low voltages, the discharge current follows the shape, and is more or less proportional to the magnitude, of the electron beam pulse. When operated with the minimum electron beam current required for switching, the discharge current in this region is very small. Above a threshold voltage, the discharge current rises rapidly into the discharge regime. At the highest voltages, the peak current approaches the short circuit current available from the power supply. In this regime, the discharge current is independent of the electron beam current. The threshold voltage for discharge operation increases with total pressure and F_2 density.

The differences between EBSD and preionized discharge operation are primarily in the details of the initial rise in the electron density and current in the discharge. The power input to the discharge is about 1 to 10 MW/cm^3. The power density deposited by the electron beam that is required to initiate the discharge is about 1000 W/cm^2; this represents an intrinsic power gain of 10^3 to 10^4. The corresponding power density for preionization discharge is only 1 W/cm^3. Attempts to operate an ultraviolet preionized discharge in the EBSD mode result invariably in arcing and no laser output.

The EBSD displays a well-defined and reproducible delay between the start of the electron beam pulse and the rise of the major portion of the discharge current pulse. A typical current waveform is shown in Fig. 10-58. The time delay is shown in Fig. 10-59 as a function of total pressure for fixed voltage and as a function of voltage for fixed pressure. The mixture is typical of KrF laser operation. Laser output is obtained only if the delay is smaller than a nominal 30 ns. The measured delays are consistent with predictions of a model that considers the growth of the electron density from the

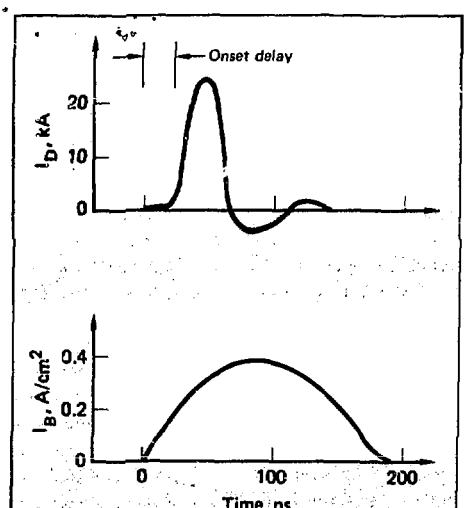

Fig. 10-58. Variation of total discharge current, I_D, and electron beam current density, J_B, under typical EBSD operating conditions in argon, illustrating discharge onset delay (discharge area, 30 cm^2).

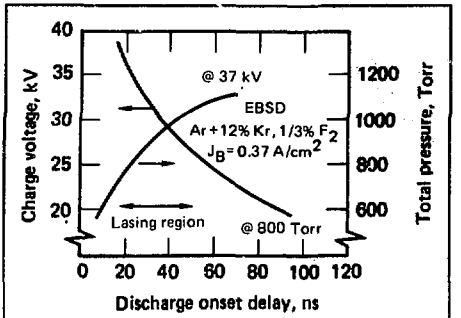

Fig. 10-59. Variation of discharge onset delay with charge voltage and total gas pressure for EBSD.

initial values produced by the electron beam, through exponentiation by one-step ionization balanced by attachment losses, and finally to a nonlinear increase by multistep ionization. The sharp increase in the current corresponds to the onset of multistep ionization. The electron beam requirements for stable switching can be related to a threshold for stabilization of one-step ionization instabilities by collisional processes.

The switched discharge operates in a parameter regime distinct from other discharge techniques and is a relatively general phenomenon. The electron beam supplies more than just an improved preionization. The EBSD appears intrinsically more stable than other discharges. The primary power input is through the discharge rather than an electron beam sustainer mode. Switched discharge operation is not confined to RGH laser gas mixtures but has been observed in pure Ar as well as in He:F_2 mixtures. The generation of discharges in Ar is indicative of the intrinsic stability of the EBSD. Such discharges are prone to constrictive instabilities at high pressures. Another indication of stability is an observed insensitivity of the discharge to the structure of the cathode. Stable KrF laser operation has been obtained with widely spaced individual wires instead of the normal fine-mesh screen on the cathode.

The electron-beam-switched discharge represents an important technological advance in the excitation techniques for RGH lasers. This approach reduces the peak power requirements on the main switches driving the discharge. The reduced power loading on the switches and other components may also lead to improvements in overall system efficiency. Additional power gain, for further system simplification, may be possible within the electron beam generator itself.

References

120. J. J. Ewing and C. A. Brau, "High Efficiency UV Lasers," in *Tunable Lasers and Applications*, Springer Verlag, Berlin (1976).
121. C. A. Brau, "Rare Gas Monohalides," in *Eximer Lasers*, C. K. Rhodes, Ed., Springer Verlag, Berlin (1978).
122. J. J. Ewing, "Rare Gas Halide Lasers," *Phys. Today* **31**, 32 (1978).
123. J. J. Ewing, "Eximer Lasers," in *Laser Handbook*, **Vol. 3**, M. Stitch, Ed., North Holland, Amsterdam (to be published).
124. R. Burnham, N. W. Harris, and N. Djeu, "Xenon Fluoride Laser Excitation by Transverse Electric Discharge," *Appl. Phys. Lett.* **28**, 86 (1976).
125. S. K. Searles and G. A. Hart, "Stimulated Emission at 281.8 nm from XeBr," *Appl. Phys. Lett.* **27**, 243 (1975).
126. C. A. Brau and J. J. Ewing, "354-nm Laser Action on Xe-F," *Appl. Phys. Lett.* **27**, 435 (1975).
127. J. A. Mangano and J. H. Jacobs, "Electron-Beam-Controlled Discharge Pumping of the KrF Laser," *Appl. Phys. Lett.* **27**, 495 (1975).
128. *Laser Program Annual Report—1976*, Lawrence Livermore Laboratory, Livermore, Calif., UCRL-50021-76 (1977).

Authors

L. D. Pleasance
W. R. Rapoport

10.6.6 Annular Copper Vapor Laser

The copper vapor laser (CVL) is an efficient (~1%) source of visible radiation, capable of moderately high powers (~20 W) and high repetition frequencies (prf ~20 kHz). Because it operates on a transition whose lower level is metastable, repetitive operation of the laser depends on depopulation of that metastable level by collisional means. In the metal vapor laser system, all present experimental evidence indicates that diffusion to and quenching at the tube walls constitute the dominant metastable deactivation mechanisms. With a laser geometry based on cylindrical tubes, the laser diameter d and prf f are constrained by diffusion to obey a relation of the form $d^2f \sim$ constant.

Annular Laser. A laser geometry that could potentially circumvent the diffusion constraint is an annular configuration. A copper vapor laser using this concept was therefore built and tested.

The active volume of the laser is formed between two cylindrical ceramic tubes, 3.8 and 7.6 cm in diameter, respectively, and each 122 cm long. The

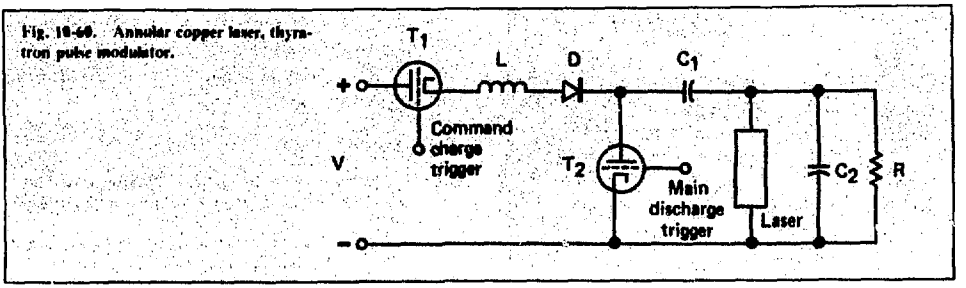

Fig. 10-60. Annular copper laser, thyratron pulse modulator.

inner tube is centered and supported within the outer tube by a number of cradles, copper vapor being introduced into the discharge plasma from two thin, effusive sources located around the inside of the outer ceramic tube. The discharge, with He as the buffer gas, takes place longitudinally along the length of the annular volume between two cylindrical electrodes attached to each end of the larger ceramic tube. A metal vacuum envelope, which also serves as a coaxial return for the discharge current, surrounds the entire tube structure. Near-normal-incidence quartz windows, held in water-cooled mounts, terminate the two ends of the vacuum enclosure and serve as the optical aperture windows. The laser operates in the self-heated mode, where the discharge power that excites the laser medium also acts as the power source to heat the tube to its operating temperature. In this case, the length of the lasing region is determined approximately by the length of the 91-cm-long radiation heat shield surrounding the tube assembly.

Pulse Modulator. Excitation of the discharge was accomplished by a pulse modulator (Fig. 10-60) whose primary energy store, capacitor C_1, is command-charged from the dc power supply through an EG&G 1802 thyratron T_1. Switching of the laser discharge is done by an EG&G HY-53 thyratron T_2 housed in a low-inductance coaxial current return structure. The thyratrons, charging inductors, and diodes are all cooled to maintain component temperatures within adequate operating limits. To maintain low inductance and reduce thermal dissipation, capacitors C_1 and C_2 actually comprise an array of low-dissipation Teflon-insulated rf capacitor units. Under typical operating conditions, 10 kW of electrical power can be dissipated by the pulser at prf 's exceeding 10 kHz.

Laser Characteristics. The discharge in the annular volume is not always uniform. Below a hot zone temperature of about 1300°C, the glow discharge tends to be filamentary and unstable. As the tube temperature increases, the discharge becomes more diffuse, completely and uniformly filling the entire volume as the tube approaches operating temperatures in the range of 1400 to 1500°C. The uniformity of the discharge at optimum operating temperatures can be explained in part by the presence of a thermally generated source of uniform preionization in the volume, because of the presence of the low-ionization-potential species Cu. At 1500°C, the Saha equation predicts a background electron density of about 7×10^6 cm^{-3}. Higher levels of ionization probably exist when the laser is operated repetitively at 6 kHz because of residual ionization left from the decay of the electron density following each pulse.

Laser power is extracted from the device in an annular beam with a flat–flat resonator consisting of one totally reflecting mirror and an uncoated optical flat as the output coupler. Figure 10-61 illustrates an oscillogram of the laser current pulse measured with a current viewing resistor and the

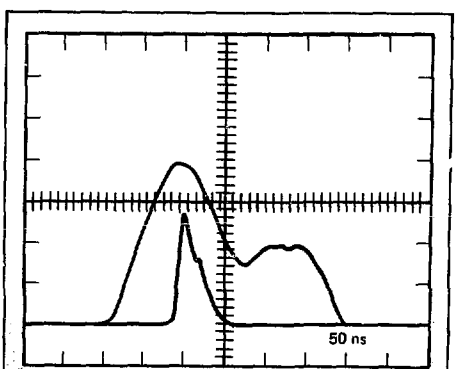

Fig. 10-61. Oscillogram of laser current pulse and stimulated emission pulse (current pulse amplitude, 400 A/cm).

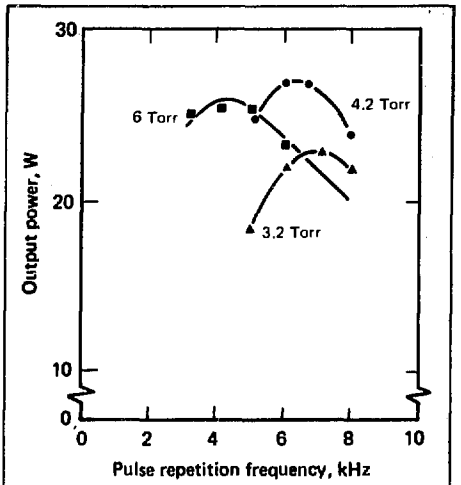

Fig. 10-62. Output power data as a function of pulse repetition frequency in helium buffer gas.

associated stimulated emission pulse. The measured current pulse with a peak amplitude of 1.6 kA and FWHM width of 200 ns agrees well with calculated current pulse shapes, using a circuit code that models the time-dependent conductivity of the Cu + He discharge. Figure 10-62 shows typical data on the operating characteristics of the laser as a function of the He buffer gas pressure and prf. Laser powers of 20 to 35 W at a prf of 6 kHz have been observed from this device.

Authors

T. Kan
D. Ball

10.6.7 Dye Development

The tunable dye laser is inexpensive to operate and is scalable; thus, it is the principal means of frequency conversion from a laser pump (copper vapor, doubled neodymium, rare gas halide) to the wavelengths and line widths needed for atomic uranium separation. For a three-step ionization process, this conversion means wavelengths centered at 600 nm; for a two-step ionization process, it means wavelengths centered at 400 nm. The dye facility presently concentrates on understanding the physical and chemical parameters that influence performance—conversion efficiency, laser threshold, tuning range, optimum response, and photochemical stability.

Short-pulse, focused laser excitation of dye media generates high concentrations of the lowest excited singlet state S_1 of the dye. Although this S_1 state is essential for gain, it introduces its own absorption. If such absorption appears at the pump wavelength, it wastes pump power. Thus, a knowledge of the spectral properties of the S_1 state is important in determining optimum pumping conditions and is essential to the design of improved laser dyes.

We have measured the S_1 spectrum of rhodamine 6G as well as other materials by means of the experimental setup illustrated in Fig. 10-63. A weak tunable probe beam B_2 interrogates the sample in cuvette C, which is pumped simultaneously by a strong laser B_1 operating at the dye absorption maximum. Because the pump saturation flux is a minimum at this wavelength, attention can be concentrated on a uniform pumping field by sacrificing power for beam homogeneity. Plots of pump transmission against incident pump flux show sigmoid-shaped curves. All experiments were conducted at only the fully saturated condition. A correction to the directly measured excited state spectrum must be applied because the dye has a strong fluorescence and, hence, a nonzero stimulated emission cross section even at the absorption maximum.[129]

The induced spectra for the ground-state S_0 and the lowest excited singlet state S_1 are shown in Fig. 10-64. The ground-state absorption cross-section (σ_0) is determined simply from the ratio of the incident (I_1) and emerging (I) intensities of the monochromatic beams on a dye sample in conventional equipment, such as a Cary spectrophotometer, according to

$$\ln \frac{I}{I_1} = -N d \sigma_0, \qquad (30)$$

where N is the dye concentration (molecules/cm^3) and d is the cell path length. If the ground-state dye molecules could now be converted entirely to the S_1 state, the induced spectrum would be as shown. Here, σ^* and σ_e are the cross sections for excited state absorption from the S_1 state and stimulated emission from $S_1 \rightarrow S_0$, respectively. At wavelengths

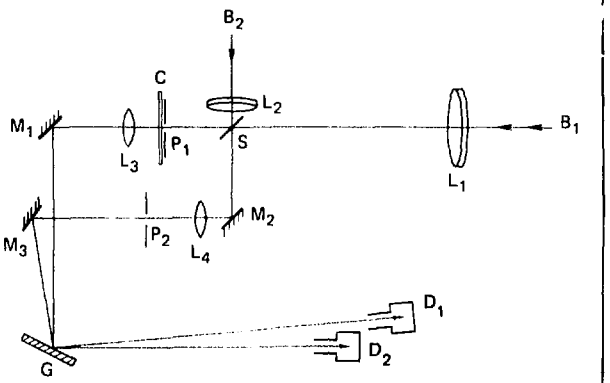

Fig. 10-63. Apparatus for measurement of dye-excited singlet absorption.

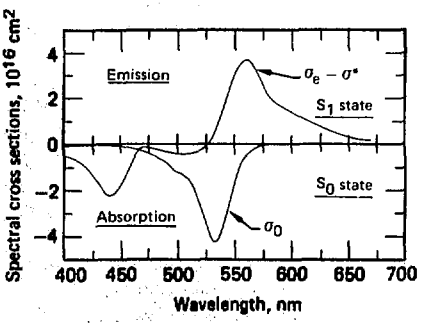

Fig. 10-64. Spectra of the S_1 and S_0 state of Rhodamine 6G fluoroborate in ethanol.

shorter than 526 nm, there would again be absorption, whereas for longer wavelengths in the yellow and red, the signal would come through amplified. Because rhodamine 6G is a laser dye, the spectrum shows a crossover point from absorption to gain. For the gain region, $(\sigma_e - \sigma^*)$ is positive. It is this *effective* stimulated emission cross section that is the basic parameter defining lasing behavior. It is related, just as for σ_0, by

$$\ln \frac{I}{I_I} = N d (\sigma_e - \sigma^*) . \tag{31}$$

Determination of the S_1 spectrum must be under small-signal conditions, so that there is no distortion of level population, just as it must be for the ground-state spectrum.

If we knew σ_e, then σ^* could be resolved unambiguously. The former can be obtained from the fluorescence spectrum[130,131] with the observation that, for such compounds (the rhodamines), the Einstein B coefficients for induced absorption and emission are identical at the maxima; i.e.,

$$B(\nu_0)_{absorption} = B(\nu_e)_{emission}, \tag{32}$$

or

$$\frac{\sigma_0 c}{h \nu_0 n_0} = \frac{\sigma_e c}{h \nu_e n_e}, \tag{33}$$

or

$$\frac{\sigma_{0\,max}}{\nu_{0\,max}} = \frac{\sigma_{e\,max}}{\nu_{e\,max}}, \tag{34}$$

assuming no dispersion in the medium for the small Stokes-Shift dye.

Along with the calculated σ_e curve, Fig. 10-65 shows both the experimental points from which Fig. 10-64 is plotted and the fluorescence spectrum $E(\lambda)$. The emission cross section is larger than the measured points up to 550 nm and indicates small σ^* values, about 0.4×10^{-16} cm^2. The curves nearly coincide at 580 nm and longer wavelengths, where the excited-state absorption appears to be minute. Support for this conclusion comes from the probe measurement at 670 nm. Although the fluorescence is extremely weak, the dye still has gain with a

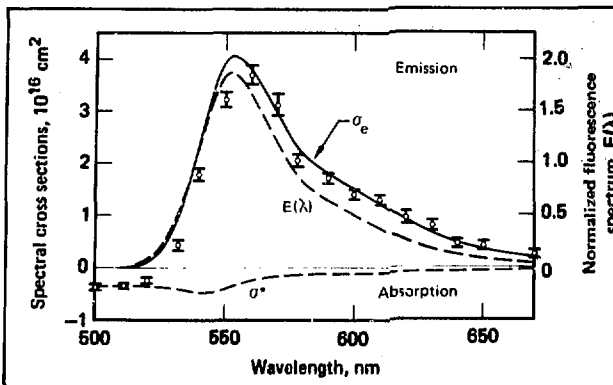

Fig. 10-65. Resolution of cross sections for stimulated emission σ_e and excited state absorption σ^*, and their comparison with the fluorescence spectrum E(λ) — Rhodamine 6G.

measured and predicted cross section of only about 0.2×10^{16} cm^2. Thus, apart from the continuation of the weak excited state absorption from beyond 500 nm to about 550 nm, σ^* is very small, probably less than 0.2×10^{-16} cm^2, across the rest of the fluorescence band. Such trends are implied in the σ^* curve of Fig. 10-65.

A comparison can be made between the $S_n \leftarrow S_1$ absorption and the related transition accessing the S_n state from the ground S_0. In Fig. 10-66(a) the σ_e curve is redrawn on the $S_n \leftarrow S_0$ ground-state absorption spectrum, offset by 18,450 cm^{-1} (the position of the S_1 state). We have used the symmetry point between the $S_1 \leftarrow S_0$ absorption and mirror-image $S_1 \leftarrow S_0$ fluorescence to approximate the origin of S_1. If the absorption shown were a true measure of σ^*, such curves would predict that rhodamine 6G is a laser dye ($\sigma_e > \sigma^*$) but would not predict gain at 670 nm.

However, we can develop some insight by inquiring about the directions of the transition moments within the molecule. Figure 10-66(b) shows the long-axis polarized absorption determined according to the method of Albrecht[132] from the fluorescence polarization measurements of Jakobi and Kuhn.[133] The estimated σ^* values are now close to the predicted values; the dye not only has gain at 670 nm but even the crossover point at 523 nm agrees with the experimental value (526 nm). Moreover, the band at 4.0×10^4 cm^{-1} in Fig. 10-66(b) and the excited state absorption at 440 nm in Fig. 10-64 are near-coincident.[134] We can use symmetry arguments to interpret this observation. If we assign the dye chromophore C_{2v} symmetry, we can infer that the transition moments for the stimulated emission process and for excited state absorption are perpendicular to each other within the plane of the molecule.

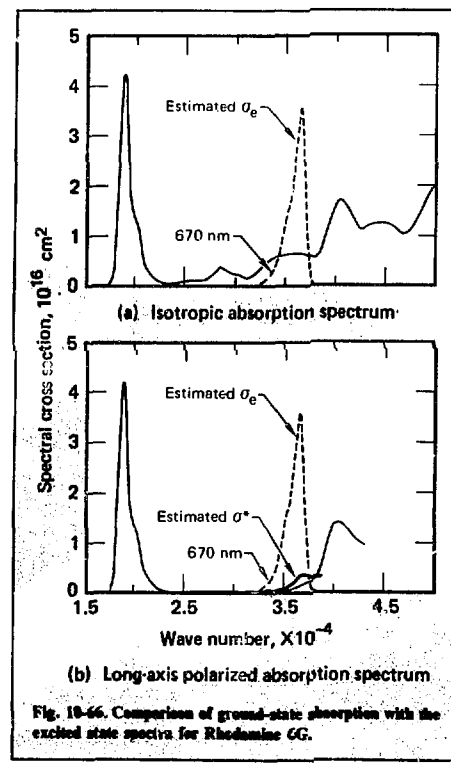

Fig. 10-66. Comparison of ground-state absorption with the excited state spectra for Rhodamine 6G.

The results of these studies bear on the optimum pumping geometry and wavelengths for a specific dye Rh6G. Our ultimate goal is to understand systematically the effect of excited state absorption and orientation on dye laser performance. Hopefully this understanding will aid in our selection of existing dyes and the construction of new dyes for uranium LIS.

129. P. R. Hammond, "Saturable Absorber Properties of a Laser Dye," *Appl. Opt.* **18**, 536 (1979).
130. A. Yariv, *Quantum Electronics* (Wiley, New York, 1975), pp. 158-165.
131. B. B. Snavely and O. G. Peterson, "Measurement of the Critical Population Inversion for the Dye Solution Laser," *IEEE J. Quantum Electron.* **QE-4**, 540 (1968).
132. A. C. Albrecht, "Polarizations and Assignments of Transitions," *J. Mol. Spectros.* **6**, 84 (1961).
133. H. Jakobi and H. Kuhn, "Direction of the Transition Moment for the Absorption Bands of Xanthene Dyes with Respect to the Dichroism and Fluorescence Polarization," *Zeit. Elektrochem.* **66**, 46 (1962).
134. G. Dolan and C. R. Goldschmidt, "Measurement of Rhodamine 6G Excited Singlet Absorption Cross-Sections," *Chem. Phys. Lett.* **39**, 320 (1976).

Author

P. Hammond

10.6.8 Laser Systems Capability

In late 1977, a major effort was undertaken to build the VENUS laser system. The facility, when completed, will provide a significant increase in the tunable laser power available for AIS experiments.

The concept of the VENUS project is to transport spectrally tailored dye oscillator beams from the SPP-II laboratory (see §8.4 of the 1976 Laser Program Annual Report[135]) into the VENUS facility, where the dye beams will be increased in average power, using CVL pumped-dye amplifiers. The beams will then be spatially combined and transported to the separation chamber (Fig. 10-67). Thirty-two nominal 15-W copper lasers will provide the necessary dye amplifier pump power. The CVL and associated mounting structures were designed and fabricated under contract with the General Electric Company. A single space frame rigidly supports the laser heads, which are arranged optically into a number of master oscillator-power amplifier (MOPA) chains.

The VENUS system is housed in an addition to Bldg. 117, which was completed in August 1978. A

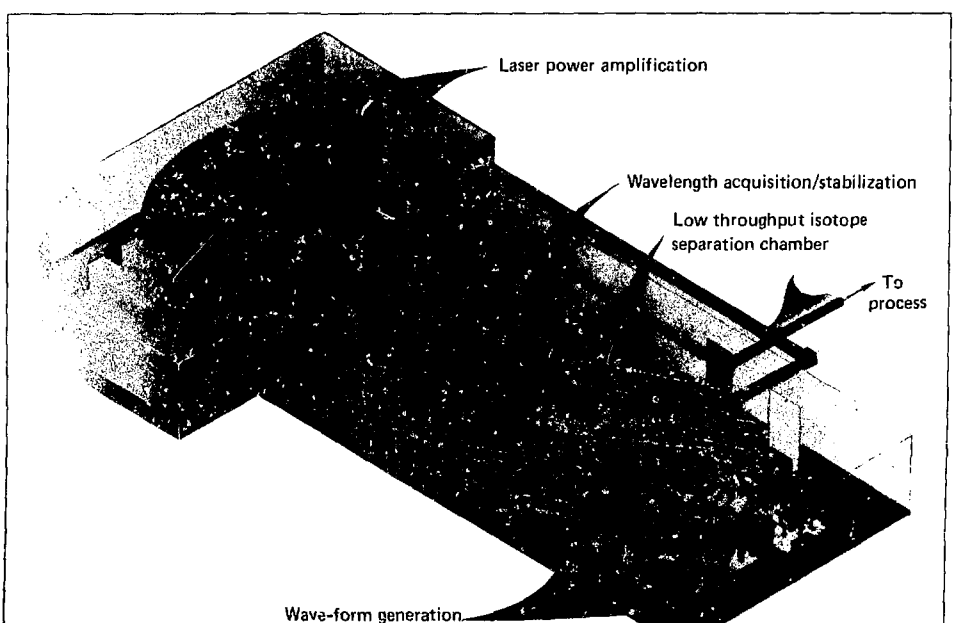

Fig. 10-67. The SPPII-VENUS Laser Facility.

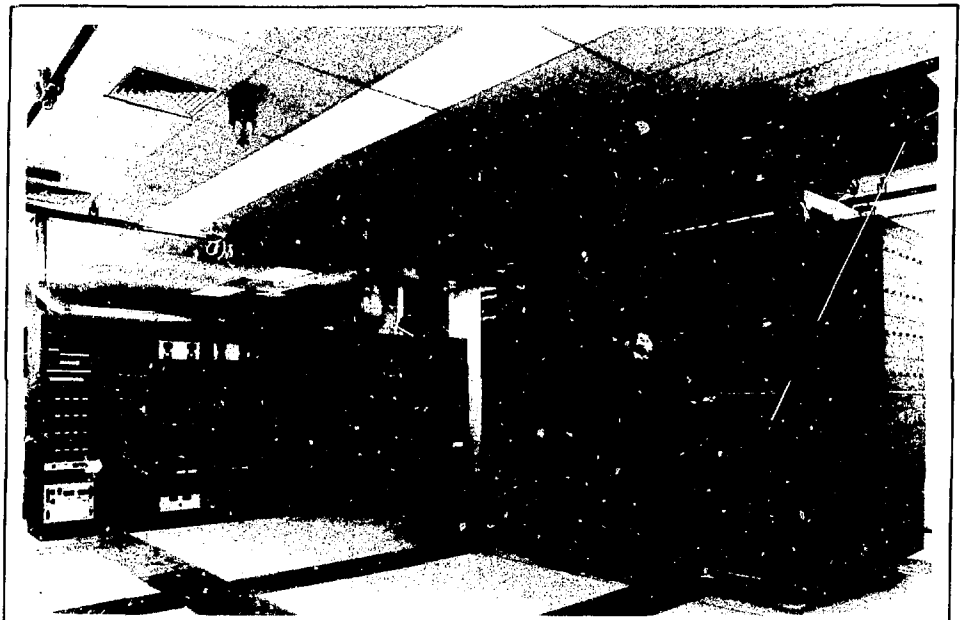

Fig. 10-68. VENUS laboratory, showing copper vaper laser modules (on right) seen from rear.

photograph of the facility is shown in Fig. 10-68. The 2000-ft^2 laboratory is divided into the laser area, power supply room, and technician work area. The CVL space frame and a granite table for the dye amplifiers rest on a 3-ft-thick concrete pad located near the north end of the room. The pad is isolated from the surrounding concrete floor to provide an extremely stable platform for the VENUS lasers.

The emphasis throughout the development of the VENUS system has been placed on the use of components designed for ease of maintenance and rapid replacement, and on the use of existing technology, wherever possible, to ensure the successful, timely completion of the project.

Copper-Vapor-Laser Pump System. Because of their present advanced state of development, copper vapor lasers were chosen to provide the pump power required to drive the VENUS dye amplifiers. The CVL's have been supplied by the General Electric Company in eight modules, each containing four laser heads and common service manifolds.

An improved version of the G.E. Model 15-6 commercial CVL is used in the VENUS system. The laser consists of a water-jacketed center section, a ceramic break, and water-cooled, easily removable end window assemblies. Reference surfaces are machined onto the jacket to provide a reproducible mounting surface. An evacuated region separates the water jacket from the heat shields surrounding the alumina discharge tube. The heat shields, made up of alternating layers of molybdenum foil and tungsten screen, sufficiently insulate the alumina tube to enable the waste heat from the discharge to raise the tube to an operating temperature of 1400°C. Bellows at both ends of the alumina tube adequately seal the buffer gas region inside the tube from the evacuated heat shield volume, permitting a constant, reproducible flow of buffer gas through each laser head. The plasma tube itself is 107 cm in length with a bore of 2.5 cm and is supported at each end by tantalum electrodes. Copper sources located near each end of the plasma tube provide the lasing medium.

At a pulse repetition frequency of 6 kHz, the VENUS CVL produces more than 15 W of average power in a 30-ns pulse, with about two-thirds of the output in the 5106-Å line.

The CVL heads are arranged in eight four-laser-head modules (Fig. 10-69). Each module con-

Fig. 10-69. VENUS copper vapor laser system (four modules are shown in installed in VENUS space frame).

tains manifolds for all mechanical and electrical services, including vacuum, water cooling, exhaust air, buffer gas, compressed air, and interlocks. For ease of servicing, the laser heads swing out from the interior of each laser cell on a hinged plate (Fig. 10-70). Precision support cradles for the heads are expected to permit replacement head installation with a reproducibility of ±0.5 mm, eliminating the need for realignment. Quick-disconnect vacuum, buffer gas, and water cooling lines should reduce head replacement time to less than 10 min. The resonant-charge circuit electrical components are located in a drawer assembly installed and removed from the rear of each laser cell of the module (Fig. 10-71). Thus, in the event of a suspected electronics failure, the entire charging circuit can be rapidly replaced.

Optics for the CVL heads are mounted on steel plates bolted to the space frame. Because of their modular design, the same optical mounts can be used for all master oscillator-power amplifier (MOPA) configurations. To maintain the stringent (~20 μrad) alignment tolerances, the space-frame members must be kept free from thermal distortion. For this reason, only one end of each module will be rigidly attached to the space frame, and water can be slowly circulated through the frame columns if required.

MOPA Operation. The limitation on bore diameter in high-prf CVL's, because of wall effects, restricts volume scaling of cylindrical CVL'S to an increase in active length. For the VENUS system, length scaling is achieved by staging the heads in a

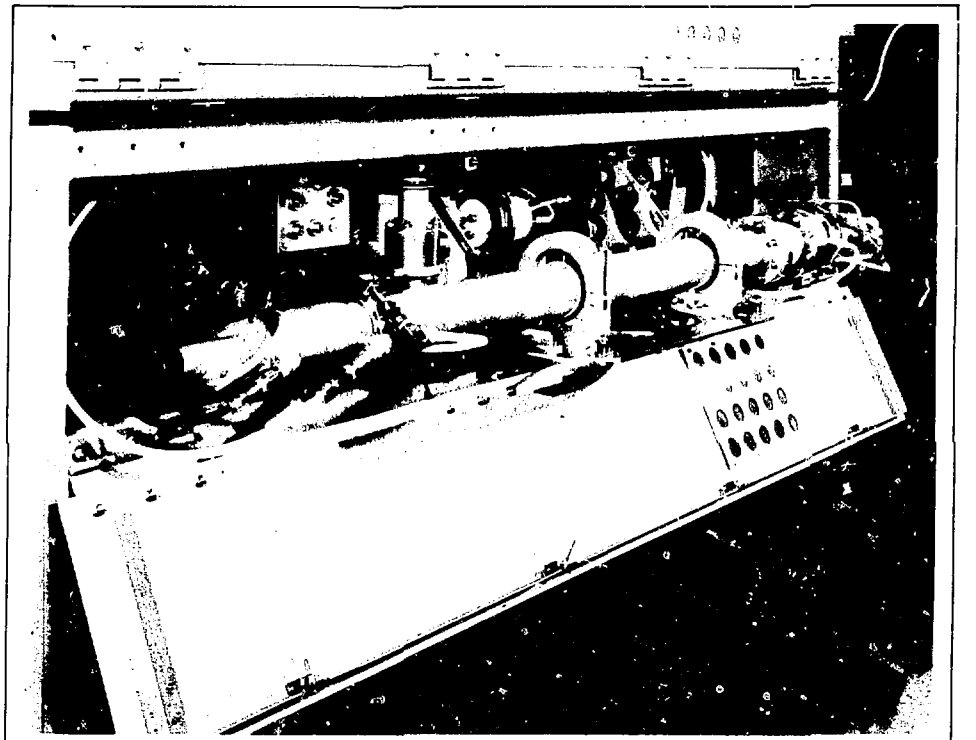

Fig. 10-70. VENUS copper vapor laser shown swung out from its laser cell for servicing.

MOPA configuration. The copper gain medium is well suited to MOPA operation because of its high stored energy and low saturation flux.[136] Earlier measurements with a 5-W CVL indicated that the device, when used as an amplifier, has a stored energy somewhat higher than when it is used as an oscillator, although some of this advantage is offset by coupling losses between amplifier stages.

To provide flexibility in the maximum output power available from each of the VENUS dye amplifiers, the CVL heads and associated optics have been designed to permit a variety of different MOPA configurations. By a simple rearrangement of resonator optics, any CVL head on the space frame can serve as a master oscillator for a MOPA chain. Any number of completely independent amplifier chains can be configured, the number being limited only by the total laser heads available.

The timing of each CVL discharge must be precisely controlled (to ~2 ns) to effectively extract the stored energy in a MOPA configuration. For the VENUS lasers, a microprocessor-based servosystem monitors and adjusts the firing time of each head. The computer is also used for active stabilization of input power to each laser head, automatic warmup of the copper lasers, data acquisition, and system status display.

When completed, the VENUS laser system is expected to be a versatile, reliable laser amplification facility. Operated in conjunction with the SPP-II laboratory, it will provide a substantial increase in the tunable average power available for isotope separation experiments. The CVL pump source at the heart of the VENUS system is believed to be practical because of the advanced head design, the efficient MOPA operation, and the use of rapid replacement components. The VENUS system has been based almost entirely on existing technology to ensure dependable operation; yet at the same time the relevance of the technical approach to future

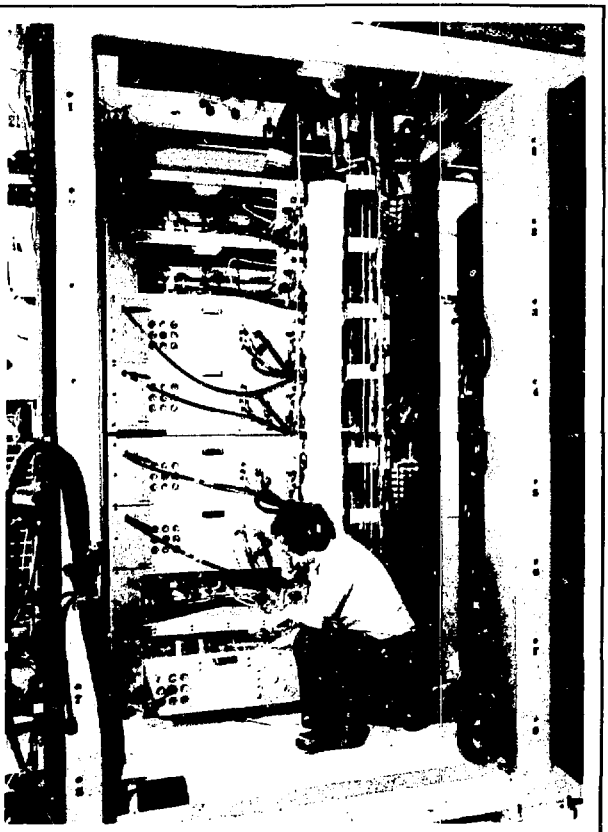

Fig. 10-71. Copper laser modules seen from rear (resonant charge drawer has been opened for routine inspection).

systems has been maximized, within schedule and cost constraints, to provide a sound foundation for the design of large AIS experiments.

References

135. *Laser Program Annual Report—1976*, Lawrence Livermore Laboratory, Livermore, Calif., UCRL-50021-76 (1977).

136. R. S. Hargrove, R. E. Grove, and T. Kan, *Copper Vapor Laser Unstable Resonator Oscillator and Oscillator-Amplifier Characteristics* (to be published).

Author

R. E. Grove

U.S. Government Printing Office: 1979/12 — 689-159/16